ORNL-3445
UC-80 – Reactor Technology

GAS-COOLED REACTOR PROGRAM

SEMIANNUAL PROGRESS REPORT

FOR PERIOD ENDING MARCH 31, 1963

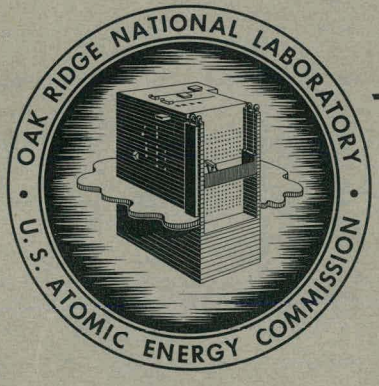

OAK RIDGE NATIONAL LABORATORY
operated by
UNION CARBIDE CORPORATION
for the
U.S. ATOMIC ENERGY COMMISSION

DISCLAIMER

Printed in USA. Price: $4.50 Available from the
Office of Technical Services
U. S. Department of Commerce
Washington 25, D. C.

ORNL-3445

Contract No. W-7405-eng-26

GAS-COOLED REACTOR PROGRAM SEMIANNUAL PROGRESS REPORT

For Period Ending March 31, 1963

W. D. Manly, Program Director

Date Issued
JUL 23 1963

OAK RIDGE NATIONAL LABORATORY
Oak Ridge, Tennessee
operated by
UNION CARBIDE CORPORATION
for the
U.S. ATOMIC ENERGY COMMISSION

THIS PAGE

WAS INTENTIONALLY

LEFT BLANK

CONTENTS

PART 2. ADVANCED REACTOR DESIGN AND DEVELOPMENT

SUMMARY

Part 1. Investigations in Support of the Experimental Gas-Cooled Reactor

1. Performance Analyses

Efforts to correlate data based on the Hanford exposure unit (Mwd/At) for the exposure and shrinkage or growth of graphite with an appropriate flux unit to make the dimensional changes independent of the reactor type resulted in a change of the conversion factor. A lower threshold was found to be more reasonable and the resulting exposures were 40% lower than calculated previously for the 20-year design lifetime of the EGCR. Based on a duty factor of 0.8, the 20-year exposure at the position of average power density is 34,300 Mwd/At. At the peak power position, the exposure is 74,000 Mwd/At in 20 years at a duty factor of 0.8. A lower duty factor would, of course, lower the exposure. The graphite temperature at the peak exposure position was estimated to be 680°F.

The predicted fission-product activity release from the EGCR fuel pellets was recalculated based on data from low-burnup irradiation tests of prototype EGCR fuel elements with thermocouples for central UO_2 measurements. The peak central UO_2 temperature was found to be only 2390°F, the apparent diffusion coefficient was much less than originally assumed, and the fission-product-release rate was a factor of 200 less than previously predicted. The predicted equilibrium total activity release based on the test data is 380 curies. The EGCR coolant system shielding is designed for 1000 curies of fission products with an effective gamma energy of 1 Mev per disintegration.

The temperature distribution to be expected in the graphite surveillance specimens in the EGCR was calculated. The specimens will be irradiated in a fuel channel with a local power level of 1.25 times the average and will then be removed to determine whether any physical changes have occurred. The temperature distribution data will permit correlation of the specimen properties with changes to be expected in the moderator blocks.

The number of fuel element failures that would result from the maximum credible accident was recalculated. A refined calculational procedure was used, and the analysis was extended in time to approximately 3 min. The fractional-life technique used resulted in an increase in the number of failures to 751. Since the cesium-rubidium isotope will not exist in the maximum quantities in all locations, as was assumed, it seems likely that the number of failures would actually be much less than 751.

The EGCR graphite oxidation code was used for the calculation of hydrogen generation rates in accidents involving an internal rupture of a steam generator. Both overpressurization and depressurization accidents were considered. The conditions necessary to prevent hydrogen flammability in the event of either accident were then established.

Experiments were conducted to determine the source-neutron multiplication of EGCR fuel assemblies under conditions which might exist in transportation and storage. It was found that 28 assemblies arranged to yield maximum nuclear reactivity could not be made critical when water-moderated and -reflected.

2. Component Development and Testing

Flow tests were continued with the fuel channel top and bottom dummey assembly. An adjustable orifice for the bottom dummy was developed that provides the flow control needed.

Venturis for EGCR instrumented channels were tested. It was found that minor variations from design dimensions had insignificant effects on the measurements.

Fabrication work on the instrumented fuel assemblies for the first core loading of the EGCR continued. Many dimensional measurements are being made and recorded for use in later comparisons.

The facility for testing the EGCR prototype control-rod drive was completed and placed in standby condition. Operating procedures were prepared.

Work continued on the fabrication of the main coolant blowers and the pressure-vessel cooling-system compressors. Delivery of the first blower is expected in September and the second in November 1963.

The three bottom in-pile loop tees and the tee for the emergency cooling loop were received and are being installed. Work is under way on the top tees and closures.

Stainless steel baked at 500°C in helium containing fission products was successfully decontaminated with hot oxalic acid solutions containing fluoride and hydrogen peroxide and with steam spray techniques. Carbon steel similarly contaminated was decontaminated by blasting with a steam jet into which an oxalate-citrate-peroxide solution was aspirated.

3. Materials Development

Several standard ORR poolside irradiation capsules containing EGCR production-quality UO_2 pellets were fabricated for testing in the ORR poolside facility, and a roughened surface fuel element designed to operate at an estimated power output of 65,000 Btu/hr·ft was fabricated for irradiation in ORR loop No. 1. The roughened-surface element has a shroud that is instrumented to measure the pressure drop across the element length.

Components for 20 instrumented EGCR fuel assemblies are being fabricated. The UO_2 bushings to be used were sanded lightly on their end faces to increase the land width. The bushings are slotted to receive cladding-inner-surface thermocouples. Special attention is being given to the production and inspection of the assemblies, and records are being kept for comparison after irradiation. An ultrasonic testing technique was developed that is capable of determining unbonded areas approximately 1/32 × 1/16 in. in the thermocouple-to-tube wall brazed joints.

The oxidation behavior of nitrided type 304 stainless steel under EGCR operating conditions was determined to be a direct function of the thickness of the oxide layer in experiments run to examine the properties of the nitrided surface layer being applied to the nozzles of the pneumatic temperature measurement system of the EGCR. The experiments showed that the surface properties of the nitrided case tended to change to those of an oxide film and to become increasingly susceptible to dimensional change. Nitriding might therefore have a detrimental effect on the stability and reliability of the nozzles.

A surveillance testing program for monitoring changes in EGCR moderator graphite was planned. Test specimens are to be placed in appropriate core positions. The surveillance program provides for the removal and testing of 21 sets of specimens over a 20-year period. The specimens removed will be tested to determine the room-temperature tensile properties, irradiation-induced creep, oxidation rates in air, thermal expansion, thermal conductivity, and stored energy.

Postirradiation examination of EGCR fuel bushings indicated a tendency toward chipping and cracking at the edges formed by the end faces and outer cylindrical surfaces. Severe out-of-pile quench tests indicated deterioration along the outer cylindrical edges which progressed with the number of quench cycles. This deterioration resulted in the formation of ridges and protrusions in the cladding and elongation of the cladding. The behavior of the bushings was attributed to axial compressive loading during the thermal quench. Removal of axial restraint drastically reduced the damage noted. Close examination of the EGCR bushings revealed that the end face dishing extended to the outer cylindrical surfaces, markedly reducing the expected 0.050-in. land. Light sanding of the end faces produced the desired lands and reduced the tendency of the bushings to chip. Modifications were therefore made to the vendor's dies to produce bushings with a uniform 0.025- to 0.050-in. land. Tests indicated that the modified bushings did not chip under high axial compressive loadings. It was decided to load the remaining EGCR elements alternately with modified and original fuel bushings. As of March 1, 1963, the Laboratory had received and accepted 756 EGCR fuel assemblies from the Westinghouse Electric Company, Atomic Fuel Department.

Arrangements were made for the dissimilar-metal welding required in the EGCR primary cooling system to be done by Laboratory personnel.

Radiographic and phase-sensitive eddy-current techniques were found to be effective in detecting voids, cracks, and laminations in extruded graphite cylinders. Pulse-reflection and through-transmission ultrasonic techniques were not usable.

4. Irradiation Testing of Components and Materials

Eight instrumented fuel elements have been operated in GCR-ORR loop No. 1 in the power range 21,000 to 42,000 Btu/hr·ft. Two of these elements are now known to have leaked during irradiation; however, the radioactivity in the piping was not great enough to be detected by radiation monitors sensitive to 1 mr/hr measured at pipe-wall contact. It appears therefore that leaking, ruptured, or ventilated elements may constitute a much smaller problem than supposed earlier.

Fuel elements with roughened surfaces have also been tested. Such elements are of interest for the second core of the EGCR. The roughened surface significantly improved the heat transfer.

Capsule E-8, which contains EGCR prototype-diameter fuel pellets and which was irradiated with a cladding surface temperature of 1600°C, was discharged from the ETR. This capsule will be compared with capsules E-6, E-1A, and E-4. Irradiation of ten capsules is continuing. Capsules 03-6, 05A-6, and 06-A were discharged from the ORR.

Examinations were made of capsules 02-5 and 07-5, which were irradiated about 5 months in the ORR poolside facility at an average cladding temperature of 1400°F. The capsules contained EGCR prototype diameter UO_2 pellets. There were several failure areas in the cladding and the pressure-transducer capillary tubing. The UO_2 pellets, which were taken from production runs, were severely fractured.

Two capsules fabricated by the French Commissariat a l'Energie Atomique were examined that had been irradiated in the ORR poolside facility. These thin-walled (0.012-in.-wall) type 347 stainless steel-clad capsules contained solid UO_2 pellets. The dimensions of the capsules did not change during irradiation. Columnar grains and lenticular voids were found in the central region of the fuel column in one capsule.

Metallographic examination of ETR-irradiated capsule E-4 showed results similar to those reported previously for capsule E-1A. Both these capsules fractured during irradiation. The two major causes of the failure appeared to be embrittlement of the cladding by nitride formation from nitrogen in the fuel and overheating of the UO_2 fuel during irradiation. There was no evidence of cladding failure in the preliminary

examination of capsule E-6, which was similar to capsules E-4 and E-1A. Fission-gas release was comparatively high, and there was appreciable cladding distortion.

Fission-gas-release studies were continued with thin-slab specimens of single-crystal UO_2. Reduction of the fission-gas-release rate with time was observed, and the influence of the production rate on the release rate was determined under steady-state conditions.

Work continued on the preparation of specimens for the EGCR pressure-vessel surveillance program. In accordance with ASTM Tentative Recommended Practices, specimens from a "reference plate" of ASTM A-212, grade B, steel will be included in the surveillance tests. Specimens from this plate are included in a number of irradiation tests being conducted at various sites. Further examinations were made of surveillance specimens from the SM-1 reactor. Metallographic examinations revealed the same fracture mode for irradiated and unirradiated specimens for the same fracture energy.

Part 2. Advanced Reactor Design and Development

5. Development of Fueled-Graphite Bodies

Comparison of crushing strength with in-pile performance has shown a direct relation between the number of cracked coated particles found after irradiation and the minimum crushing strength measured for samples from the same lot of particles. Monolayers of coated particles were crushed under loads of 2,500 to 20,000 lb and then acid leached to remove the exposed uranium. The uranium recovered was less than that contained in one particle until the load exceeded 10,000 lb.

Tests were conducted for determining fuel migration in coated fuel particles held at 1000 to 2000°C for periods up to 1000 hr. Measurements taken adjacent to the fueled particle and at points of farthest migration in the coating showed wide variations. Some diffusion was apparent at the fueled core-to-coating interfaces, but the fuel found at the surfaces of both treated particles and the control samples was attributed to superficial deposits from external sources.

Equipment for the deposition of pyrolytic-carbon coatings was installed, and a few runs were completed. Coating microstructures ranging from laminar to columnar and combinations of these were prepared. Additional equipment is being installed for operation at temperatures up to 2000°C.

An apparatus for measuring the thermal conductivity of powder in a controlled atmosphere was operated at temperatures up to 820°C. Low-temperature results agreed with literature values and were reproducible. Adaptations are being made to the equipment to improve high-temperature operation.

Two neutron-activation tests were made to obtain quantitative information on the release, transport, and deposition of I^{131}, Ba^{140}, Sr^{89}, and Te^{132} from uncoated UC_2 particles. The release rates for Xe^{133} in helium at 560 and 790°C were high in comparison with the rates for duplicate samples sintered in vacuum at the same temperature. The difference is attributed to partial oxidation of the UC_2 to UO_2. At 790°C, the release rate for I^{131} was comparable with that for the Xe^{133}, whereas only traces of I^{131} were found at 560°C. The distribution of activities after the 790°C test was plotted. Most of the Te^{132} was found at a point which was ~600°C during the test. The I^{131} was first noted at a point operating at ~440°C and displayed a maximum at 300°C. A theoretical explanation for the I^{131} deposition was proposed.

Attempts to "isostatically" form fueled-graphite spheres with polyvinyl chloride gel molds were abandoned. Light cold forming followed by isostatic compression was more successful. Experimental work is continuing on the fabrication of dense high-strength graphite bodies by molding and baking.

Evaluation studies of fueled graphite spheres from several vendors were continued. The specimens were visually examined, and the bulk densities and net carbon densities were determined. Radiographic techniques indicated deviations in the thicknesses of unfueled graphite shells. The contained coated particles were examined by alpha counting, acid electrolysis, and neutron activation. The uranium contamination on the surfaces of the spheres was found to vary markedly within a given lot. The

internal uranium contamination resulting from defective coated particles varied from 0.005 to 16.5% of the contained uranium. High Xe^{133} rates were found to be associated with high values of internally exposed uranium. Chlorine gas treatment of the spheres at 800 to 1000°C was found to be partially effective in removing exposed uranium, and additional experiments are in progress to improve the effectiveness of this treatment. Metallographic examinations were performed to determine distributions of coated particles, quality of bond between matrix and particles, and the structure of the graphite matrix.

6. Investigations of Fueled-Graphite Systems

The incidence of failures of coatings on uranium carbide fuel particles in experiments MTR-48-6 and ORR-08-5 were 10 and 16%, respectively, as determined by metallographic examination. Appreciable fractions of the uranium-thorium fuel in the MTR-48-6 specimen had migrated from the fuel specimen to the surrounding graphite sleeve.

Uranium carbide fuel particles of the same size but fabricated by two manufacturers were irradiated in capsules 01-5 and 08A-5. Postirradiation examination showed the fuel pellets from the two capsules to be quite different. All pellets in capsule 01-5 were fractured, and none of those in capsule 08A-5 were fractured. There were small dimensional increases in both cases.

Uranium carbide fuel particles with columnar, duplex, and laminar coatings were examined after irradiation in the facility for studying instantaneous fission-gas release. These particles were not incorporated into a graphite matrix. The irradiation effects on the columnar and laminar coatings were comparable in that 2 to 5% of the coatings cracked at burnups of up to 15 at. % uranium. The duplex coating, on the other hand, exhibited superior performance, even up to 30 at. % uranium burnup. This was especially noticeable during irradiation, because the fission-gas-release rate from the duplex coating was much lower than that from the other coatings. These findings indicate that the percentage of broken particles in a capsule can be accurately predicted from the fission-gas-release rates during irradiation.

Group VI irradiation experiments in the ORR poolside facility were continued. Fourteen specimens are currently being irradiated. Modifications were made to the facility that included changing the capsule mounting rigs to accommodate the larger capsules housing the graphite-matrix fuel specimens and relocating the capsule weight-loading points to relieve the forces on the capsule-positioning mechanisms.

Test assemblies are being fabricated for irradiation of fueled spheres in GCR-ORR loop No. 2. The experiment is designed for ascertaining the effects of nuclear heating on fueled-graphite spheres exposed in a configuration in which the heat transfer is nonuniform and in which four spheres are held in straight-line contact. A secondary purpose is to study the deposition on the loop surfaces of the fission products that may be released from the spheres.

Fission-product transport and deposition in coolant circuits are also being studied out of pile in a forced-circulation loop at BMI. In this loop, helium heated to 1200°F is passed over a preirradiated uranium carbide fuel specimen at 1800°F and then over simulated reactor cooling system components. Following completion of a test run, the loop is dismantled and the fission-product contamination on the type 347 stainless steel loop tubing is determined. The initial test was completed and the data were correlated with analytical relations. The agreement was considered to be reasonably good. Samples of three portions of the test-loop piping were taken for decontamination studies, and it was found that oxalate-peroxide solutions were satisfactory for this purpose. Other reagents and a steam spray were also used successfully.

Two methods for determining the form of the radioactivity in the gas circulating in the BMI loop were investigated. In the first method, diffusion coefficients for fine particles and for radioactive vapors, such as iodine, were determined by measuring the distribution of radioactivity of the walls of a channel previously exposed to gas carrying radioactive materials and flowing under laminar conditions. This method was applied to the problem of removing millimicron-diameter radioactive particles from air streams. In tests using I^{131}-labeled Al_2O_3 particles with a nominal diameter of 0.004 μ, high-efficiency, low-pressure-drop particulate filters exhibited an efficiency ranging from less than 10 up to about 75%. With

activated-carbon beds 0.75 in. deep and 6 × 16 mesh, iodine-vapor removal was essentially complete, but the removal efficiency for 0.003- to 0.006-μ particles was observed to be only 75 to 90%, the higher efficiency being associated with the finer particles. Similar tests were carried out using fog condensation and foam encapsulation to remove millimicron-sized particles from air. In these tests removal efficiencies of 85 to 99% were observed.

In the second method for measurement of the characteristics of radioactive aerosols, fibrous filters were used to measure aerosols in terms of their response to the processes of inertial impaction, interception, and diffusion under carefully controlled conditions. A filter was developed that has a uniform fiber diameter to permit theoretical analysis and a layered structure to facilitate separation of the fiber bed into discrete layers for radioassay after exposure to the aerosol. Preliminary results with a radioactive aerosol of 0.004- to 0.03-μ particles containing Zn^{65} indicate that the techniques used are satisfactory and should provide useful information on aerosol character and on filtration mechanisms.

Specimens of type 347 stainless steel, Croloy, AGOT graphite, and silver were exposed to fission products in the purge-gas stream from experimental assembly MTR-48-6. Upon removal from the reactor, the specimens were leached in nitric acid and the solute was analyzed for the common fission products. Silver retained the most fission products, and type 347 stainless steel retained the least.

Three experiments were conducted in the ORR to study the release of fission products that would occur in a reactor accident in which air became admixed with the helium coolant. In these in-pile experiments, pyrolytic-carbon-coated uranium carbide particles in a graphite matrix were exposed to air during high-temperature operation in the ORR and partially burned. Approximately half the specimen was consumed in the 15-min period of burning, during which the temperature reached 1400°C. Radiochemical analysis showed that if combustion of graphite-uranium fuel occurred in a reactor accident under the conditions of these experiments, all but a small fraction of the strontium, zirconium, barium, cerium, and uranium would remain in the vicinity of the fuel, and significant amounts

of iodine, tellurium, and cesium would be released. The release of ruthenium was variable. The association of a disproportionate amount of the uranium with the unburned fuel indicated that the uranium-lean part of the specimen burned preferentially.

Coated uranium carbide-fueled particles from lot 3M-117 were exposed to steam-helium mixtures having a partial pressure of steam of 355 or 635 mm Hg at temperatures from 800 to 1100°C. The rate of reaction of the pyrolytic-carbon coating with steam and the integrity of the coating after the steam treatment were determined. Good protection of the core by the coating was observed at 800°C for an exposure of 4 hr to a partial pressure of steam of 355 mm Hg. Drastic attack and high incidence of failure of the coatings was found at 1100°C for a 1-hr exposure to a partial pressure of steam of 635 mm Hg. Less extensive damage was observed at 900 and 1000°C.

The rate of diffusion of thorium in pyrolytic carbon was studied at 1900°C by a new technique of sample preparation. The samples were square coupons of pyrolytic carbon with an infinitely thin layer of thorium placed by bombardment with Th^{++} ions in an electromagnetic separator. At 1900°C an average value of the diffusion coefficient of 5.47×10^{-11} cm^2/sec was obtained for diffusion along the "c" direction.

Studies of the rates of migration of uranium from uranium carbide through porous graphite were initiated to provide information for the design of reactors employing fuel elements comprised of uncoated and coated fueled-graphite bodies. Some experimental results were obtained from couples of a furfural-impregnated graphite and an uncoated graphite matrix containing 25 wt % uranium carbide. The results indicated that the penetration of uranium was much faster than that expected for solid-state migration. In addition the results suggest that there is an additional source of uranium within the couple beyond the interface. Such a source could presumably originate from pore and surface effects coupled with adsorption-desorption phenomena in addition to solid-state migration. It thus appears that the mechanism of uranium mass transfer is complex and associated with the graphite structure.

In decontamination studies, treatment with 0.4 to 0.5 M oxalic acid or oxalate salt solutions containing 0.1 M fluoride and various amounts of hydrogen peroxide was found to be satisfactory for removing I^{131} and Te^{132} deposited at 800°C and below from helium onto type 304 stainless steel pipe. The pipe had been contaminated from heated, irradiated UC_2 and UO_2. Resistance to decontamination was highest in the high-temperature zone where some metal oxidation had occurred because of slight inleakage of air. Decontamination was much easier where the metal was unoxidized and the temperature had been lower.

7. Clad Fuel Development

Irradiated fuel rods containing vibratory compacted ThO_2-UO_2 were examined. The fuel was clad with type 304 stainless steel and tested in the ORR poolside facility at 1000 to 1300°F. Although there was some dimensional distortion of the element, no distinct fuel shifting was indicated.

Thermal and pressure cycling tests of simulated fuel elements showed that interactions of fuel and cladding could result in strains sufficient to rupture the cladding. The problem of circumferential ratchetting could be the limiting factor in the use of thin-walled cladding.

In-pile stress-rupture tests of British stainless steel tubing indicated a slight loss in strength at 650°C and no effect at 750°C. This tubing was fabricated from 25% Cr-20% Ni material stabilized with 0.6% Nb. The average strains at failure were 30 to 50% lower in-pile than out of pile. Failures of several specimens at or near the end welds indicated possible irradiation-induced embrittlement.

Air-melted type 347 stainless steel and air- and vacuum-melted type 304 stainless steel specimens are being irradiated at temperatures from 150 to 815°C to total neutron doses of 10^{19} to 10^{21} neutrons/cm^2. After irradiation, tensile tests will be performed under various conditions.

The wetting behavior of several liquid metals and alloys on beryllium in argon and in vacuum were determined. These tests are being made for the selection of a brazing alloy for joining beryllium.

Metallographic examinations of welded joints of ferritic steel to austenitic stainless steel indicated that the carburized zone of the

austenitic material demonstrated carbon migration. The addition of a carbon-forming element to the ferritic material did not change the over-all carbon diffusion from ferrite to austenite.

The thermal conductivity of UO_2 was measured at temperatures up to approximately 1400°C after modifications were made to the system to extend the operating temperature. The data indicate the existence of a heat-transfer mechanism above 1200°K that is more powerful than internal radiation.

8. Investigations of Moderator Materials

Tensile and compressive tests were conducted on various grades and extruded sizes of graphite. There was much scatter of the data for large extrusion sizes. Some resistance to crack propagation was noted.

An in-pile creep experiment on graphite at approximately 450°F and a neutron flux (>0.2 Mev) of about 1×10^{17} neutrons/cm^2·hr indicated that a successful method for measuring in-pile creep has been developed and that the creep of graphite both in pile and out of pile is a linear function of stress. Once it is established that a linear creep rate will or will not be attained, the stress levels will be raised to expedite conclusion of the test.

Tests on the compatibility of type 304 stainless steel and graphite in vacuum at 1000 to 1300°F indicated interdependence of contact pressure and extent of carburization. Tests were run using a high initial test load followed by a lower load for the duration of the test to illustrate that the contact pressure causes permanent deformation that results in a greater effective contact area. The data obtained did not confirm the hypothesis.

The rates of reaction of Speer Moderator-2 graphite with helium-CO_2 mixtures having CO_2 concentrations of 100, 300, 550, 1100, and 1800 ppm by volume were measured at 975°C. The apparent order of the reaction with respect to partial pressure of CO_2 is less than unity over this concentration range, but the precise fractional order has not been established. The Burrell K-7 gas chromatograph was extensively modified prior to these measurements in a partially successful attempt to increase the stability of its output. The blank arising from contaminants in the

helium stream was reduced by elimination of inleakage in the gas-handling system.

The "dusty-gas" model for gas transport through porous media was theoretically extended to include the flow behavior of pure gases under the influence of temperature gradients, and exploratory experiments were conducted for studying the phenomenon. Investigations were completed on the flow characteristics of stratified graphite, and no deviations attributable to the inhomogeneity of the graphite were observed under the conditions employed.

Studies are being made of the stresses and distortions associated with irradiation-induced changes in graphite. A generalized study applicable to all reactors cannot be made because of differences in fast-neutron damage, but the results for specific cases will provide a guide for evaluating the geometry effects for other applications.

The tensile strength of graphite and the fracture elongations are low when compared with the stresses or total strains to be sustained by graphite bodies used in nuclear reactors, and calculations indicate that fracture of these bodies will occur during service. Experimental and analytical studies are therefore under way for establishing adequate design criteria for graphite components of reactor cores.

Two additional tests were completed in the investigation of the reactions of hydrogen, graphite, and metals at high temperatures in autoclaves. Type AGOT graphite, specimens of type 304L and 310 stainless steel, Inconel, and a control specimen of 19-9DL steel were used in both tests, which were conducted at 1500°F for 1000 hr with a hydrogen pressure of 850 psig. Analyses of the hydrogen during the tests showed a steady increase in CH_4 concentration.

Studies of the behavior of beryllium oxide compacts under fast-neutron irradiation were continued. Most of the changes in physical properties caused by doses in the range 1.2 to 3.65×10^{21} neutrons/cm^2 at temperatures from 580 to 1100°C can be attributed to grain-boundary separation. There is a correlation of the increase in volume of irradiated samples with the degree of grain-boundary separation estimated from visual inspection of photomicrographs of as-polished specimens. Hot-pressed samples were observed to have undergone more extensive grain-boundary

separation and greater volume increases than cold-pressed samples irradiated under the same conditions. Expansion of the lattice parameters is much less at temperatures above 900°C. The total volume increase of irradiated samples is proportional to the lattice parameter expansion, even though the increase in volume calculated from the lattice parameter increases is only 4 to 8% of the total increase in volume. Gas analyses indicated a loss of about 50% of the helium that was generated in BeO exposed to high neutron doses ($>3 \times 10^{21}$ neutrons/cm^2).

In BeO compacts exposed to low neutron dose at a very low temperature (~100°C), grain-boundary separation is primarily caused by anisotropic expansion of BeO crystals. Presently available data are not sufficient to determine whether this mechanism dominates at high temperatures and high doses or whether helium pressure causes the grain-boundary separation under these conditions. Lattice-defect agglomeration and lattice parameter expansion both contribute to a preferential growth in the direction of the c-axis. Measurements of the lattice parameters and densities of single-crystal specimens included in statistically designed experiments now in progress will permit the calculation of the volume increases caused by lattice parameter expansion and lattice defect agglomeration. From these values and the measured volume increases of corresponding sintered compacts, it may be possible to obtain a quantitative estimate of the volume increases resulting from grain-boundary separation.

9. Studies of Advanced Systems

The effects of feedwater temperature on performance of the GCR-3 power cycle were investigated in a parametric study in which the feedwater temperature was varied from 93.6 to 533°F. There was a broad, flat maximum in the efficiency and heat-rate curves between feedwater temperatures of 350 and 530°F. The change in efficiency in this range was only 0.2% of 39%. This is a much flatter efficiency peak than is common for conventional power plants. The economics also differ from those for a conventional plant, and they too must be evaluated before the feedwater temperature is established.

A parametric study of a combined gas-turbine and steam-generator power cycle was conducted that was based on the GCR-3 and was designated GCR-4. Heat balances were developed for feedwater temperatures of 96.1, 269.4, and 450.3°F, corresponding to 0, 3, and 6 stages of heating. The corresponding gas temperatures at the compressor suction were 375, 470, and 550°F. Ten gas turbine and compressor arrangements were studied as topping cycles for the three steam generators. Based on these studies, a system with a suction temperature of 470°F, a feedwater temperature of 270°F, a reactor exit temperature of approximately 1500°F, and a plant designed for a total electrical output of 1000 Mw was selected for further study.

Various coolants for gas-cooled reactors were compared on the basis of the GCR-3 design. The coolants H_2, SiH_4, CF_4, SiF_4, SF_6, and C_2F_6 were all found to be superior to helium, with SiH_4, SF_6, and C_2F_6 being best. It was also found that SO_2 would be poor as a coolant under these conditions. The effect of adding neon to helium was also evaluated. The saving required in the cost of the coolant to offset the increase in pumping power was determined.

A study was made of the heat transfer and fluid flow parameters for the core of a pebble-bed reactor designed for operation in the thermal power range 2500 to 100,000 Mw. A radial-flow core was used for this study, and it was assumed that a prestressed concrete pressure vessel could be built to contain helium at 1000 psia.

Fuel-cycle costs and conversion ratios were also calculated for large pebble-bed reactors. The study showed that the optimum reactor from an economic standpoint would have a conversion ratio somewhat greater than 90%. A further study was made to determine the conditions that would yield a breeder reactor. It was found that a breeding gain would be possible with little cost penalty for unit processing costs of the order of $10 to $20 per kilogram of heavy metal.

A study of fuel-management procedures for the German pebble-bed reactor is in progress. An attempt is being made to achieve a high burnup rate with fuel representative of that which would be used in a large power reactor of the pebble-bed type. The fuel must meet the requirement

that there would be no reactivity rise in the event of an accident in which steam entered the core.

An experimental program is in progress for examining the stress distributions around both radially and nonradially attached nozzles. The information being obtained will be used in the design of nozzle attachments to pressure vessels and in correlating theoretical methods for evaluating designs for nozzle attachment.

A study of neutron captures in second- and higher-generation fission-product poisons was conducted to establish the magnitude of the contribution of secondary poisons to the total neutron capture rate under conditions of interest to the gas-cooled reactor program. The individual contribution of each nuclide in the group ranging from Nd^{145} to Eu^{155} was calculated and recorded. Data that are sufficient to show the significance of the secondary captures and to illustrate their dependence on key reactor parameters were obtained.

10. Experimental Investigations of Heat Transfer and Fluid Flow

The constants in the equation correlating the heat transfer in a seven-rod cluster geometry with the flow and the axial position were redetermined using all available data. The resulting equation was

$$N_{Nu,x} = 0.041 \ (N_{Re,x})^{0.77} \ (x/d_e)^{-0.15} ,$$

for Reynolds moduli $N_{Re,x}$ in the range of 38,000 to 63,000 and axial positions x/d_e (as measured from the nearest upstream obstruction) between 5 and 25.

The pressure-loss coefficients associated with rough surfaces were determined in two long-rod clusters of somewhat different geometries. In the first of these, the mid-cluster spacer was omitted and the cluster lengthened to provide an uninterrupted flow path of 85 diameters. Only the reference smooth-tube experiments were completed. The results in the Reynolds modulus range of 20,000 to 80,000 suggest a sensitive dependence on the inlet geometry. In the second arrangement the cluster was approximately 60 diameters in length and was subdivided into five sections by the mid-cluster spacers. Results obtained for Reynolds moduli between 2000 and 200,000 with bare rods and rods spirally wrapped with

0.006-in. wire on a 0.036-in. pitch showed the pressure-loss coefficient for the rough surface to be consistently higher than that for the smooth surface. The difference between the two was of the order of a factor of 2 for $N_{Re} > 10^5$.

The assembly of the apparatus and the installation and check-out of instrumentation for the study of heat transfer from rough surfaces was continued. Experimental difficulties led to the termination of studies of the transfer characteristics of rough surfaces by the naphthalene mass-transfer technique.

An experimental facility was placed in operation for studying the friction factor and heat transfer coefficient of air in an annulus with a roughened inner surface and a smooth outer surface. The friction factor goes through a maximum as a function of roughness pitch at a constant Reynolds number.

The problem of "hot spots" in a gas-cooled bed of fueled spheres was studied. Factors relating to gas flow distribution, heat transfer, bed movement, physics, manufacturing tolerances, and operation were defined and estimated for a pebble-bed reactor. These factors were then combined to give a maximum temperature allowance on the mean temperature rise through the reactor; the calculated temperature increment was 500 to 650°F. When a term was introduced to allow for the probability of occurrence of each specific factor and for the probability of adverse simultaneous occurrence of factors, the calculated temperature increment was reduced to 250 to 325°F.

The study of the static and dynamic characteristics of a random bed of 1 1/2-in.-diam graphite spheres within a full-scale model of the pebble-bed core was continued. Measurements were made of the void fraction, angle of sphere repose, gas velocity profile, pressure distribution, and levitation velocity for a number of differently formed beds. Results on the void fraction for two beds created by injecting spheres singly at the core top fell within the scatter band of previous measurements (0.401 ± 2%). In contrast, beds formed by levitating a previous bed showed an approximately 5% expansion (void fraction = 0.419). Data on the mean angle of repose of the spheres on the upper face of the bed were in good agreement with earlier results obtained before inclusion of the core model in the

mockup facility. Experiments in which the spheres were injected against a counterflow of air showed less scatter in the angle-of-repose data.

Friction factors were calculated from data obtained for the pressure distribution in the various beds. An over-all factor, specific to the geometry studied and based on the total pressure difference across the bed, was found to be less than a more general factor characterizing fully developed flow in a bed, as calculated from the constant-slope portion of the pressure-gradient curve. This resulted from the lower pressure gradients in the inlet region of the core. Both the over-all and the established-flow factors showed a -0.2 dependence on the Reynolds modulus over the full range of the experiments ($25{,}000 < N_{Re,p} < 100{,}000$). Further, the friction factor did not appear to depend simply on the void fraction; the existence of flow channeling in some of the beds was indicated. The data are in good agreement with measurements obtained with smooth plastic spheres in a smaller scale model.

Bed levitation phenomena were studied by observing the behavior of the spheres on the top face of the bed, while the air flow was slowly increased and decreased at a velocity near that required to levitate the full bed. Levitation was characterized in terms of the ratio of the pressure gradient across the bed to the bulk bed density ($dp/\rho dz$) rather than in terms of the gas velocity. Three distinct phenomena were observed as full levitation was approached: (1) rocking motion of a few spheres at $dp/\rho dz = 0.6$, (2) spinning of spheres at $dp/\rho dz = 0.8$, and (3) physical lifting of some spheres at $dp/\rho dz > 0.9$. If the bed had been previously levitated, subsequent levitation was achieved at pressure gradients equal to only 60% of the bulk density. Other indications of approaching levitation were observed at correspondingly lower values of the pressure gradient.

The gas velocity distribution at the exit face of the bed was determined by traverse with a hot-wire probe. It was observed that, at any given radial distance from the core wall, the local velocity varied significantly with angular position. This was believed to reflect local variations in the void fraction in the uppermost layers of the bed. Mean values, averaged over the full 360-deg sector at any radial distance,

showed the characteristic peaking in the velocity near the core wall resulting from the higher void fraction in this region. Secondary maxima were associated with channeling effects and with the shape of the bed top and bottom faces. No significant effect of the bed average velocity on the profile shape was detected. Prior levitation of the bed caused a shift toward the core center of the velocity maximum occurring near the wall and a flattening of the profile over the central region.

Development of an apparatus and technique for studying mass transfer from benzoic acid spheres within and in the wake of closely packed sphere clusters was continued. Modification of the instrumentation used in determining local mass-transfer factors from spheres in ordered arrays was completed. A solid replication of a random bed, formed by filling the voids with a polymerizable resin, was constructed. This replication was then sectioned into 3/4-in.-thick disks; photometric density analysis of x-ray photographs of these disks to establish the radial, axial, and circumferential void-fraction distribution was initiated.

11. Facilities and Equipment

Installation of the in-pile section and the first experimental assembly was completed, and operation of GCR-ORR loop No. 2 was initiated. The experimental assembly is a low-power unit for determining the neutron flux by the argon-activation technique.

Work continued on the development of gas-bearing compressors. The regenerative grease-lubricated compressor in GCR-ORR loop No. 1 continued to operate satisfactorily.

Development work was completed on the Greenbrier process chromatograph, which was adapted for analysis of radioactive helium samples from GCR-ORR loop No. 2. The instrument is now in service. In measurements at the 100-ppm concentration level, the reproducibility is better than 5 ppm for all components except hydrogen and better than 40 ppm for hydrogen.

Thermocouple materials are being tested out-of-pile under environmental conditions approaching those conceived for a pebble-bed reactor. In these tests, 25 types of wires, which are isolated from each other,

are being exposed to graphite and helium containing 500 ppm H_2 and 500 ppm CO at two temperatures, 1400 and 1800°F. Of the nine wires checked thus far after a 36-day exposure, only Chromel-A and type 347 stainless steel showed significant error at the lower temperature. At 1800°F, however, all wires were in error except one with the composition 50% Mo—50% Re.

Metallographic samples were taken from sheathed Chromel-P-vs Alumel couples exposed to various atmospheres (CO, He, H_2). The changes in microstructure revealed by photomicrographs corresponded with the temperature profile error curves. In each case emf peaks in the error curve occurred at the same geometrical location as the maximum oxidation on the wires.

The spiral graphite furnace used to test tungsten-rhenium couples in helium-CO atmospheres was improved by doubling the length of the heating section of the helix and thus producing a flat temperature zone for the calibration of thermocouples.

PART 1. INVESTIGATIONS IN SUPPORT OF THE EXPERIMENTAL GAS-COOLED REACTOR

THIS PAGE

WAS INTENTIONALLY

LEFT BLANK

1. PERFORMANCE ANALYSES

Lifetime Graphite Exposure in EGCR

A. M. Perry C. A. Preskitt

Several studies were performed during the past three years to provide information on the fast-neutron exposure accumulated by the EGCR graphite during the 20-year design lifetime of the plant. Both multigroup one-dimensional and four-group two-dimensional calculations were performed to study various aspects of the exposure, for example, the detailed neutron energy spectrum and the detailed spatial distribution of the neutrons. Since the early experimental information on the correlation between exposure and shrinkage or growth was based on the Hanford exposure unit, megawatt days per adjacent ton (Mwd/At), the need to use this information resulted in the development of equivalent neutron flux units. When correlated against the unit Mwd/At, the dimensional change depends on the reactor in which the irradiation takes place, whereas, presumably, if correlated against the appropriate flux unit, the dimensional change is independent of the reactor type. Unavoidably the efforts to establish an appropriate flux unit made obsolete the normalization of some of the earliest work. In particular, the distribution shown in ref. 1 was based on the conversion

$$1 \times 10^{20} \text{ neutrons/cm}^2 \ (E > 1 \text{ Mev}) = 2300 \text{ Mwd/At},$$

which was estimated at that time.[2] Subsequent investigations indicated that a lower threshold was more reasonable, and this, together with more detailed calculations of the neutron-energy spectrum, indicated that the exposures shown in ref. 1 are high by about 40%.

The conversion factor used in producing the exposure variations found in ref. 3 was

$$1.23 \times 10^{17} \text{ neutrons/cm}^2 \ (E > 0.18 \text{ Mev}) = 1 \text{ Mwd/At},$$

which is quite close to the current estimates, which lie in the range 1.25×10^{17} to 1.30×10^{17} neutrons/cm^2 ($E > 0.18$). With these more recent values for the flux-exposure conversion, the estimated exposure at

the position of average power density in the EGCR is 42,900 Mwd/At for 20 years of continuous full-power operation. If the conventional duty factor of 0.8 is assumed, this is reduced to 34,300 Mwd/At at the average position. Averaged over a period of time, the radial peaking factor should be about 1.2 and the axial factor about 1.8 so that the peak exposure position should accumulate an exposure of near 74,000 Mwd/At in 20 years at a duty factor of 0.8. In terms of flux units, this exposure corresponds to 9.4×10^{21} neutrons/cm^2 ($E > 0.18$ Mev). If lower duty factors result, the exposures will, of course, be reduced proportionally.

An assessment was made of the correlation between exposure and graphite temperature for maximum-exposure core columns in the EGCR. The location of the column was not specified; it was assumed only that the channel power would average about 1.2 times the mean channel power. The temperature distribution given in ref. 4 was used to represent the axial temperature distribution in the column. The result is given in Fig. 1.1 for 20 years of continuous full-power operation. The maximum exposures may be seen to occur at positions in the graphite where the temperature is in the interval between 580 and 800°F. At the peak exposure position the graphite temperature will be about 680°F.

EGCR Fission-Gas-Release Activity

G. Samuels

Calculations were completed to update the predicted fission-product activity release from the EGCR fuel pellets. The original estimates were based on an apparent diffusion coefficient of 10^{-10} sec^{-1} at 1400°C and

---

[1]Oak Ridge National Laboratory, "GCRP Quar. Prog. Rep. Dec. 31, 1959," USAEC Report ORNL-2888, p. 19.

[2]D. R. de Halas, Hanford Atomic Products Operation, personal communication to C. A. Preskitt, Oak Ridge National Laboratory, October 1959.

[3]L. E. Hulbert and R. F. Redmond, "Numerical Results for EGCR Moderator-Element Stress Problems," p. 67, USAEC Report BMI-1526, Battelle Memorial Institute, July 3, 1961.

[4]S. E. Moore and F. J. Witt, Temperature Distributions and Thermal Stresses in an EGCR Graphite Column, p. 38, "GCRP Semiann. Prog. Rep. Sept. 30, 1962," USAEC Report ORNL-3372, Oak Ridge National Laboratory.

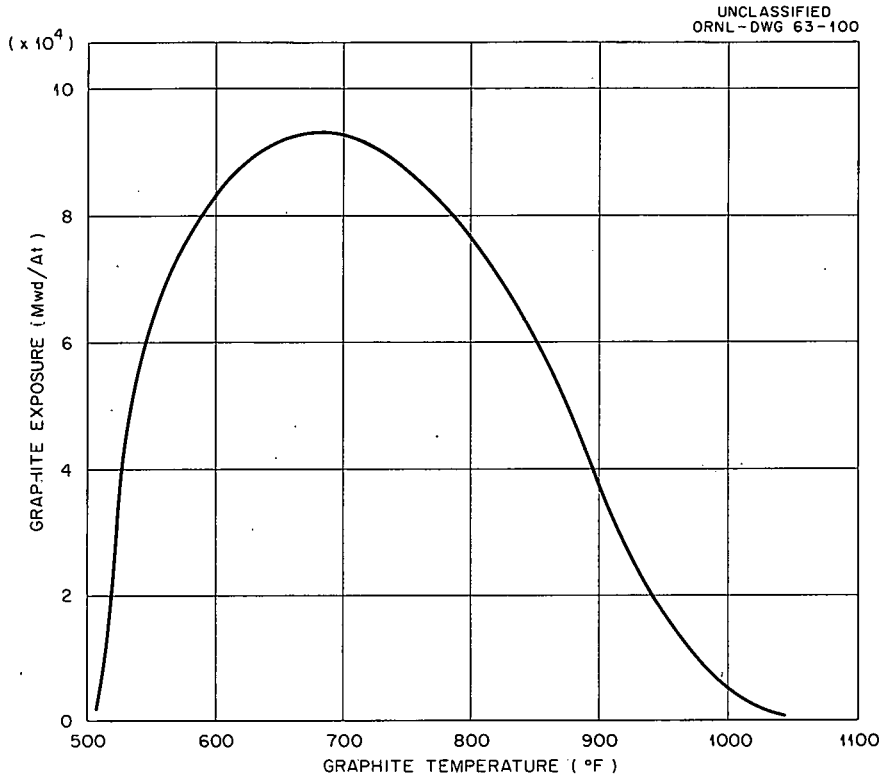

Fig. 1.1. Correlation Between Exposure and Temperature for the Maximum-Exposure Column After 20 Years of Continuous Full-Power Operation of the EGCR.

an activation energy of 70 kcal/g·mole. The temperature in the UO_2 was based on the thermal-conductivity measurements of Hedge and Fieldhouse[5] and contact resistance between the UO_2 and the cladding equivalent to a 0.001-in. gas gap.

The results of low-burnup irradiation tests on prototype EGCR fuel elements with thermocouples for central UO_2 temperature measurements have consistently given an over-all equivalent thermal conductivity from the center of the UO_2 to the cladding of about 1.7 Btu/hr·ft·°F. In these tests the internal gas in the capsule was essentially all helium. Applying the thermal conductivity value obtained from these tests to the maximum-power element in the EGCR, the peak central UO_2 temperature was found to be only 2390°F.

---

[5]J. C. Hedge and J. B. Fieldhouse, Measurement of Thermal Conductivity of Uranium Oxide, Armour Research Foundation Report G022D3 (1956).

The first results of measurements of the apparent diffusion coefficient of EGCR fuel pellets showed the coefficient to be much less than originally assumed. The results for three samples of one batch of UO_2 were 5.95×10^{-14}, 2.75×10^{-14}, and 2.78×10^{-14} sec^{-1} at 1400°C. With such small diffusion coefficients, the amount of fission products leaving the UO_2 will be less than 1% of that used in the original EGCR calculations, and the dilution of the helium in the capsule will be negligible. Thus, the temperature in the UO_2 fuel should not change any appreciable amount during operation, and the central temperatures to be expected should be those measured in the prototype in-pile tests.

In determining the quantity of fission products diffusing from the UO_2, the fuel volume of the maximum-power element in the core was divided into 40 equal parts, and the temperatures were determined for each part. The element was divided into eight axial and five radial sections, as shown in Fig. 1.2. The temperature difference between the outer surface of the UO_2 and the cladding was determined by assuming the contact resistance to be that equivalent to a 0.001-in. gap of helium. The temperature difference between the inner UO_2 surface and the cladding was determined by using an equivalent thermal conductivity of 1.7 Btu/hr·ft·°F. In calculating the intermediate radial temperatures, the UO_2 thermal conductivity and the heat generation rate in the UO_2 were assumed to be uniform.

The equation for the diffusion of fission products from the fuel, assuming equilibrium conditions, is

$$F = 3 \left(\frac{D'}{\lambda}\right)^{1/2} \left\{\left[\coth \left(\frac{\lambda}{D'}\right)^{1/2}\right] - \left(\frac{D'}{\lambda}\right)^{1/2}\right\} ,$$

where F is the fraction of the equilibrium quantity of a nuclide outside the fuel, D' is the apparent diffusion coefficient, sec^{-1}, and λ is the nuclide decay constant, sec^{-1}. For the EGCR conditions, the value of D' will be much smaller than the value of λ for the nuclides of interest, and the equation reduces to

$$F = 3 \left(\frac{D'}{\lambda}\right)^{1/2} .$$

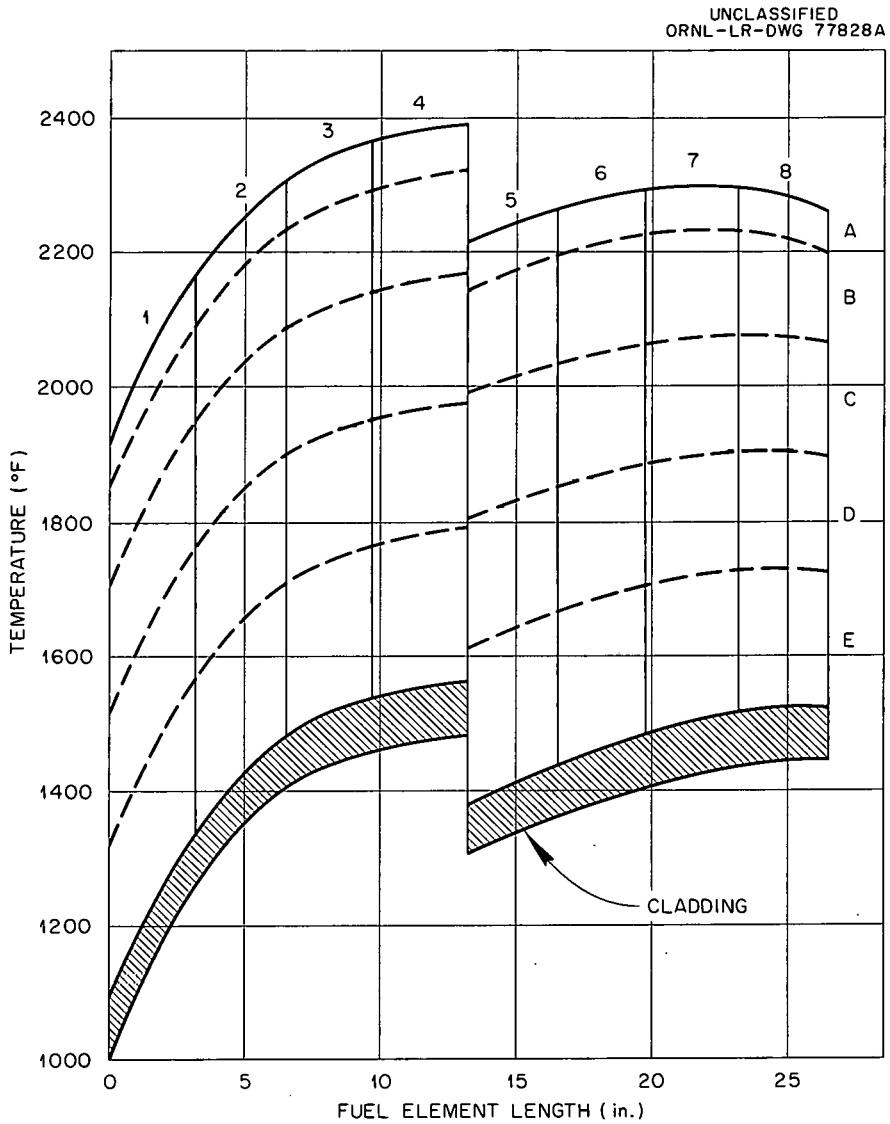

Fig. 1.2. Temperatures of UO_2 in Maximum-Power EGCR Fuel Element.

Thus the activity released from the fuel is proportional to the $\sqrt{D'}$. Assuming a D' of 5.95×10^{-4} sec^{-1} at 1400°C and an activation energy of 70 kcal/g·mole, the average value of $\sqrt{D'}$ for the maximum-power fuel element is 4.4×10^{-8}. Using I^{133} as an example, the activity release was found to be 0.049 curies per element. The corresponding activity previously reported[6] for the EGCR was 10 curies. Thus the use of the latest

[6] "Experimental Gas-Cooled Reactor Final Hazards Summary Report," USAEC Report ORO-586, Vol. 1, pp. 8.3–8.7, Oct. 10, 1962.

data reduces the release rate by a factor of about 200. Reducing all the nuclide release rates by a factor of 200 gives the following results for the maximum-power element, assembly, and channel:

	Activity Release (curies)
Fuel element	0.50
Fuel assembly	3.50
Fuel channel	4.30

In order to estimate the total activity release in the reactor, the core was divided into a number of approximately equal power channels, as shown in Table 1.1, which also gives the number of channels in each power

Table 1.1. Radial Distribution of Power and Temperature in EGCR Core

Channel Power Ratio	Number of Channels	Maximum Fuel Temperature (°F)	Number of Equivalent Maximum-Power Channels
1.30–1.35	36	2390	36.00
1.25–1.30	16	2350	13.13
1.20–1.25	8	2310	5.31
1.15–1.20	20	2270	10.71
1.10–1.15	16	2230	6.89
1.05–1.10	8	2190	2.74
1.00–1.05	8	2150	2.14
0.95–1.00	16	2110	3.34
0.90–0.95	12	2070	1.97
0.85–0.90	12	2030	1.53
0.80–0.85	16	1990	1.56
0.75–0.80	24	1950	1.78
0.70–0.75	16	1905	0.89
0.65–0.70	8	1860	0.32
0.60–0.65	8	1815	0.23
0.55–0.60	8	1770	0.16
	232		88.70

range, the maximum UO_2 temperature, and the number of equivalent peak-power channels in each group. The number of equivalent peak-power channels was determined from

$$N = \frac{D_1}{D_2} N_c \frac{P_R}{1.35},$$

where

D_1 = diffusion coefficient at maximum central UO_2 temperature,

D_2 = diffusion coefficient at maximum UO_2 temperature (2390°F),

N_c = number of channels in each power-ratio group,

P_R = ratio of channel power of group to the reactor average power.

The value of N for the core was found to be 88.7 channels, and the equilibrium total activity release was 380 curies. The EGCR coolant system shielding is designed for 1000 curies of fission products with an effective gamma energy of 1 Mev per disentegration.

Temperature Distribution in EGCR Graphite Surveillance Specimens

M. E. Lackey R. S. Holcomb

Specimens of the EGCR moderator graphite will be placed in one of the fuel channels in the reactor core to be irradiated and then removed to determine whether any changes in the physical properties have occurred (see chap. 3, this report). In order to relate the changes of properties of the specimens to those that might be expected to occur in the moderator blocks, it will be necessary to know the approximate temperature at which the specimens will be irradiated.

The moderator specimens will be placed inside graphite fuel assembly sleeves. Six of these sleeves, filled with specimens and fitted with top and bottom dummies, will be loaded into a fuel channel. The heat-generation rate in the graphite specimens, sleeve, and surrounding moderator will be lower than the heat-generation rate in the sleeve and moderator surrounding a fueled channel, since no fissions will occur in the specimen channel. Therefore, for the same axial gas temperature distribution, the annulus coolant flow must be adjusted to match the actual heat generated in the low-power channel.

The fuel channel designated No. 140 and located in moderator block No. 270-65 was recommended from a physics standpoint as the best location

of the graphite specimens. The local power level for this channel is 1.25 times the average.

The average energy deposition rate for this channel was calculated to be 0.110 w/cm^3. The local energy deposition rate as a function of axial position in the channel is given below for the case of 47-in. bank insertion of the control rods.

Distance from Bottom of Core (in.)	Energy Deposition in Graphite (w/cm^3)
0	0.017
20	0.100
10	0.162
60	0.195
70	0.199
80	0.194
100	0.157
120	0.092
140	0.0303
160	0.0083
174	0.0044

These were the heat-generation rates assumed to exist in the graphite specimens and specimen sleeve for this study.

The heat-generation rates in the moderator block were determined previously for calculating the temperature distribution in the moderator surrounding a normal fuel channel operating at the average power. These rates were multiplied by 1.25 to correspond to the local power level of the region around the specimen channel. The graphite specimen assembly consists of a number of small specimens stacked on graphite spacer disks at nine levels inside a fuel assembly graphite sleeve. The entire assembly of spacers and specimens is held together by a stainless steel rod through the center of the assembly. There are two arrangements of specimen loading in the assembly; one type is used in the three odd-numbered assemblies and the other is in the three even-numbered assemblies.

A simplified model of the specimen assembly was assumed for the temperature calculations. At the level of each type of specimen, the specimens were considered to be homogenized into a single cylinder of the same cross-sectional area. The spacers were combined at a single axial position

within a half-assembly in order to reduce the number of axial parts needed to describe the assembly. The models used for the odd and even assemblies are shown in Fig. 1.3.

The temperature distribution was calculated within the half-block containing the specimen channel at 36 axial positions within the reactor on the IBM-7090 computer. The model assumed for these calculations is shown in Fig. 1.4. The half-block was assumed to have no heat flow across its boundary and no heat flow in the axial direction.

The helium flow rate in the adjacent fuel channels is 121 lb/hr, and it was assumed that one third of the heat generated in the graphite sleeves of the fuel assemblies was transferred to the fuel channel annulus gas. The helium flow rate in the graphite-specimen channel annulus was therefore chosen to be 104 lb/hr.

The temperature calculated to be representative of the specimen was the surface temperature of the equivalent cylinder used in the model. The temperatures of the specimen, sleeve, and annulus gas were assumed to be constant with angular position around the channel.

Static helium was assumed to exist between the specimen and sleeves, and an average value of 0.16 Btu/hr·ft·°F was used for the thermal conductivity of the helium. The axial locations at which the temperatures were calculated, the specimen equivalent cylinder diameter, and the heat generated in the specimen and sleeve are shown in Table 1.2.

The computer calculated the temperature distribution at the center of each axial segment using the gas temperatures at the beginning of the segment. The heat transferred to the gas at the midpoint of the segment was calculated from the temperature differences, and this heat was added to the gas to calculate the gas temperature at the end of the segment. Heat transfer by radiation was neglected in the computer program. The moderator block central temperature, the surface temperature of the 2.75-in.-diam specimens, and the surface temperature of all other diameter specimens, as calculated by the computer, are shown as a function of axial position in Fig. 1.5.

These temperatures were then recalculated to determine the effect of radiation heat transfer. One effect of including radiation was to lower

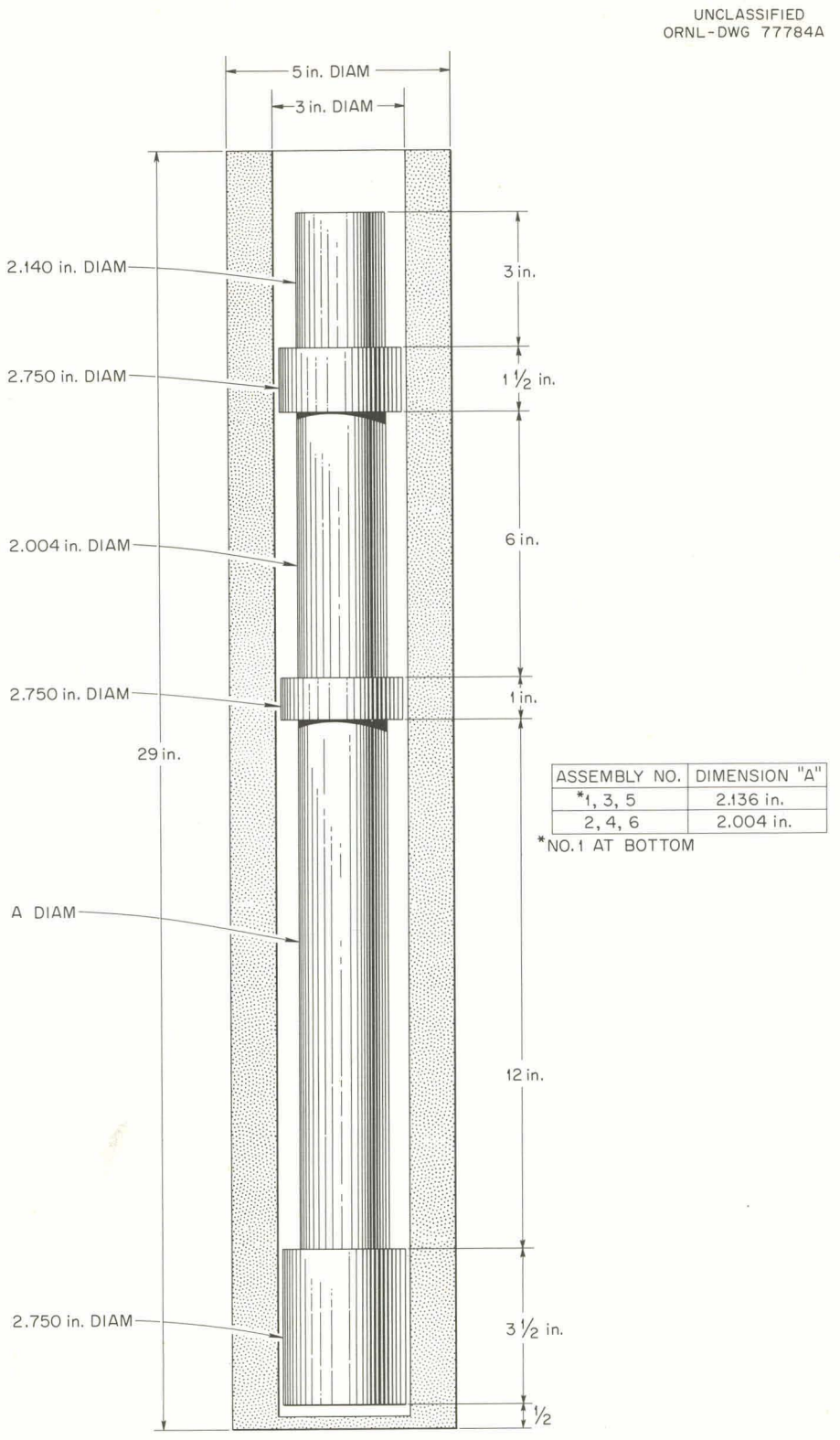

Fig. 1.3. Graphite-Surveillance-Specimen Assembly Model Assumed for Temperature Calculations.

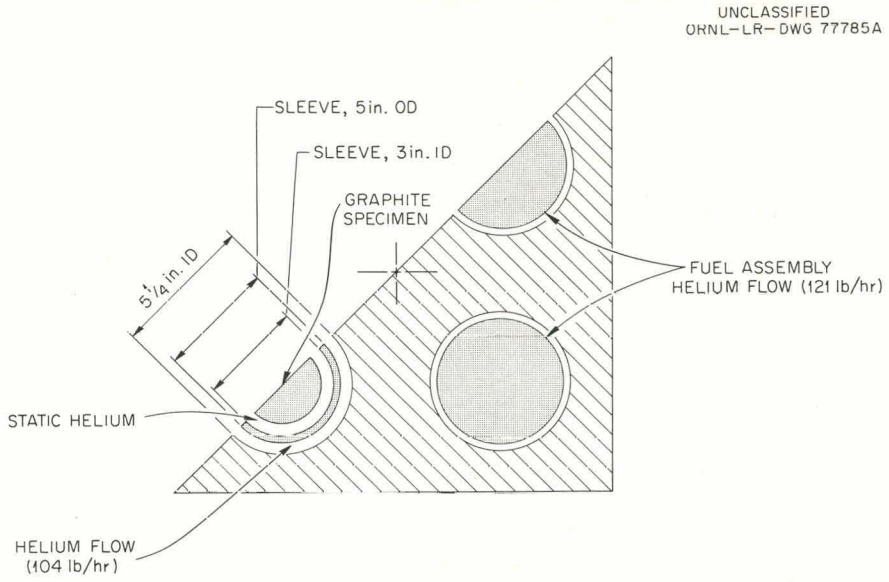

Fig. 1.4. Heat-Conduction Model of Moderator Block Containing Graphite Specimen.

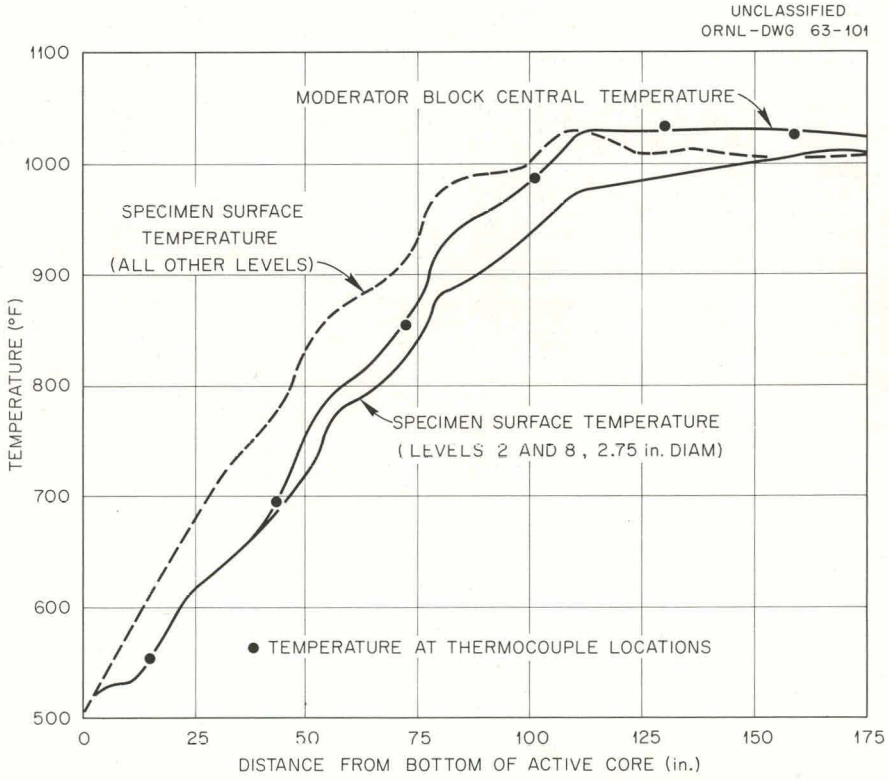

Fig. 1.5. Calculated Temperature of Moderator Block Center and Specimen Surface, Neglecting Radiation, Versus Axial Position.

Table 1.2. Heat Generation in Specimen Channel

Axial Position No.	Distance from Bottom of Active Core (in.)	Heat Generation Rate in Graphite (Btu/hr·in.^{3})	Heat Generated in Specimen (Btu/hr·in.)	Specimen Equivalent Diameter (in.)	Heat Generated in Specimen Sleeve (Btu/hr·in.)
1	2.25	1.5	9.182	2.75	18.84
2	10	3.25	12.241	2.136	40.82
3	16.5	4.6	28.159	2.75	57.76
4	20	5.45	18.023	2.004	67.824
5	23.75	6.3	38.565	2.75	79.756
6	26	6.75	25.514	2.14	84.78
7	31.25	7.7	47.13	2.75	96.71
8	39	8.8	29.1	2.004	110.53
9	45.5	9.7	59.37	2.75	121.83
10	49	10	33.07	2.004	125.6
11	52.75	10.4	63.66	2.75	130.62
12	55	10.55	39.88	2.14	132.51
13	60.25	10.9	66.72	2.75	136.9
14	68	11.1	41.8	2.136	139.42
15	74.5	11.05	67.64	2.75	138.79
16	78	10.9	36.05	2.004	136.9
17	81.75	10.7	65.49	2.75	134.4
18	84	10.6	40.07	2.14	133.14
19	89.25	10.1	61.82	2.75	126.86
20	97	9.2	30.42	2.004	115.55
21	103.5	8.2	50.19	2.75	102.99
22	107	7.6	25.13	2.004	95.46
23	110.75	6.85	41.93	2.75	86.04
24	113	6.5	24.57	2.14	81.64
25	118.25	5.55	33.97	2.75	69.71
26	126	3.8	14.31	2.136	47.73
27	132.5	2.8	17.14	2.75	35.17
28	136	2.2	7.28	2.004	27.63
29	139.75	1.8	11.02	2.75	22.61
30	142	1.55	5.86	2.14	19.47
31	147.25	1.1	6.73	2.75	13.82
32	155	0.7	2.31	2.004	8.79
33	161.5	0.5	3.061	2.75	6.28
34	165	0.4	1.32	2.004	5.02
35	168.75	0.35	2.14	2.75	4.40
36	171	0.3	1.13	2.14	3.77

the temperature difference between the moderator and annulus gas streams. From the calculated temperatures it could be seen that including radiation would have practically no effect on the percentage of the moderator heat that would be removed by each of the three gas streams. Therefore it was assumed that the gas temperature in the specimen channel annulus would be unchanged, and likewise the temperature difference from the moderator surface at the specimen channel annulus to the moderator center would be unchanged.

The moderator central temperature was reduced a maximum of 8°F by radiation. The greatest change in the specimen surface temperature was for the smaller equivalent-diameter specimens. The over-all effect of including radiation was to make the specimen temperature more nearly equal to the moderator central temperature. The temperatures of the moderator center and the specimens at the surface as calculated including radiation heat transfer are shown in Fig. 1.6.

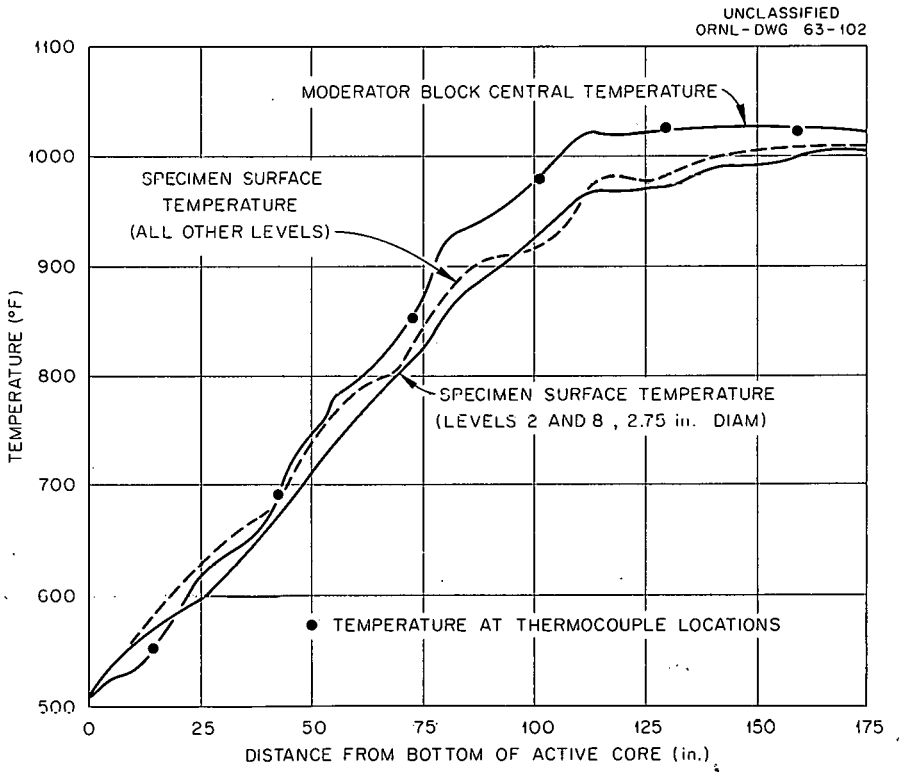

Fig. 1.6. Calculated Temperature of Moderator Block Center and Specimen Surface, Including Radiation, Versus Axial Position.

Taking into account axial heat conduction would require a complicated computer program. This effect will cause the moderator to be colder by a few degrees in the middle third of the reactor and a little hotter in the bottom third. Axial conduction will have practically no effect on the specimen temperature, since the gaps between the pieces will provide a high resistance to axial heat flow.

EGCR Fuel Element Failure Analyses

T. H. Row

A previous analysis indicated that 330 fuel element failures would result from the EGCR maximum credible accident.[7] Experimental stress-rupture data were compared with information derived from accident analyses of fuel element cladding transients to arrive at the estimate of failures. This failure analysis was examined to determine the effect of several refinements in the calculational procedure. The changes in the calculations include an allowance for the actual decrease in the central temperature after shutdown, consideration of the effect of the partial pressure of cesium and rubidium, and the use of larger subdivisions of the EGCR core.

The internal fuel element pressure values calculated previously[7] were recalculated with a revised form of the Pandora code[8] used originally. The code was designed for use on the IBM-704 but was reprogrammed for the IBM-7090 to take advantage of the more efficient machine operation and additional information. The revised internal pressure data, given in Table 1.3, show a reduction of as much as 20 psia in cases of high fuel exposure. In addition, it was previously assumed that the calculated internal pressure remained the same for the duration of the accident. Actually, the UO_2 temperature in the region surrounding the central void

---

[7]T. H. Row and W. B. Cottrell, Fuel Element Failures in Depressurization Accident, pp. 6–9, "GCRP Quar. Prog. Rep. March 31, 1962," USAEC Report ORNL-3302, Oak Ridge National Laboratory.

[8]M. W. Rosenthal, Pandora — A Computer Program for Estimating Fission-Gas Release and Its Effect on the Mechanical Life of Clad Fuel Elements, Oak Ridge National Laboratory, unpublished report.

Table 1.3. Fuel Exposures, Temperatures, and Internal Fuel Element Pressures for EGCR Equilibrium Core

Core Group	Fuel Element Assembly	Fuel Exposure (Mwd/MT)	Fuel Element Cladding Temperature (°F)	Fuel Element Internal Pressure (psia)
		First Half of Fuel Cycle		
P-1	1[a]	240	1054	41.5
	2	1,360	1086	43.8
	3	5,730	1223	54.0
	4	9,860	1279	62.8
	5	9,310	1099	55.7
	6[b]	4,500	739	37.7
P-2	1	245	1054	41.6
	2	1,380	1087	44.3
	3	5,840	1224	56.6
	4	10,000	1282	69.4
	5	9,460	1102	60.1
	6	4,570	741	39.3
P-3	1	242	1054	41.7
	2	1,360	1087	44.9
	3	5,750	1225	59.1
	4	9,870	1285	79.2
	5	9,300	1105	64.8
	6	4,490	742	40.9
		Second Half of Fuel Cycle		
P-4	4	10,480	1080	44.9
	5	10,940	1123	48.5
	6	9,970	1280	64.7
	1	9,320	1367	105.0
	2	9,970	1167	73.8
	3	10,110	774	44.5
P-5	4	10,770	1080	46.1
	5	11,200	1123	48.9
	6	10,070	1281	66.5
	1	9,320	1369	126.1
	2	10,000	1169	79.5
	3	10,270	775	45.4
P-6	4	10,750	1081	49.1
	5	11,150	1123	49.5
	6	9,950	1282	68.4
	1	9,150	1370	156.7
	2	9,830	1170	86.1
	3	10,190	776	46.3

[a]Top of core.

[b]Bottom or core.

in the EGCR fuel elements drops rapidly following scram action. This decrease in UO_2 temperature and a corresponding decrease in the equilibrium pressure are shown in Fig. 1.7. Thus the first two factors considered had the effect of reducing internal fuel element pressures.

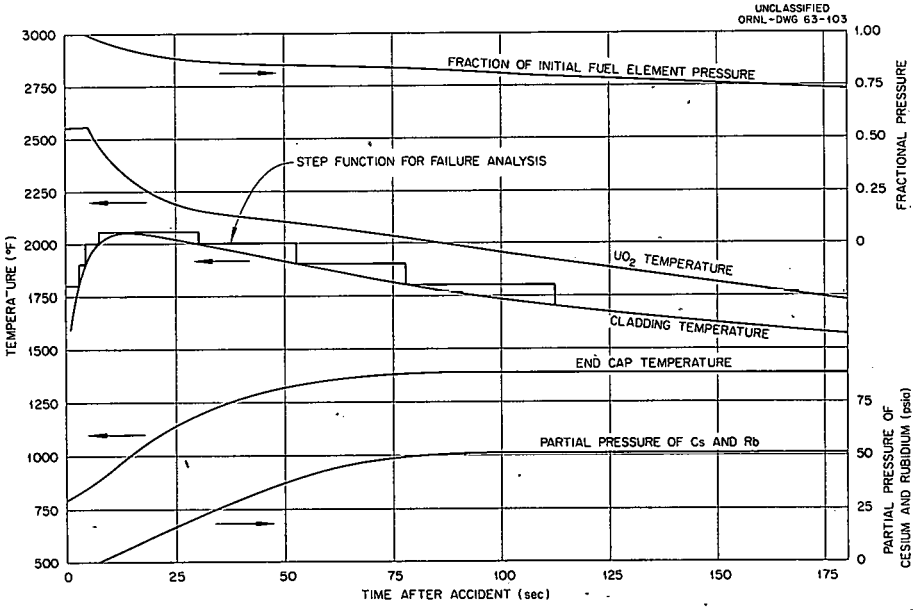

Fig. 1.7. Fuel Element Parameters During Maximum Credible Accident Group P-3, Axial Position 5.

On the other hand, consideration of the effect of the stable isotopes of cesium and rubidium increased the internal fuel element pressure. This effect was investigated previously,[9,10] but recent experimental work has indicated that cesium and rubidium may be released in the same proportion as the noble gases.[11] It was determined previously that at EGCR

---

[9]W. B. Cottrell et al., "Fission-Product Release from UO_2," USAEC Report ORNL-2935, pp. 129–130, Oak Ridge National Laboratory, Sept. 13, 1960.

[10]M. W. Rosenthal and S. Cantor, "Some Remarks on the Contribution of Fission-Product Cesium to the Pressure Buildup in UO_2 Fuel Elements," USAEC Report ORNL-CF 60-3-81, Oak Ridge National Laboratory, March 18, 1960.

[11]G. W. Parker et al., Influence of Irradiation Level on Fission Product Hazards Associated with UO_2-Fueled Reactors, pp. 11–17, "Nuclear Safety Program Semiann. Prog. Rep. June 30, 1962," USAEC Report ORNL-3319, Oak Ridge National Laboratory.

operating conditions, the partial pressure of the isotopes of cesium and rubidium would add approximately 10 psia[9] in the maximum-power channel. This would be true only if the temperature of the coldest part of the element, that is, the lower end cap, did not exceed 1100°F. During the EGCR maximum credible accident, however, the end-cap temperature would exceed this value for the majority of the accident and thus would subject the capsule to the cesium-rubidium partial pressure associated with the end-cap temperature transient. The expected partial pressure for one case is shown in Fig. 1.7.

The analysis was also extended in time to approximately 3 min. This was made possible by the use of information resulting from analysis of graphite oxidation in the EGCR core following the accident.[12] By the end of 3 min, the temperature of most of the cladding will have dropped to below 1800°F, which is considered as the upper limit for long-term operation without failure.[13]

In the previous analysis the probability of fuel element failure had been determined from the transient curve by assuming a constant peak pressure for the different temperature intervals. The transient curve was taken as a step function, with each step representing the time at which the cladding was at or above a certain temperature value. In the present analysis, it became impossible to proceed on this basis because of the variation with not only the cladding temperature but also the internal pressure. Therefore the method of analysis used was the fractional-life technique.[14,15] The use of the fractional-life method, where each step along the curve is analyzed for failure, is illustrated in Fig. 1.7. A ratio is obtained of the time at each step to the failure time indicated

---

[12]J. O. Kolb and W. B. Cottrell, Graphite Oxidation, pp. 23–37, "GCRP Semiann. Prog. Rep. Sept. 30, 1962," USAEC Report ORNL-3372, Oak Ridge National Laboratory.

[13]"EGCR Final Hazards Summary Report," Vol. 1, USAEC Report ORO-586, pp. 4-3 to 4-8, Oct. 10, 1962.

[14]C. R. Kennedy, Stress-Rate Testing, pp. 44–45, "Metals and Ceramics Div. Ann. Prog. Rep. May 31, 1962," USAEC Report ORNL-3313, Oak Ridge National Laboratory.

[15]John E. Dorn (Ed.), Mechanical Behavior of Materials at Elevated Temperatures, McGraw-Hill, New York, 1961.

for the particular cladding conditions at each step, and these fractions are summed over the entire transient curve. Failure is indicated if the sum equals or exceeds unity.

This study conservatively introduced many refinements into the calculation of the number of fuel element failures, and the net result was to indicate a failure number of 751. Since the cesium-rubidium isotopes will not exist in the maximum quantities in all locations, as was assumed, it seems likely that the number of failures would actually be substantially less than 751.

Graphite Oxidation and Hydrogen Generation

J. O. Kolb W. B. Cottrell

The EGCR graphite oxidation code[16] was used for the calculation of hydrogen generation rates in accidents involving an internal rupture of a steam generator. The hydrogen generation rates thus obtained were then used in a study of methods for preventing hydrogen flammability in the EGCR containment vessel.

Method for Calculating Hydrogen Generation Rates

The hydrogen generation calculations for an EGCR channel were based on surface reaction rates that are a function of graphite temperature only.[17] The reaction rate was assumed to apply to a reaction between graphite and water vapor:

$$C(\text{solid}) + 2H_2O \rightarrow CO_2 + 2H_2 \ .$$

This reaction yields the greatest amount of hydrogen; that is, two moles per mole of carbon reacted. An endothermic heat of reaction of 31.4 kcal/g·mole of carbon was used in the oxidation code. Since the graphite

---

[16]J. O. Kolb and W. B. Cottrell, Graphite Oxidation, pp. 9–18, "GCRP Quar. Prog. Rep. March 31, 1962," USAEC Report ORNL-3302, Oak Ridge National Laboratory.

[17]J. O. Kolb and W. B. Cottrell, Graphite Oxidation, pp. 23–37, esp. Fig. 1.15, "GCRP Semiann. Prog. Rep. Sept. 31, 1962," USAEC Report ORNL-3372, Oak Ridge National Laboratory.

oxidation code output includes oxidation heat "generation" rates, which are negative in this case, for the inner sleeve and annular graphite, hydrogen generation rates could be conservatively calculated from the heat generation rate, the heat of reaction, and the hydrogen yield of two moles per mole of carbon reacted.

The value of 31.4 kcal/g·mole for the endothermic heat of reaction actually applies to the gasification reaction

$$C(\text{solid}) + H_2O \rightleftharpoons CO + H_2 \ .$$

The water-gas reaction,

$$CO + H_2O \rightleftharpoons CO_2 + H_2 \ ,$$

is exothermic with a heat of reaction of 9.9 kcal/g·mole. Since the endothermic heat of reaction is drawn from the graphite enthalpy in the oxidation code, a lower value than 31.4 kcal/g·mole would have been more conservative by allowing higher graphite temperatures. In the calculations performed, however, the oxidation heat generation was a negligible fraction of the total heat generation, so a lower heat of reaction would not have affected the temperature and hydrogen generation transients significantly.

The hydrogen generation rate for the inner sleeve surface was obtained in the manner outlined above. The hydrogen generation rate in the annulus based on the calculated oxidation heat generation rate usually exceeded the rate of hydrogen flow into the annulus in the form of H_2O. This situation was caused by the combination of (1) a zero-order reaction, which was used because the mass-balance equations in the code were programmed for air rather than steam, and (2) low annulus flow rates. (Since the percentage of the total flow passing through the annulus at low flow rates was not known, a relative annulus flow of 3% was chosen as a conservatively high value.) Therefore the annulus hydrogen generation rate was determined from two limiting conditions. First, the hydrogen outflow from the annulus was limited by the hydrogen partial pressure allowable from equilibrium considerations. The hydrogen partial pressure variation as a function of temperature at 1.5 and 25 atm total pressure shown

in Fig. 1.8 was calculated from standard equilibrium constants[18] for the gasification and water-gas reactions. The highest annulus graphite temperature calculated by the oxidation code was then used to select the hydrogen partial pressure in the annulus stream at a given time. The second limiting condition was that the hydrogen generation rate in the annulus would not exceed the inner sleeve generation rate times the annulus-to-inner sleeve area ratio, 3.42, when the inner sleeve and moderator block temperatures were about the same. This condition is satisfied within 30 sec after the reactor is scrammed, so this limit was applicable to all cases analyzed.

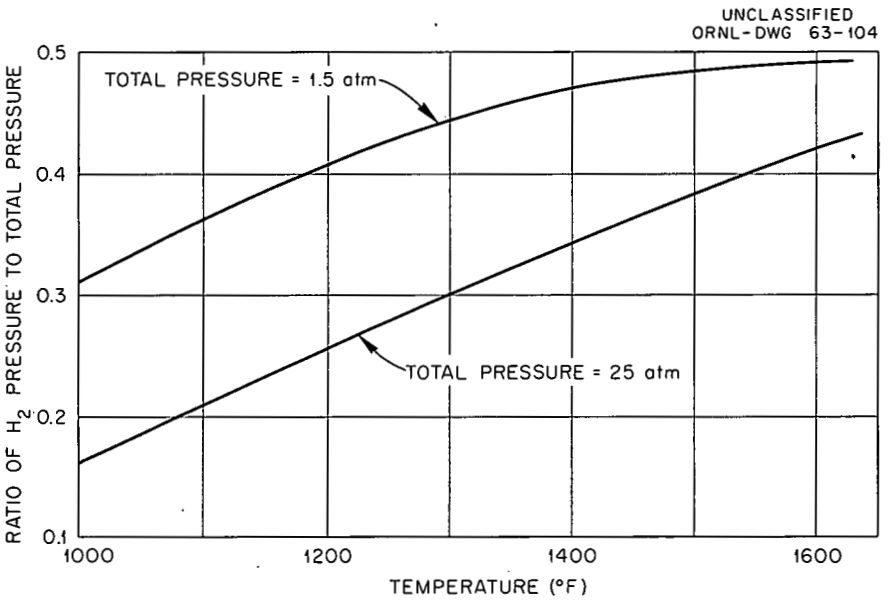

Fig. 1.8. Calculated Hydrogen Equilibrium Partial Pressures for Graphite-Water Reactions.

Hydrogen Generation Following Overpressurization or Depressurization Accidents

Hydrogen could be generated following a steam generator internal failure in an overpressurization or depressurization accident. The overpressurization accident is worse from the standpoint of the higher

[18] Tables of Selected Values of Chemical Thermodynamic Properties, National Bureau of Standards, Washington, D.C., 1949.

reaction rate for forming hydrogen but better because of the natural circulation cooling that would be available. In the EGCR hazards analysis, it was assumed that no means of forced circulation was available during the first hour after the accident but that at least 7000 lb/hr of steam would flow through the core after an overpressurization accident.

Calculations were performed for maximum- and average-power channels with core steam flow of 7000 lb/hr at 300 psig starting after 30 sec of no cooling. The generation rate and cumulative amount of hydrogen generated per channel are shown in Fig. 1.9 for these conditions. The calculated generation rate is high for many hours and would lead to large amounts of hydrogen being formed if no remedial action were taken.

Two cases were also calculated for a maximum power channel with core flows of 197,500 and 98,750 lb/hr from a main blower starting 1 hr after scram. (These flows are 50 and 25%, respectively, of the normal helium mass flows.) The initial temperature profile was the conservatively high C-K temperature envelope used for air oxidation calculations.[17] The calculations were performed to investigate the magnitude of steam cooling necessary to reduce the hydrogen generation rates to negligible levels. It was found, as shown in Fig. 1.10, that the calculated generation rates decreased several orders of magnitude within 1 hr of the initiation of forced cooling. The generation rates in the annulus were based on the area ratio limit described above.

A depressurization accident that included an internal steam generator rupture could expose the core for up to 1 hr with little cooling until some means of forced-circulation cooling was initiated. The first depressurization calculation was for the first hour after a scram with no cooling and a 1-atm steam-graphite reaction occurring on all graphite surfaces of a maximum power channel. The results for this case are presented in Fig. 1.11.

By 1 hr after a depressurization accident in the EGCR, the emergency cooling loop will provide core flow and nitrogen purging of the circulating volume if a main blower is unavailable for use. Therefore, a calculation was performed for a maximum-power channel to simulate the initial

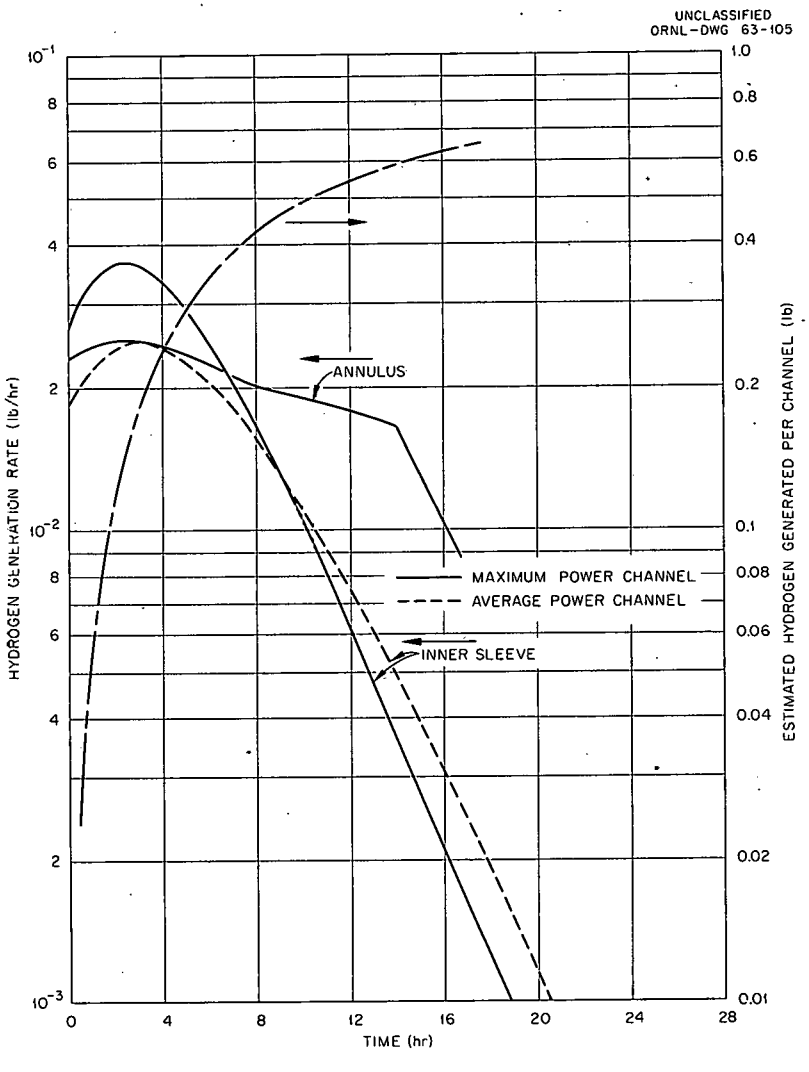

Fig. 1.9. Hydrogen Generated Per Channel During Overpressurization Accident Based on 7000-lb/hr Steam Flow from Natural Circulation at 300 psig and the Temperatures Existing After 30 sec of No Cooling.

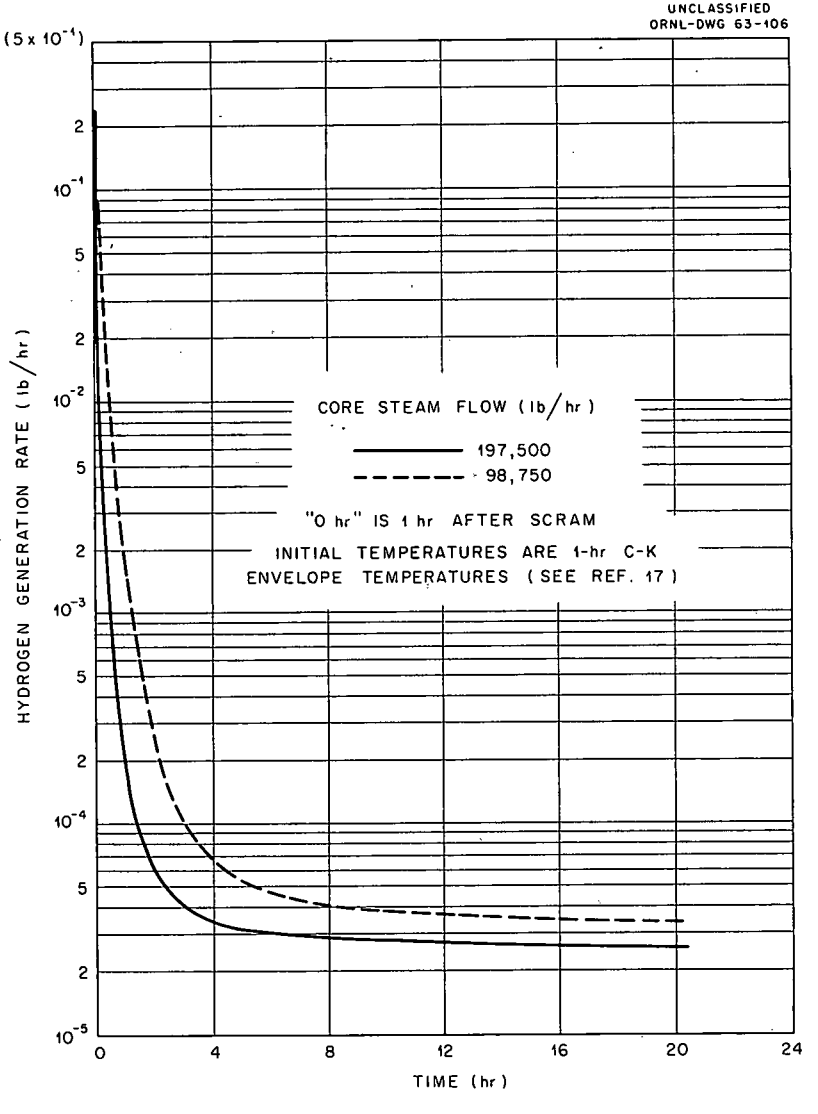

Fig. 1.10. Hydrogen Generation Rate in Maximum-Power Channel with Core Steam Flow from a Main Blower Operating at 300 psig.

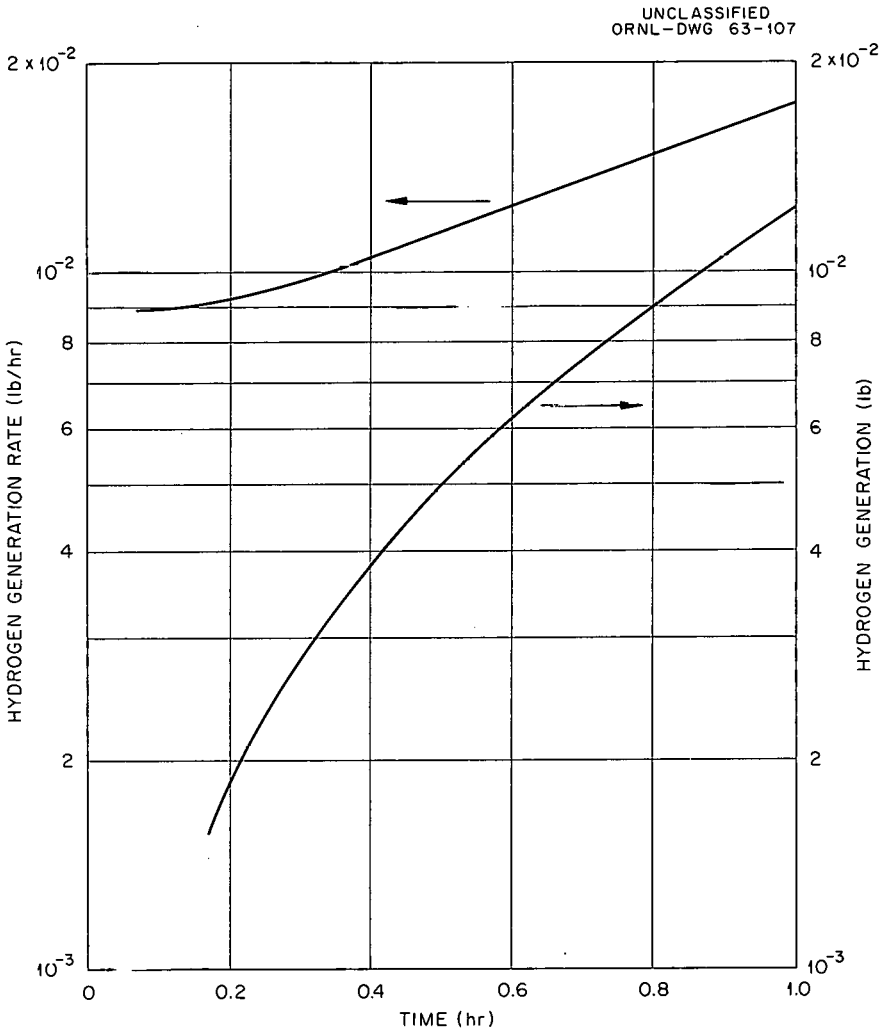

Fig. 1.11. Hydrogen Generation from a Maximum-Power Channel with No Cooling During First Hour After a Scram Caused by a Depressurization Accident. Calculations based on a 1-atm steam-graphite reaction occurring on all graphite surfaces of the channel.

circulation of steam by the emergency cooling loop. A steam flow of 3830 lb/hr, which is volumetrically equivalent to the 7000-lb/hr nitrogen flow of the emergency-cooling loop, and the C-K temperature envelope for 1 hr after scram were used. The results for this case are presented in Fig. 1.12; the generation rate in the annulus was obtained from both the area ratio and equilibrium limits at different times during the transient.

Circulation of 1-atm steam by a main blower was investigated by calculations starting at 1/2 and 1 hr after scram. Steam flows of 15,800 and 22,130 lb/hr were used to correspond to the air flows of 25,000 and

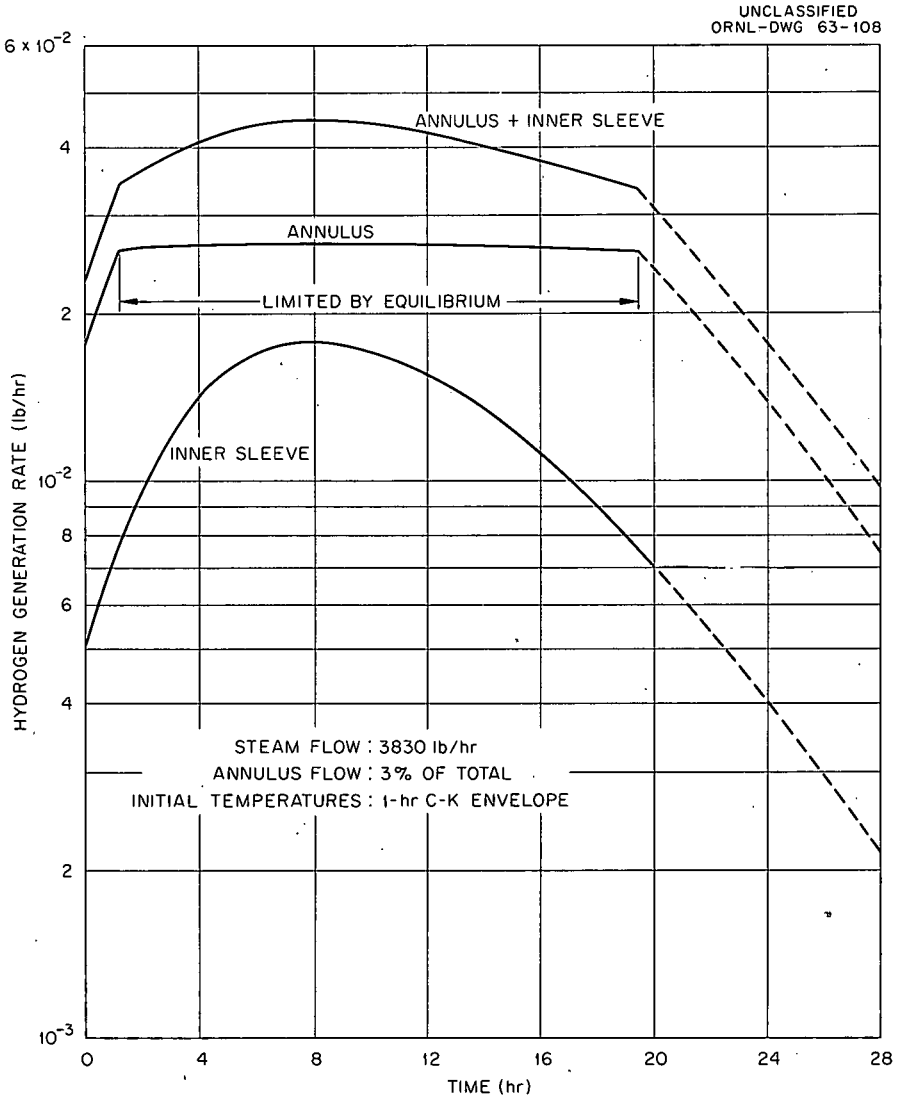

Fig. 1.12. Hydrogen Generation Rate for a Maximum-Power Channel Versus Time with Steam Cooling by the Emergency Cooling Loop Starting 1 hr After Scram.

35,000 lb/hr required at 1/2 and 1 hr after scram to prevent runaway air oxidation.[17] The initial temperature profiles used were again the conservative C-K envelopes. The results for these two calculations are presented in Fig. 1.13.

Prevention of Hydrogen Flammability

The amounts of hydrogen generated, the dispersion of the hydrogen into the various internal volumes of the EGCR containment vessel, and

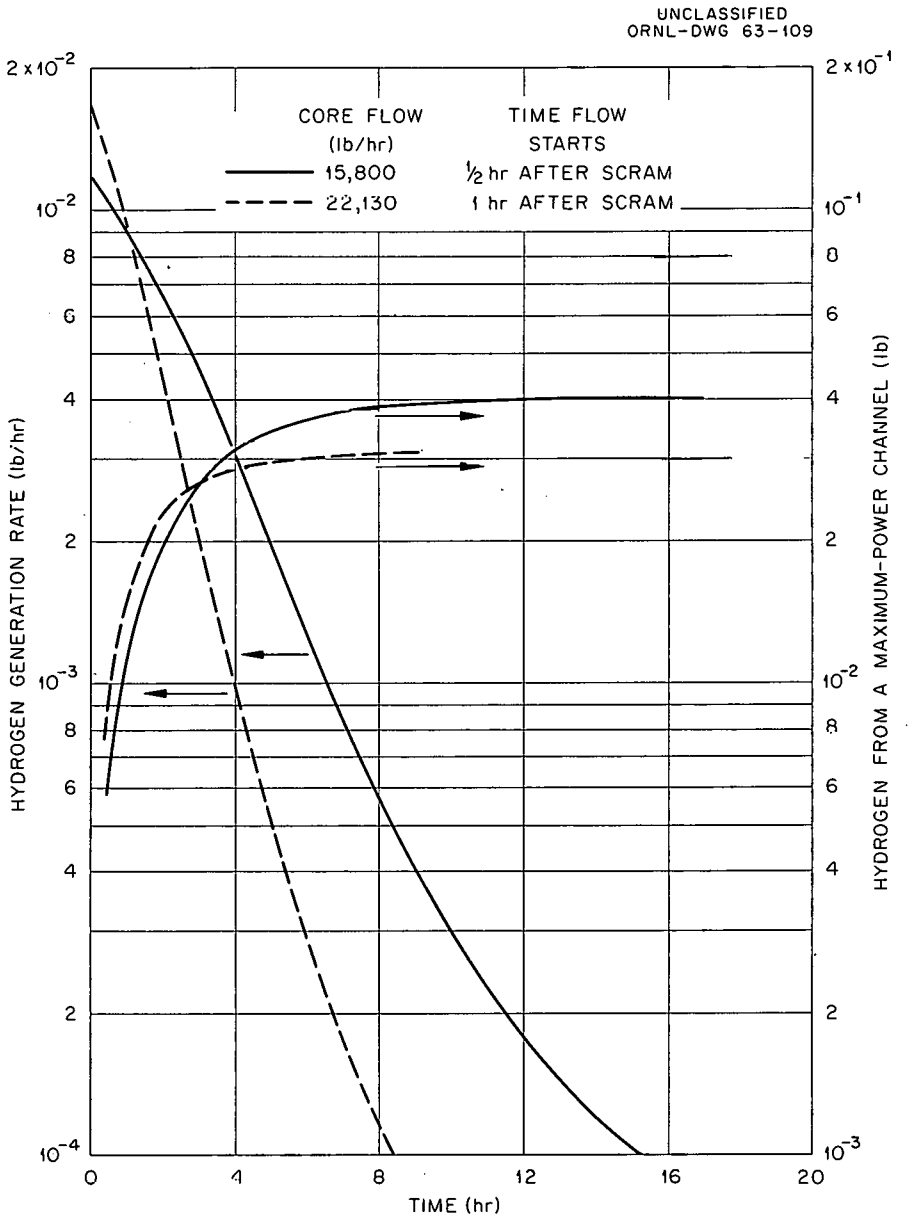

Fig. 1.13. Hydrogen Generation from a Maximum-Power Channel with 1-atm Steam Flow from a Main Blower.

the means for preventing the accumulation of flammable volumes of hydrogen were studied by Allis-Chalmers, Kaiser Engineers, and ORNL members of the EGCR hazards team and were reported by Kaiser Engineers in a report documented for the EGCR Hazards Summary Report.[13] It was decided to limit conservatively calculated hydrogen concentrations to the flammable range so that no self-supporting reaction could occur even in the presence

of an ignition source. Therefore two working criteria were established: (1) hydrogen concentrations in air would be kept to less than 4 vol %, the lower limit of flammability for upward propagation; and (2) volume ratios for steam to hydrogen[19] and nitrogen to hydrogen[20] in mixtures released to the containment vessel would be at least 4.5 and 16.5, respectively. The latter criteria establish "ever-safe" mixtures of hydrogen and the diluent nitrogen or water vapor in air so that flammability cannot occur as the hydrogen is released from the primary cooling system and mixed with the atmosphere in the containment vessel.

In the Kaiser Engineers study, it was assumed conservatively that the shield cooling system and the reactor chamber were the locations into which hydrogen would disperse in overpressurization and depressurization accidents, respectively. Based on the results presented in Figs. 1.9, 1.10, and 1.12, the following sequence of events was shown to be acceptable after overpressurization: (1) 1 hr of natural circulation from overpressurization followed by (2) core cooling by 98,750 lb/hr of core steam flow from a main blower or (3) depressurization of the primary cooling system within 1 hr if a main blower was inoperable and use of the emergency cooling loop for core cooling and purging of the primary system. Depressurizing the primary system to 9 psig in about 1/2 hr has been made possible by recent piping revisions, so this action would not be taken until 1/2 hr after the accident if a main blower were not operable.

For a depressurization accident, the results presented in Fig. 1.11 were used for the first hour. If a main blower were operable, the Kaiser study showed that core flows of 21,400 and 26,000 lb/hr should begin at 1/2 and 1 hr, respectively. These values were derived by interpolating and extrapolating the results presented in Fig. 1.13. If a main blower could not provide the required steam flow, the emergency cooling loop would be used. The nitrogen purge rates would be sufficient to remove

---

[19]M. S. Zabetaki, "Research on the Combustion and Explosion Hazards of Hydrogen-Water Vapor-Air Mixtures," AECU-3327, Sept. 4, 1956, Fig. 1.

[20]H. F. Coward and G. M. Jones, "Limits of Flammability of Gases and Vapors," Bulletin 503, Bureau of Mines, 1952, Fig. 1.

essentially all water vapor and hence the source of hydrogen from the core during the first hour of operation. It appears therefore that the amounts of hydrogen generated in the depressurization situations would be tolerable even in the relatively small reactor chamber volume.

Experimental Measurements of the Reaction of Steam and Graphite

R. E. Helms R. E. MacPherson

A high-pressure forced-convection loop is being assembled for measuring the reaction rate of graphite and steam over the temperature range 1000 to 1800°F at system pressures from 20 to 362 psia and steam flow rates up to 120 lb/hr. The data obtained will be used to verify the calculations described in the preceding section.

Neutron Multiplication by Experimental Gas-Cooled Reactor Fuel Assemblies

E. B. Johnson R. K. Reedy, Jr.

Experiments were conducted to determine the source-neutron multiplication of EGCR fuel assemblies under conditions which might exist in transportation and storage. Twenty-eight fuel assemblies were arranged to yield maximum nuclear reactivity under conditions that might be expected for out-of-pile environments. It was found that these 28 assemblies could not be made critical when water moderated and reflected.[21]

---

[21]E. B. Johnson and R. K. Reedy, Jr., "Neutron Multiplication by Experimental Gas Cooled Reactor Fuel Assemblies," USAEC Report ORNL-TM-433, Oak Ridge National Laboratory, Nov. 27, 1962.

2. COMPONENT DEVELOPMENT AND TESTING

Fuel Channel Top and Bottom Dummy Assembly Flow Tests

R. E. Helms R. E. MacPherson

An adjustable orifice in the bottom dummy was designed and tested that will provide the control needed to assure more linear flow for the full 5 in. of travel of the adjustable plug. The calculated helium pressure drop versus flow for this design is presented in Fig. 2.1. The helium flow as a function of plug position is presented by Fig. 2.2.

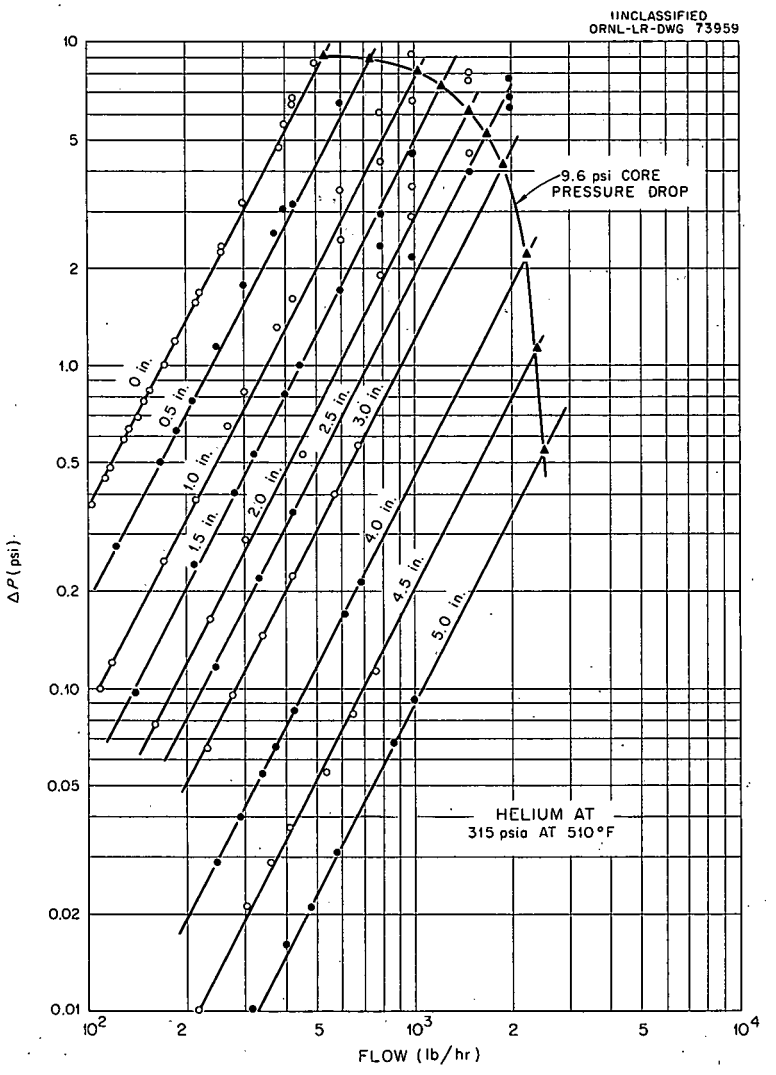

Fig. 2.1. Modified Plug and Orifice Pressure Drop vs Flow.

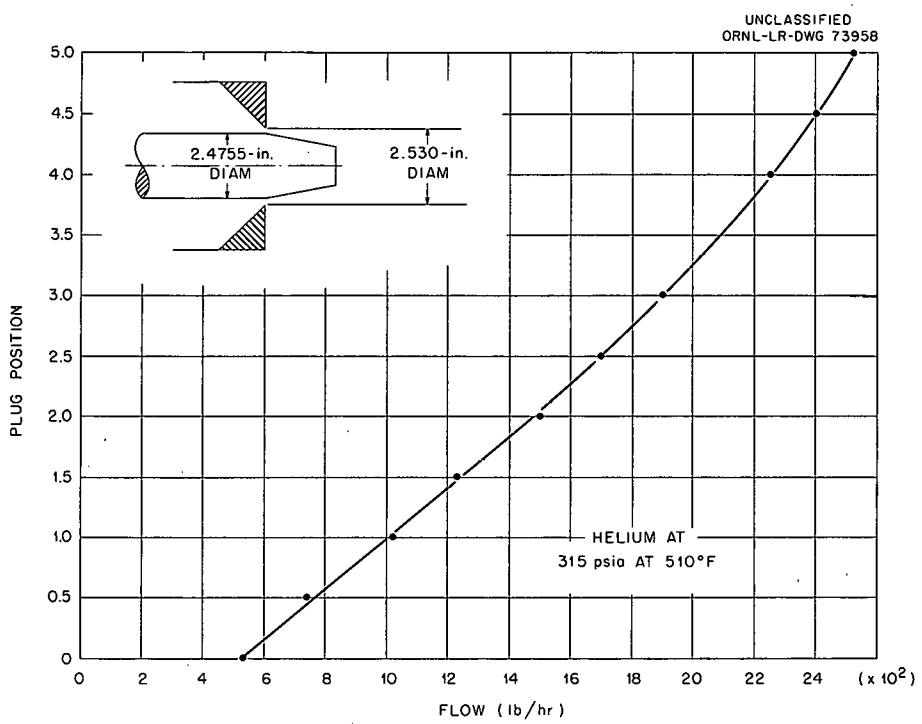

Fig. 2.2. Helium Flow vs Modified Adjustable Plug Position.

A retest of the prototype top dummy following machining to the dimensions of the mockup top dummy gave essentially the same flow versus pressure drop relationship as that measured in tests of the mockup. The data on flow versus pressure drop for the mockup top dummy were reported previously.[1]

Evaluation of Venturis for EGCR Instrumented Channels

R. E. Helms R. E. MacPherson

Venturis 1, 2, and 3 for the EGCR instrumented channels were tested to determine the effect of variations from design dimensions. The design dimensions and the dimensions of the five units that have been fabricated are listed below:

---

[1]R. E. Helms and R. E. MacPherson, Fuel Channel Top and Bottom Dummy Assembly Flow Tests, pp. 61–64, GCRP Semiann. Prog. Rep. Sept. 30, 1962, USAEC Report ORNL-3372, Oak Ridge National Laboratory.

	Entrance Diameter (in.)	Throat Diameter (in.)
Design	3.000 ± 0.001	1.625 ± 0.001
Unit 1	2.999	1.6248
Unit 2	2.9989	1.6250
Unit 3	2.9993	1.6243
Unit 4	2.9996	1.6255
Unit 5	2.9993	1.6243

The calculated values of helium flow versus pressure differential are presented in Fig. 2.3 for units 1, 2, and 3, which had the greatest dimensional variations. The results for all three units agree within 1%; therefore no tests are planned on the remaining two units.

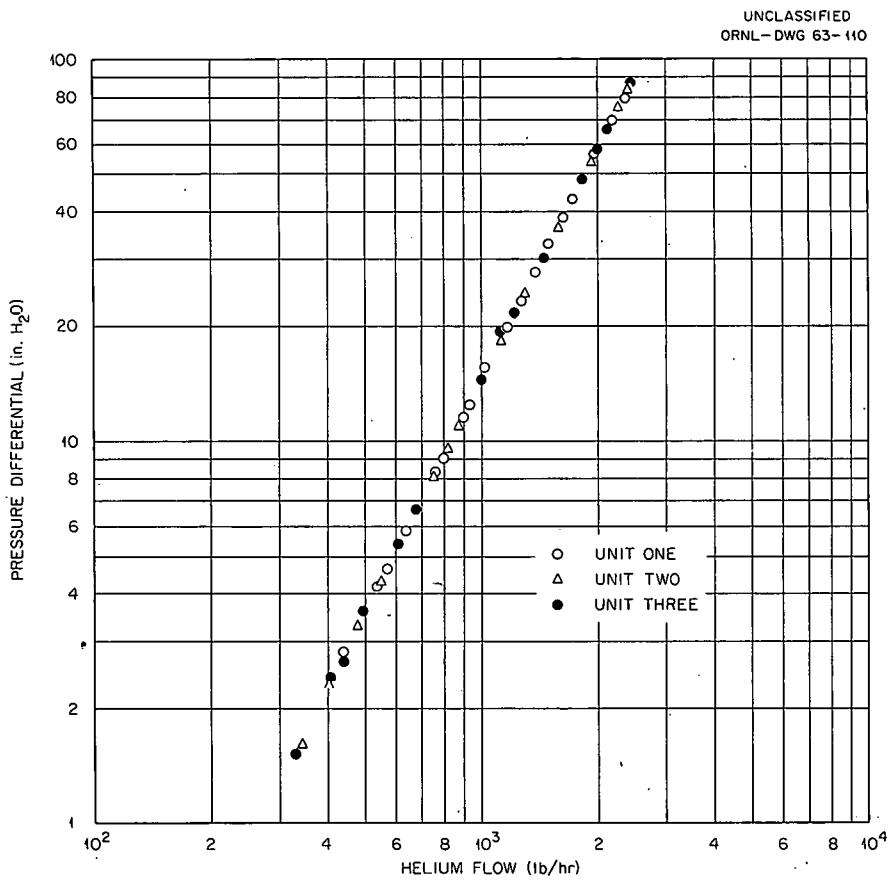

Fig. 2.3. Calculated Helium Flow Versus Pressure Differential for Venturis 1, 2, and 3 Fabricated for EGCR Instrumented Channels. Helium initially at 1050°F and 305 psia.

Instrumented Fuel Assemblies

R. L. Senn W. G. Cobb
E. A. Franco-Ferreira

Fabrication work on the instrumented fuel assemblies for the first core loading of the EGCR continued. The final assembly of the first four units was rescheduled for October 1963 as a result of delays in the expected shipping date for the top closures and shield plugs.

The design and fabrication of assembly fixtures was completed and assembly of the seven-rod cluster fuel element assemblies is in progress (see chap. 3, this report). Numerous special dimensional inspections are being performed on the fuel rods, graphite sleeves, and fuel element assemblies. These include lengths, diameters, and straightness of the rods and sleeves. Upon completion of each assembly, the spacings between the rods near the top spider, bottom spider, and midplane spacers are measured. A record of these inspections is maintained for each unit.

Control-Rod-Drive Testing Facility

W. F. Ferguson

The EGCR control-rod-drive testing facility was completed and placed in standby condition pending delivery of the prototype drive mechanism. This completes all installation work, except for the calibration of certain instruments, which cannot be accomplished until after the drive mechanism is installed. Operating procedures were prepared for the test facility.

Compressor Procurement

W. F. Boudreau

Main Coolant Blowers (E. R. Taylor)

The progress on the casings for the Joy Manufacturing Company blowers was extremely slow during the report period, even though no further problems were encountered in welding. The latest tentative schedule received from the Joy Manufacturing Co. indicates delivery of the first blower in

September and the second in November 1963. All other components for the blowers are essentially complete, except for the static seals, which are now in the latter stages of design and testing. Design changes are being made to improve the endurance life of the bellows.

Pressure-Vessel Cooling-System Compressors (E. R. Taylor)

The welding of the first casing was completed by the Battelle Memorial Institute on February 15, 1963. This unit is in the Roots-Connersville Plant for final machining, hydrostatic testing, assembly, and performance testing. The remaining work on this unit is estimated to require between two and three months. The progress schedule for the second unit is about two months behind that of the first. All other parts for these two units are essentially complete, except for the static seals, which have the same status as those for the main blowers. The Chicago Rawhide Company is providing the static seals for both the vessel cooling compressors and the main cooling blowers.

EGCR In-Pile Loops

W. F. Ferguson

The experimental loop nozzle tees, which provide access for the loops through the pressure vessel, are being fabricated by the Baldwin-Lima-Hamilton Corporation of Philadelphia, Pennsylvania. The three bottom loop tees and the tee for the emergency cooling loop were delivered to the reactor site and are being installed by the H. K. Ferguson Company. The major production effort has been expended on the bottom tees, and little progress has been made toward completion of top tees.

The lower experimental piping for loops TS-2, TS-3, and TL-4 was installed by the H. K. Ferguson Company, and all welding of both stainless and carbon steel was completed, except for the welds that connect the loop piping to the bottom nozzle tees. Inspection and testing of all finished welds was satisfactorily completed.

The top closures for the loops are being designed and fabricated by the General Electric Company. The design of the closures is approximately

80% complete. Since the design is similar to the design of the EGCR closures, which are also being supplied by GE, the General Electric Company has elected to defer completion of loop closure design and fabrication until after a prototype of the EGCR closures has been fabricated and has satisfactorily undergone all required testing.

The bottom closures are being supplied by Flight Refueling, Inc. of Baltimore, Maryland. A prototype closure was tested using Viton "O" rings, and the leakage across the seal was far in excess of the specification requirements. Consequently, the closure was retested using Selastic S-2097-U "O" rings. The closure met all requirements of the specification in the second test. Approximately 50% of the parts for the closures have been completed.

Decontamination Studies

A. B. Meservey

Decontamination of Stainless Steels Baked in Helium at 500°C

Stainless steel blowers and piping exposed to contaminated helium at the operating temperatures of the EGCR can probably be adequately decontaminated without damage by hot oxalic acid solutions containing fluoride and hydrogen peroxide. Decontamination can be by means of an aqueous bath containing 0.4 M $H_2C_2O_4$ + 0.1 M F^- + 0.1 to 1 M H_2O_2 for 2 to 4 hr at 90 to 95°C. This decontaminating solution has a corrosion rate of 0.003 ± 0.001 mil/hr. For increased effectiveness, a similar but more corrosive bath, with a penetration rate of 0.02 ± 0.01 mil/hr, can be used. The latter solution differs from the first only in the H_2O_2 content, which is 0.01 to 0.02 M, and in its increased corrosivity. Typical laboratory data illustrating the effectiveness of the two types of solutions compared with noncorrosive (pH = 4) solutions are shown in Table 2.1 for types 302 and 347 stainless steels contaminated with the most tenacious of the fission products. The noncorrosive oxalate-peroxide solution produces decontamination factors of 10^2 to 10^3 or more on carbon steels and stainless steels not heated above about 200°C and also decontaminates carbon steels and aluminum that have been contaminated and then

Table 2.1. Decontamination Factors with Oxalate-Peroxide Solutions on Stainless Steels Baked at 500°C in Helium

Fission Product	Decontamination Factor		
	Noncorrosive Solution (pH = 4)	Corrosive Solution (0.003 mil/hr)	Corrosive Solution (0.02 mil/hr)
$Zr\text{-}Nb^{95}$	2–4	25–45	100–200
$Ce\text{-}Pr^{144}$	6	20	200–300
$Ru\text{-}Rh^{106}$	2	17	70
$Ba\text{-}La^{140}$	7		70

heated to 500°C in helium, but it fails to decontaminate stainless steels baked at 500°C. The increased acidity provided by oxalic acid combined with the complexing properties of the oxalate and fluoride ions and the oxidizing-reducing behavior of the peroxide results in a superior decontaminating, oxide-dissolving, and metal brightening solution for heated stainless steels. The decontamination of contaminated loop specimens and of piping exposed to heated helium containing fission products was successful with these solutions and with steam-spray techniques.

Decontamination of Carbon Steels by Steam Spray

Blasting with a 15-psig steam jet into which was aspirated approximately 12 wt % 0.4 M oxalate + 0.16 M citrate + 0.5 M H_2O_2 at a pH of 4.0 was satisfactory as a low-corrosion decontaminating technique for carbon steel at distances of 2 to 24 in. from the nozzle. The corrosion rate was 0.002 to 0.006 mil/hr. At lower peroxide concentrations, such as 0.3 M, the corrosion rate rose abruptly to 0.17 mil/hr as inhibition was lost. After $Zr\text{-}Nb^{95}$ was baked onto carbon steel in helium at 500°C, decontamination factors in 1 hr at 2 and 24 in. from the jet were 1.2×10^3 and 520, respectively, in the 0.5 M H_2O_2 mixture.

3. MATERIALS DEVELOPMENT

A. Goldman

Fabrication of Instrumented Capsules and Fuel Elements for Irradiation Tests

E. A. Franco-Ferreira

ORR Poolside Irradiation Capsules

Six standard uninstrumented capsules were fabricated for tests of UO_2 pellets in the ORR poolside facility (see Chap. 4). The sources of the UO_2 in these capsules, designated group VI, are listed below:

Capsule No.	UO_2 Source
03-6	Oak Ridge National Laboratory
02A-6	Westinghouse virgin oxide
03A-6	Westinghouse virgin oxide
05A-6	Westinghouse reprocessed oxide
06A-6	Westinghouse reprocessed oxide
05B-6	Modified Westinghouse reprocessed oxide

Test Fuel Elements for Irradiation in GCR-ORR Loop No. 1

A special roughened-surface fuel element, designated 10-P, was fabricated for measuring the effect of the roughened surface on the pressure drop in the coolant gas. The roughened surface was produced by wrapping the outside of the cladding with 0.0063-in.-diam Nichrome wire on a pitch of 24 turns per inch and copper brazing it in place. Standard procedures were used in the installation of four internal cladding thermocouples. The element was designed for a higher power output (estimated at 65,000 Btu/hr·ft) than those manufactured previously, and both the over-all length of the element and the length of the fuel column were less. As in the past, two complete elements were fabricated for the experiment.

Each element was encased in a shroud designed to direct the flow of cooling gas around the element. Normally each shroud contains two thermocouples to measure the exit-gas temperature, and the thermocouples, as well as the gas sealing rings, are brazed in place as a routine portion of the fabrication program. The shroud used for element 10-P was somewhat

more complicated, however, in that it contained provisions for gas pressure-drop measurements, as well as temperature measurements. The completed shroud is shown in Fig. 3.1. The two girth rings contain gas annuli that are connected to the inside of the shroud by a number of accurately sized holes. The annuli are connected to pressure transducers by brazed-in capillary tubes, one of which can be seen in Fig. 3.1. Also evident are the two gas-temperature thermocouples. All components were simultaneously brazed in place.

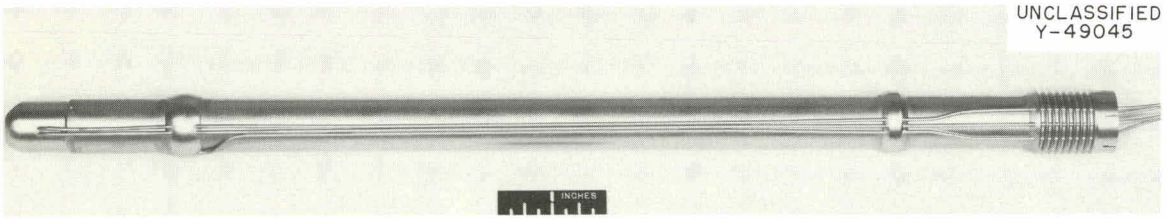

Fig. 3.1. Completed Shroud for Fuel Element 10-P. The girth rings, capillary tubes, and gas-temperature sensing thermocouples are shown.

Fabrication of EGCR Instrumented Fuel Elements

E. A. Franco-Ferreira

Fabrication of components for the 20 instrumented fuel elements that will be installed in four-assembly stringers with the first core loading is progressing rapidly. All the fuel rods for the first two instrumented stringers were completed (see Chap. 2). The various phases involved in this work are discussed below.

Fuel Processing

All the UO_2 bushings are standard EGCR units removed from Westinghouse's normal assembly stream. After the bushings were received at ORNL, it was discovered that the flat lands on the dished ends of the bushings were too narrow. This condition was corrected by hand grinding both ends of each bushing in order to widen the lands. The bushings can be processed in this way at a maximum rate of approximately three per minute.

The bushings were then slotted by an Elox process to accommodate the internal thermocouple of the instrumented fuel tube. After the grinding and slotting operations were completed, the bushings were ultrasonically cleaned in trichlorethylene to remove oil and grease, as well as any UO_2 dust produced by machining.

Because of variations that occur during manufacturing, the UO_2 bushings are not all the same length. Therefore the fuel bushings for each rod must be individually selected so that their stacked height will be within the specified tolerance. After each stack is made up, it is weighed and loaded into a fuel rod that has one end cap welded in place. Loaded rods are then placed in a special furnace extension on the inert-atmosphere welding chamber. This extension is the aluminum-foil-insulated portion in Fig. 3.2. The chamber is evacuated to at least 2×10^{-5} torr and outgassed for 4 hr at a temperature of 400°C. The chamber is then backfilled with helium, and the final end-cap welds are made.

Uninstrumented Fuel Rods

Each instrumented fuel assembly stringer has 25 uninstrumented rods and 3 instrumented rods, and the uninstrumented rods are fabricated with the same care as the instrumented rods. The upper end caps are welded into the tubes outside the welding chamber, helium-leak tested, dye-penetrant inspected, and radiographed. The rods are then loaded with fuel and outgassed as described above. The bottom end caps are pressed in and welded automatically inside the welding chamber in the unit shown in Fig. 3.3, which is a view through the port of the welding chamber with an actual weld setup shown. The bottom end-cap welds are subjected to the same nondestructive tests as the top end-cap welds.

In addition, special dimensional measurements are made of each fuel rod. These data and the weld inspection reports, welding current traces, and fuel weights are compiled into a record file.

Instrumented Fuel Rods

Two of the three instrumented fuel rods in each stringer have two cladding thermocouples and one central thermocouple (Fig. 3.4); the other

rod has only one cladding thermocouple and no central thermocouple. In the fabrication of these rods, the top end caps are first welded and inspected as above. The cladding thermocouples are then brazed in place using procedures developed and reported previously. The brazed joints

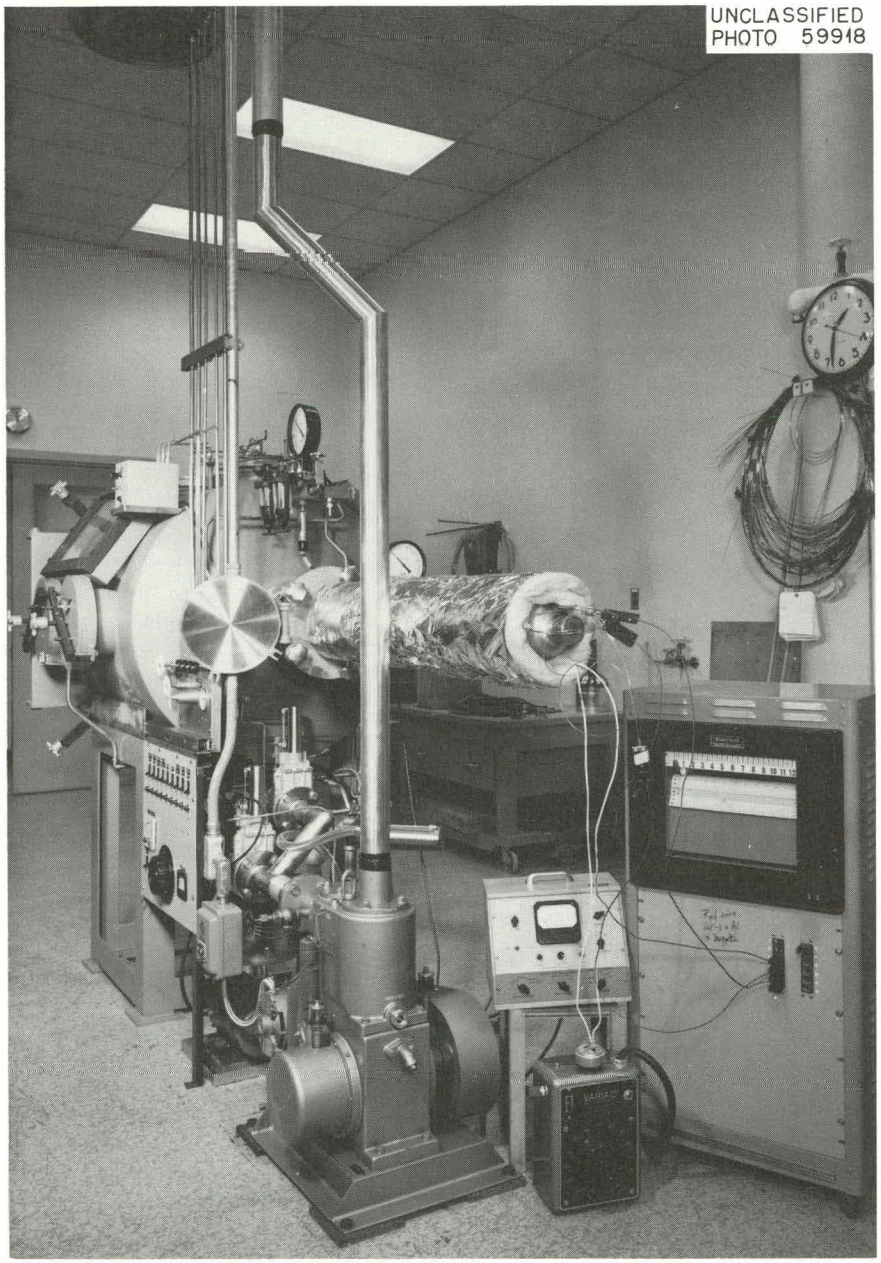

Fig. 3.2. Furnace Extension Used for Outgassing Fuel Rods Loaded with UO_2 Bushings. This unit is attached directly to the welding chamber shown in the background.

are tested as described in the following section, and the fuel bushings are loaded into the rod. If the rod is to include a central thermocouple, the central thermowell is welded in place and leak checked before the bottom end cap is welded in. The only other variation from the assembly

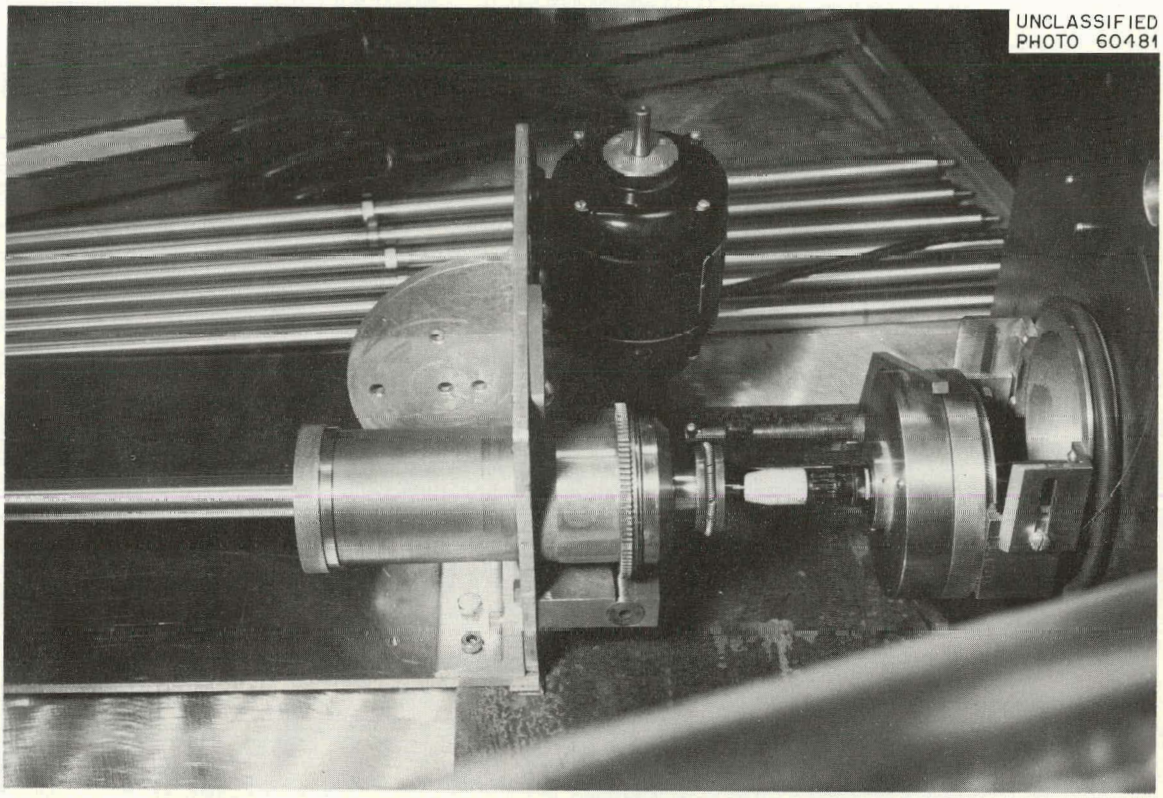

Fig. 3.3. Apparatus for Welding Bottom End Caps of Fuel Rods Inside the Controlled-Atmosphere Welding Chamber.

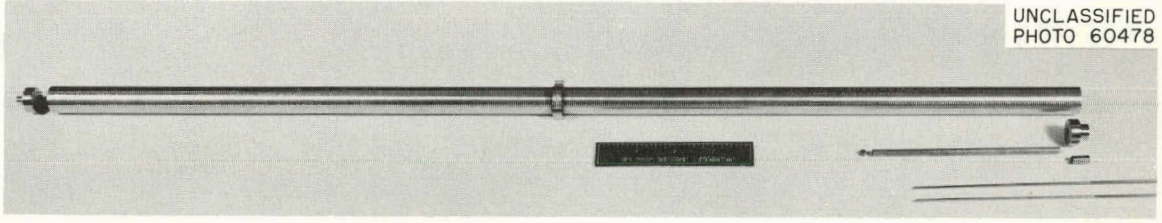

Fig. 3.4. Components of Typical Instrumented Fuel Rod Showing End Caps, Central Thermocouple, and Two Cladding Thermocouples.

sequence described for the uninstrumented rods is that the bottom end cap must be manually welded because the thermocouples prevent automatic rotation of the rod. Special inspections, dimensional measurements, and reports are completed as described for the uninstrumented rods.

Nondestructive Evaluation of Thermocouple-to-Tube Brazed Joints

K. V. Cook

Various inspection methods were investigated, and it was found that a "ringing" ultrasonic technique was applicable for evaluating the brazed joints between the thermocouples and the inner surface of the type 304 stainless steel tubes used in the instrumented fuel assemblies. Preliminary ultrasonic data were generated for a specimen with four thermocouples attached; subsequent destruction of two of the thermocouple-to-tube brazed joints demonstrated that the method could differentiate between unbonded and bonded areas approximately 1/32 × 1/16 in. The two remaining brazed joints contained unbonded areas of comparable size, and hence they served as standards. Nine additional thermocouple-to-tube brazed joints were evaluated, and the results indicated acceptable bonding in all cases.

Oxidation Studies of Nitrided (Malcomized) Type 304 Stainless Steel

B. Fleischer

An experiment was conducted to evaluate the oxidation behavior of nitrided type 304 stainless steel under EGCR coolant conditions. The purpose of the experiment was to examine the properties of the nitrided surface layer being applied to the nozzles of the pneumatic temperature measurement system of the EGCR, since the accuracy of the temperature measurements of the system will be significantly affected by extremely small variations in the nozzle throat area. Also, an alteration of the surface smoothness of the throat would produce a change in the flow characteristics of the nozzle that would, in effect, be similar to that produced

by a variation of the throat diameter. It is clear from these considerations that dimensional stability of the nozzle throat is extremely critical and that tests designed to determine the stability of the surface layer would have to be concerned with extremely small dimensional changes.

Test specimens consisting of four 1/2-in.-diam, 3/4-in.-long rods of cold-rolled type 304 stainless steel were obtained from the Atomic Power Equipment Department of the General Electric Company. Pretest metallographic examinations of the four samples revealed a thin, continuous, nitride case that varied in depth from about 0.004 to 0.007 in., as indicated in the data of Table 3.1, and many imperfections in the nitride layers in the form of circumferential and radial cracks. A system of circumferential cracks that was apparent around the outer edges of specimens 1 and 2 is shown in Fig. 3.5; specimens 3 and 4 had radial cracks such as those shown in Fig. 3.6. Hardness impressions made across the nitrided layers gave an average value of 595 DPH, and the hardness of the base metal averaged 191 DPH.

Table 3.1. Results of Measurements and Oxidation Tests of Nitrided Type 304 Stainless Steel Specimens

Specimen No.	Original Depth of Nitride Case (in.)	Thickness of Layer Removed (in.)	Oxidation Rate in 1000 hr ($mg/cm^2 \cdot hr$)
			$\times 10^{-4}$
1[a]	0.0067		4.39
2	0.0059	0.003	2.35
3	0.0045	0.004	0.668
4	0.0045	0.006[b]	0.314

[a]Tested as received.

[b]Nitride layer completely removed.

Three of the specimens, Nos. 2, 3, and 4, were surface ground to remove 0.003, 0.0045, and 0.006 in., respectively, of the nitride case, and specimen No. 1 was tested in the as-received condition. Oxidation exposures of the specimens were carried out in slowly flowing, 40 cm^3 (STP)/min,

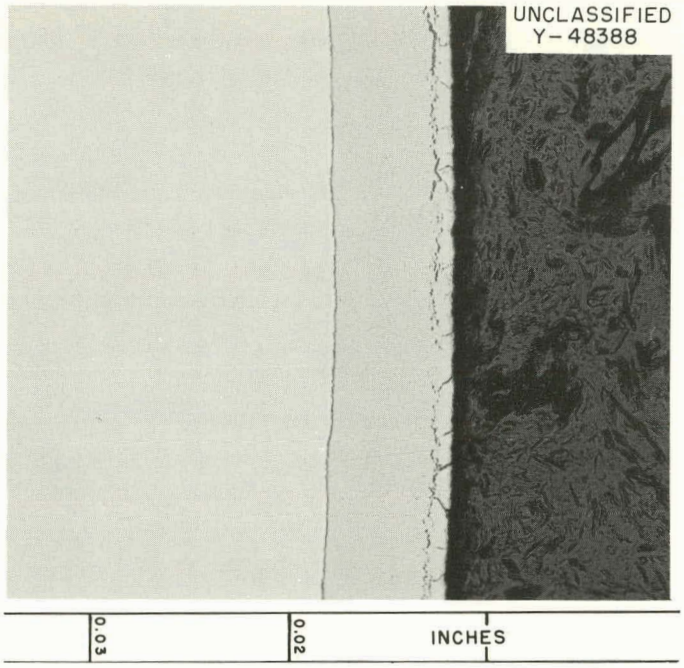

Fig. 3.5. Circumferential Cracks in Nitride Layer of Type 304 Stainless Steel Specimen No. 1. As received. 100X

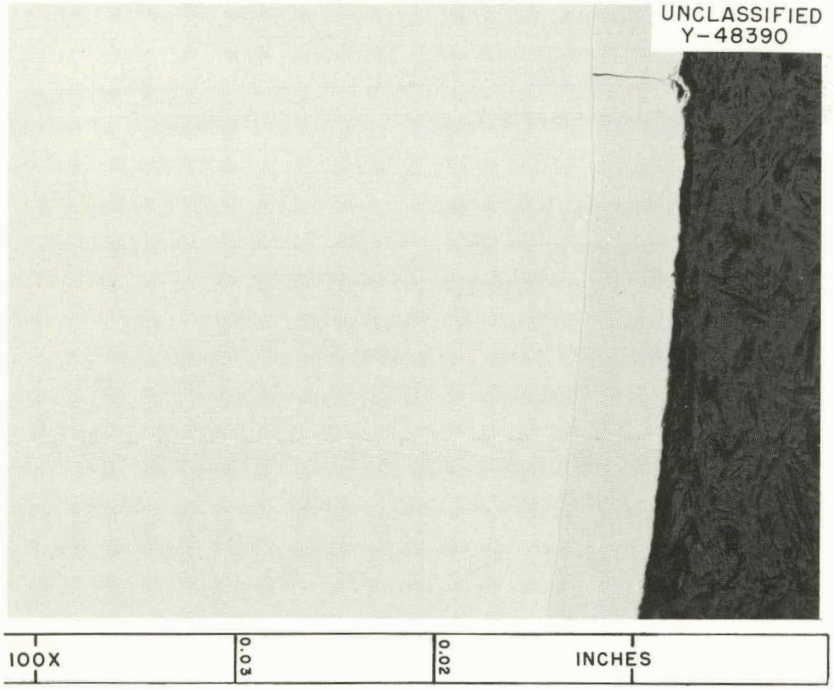

Fig. 3.6. Radial Crack in Nitride Layer of Type 304 Stainless Steel Specimen No. 3. As received.

impure helium at 1050°F. The test gas composition is given below:

Element	Quantity by Volume
CO	0.01%
CO_2	0.13%
H_2	0.17%
N_2	0.013%
H_2O	10 ppm
He	Balance

The weight gains of the surface-ground and as-received nitrided specimens after 1000 hr are listed in Table 3.1. As may be seen, the oxidation rate decreased as a function of the depth of the layer removed by surface grinding. The oxidation rate of the as-received nitrided specimen (No. 1) was about 14 times that of type 304 stainless steel from which the nitride layer had been completely removed. The metallographic appearance of the as-received nitride layer after oxidation is shown in Fig. 3.7. The

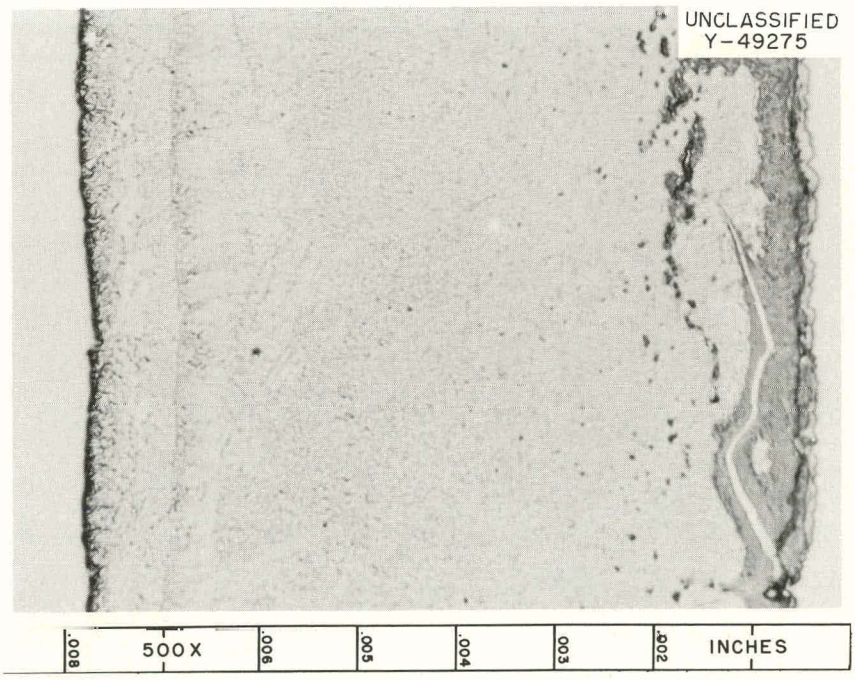

Fig. 3.7. Typical Cross Section of As-Received Nitrided Specimen No. 1 Showing Oxide Layer Produced by 1000 hr of Exposure to Impure Helium at 1050°F.

specimens from which most or all of the nitride had been removed revealed no detectable oxide layer.

Hardness measurements of the nitride layer after exposure to impure helium gave an average value of 513 DPH, a decrease of approximately 80 DPH points from the pretest hardness. The base metal hardness remained unchanged.

The experimental results show that the surface properties of a nitrided case under EGCR conditions tend to change to those of an oxide film. Since the decreased oxidation resistance of the nitrided surface results in increased susceptibility to dimensional change, nitriding may have a detrimental effect on the stability and reliability of the pneumatic temperature measurement nozzles.

Graphite Surveillance Program

M. P. Davis

Surveillance Specimens

A graphite surveillance program is to be carried out in the EGCR to monitor the changes in certain physical, mechanical, and chemical properties of the moderator graphite as a result of neutron irradiation and exposure to oxidizing impurities in the coolant gas. The surveillance will be accomplished by placing various types of AGOT graphite test specimens in channel No. 140, where conditions will be the most severe with respect to neutron flux and temperature (see Chap. 1). The specimens will be placed in graphite sleeves similar to those used for the fuel assemblies and can therefore be handled by the service machine. A schematic drawing of a graphite surveillance assembly, which indicates the relative positions of the graphite specimens and the other components, is shown in Fig. 3.8. The specimens will be identified and arranged in seven layers separated by graphite spacers within each assembly.

The surveillance program calls for removal and testing of 21 sets of specimens over a 20-year period, one set after each of the first two 6-month periods and annually thereafter. Vacated positions in the assemblies

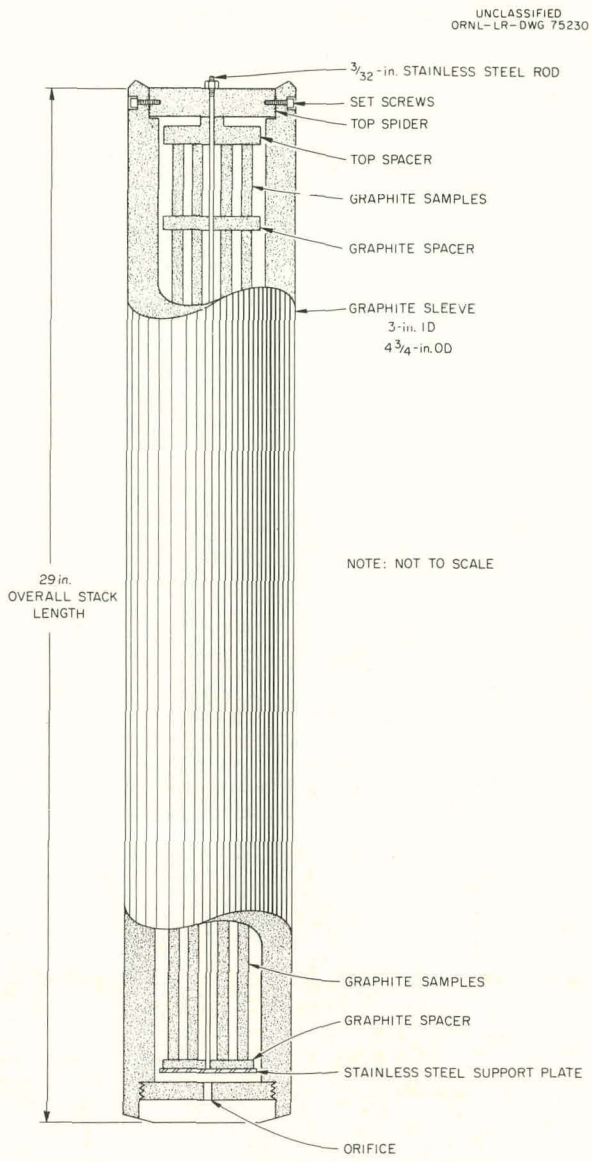

Fig. 3.8. Graphite Surveillance Assembly (Schematic) Showing Positions of Test Specimens and Position of Orifice at the Bottom.

will be filled with "dummy" specimens in the interest of over-all structural stability.

Temperature measurements will be made by the "melt-wire" method; there are no provisions for instrumenting the graphite surveillance channel for temperature measurements by thermocouples. Ten metals or alloys with low neutron-absorption cross sections and known melting temperatures were selected to cover the range 200 to 650°C in 50°C increments. Wires of

these materials will be placed in the center of each assembly in special graphite holders that serve as spacers. An estimate of the maximum temperature achieved will be made by visual examination of the wires upon removal of the assembly. Flux monitors for the graphite surveillance channel are being considered.

The test program has been planned under the assumption that the specimens can be handled outside hot cells with appropriate precautions. Brief descriptions of the planned tests are given below.

Test Program

Dimension and Weight Measurements. The weights and dimensions of all test specimens will be recorded before and after exposure. In addition, certain specimens will be measured and weighed at each scheduled removal and returned to their original positions. Specimens cut with longitudinal axes both parallel and perpendicular to the extrusion direction will be represented.

Room-Temperature Tensile Properties. Load-elongation curves will be prepared for axially loaded tensile specimens to determine the fracture stress, fracture strain, and modulus of elasticity. The limited space available and the large number of samples required to give a statistically meaningful measurement necessitate that tensile properties be measured only parallel to the extrusion axis.

Irradiation-Induced Creep. The permanent set in prestressed specimens of the type shown in Fig. 3.9 will be measured. These data will be used to determine the irradiation-induced creep characteristics of the moderator graphite.

Oxidation Rate in Air. The oxidation rate of irradiated graphite specimens will be determined in flowing air and compared with the oxidation rate of unirradiated specimens taken from the same graphite stock. Oxidation rates will be determined at several temperatures up to 650°C.

Thermal Expansion. The coefficient of thermal expansion will be measured over the temperature range 25 to 1000°C on specimens with axes both parallel and perpendicular to the extrusion direction.

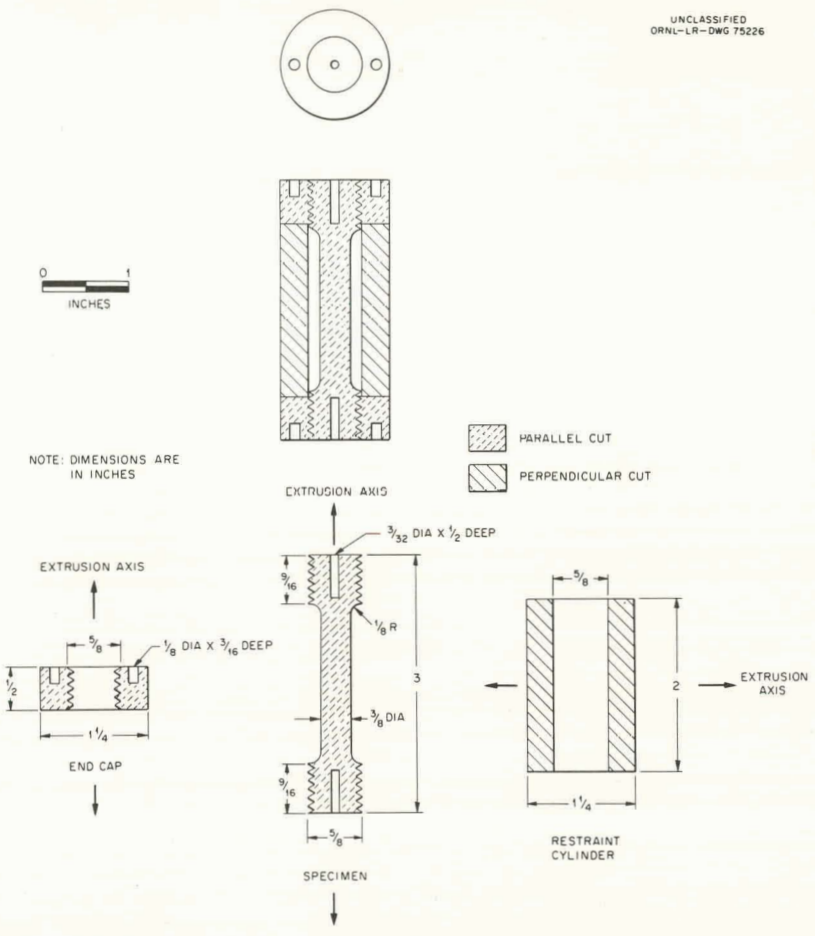

Fig. 3.9. Specimen for Determination of Irradiation-Induced Creep in Graphite.

Thermal Conductivity. The thermal conductivity of irradiated graphite in directions both parallel and perpendicular to the extrusion direction will be measured on cubical specimens.

Stored Energy. Both the total stored energy and the temperature dependence of stored energy release will be determined by heat of combustion and adiabatic calorimeter techniques, respectively.

Quench and Compression Tests of EGCR Fuel Bushings

C. Michelson J. L. Scott

Examinations of capsules containing EGCR prototype fuel bushings that had been irradiated in the ORR poolside facility indicated a tendency of

these bushings to chip and crack, particularly at the edges formed by the intersection of the flats and the outer cylindrical surface. During repeated thermal cycling, many chips formed and migrated into the annulus between the bushing and the cladding and produced easily detectable protrusions and ridges on the cladding surface. Excessive cracking at some bushing-to-bushing interfaces plus external pressure on the cladding also produced localized collapse of the bushings and visible depressions in the cladding. An out-of-pile study of these problems was initiated, and the results of tests of bushing performance under repeated severe thermal cycling and under axial loading are reported here.

One out-of-pile test performed during the development of fuel for the EGCR consisted of successive heatups of a capsule to 1500°F followed by a water quench. Although admittedly a severe test, it was performed at that time on ORNL-fabricated UO_2 bushings to demonstrate the effect of a maximum possible thermal shock. After 100 quenches, radiographs of these bushings showed radial cracks from surface to center and a few axial cracks, but there were no fine chips and no UO_2 fell down the central void in the bushings. In view of this prior favorable test experience, the quench test was selected for evaluating the gross effects of severe thermal cycling on fuel bushings fabricated for the EGCR fuel loading. A cross section of a quench-test capsule is shown in Fig. 3.10.

The first quench-test capsule (XP-TCA) was loaded with fuel bushings from the batch used in the irradiated capsules (ORNL inspection batch No. 3008), and it was subjected to 50 quench cycles. The radiographs shown in Fig. 3.11 were taken at the end of 0, 10, and 50 cycles. Deterioration of the bushings along the external cylindrical surfaces was detectable at the end of 10 cycles and was pronounced at the end of 50 cycles. The fines produced by surface deterioration filled gaps between the bushings and the capsule cladding and formed ridges and protrusions in the cladding during subsequent thermal cycling. Deformation of the cladding was visible at the end of three cycles and continued throughout the test. Diametral growth of 0.030 to 0.050 in. was measured in the region of severest ridging at the end of 50 cycles. An axial growth of 1/4 in. occurred during the test.

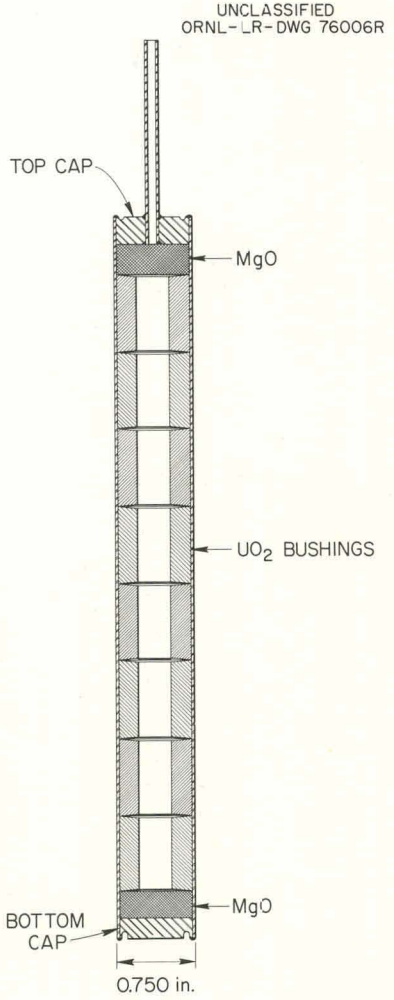

Fig. 3.10. Cross-Section of Quench Test Capsule.

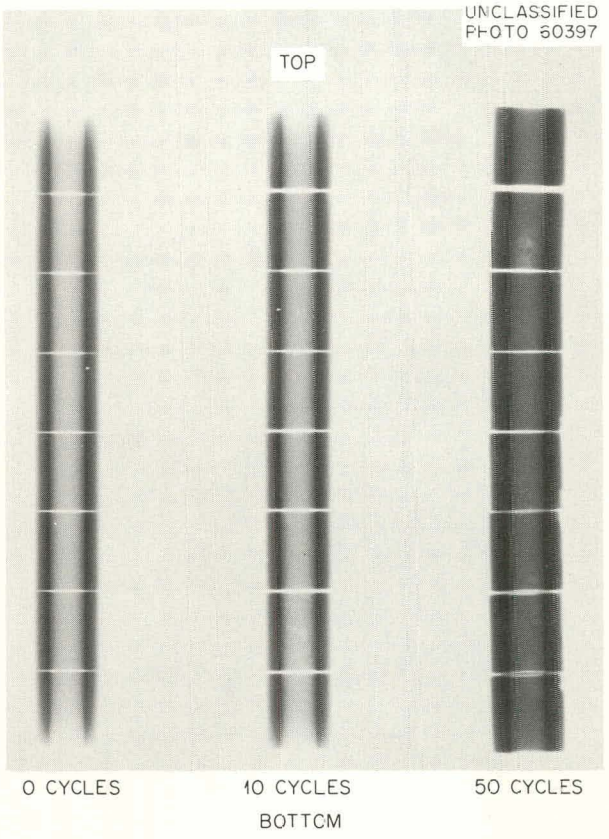

Fig. 3.11. Radiographs of Capsule XP-TCA Before Quench Cycling and After 10 and 50 Cycles.

After dimensioning and radiographing, the cladding on capsule XP-TCA was bisected on a milling machine. The interior of the capsule is shown in Fig. 3.12. The surface deterioration noted on the radiographs appeared as gross chipping of the outer cylindrical surfaces. The capsule elongation appeared as headspace at the top. One favorable observation was the ability of the UO_2 bushings to lock into place instead of falling into the central void.

In order to confirm the previous favorable experience with the quench test, a second test capsule (XP-TCB) was loaded with ORNL-fabricated fuel bushings (ORNL inspection batch No. 3005). These bushings had the same inside and outside diameters as the EGCR bushings but were 3/8 in. instead of 3/4 in. long and had flat faces instead of dished faces. In all other respects, capsule XP-TCB was identical to capsule XP-TCA, including the elimination of all headspace.

Capsule XP-TCB was subjected to 50 quench cycles, and the radiographs shown in Fig. 3.13 were taken at the end of 10 and 50 cycles. No degradation of the UO_2 was observed at the end of 10 cycles. After 50 cycles some axial cracks were detectable, but no deterioration of the cylindrical surfaces was evident. Ridges became visible in the cladding after several cycles, but they did not grow appreciably during the test. A diametral growth of 0.005 to 0.015 in. was measured in the region of severest ridging at the end of 50 cycles. Noises heard when shaking the capsule indicated that some fines were present and that the bushings were free to move. An axial growth of 1/2 in. occurred during the test.

The interior of capsule XP-TCB is shown in Fig. 3.14. The rather disorganized appearance of the bushings is due to penetration of the milling cutter. The significant aspect is the absence of surface deterioration such as that present in Fig. 3.12. Each piece of UO_2 was examined for surface damage, but none was found. Fragments of the ORNL-fabricated bushings demonstrated a marked ability to key into place, as evidenced by the freedom of the bushings to move within the capsule without fragments falling into the central void.

The results of these two quench tests verified the unusual behavior of the EGCR bushings noted following the irradiation tests. A subsequent investigation of possible bushing and cladding interactions indicated

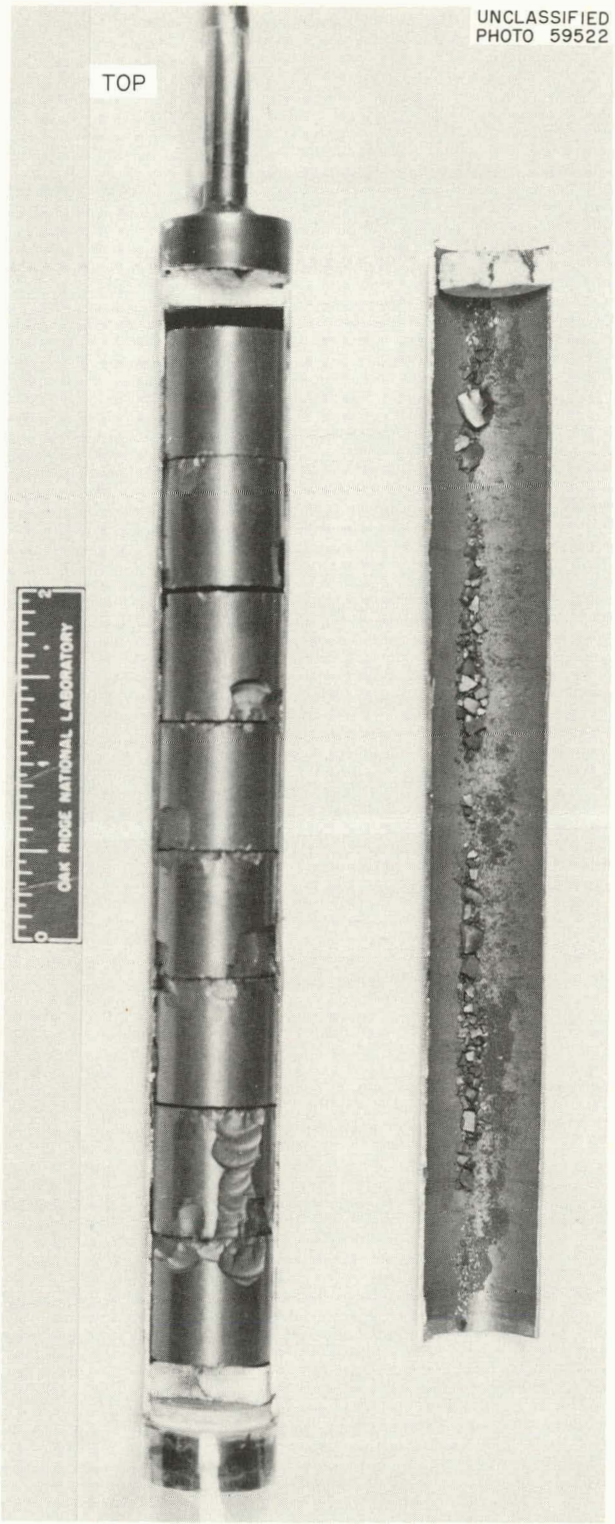

Fig. 3.12. Interior of Capsule XP-TCA after 50 Quench Cycles.

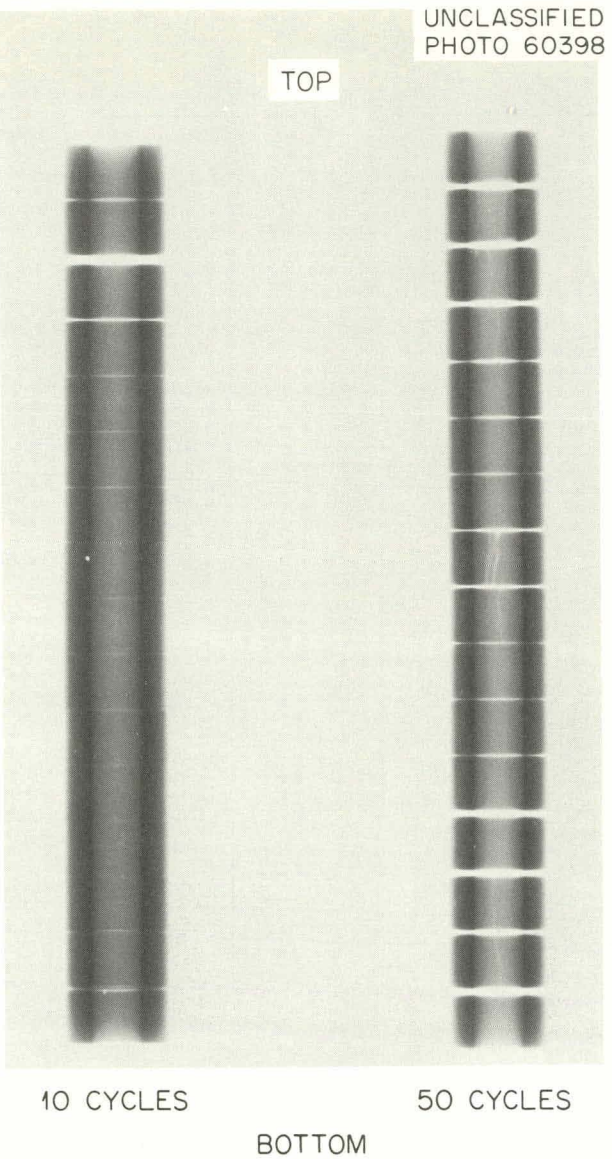

Fig. 3.13. Radiographs of Capsule XP-TCB After 10 and 50 Quench Cycles.

that the principal contributor to EGCR bushing damage was the axial compressive force produced by the cladding during the thermal quench. Similar bushing damage could be expected because of end constraints when the UO_2 is heated rapidly in the reactor.

A third test capsule (XP-TCE) was built to demonstrate that axial constraint produced the bushing damage in capsule XP-TCA. In this capsule a headspace of 0.090 in. was provided to remove the end constraints;

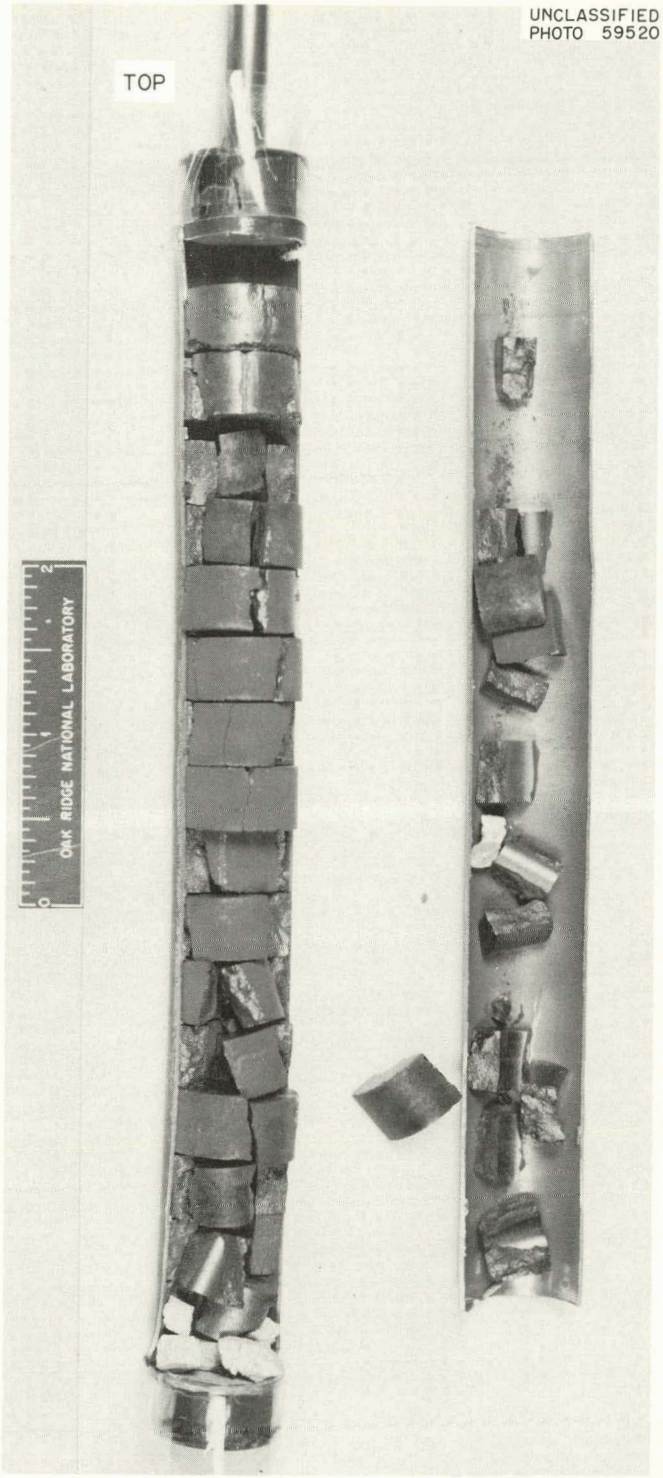

Fig. 3.14. Interior of Capsule XP-TCB After 50 Quench Cycles.

otherwise the capsule was identical to capsule XP-TCA in all respects. Capsule XP-TCE was subjected to 50 quench cycles. Ridges formed on the cladding after several cycles, but they did not expand significantly during the test. The capsule grew about 5/32 in.

An interior view of capsule XP-TCE is shown in Fig. 3.15, the significant aspect of which is the absence of surface chips and the type of deterioration shown in Fig. 3.12. Each bushing was examined, but no chips were found. Considerable milling-cutter damage did occur, however.

A fourth capsule (XP-TCF) was tested to verify that the bushing damage observed in capsule XP-TCA occurred during the first few thermal cycles. This capsule, which was identical to capsule XP-TCA, was subjected to three quench cycles. Severe ridges and protrusions were detectable after the second cycle. Subsequent bisection of the cladding showed that the predicted gross chipping along the outer surfaces did occur during the first three cycles.

After identifying the axial compressive force as the principal damage mechanism, it was necessary to determine the individual bushing features that made them susceptible to damage. To accomplish this, a series of 29 compression tests was performed on ORNL-fabricated and EGCR bushings to study their response to axial loading. For these tests, three or more bushings were placed in a length of capsule tubing (EGCR size) and compressed in a hydraulic press. Total loads of up to 2000 lb were applied. This is the maximum load that room-temperature capsule tubing can apply between end constraints before yielding, and thus represents an upper limit on the axial compressive force in a test capsule or fuel element using EGCR-type cladding.

For the first series of compression tests, EGCR bushings from the batch used in capsule XP-TCA were placed in a 2-in. length of capsule tubing and compressed with loads of 200 to 2000 lb. At 400 lb, visual inspection disclosed a small amount of chipping along the edges formed by the intersection of the cylindrical surface and the end faces. At 800 lb the chips were larger and more numerous. In the range of 1000 to 2000 lb most of the bushings formed many large chips, some extending the full axial length. The amount of chipping at reduced loads varied considerably, but

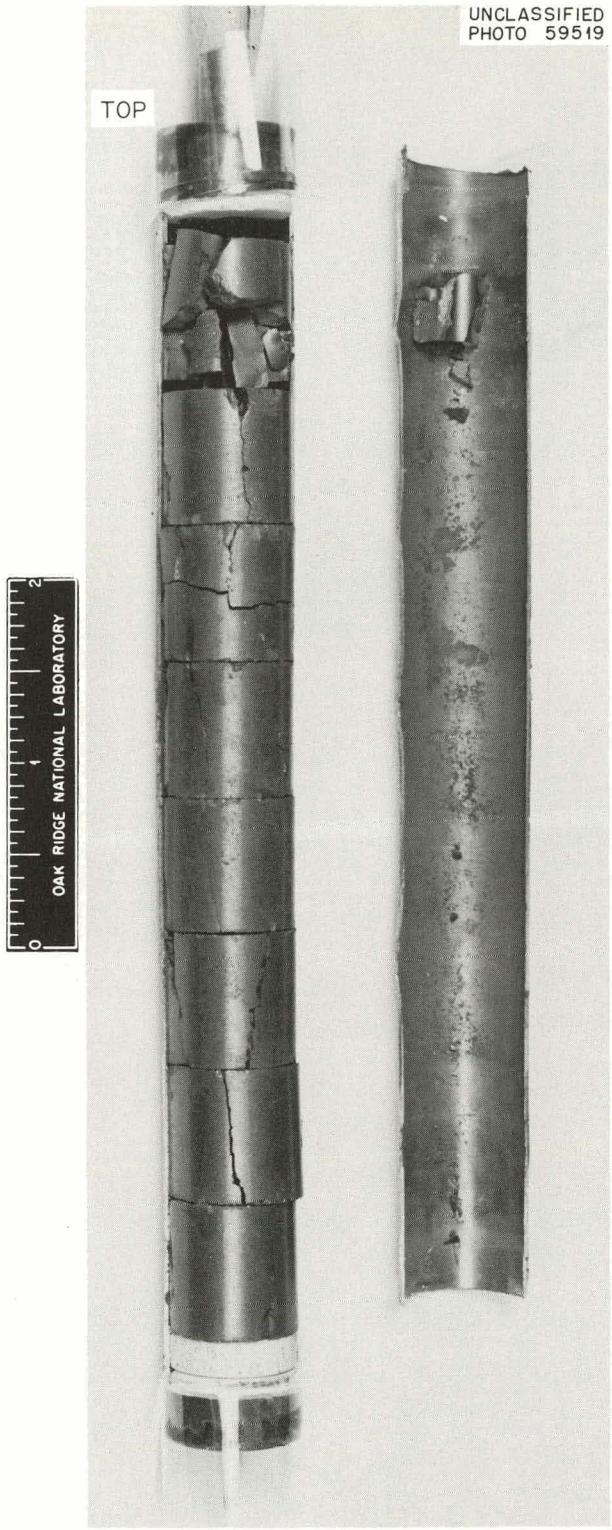

Fig. 3.15. Interior View of Capsule XP-TCE After 50 Quench Cycles.

the surface degradation was of the same general type as observed with similar bushings during the quench tests.

A preponderance of chips along the edges formed by the intersection of the cylindrical surface and the end faces prompted a careful examination of this area. It had been assumed that the bushing faces were dished to a depth of approximately 0.005 in. at the inner surface of the bushing and that the diameter of the dish was approximately 0.600 in. This should have left a relatively flat area approximately 0.053 in. wide between the dish and the outer cylindrical surface.

Depth measurements on several bushings showed the end faces to be dished to a depth of 0.005 to 0.007 in., but in many cases the dish extended to the bushing outer edge and thus provided line or multiple-point contact along the outer edges. In some cases a small flat area was detected, but numerous surface irregularities resulted in multiple-point contact with adjacent bushings. It was along these lines and points of contact that most of the chips and fractures initiated under axial loading.

A second series of compression tests was therefore performed to evaluate possible beneficial effects of removing the line or multiple-point contact by creating a smooth, flat, contact surface. Bushings were selected from the batch used in capsule XP-TCA, and the end faces were deburred until a flat approximately 0.050 in. wide was achieved. When these bushings were compressed, fracture occurred at 1800 lb, and some fines were formed. The significant point was that the absence of chipping and flaking at lower axial loads alleviated the problem of the formation and migration of fines into the interface between the bushings and the cladding.

A quench capsule (XP-TCG) was then tested to verify the beneficial effects of deburring the fuel bushings. This capsule was identical to capsules XP-TCA and XP-TCF, except for the use of deburred bushings. The interior of the capsule is shown in Fig. 3.16 after being subjected to three quench cycles. The bushings were essentially undamaged. Only the bottom bushing was cracked, and no new chipped surfaces appeared on the other bushings.

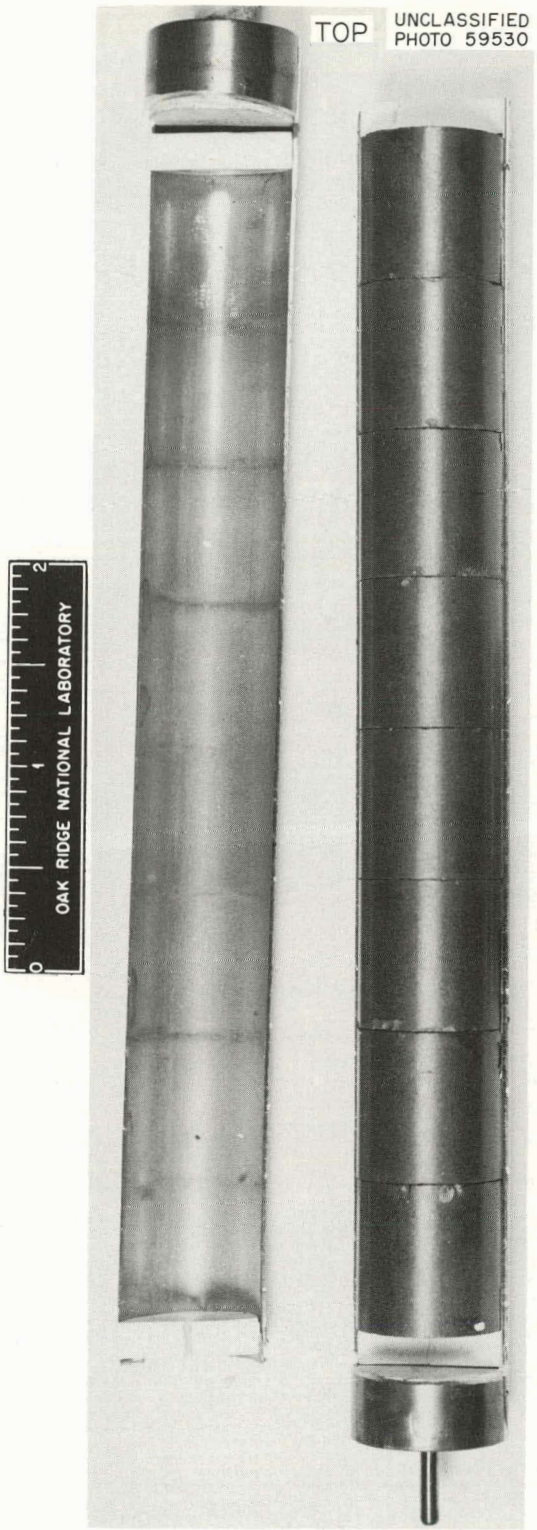

Fig. 3.16. Interior of Capsule XP-TCG After Three Quench Cycles.

Since bushings from many oxide blends were being fabricated for the EGCR, it was necessary to evaluate their behavior under similar test conditions. The test results were essentially the same. In the as-received condition, all bushings cracked and chipped at the edges when compressed with 200- to 400-lb loads. In all cases, such chip formation was significantly reduced by deburring the bushing faces. Although most bushings fractured upon loading to 1200 to 1800 lb, there were significant differences in the nature of the fractures. Bushings fabricated from some oxide blends demonstrated a marked tendency to form numerous fines during fracture.

After completing this phase of the investigation, a die modification was made by the bushing vendor to provide uniform contact at the bushing-to-bushing interfaces. The modified die produced bushings with a uniform flat surface 0.025 to 0.050 in. wide extending inward from the outer cylindrical surface. The flat surface was tapered slightly toward the outer edge to shift the contact between adjacent bushings to a broadly defined line inward from the bushing edge. This line became the high point on the bushing face and was approximately 0.001 in. higher than the bushing face at the outer edge. A production sample from this new die demonstrated satisfactory performance in the compression test. No chips formed below an initial compressive load of 1200 to 1800 lb.

The modified bushing faces were also tested in contact with unmodified faces to determine whether the inverse taper was sufficient to prevent bushing-to-bushing contact along the outer edge. The test results demonstrated the feasibility of this arrangement. In nearly all tests, no chips formed below a compressive load of 1200 to 2000 lb for the bushing stack. The results demonstrated the desirability of alternating modified and unmodified bushings to obtain a reasonably chip-resistant arrangement.

Manufacture of the EGCR Fuel Assemblies

G. M. Tolson

As of March 1, 1963, 756 EGCR fuel assemblies had been received and accepted at ORNL. About 100 more assemblies were at the vendor's plant

awaiting final inspection or shipment. The assemblies are being manufactured by the Westinghouse Electric Company, Atomic Fuel Department, at Cheswick, Pennsylvania.

Pressing and sintering of the UO_2 fuel bushings were halted for approximately three months during this period because of the problems described in the preceding section. Production has been resumed with the modified fuel bushings.

The vendor is now making a precise dimensional inspection of 30 special fuel assemblies destined for thorough postirradiation examination.

EGCR Welding Assistance

G. M. Slaughter

Arrangements were completed for the dissimilar-metal welds in the EGCR primary coolant system to be made at ORNL. Estimates of the cost of the task were prepared, and a purchase order was placed with the International Nickel Company for the necessary welding electrodes. Welding will be initiated as soon as the component pipes arrive from the manufacturer.

Nondestructive Evaluation of EGCR Graphite Cylinders

R. W. McClung

Several 4 1/2-in.-diam, 5-ft-long graphite cylinders were evaluated by radiographic, eddy-current, and ultrasonic methods prior to destructive testing. The pieces tested were removed from the EGCR moderator columns when the fuel channels were machined.

Calibration tests indicated that a radiographic technique was applicable for the detection of voids having dimensions greater than 0.045 in. and cracks or laminations oriented sufficiently parallel to the x-ray beam axis. During the inspections, no voids were detected but several small crack-like indications were noted.

A phase-sensitive eddy-current scan was performed to detect nonlaminar discontinuities near the surface. One cylinder was scanned both helically and longitudinally with circumferential indices. The helical scan

was determined to be the most sensitive to longitudinal defects and was used on the remaining cylinders. Longitudinally machined notches were used for calibration. Those which were 0.100 in. or more in depth were readily detected. Although no direct relation has been established between these notches and actual discontinuities, they do provide a qualitative indication of flaw size. The scan recordings revealed considerable variation in electrical conductivity in each cylinder but nothing that could be readily identified as an abrupt discontinuity, such as a crack.

Both pulse-reflection and through-transmission ultrasonic inspection techniques were applied to the cylinders. In both cases the variable ultrasonic attenuation and the inhomogeneous ultrasonic properties created so many signals that interpretation was impossible.

4. IRRADIATION TESTING OF COMPONENTS AND MATERIALS

D. B. Trauger O. Sisman

Instrumented Fuel Element Irradiations in GCR-ORR Loop No. 1

J. K. Franzreb

ORR gas-cooled loop No. 1, which was designed to test metal-clad fuel elements, has now been in continuous service for 22 months. To date, the loop has been used for evaluating EGCR pressure-vessel steel weld metal specimens, fuel elements that simulate those of the EGCR first core design, EGCR instrumented fuel elements, and new elements having roughened surfaces applicable to future designs, including the second core for the EGCR. The eight instrumented fuel elements that have been tested operated in the power range 21,000 to 42,000 Btu/hr·ft. The reliability of the loop has been excellent, and the helium and water leaks encountered earlier have largely been eliminated.

Two fuel elements tested in the loop are now known to have leaked during irradiation. Element No. 7C was observed to have four pin-holes randomly spaced in the cladding upon examination in the hot cell. Element No. 9 had a section of small tubing connected to the top end cap to facilitate sampling for fission-gas-release determinations in the hot cell, and a leak was found in this tubing following irradiation. It is significant to note that during loop operation with these elements, the radioactivity in the piping was not great enough to be detected by radiation monitors sensitive to 1 mr/hr measured at pipe-wall contact. Very small amounts of Xe^{133} were found by gamma-ray spectrometer analysis of gas samples taken from the loop. Beta-gamma activity inside the compressors at shutdown was approximately 20 mr/hr, compared with 10 mr/hr following operating periods with no fuel element leakage. This indicates that leaking, ruptured, or ventilated elements may constitute a much smaller problem than supposed earlier. In fact, this experience indicates the desirability of further tests in the loop with deliberately vented elements to determine whether such elements can be used in the EGCR. Ventilation would permit the use of thinner cladding and an improved fuel element design.

Fuel elements with roughened surfaces have also been tested in the loop, one for a single ORR cycle and a second for two cycles. The performance of these elements, Nos. 8 and 8S, is compared with that of a smooth surface element, No. 9, in Table 4.1. These elements were of approximately the same power rating and general design and were tested under similar conditions of maximum cladding temperature and gas flow in the loop. It is apparent in Table 4.1 that a significant improvement in heat transfer is achieved with the roughened surface elements. Additional tests will be conducted with new elements operating at higher specific powers to further evaluate the potential of the roughened surface elements.

Table 4.1. Comparison of Performance of Fuel Elements 8, 8S, and 9

Cladding material: type 304 stainless steel
Cladding outside diameter: 0.750 in.
Cladding wall thickness: 0.020 in.
Element heat rate: 40,000 ± 2,000 Btu/hr·ft
Maximum cladding temperature: 1500°F

Element No.	Cladding Surface	Gas Exit Temperature (°F)	Difference Between Cladding and Gas Exit Temperature (°F)	Gas Temperature Rise from Inlet to Outlet (°F)	Central Fuel Temperature (°F)
9	Smooth	920	540	230	2400
8	Roughened with 0.0063-in.-diam wire at a 0.090-in. pitch	1100	400	210	2400
8S	Roughened with 0.0063-in.-diam wire at a 0.040-in. pitch	1250	250	220	(a)

[a]Thermocouple failed.

Fueled Capsule Irradiations in ETR

F. R. McQuilkin

Capsule E-8, which is an EGCR prototype-diameter specimen, was discharged from the ETR February 18, 1963. Irradiation of the remaining ten

capsules continues. A summary of the status of the program at the end of ETR cycle 52 (Feb. 18, 1963) is presented in Table 4.2.

When discharged, capsule E-8 had only one operating thermocouple. Although continuation of irradiation would have been acceptable under special operating procedures, the capsule was discharged for examination to obtain comparisons with capsule E-6 and capsules E-1A and E-4, which had ruptured.[1,2] Capsule E-5, which was scheduled for removal, will remain in the reactor to achieve the high burnup scheduled for capsule E-8. Since capsule E-5 now has a higher burnup than capsule E-8, the time required for obtaining the original target burnup of 13,000 Mwd/MT for one capsule has been decreased. Capsule E-8 had operated appreciably above the rated design power during portions of its irradiation, as had capsule E-1A, E-4, and E-6; however, capsule E-8, which was fueled with hollow pellets, was the only one operated with a cladding surface temperature of 1600°F.

Fueled Capsule Irradiations in ORR Poolside Facility

V. A. DeCarlo F. R. McQuilkin

Capsules 03-6, 05A-6, and 06A-6 were discharged from the ORR poolside irradiation facility during this reporting period. Operating data for these capsules, which contained EGCR fuel specimens, are presented in Table 4.3. Capsules 03-6 and 05A-6 were replaced with capsules 03A-6 and 05B-6. Capsule 03A-6 is a duplicate of capsule 03-6, but it is operating at a maximum cladding temperature of 1300°F, as compared with 1600°F for capsule 03-6. Capsule 05B-6 is similar to capsule 05A-6, except that it contains UO_2 pellets prepared from virgin UO_2 powder and the outer edges of the dished ends were ground flat to obtain lands 0.002 to 0.005 in. wide. The pellets in capsule 05A-6 were fabricated from reprocessed fuel

---

[1]F. R. McQuilkin, Fuel Capsule Irradiations in ETR, pp. 61 and 63, "GCRP Quar. Prog. Rep. March 31, 1962," USAEC Report ORNL-3302, Oak Ridge National Laboratory.

[2]F. R. McQuilkin, Fuel Capsule Irradiations in ETR, pp. 93–95, "GCRP Semiann. Prog. Rep. Sept. 30, 1962," USAEC Report ORNL-3372, Oak Ridge National Laboratory.

Table 4.2. Status of EGCR Prototype-Diameter Capsule Irradiations in ETR Through Cycle 52

Capsule No.	Fuel		Design Cladding Temperature (°F)	Effective Thermal Neutron Flux (neutrons/cm^2·sec)	Design Burnup Rate[a] (Mw/MT of UO_2)	Total Burnup (Mwd/MT of UO_2)		Ratio of Actual Power to Design Power[a]			Discharge Date
	Type	Number of Pellets				Target	Estimated Actual[b]	Maximum	Minimum	Cycle 52	
Capsules Currently Operating											
E1R	Solid	10	1600 max	4.2×10^{13}	12.71	6,000	4,400	1.12	0.38	0.73	
E2	Solid	10	1300 av	4.2×10^{13}	12.70	13,000	2,500	0.60	0.19	0.50	
E3	Solid	10	1600 max	4.2×10^{13}	12.70	13,000	5,000	1.11	0.20	0.99	
E4R	Solid	10	1300 av	4.2×10^{13}	12.91	6,000	3,900	0.97	0.23	0.80	
E5[c]	Hollow	12	1300 av	3.7×10^{13}	16.55	6,000	7,300	0.99	0.41	0.96	
E5R	Hollow	12	1600 max	3.9×10^{13}	16.68	6,000	5,700	1.17	0.43	0.76	
E7[c]	Hollow	12	1300 av	3.6×10^{13}	16.25	13,000	10,200	1.70	0.71	0.90	
E10	Central BeO rod	12	1600 max	3.7×10^{13}	16.09	6,000	5,900	1.06	0.25	0.88	
E11	Central BeO rod	12	1300 av	3.9×10^{13}	16.47	6,000	4,300	0.79	0.25	0.63	
E12R	Hollow	12	1600 max	3.9×10^{13}	16.47	13,000	3,400	0.98	0.63	0.63	
Discharged Capsules											
E1[c]	Solid	12	1300 av	4.3×10^{13}	12.8	1,000	630[d]				10-18-59
E1A[c]	Solid	11	1300 av	4.3×10^{13}	13.1	3,000	5,050[e]	1.61	0.76	1.61	10-2-61
E4[c]	Solid	10	1300 av	4.3×10^{13}	13.1	6,000	7,300[e]	1.66	0.75	1.35	3-21-62
E6[c]	Hollow	12	1300 av	3.7×10^{13}	16.5	6,000	7,550	1.49	0.57	0.95	9-19-62
E8	Hollow	12	1600 max	3.6×10^{13}	16.24	13,000	6,900	1.27	0.24	0.95	2-18-63
E9[c]	Central BeO rod	12	1300 av	3.6×10^{13}	16.3	3,000	2,300[e]	1.20	0.73	0.73	11-2-60
E12	Central BeO rod	12	1600 max	3.9×10^{13}	16.5	13,000	1,140[e]	0.46	0.34	0.41	6-7-61

[a] Design power rating for ETR capsules is 35,000 Btu/hr·lin ft.

[b] Burnup estimated as of Feb. 18, 1963 based on temperature measurements, except where noted.

[c] These capsules were fabricated with a 0.005-in. gas gap.

[d] Based on Cs^{137}.

[e] Based on Ce^{144}.

Table 4.3. Summary of Operating Data for Capsules 03-6, 05A-6, and 06A-6 Fabricated from Westinghouse EGCR Tubing and Westinghouse-Fabricated Fuel

Type of capsule: eight UO_2 pellets in type 304 stainless steel tubing
Maximum cladding outer surface pressure: 300 psig
Estimated fuel central temperature: 2200°F
Calculated effective thermal-neutron flux: 1.62×10^{13} neutrons/cm^2·sec
Fuel density: 95.44% of theoretical
Fuel enrichment: 2.46% U^{235}
Fuel oxygen-to-uranium ratio: 2.001
Total calculated power: 30,000 Btu/hr·ft
Total heat flux: 152,860 Btu/hr·ft^2

Capsule number	03-6	05A-6	06A-6
Origin of fuel specimen	Virgin material	Reprocessed material	Reprocessed material
Fuel batch identification	3008	3013	3013
Irradiation starting date	9-23-62	11-25-62	11-25-62
Irradiation ending date	11-25-62	1-13-63	1-13-63
Irradiation time normalized to operation for 30 Mwd	51.9	41	41
Calculated total burnup, Mwd/MT of UO_2 specimen	721	570	570
Burnup rate, Mw/MT of UO_2 per day at full power	13.9	13.9	13.9
Cladding outer surface temperature, °F			
Design maximum	1600	1600	1600
Highest reading for entire run	1610	1600	1600
Lowest reading for entire run	1330	1180	1165
Average reading for entire run	1480	1420	1415

and the dished ends were not ground to obtain flat edges. The other group VI capsules are described in Chapter 6, this report.

Examination of Irradiated Capsules and Fuel Elements

J. G. Morgan H. E. Robertson
D. F. Toner E. L. Long, Jr.
M. F. Osborne C. D. Baumann

ORR-Irradiated EGCR Prototype-Diameter Capsules 02-5 and 07-5

Capsules 02-5 and 07-5 were irradiated for about 5 months in the ORR poolside facility at an average cladding temperature of 1400°F. Preliminary postirradiation examination revealed several failure areas in the cladding and the pressure-transducer capillary tubing.[3] These failures were confirmed when Cs^{137} activity was found in the NaK coolant, and metallographic sections were taken at some of the failed areas. Dimensional data for each fuel element showed that the maxium deviation from preirradiation diameters was 0.005 in., except at depressions associated with missing fuel. Capsule 02-5 had a 0.012-in. bow, and capsule 07-5 had a 0.016-in. bow, both at midplane.

When these capsules were sectioned, NaK was found inside. The fractured capillary tubes were the most probable points for NaK entrance, although NaK may have been forced through holes in the cladding. Studies are currently under way to determine the size of hole required to allow NaK passage at a pressure of 300 psig. The fractured pellets from the lower half of capsule 02-5 are shown in Fig. 4.1. The severe fracturing shown is irregular and may be associated with the method of pellet fabrication. A similar fracture pattern was found in capsule 07-5 (Fig. 4.2). The pellets in both of these capsules were taken from Westinghouse production batches. A depression in the cladding, which was reported previously,[1] may be seen at the pellet-to-pellet interface in Fig. 4.2. Although the UO_2 in both elements was severely fractured, no UO_2 was found at the bottom of the central void, as previously suggested.[1]

---

[3]J. G. Morgan et al., Examination of Irradiated Capsules, pp. 95–100, "GCRP Semiann. Prog. Rep. Sept. 30, 1962," USAEC Report ORNL-3372, Oak Ridge National Laboratory.

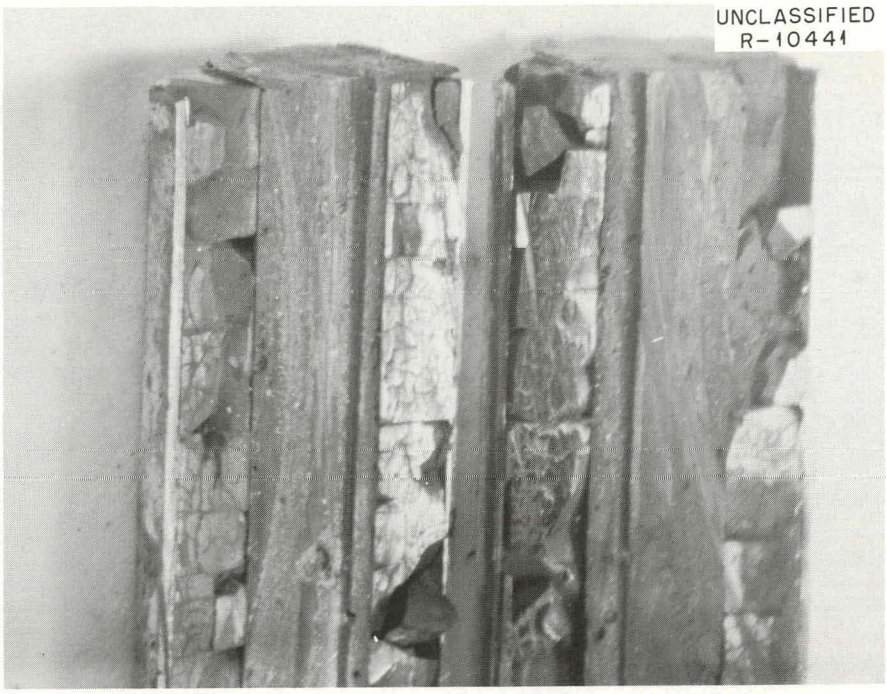

Fig. 4.1. Cracked UO_2 Pellets in Capsule 02-5. The central void was filled with epoxy resin. Mating halves of the capsule are shown.

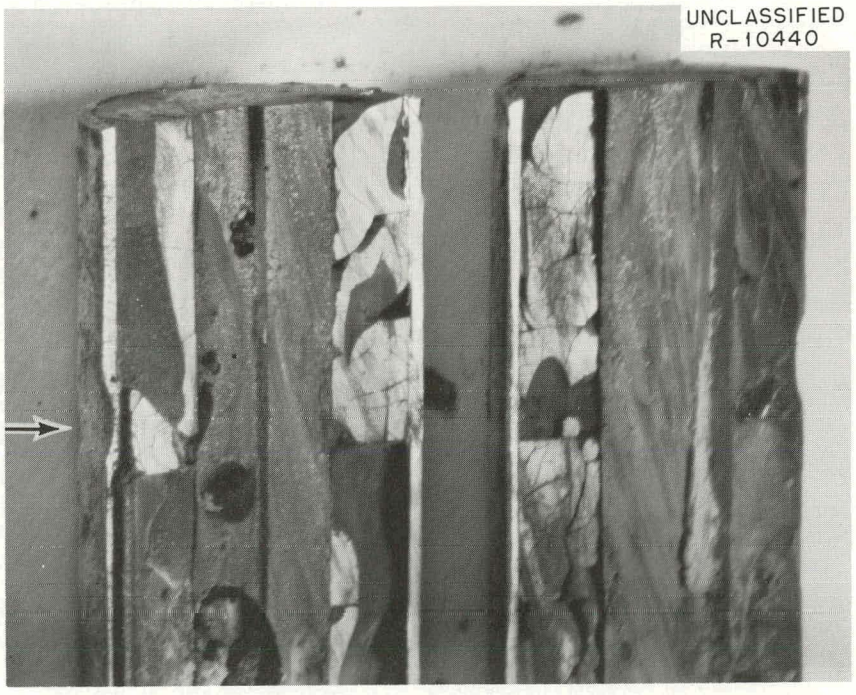

Fig. 4.2. Cracked UO_2 Pellets from Capsule 07-5. The depression and fracture pattern at the pellet-to-pellet interface is indicated by the arrow. Mating halves of the capsule are shown.

Burnup was determined by radiochemical analyses for Cs^{137}, Ce^{144}, and Zr^{95} on specimens from the mid-length of both capsules. The values for these three isotopes respectively were 1711, 1424, and 1746 Mwd/MT of uranium for capsule 02-5 and 1637, 1367, and 1600 Mwd/MT of uranium for capsule 07-5. The Ce^{144} value was low in both cases and is thought to be wrong.

Metallographic Examination of Capsule 02-5. A metallographic examination was made of the capillary tube that had fractured at the juncture with the pressure-sensing transducer of capsule 02-5. The fracture region is shown in Fig. 4.3. The examination revealed several facts: (1) the end of the capillary tubing that was attached to the transducer had been drilled off center prior to assembly and as a result the wall thickness in one area was approximately one-half the original thickness; (2) the tubing was probably type 347 stainless steel rather than type 304 stainless steel; (3) the failure did not occur in a weld, as was presupposed; (4) the fracture was a rapid, ductile break and occurred while the capsule was in the reactor, as evidenced by the absence of twinning and creep cracks and by the presence of recrystallization along the fracture surfaces.

A transverse section of the cladding about 2 in. from the bottom of the capsule was examined for a leak that was observed during leak testing in the hot cell. Although the actual leak was not found, a region was found in the cladding where many intergranular voids were present. The cladding was slightly deformed in this region. This region and a typical region of the cladding are shown in Fig. 4.4. Other regions examined included the top end plug welds and brazed joints and the capillary sleeve joints. These specimens contained leak-suspect areas, but no leaks were found metallographically.

Metallographic Examination of Capsule 07-5. A metallographic examination was made of a depression found in the cladding near the bottom of capsule 07-5. A longitudinal section through the depression did not reveal a continuous break through the cladding; however, the frequency of intergranular voids was high. Most of the intergranular voids were parallel to the surface of the cladding. A portion of the depression is shown in Fig. 4.5. Deformation of the cladding ranged from 4 to 10% on the

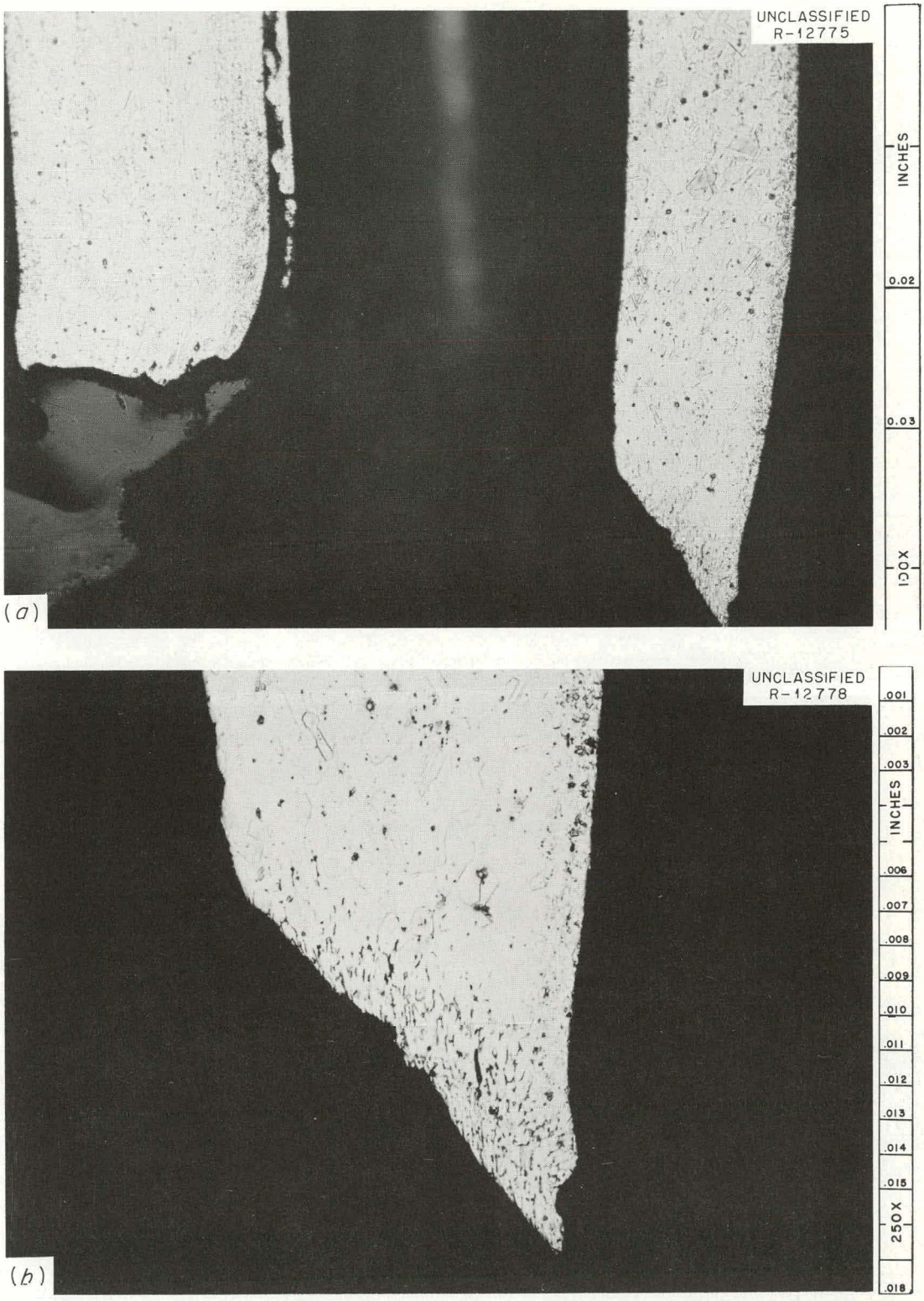

Fig. 4.3. Fractured Capillary Tube that Connected the Pressure Sensing Transducer to Capsule 02-5. (a) Note difference in wall thickness. (b) Note small grains along fracture. Etched.

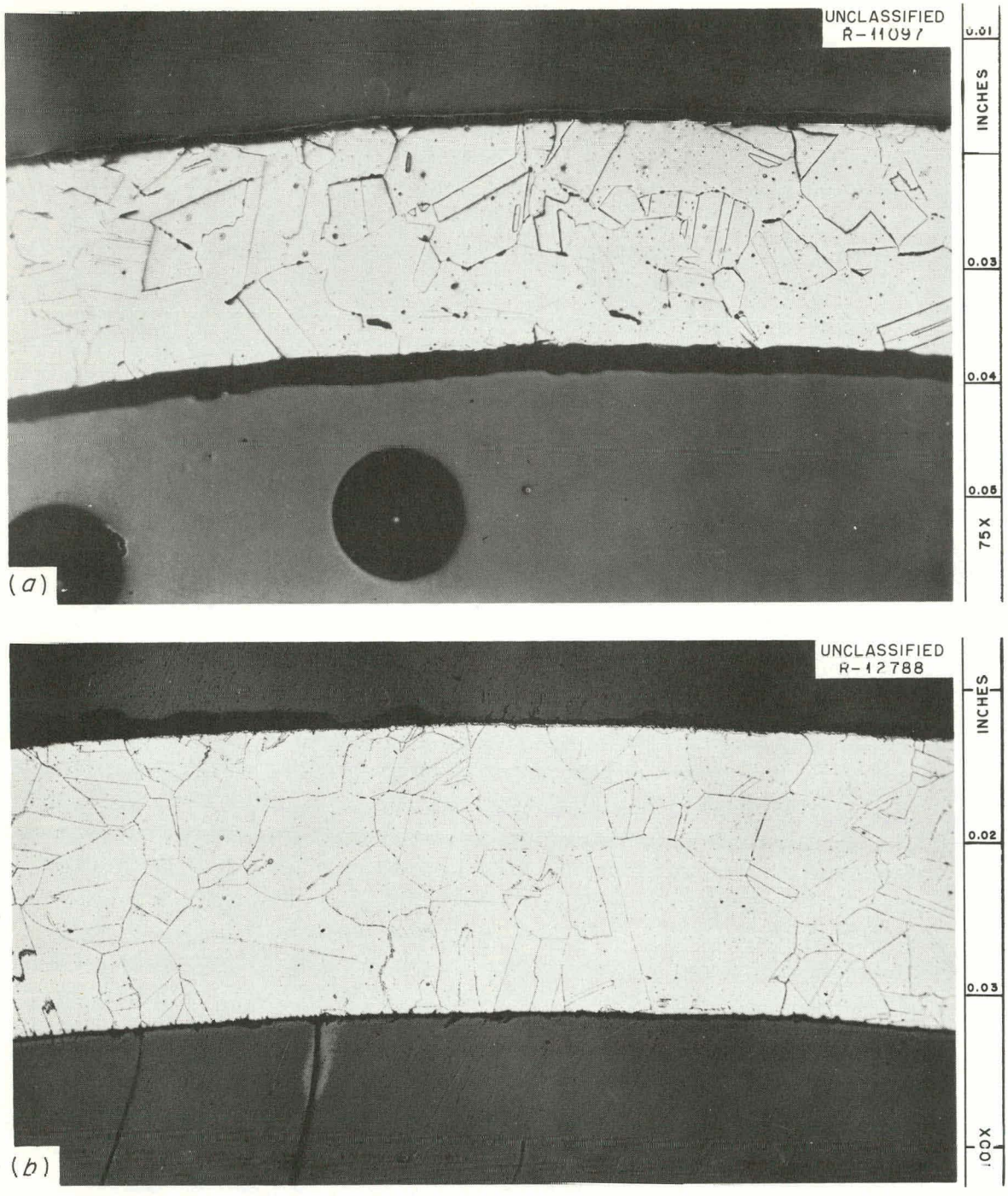

Fig. 4.4. Areas from Transverse Sections Through the Type 304 Stainless Steel Cladding of Capsule 02-5. (a) Region near a leak; note intergranular voids. (b) Typical appearance of cladding. Etched.

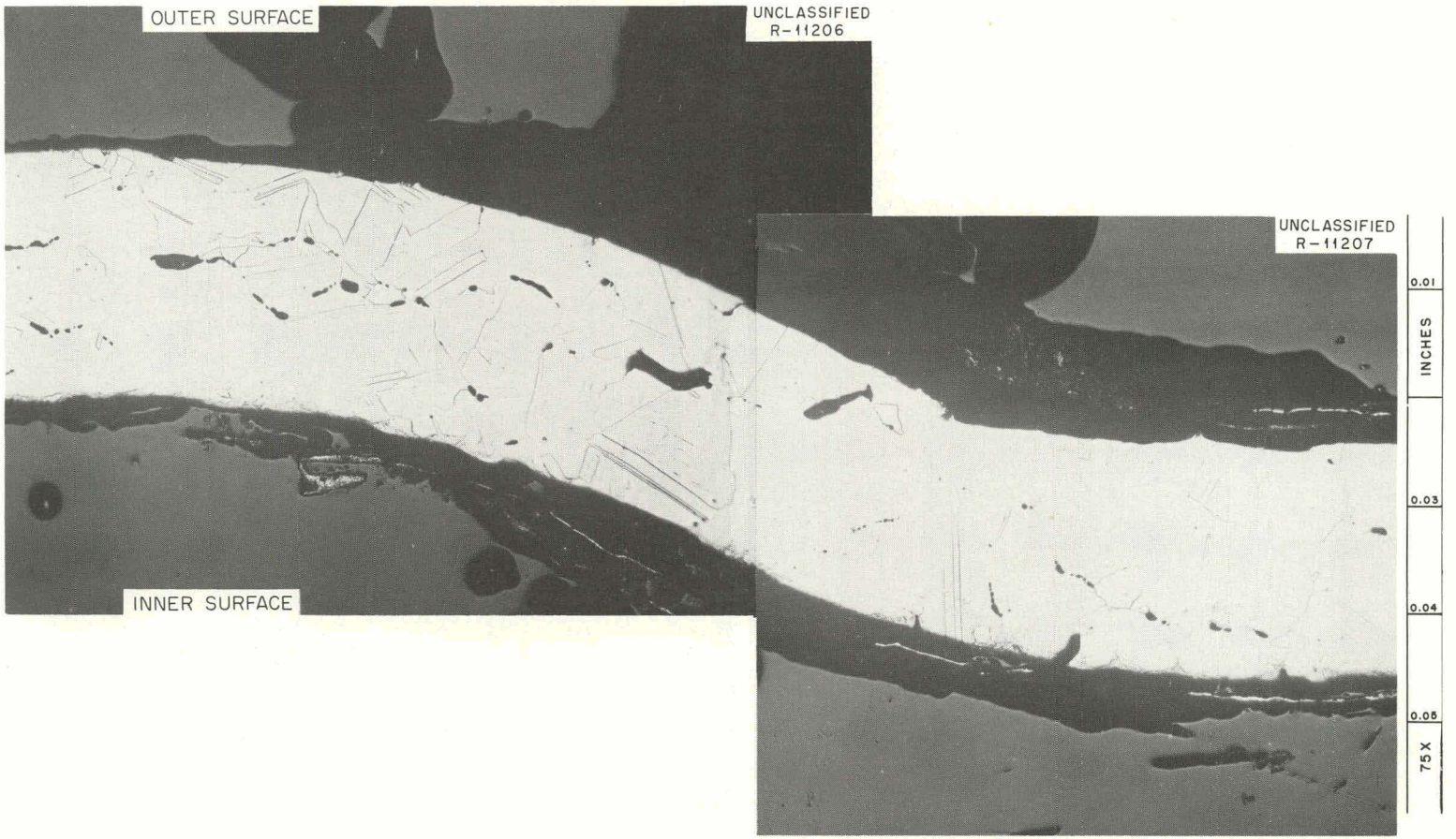

Fig. 4.5. Portion of Longitudinal Section Through the Depression in the Cladding of Capsule 07-5. Etched.

outer surfaces in the depressed region. Intergranular separation normal to the surfaces of the cladding was observed at the edges of the depression.

A longitudinal section was made through the top end plug in order to examine the capillary tube brazed joint, which apparently leaked during the in-cell leak test. While lapping the longitudinal section, it was found that the capillary tube was not parallel to the long axis of the capsule but, rather, was slanted about 15°; thus examination of the entire braze was impossible. A fracture was found in the braze, however, that originated at the outer surface of the top end plug and penetrated the braze to a depth of at least 0.08 in., that is, slightly less than one-half the thickness of the end plug in this region. The fracture in the brazed joint is shown in Fig. 4.6.

Sections through the lead tube weld, the capillary tube sleeve, and the plug head from the lead tube were examined for leaks. None of these areas showed evidence of actual or potential failure.

ORR-Irradiated French Capsules 04-5 and 05-5

Two thin-walled type 347 stainless steel-clad UO_2-fueled capsules fabricated by the French Commissariat a l'Energie Atomique were irradiated in the ORR poolside facility. These capsules were about 6 in. long and 0.46 in. in diameter, and they contained solid UO_2 pellets about 0.4 in. long and 0.43 in. in diameter. The irradiation conditions are listed in Table 4.4. During irradiation, temperature oscillations of ±100°F and ±50°F occurred in capsules 04-5 and 05-5, respectively, because of unstable heat transfer conditions in the NaK coolant.

The postirradiation examination of capsule 04-5 revealed that even burnup had been obtained. No separations between pellets were noted, and dimensional stability during irradiation was excellent. No changes in length or diameter were noted, except for a 0.002-in.-diam collapse of the cladding in the midsection of the fuel column. Two pinhole leaks were found in the cladding by noting a stream of bubbles when the capsule was submerged in oil under vacuum. These leaks, which were not found during metallographic examination of the failure areas, were substantiated by analysis of a white deposit between the fuel and cladding in the area

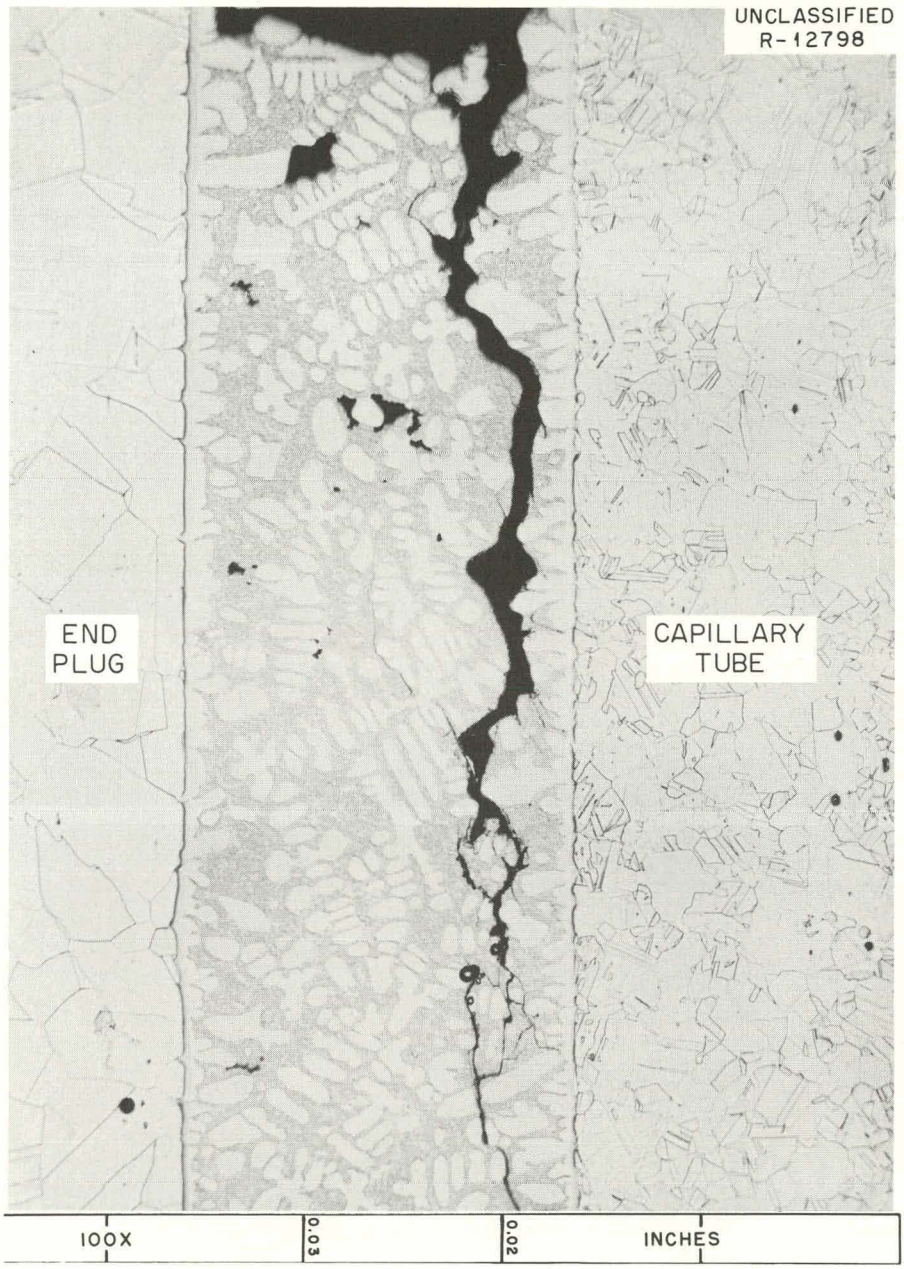

Fig. 4.6. Longitudinal Section Through Capillary Tube to Top End Plug Brazed Joint of Capsule 07-5. Etched.

of one of the leaks (see Fig. 4.7). The deposit was principally sodium, potassium, iron, chromium, and nickel. The sodium and potassium were probably present because of NaK leakage into the capsule.

The results of the postirradiation examination of capsule 05-4 were identical with those for capsule 04-5 except that no leaks or white deposits

Table 4.4. Conditions of ORR Irradiation of French Capsules 04-5 and 05-5

	Capsule 04-5 (CEA I-4)	Capsule 05-5 (CEA I-1)
Cladding thickness, in.	0.0126–0.0134	0.0118–0.0126
Cladding temperature, °F		
Maximum	1370	1270
Average	1140	1154
Cladding outer surface pressure, psig	850	850
Thermal-neutron flux, neutrons/$cm^2 \cdot sec$	5.4×10^{13}	4.8×10^{13}
Burnup, Mwd/MT of U	7470	7610

Fig. 4.7. UO_2 Pellets from Capsule 04-5 Showing White "NaK" Deposit.

were found. The pellets were cracked as in capsule 04-5, as shown in Fig. 4.8.

Samples of gas were removed from each capsule prior to sectioning, and the mass spectrometer analyses of the samples are listed below:

	Gas Analysis (vol %)	
	Capsule 04-5	Capsule 05-5
H_2	0.23	0.60
He	2.45	4.31
CH_4	0.02	0.03
H_2O	0.56	3.48
Hydrocarbon	0.02	
N_2 + CO	0.43	0.49
O_2	0.01	0.01
Ar	0.04	0.01
Kr	9.92	9.29
Xe	86.32	81.77

There is little difference between the two analyses, except for the high water content in capsule 05-5, which has not been explained. The fission-gas release was determined by measuring the Kr^{85} present in each capsule and dividing by the total generated during irradiation. Capsule 04-5 released 3.3% of the Kr^{85} generated and capsule 05-5 released 5.4%. Some of the gas from capsule 04-5 may have escaped through the cladding fracture during irradiation.

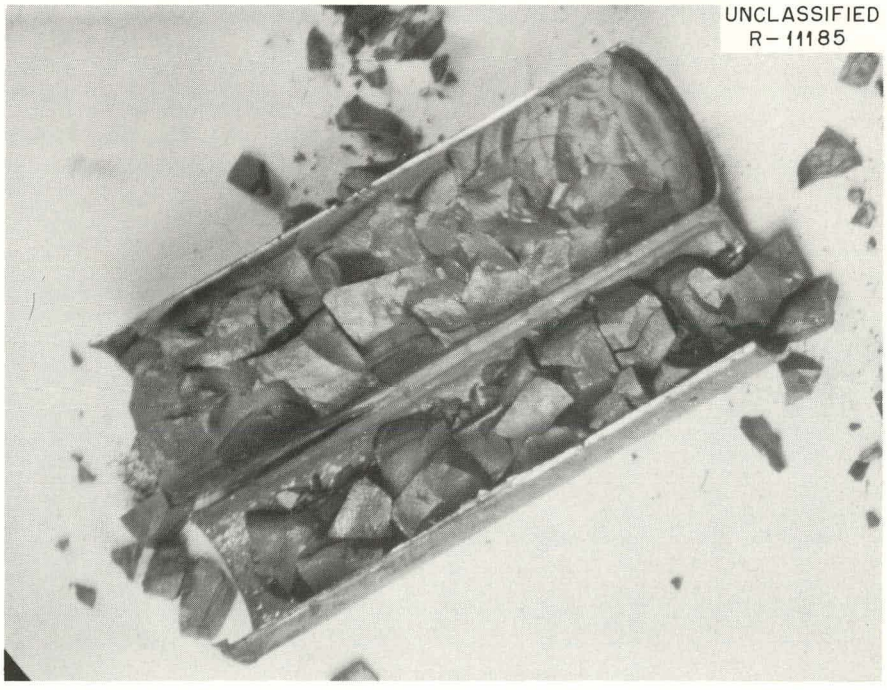

Fig. 4.8. UO_2 Pellets from Capsule 05-5. No white deposits are visible on the pellets.

Two specimens from an unirradiated control capsule were sectioned for metallographic examination of a transverse section from near the mid-length and a longitudinal section through the top portion. Longitudinal sections through the top and bottom portions and transverse sections near the mid-length were taken from each irradiated capsule. The longitudinal specimens permitted examination of the end cap welds, Al_2O_3 end spacers, and the pellet-to-pellet interfaces. The cladding remained in place in each section prepared metallographically.

An area from the transverse section of the unirradiated capsule is shown in Fig. 4.9 that is typical of the UO_2 and the UO_2-to-cladding interface. Colonies of large grained UO_2 were found dispersed throughout the unirradiated pellets that averaged 18 μ in diameter; the remainder of the UO_2 had an average grain size of 10 μ. The grain colonies were a result

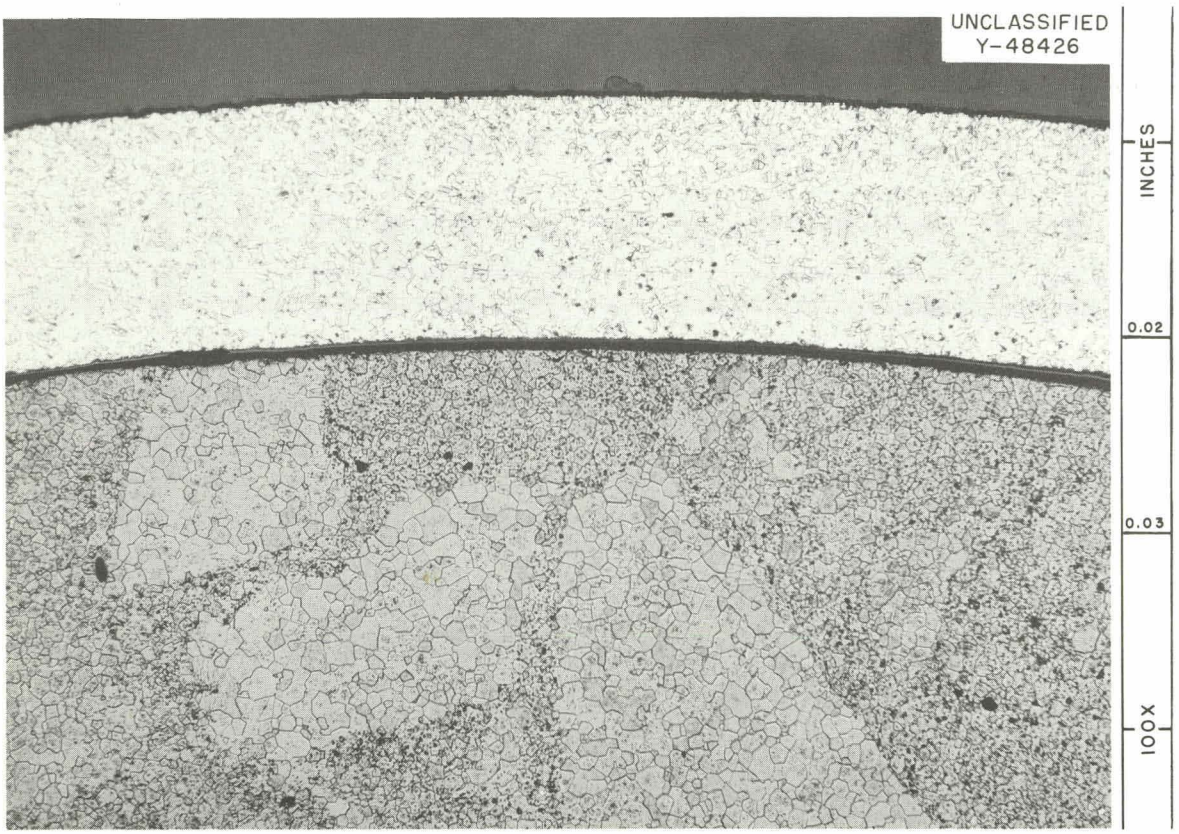

Fig. 4.9. Interface of UO_2 Pellet and Type 347 Stainless Steel from a Transverse Section Through an Unirradiated Control Capsule Like Capsules 04-5 and 05-5. Etched.

of blending two batches of UO_2 to achieve the desired enrichment of 1.9%.[4] Areas through the top portion of the control capsule that illustrate a typical Al_2O_3–UO_2–type 347 stainless steel cladding interface and a pellet-to-pellet-to-cladding interface are shown in Fig. 4.10. Flats, approximately 0.04 in. across, had been ground on the dished ends of the pellets; only one end of each pellet was dished. The cladding had a measured grain size of ASTM 10-11 and an average microhardness of 170 DPH (0.5-kg load).

The results of the metallographic examinations of the sections from the two irradiated capsules, 04-5 and 05-5, were similar, with one exception. There was no evidence of deformation of the cladding at any of the pellet-to-pellet interfaces examined. Although there were many fractures in the fuel pellets, no small pieces of UO_2 were found that had been dislodged or had shifted at the pellet-to-cladding interfaces. A typical pellet-to-cladding interface is shown in Fig. 4.11. In a few areas the UO_2 adhered to the cladding; this indicated contact during irradiation. An intermittent reaction product was found in the inner surface regions of the cladding that is believed to have resulted from the fuel-to-cladding contact. The reaction product, which was found to a maximum depth of 0.001 in., was probably formed by an oxidation-reduction mechanism. The reaction product and a metallic film between the reaction product and the UO_2 can be seen in Fig. 4.12. The grain size and the microhardness of the cladding remained unchanged. None of the cladding specimens examined, including the end cap welds, suggested potential failure.

Small, intergranular voids were found in the UO_2 at approximately mid-radius and increased in size and frequency toward the center of the fuel columns. The only significant microstructural differences in the two elements was seen in the UO_2. In capsule 05-5, columnar grains and lenticular voids were found in the central region of the fuel column, which suggested that the central temperature in this element was higher than had been thought. It has been reported in the literature[5] that the type of

---

[4]A. E. Goldman, "Preirradiation Examination of CEA Group V ORR Capsules No.'s 1, 2, 3, & 4," unpublished report, Oak Ridge National Laboratory.

[5]V. B. Lawson and J. R. MacEwan, "Thermal Simulation Experiments with a UO_2 Fuel Rod Assembly," Canadian Report CRFD-915, March 1960.

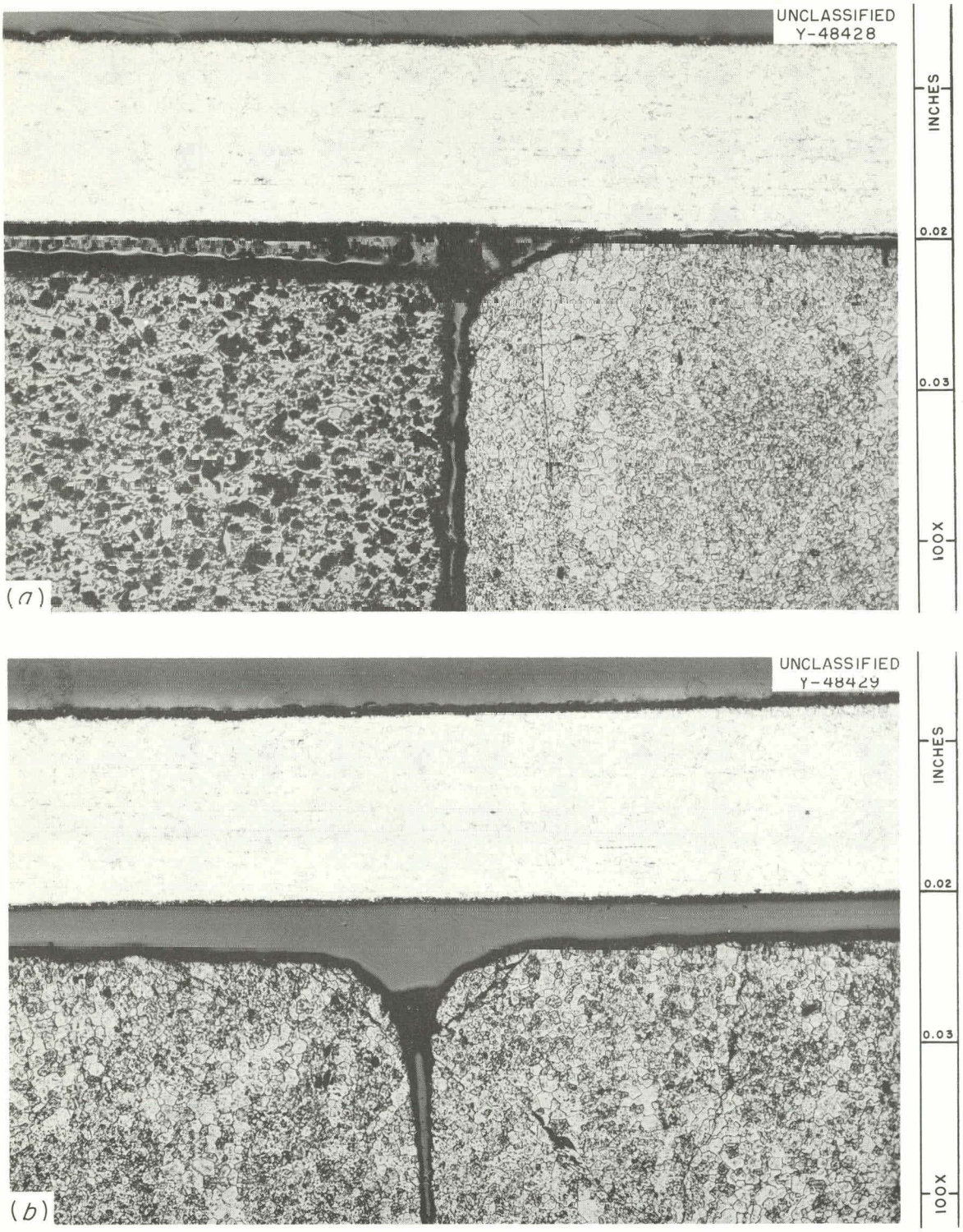

Fig. 4.10. Areas from a Longitudinal Section Made Near the Top of the Control Capsule. (a) Al_2O_3-UO_2-cladding interface. (b) UO_2 pellet-to-pellet-to-type 347 stainless steel cladding interface. Etched.

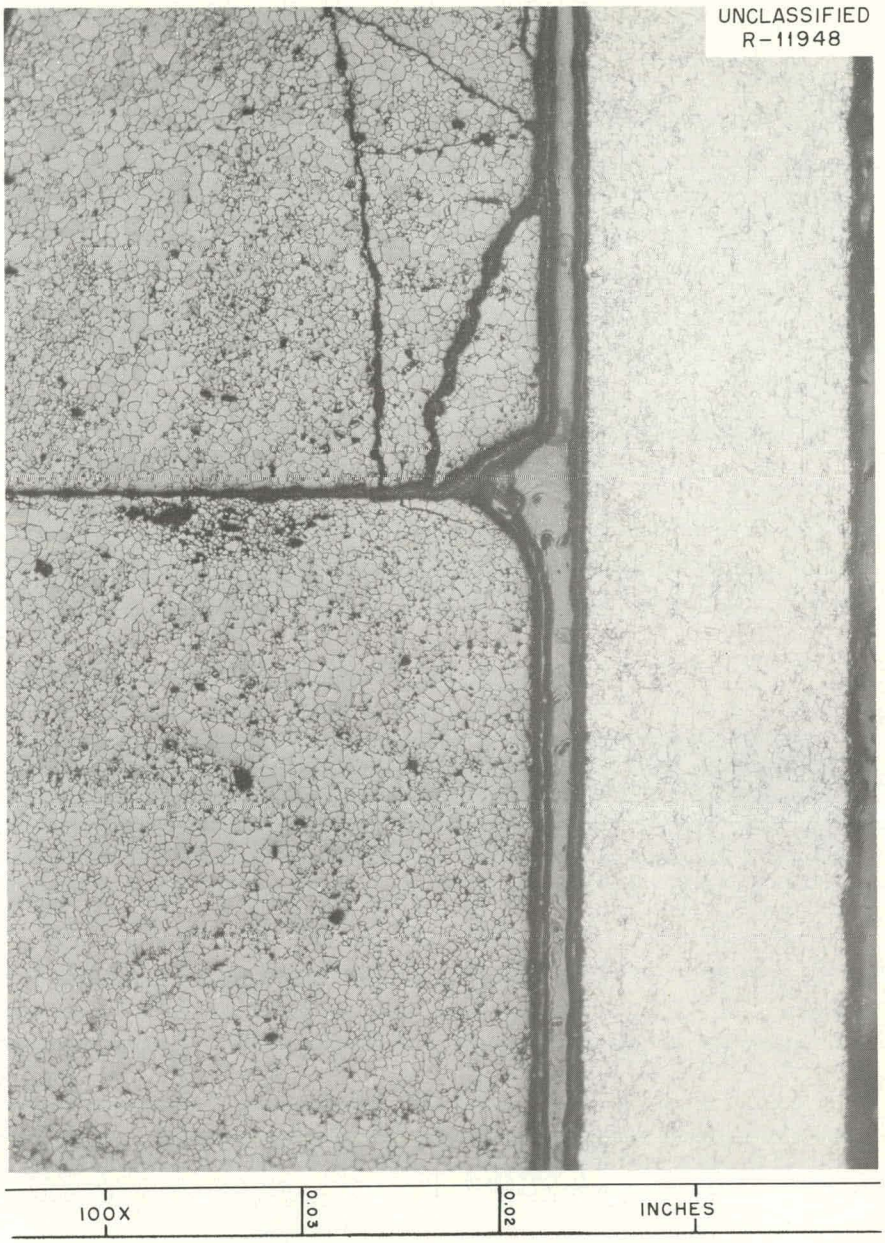

Fig. 4.11. Typical Pellet-to-Pellet-Cladding Interface from the Bottom Portion of Capsule 05-5. Etched.

microstructure found occurs at a minimum temperature of 1600°C. Areas from the outer, mid-radius, and central regions of the fuel columns of both capsules are shown in Figs. 4.13 and 4.14. The grain size of the UO_2 in the outer regions showed no increase in size compared with the unirradiated fuel. The grain size of the UO_2 in the center of the fuel pellets from capsule 04-5 measured 35 μ and 28 μ in capsule 05-5. No

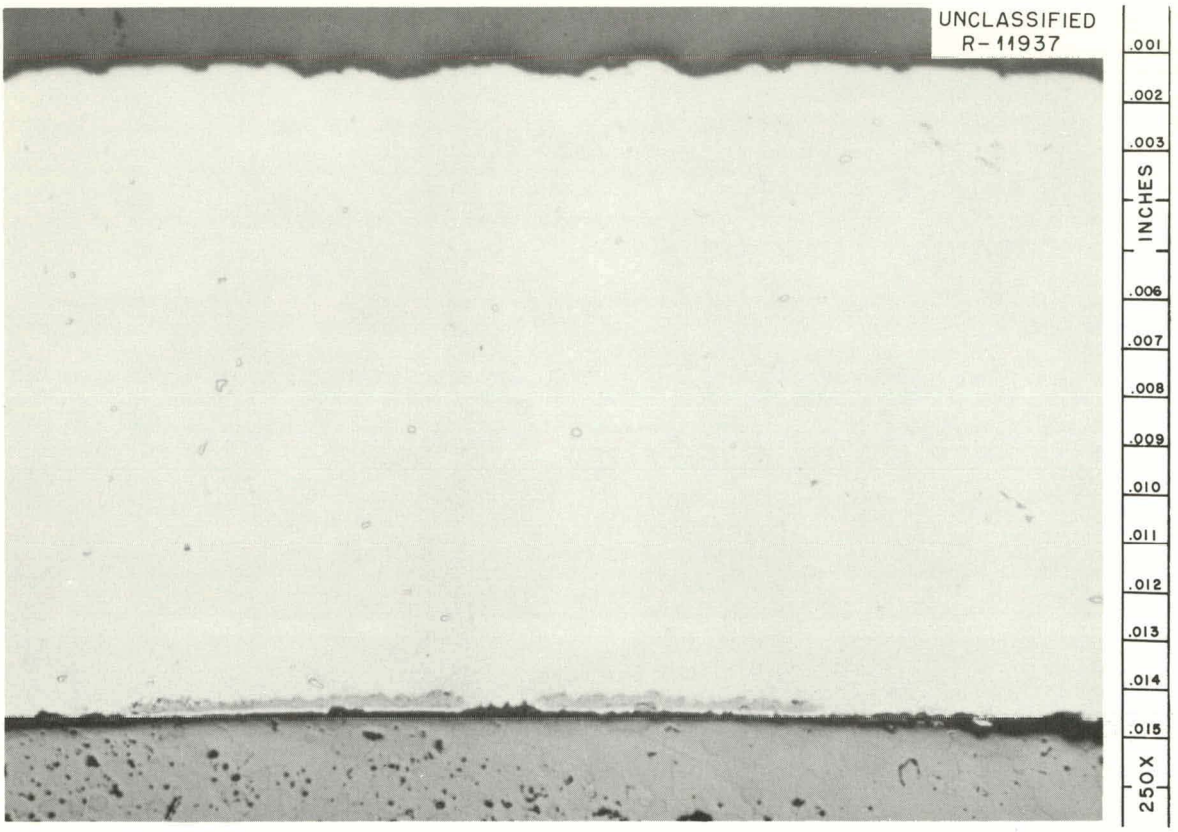

Fig. 4.12. Intermittent Reaction Product Found in Irradiated Capsules 04-5 and 05-5. Note metallic layer between reaction product and UO_2. As polished.

reaction products were present at the Al_2O_3 end spacer-to-cladding-to-UO_2 interfaces. Based on these comparisons of the unirradiated control capsule with the two irradiated capsules, it is concluded that although a leak was detected during the leak test and subsequent analysis of the NaK coolant deposit, this failure of the cladding was not typical.

Instrumented Fuel Elements Irradiated in GCR-ORR Loop No. 1

Fuel Element 7A. The disassembly, macro, and partial metallographic examination of instrumented fuel assemby 7A has been reported.[6,7] The

---

[6]D. F. Toner et al., Examination of Irradiated Capsules, pp. 94–96, "GCRP Quar. Prog. Rep. March 31, 1962," USAEC Report ORNL-3302, Oak Ridge National Laboratory.

[7]J. G. Morgan et al., Examination of Irradiated Capsules, pp. 111–117, "GCRP Semiann. Prog. Rep. Sept. 30, 1962," USAEC Report ORNL-3372, Oak Ridge National Laboratory.

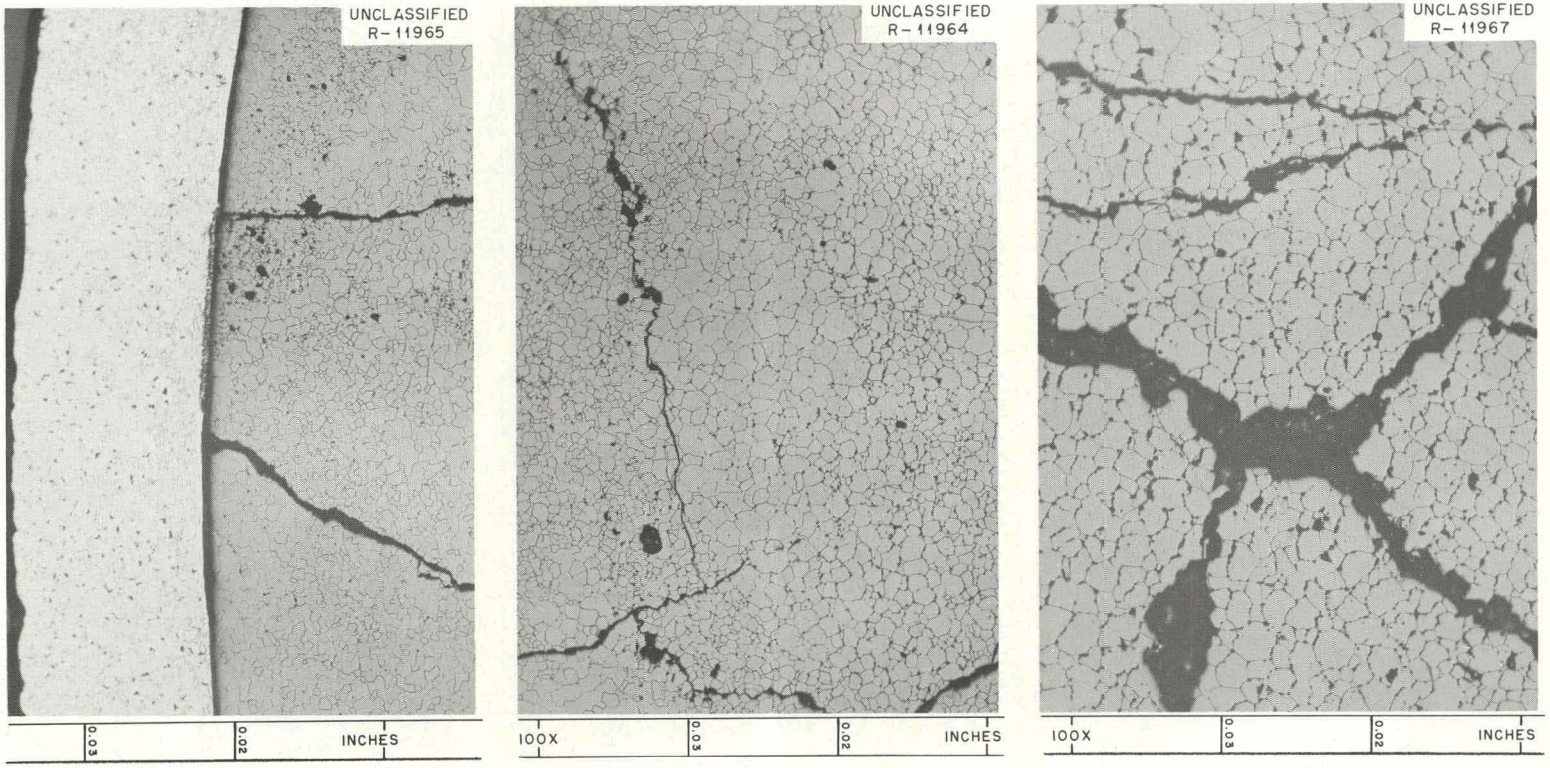

Fig. 4.13. Areas from a Transverse Section Near the Mid-Length of Capsule 04-5. Etched. (a) UO_2—type 347 stainless steel cladding interface. Note slight reaction between the UO_2 and cladding. (b) Area from approximately mid-radius. Note increase in intergranular voids. (c) Typical area from center of fuel column. Note size of intergranular voids and increase in grain size.

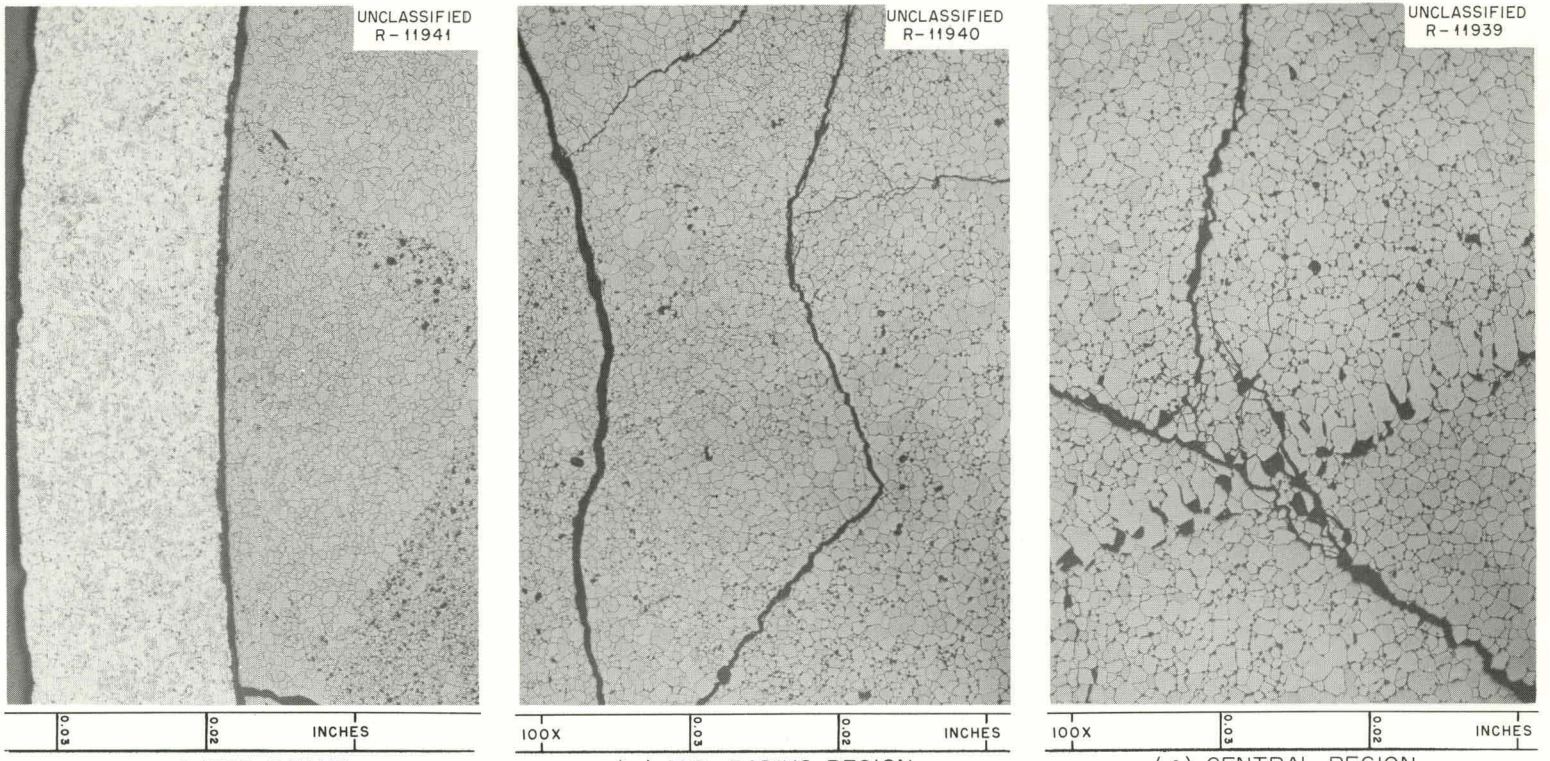

Fig. 4.14. Areas from a Transverse Section Near the Mid-Length of Capsule 05-5. Etched. (a) UO_2—type 347 stainless steel cladding interface. Note slight reaction between the UO_2 and cladding. (b) Area from approximately mid-radius. Note increase in intergranular voids. (c) Area from center of fuel column. Note increase in intergranular voids, lenticular voids and subsequent columnar grains, and increase in grain size.

only portion of the examination of this element that has not been reported is the result of metallographic examination of a specimen taken at the bottom of the type 304 stainless steel insert that fractured during sectioning. The bottom portion of the shroud was irradiated at a temperature estimated to be about 1000°F and had rusted badly while in storage in the pool of the ORR. Metallographic examination of the transverse section taken at the bottom of the insert (Fig. 4.15) revealed an intermittent oxide that penetrated the outer surface to a maximum depth of 0.5 mil. Examination of the crack that developed during sectioning showed severe intergranular separation and evidence of an intergranular corrosion product in the fracture region (Fig. 4.15b).

Fuel Element 7C. The irradiation conditions and preliminary examination of fuel element 7C were reported previously.[7] Subsequent post-irradiation examination has included dimensional measurements, gamma scanning, burnup determinations, leak checking, and metallography.

No changes in the diameter or length of the fuel element were observed; however, a bow of 0.040 in. was found in the central portion. The scan of gross gamma activity, shown in Fig. 4.16, indicates the variation of activity resulting from the different UO_2 enrichments in the pellets. Comparison of the burnup data, given in Table 4.5, with the flux pattern calculated from the gamma activity showed close agreement.

Four failures were found in the cladding when the element was submerged in oil under a vacuum. Two holes were found 1/4 in. below the top end cap and two were found about 3 1/2 in. above the bottom end cap. These failures were substantiated by the presence of Xe^{133} activity in the helium sweep gas during operation. The metallographic examination of these failure areas is still in process.

During the examination of the experimental assembly in which element 7C was irradiated, loosely adhering rust was observed over the entire length of the shroud. The formation of the rust was attributed to the presence of water in the loading tube while it was in storage in the ORR pool.[7] A section was therefore made at the bottom of the shroud and prepared for transverse metallographic examination. As shown in Fig. 4.17, lack of grain-boundary integrity permitted entire grains to fall out of

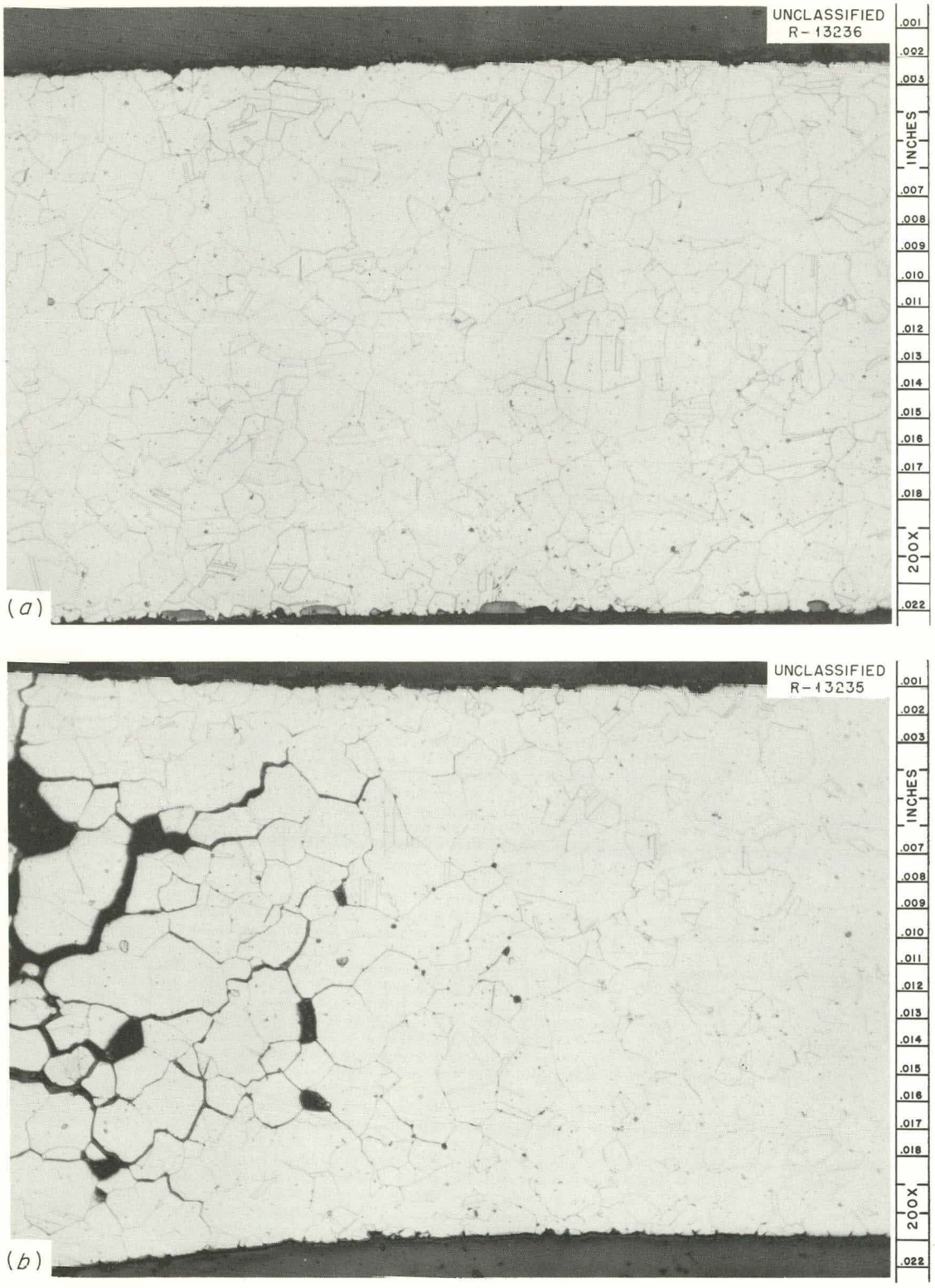

Fig. 4.15. Transverse Section Through Bottom of Insert from Irradiated Fuel Element 7A. (a) Note intermittent oxide in outer surface and (b) intergranular separation. Etched.

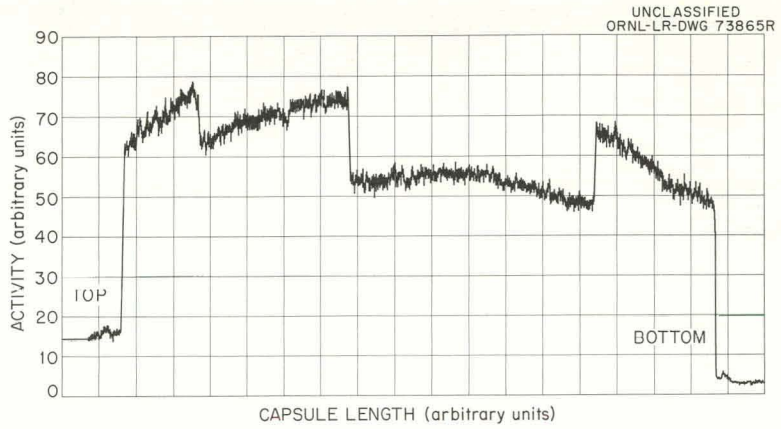

Fig. 4.16. Gamma Scan of Instrumented Fuel Element 7C After Operation in GCR-ORR Loop No. 1.

Table 4.5. Burnup Data on Irradiated Fuel Element 7C

Pellet No.	Burnup (Mwd/MT of Uranium)					
	Based on Ce^{144} Analyses			Based on Cs^{137} Analyses		
	Analysis 1	Analysis 2	Average	Analysis 1	Analysis 2	Average
13	864	942	903	1141	1067	1104
29	713	713	713	870	945	907
44	691	717	704	861	897	879

the inner surface region of the shroud during metallographic preparation. Such lack of grain-boundary integrity was observed in only three areas.

ETR-Irradiated EGCR Prototype-Diameter Capsules

Capsules E-4 and E-1A. The metallographic examination of capsule E-4, which fractured during irradiation in the ETR, was completed. The disassembly and macro examination of this capsule were previously reported.[8] Three metallographic specimens were taken from this capsule; two transverse sections through the cladding fracture region, which included the cladding and the fuel, and a longitudinal section of the cladding at a pellet-to-pellet interface. Metallographic examinations were

[8]Ibid., pp. 106–108.

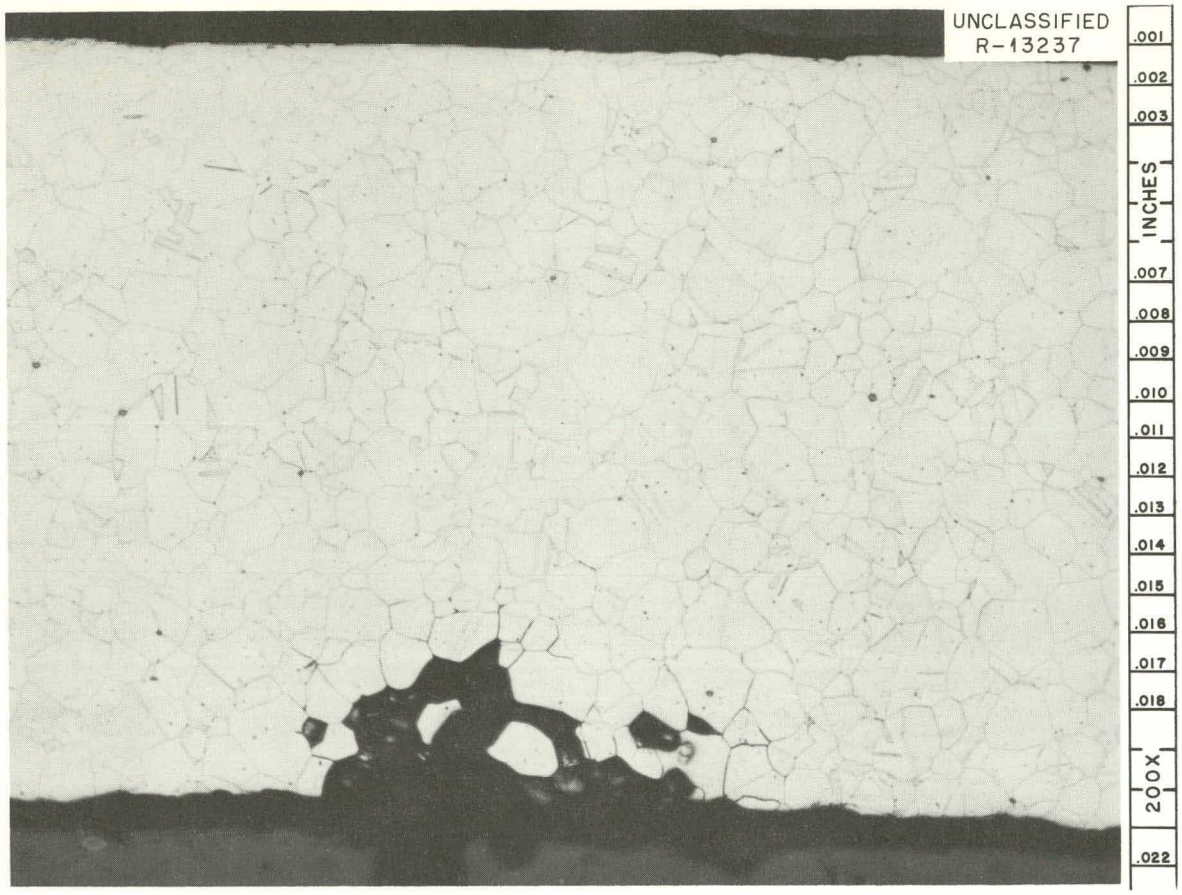

Fig. 4.17. Area from Bottom Portion of the Shroud of Element 7C. Lack of grain-boundary integrity is evident at inner surface. Etched.

also made of unirradiated control specimens of the fuel and cladding material. Photomicrographs of a transverse section through one of the control pellets are shown in Fig. 4.18. The second phase evident in the peripheral region of the UO_2 pellet was identified as primarily UN_2, with trace amounts of UN. A transverse section of the unirradiated type 304 stainless steel cladding is shown in Fig. 4.19. The microhardness of the cladding averaged 158 DPH (0.5-kg load). The same materials[9] were used in capsules E-4 and E-1A, both of which failed during irradiation.

The microstructural features of both transverse sections from capsule E-4 were similar. The outer surface, mid-radius, and edge of the

[9]R. L. Heestand and R. M. Evans, "GCR Irradiation Program Fuel Data Summary," unpublished data, Oak Ridge National Laboratory.

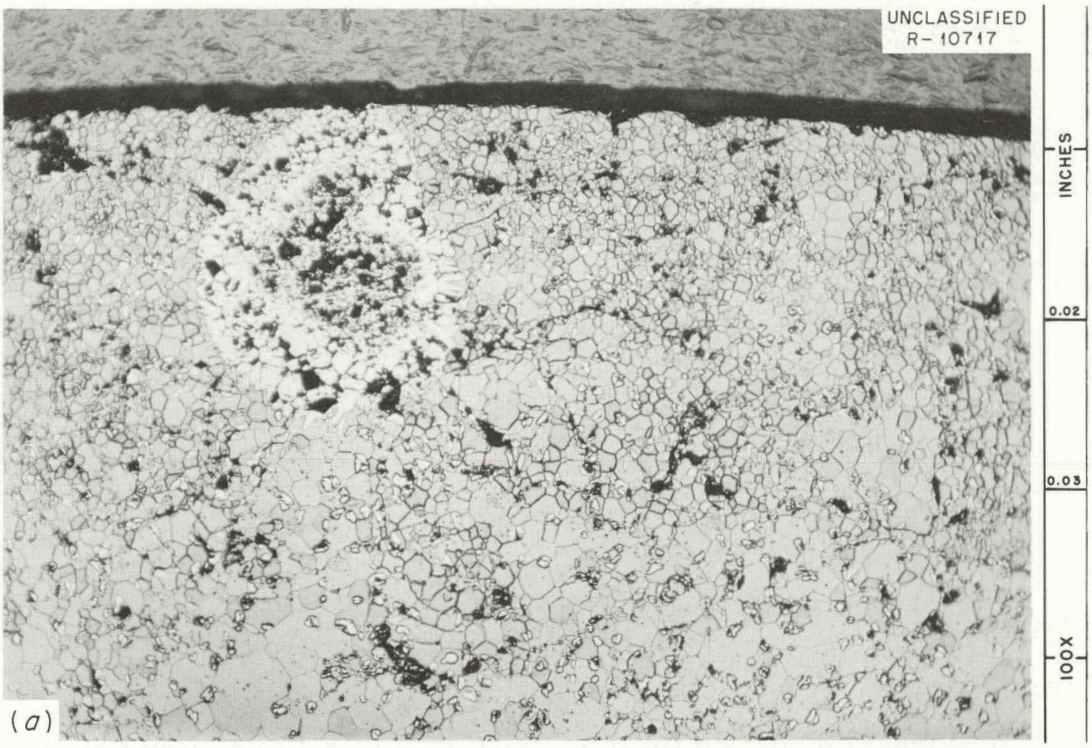

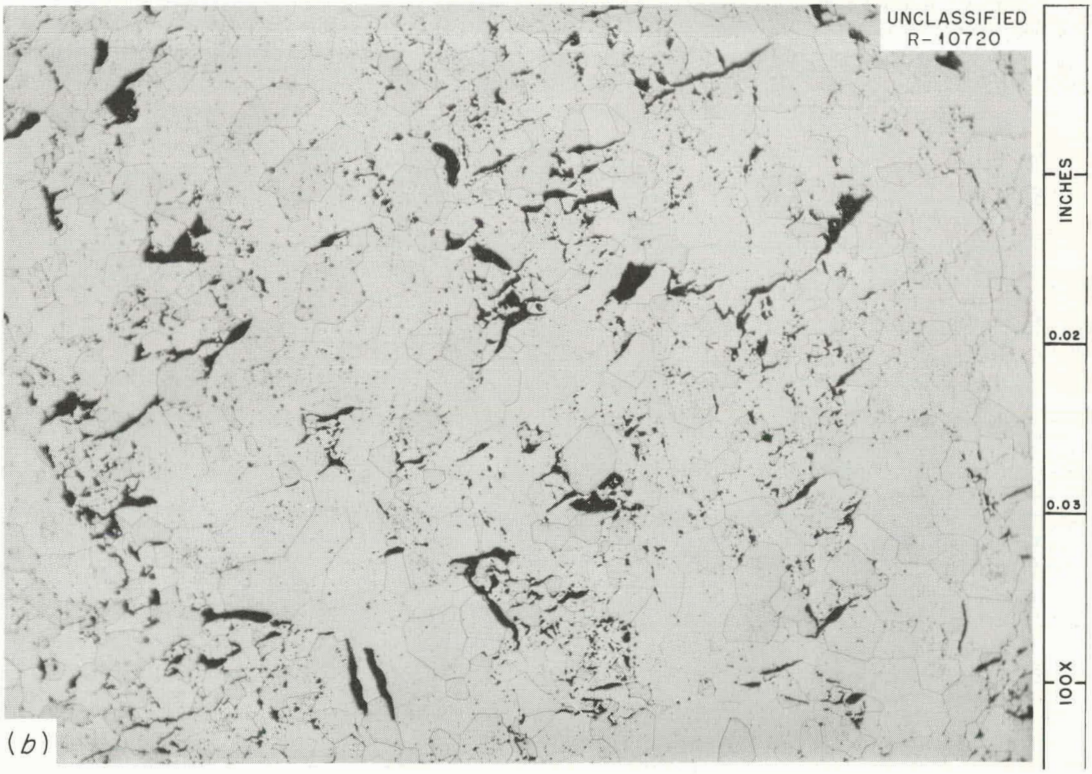

Fig. 4.18. Areas from an Unirradiated UO_2 Pellet from the Batch Used to Load Capsules E-1A and E-4. (a) Outer region. (b) Central region. Second phase present in outer region is primarily UN_2. Etched.

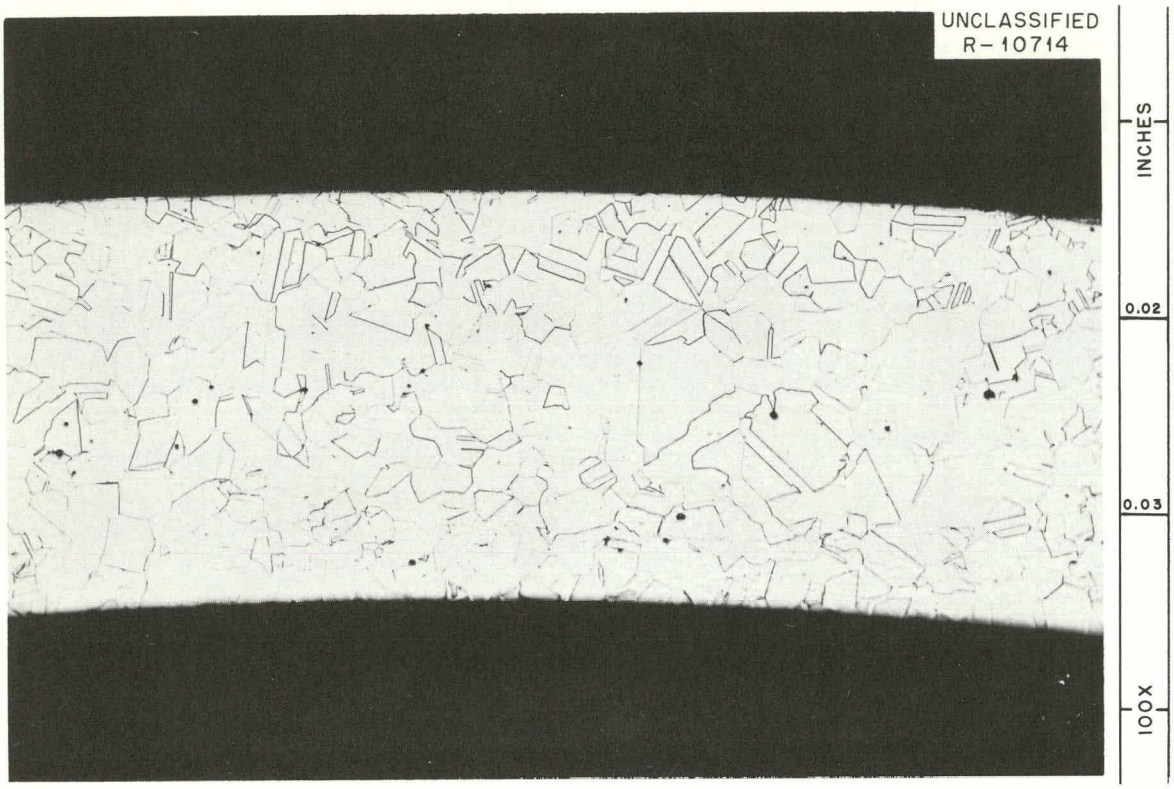

Fig. 4.19. Transverse Section of Unirradiated Type 304 Stainless Steel Cladding for Capsule E-4. Etched.

central void in the UO_2 pellet are shown in Fig. 4.20. The uranium nitride phase present in the peripheral regions of the UO_2 fuel pellets before irradiation was not evident after irradiation. Although columnar grains were observed in the inner two-thirds of the pellets in both capsules E-1A and E-4, the lenticular voids normally associated with columnar grain growth in UO_2 were not found in capsule E-4, except near the central void. Voids were observed in the columnar grained UO_2 in capsule E-4, but they were confined mainly to grain boundaries. There was no evidence that the UO_2 had been molten during irradiation. The unidentified metallic globules near the central voids in the UO_2 from capsule E-1A were also present in capsule E-4.

A longitudinal section through the type 304 stainless steel cladding of capsule E-4 at a pellet-to-pellet interface and a transverse section through the fracture are shown in Fig. 4.21. The fine precipitates in the inner surface regions are believed to be nitrides from the uranium

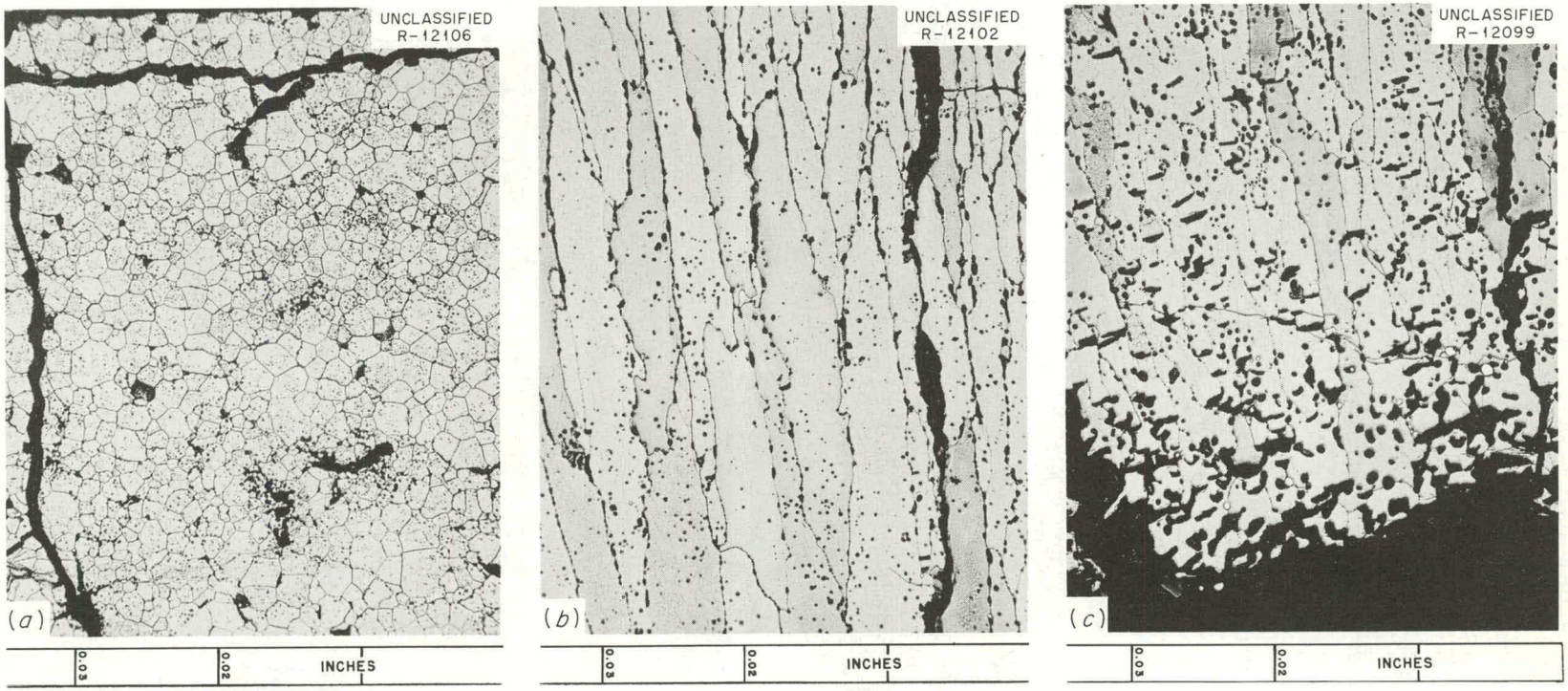

Fig. 4.20. Microstructure of a UO_2 Pellet from Capsule E-4. Etched. 100X. (a) Outer surface region. (b) Mid-radius region. (c) Edge of central void that formed during irradiation.

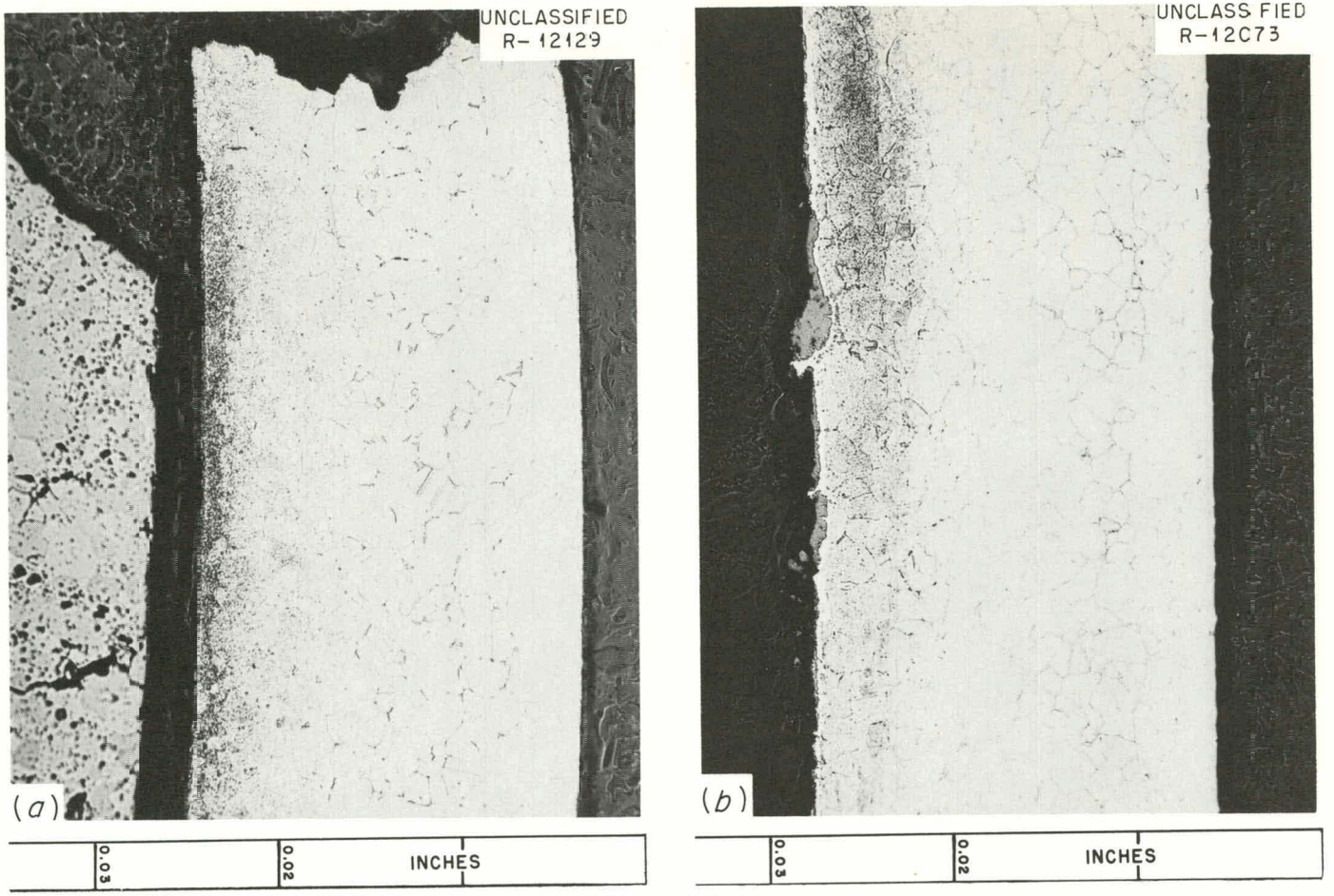

Fig. 4.21. Areas from the Type 304 Stainless Steel Cladding of Capsule E-4. (a) Transverse section through a fracture region. (b) Longitudinal section adjacent to a pellet-to-pellet interface. Precipitate in inner surface regions believed to be a nitride. Chips of UO_2 were found embedded in the cladding at a pellet-to-pellet interface. Etched. 100X.

nitride present in the UO_2. The precipitate was more heavily concentrated at the pellet-to-pellet interface than elsewhere in the longitudinal section, which was indicative of the effect of stress on the development of the precipitate; McCoy and his co-workers[10] also made this observation. Closer examination revealed the presence of the fine precipitate along the fracture region shown in Fig. 4.22. Although sigma phase material was observed in the grain corners in the outer surface regions of the cladding, it is not believed that the presence of the sigma phase material was a major factor in the cladding failure. A 5% reduction in wall thickness at the fracture was measured, and most of the reduction occurred at the outer surface region. The microhardness of the cladding was 170 DPH at the outer surface, 180 DPH at the center, and 202 DPH at the inner surface; all impressions were made using a 0.5-kg load. Attempts to identify the fine precipitate by x-ray diffraction have been unsuccessful so far.

It is concluded that the primary causes of failure were essentially the same for capsule E-4 as for capsule E-1A: (1) the formation of nitrides in the inner surface region of the cladding and (2) overheating of the UO_2. Large amounts of UN_2 were present near the peripheral regions of the unirradiated fuel pellets. The UN_2 apparently disassociated during irradiation and released nitrogen. Consequently, nitrides were formed in the type 304 stainless steel cladding. Although sigma phase material was found in large quantities in the cladding, it was apparently not related to the failure because the outer regions of the cladding were still relatively ductile, as evidenced by the reduction in thickness in that area. Furthermore, it is believed that capsule E-4 experienced a higher heat rating than capsule E-1A sometime in the course of its irradiation history. This would explain the increased depth of precipitate in the inner surface regions of the cladding and the formation of columnar-grained UO_2 without lenticular voids.

Capsule E-6. General examination of capsule E-6 disclosed nothing unusual. Fabrication and irradiation data for capsules E-4 and E-6 are

---

[10]H. E. McCoy et al., "Effect of Environment on the Mechanical Properties of Metals," pp. 166–167 in Proceedings of the Institute of Environmental Sciences National Meeting, April 5–7, 1961, Washington, D.C.

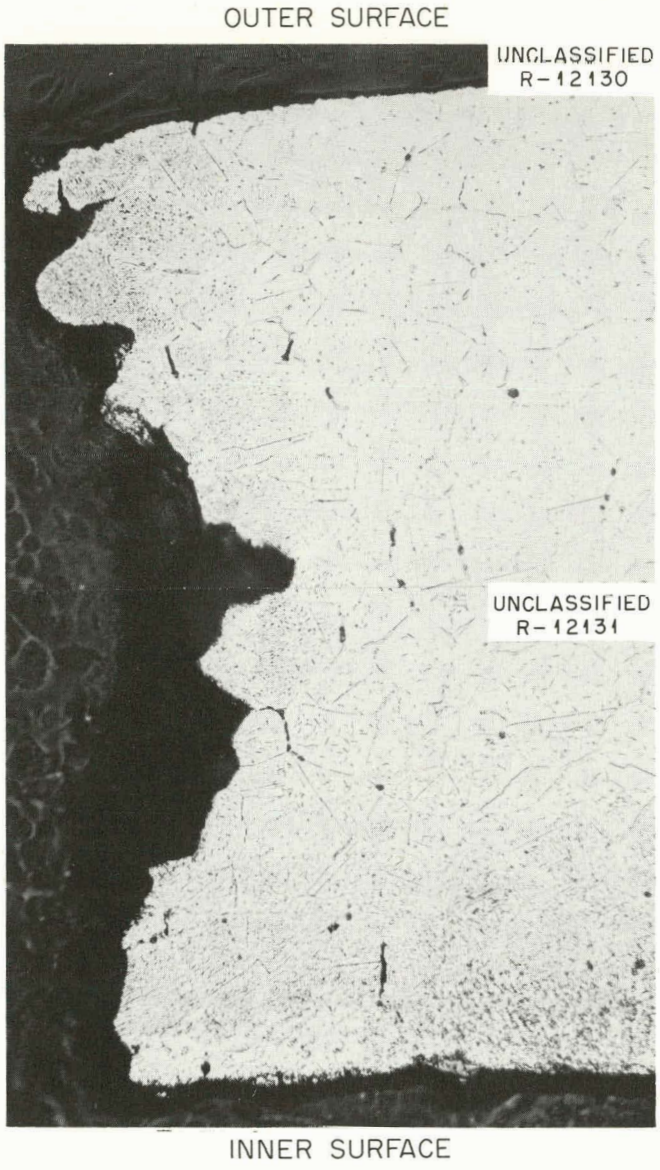

Fig. 4.22. Fracture Region Shown in Fig. 4.21 at a Higher Magnification. Note precipitate concentration along the fracture. Sigma phase material can be seen in some of the grain corners near the outer surface. Etched. 250X.

compared in Table 4.6. There were no obvious flaws in the cladding of capsule E-6, and a leak test in an oil bath under vacuum indicated no leaks. Dimensional measurements showed significant diameter changes, but only slight bowing. The eccentricity of the middle part of the capsule had increased from about 0.001 in. to a maximum of 0.058 in., with a net increase in over-all size. There was no significant change in capsule

length. The results of gas analyses indicated that a large fraction of the fission-product xenon and krypton was released. Pending an accurate measurement of fuel burnup, the Kr^{85} release from the fuel was estimated to be about 17%. Upon capsule disassembly, the fuel pellets were each found to be cracked into several pieces; however, there was no appreciable displacement of the fuel, as shown in Fig. 4.23. The results of metallographic examination of fuel and cladding samples will be reported later.

Table 4.6. Fabrication and Irradiation Data for Capsules E-4 and E-6

Capsule No.	Pellet Type	Cladding Temperature (°F)	Maximum Power[a] Level (% of design)	Burnup (Mwd/MT of UO_2)
E-4	Solid	1320	157	7300
E-6	Cored	~1300	116	~7500

[a]Based on heat balance calculation.

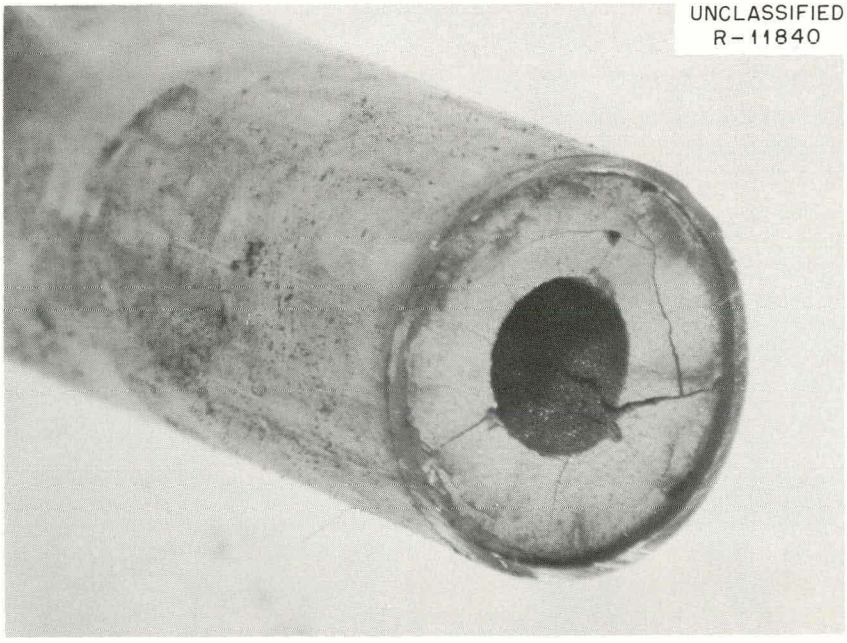

Fig. 4.23. Transverse Section Through Capsule E-6, Showing Fourth Fuel Pellet from Bottom End. Note pellet cracking without fuel displacement. 3X.

Instantaneous Fission-Gas-Release Experiments

R. M. Carroll J. G. Morgan
P. E. Reagan M. T. Morgan

Thin-slab specimens of single-crystal UO_2 are now being irradiated in the C-1 facility of the ORR. In the C-1 facility the specimens can be positioned at different flux levels and temperatures can be independently controlled.[11] The fission gas is removed by a stream of inert gas, and the neutron flux is measured by adding argon to this sweep gas.[12] The initial results of the current irradiation experiment and in-pile electrical measurements have been reported.[13,14]

All of the measured isotopes (Xe^{135}, Xe^{133}, Kr^{88}, Kr^{87}, and Kr^{85m}) are released from the single-crystal specimen with the same temperature dependence. This is illustrated in Fig. 4.24, which gives the temperature dependence of the Kr^{88} release. The typical gas-release pattern shown in Fig. 4.24 was observed for all previously tested UO_2 specimens, as well as for the single crystal. The temperature-independent release is usually assumed to be from fission products recoiling free of the specimen and the temperature-dependent release is assumed to be the result of diffusion. The temperature-dependent release has an activation energy of 50 kcal/mole for the single-crystal UO_2 specimen.

Fission-Recoil-Activated Release

It has been shown that the proportions of isotopes in the fission gas are characteristic of the manner in which the gas escaped from the

---

[11] R. M. Carroll and C. D. Baumann, "Experiment on Continuous Release of Fission Gas During Irradiation," USAEC Report ORNL-3050, Oak Ridge National Laboratory, Feb. 9, 1961.

[12] R. M. Carroll, "Argon Activation Measures Irradiation Flux Continuously," Nucleonics, 20(2), February 1962.

[13] R. M. Carroll et al., Instantaneous Fission-Gas-Release Experiment, pp. 116–120, "GCRP Semiann. Prog. Rep. Sept. 30, 1962," USAEC Report ORNL-3372, Oak Ridge National Laboratory.

[14] M. D. Karkhanavala and R. M. Carroll, "In-Pile Measurement of the Electrical Resistivity and Thermoelectric Power of Sintered UO_2," USAEC Report ORNL-3093, Oak Ridge National Laboratory, April 1961.

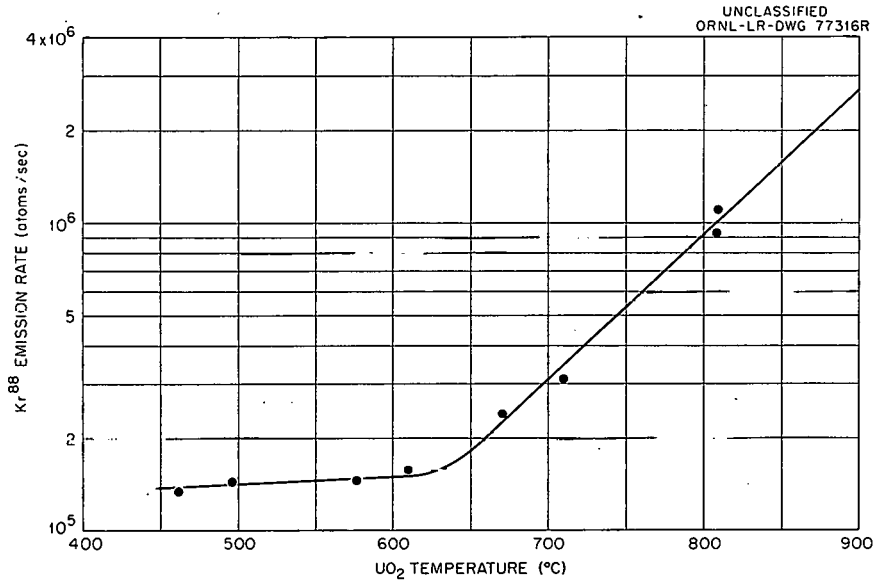

Fig. 4.24. Steady-State Release Rate of Kr^{88} from Single-Crystal UO_2 During Irradiation at a Thermal-Neutron Flux of 2.0×10^{13} Neutrons/cm^2·sec.

specimen.[15] Plots of the steady-state fractional release of the krypton and xenon isotopes vs their radioactive decay constants are given in Fig. 4.25. In a plot of this type, direct recoil emission results in a horizontal line, whereas a mixture of recoil and diffusion gives a slope that increases as the temperature increases. The increasing slope was not observed, and the slope of the low-temperature emission indicates that direct recoil was not the mechanism of escape.

An explanation for the constant proportions of isotopes in the fission gas is that the recoils leave the specimen surface with sufficient energy to be embedded in the surrounding capsule material and are not released to the sweep gas; however, each fission spike penetrating the specimen surface evaporates an estimated 2000 UO_2 atoms.[16] This process would liberate fission gas that had diffused to the specimen surface and would produce a temperature-independent gas release that had the same ratio of isotopes as the temperature-dependent gas release.

---

[15]R. M. Carroll, "Continuous Release of Fission-Gas From UO_2 During Irradiation," ASTM Special Tech. Publication No. 306, pp. 118–120 (1961).

[16]M. D. Rogers and J. Adam, "Ejection of Atoms from Uranium by Fission Fragments," J. Nuc. Matls., 6(2): 182–189 (1962).

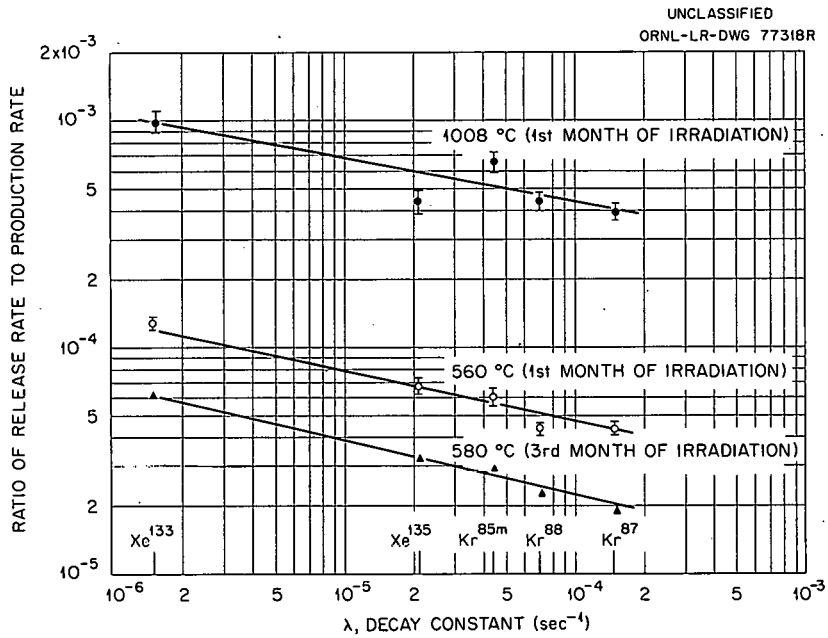

Fig. 4.25. Dependence of Fractional Fission-Gas Release from UO_2 Single Crystal on Decay Constant (Kr^{85m} Plotted for Fission Yield of 2%).

Reduction of Fission-Gas-Release Rate with Time

The rate of fission-gas release from the single-crystal specimen is decreasing as the irradiation continues. The decreasing of the release rate, indicated in Fig. 4.26, was rapid at first, but the release rate appears to be approaching stability after about 6 months of irradiation (2.1×10^{19} fissions/cm^3). The reduction of the gas release rate was the same for both the temperature-dependent and -independent processes and for all isotopes, as shown in the lower line of Fig. 4.25. It has been postulated that microscopic imperfections in the crystal surface are smoothed out by radiation, and thus the surface area is reduced, as has been demonstrated in metals bombarded with alpha particles.[17]

Influence of Production Rate on Release Rate

The effect of production rate on the Kr^{88} release rate was investigated by irradiating the specimen at different fission rates but at the

[17]R. Sizman and U. Däurent, "Radiation Induced Diffusion in Metals," Symposium on Radiation Damage in Solids and Reactor Materials, Venice, Italy, May 1962.

same temperatures. The Kr^{88} release, as a function of temperature, is given in Fig. 4.27 for thermal-neutron flux levels ranging from 1.1×10^{13} to 3.6×10^{13} neutrons/cm^2·sec. As the specimen temperature was increased, the Kr^{88} release rates converged to the same values for all flux levels. This result was unexpected, since the temperature-dependent release is usually considered to be by diffusion and thus directly proportional to the fission rate (which is here directly proportional to the neutron flux). The fact that the curves converge at the high temperatures implies that the release is not the result of simple diffusion.

The temperature-independent gas release is a direct function of the neutron flux, as would be expected of a fission-activated process. This is illustrated in Fig. 4.28, where the release rate below 600°C is plotted vs the neutron flux. To find the gas emission by the temperature-dependent process, the recoil release rate was subtracted from the total release rate. The temperature-dependent release rates are given in an Arrhenius plot in Fig. 4.29. They demonstrate that the fission-gas-release rate is essentially independent of the fission rate. These recent observations are contrary to the current concepts that the fission-gas-release should be directly proportional to the fission rate.

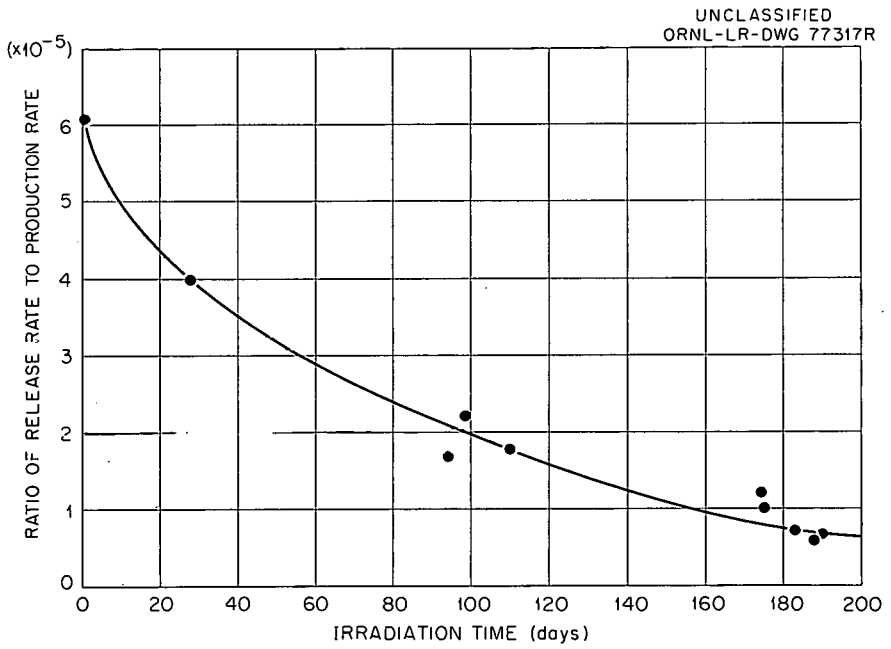

Fig. 4.26. Fractional Steady-State Release Rate of Kr^{88} from a UO_2 Single Crystal at Temperatures Below 600°C.

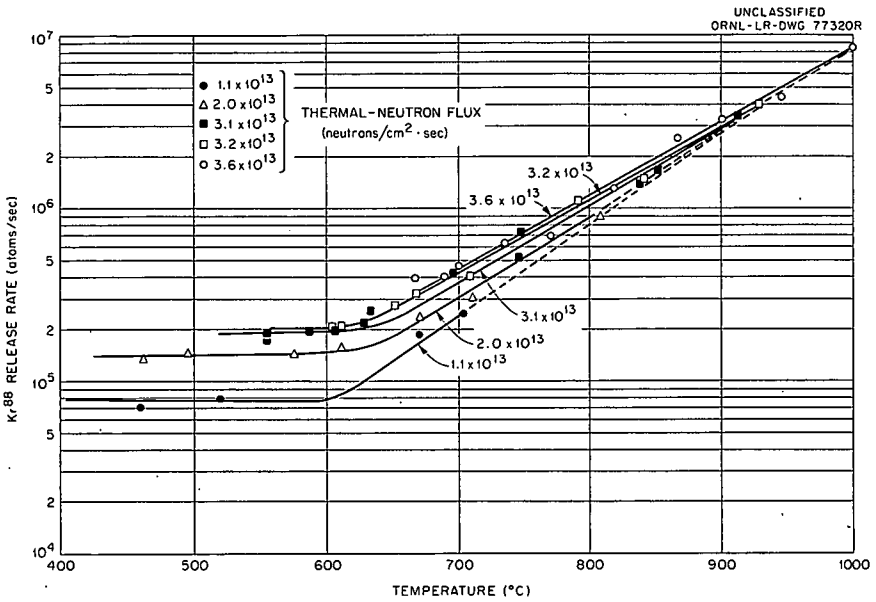

Fig. 4.27. Steady-State Release Rate of Kr^{88} from UO_2 Single Crystal.

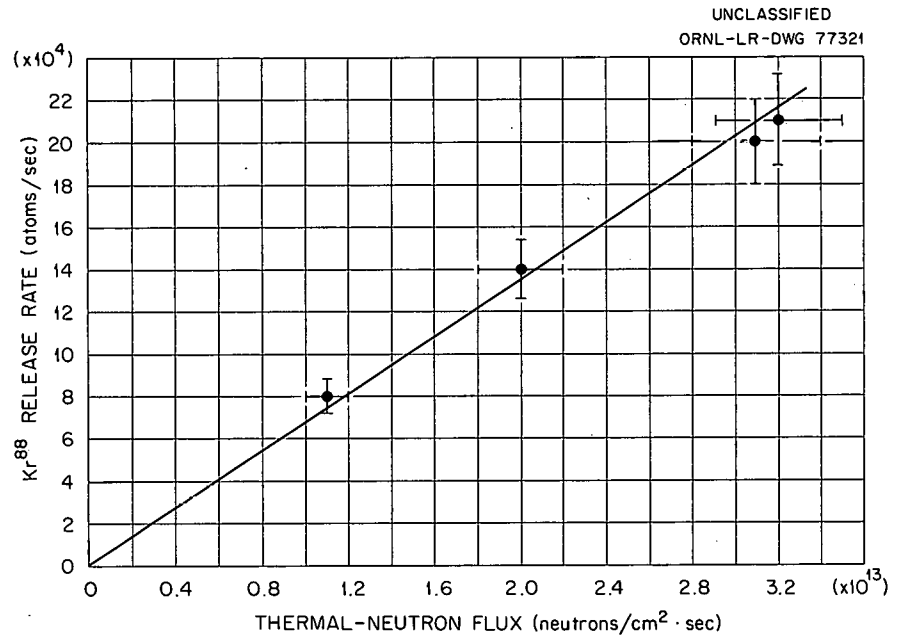

Fig. 4.28. Temperature-Independent Steady-State Kr^{88} Release Rate from UO_2 Single Crystal vs Thermal Flux Measured by Ar^{41} Analysis.

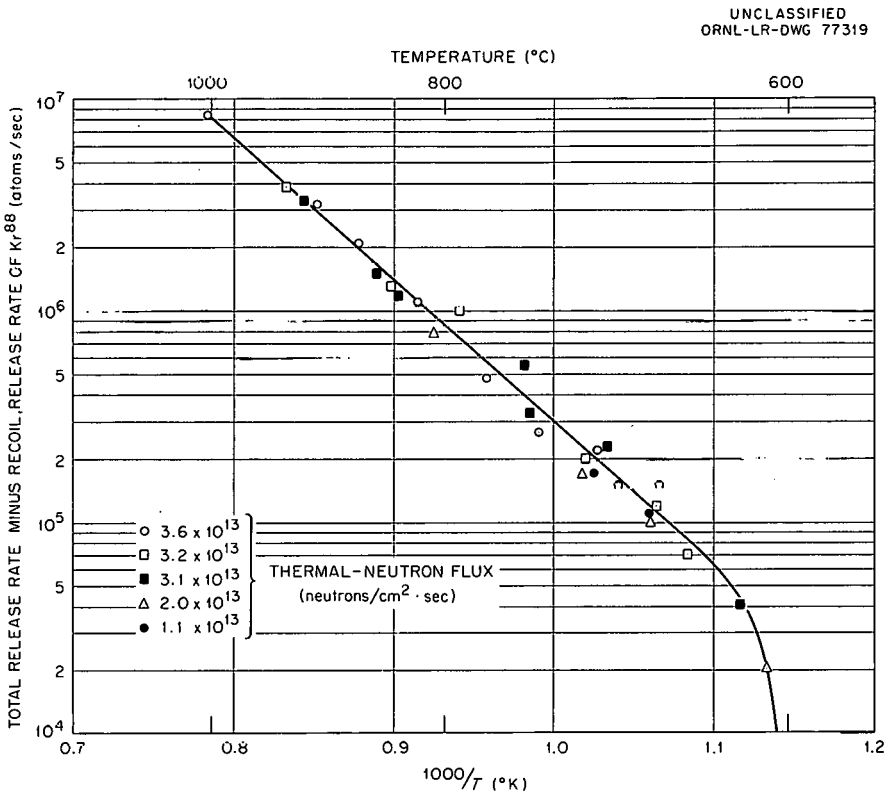

Fig. 4.29. Steady-State Temperature-Dependent Release of Kr^{88} from Single-Crystal UO_2 During Irradiation (Temperature Independent Contribution Subtracted).

Heating-Burst Studies

Postirradiation heating of irradiated fuel produces a heating burst when the specimen temperature is increased. If the specimen temperature is again increased, another heating burst occurs. If the specimen is cooled and then reheated to the same temperature, the heating burst is greatly diminished or does not occur. The size of the burst is increased by increasing the surface area of the specimen. The two most likely causes of the heating burst are either the annealing of gas traps located near the specimen surface or a rapid change in concentration gradient.

Some in-pile experiments were conducted to try to find the causes of the heating burst. For one of these experiments, the single-crystal specimen was set at a constant neutron flux and temperature for several days until the fission-gas release was at steady state. The specimen temperature was then cycled from 945 to 525 to 945°C within 10 min by withdrawing

the specimen from the neutron flux and then reinserting it to the original position. The Kr^{88} release during this period is shown in Fig. 4.30; it did not give any evidence of a heating burst. This demonstrates that the heating burst is not caused by thermal stresses when the specimen is being heated or cooled.

In another experiment, the single-crystal specimen was irradiated at 660°C until the krypton isotope release rate was at equilibrium. The specimen temperature was then cycled from 660 to 940 to 660°C without changing the neutron flux; the entire cycle required 13 min. The number of atoms released during the resultant heating burst is listed in Table 4.7. The atoms released were accumulated during approximately 9.2 hr of steady-state release at 660°C.

The most significant observation of this heating burst is that the isotopes were released during the burst in the same proportions as in steady-state release. This implies that this burst was an accelerated version of the same process as the steady-state release. If the gas in the burst had come from deep within the fuel or from a region of the fuel that normally retained the fission gas, the gas would have been rich in long-lived isotopes.

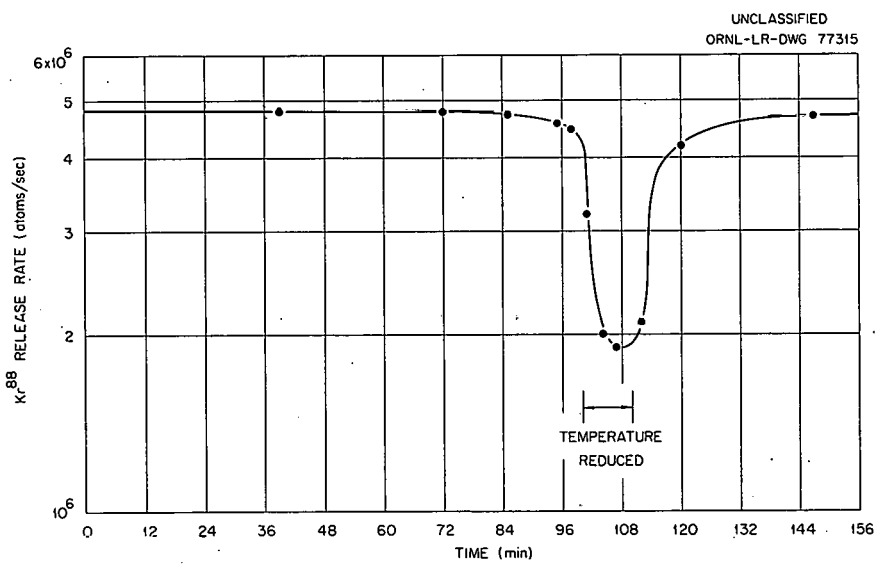

Fig. 4.30. Kr^{88} Release Rate from Single-Crystal UO_2 for a Temperature Cycle from 945 to 525 to 945°C in 10 min.

Table 4.7. Fission-Gas Released by a UO_2 Single Crystal During a Heating Burst

Isotope[a]	Release Rate (atoms/sec)		Number of Atoms Released in Burst
	At 660°C	At 940°C	
	$\times 10^5$	$\times 10^6$	$\times 10^{10}$
Xe^{133}	13.0	5.7	3.86
Xe^{135}	2.2	0.84	0.75
Kr^{85m}	3.0	3.6	1.2
Kr^{88}	3.5	4.8	1.4
Kr^{87}	2.0	2.8	0.38

[a]The steady-state xenon release was corrected for iodine decay.

Fission-Gas Release from High-Burnup UO_2

M. T. Morgan
D. C. Evans* R. M. Martin*

An apparatus has been developed for postirradiation annealing experiments to study the effects of high burnup on fission-gas release from UO_2 and other reactor fuel materials. The system can also be used to study fission-gas release from prototype fuel elements and from a wide variety of advanced fuel materials.

A molybdenum susceptor containing the fuel sample is heated by an induction current supplied by a high-frequency electron generator with an output of 10 kw. Purified helium sweep gas passes over the sample and carries the Kr^{85} released through the filter, to remove radioactive dust, and into the counting and collection systems in an evacuated enclosure. The Kr^{85} is continuously monitored as it flows through a GM counter and is collected in molecular sieve traps at −196°C. The helium carrier gas passes through the traps and is exhausted. Two traps are used alternately and switched at intervals so that one trap is collecting while the other is being exhausted. The trap being exhausted is

*Co-op student, University of Tennessee.

heated and the Kr^{85} is pumped into a totalizing counting system by means of a Toepler pump. This gas is later transferred into collection bulbs for further analysis.

The furnace tube and filter are housed in a glove box shielded with 4 in. of lead and fitted with modified Castle manipulators. The vacuum, counting, and collection systems are contained in a separate closed hood. The counting cells consist of coaxial tubes enclosing thin-walled GM tubes for measuring low count rates and a scintillation beta counter for high count rates. Calibration tests have shown that the GM tube measurements are reproducible between 200 to 10,000 counts/min to within 4% and accurate to 10%. The scintillation-detector measurements have a reproducibility of 12% and an accuracy of 20% above 10,000 counts/min. The system was designed to analyze for Kr^{85} in gases released by the fuel sample, since this gas has a 10-year half-life and other radioactive gases would have decayed in most of the samples to be used.

The first studies were made on high-density UO_2 samples from LITR-irradiated experimental capsule L-22a. This material was irradiated to a burnup of 12,000 Mwd/MT at a temperature of approximately 730°C. A rapid increase in the rate of Kr^{85} release as a function of time was observed in the temperature range 1500 to 1600°C that caused the slope of the curve in the plot of the fractional release, F, vs the square root of time, t, to increase with time, as shown in Fig. 4.31. The linear portion of the graph, based on data obtained during the first 4 1/2 hr, indicates a steady-state condition from which erroneous assumptions might have been drawn if the experiment had been terminated at that point.

Evidence of unusual behavior at 1500°C was indicated by bursts of Kr^{85} during steady operation. This phenomenon was observed for two samples. The magnitude of the largest burst was 175,000 counts/min or a fractional value of 1×10^{-4} of the total Kr^{85} contained in the sample. This release might be too small to be noticed if it occurred below 1500°C and would be obscured by the higher steady-state release above 1500°C.

The value of the diffusion parameter

$$D' = D/a^2$$

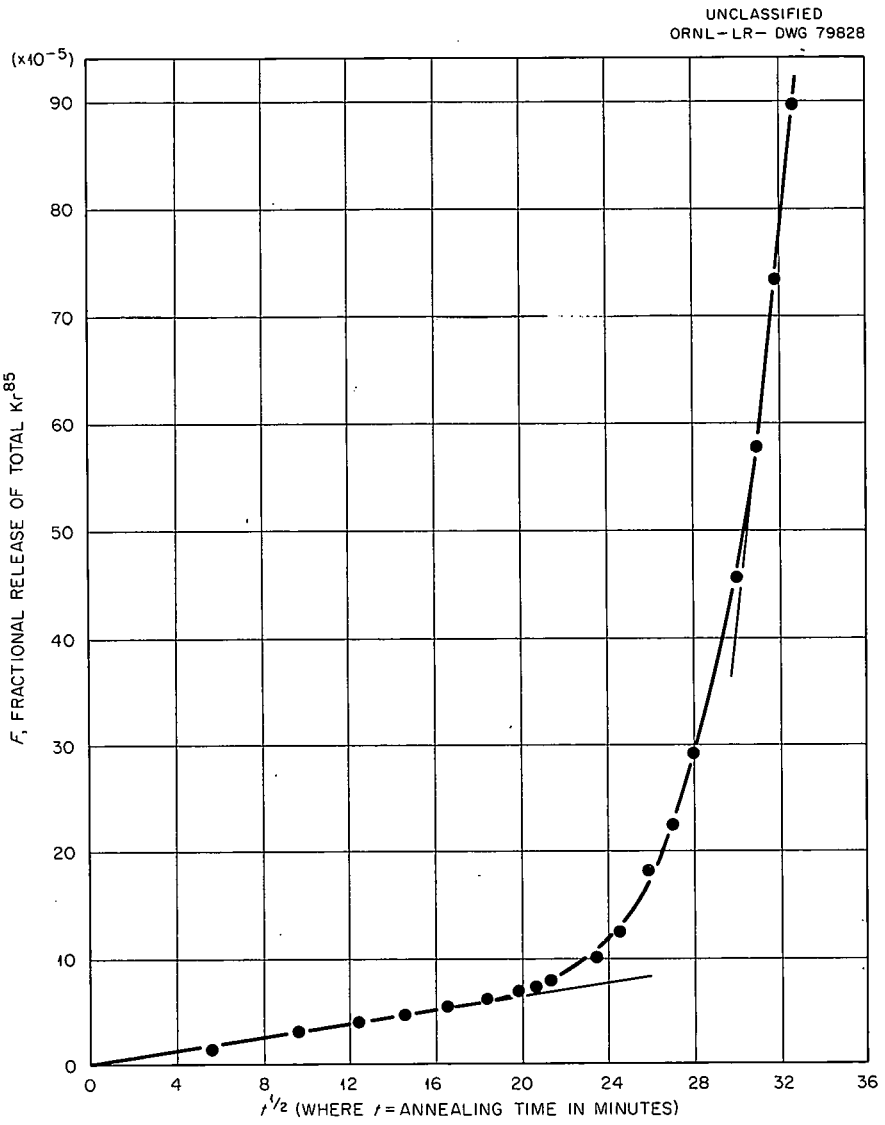

Fig. 4.31. Fractional Release of Kr^{85} from LITR-Irradiated UO_2 Upon Annealing at 1500°C. Heating-burst release was subtracted.

calculated from the equation

$$F = 6\left(\frac{D't}{\pi}\right)^{1/2},$$

where

D = diffusion coefficient,

a = equivalent sphere radius,

F = fraction of total gas released,

t = time of heating,

was 1×10^{-15} sec^{-1} for a sample annealed at 1400°C. Values of D' for higher temperatures are not given because the phenomena observed show that the gas release at higher temperatures is partly due to mechanisms other than diffusion.

Some experiments[18] have indicated that the starting point of serious damage in UO_2 is 1×10^{21} fissions/cm^3 (3.5×10^4 Mwd/MT). Data on material irradiated to such high burnups are scarce, and it is felt that it would be worthwhile to irradiate single crystals of UO_2, as well as other materials, to burnups greater than 1×10^{21} fissions/cm^3 specifically for this study. The use of single crystals would simplify the study of fission-gas release by eliminating the effects of grain boundaries and would permit geometrical calculation of surface areas ordinarily obtained by BET measurements[19] on porous materials; BET measurements can only be made on large quantities of high-density materials. Single crystals of naturally enriched UO_2 are available from several sources, but to achieve high burnups in a short time, small crystals of high enrichment will be needed. Preliminary experiments have shown that UO_2 crystals about 1 mm wide can be grown by electrolysis of uranyl chloride in solution with lithium and potassium chlorides. It is planned to produce a number of these crystals enriched to 50% U^{235} and to irradiate them to burnups in excess of 1×10^{21} fissions/cm^3.

A sample of duplex pyrolytic-graphite-coated UC_2 particles from experimental capsule B9-8 is being prepared for the next experiment. These particles have a burnup of about 30% of the uranium.

Pressure-Vessel Surveillance Program

R. G. Berggren M. S. Wechsler
W. J. Stelzman T. N. Jones

EGCR Pressure-Vessel Surveillance Specimens

Work continued on the preparation of specimens for the EGCR pressure-vessel surveillance program described previously.[20] Four strings of

[18] J. Belle (Ed.), Uranium Dioxide Properties and Nuclear Applications, pp. 559, 569, U.S. Government Printing Office, 1961.

specimen capsules will be suspended from each of two special nozzles. One string will be removed for testing after each selected period of operation. Each string consists of eighteen containers, each containing four test specimens of EGCR pressure-vessel material. The specimens include Charpy notch-impact samples and tensile samples. The material for the notch-impact samples will be representative of base plate, weld material, and heat-affected zone material. All surveillance and control specimens of base plate material have now been machined. The weld specimens are to be machined from a special weldment fabricated by the Baldwin-Lima-Hamilton Corporation according to specifications similar to those used in the welding of the actual EGCR pressure vessel. This weldment has been received at ORNL; ultrasonic and radiographic examinations have been completed; and the machining of specimens is under way. Specimen blanks have been shipped to Rensselaer Polytechnic Institute for preparation of the heat-affected zone specimens. They will be given a thermal-cycling treatment for the synthetic formation of the heat-affected zone microstructure. The appropriate thermal-cycling treatment is being determined at RPI on the basis of welding procedures used in the fabrication of the EGCR pressure vessel. To permit the correlation of results from this surveillance program with those from other programs, it is desirable to include test specimens from a "reference plate" of ASTM A-212, grade B, steel. In accordance with ASTM Tentative Recommended Practices E184-61T and E185-61T,[21] specimens from this plate are included in a number of irradiation studies being conducted at various sites in the United States. The EGCR surveillance schedule has been modified to include two tensile specimens from the reference plate in container 12 of each string. These specimens are on hand.

---

[19]S. Brunauer, P. H. Emmett, and E. Teller, "Adsorption of Gases in Multi-Molecular Layers," J. Am. Chem. Soc., 60: 309 (1938).

[20]R. G. Berggren, M. S. Wechsler, and L. D. Schaffer, Pressure-Vessel Surveillance Program, pp. 120–127, "GCRP Semiann. Prog. Rep. Sept. 30, 1962," USAEC Report ORNL-3372, Oak Ridge National Laboratory.

[21]ASTM Standards, 1961, Part 3, pp. 322 and 327, American Society for Testing and Materials.

Because of the long exposure periods involved in the surveillance program, a special problem arises with regard to neutron dosimetry. The thermal-neutron dose may be determined with cobalt detectors placed in the surveillance containers. The activity of the induced Co^{60} isotope, which has a half-life of 5.3 years, will be measured. For the measurement of fast-neutron dose, use of the $Fe^{54}(n,p)Mn^{54}$ reaction is being considered. The Mn^{54} product has a 314-d half-life; however, the cross section for the reaction is not well known. Work is now in progress to obtain the necessary information. This reaction has the advantage that the steel samples themselves may be used as the monitoring material.

Preirradiation Charpy-V impact tests have been delayed because of deviations from specifications discovered in the impact testing machine. An attempt was made to calibrate the testing machine in accordance with the ASTM "Standard Method for Notched Bar Impact Testing of Metallic Materials," ASTM E23-60.[22] The machine met all the requirements except for apparently small deviations in the dimensions of the anvil. Tests conducted on standard specimens provided by the Watertown Arsenal Laboratory indicated, however, that these deviations resulted in significant errors in the impact-energy readings. Motion pictures taken at 4000 frames per second showed interference between the broken specimens and the pendulum. Work is in progress to correct this condition.

Drop-weight impact tests are also planned. These will be carried out after the Charpy-V impact tests are completed.

SM-1 Reactor Surveillance Tests

The results of subsize Izod impact tests on surveillance specimens from the SM-1 reactor were reported previously.[20] The surveillance specimens have subsequently been analyzed by radiochemical methods for Mn^{54}, and computation of fast-neutron fluxes, based on the $Fe^{54}(n,p)Mn^{54}$ reaction, is in progress. Metallographic examination of the fractures in the surveillance specimens indicates the same fracture mode for irradiated and unirradiated specimens for the same fracture energy.

---

[22] ASTM Standards, 1961, Part 3, p. 79, American Society for Testing and Materials.

PART 2. ADVANCED REACTOR DESIGN AND DEVELOPMENT

THIS PAGE

WAS INTENTIONALLY

LEFT BLANK

5. DEVELOPMENT OF FUELED-GRAPHITE BODIES

A. Goldman

Characterization of Unsupported Fuel Particles

E. S. Bomar
F. L. Carlsen, Jr.
J. L. Cook
R. J. Gray

Crushing Load

Additional data were obtained that supplement those previously reported[1] on the load necessary to crush individual particles of pyrolytic-carbon-coated and uncoated uranium carbide from various lots of particles. These data are presented in Table 5.1.

Comparison of the crushing strength with in-pile performance has shown[1] that a direct dependence exists between the number of cracked coatings found after irradiation and the minimum crushing load for a sample from a given lot of particles. This suggests that the behavior of the particles in the reactor is determined by the weakest members. Examination of the data of Table 5.1 shows that the minimum crushing loads may be less than one-half the average value.

Consideration was given to an alternate test for determining the crushing load that would permit the simultaneous examination of a large number of particles. In the alternate test, a monolayer of coated particles was placed between a steel punch and a neoprene pad in a die and loaded into a press. A series of samples was pressed with loads ranging from 2,500 to 20,000 lb. The particles thus treated were leached with nitric acid and analyzed for exposed uranium. The results given in Table 5.2 show that the exposed uranium amounted to less than that contained in a single particle until the load exceeded 10,000 lb. If it can be demonstrated that this test causes selective destruction of the weakest particles present, such a treatment might be used to remove such particles.

---

[1]E. S. Bomar et al., Characterization of Unsupported Particles, pp. 186–189, "GCRP Semiann. Prog. Rep. Sept. 30, 1962, USAEC Report ORNL-3372, Oak Ridge National Laboratory.

Table 5.1. Data on Load Required to Crush Pyrolytic-Carbon-Coated and Uncoated Uranium Carbide Particles

Lot No.	Crushing Load (g)			
	Average[a]	Standard Deviation	Maximum	Minimum
GA-301	970	250	1362	530
-302	1168	342	2105	615
HTM-20[b]	472	278	982	86
-40N	622	114	904	452
3M-A	259	74	441	148
-E	984	175	1479	706
-G	227	53	363	90
-101-61	1180	513	2644	755
-101-62	754	139	999	487
-101-63	1147	337	2165	615
-117	1252	256	1973	658
-118	1776	304	2404	1180
-119	1796	339	2482	1200
-120	1318	304	2454	755
-10695-47	1461	419	2394	877
NCC-SF[b]	699	238	1224	300
-G	1293	182	1505	924
-208-1	1438	197	2364	1000
-208-2	1422	238	1865	921
-208-3	1560	183	1833	1220
-209	1022	142	1300	702
NUMEC-400	836	212	1288	548
-915	1690	353	2285	917
OSAE-1	1712	681	3912	846

[a]Values based on data obtained by crushing 50 particles from each lot.

[b]Uncoated particles.

Coated-Particle Dimensions

The results of irradiation tests also suggest that coating thickness may be an important factor in characterizing coated particles. A systematic examination of coated particles from various sources is being made to provide data both for comparison with in-pile behavior and observation of the effect of coating thickness on fueled-graphite fabrication. Measurements taken from microradiographs are presented in Table 5.3.

Table 5.2. Effect of Various Loads Applied to Monolayers of Coated Particles from Batch 3M-119

	Sample							
	1	2	3	8	6	5	7	4
Load on 1.182-in. punch, lb	2,500	5,000	10,000	12,000	14,000	16,000	18,000	20,000
Number of particles in sample	5,100	5,100	5,000	5,000	5,000	5,100	5,100	5,100
Load per particle, g	220	450	910	1,090	1,270	1,430	1,600	1,780
Total uranium leached,[a] µg	3.43	1.31	1.43	94	149	700	2,180	3,480
Equivalent broken coated particles	0.2	0.1	0.1	5	8	36	113	180

[a]Uranium content of average particle was 19 µg.

Table 5.3. Dimensional Measurements of Pyrolytic-Carbon-Coated Fuel Particles Based on Microradiographic Examination of Samples Containing 50 Particles

Lot No.	Core Diameter (μ)			Coating Thickness (μ)			Total Particle Diameter (μ)		
	Mean	Standard Deviation	Minimum	Mean	Standard Deviation	Minimum	Mean	Standard Deviation	Minimum
HTM-40N	194	30	145	42	9	12	276	21	220
-80N	183	23	155	62	9	40	307	10	285
3M-108	172	18	130	36	8	25	245	20	210
-111	210	38	160	34	4	25	278	40	210
-113	196	21	110	137	14	105	470	24	420
-114	188	33	130	84	6	70	357	36	300
-116	167	12	145	98	15	75	363	29	315
-117	176	9	160	98	9	70	372	16	330
-118	173	9	160	133	7	96	400	20	360
NCC-K	226	21	185	102	17	88	425	22	360
-104	256	29	175	122	24	62	499	62	405
-105	243	26	185	76	8	55	395	31	310
-106	230	29	180	41	4	35	314	33	260
-201	230	28	150	107	11	92	443	26	405
-207	220	20	185	101	7	90	422	20	395

Measurement of Exposed Fuel

The initially exposed fuel establishes the minimal release of fission products that can be expected in the reactor. Specifications have been selected which require that surface contamination of either as-received or thermally cycled particles, as determined by alpha counting, should not exceed $5 \times 10^{-3}\%$ of the contained fuel. Similarly, leachable fuel must not exceed $5 \times 10^{-3}\%$ of the contained fuel for either of these conditions. The results of measurements on several lots of coated particles with regard to these variables are presented in Table 5.4.

Effect of Heat Treatment on Fuel Migration

Movement of fuel through the pyrolytic-carbon coating can cancel the benefit of the coating in two ways: (1) fuel located near the coating surface will release fission products to the matrix surrounding the particle by recoil, and (2) the presence of uranium in a pyrolytic-carbon coating might result in a sensitivity to moisture that could cause failure of the coating.[2] Tests for extended periods of up to 1000 hr are under way to determine fuel migration in a number of types of coated particle at temperatures of 1000 to 2000°C, and measurements have been made on 23 samples heat treated by vendors. The measurements were made by microscopic examination at 200X of contact microradiographs. Fuel migration was characterized by two zones in each particle: (1) a region of high concentration in the coating adjacent to the core fuel particles and (2) a point of farthest migration of fuel from the core particle, even if this migration appeared as a small, isolated spot. The results of these measurements are listed in Table 5.5. Data for the NCC series provide a comparison with the 3M series of the behavior of six lots of particles prepared under different conditions. The control particles for each of the NCC samples showed an initial movement of fuel; the 3M control particles showed none. Relative movement of fuel in the NCC coatings during subsequent heat treatments was both greater and less than observed for

[2] J. L. Scott et al., Fission-Product-Retention Characteristics of Coated Fuel Particles, pp. 194–197, "GCRP Semiann. Prog. Rep. Sept. 30, 1962," USAEC Report ORNL-3372, Oak Ridge National Laboratory.

Table 5.4. Measurements of Exposed Fuel on Pyrolytic-Carbon-Coated Fuel Particles Before and After Thermal Cycling

Lot No.	As-Received				After Thermal Cycling[c]			
	Surface Contamination[a] (%)	Material Removed by HNO_3 Leach[b]		Surface Contamination After Leaching[a] (%)	Surface Contamination[a] (%)	Material Removed by HNO_3 Leach[b]		Surface Contamination After Thermal Cycling and Leaching[a] (%)
		U (%)	Th (%)			U (%)	Th (%)	
	$\times 10^{-3}$	$\times 10^{-3}$	$\times 10^{-3}$	$\times 10^{-3}$	$\times 10^{-3}$	$\times 10^{-3}$	$\times 10^{-3}$	$\times 10^{-3}$
GA-301	<1.7	2.9	10.6	<1.0	<1.7	<0.2	<5.7	<1.7
-302	0.30	3.6	1.7	<0.06	0.10	<0.2	<6.1	0.17
3M-D	70.0	24.8		27.6	21.0	0.2		12.4
-F	17.4	237.0		10.3	26.7	0.2		22.8
-G	27.5	14.0		1.1	33.8	450		448
-101-61	<0.01	15.2		<0.01	2.9	39.9		3.0
-116	<1.7	182.0		<2.5	7.6	1.2		5.1
-117	<1.8	0.09		<0.6	<3.6	7.1		<0.6
-118	0.2	0.4		<0.01	<0.01	0.2		<0.01
-119	<0.4	<0.03	<0.2	<0.4	1.3	<0.03	<0.9	1.3
NCC-J	8.4	3.3		12.6	18.6	34.6		10.8
-K	2.8	3.7		6.8	6.3	6.6		10.2
-201	2.4	124.0		1.2	3.6	8.5		1.8
-207	0.3	<0.1		0.3	0.4	2.1		0.4
-208-2	1.43	<0.5	<7.8	1.41	1.29	<0.5	<7.8	1.4
-209	4.9	<0.2		3.8	4.0	<0.2		3.7
NUMEC-400	0.5	8.2		<0.1	2.8	9.9		2.6
-915	<0.8	0.2		<0.8	7.6	3000		0.8

[a] Determined by alpha counting and expressed as percentage of total fuel in particles.

[b] Treated with 8 M HNO_3 at 95°C for 8 hr; material removed expressed in terms of total quantity of uranium vs thorium in particles.

[c] Sample cycled three times between 200 and 1450 to 1500°C with a 1-hr hold time at the temperature extremes.

Table 5.5. Fuel Migration in Coatings During Heat Treatment of Pyrolytic-Carbon-Coated Uranium Carbide Particles

Coated Particle Identification	Conditions of Heat Treatment[a]	Fuel Diffusion[b] (μ)	
		Average[c]	Maximum[d]
CA-1332-4N[e]	6 hr at 2000°C	10	38
3M-102B-4	Control	0	0
-1	3 hr at 1500°C	0	0
-2	3 hr at 1750°C	6	11
-3	5 min at 1950°C	10	14
NCC-3M	Control	0	0
-3M-15	300 hr at 1500°C	2	28
-3M-17	307 hr at 1700°C	4	107
NCC-202	Control	15	20
-202-15	300 hr at 1500°C	17	21
-202-17	307 hr at 1700°C	21	104
NCC-203	Control	9	13
-203-15	300 hr at 1500°C	16	82
-203-17	307 hr at 1700°C[f]	44	90
NCC-204	Control	7	10
-204-15	300 hr at 1500°C	7	75
-204-17	307 hr at 1700°C	9	97
NCC-205	Control	19	35
-205-15	300 hr at 1500°C	23	111
-205-17	307 hr at 1700°C[f]	37	90
NCC-206	Control	7	13
-206-15	300 hr at 1500°C	8	92
-206-17	300 hr at 1700°C	14	97

[a] Performed by supplier.

[b] Distance measured from original interface between fuel particle and coating. Measurements taken from contact microradiographs.

[c] Region of heavy concentration adjacent to fuel particle. Two measurements made on each of 50 particles.

[d] Region of farthest movement of fuel into coating, even though a small, isolated spot.

[e] As-deposited control particles not supplied.

[f] The original interface was obscured by gross fuel movement. Measurement of both zones of diffusion possibly in error. Note inverse values of maximum diffusion zones for NCC-205-15 and -17.

3M material. Coatings in the NCC-204 lot resisted fuel movement best, showing no change in the core zone after 300 hr at 1500°C and only a 2-μ change after 307 hr at 1700°C.

The appearance in the microradiographs of a heavy concentration of high-density material at the surface of many particles in several different lots without a commensurate change in diffusion zone at the core led to a suspicion that the apparent extensive diffusion was in fact a superficial deposit of high-density material from an exterior source. Microradiographs of two samples showed the contaminant to be removed after either treating in a nitric acid solution or chlorine-bearing argon at 800°C for 1 1/2 hr. Particles from lot No. NCC-203-17 are shown in Figs. 5.1 and 5.2 before and after the chlorine treatment. Except for the

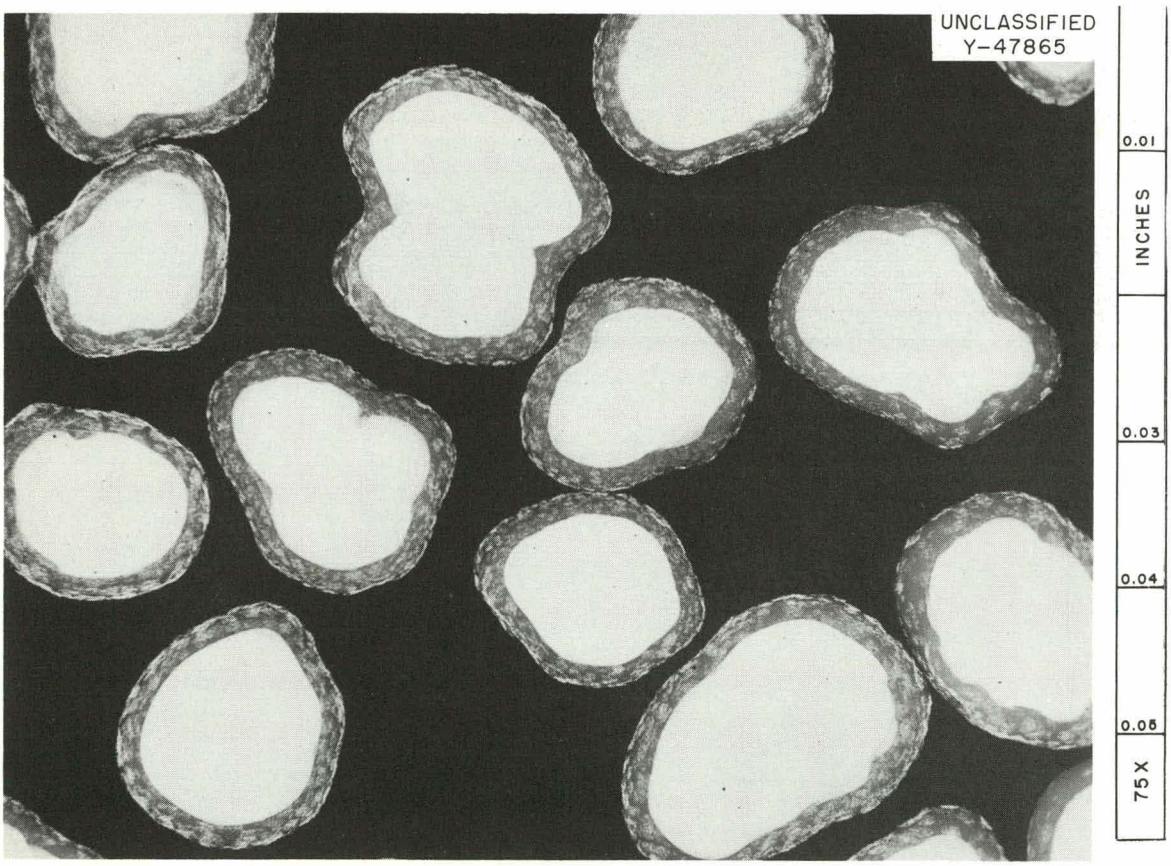

Fig. 5.1. Sample NCC-203-17 Which Has Been Heated at 1700°C for 307 hr. The spotty regions of high density in the coating are superficial contamination rather than fuel migration from core.

Fig. 5.2. Sample NCC-203-17 Following Supplemental Treatment with a Chlorine-Argon Mixture at 800°C. The surface contamination has been removed.

diffusion which occurred at the interface of the core particle and coating, the coating of the chlorine-treated sample had the same appearance as the control sample, which was not heat treated.

Pyrolytic-Carbon-Coating Equipment

Equipment was assembled to permit deposition of pyrolytic-carbon coatings on particles under known conditions. The relationship between the conditions of coating application and the resulting coating properties will be established. The equipment features a graphite nozzle in a mullite tube. The feed material is fluidized by a gas stream that contains a carbonaceous gas. The maximum temperature capability is about 1400°C.

A limited number of runs has been made, and coating microstructures ranging from laminar to columnar and combinations of these have been

prepared. Information was obtained on how to minimize defects such as multiple particles in a common coating and delamination of coatings. It was demonstrated that the particles could be fluidized and the coatings applied at reduced pressures, thus offering the possibility of a large reduction in the amount of gas used. Coating equipment for operation up to 2000°C is being assembled.

Fission-Product-Retention Characteristics of Coated Fuel Particles

R. B. Fitts

The results of a series of neutron-activation tests on coated particles are presented in Table 5.6. These tests were made to determine the integrity of the particle coating based on its ability to retain the fission gases generated during irradiation.

Thermal Conductivity of Coated-Particle Fuels

P. DeNee D. L. McElroy

An apparatus for measuring the thermal conductivity of powder in a controlled atmosphere was tested at temperatures up to 820°C with a magnesium oxide specimen in vacuum and in helium. The technique employed consisted of measuring, as a function of time, the temperature rise of a 1/8-in. tantalum tube immersed in the powder specimen when the tube was heated by a constant power input. Prior to a run, the specimen was brought to the desired temperature in a tubular furnace, which enclosed the specimen. The temperature rise of the probe above this temperature (usually a 10 to 20° rise) was measured when the power to the probe was turned on. Radial heat flow in the specimen was ensured by providing special radiation shields over the ends of the furnace so that the temperature profile along the axis of the furnace was essentially flat in the region of the specimen. The furnace and specimen were enclosed in a chamber that could be evacuated or filled with gas to a pressure of 2 atm.

The low-temperature results agreed with literature values and were reproducible to ±5%; however, the high-temperature results displayed

Table 5.6. Fission-Product Release from Pyrolytic-Carbon-Coated Fuel Particles

Sample No.	Core Material	Xe^{133} Released During Capsule Puncture Test (ppm)	Xe^{133} Released During Vacuum Annealing		
			Temperature (°C)	Time (hr)	Release (ppm)
NCC-201	UC_2	<1	1400	3	<20[a]
3M-116	UC_2	2.07	1400	3	<10[a]
-118	Monocrystalline UC_2	<1	1000	24	<1
-1178-A[b]	$(U + Th)C_2$	<1	1000	3	<1
-1178-B	$(U + Th)C_2$	<1	1000	3	<1
-1178-C	$(U + Th)C_2$	<1	1000	3	<1
-1178-G	$(U + Th)C_2$	1.33	1000	3	<1
-1178-H	$(U + Th)C_2$	<1	1000	3	<1
-1178-I	$(U + Th)C_2$	<1	1000	24	<1
-1178-EI	$(U + Th)C_2$	<1	1000	24	<1
-1178-TE-2	$(U + Th)C_2$	<1	1000	24	<1
GA-302	$(U + Th)C_2$	<1	1000	24	8.2

[a] Low sensitivity because of low U^{235} content of sample.

[b] All 3M-1178 samples and sample GA-302 had a thorium-to-uranium ratio of 0.61.

certain anomalies that indicated the need for both a larger specimen container to more nearly fulfill the boundary conditions of the method and for an improved electrical system. These changes were nearly completed, and, in addition, an all-metal gas-purification train was added to the system to allow measurements up to several atmospheres. Measurements of coated-particle fuels will be initiated in the near future.

Fission-Product Deposition Studies

J. L. Scott

Most studies of fission-product release have involved measurement of the rates of release of the inert gases xenon and krypton. Relatively little work has been done on measurements of the release of other fission-product species. For clad fuels, emphasis on the inert gases is logical, since pressure buildup within the cladding is the main problem. In unclad fuel systems, however, contamination of the primary coolant circuit with long-lived gamma emitters is a major concern. Thus it is necessary that quantitative information be obtained on the release, transport, and deposition of other fission-product species from such fuels.

A small loop was developed for obtaining deposition data on species such as I^{131}, Ba^{140}, Sr^{89}, and Te^{132}. Except for the test section, the loop consists of 3/8-in.-diam stainless steel tubing, and it contains a flow meter, a diaphragm-type circulating pump, and a bypass line to a liquid nitrogen-cooled charcoal trap, which is continuously monitored for Xe^{133}. Provisions are made for helium pressurization or evacuation.

The test section consists of a 27.5-in. length of 3/4-in.-diam, 20-mil-wall, stainless steel tubing. A small resistance furnace is used to heat a 9-in. length of the test section to 1000°C. Twelve thermocouples are spot welded at intervals along the test section to measure the temperature distribution. A sheathed thermocouple is inserted within the fuel sample holder to measure the actual fuel temperature. A stainless steel holder containing copper- and silver-impregnated charcoal (Whetlerite) is installed at each end of the test section to contain the fission-product species within the test section.

Two tests have been completed to date. Both specimens were uncoated uranium carbide particles from batch 3M-112U. The samples were irradiated at room temperature to a burnup of about 10^{15} fissions per sample. In the first test the sample was placed in the loop after neutron activation and was held at 560°C for 24 hr. The helium pressure was 10 psig and the flow rate was 8 liters/min. The temperature gradient along the tube varied from 36°C at the ends of the tube to 660°C at the center of the furnace adjacent to the fuel samples. During the run, the Xe^{133} content of the charcoal trap increased continuously at approximately a linear rate, and the total fractional release of Xe^{133} was 0.21. This amount was much higher than that observed to be released from duplicate samples sintered in vacuum at the same temperature and was attributable to the partial oxidation of the uranium carbide to uranium oxide during the run. At the end of the heating period, the fuel sample was removed from the loop, and the deposition tube was monitored for gamma activity by autoradiography and scintillation spectrometry. No detectable activity was found on the deposition tube by either technique. There were, however, traces of I^{133} in the upper Whetlerite trap.

In order to increase fission-product release, the second test was run at a considerably higher temperature (~790°C). Again the duration of the run was 24 hr. The helium pressure was 6 psig and the flow rate was 4.8 liters/min. The fractional release of Xe^{133} was 0.42. The high release was again attributable to oxidation of the uranium carbide. As the uranium carbide is converted to uranium oxide, a phase boundary moves across each fuel particle and acts as a short-circuit diffusion path for the release of volatile fission products. When the fuel sample was removed, the deposition tube was found to be highly radioactive, in contrast to the first run, and both I^{131} and Te^{132} were found along the tube. Since the specimen was 23 days old, most of the 77-h Te^{132} had decayed, and the predominant activity came from 8.05-d I^{131}. The total fractional release values were 0.06 for Te^{132} and 0.41 for I^{131}. Since the release of I^{131} was about the same as the release of Xe^{133} at 790°C, whereas only traces of I^{131} were found at 560°C, it is suspected that the iodine was adsorbed by the graphite bottle at the lower temperature.

The distribution of activity and the temperature distribution in the second loop are shown in Fig. 5.3. Although traces of I^{131} and Te^{132} were found at the hottest points of the deposition tube, most of the Te^{132} was found at a point 11 in. from the bottom of the tube. At this location the tube-wall temperature was about 600°C. The I^{131} began to deposit in more than trace amounts where the tube was at 440°C and showed a very intense maximum where the tube was at 300°C.

A theoretical interpretation of the I^{131} distribution is possible. First, the point x = 0 is arbitrarily chosen at a point 11.9 in. from the bottom of the deposition tube. The temperature distribution is then assumed to fit an equation of the form

$$T = \frac{a}{x + b} , \qquad (1)$$

where T is the absolute temperature, x is the distance along the tube, and a and b are constants. If it is assumed that $T = T_0$ at x = 0 and

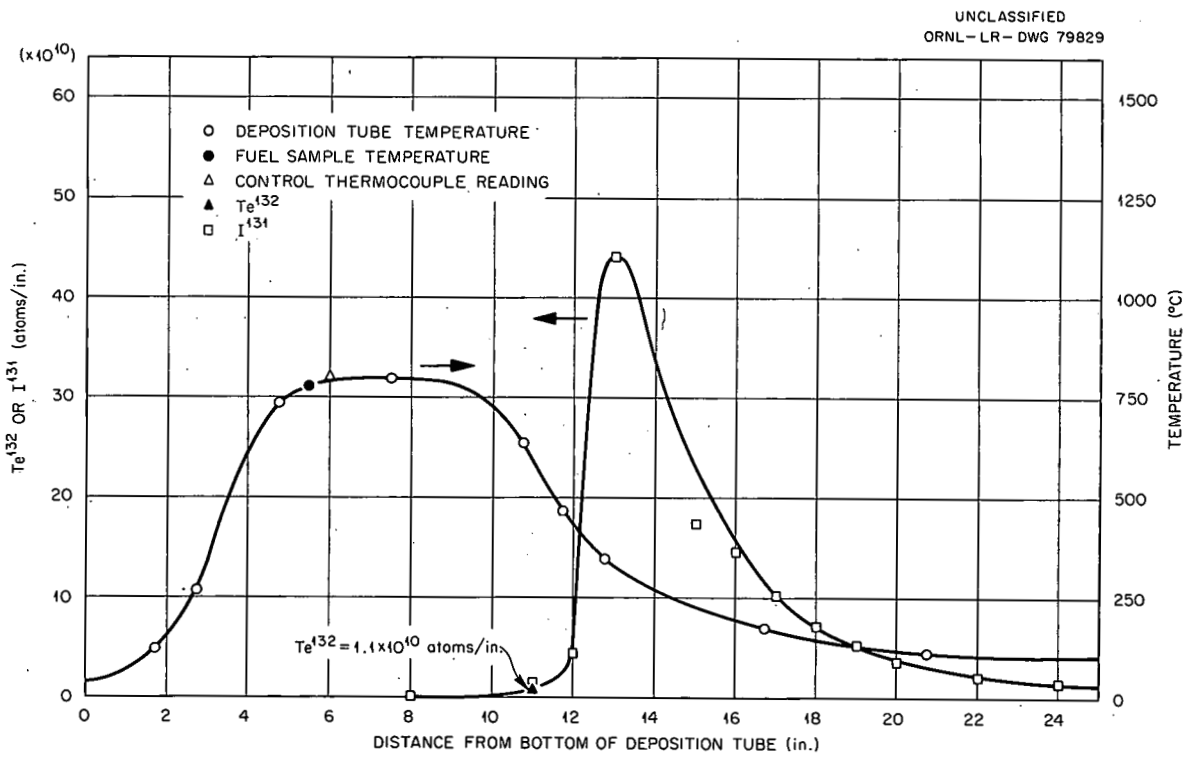

Fig. 5.3. Distribution of Fission Products on Deposition Tube.

$T = T_f$ at $x = \ell$, where ℓ is the distance to the end of the tube, then

$$T = \frac{\dfrac{T_0 T_f \ell}{T_0 - T_f}}{x + \dfrac{T_f \ell}{T_0 - T_f}} . \tag{2}$$

Next, it is assumed that deposition occurs by an adsorption process and that the gas in equilibrium with a given deposit obeys the Arrhenius equation

$$P^* = P_0^* \, e^{-\Delta H_a / RT} , \tag{3}$$

where P^* is the vapor pressure of the adsorbed species, ΔH_a is the heat of adsorption, R is the gas constant, and P_0^* is a constant. The equilibrium concentration, C^*, of the deposited species in the gas phase is then given by the equation

$$C^* = \frac{P^*}{RT} = \frac{P_0^*}{RT} e^{-\Delta H_a / RT} \approx \frac{P_0^*}{RT_0} e^{-\Delta H_a / RT} . \tag{4}$$

By combining Eqs. (2) and (4),

$$\frac{C^*(x)}{C^*(0)} = e^{-\alpha x} , \tag{5}$$

where

$$\alpha \equiv \frac{\Delta H_a \, (T_0 - T_f)}{R T_0 T_f \ell} . \tag{6}$$

By a material balance the gas composition is found to obey an equation of the form

$$\frac{dC}{dx} + \beta C = \beta C_0^* \, e^{-\alpha x} , \tag{7}$$

where

$$\beta \equiv \frac{2K_D}{rv} . \tag{8}$$

In Eq. (8), K_D is the deposition rate constant, r is the tube radius, and v is the linear gas velocity. Solving Eq. (7) and making use of the following relationship for the fraction of the species deposited per unit length,

$$\frac{df}{dx} = \beta \frac{C - C^*}{C_0^*} , \tag{9}$$

the fission-product distribution is

$$\frac{df}{dx} = \frac{\alpha\beta}{\beta - \alpha} (e^{-\alpha x} - e^{-\beta x}) . \tag{10}$$

The actual values of α and β for the data in Fig. 5.3 were $\alpha = 0.51$ cm^{-1} and $\beta = 0.19$ cm^{-1}. From the experimental value of α and Eq. (6), the heat of adsorption was determined to be 26.2 kcal/mole. Similarly, from β the value of K_D was calculated to be 2.73 cm/sec. Both values appear to be reasonable. The heat of adsorption is consistent with a chemisorption process either of I, I_2, or CsI species. In view of the small number of atoms of I^{131} present (1.62×10^{12}), the chemisorption of iodine ions is probably the correct process. The small amounts of I^{131} observed to be deposited at 800°C are adsorbed by a different mechanism, probably by van der Waal's forces.

When the tube-wall temperature is below about 300°C, the tube wall becomes an infinite sink for I^{131} atoms in the concentration range under discussion, and the rate of deposition is controlled by the rate at which the I^{131} ions strike the surface. For laminar gas flow, the deposition constant is approximately

$$K_D = \frac{48 D_G}{11 D} , \tag{11}$$

where D_G is the diffusion coefficient of the depositing species in the gas phase, and D is the tube diameter. If D_G is taken as 1 cm^2/sec, then $K_D = 2.2$ cm/sec. This compares well with the value 2.73 cm/sec found experimentally.

Fueled-Graphite Fabrication

J. M. Robbins A. J. Taylor

Attempts to "isostatically" form fueled-graphite spheres with polyvinyl chloride gel molds[3] were abandoned because of the problems associated with filling the mold cavity and the nonuniformity of forces applied under uniaxial loading. A second approach involving light cold forming followed by high isostatic compression in oil was more successful. The preforming operation was carried out at room temperature with a Lucite die and hemispherical concave Lucite punches. The dimensions of spheres preformed at low pressures (approximately 100 psi) were reduced uniformly on subsequent compaction under high isostatic pressure (approximately 35,000 psi). The simple three-piece forming die was not entirely suitable, however, because (1) the sharp edges of the punches were highly susceptible to chipping, (2) a molding flash was formed at the equator of the spheres, and (3) the die design did not readily lend itself to the fabrication of spheres with molded unfueled shells. A new die was designed to eliminate these objectionable features and was ordered.

Experimental work was continued to obtain a better understanding of the variables associated with the fabrication of high-density, high-strength graphite bodies by molding and baking techniques. Graphite bodies were prepared from mixtures of fine-grained natural and synthetic graphite powder and a furan resin binder. Cylindrical pellets representing eight compositions of these ingredients were formed at a low-forming pressure (100 psi) and then isostatically pressed at various pressures ranging from 500 to 35,000 psi. All specimens were baked in hydrogen on a 24-hr schedule at 1000°C. While densities greater than 1.7 g/cm^3 were achieved, the isostatic-forming pressures required to obtain these densities (>20,000 psi) were higher than can be tolerated when pyrolytic-carbon-coated fuel particles are incorporated in the body. To clarify this point, an experiment is being performed using fueled-graphite cylinders fabricated

---

[3]J. M. Robbins and A. J. Taylor, Fueled-Graphite Fabrication, pp. 201–202, "GCRP Semiann. Prog. Rep. Sept. 30, 1962," USAEC Report ORNL-3372, Oak Ridge National Laboratory.

with a graphite matrix of known fabrication characteristics. Fuel concentrations of 8, 14, 20, and 26 vol % pyrolytic-carbon-coated carbide particles are being used. The several bodies were formed into cylindrical pellets (approximately 1 in. OD and 1 in. long) at a pressure of 100 psi and then isostatically pressed at 3,000, 6,000, 9,000, 12,000, 15,000, 20,000, 25,000, or 35,000 psi. Standard baking and testing techniques were used. Baking was done on a 24-hr schedule in hydrogen at 1000°C. Testing has not been completed but consists of radiography, metallography, and anodic disintegration followed by acid leaching. A sample of the as-received pyrolytic-carbon-coated fuel particles was acid-leached and analyzed in order to determine the background uranium value.

Evaluation of Fueled-Graphite Spheres

E. S. Bomar
F. L. Carlsen, Jr.
J. L. Cook
R. W. McClung

The evaluation studies of graphite spheres fueled with pyrolytic-carbon-coated uranium carbide particles were continued.[4] The lots of spheres received during this report period are described in Table 5.7. The spheres are all 1 1/2 in. in diameter, although they vary in design and fuel loading. With the exceptions noted in Table 5.7, the spheres contain thorium-uranium carbide particles with a thorium-to-uranium ratio of approximately 0.6.

Visual and Dimensional Examinations

Spheres from several lots are shown in Fig. 5.4. The GA-S-1, GA-S-9, NCC-S-2, and 3M-S-4 spheres do not have unfueled shells, and the coated particles present on the surface are discernible. No coated particles are present on the surfaces of the spheres that have unfueled shells. The GA spheres have very smooth surfaces, evidently produced by machining and polishing.

---

[4]E. S. Bomar et al., Evaluation of Fueled Graphite Bodies, pp. 203–213, "GCRP Semiann. Prog. Rep. Sept. 30, 1962," USAEC Report ORNL-3372, Oak Ridge National Laboratory.

Table 5.7. Descriptions of 1 1/2-in.-diam Fueled-Graphite Spheres Containing Pyrolytic-Carbon-Coated Fuel Particles That Were Received for Evaluation

Lot Designation	Thickness of Unfueled Shell (in.)	Coated Particle Batch Number	Uranium Enrichment (at. %)	Heavy Metal Content (wt %)
GA-S-1	0	302	93	6
-2	1/4	302	93	6
-3	0	301	0.7	6
-4	1/4	301	0.7	6
-5[a]	0	301	0.7	6
-6[a]	1/4	301	0.7	6
-7	1/4	301	0.7	6
-8	1/4	302	93	6
-9[a]	1/4	302	93	6
-10[a]	0	302	93	6
NCF-S-1	0		0.7	6
-2	0	208	93	6
-3	0		0.7	6
-4[b]	0	209	93	10
-5	0	208	18.6	5
-6	1/4	208	18.6	5
-7	1/4	208	93	6
NCP-SS-1[b,c]	1/4–7/16	207	93	1.2
3M-S-1	0		93	6
-2	0		0.7	6
-3	1/16		0.7	6
-4	0		93	6
-5	1/16		93	6

[a] Impregnated to reduce permeability.

[b] Spheres contained no thorium.

[c] Fuel contained in a cylindrical insert approximately 0.6 in. in diameter and 0.6 in. high.

Many of the spheres in the NCF lots have hairline cracks around the smaller diameter die marks, but no cracks were observed on the spheres from GA and 3M. The diameters of nearly all the spheres were within the specified tolerance of ±0.032 in. Only two of a total of 300 spheres were out of tolerance and these by only 0.001 to 0.002 in. The maximum deviations from sphericity (defined as the difference between maximum

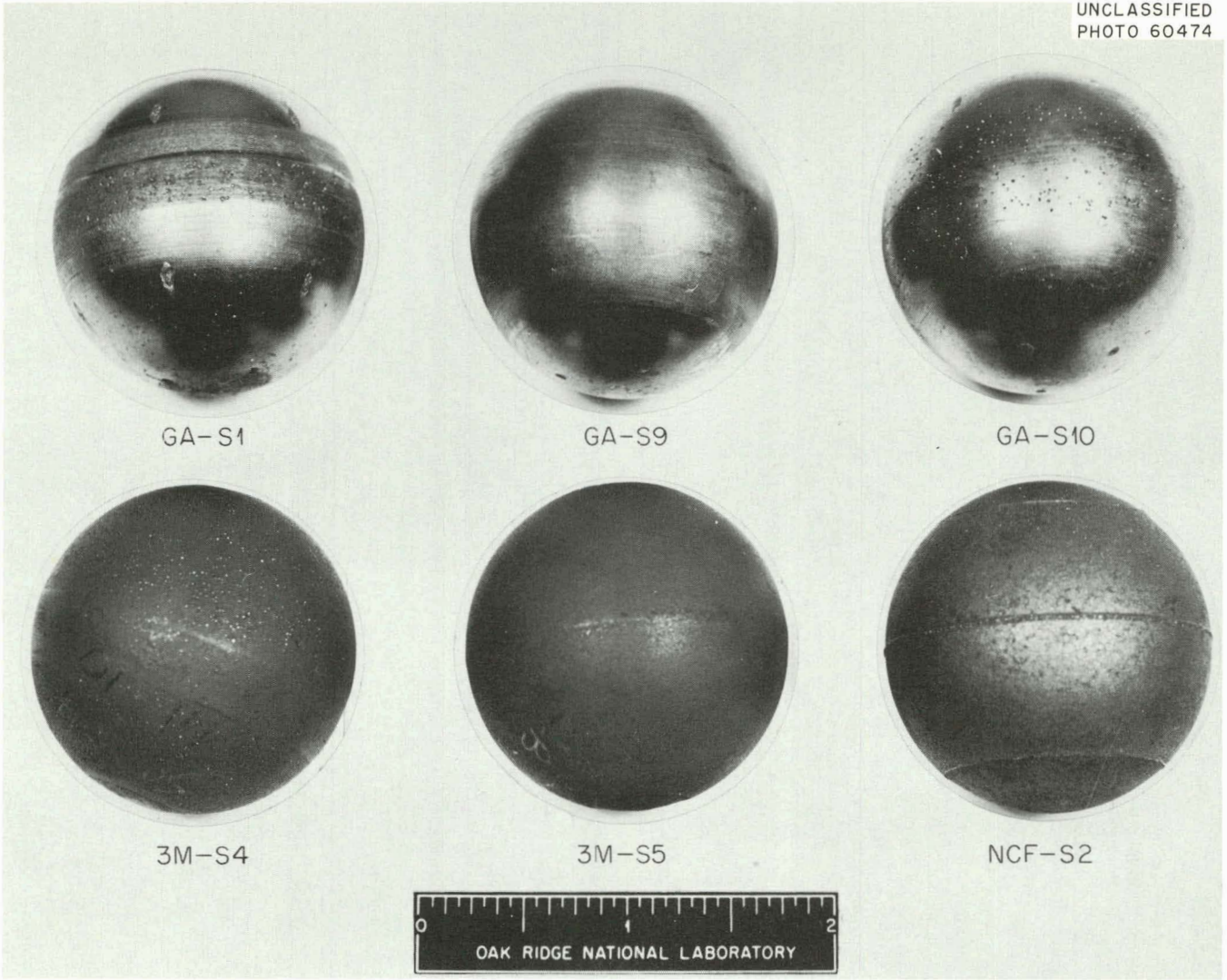

Fig. 5.4. Fueled-Graphite Spheres Representative of Lots GA-S-1, GA-S-9, GA-S-10 in the Top Row and Lots 3M-S-4, 3M-S-5, and NCF-S-2 in the Lower Row.

and minimum diameters on a sphere) for the lots are given in Table 5.8 and range from 0.011 to 0.045 in.

Table 5.8. Sphericity and Density of Fueled-Graphite Spheres

Lot Designation	Maximum Deviation from Sphericity (in.)	Bulk Density (g/cm^3)		Net Carbon Density (g/cm^3)
		Average	Range	
	$\times 10^3$			
GA-S-1	40	1.87	1.86–1.90	1.76
-2	45	1.88	1.86–1.89	1.77
-3	34	1.91	1.89–1.93	1.80
-4	26	1.91	1.86–1.96	1.80
-5	17	1.95	1.93–1.98	1.84
-6	28	1.94	1.90–1.96	1.84
-7	25	1.92	1.88–1.95	1.81
-8	33	1.90	1.87–1.93	1.78
-9	27	1.93	1.90–1.95	1.82
-10	27	1.87	1.84–1.88	1.76
NCF-S-1	12	1.79	1.77–1.81	1.68
-2	28	1.78	1.75–1.81	1.67
-3	26	1.79	1.75–1.82	1.72
-4	29	1.82	1.79–1.85	1.65
-5	32	1.82	1.79–1.85	1.73
-6	13	1.78	1.77–1.81	1.67
-7	14	1.80	1.78–1.82	1.69
3M-S-1	11	1.81	1.80–1.82	1.70
-2	23	1.81	1.80–1.83	1.70
-3	19	1.82	1.81–1.83	1.71
-4	14	1.78	1.77–1.78	1.67
-5	24	1.79	1.78–1.79	1.68

The bulk densities and net carbon densities are also given in Table 5.8. The densities of the GA spheres were considerably higher than those of the other spheres, although all spheres exceeded the required minimum bulk density of 1.70 g/cm^3. The variation in the bulk density of all the spheres within any particular lot is less than 10%.

Evaluations of Unfueled Graphite Shells

Radiographic examinations of elements with unfueled graphite shells permit the determination of the thickness and quality of the shell. In general, the unfueled shells are slightly thicker parallel to the molding direction than they are perpendicular to the molding direction. For example, the thickness of the unfueled shell on a sphere from lot NCF-S-6 was 5/16 in. in the parallel direction and 1/4 in. in the perpendicular direction. The axes of the fueled region were 7/8 and 1.0 in. in these directions, respectively.

Integrity of Contained Coated Particles

The integrity of the coated particles in the spheres was determined by alpha counting, acid electrolysis, and neutron-activation studies. The alpha activity of a sphere is a measure of the uranium contamination on the surface. The values given in Table 5.9 show that the contamination varies considerably within a lot. The relatively high contamination of the GA spheres may have resulted from coated particle damage when the die marks were removed by machining. Attempts to minimize this contamination by leaching the spheres in 16 M HNO_3 at room temperature were not effective.

The acid electrolysis treatment consists of placing a fueled-graphite body on a platinum electrode, submerging the body and electrode in 8 M HNO_3, and establishing a direct current of approximately 5 amp between the fueled-graphite body and a second platinum electrode. The graphite body disintegrates after 8 to 24 hr under these conditions. The coated particles contained in the matrix are thus exposed to the 8 M HNO_3, which removes the uranium from particles with defective coatings. Analyses of the 8 M HNO_3 for uranium permit determination of the amount of exposed uranium within the spheres. Only one determination is made for each lot because of the destructive nature of the test.

The high values of internally exposed uranium given in Table 5.9 for lots GA-S-2 and GA-S-4 are attributed to excessive pressure during fabrication. The fabrication process has been altered to produce elements

Table 5.9. Exposed Uranium and Fission-Gas Release from Fueled-Graphite Spheres

Lot Designation	Exposed Uranium (%)		Xenon Release[c] (%)	Ratio of Xe^{133} Release to Internally Exposed Uranium
	Surface[a]	Internal[b]		
	$\times 10^{-4}$			$\times 10^{-2}$
GA-S-1	10–40	0.5	8.0×10^{-3}	1.6
-2	0.1–0.4	16.5	1.1	6.7
-3	4–400	0.35	(d)	
-4	3–240	6.7	(d)	
-5	8–110	0.31	(d)	
-6	(d)	0.34	(d)	
-7	(d)	0.25	(d)	
-8	0.01–0.02	1.03	(d)	
-9	0.01–0.014	(d)	(d)	
3M-S-1	0.01–0.2	0.005	1.5×10^{-3}	30
NCF-S-1	<1	0.09		
-2	0.01–0.8	0.09	6.2×10^{-3}	6.9
NCP-SS-1	0.01–0.2	0.002	$<1 \times 10^{-4}$	<5

[a]Calculated from alpha-activity measurements of several spheres from each lot.

[b]Based upon uranium analysis of acid used in acid electrolysis of one sphere from each lot.

[c]Total release of Xe^{133} after neutron activation during puncture and heating to 1000°C for 12 to 24 hr. One sphere from each lot was tested.

[d]Not determined.

with lower amounts of exposed uranium, as shown by the values reported for lots GA-S-6 through GA-S-9.

Neutron-activation tests also measure the integrity of the coated particles contained in fueled-graphite spheres. The Xe^{133} release values reported in Table 5.9 show that high release values are associated with high values of internally exposed uranium; however, the ratio of Xe^{133} release to internally exposed uranium ranges from 1.6×10^{-2} to 30×10^{-2}. This range of values could result from variations in the amount of exposed uranium or the incomplete removal of uranium by the 8 M HNO_3 or both.

Removal of Exposed Fuel

Studies were initiated to develop a nondestructive method for removing exposed uranium that would be suitable for production use. The first experiments involved passing dry chlorine gas diluted with argon over samples at temperatures of 800 and 1000°C for periods up to 9 1/2 hr. A summary of the results of these experiments is presented in Table 5.10. These experiments showed that the chlorine treatment was effective in reducing the amount of exposed uranium; however, under the conditions used, only partial removal was achieved. Additional experiments are in progress to improve the effectiveness of the treatment.

Metallographic Examinations of Fueled-Graphite Spheres

Metallographic examinations were performed to determine the distribution of the coated particles, the quality of the bonding between the coated particles and the graphite matrix, and the structure of the graphite matrix. The microstructures of the 3M and NCC spheres were basically the same as those previously described for fueled-graphite bushings.[4] Fuel distribution in the 3M spheres was quite uniform and better bonding of the coated particles in the matrix had been achieved.

The GA sphere matrix is characterized by plate-like grains similar to those of the NCC spheres; however, the pores are, in general, smaller and more uniformly distributed than those in the NCC spheres. A slight change in the structure at the interface between the fueled region and the unfueled shell was noted on a GA-S-2 sphere that had a 1/4-in. unfueled shell. This change was not apparent at low magnification but was observed at 250X under polarized light. The structure of the interface is shown in Fig. 5.5a with bright field illumination and in Fig. 5.5b with polarized light. The interface runs diagonally across the field and is most evident in Fig. 5.5b.

Fission-Gas Retention in Fueled-Graphite Spheres

R. B. Fitts

Five 1 1/2-in.-diam fueled graphite spheres were evaluated by low-temperature neutron activation and postirradiation vacuum annealing to

Table 5.10. Results of Chlorine Treatments to Remove Exposed Uranium

Sample Description	Treatment Conditions	Results
	Unsupported Coated Particles	
NCC-203-17 with high surface contamination	3 hr at 800°C	Heavy uranium surface contamination completely removed, as determined by microradiography
NCC-104 and -105 with 15% and 0.6% cracked coated particles, respectively	4 hr at 800°C	Alpha activity reduced by a factor of 2; partial removal of uranium in cracked coated particles, as determined by microradiography
	Fueled-Graphite Specimens	
Machined parts with high surface contamination	8 hr at 800°C	Alpha activity reduced from more than 1000 counts/min to 75 to 110 counts/min
Sphere containing a few cracked coated particles on the surface	9 1/2 hr at 800 to 850°C	Uranium and thorium removed from cracked coatings, as determined by metallography
As-received spheres GA-S-3 and GA-S-4 with 0.35% and 6.7% cracked coated particles, respectively	2 hr at 1000°C and 4 hr at 800°C	Partial removal of uranium and thorium; alpha activity reduced by a factor of 2

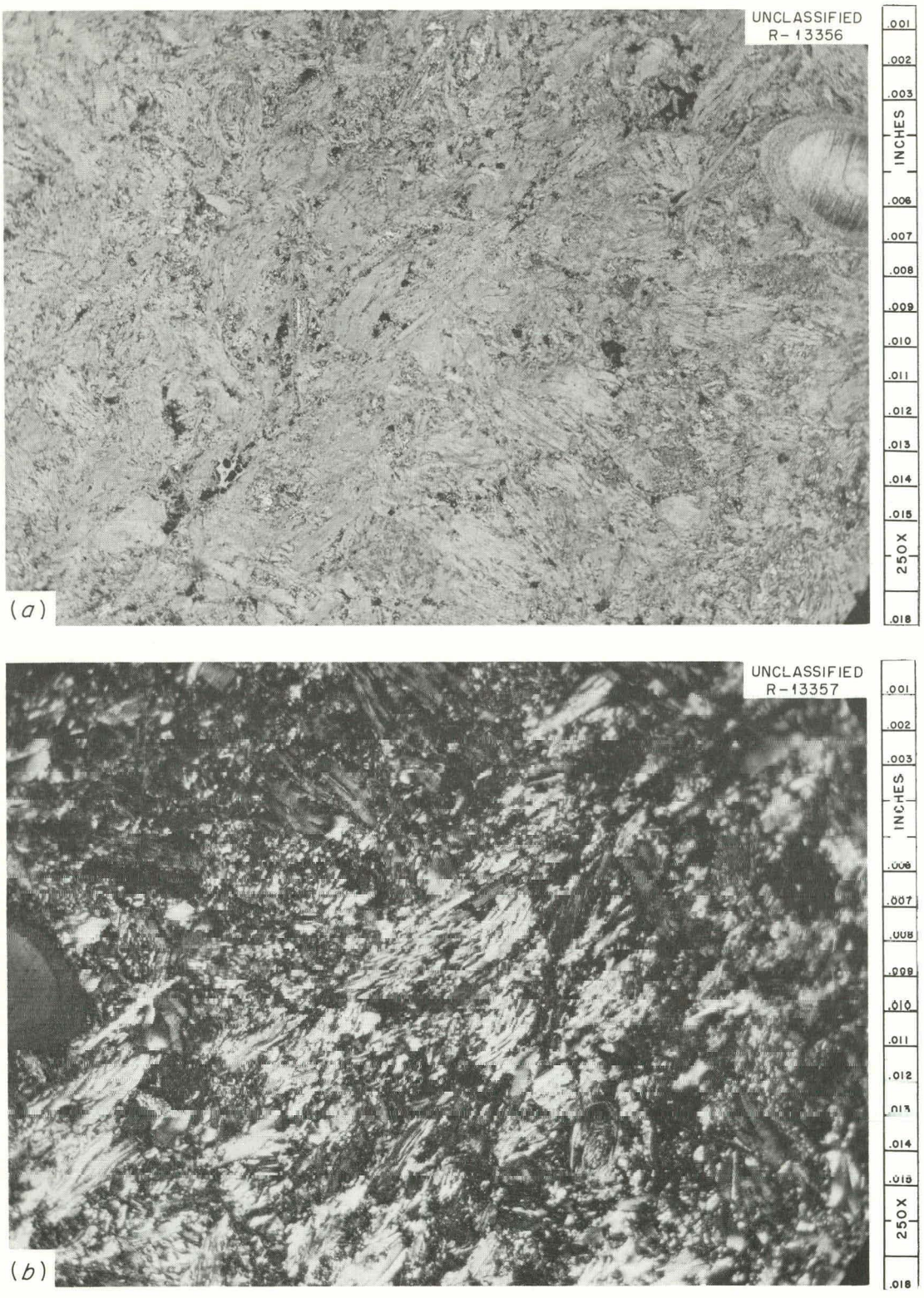

Fig. 5.5. Cross Section of Sphere GA-S-2-9 Showing the Interface Between the Fueled Region and the Unfueled Shell. (a) Bright field. (b) Polarized light. 250X

obtain relative measures of their fission-gas-retention characteristics. The results of the tests are presented in Table 5.11. The very high release from sample GA-S-2-10 was expected since similar samples had shown a high percentage of exposed uranium when leached with HNO_3.

Table 5.11. Fission-Gas Release from 1 1/2-in.-diam Fueled-Graphite Spheres

Sample No.	Fuel Loading (g)			Xe^{133} Released During Capsule Puncture Test (ppm)	Xe^{133} Released During 24-hr 1000°C Vacuum Annealing (ppm)
	Th	U	U^{235}		
3M-S-1-6	1.20	1.96	1.82	13.8	1.39
NCF-S-2-W	1.20	1.96	1.82	3.0	59.0
NCP-SS-1		0.65	0.60	<1	<1
GA-S-1-2	1.20	1.96	1.82	42.5	38.0
GA-S-2-10	1.20	1.96	1.82	2900	8400

6. INVESTIGATIONS OF FUELED-GRAPHITE SYSTEMS

O. Sisman
H. W. Savage
D. B. Trauger
G. M. Watson

Postirradiation Examination of Pyrolytic-Carbon-Coated Uranium Carbide Particles Dispersed in Graphite

M. F. Osborne
E. L. Long, Jr.
D. F. Toner
J. G. Morgan

Studies were continued of two types of irradiated assemblies containing pyrolytic-carbon-coated uranium carbide particles dispersed in graphite. Fabrication and irradiation data for these assemblies are summarized in Table 6.1. Some results of the postirradiation examinations were reported previously,[1,2] and the examinations of capsules 01-5 and 08A-5 are not yet complete.

---

[1] J. G. Morgan et al., Postirradiation Examination of Fueled-Graphite Bodies, pp. 190–195, "GCRP Quar. Prog. Rep. March 31, 1962," USAEC Report ORNL-3302, Oak Ridge National Laboratory.

[2] M. F. Osborne et al., Postirradiation Examination of Pyrolytic-Carbon-Coated Uranium Carbide Particles Dispersed in Graphite, pp. 220–228, "GCRP Semiann. Prog. Rep. Sept. 30, 1962," USAEC Report ORNL-3372, Oak Ridge National Laboratory.

Table 6.1. Fabrication and Irradiation Data for Fueled-Graphite Specimens

Experimental Assembly No.	Number of Specimens	Specimen Size (in.)			Manufacturer Designation[a]	Average Fuel Temperature (°F)	Fuel Burnup (at. % of U)	Coating Failure (%)
		Outside Diameter	Inside Diameter	Length				
MTR-48-5	1	1.0	0	1.5	3M	2500	17	100
MTR-48-6	1	1.0	0.25	1.5	GA	2000	1.6[b]	10
01-5	12	0.6	0.25	0.5	3M	2000	8.4	(c)
08-5	12	0.6	0.25	0.5	3M	1700	~3	16
08A-5	12	0.6	0.25	0.5	NCC	1700	7.4	(c)

[a] 3M = Minnesota Mining and Manufacturing Company.
GA = General Atomic Div., General Dynamics Corp.
NCC = National Carbon Company.

[b] Burnup of uranium and thorium (at. %); uranium burnup was 5.0 at. %.

[c] Examination incomplete.

Experiment MTR-48-6

The examination of experimental assembly MTR-48-6 was completed. Analyses of core drillings from the graphite sleeve surrounding the fuel specimen indicated that thorium was much more mobile than uranium, as shown in Table 6.2. The ratios of the concentrations of uranium and thorium in the graphite sleeve after irradiation to those in the fuel specimens before irradiation were about 0.002 and 0.04 for uranium and thorium, respectively. Since only about 10% of the fuel-particle coatings had fractured, these values indicate fairly high migration rates, especially for thorium. The burnup of uranium and thorium in this specimen was determined by mass spectrometry to be 1.57 at. % at the outer surface and 1.55 at. % at the inner surface. Thus very little self-shielding was indicated.

Table 6.2. Analyses of Core Drillings from Graphite Sleeve Surrounding Fuel Specimens in Assembly MTR-48-6

	Average Concentration (atoms per mg of graphite)	
	Uranium	Thorium
In fuel specimen before irradiation	1.16×10^{17}	2.41×10^{17}
In graphite sleeve after irradiation	2×10^{14}	1×10^{16}

Experiment ORR-08-5

The disassembly and results of macro examination of experimental assembly 08-5 were described previously.[2] The most severely cracked pellet was fractured further to see whether a crack in the graphite matrix would cause the coated particles to fail. Two pieces of the fractured pellet were selected for metallographic examination. One piece was a longitudinal section, and the other was a transverse section with respect to the long axis. It was determined from stereo examination that fracturing of the graphite matrix (in this case a mechanical stress rather than thermal) could cause failure of the coated particles, and this finding was confirmed by metallography. Fractures in the matrix had progressed through

and around the coated particles, as shown in Fig. 6.1. A count of more than 200 coated particles showed that 16% had failed. A comparison of typical unirradiated and irradiated particles is shown in Fig. 6.2. A lack of definite grain structure in the uranium carbide core and a separation between the pyrolytic coating and the graphite matrix were the only microstructural changes observed. There was no evidence of a reaction at the core-to-coating interface. The apparent void at the core-to-coating interface is an unavoidable artifact that occurred in the final stages of metallographic preparation.

Experiments ORR-01-5 and ORR-08A-5

The examinations of experimental assemblies 01-5 and 08A-5 were completed except for metallography. As in several previous experiments, the

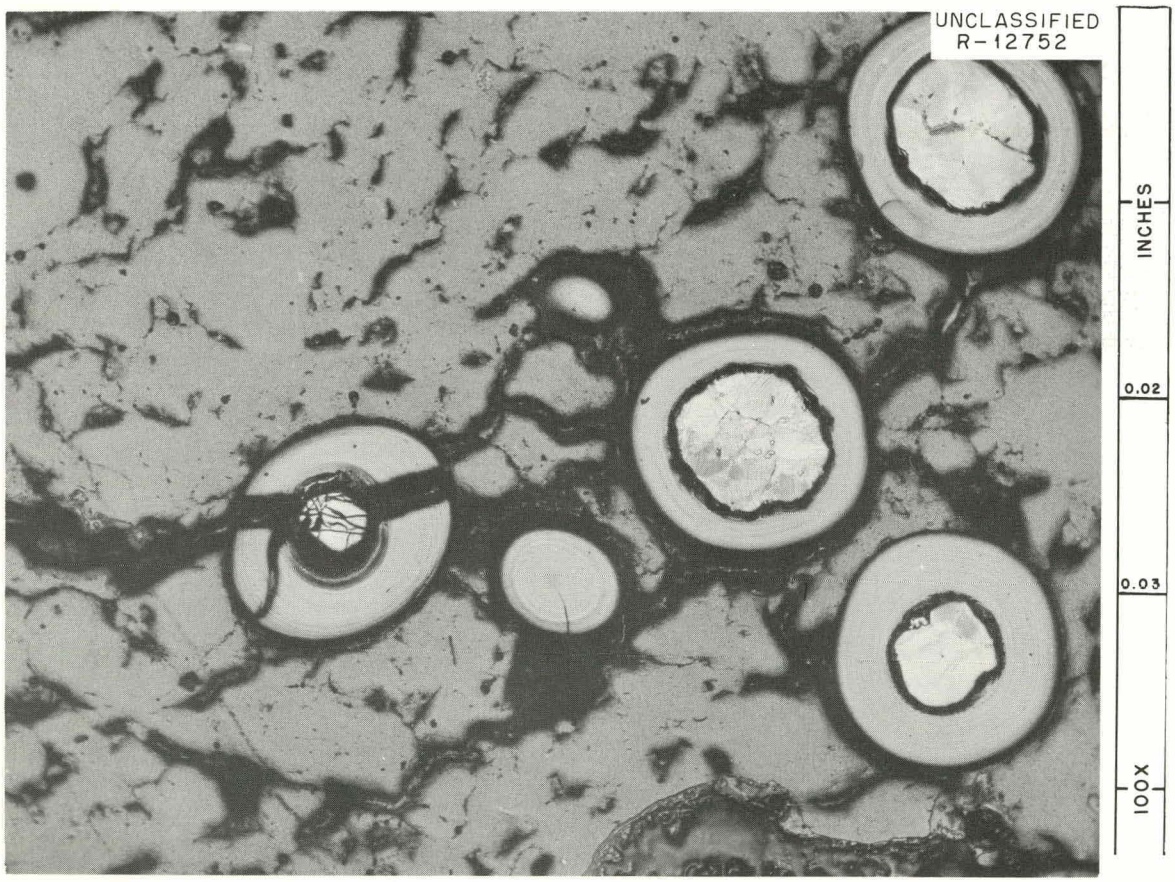

Fig. 6.1. Area from Pellet No. 31 from ORR-Irradiated Experimental Assembly 08-5. Note that the fracture in the graphite matrix went both through and around the coated particles. Etched.

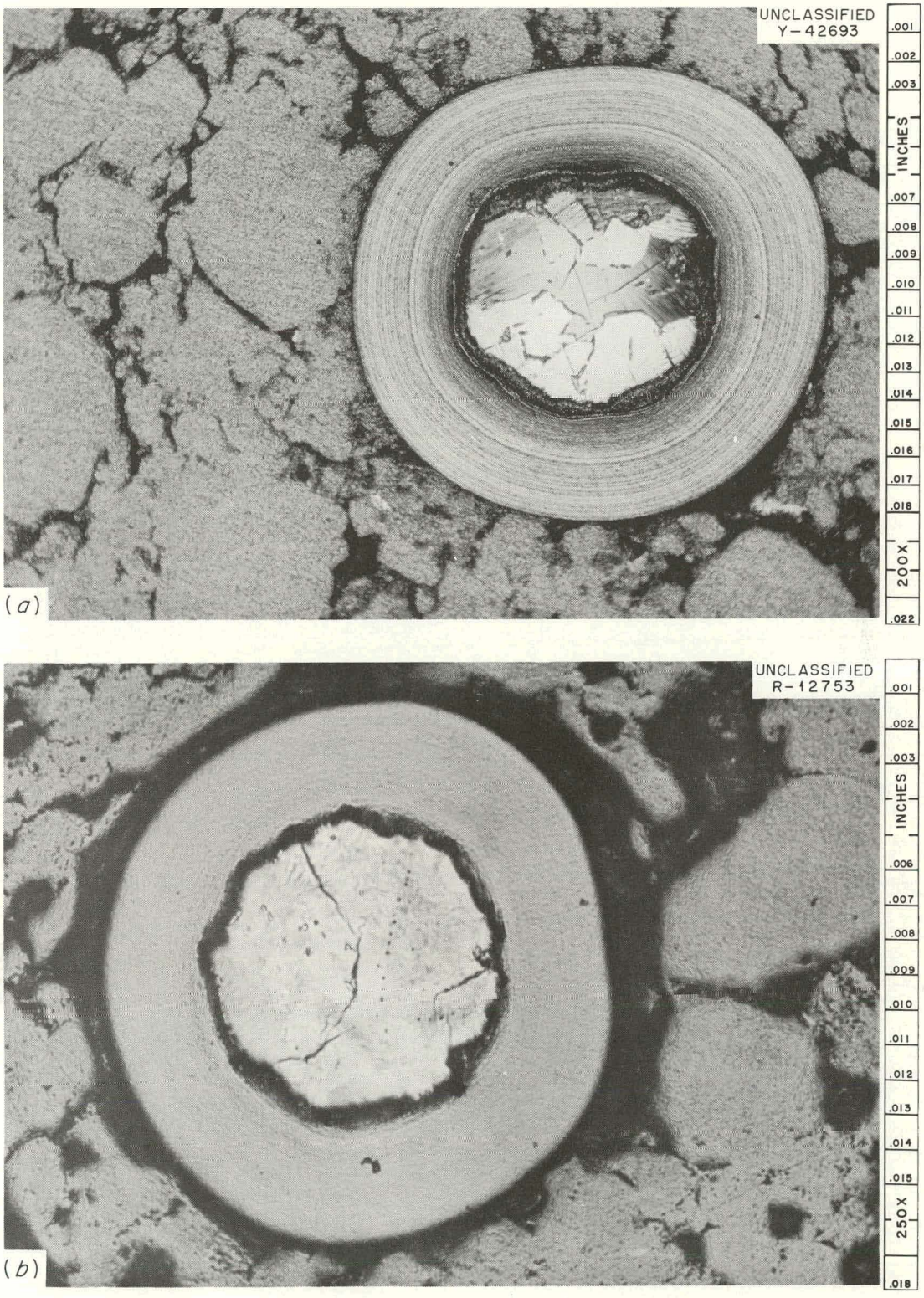

Fig. 6.2. Pyrolytic-Carbon-Coated Uranium Carbide Particles from Experimental Assembly 08-5. (a) Unirradiated. Etched. (b) Irradiated. Etched.

gamma scans were quite irregular, indicating inhomogeneous fuel loading. There were no significant dimensional changes in the stainless steel cladding of either capsule. The dimensions of the fuel pellets had increased 1 to 2%, causing corresponding volume increases of about 5%. All twelve fuel pellets in capsule O1-5 fractured, but they remained intact, as shown in Fig. 6.3. Each end pellet appeared to be slightly oxidized, possibly because of impure sweep gas. No fuel pellets in capsule O8A-5 fractured, and there was no evidence of oxidation. Typical pellets are shown in Fig. 6.4.

Instantaneous Fission-Gas-Release Experiment

P. E. Reagan R. M. Carroll
T. W. Fulton

The in-pile test facility and capsule for studying instantaneous fission-gas release from pyrolytic-carbon-coated uranium carbide particles was described previously.[3] Particles with three types of coatings are being studied: laminar, columnar, and duplex. The duplex coating consists of a laminar inner coating and a columnar outer coating.

Particles with Laminar Coatings

Particles from batch 3M-SP-2 were irradiated to 15 at. % uranium burnup in capsule C1-7, and when viewed at 30X, a fair estimate of the number of broken particles could be made. About 5% of the particles had broken coatings, and a few of the carbide cores were completely separated from the laminar coating, as shown in Fig. 6.5. An irradiated particle is compared with an unirradiated particle in Fig. 6.6, and a typical broken particle is shown in Fig. 6.7. A reaction zone may be seen at the fuel-to-coating interface that produced protrusions outward into the coating.

---

[3]R. M. Carroll, J. G. Morgan, and P. E. Reagan, "Instantaneous Fission-Gas-Release Experiment, pp. 228–237, "GCRP Semiann. Prog. Rep. Sept. 30, 1962," USAEC Report ORNL-3372, Oak Ridge National Laboratory.

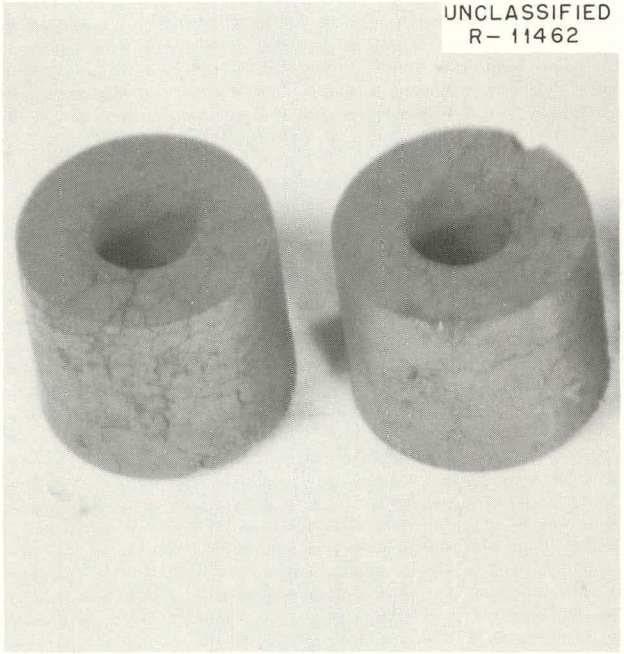

Fig. 6.3. Typical Fuel Pellets from Capsule 01-5 After Removal from Graphite Sleeve. 2X.

Fig. 6.4. Typical Fuel Pellets from Capsule 08A-5 After Removal of Graphite Sleeve. 2X.

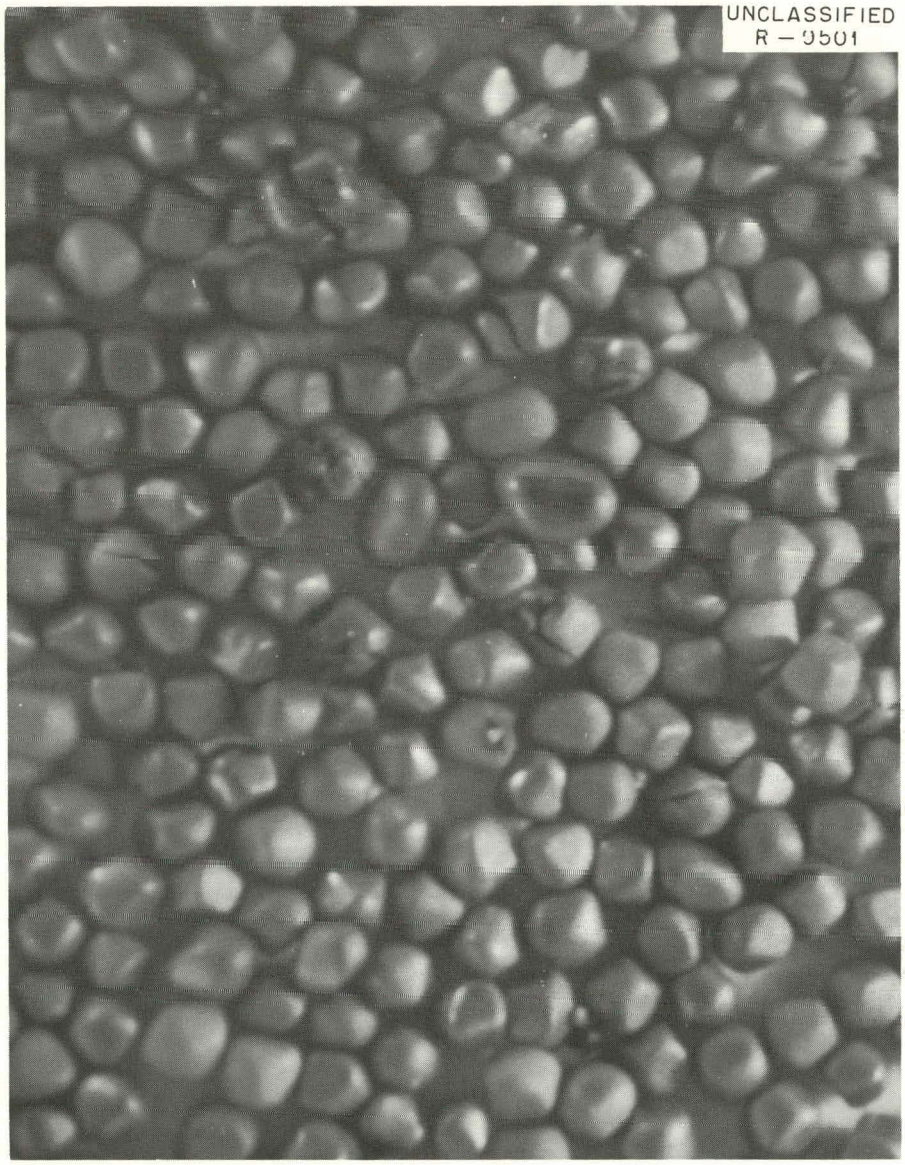

Fig. 6.5. Pyrolytic-Carbon-Coated Uranium Carbide Particles with Laminar-Type Coatings After Irradiation in Capsule C1-7 to a Burnup of 15 at. % Uranium at 1500 to 1800°F. 30X.

Particles with Columnar Coatings

Pyrolytic-carbon-coated uranium carbide particles from capsule B9-7 were examined after being irradiated to 12 at. % uranium burnup. These particles were from batch HTM-1, and they had columnar-type coatings. When viewed at 30X, about 2% of the particles showed broken coatings, and several doublet particles were evident, as shown in Fig. 6.8. When

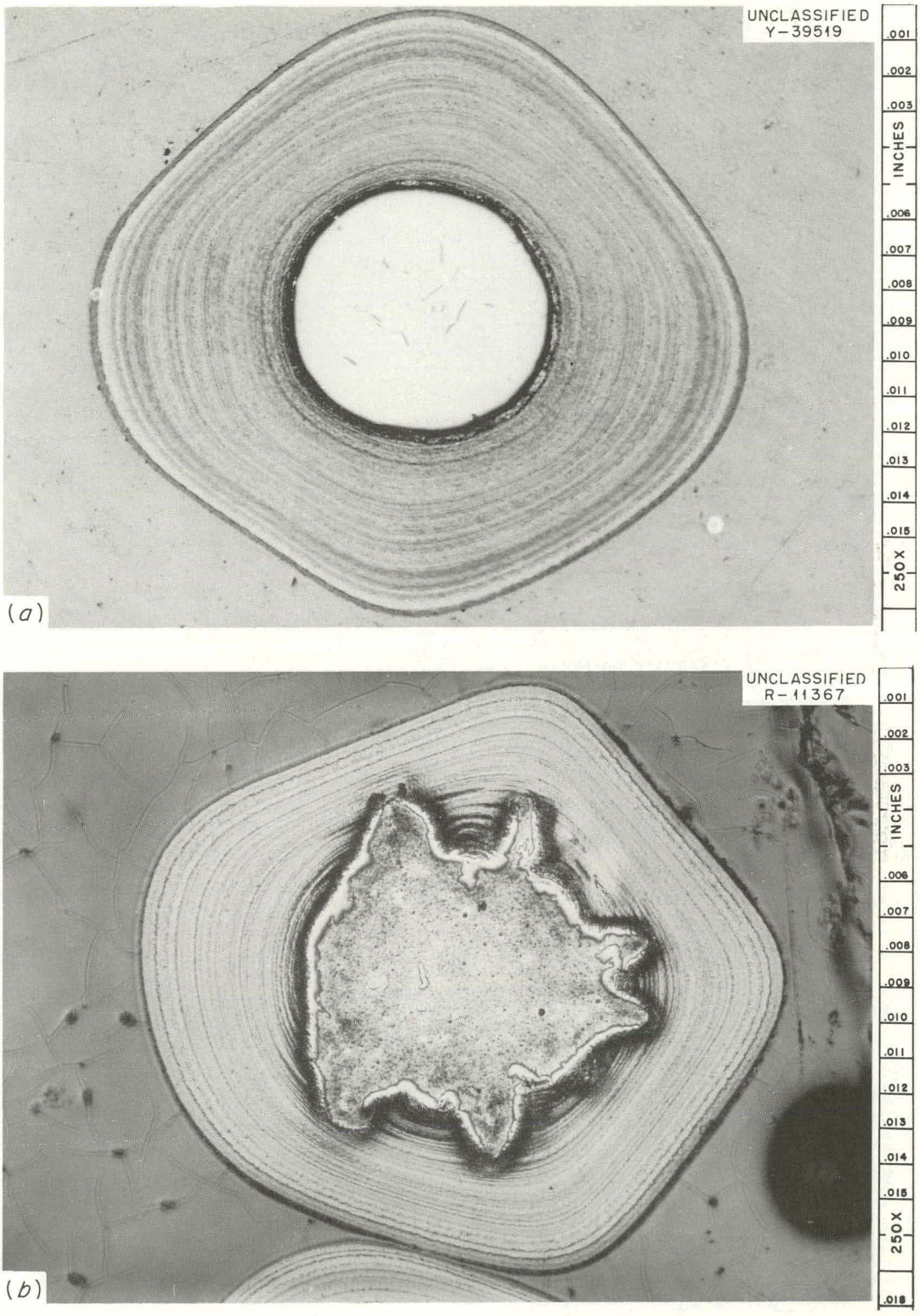

Fig. 6.6. Sectioned, Laminar-Type, Pyrolytic-Carbon-Coated Uranium Carbide Particles. (a) Unirradiated. (b) Irradiated to 15 at. % uranium burnup at 1500 to 1800°F.

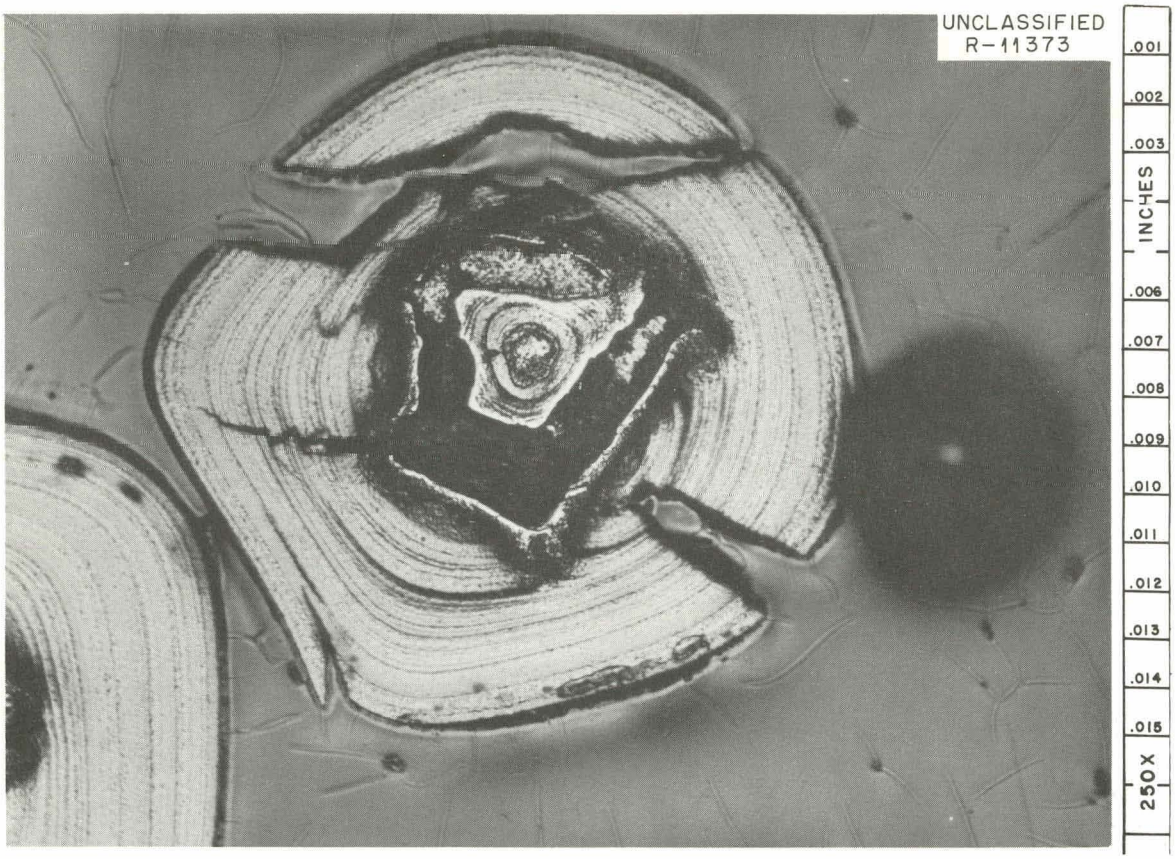

Fig. 6.7. Sectioned, Irradiated, Laminar-Type, Pyrolytic-Carbon-Coated Uranium Carbide Particle Showing Broken Coating.

the particles were sectioned, two areas of damage were noted. There was severe damage by reaction at the fuel-to-coating interface and the columnar coating showed numerous voids. An irradiated particle is compared with an unirradiated particle in Fig. 6.9. The volume of the fuel, including the void space, increased by a factor of about 4 and the coating thickness decreased to about one-half.

Particles with Duplex Coatings

Particles were removed from capsule B9-8 after irradiation to a burnup of 30 at. % uranium. These particles had duplex-type coatings and were from batch NCC-AD. No broken particles or doublets were found when viewed at 30X. These particles are shown in Fig. 6.10.

Sectioned particles from this group showed very few voids in the columnar part of the coating, but in many instances a reaction zone at

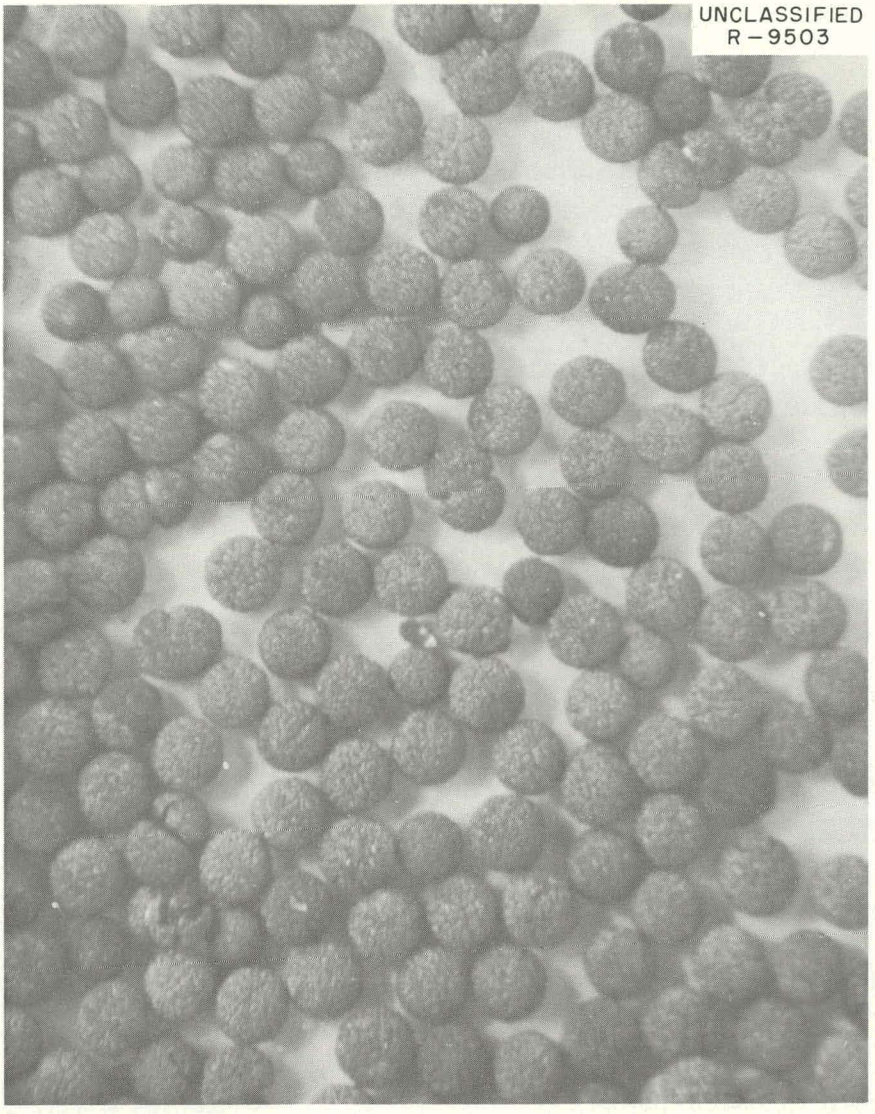

Fig. 6.8. Pyrolytic-Carbon-Coated Uranium Carbide Particles with Columnar-Type Coatings After Irradiation in Capsule B9-7 to a Burnup of 12 at. % Uranium at 1500 to 1650°F. 30X.

the fuel-to-coating interface had completely penetrated the laminar layer of the coating. An irradiated particle from capsule B9-8 is compared with an unirradiated particle in Fig. 6.11. After being irradiated for 88 days at 7.5×10^{13} neutrons/cm^2·sec, the columnar part of the duplex coating appeared to have retained its structure quite well. About one-third of the particles were leached with acid to remove uranium from the broken particles, and, based on the uranium removed, about 1.5% of the particles had broken.

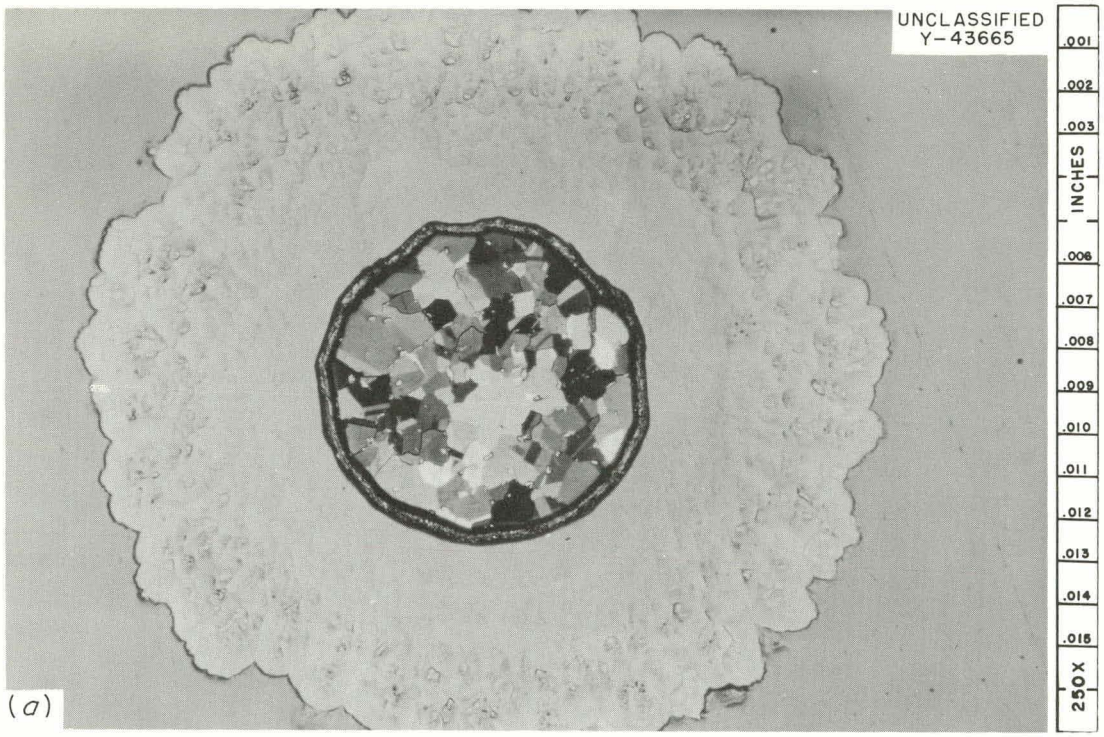

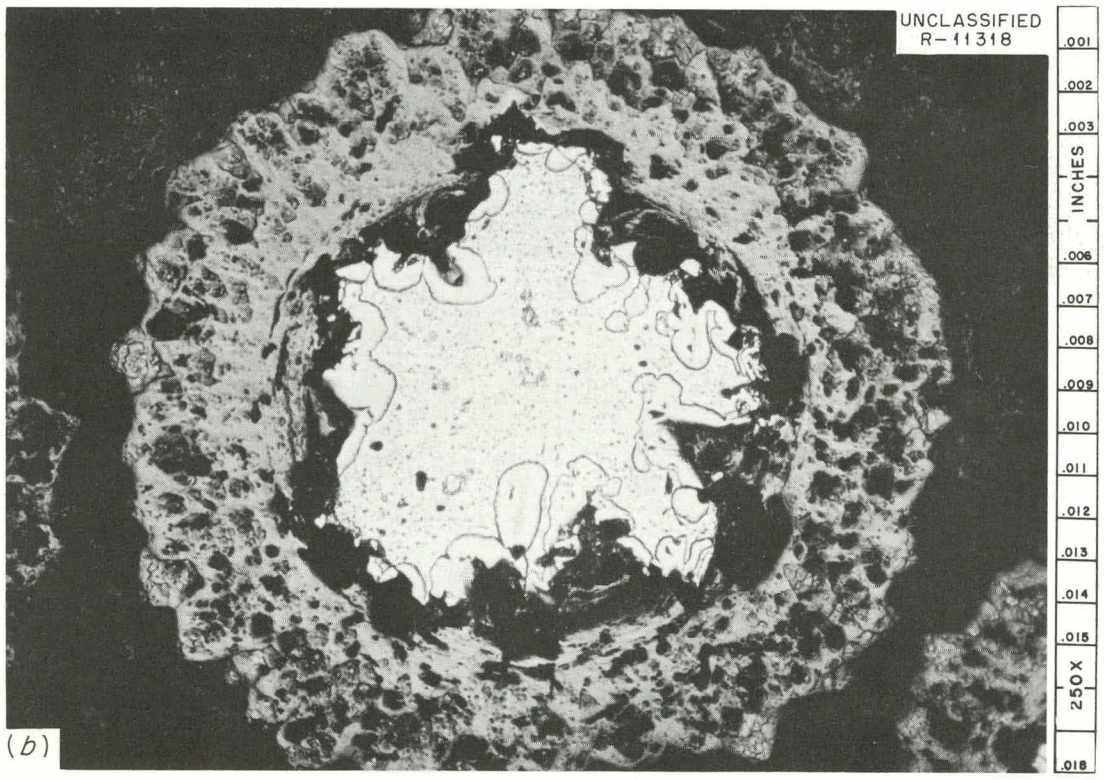

Fig. 6.9. Sectioned, Columnar-Type, Pyrolytic-Carbon-Coated Uranium Carbide Particles. (a) Unirradiated. (b) Irradiated to 12 at. % uranium burnup at 1500 to 1650°F.

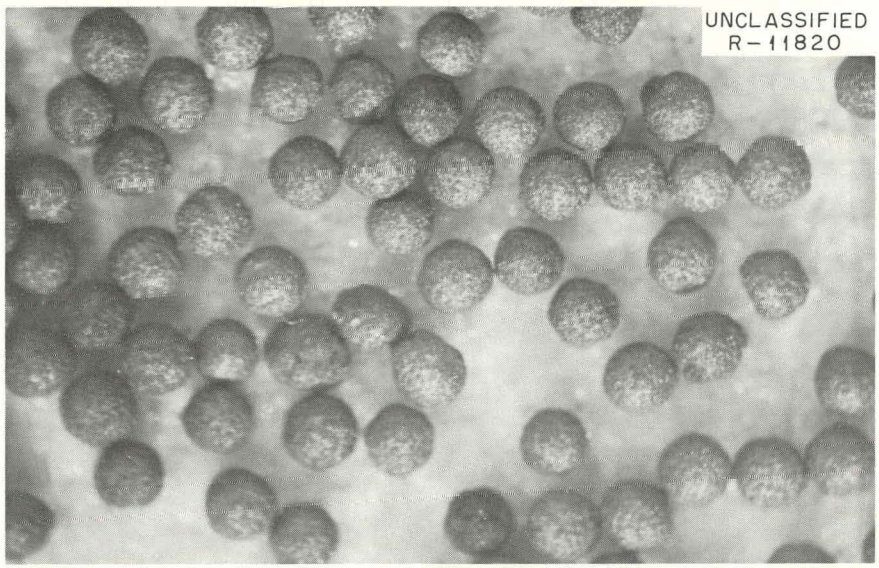

Fig. 6.10. Pyrolytic-Carbon-Coated Uranium Carbide Particles with Duplex-Type Coatings After Irradiation in Capsule B9-8 to a Burnup of 30 at. % Uranium at 600 to 1750°F. 30X.

Capsule B9-9, containing a third group of pyrolytic-carbon-coated uranium carbide particles of the NCC-AD duplex-coating type, was irradiated to nearly 19 at. % uranium burnup. These particles were first irradiated to 9.4% burnup at 800°F to study particle-coating damage by irradiation at low temperature. The fission-gas-release rates remained nearly constant during irradiation at 800°F, with no increase with burnup. The average fractional fission-gas-release rates at 800°F are shown in Fig. 6.12. After 9.4% burnup was reached at 800°F, the temperature was increased to 1200°F for a short time, then to 1600°F, and finally to 1750°F. The burnup and fractional fission-gas-release rates at each of these temperatures are also given in Fig. 6.12. During the 1600 and 1750°F irradiation periods, small bursts of activity were noted that were similar to those noted during the irradiation of capsules C1-7, B9-7, and B9-8.[3]

Of the three coatings that have been studied, the duplex type has demonstrated greater ability to retain fission gases than the other two. In all three types of coating, a reaction zone was found at the fuel-to-coating interface after high burnup. Based on results from postirradiation examination, it appears that the percentage of broken particles in

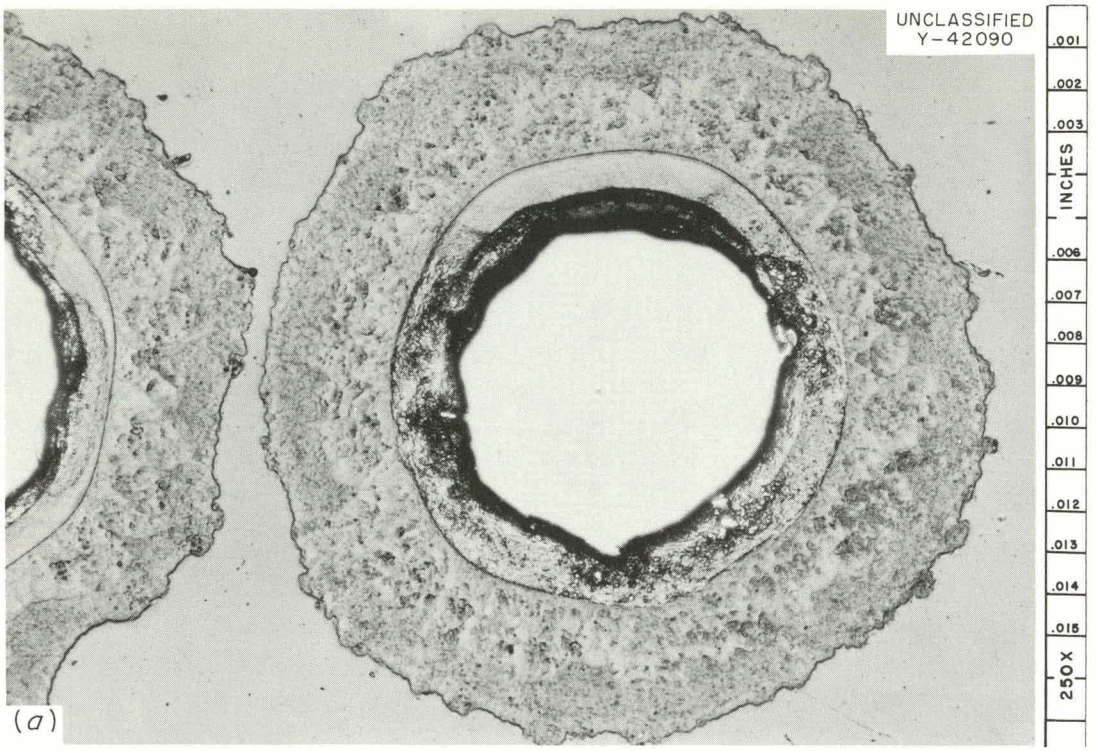

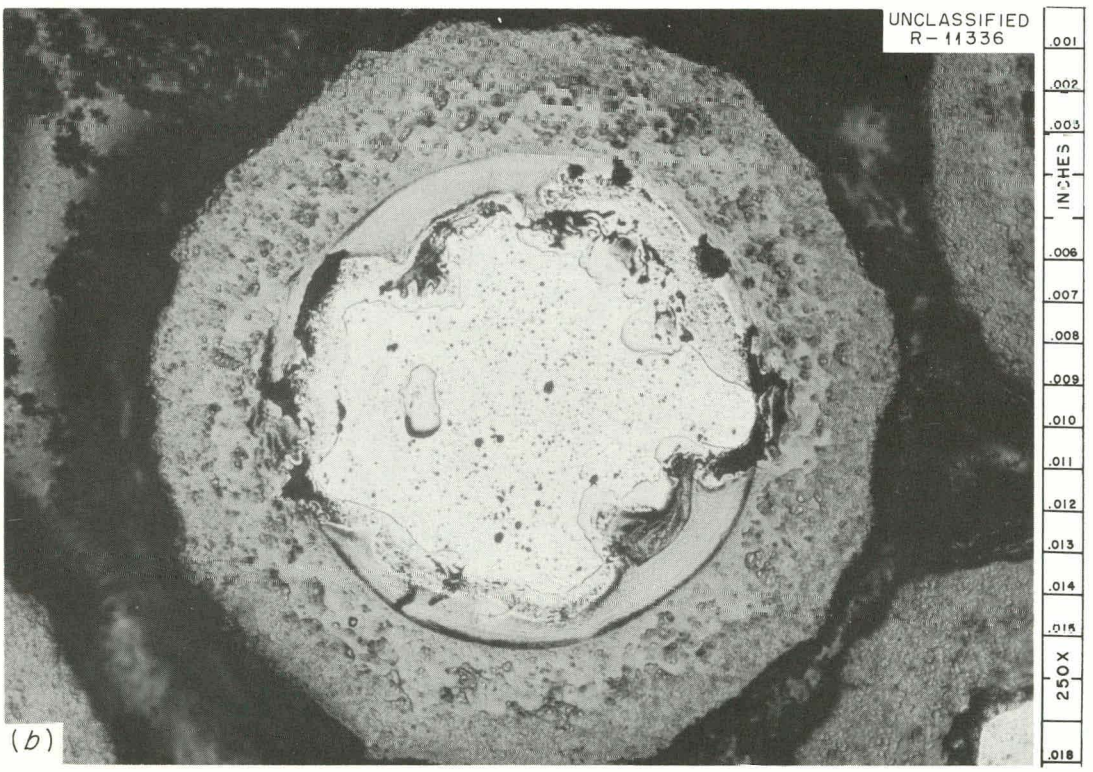

Fig. 6.11. Sectioned, Duplex-Type, Pyrolytic-Carbon-Coated Uranium Carbide Particles. (a) Unirradiated. (b) Irradiated at 30 at. % uranium burnup at 600 to 1750°F.

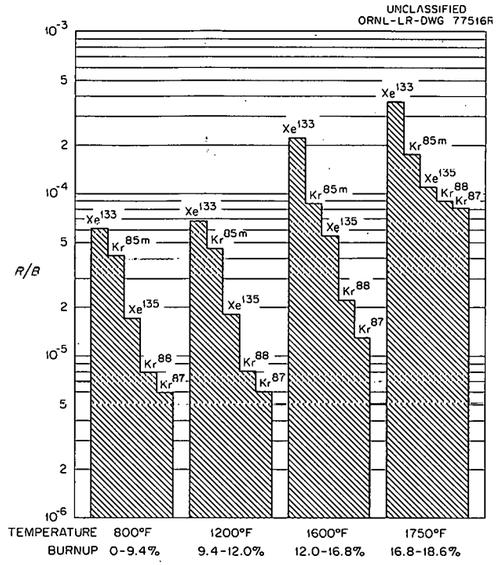

Fig. 6.12. Fractional Fission-Gas Release at Various Temperatures and Burnups for Pyrolytic-Carbon-Coated Uranium Carbide Particles with Duplex-Type Coatings. Batch NCC-AD irradiated in capsule B9-9.

a capsule can be accurately predicted from the fission-gas-release rates during irradiation.

Capsule Irradiations in ORR Poolside Facility

V. A. DeCarlo F. R. McQuilkin

There are 14 capsules in group VI now being irradiated in the ORR poolside facility. During this reporting period, three capsules were discharged (03-6, 05A-6, and 06A-6; see chap. 4); seven were operating (01-6, 02A-6, 03A-6, 04-6, 05B-6, 06Z-6, and 08-6); and four were readied for insertion during the May 1963 shutdown (01A-6, 05Z-6, 06X-6, and 08A-6). The designs and planned operating conditions for the seven capsules now being irradiated are described in Table 6.3, and typical operating data for these capsules are presented in Table 6.4.

Capsule 06Z-6, which replaced capsule 06A-6, is referred to as a "four-ball" capsule and is similar in design to capsule 08-6, which was

Table 6.3. Summary of Design and Planned Operating Conditions for Group VI ORR Poolside Capsule Irradiations

Capsule number	01-6	02A-6	03A-6	04-6	05B-6	06Z-6	08-6
Experiment code	F BeO bushing	EGCR bushing	EGCR bushing	Advanced GCR bushing	EGCR bushing	CP sphere	Graphite sphere
Capsule type	Sweep capsule with central thermocouple[a]	Static	Static	Static capsule with central thermocouple; type 304 stainless steel cladding wire wrapped	Static	Upper sweep compartment; lower static compartment	Upper sweep compartment; lower static compartment with central thermocouple
Specimen data							
Specimen type	UO_2 particles in BeO matrix	UO_2	UO_2	UO_2	UO_2	Fueled-graphite sphere containing pyrolytic-carbon-coated $(U,Th)C_2$ particles	Fueled-graphite insert containing pyrolytic-carbon-coated UC_2 particles
Specimen origin	ORNL	Westinghouse	Westinghouse	ORNL	Westinghouse	Specimens 1, 2, 3 from batches NCF-S-2-G, K, and T; specimen 4 from batch GA-S-1-7	National Carbon-Parma, three spheres; ORNL,[b] one sphere
Number of fueled specimens per capsule	11	8	8	8	8	4	4
Fuel loading							
U^{235} as wt % of total U	19.78	2.46	2.46	4.6	2.46	93.2	93.2;[c,d] 38.2[e]
U as wt % of fueled specimen	54.0	88.2	88.2	88.2	88.2	3.76	1.2;[c,d] 2.85[e]
Total U^{235}, g	7.2	6.8	6.8	12.97	6.8	1.8[d]	0.6;[c,d] 0.6[e]
Total U, g	36.6	278.0	278.0	281.99	278.0	1.96[d]	0.65;[c,d] 1.57[e]
Fueled specimen density							
g/cm^3	5.14	10.47	10.47	10.47	10.47	1.8	
% theoretical	95.0	95.44	95.44	95.44	95.44		
Power data							
Specific power, w/g of fueled specimen	88.5	13.9	13.9	23.0	13.9	25.0	8.3[d] 75.7[f]
Heat rate, Btu/hr·ft of fueled specimen	45,000	30,000	30,000	50,000	30,000	35,500	15,160
Effective thermal neutron flux, neutrons/cm^2·sec	2.3×10^{13}	1.6×10^{13}	1.6×10^{13}	1.5×10^{13}	1.6×10^{13}	1.9×10^{13}	1.9×10^{13}
Self-shielding factor	0.6	0.7	0.7	0.6	0.7		
Scheduled burnup							
Mwd/MT of fueled specimen	15,900	10,000	5,000	4,100	2,800		
U^{235}, at. %						14	14

Table 6.3 (continued)

Capsule number	01-6	02A-6	03A-6	04-6	05B-6	06Z-6	08-6
Planned operating conditions							
Temperature, °F							
Fuel can	530 (control)	1600 max (control)	1300 max (control)	1600 max (control)	1600 max (control)	600 est.	600 est.
Fuel surface	1880	1650	1350	1650	1650	1500[g] (control)	1200[g] (control)
Fuel center	2120 est.	2200 est.	1900 est.	2600[h] est.	2200 est.	1900 est.	1675[b]
Cladding pressure, psig	~1 atm (sealed)	300 (control)	300 (control)	300 (control)	300 (control)	50 (control)	50 (control)
Thermal barrier gas	He	N_2	He	He	He	N_2	N_2
Hot gap width, in.	0.005	0.005	0.014	0.015	0.020	0.004	0.010
Dimensional data							
Fuel can outside diameter, in.	0.750	0.750	0.750	0.850	0.750	2.046	2.032
Fuel can inside diameter, in.	0.710	0.710	0.710	0.820	0.710	1.9375	1.9375
Fuel outside diameter, in.	0.500	0.706	0.706	0.816	0.706	1 1/2 (sphere)	1 1/2 (sphere)
Fuel inside diameter, in.	0.250	0.323	0.323	0.520	0.323		
Assembly drawing number	D-47396	D-47794	D-47794	D-47489	D-47794	D-47490	D-47722

[a]Thermocouple is 1/16-in.-OD Ta-sheathed Pt vs Pt-Rh insulated-junction type in open-ended Mo tube.

[b]Specimen ORNL-SS-1 in bottom of 08-6 equipped with 70-mil-OD-Ta sheathed W–5% Re vs W–26% Re insulated-junction thermocouple, with 5-mil Zr sleeve inserted into 82-mil-ID thermocouple well in screw plug; original estimate of 3300°F temperature was based on thermal conductivity of fuel region being 1 Btu/hr·ft (°F/ft).

[c]National Carbon-Parma sphere.

[d]Per sphere.

[e]ORNL sphere fueled with $(U,Th)C_2$ (Th/U = 0.6).

[f]Per insert.

[g]Thermocouple is 4-mil Cu-plated type 347 stainless steel-sheathed Chromel-Alumel grounded-junction type.

[h]Thermocouple is 1/8-in.-OD type 347 stainless steel-sheathed W–5% Re vs W–26% Re type, with BeO-beaded bare wire in closed Mo well.

Table 6.4. Operating Conditions of ORR Group VI Capsules as of February 15, 1963

Capsule No.	Cladding Surface Temperature (°F)				Central Temperature (°F)	Power Density (w/cm^3)	Flux (neutrons/$cm^2 \cdot sec$)	
	Design	High	Low	Average			Calculated	Measured
							$\times 10^{13}$	$\times 10^{13}$
01-6		659	622	636	2090[a]		2.0	1.4
02A-6[b]	1600	1528	1326	1440			1.43	1.32
03A-6	1300	1295	1010	1177			1.43	1.32
04-6	1600	1583	1396	1471	2435[c]		1.36	1.18
05B-6	1600	1571	1265	1448			1.43	1.43
	Surface Temperature of Spheres (°F)				Central Temperature of Sphere No. 4 (°F)			
	No. 1	No. 2	No. 3	No. 4				
06Z-6	1403	1520	1023	960		45,[d] 15[e]	1.9[d]	1.5[d]
08-6[f]	1045	1081	1167	1135	1763	167,[g] 8.3[h]	2.3	1.8

[a] Central thermocouple TE-107 failed on Dec. 13, 1962 when indicating 2085°F and has subsequently given intermittent indications.

[b] Midcapsule cladding thermocouple TE-204 failed February 1, 1963.

[c] Central temperature is indicated intermittently to be about 2100 or 2450°F; shifts occur when the reactor power changes.

[d] Upper spheres (calculated).

[e] Lower spheres (estimated).

[f] Temperatures were 750, 770, 820, 800, and 997, in the order given, when 08-6 was operated at a power density of 13.3 w/cm^3.

[g] Power density is for fueled insert.

[h] Power density is for sphere containing fueled insert.

described previously.[4] It contains four 1 1/2-in.-diam spheres mounted in pairs in two separate compartments. The upper compartment contains spheres made by the National Carbon Company (batch NCF-S-2G, -K), which are swept continuously with helium. The lower compartment is sealed for operation under static conditions and contains one National Carbon Company sphere (batch WCF-S-2-2-T) and one sphere made by General Atomic (batch GA-S-1-7). There are no provisions for the measurement of fuel central temperatures in these spheres, as there is for one sphere in capsule 08-6.

Fission-gas-release rates for the three sweep-type capsules now installed in the ORR poolside facility, 01-6 (fueled BeO), 06Z-6 (1 1/2-in.-diam fueled-graphite spheres), and 08-6 (fueled graphite insert in 1 1/2-in.-diam graphite spheres), are summarized in Tables 6.5 and 6.6. As shown, the release rate of Kr^{88} was 1.2×10^{-3} after 0.95 at. % burnup for capsule 01-6; it was not detectable after 1.7 at. % burnup for capsule

[4]V. A. DeCarlo and F. R. McQuilkin, Capsule Irradiation in ORR Poolside Facility, pp. 238–251, "GCRP Semiann. Prog. Rep. Sept. 30, 1962," USAEC Report ORNL-3372, Oak Ridge National Laboratory.

Table 6.5. Summary of Fission-Gas-Release Data for Capsule 01-6 Containing Fueled BeO

Time of Sampling[a]	Estimated Burnup (at. % of total U)	Estimated Central Temperature (°F)	Fission-Gas Release as Ratio of Release Rate to Birth Rate, R/B				
			Kr^{85m}	Kr^{87}	Kr^{88}	Xe^{133}	Xe^{135}
			$\times 10^{-3}$	$\times 10^{-4}$	$\times 10^{-3}$	$\times 10^{-2}$	$\times 10^{-3}$
4	0.01	1640			2.0		
5	0.02	1640			2.2		
5	0.02	2100			5.5		
15.5	0.32	2100	1.9	9.0	2.0	1.1	2.8
17.5	0.36	2100	1.3	5.6	1.4		2.3
24	0.49	2100	2.2	5.8	1.5	1.45	3.1
31	0.63	2100	1.2	5.6	1.3	1.3	1.9
33	0.67	2100	0.93	4.2	1.3	1.0	3.9
38	0.73	2100	2.5		3.0	2.1	4.58
47	0.91	2100	3.1		2.5	1.2	3.1
49	0.95	2100	1.5	6.1	1.2		1.87

[a]Days of operation at 30 Mw.

Table 6.6. Summary of Operating and Fission-Gas-Release Data for Capsules 06Z-6 and 08-6

Time of Sampling[a]	Estimated Burnup (at. % of total uranium)	Average Surface Temperature of Swept Spheres (°F)	Surface Temperature of Sphere No. 4 (°F)	Central Temperature of Sphere No. 4 (°F)	Fission Power Density (w/cm^3)	Fission-Gas Release as Ratio of Release Rate to Birth Rate, R/B				
						Kr^{85m}	Kr^{87}	Kr^{88}	Xe^{133}	Xe^{135}
Capsule 06Z-6										
4	0.2	1144			33	No detectable fission gas				
7	0.3	1285			39	No detectable fission gas				
12	0.6	1431			45	No detectable fission gas				
13	0.7	1434			45	No detectable fission gas				
18	1.0	1491			45	No detectable fission gas				
20	1.3	1507			45	No detectable fission gas				
26	1.7	1455			45	No detectable fission gas				
Capsule 08-6										
4	0.2	760	800	940	122			$<10^{-10}$		
5	0.3	760	800	950	122			$<10^{-10}$		
15.5	1.0	740	785	995	122	2.1×10^{-6}	3.8×10^{-6}	1.8×10^{-7}	1.6×10^{-5}	2.7×10^{-6}
17.5	1.1	750	783	1000	122	1.9×10^{-6}	4.6×10^{-8}	1.1×10^{-7}	3.1×10^{-6}	1.6×10^{-8}
24	1.5	780	767	983	122	6.3×10^{-7}	2.3×10^{-7}	7.6×10^{-8}	5.1×10^{-7}	6.3×10^{-7}
31	2.0	1000	925	1290	152	1.7×10^{-8}	6.3×10^{-7}	1.5×10^{-6}	1.7×10^{-5}	6.8×10^{-6}
36	2.5	1100	1133	1730	167	4.5×10^{-6}	1.1×10^{-6}	4.2×10^{-6}	1.6×10^{-5}	2.7×10^{-6}
38	2.6	1100	1133	1720	167	4.8×10^{-6}	2.0×10^{-6}	4.8×10^{-6}	1.5×10^{-5}	3.2×10^{-6}
47	3.4	1070	1153	1730	167	2.6×10^{-6}	8.2×10^{-6}	2.7×10^{-5}	4.1×10^{-5}	1.6×10^{-5}
49	3.6	1085	1145	1725	167		9.1×10^{-6}	2.8×10^{-5}	5.5×10^{-5}	1.6×10^{-5}
54	3.9	1050	1135	1715	167	3×10^{-5}	2.2×10^{-6}	2.6×10^{-5}	8.3×10^{-5}	2.0×10^{-5}
55	4.0	1055	1135	1712	167		1.0×10^{-5}	3.4×10^{-5}	1.7×10^{-5}	2.0×10^{-5}
60	4.5	1095	1130	1705	167	3.4×10^{-5}	1.3×10^{-5}	3.7×10^{-5}	9.4×10^{-5}	2.3×10^{-5}
62	4.6	1112	1127	1700	167	4.3×10^{-5}	1.3×10^{-5}	4.1×10^{-5}	9.3×10^{-5}	1.7×10^{-5}
68	5.2	1051	1133	1700	167	3.0×10^{-5}	1.0×10^{-5}	3.1×10^{-5}	8.2×10^{-5}	

[a] Days at 30 Mw.

06Z-6; and it was 3.1×10^{-5} after 5.2 at. % burnup for capsule 08-6. The daughter trapping program for determining short-lived fission products was temporarily postponed, and therefore no data from this phase of the program are available.

Four capsules are being prepared for insertion in the ORR as a final subgroup of the group VI irradiation series. These include three "four-ball" capsules loaded with fuel specimens manufactured by several commercial vendors. The other capsule will be a stainless steel-clad element partially loaded with EGCR pellets shaped to avoid column loading at the edges. These pellets are alternated with pellets of the original design in this capsule to simulate this type of loading in the EGCR elements.

Since a high rate of heating may increase the strain imposed by the fuel column on the element cladding, the ORR procedures for startup and return-to-power were modified to limit the heatup rate of capsules in the poolside facility. To simulate EGCR conditions, the maximum heatup rate was limited to 150°F/min. For present EGCR-capsule power-generating rates, this corresponds to a maximum rate of increase in ORR power of 3 Mw/min. This revision was initiated at the beginning of cycle 44 (December 3, 1962), after capsule 03-6 was discharged but prior to the start of the later Westinghouse capsule irradiations of group VI.

The thermal-neutron flux of the ORR poolside capsules is now determined by measuring the radioactive Ar^{41} produced by passing argon through a tube placed adjacent to each unit. Results from the first tests are given in Table 6.4, which also lists the calculated design fluxes for comparison. The system offers an excellent method for estimating integrated thermal-neutron fluxes during irradiation. Since the Ar^{41} fluxes reported are instantaneous values, it is necessary to make Ar^{41} activation measurements during each reactor cycle of the irradiation period.

Several modifications were made to the poolside facility during the ORR cycle 44 shutdown. These changes included modification of the capsule mounting rigs to accommodate the larger capsules housing the graphite-matrix fuel specimens and relocation of the capsule weight-loading points to relieve the forces on the capsule-positioning mechanisms.

A summary of the final operating data for the group V capsules is presented in Table 6.7. Similar tabulations were published previously,[4]

Table 6.7. Final Operating Data for Group V ORR Poolside Capsules

Capsule number	01-5	02-5	03-5	04-5	05-5	06-5	07-5	08A-5
Cladding identification	J-10 (clad)	J-12 (clad)		CEA I-4	CEA I-1		J-4 (clad)	J-8 (clad)
Origin of fuel specimen	3M Co.	Westinghouse virgin material	ORNL	CEA France	CEA France	ORNL	Westinghouse virgin material	NCC
Fuel identification	3M-101-61	3008					3008	NCC-UC-6
Type	Pyrolytic-carbon-coated UC_2 fuel particles in graphite matrix	UO_2 pellets in type 304 stainless steel tubing	Vibratory-compacted ThO_2-UO_2 granules in type 304 stainless steel tubing	UO_2 pellets in 12-mil-wall type 347 stainless steel tubing	UO_2 pellets in medium thin (12-mil) walled type 347 stainless steel tubing	Vibratory compacted ThO_2-UO_2 granules in type 304 stainless steel tubing	UO_2 pellets in type 304 stainless steel tubing	Pyrolytic-carbon-coated UC_2 fuel particles in graphite matrix
Irradiation starting date	Nov. 1, 1961	Feb. 20, 1962	Dec. 27, 1961	Nov. 1, 1961	Nov. 1, 1961	Dec. 27, 1961[a]	Feb. 20, 1962	Feb. 20, 1962
Irradiation ending date	Feb. 9, 1962[b]	July 29, 1962	Sept. 23, 1962	Sept. 23, 1962	Sept. 23, 1962	Sept. 23, 1962	July 29, 1962	Sept. 23, 1962
Irradiation time normalized to operation at 30 Mwd	87.9	134.98	215.2	272.5	272.5	200.0	134.98	180.4
Effective thermal flux, neutrons/$cm^2 \cdot sec$	3.0×10^{13}	1.43×10^{13}	2.72×10^{13}	4.3×10^{13}	3.8×10^{13}	2.72×10^{13}	1.43×10^{13}	2.8×10^{13}
Fuel density, % of theoretical		95.44	86.0	94.8	94.8	86.0	95.44	
Fuel enrichment, % U^{235}	50.0	2.46	93.2	1.9	1.9	93.2	2.46	50.0
Fuel oxygen-to-uranium ratio		2.002		2.0	2.0		2.002	
Total power, Btu/hr·ft	~16,000	~30,000	~36,200	~29,800	~26,800	~36,200	~30,000	~15,600
Total heat flux, Btu/hr·ft^2	81,520	152,860	222,000	257,000	223,500	222,000	152,860	79,490
Burnup (calculated)								
Total, Mwd/MT of fueled specimen	11,934	1,968	6,456	9,130	8,180	6,000	1,968	11,934
Rate, Mw/MT of fueled specimen (at full power)	71	15	30	33.5	30.0	30	15	66
Typical irradiation conditions								
Cladding outer surface temperature, °F								
Design	1200	1600 (max)	1300 (av)	1202 (av)	1202 (av)	1000 (av)	1600 (max)	800
High for entire run	1205	1640	1480	1320[c]	1260[c]	1210	1640	940
Low for entire run	730	1090	1050	940	1020	800	1160	640
Average for entire run	1060	1340	1280	1150	1150	1020	1360	790
Central temperature range	2300–2100	2410–2200	3400–2860			2800–2420[d]	2280–1980	1800–1560
Maximum cladding outer surface pressure, psig	50	300	300	850	850	300	300	50

[a] This capsule was not positioned correctly until January 16, 1962.

[b] Capsule retracted to reduce release of fission gases; flux reduction factor, 3.4; capsule removed from reactor Sept. 23, 1962.

[c] Temperature oscillations occurred in capsules 04-5 and 05-5 of ±100°F and ±50°F, respectively.

[d] The 1/16-in.-OD bare W-5% Re vs W-26% Re wire in a molybdenum well was the only one of four of this type of central thermocouple in the group V capsules that operated successfully throughout the run.

but this revised table corrects an error in the specification of the cladding material in capsules 04-5 and 05-5 and includes flux, power, burnup, and temperature data obtained from postirradiation analyses.

Fuel-Ball Irradiation Tests in GCR-ORR Loop No. 2

C. L. Segaser R. L. Senn

The first of a series of fuel-ball test assemblies is being fabricated for irradiation in the GCR-ORR loop No. 2 facility. The experiment is designed for ascertaining the effects of nuclear heating on fueled-graphite spheres exposed in a configuration in which the heat transfer is nonuniform and in which four spheres are held in straight-line contact. A secondary purpose is to study the deposition on the loop surfaces of the fission products that may be released from the spheres.

The fuel-ball test assembly will be mounted horizontally in a 3-in.-diam tube at the end of a 4-in.-diam stepped shielding plug. The entire assembly will fit into the 18-in.-diam pressure-piping plug of the loop No. 2 facility.[5] Helium coolant will enter the outer end of the tube, flow over the fuel balls, past the fission-product-deposition tube, and then branch off to the gas outlet line, as shown in Fig. 6.13. The remainder of the assembly is primarily a composite radiation shield equivalent to about 4 ft of ferrophosphorous concrete.

The test section is arranged so that the four 1 1/2-in.-diam fueled-graphite spheres are supported by unfueled graphite retainers cut from spherical sections, as shown in Fig. 6.14. This arrangement simulates one possible configuration in a bed of fueled-graphite spheres. The test section is instrumented with ten type 347 stainless steel-sheathed Chromel-P vs Alumel thermocouples, which are copper plated where they are in contact with graphite. Three thermocouples will be located at the test section gas inlet, three in the graphite pieces near ball contact points, one at the center of a fuel ball, and three at the test section gas outlet.

---

[5]J. Zasler, GCR-ORR Loop No. 2, pp. 223–228, "GCRP Quar. Prog. Rep. Sept. 30, 1961," USAEC Report ORNL-3210, Oak Ridge National Laboratory.

UNCLASSIFIED
ORNL-DWG 63-1172

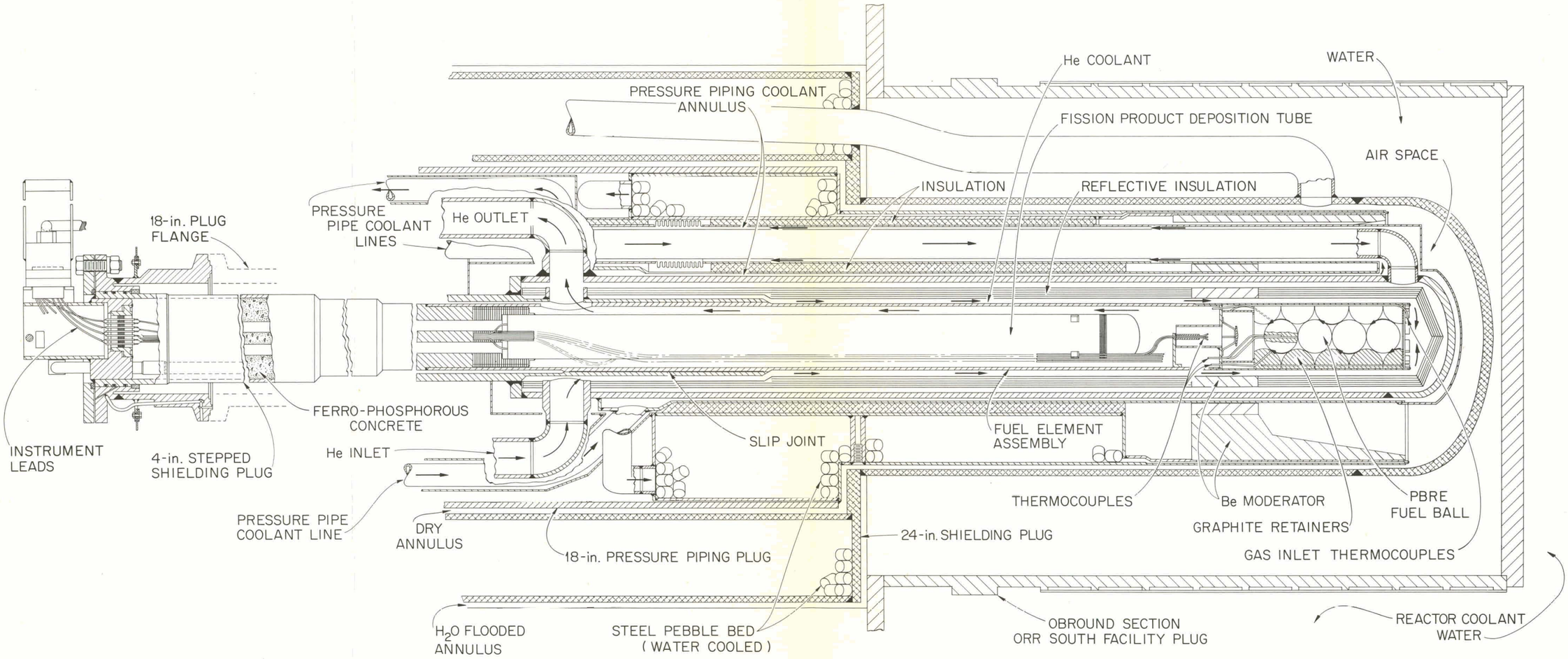

Fig. 6.13. Assembly for Tests of Fueled-Graphite Spheres in GCR-ORR Loop No. 2.

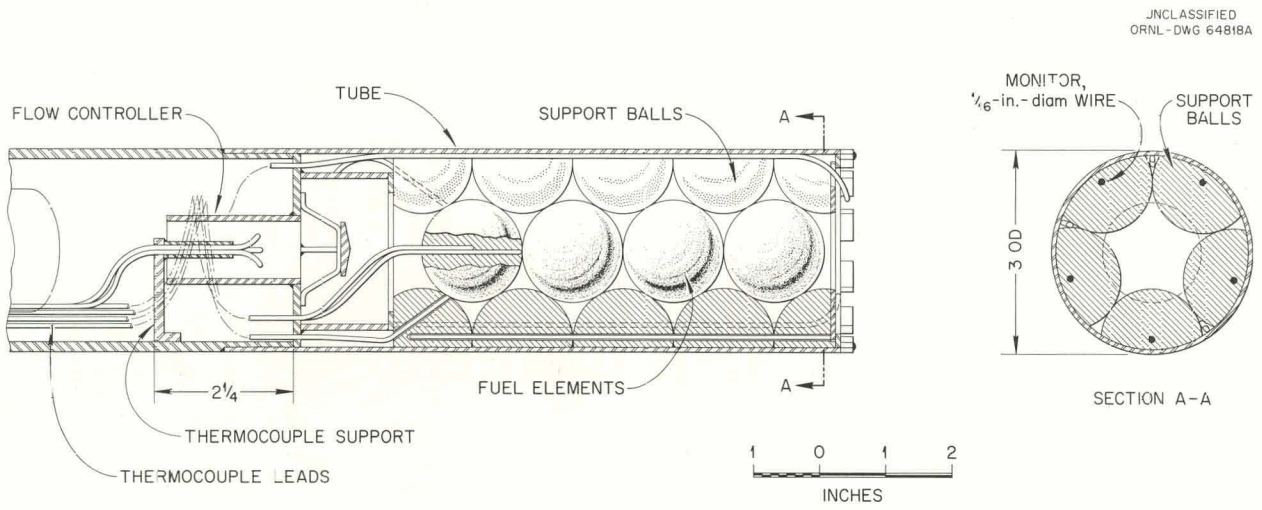

Fig. 6.14. Fuel-Ball Section of Test Assembly.

The fission-product-deposition tube is located downstream of the fuel-ball test section and extends forward approximately 28 in. from the loop outlet gas line to within 5 in. of the rear fuel ball, as shown in Fig. 6.13. The deposition tube provides a relatively large surface that can be examined after each test. The deposition surface temperature profile will be established by a water-cooled heat exchanger located within a carefully sized gas gap, as shown in Fig. 6.15. The temperatures will range from that of the gas (1500°F, maximum) at the test section outlet to about 600°F at the rear of the deposition tube. The temperatures will be measured by six type 347 stainless steel-sheathed Chromel-P vs Alumel thermocouples of varying lengths embedded in the outer wall of the deposition tube, as shown in Fig. 6.15. A seventh thermocouple, although attached to the fission-product-deposition tube, will extend into the gas stream to measure the outlet gas temperature as it leaves the test section and enters the loop piping.

The material, surface finish, and wall temperatures of the fission product-deposition tube can be varied for each test. Thus a series of parametric experiments may be conducted to study the effects of the variables involved in transport and deposition of fission products. The first test assembly will include a type 347 stainless steel tube with a 63-μin. finish (approximately the surface finish of commercial tubing). Temperature criteria will be established during the first in-pile test.

Seventeen thermocouples and the water inlet and outlet lines to the heat exchanger pass through the steel shielding section and a ferrophosphorous concrete shield in spiral tubing conduits. The thermocouple leads are attached to a hermetically sealed, multipin connector that is welded into the Marmon-Conoseal flange assembly which mates with the flange of the 18-in. plug. The water lines are seal-welded through the flange assembly. Suitable connections are made to the water lines and thermocouple connector pins within the loop containment cell.

The proposed operating conditions for the initial fuel-ball test are described in Table 6.8. After operation for two ORR cycles, the test assembly will be removed from the loop for disassembly and hot-cell examination.

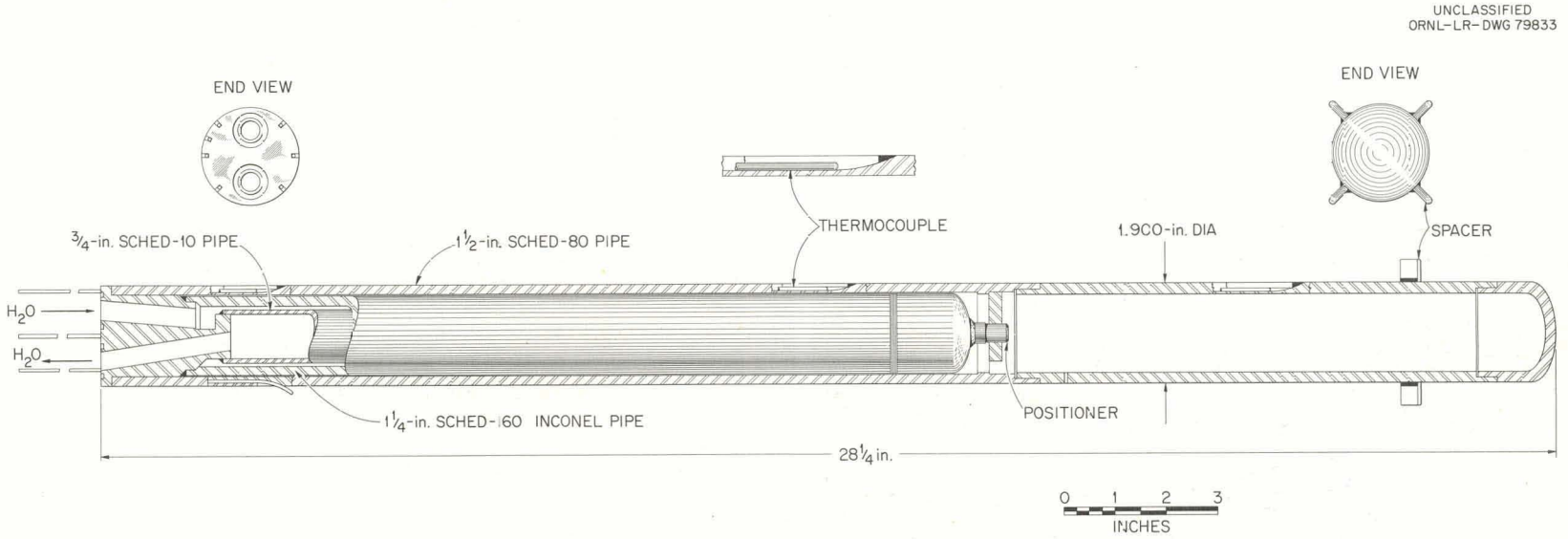

Fig. 6.15. Fission-Product Deposition Tube and Heat Exchanger in Fuel-Ball Test Assembly.

Table 6.8. Operating Conditions for Fuel-Ball Test No. 1 in GCR-ORR Loop No. 2

Fuel power density, w/cm^3	30
Power level, kw	3.48
Fuel-ball test conditions	
Surface heat flux, $Btu/hr \cdot ft^2$	60,800
Surface temperature, °F	1500–1800
Internal temperature, °F	1738–2038
Helium coolant conditions in test section	
Pressure, psia	300
Inlet temperature, °F	1200
Outlet temperature, °F	1268–1350
Flow rate, lb/hr	73.8–184
Superficial mass velocity,[a] $lb/hr \cdot ft^2$	2000–5000
Average heat transfer coefficient, $Btu/hr \cdot ft^2 \cdot °F$	125–250

[a]Design reference value was 3200 $lb/hr \cdot ft^2$.

Fission-Product Transport and Deposition in Coolant Circuits

F. H. Neill
A. B. Meservey
W. E. Browning, Jr.
O. Sisman

Out-of-Pile Loop Test at BMI (F. H. Neill)

The initial fission-product deposition experiment was completed in the out-of-pile loop[6] at Battelle Memorial Institute. Helium coolant, heated to 1200°F, was passed over a preirradiated UC_2 fuel specimen. The fission products diffusing from the fuel specimen were carried by the coolant around the loop and through simulated reactor components, that is, heaters, heat exchangers, and a compressor. At the termination of the test, the loop was dismantled, and the fission-product contamination on the type 304 stainless steel loop tubing was determined.

For the first test, the UC_2 fuel specimen was irradiated for 10 hr in a flux of 9.5×10^{11} neutrons/$cm^2 \cdot sec$. After cooling seven days, the

[6]F. H. Neill, M. N. Ozisik, and D. B. Trauger, Fission Product Transport and Deposition in Coolant Circuits, pp. 250–256, "GCRP Semiann. Prog. Rep. Sept. 30, 1962," USAEC Report ORNL-3372, Oak Ridge National Laboratory.

specimen was annealed at 1800°F with the loop operating under the following conditions:

Helium pressure, psia	240
Helium temperatures, °F	
After specimen	1200
Cooler outlet	465
Blower inlet	460
Reynolds number	4000 to 6000
Tubing outside diameter, in.	0.5

The gross gamma activity of the deposited fission products is shown in Fig. 6.16 as a function of distance from the fuel specimen. The distribution of the individual species, as determined by radiochemical analysis, is indicated in Figs. 6.17 through 6.20.

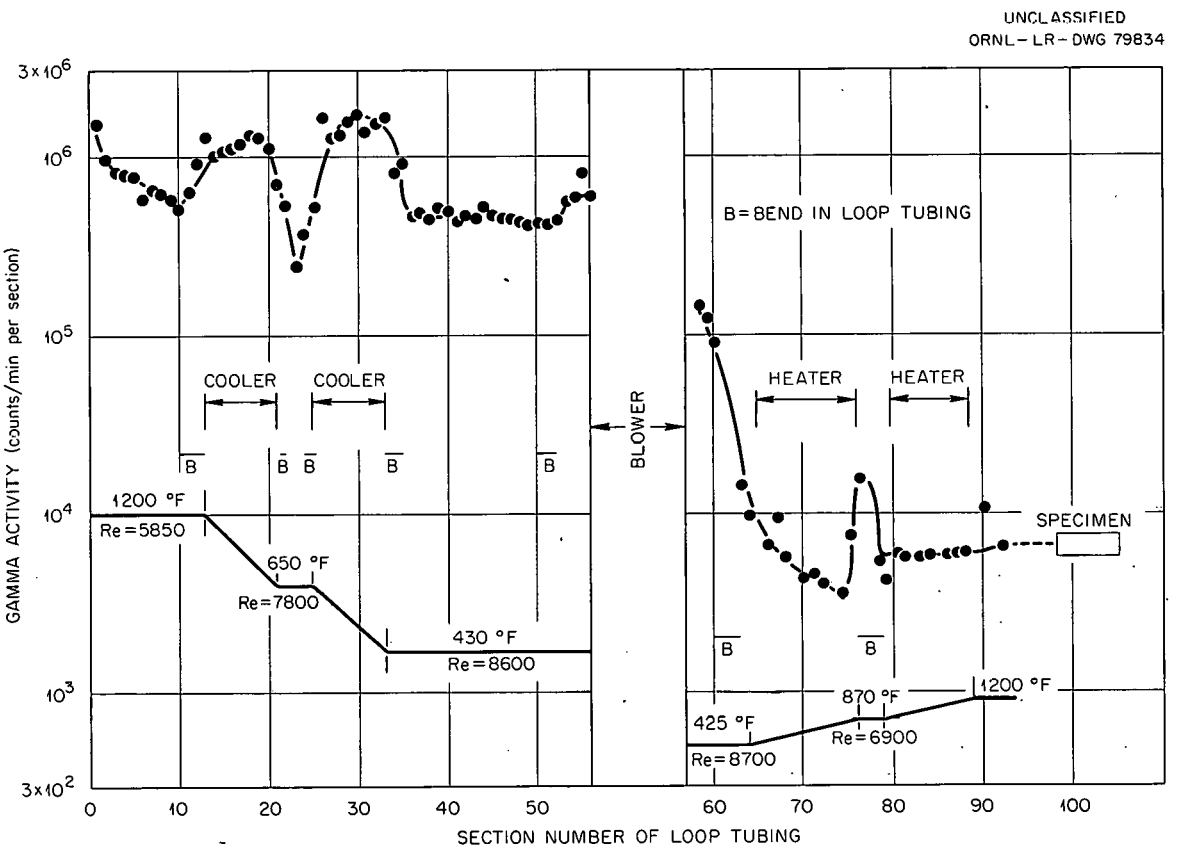

Fig. 6.16. Distribution of Gross Gamma Activity in Out-of-Pile Fission-Product-Deposition Loop at BMI.

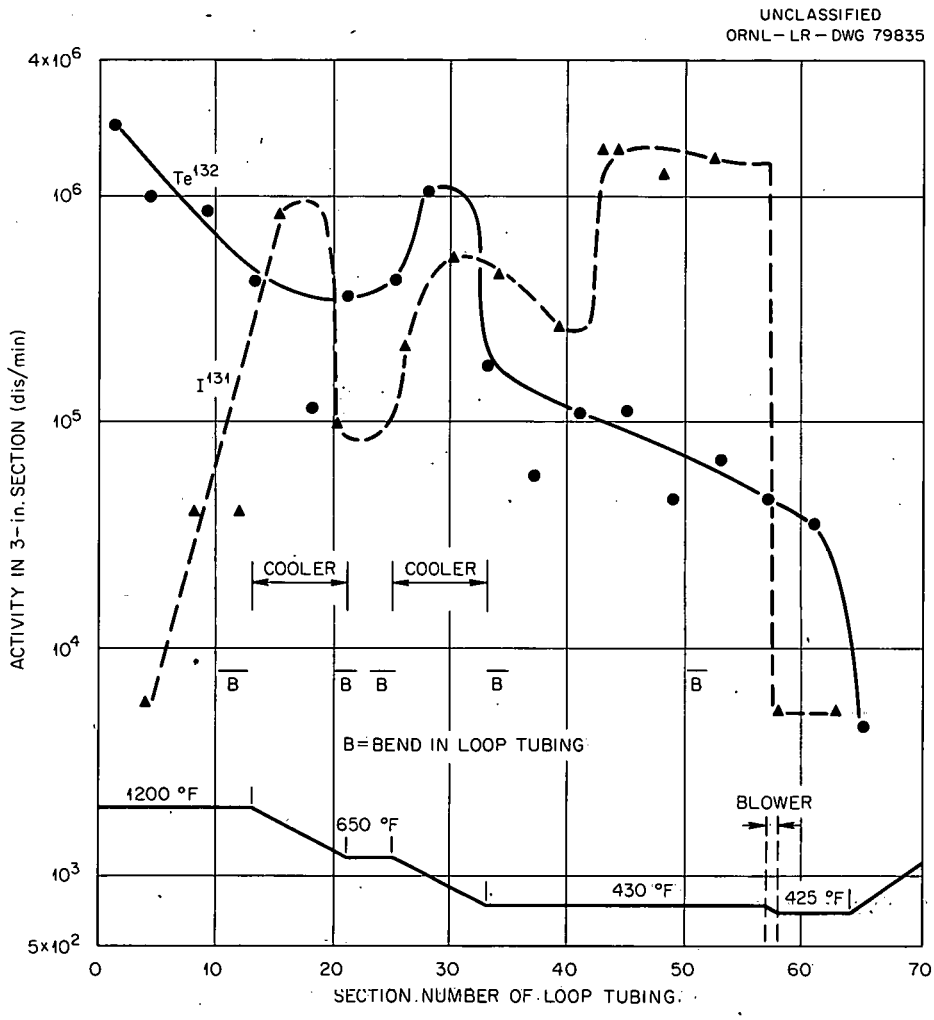

Fig. 6.17. Distribution of Te^{132} and I^{131} Activity in BMI Loop.

Analytical Model (M. N. Ozisik)

The test data for the deposition of fission products from the turbulent helium stream on the inner surface of a 0.37-in.-ID stainless steel tube in the BMI out-of-pile loop experiment (run 1) were correlated with the analytical relations developed previously.[6] As mentioned above, the fission products were produced from an irradiated fuel specimen which was heated to approximately 1800°F to allow the fission products to diffuse into the gas stream; the fuel specimen had been stored after irradiation to allow the short-lived fission products to decay.

The calculated and the experimental data are compared in Fig. 6.21 as a function of the distance along the tube for an isothermal region of

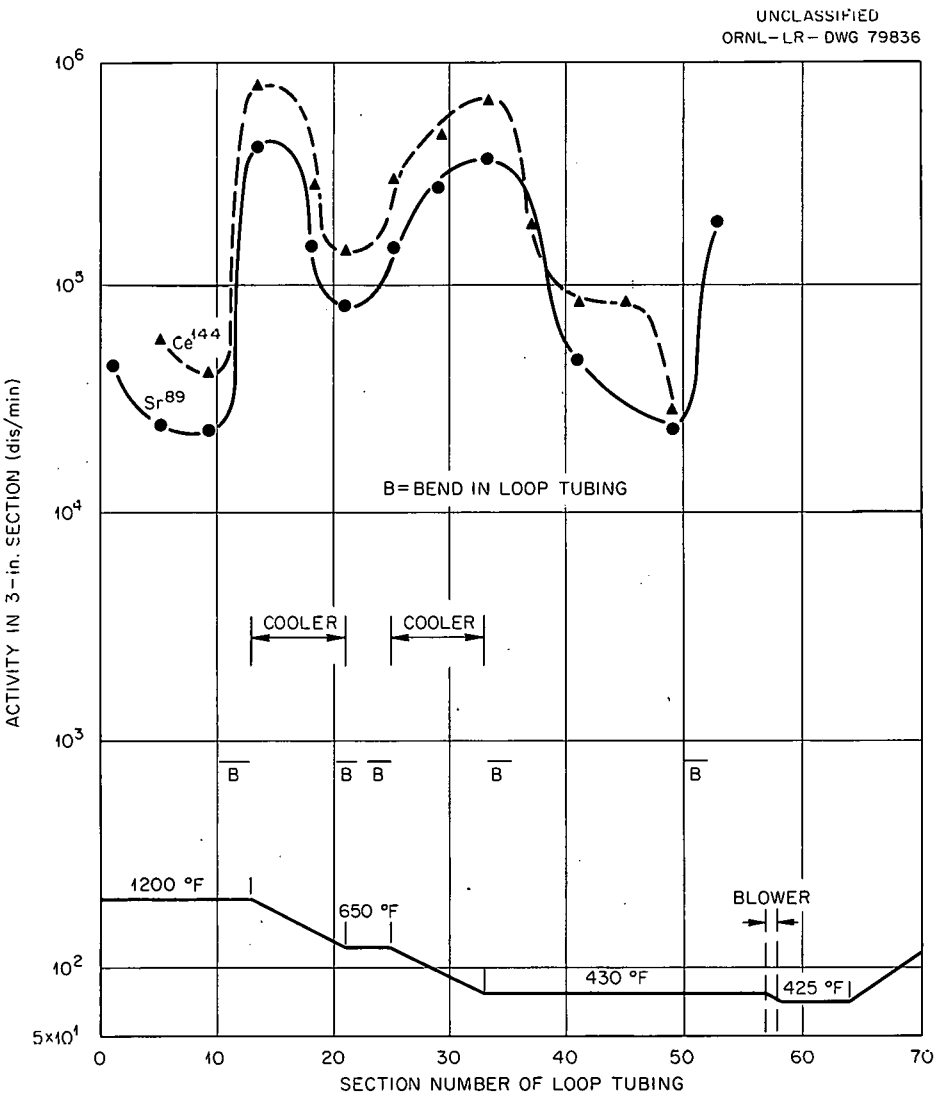

Fig. 6.18. Distribution of Sr^{89} and Ce^{144} Activity in BMI Loop.

the tube. Since the source strength of the particles in the gas was not known, no attempt was made to calculate the absolute value of the deposition, and therefore only the slope of the calculated curve is of interest. The following analytical relation was used for calculating the number of particles deposited per square centimeter:

$$\text{Particles deposited} = N_o \frac{P_o C_o}{\lambda_o} e^{-\alpha_o x} , \qquad (1)$$

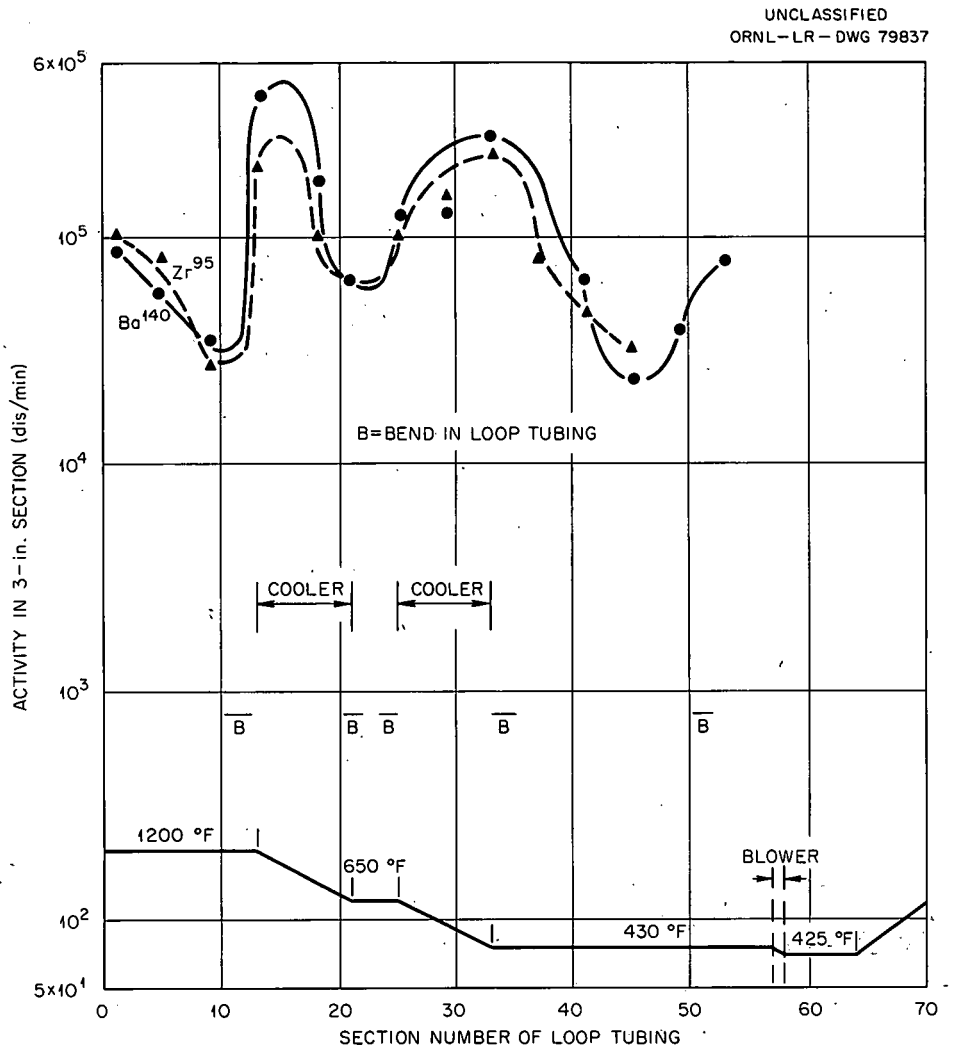

Fig. 6.19. Distribution of Ba^{140} and Zr^{95} Activity in BMI Loop.

where

$$\alpha = \frac{1}{U}\left(\lambda_o + \frac{4P_oC_o}{d}\right),$$

$$C_o = 0.023\,\frac{D^{0.7}\rho^{0.5}U^{0.8}}{\mu^{0.5}d^{0.2}},$$

d = tube inside diameter, cm,

D = diffusion coefficient, cm^2/sec,

N_o = particle concentration in the gas stream at the origin, particles per cm^3,

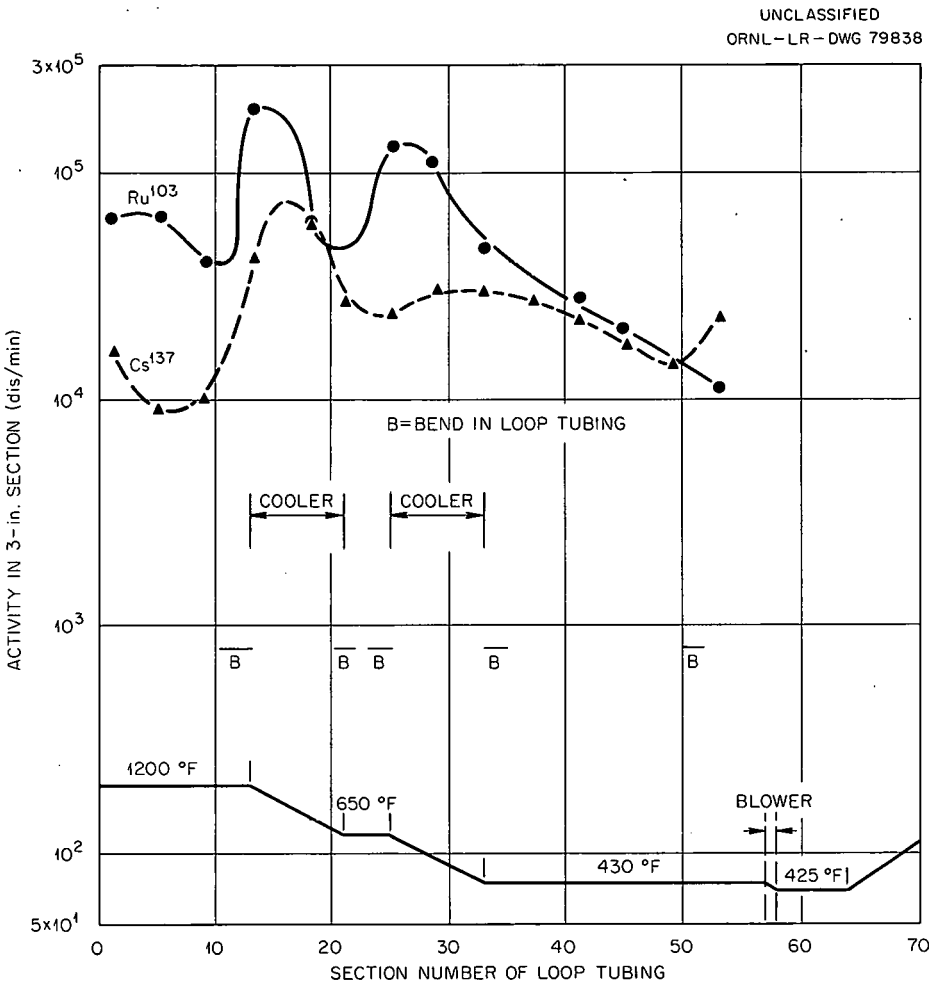

Fig. 6.20. Distribution of Ru^{103} and Cs^{137} Activity in BMI Loop.

P_o = probability that a particle or atom will stick on the wall surface, dimensionless,

U = coolant velocity, cm/sec,

μ = viscosity of coolant, g/cm·sec,

ρ = density of coolant, g/cm^3,

λ = half life, sec^{-1}.

The diffusion coefficient D was calculated from the relation

$$D = 0.185 \times 10^{-2} \frac{T^{3/2}}{\sigma^2 P} \left(\frac{1}{M} + \frac{1}{M'} \right)^{1/2} , \qquad (2)$$

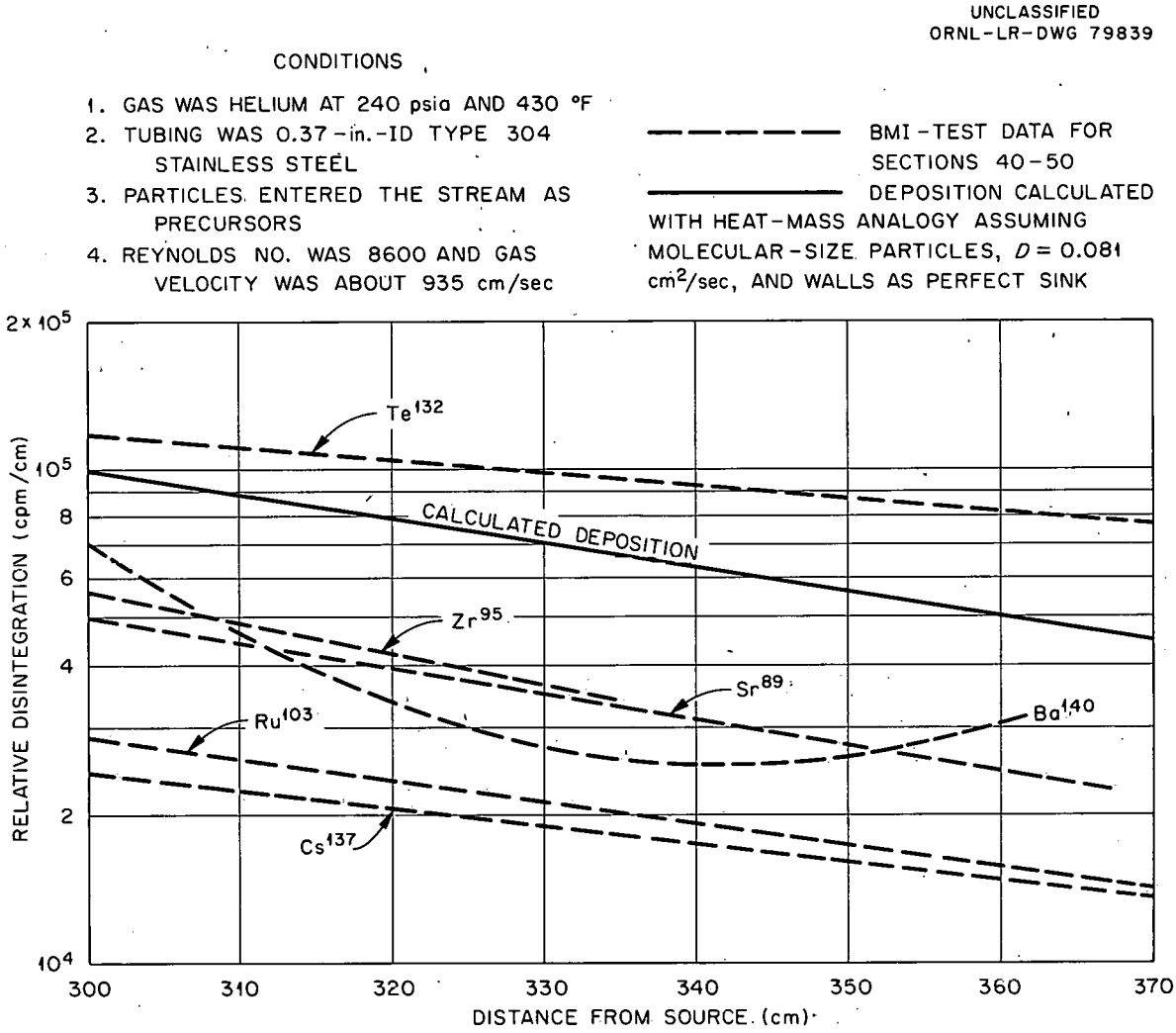

Fig. 6.21. Comparison of Calculated and Experimental Data on the Deposition of Fission Products from Gas Streams.

where

M, M′ = molecular weight of colliding spheres (i.e., gas and fission-product molecules),

P = pressure, atm,

T = absolute temperature, °K,

σ = distance between the centers of colliding spheres, A.

The wall surface was taken as a perfect sink (i.e., $P_o = 1$), and the fission products in the gas stream were assumed to be of molecular sizes with a mean diameter of 3 A. If the exact molecular diameter had been used for each type of fission product, the slopes of the calculated curves

would have varied slightly for the different species considered. The agreement between the slope of the calculated curve and slopes of the experimental curves is considered to be reasonably good.

No attempt was made to correlate the test data for the regions of the loop where the coolers were located and a temperature gradient existed from the gas stream to the wall. The effect of a temperature gradient is to increase or decrease the deposition rate depending on the direction of the temperature gradient. For the temperature gradient present in the gas stream, the total deposition can be assumed to have two components: one from ordinary diffusion (i.e., Brownian motion) and the other from thermal diffusion. With a simple analysis it can be shown that the ratio of the thermal diffusion component to ordinary diffusion component is given by[7]

$$\frac{\text{Thermal diffusion mass flux}}{\text{Ordinary diffusion mass flux}} = \frac{1}{2}\,\alpha_t \left(\frac{Pr}{Sc}\right)^{1/3} \frac{\Delta T}{T}\,, \qquad (3)$$

where

$Pr = C_p\mu/K$ = Prandtl number,

$Sc = \mu/\rho D$ = Schmidt number,

ΔT = difference between bulk-free stream and tube wall temperatures, °C,

T = mean temperature, °K,

α_t = thermal diffusion factor, dimensionless.

The quantities on the right of Eq. (3) are such that for most practical purposes the diffusion component from thermal forces is much less than that from Brownian motion of the particles.

The test data for the deposition of particles in the regions where the coolers were located were significantly different from those in the isothermal region. This difference could not be accounted for by estimating the effects of the temperature gradient on deposition from Eq. (3). Analytical work is now in progress in an attempt to resolve this apparent anomaly.

---

[7]M. N. Ozisik, "An Analytical Model for Fission-Product Transport and Deposition," USAEC Report ORNL-3379, Oak Ridge National Laboratory (to be published).

Decontamination of Samples of BMI Loop Piping (A. B. Meservey)

Samples from three portions of loop piping which had been contaminated by fission products from a UC_2 source at 1800°F were successfully decontaminated with oxalate-peroxide solutions. Samples exposed to the circulating gas at 650 and 1000°F had average decontamination factors of 125 and 64, respectively, after 1 hr at 95°C in 0.4 M oxalate–0.16 M citrate–0.34 M H_2O_2 at a pH of 4.0. Samples exposed at 1200°F had a decontamination factor of only 2.0 with this treatment. Decontamination factors during the second hour were, in the same order, 1.5, 2.3, and 1.4. The samples exposed at 1200°F were decontaminated to only twice the scintillation-counter background, with an additional decontamination factor of 15 (cumulative DF = 41), after 1 hr in a controlled-corrosion solution. This solution contained 0.5 M $H_2C_2O_4$ and 0.1 M NaF, with the H_2O_2 maintained at about 0.015 M by periodic additions. The corrosion rate on type 347 stainless steel was 0.009 mil/hr. Initial scintillation gamma-counting rates were only 1×10^4 to 3×10^4 counts/min. The high-temperature samples were thus decontaminated, but they retained a dark oxide coating.

Other reagents were also used successfully. The best was 3 M H_2SO_4 plus 1 M H_2O_2. In 1 hr at 95°C, the decontamination factors on the samples exposed at 1200, 1000, and 650°F were 140, 453, and 151, respectively. In 3 M HNO_3 + 1 M H_2O_2, the results were 21, 246, and 240, and in 6 M HNO_3 without H_2O_2 the decontamination factors were 9, 103, and 45. In 10% Turco 4512, an inhibited H_3PO_4 solution, the decontamination factors were only 2, 55, and 38, but further boiling in 50% Turco 4512 for 3 hr increased the decontamination factors to 4, 325, and 137, with partial removal of the dark coating from the sample exposed at 1200°F. A three-stage treatment with Turco 4501 in the first stage, Turco 4502 in the second, and Turco 4518 in the third gave decontamination factors of 6, 265, and 63.

A second batch of samples was decontaminated in a steam spray. The reagent was noncorrosive 0.4 M ammonium oxalate–0.16 M ammonium citrate–0.5 M H_2O_2 at a pH of 4.0, which was aspirated into a 15-psig steam jet. The treatment time was 30 min. Eight samples from different parts of the loop, representing temperatures from 590 to 1150°F and scintillation

gamma activities from zero to 2×10^4 counts/min per sample, were each run in duplicate. Samples exposed at 1150°F with activities of 1×10^4 to 2×10^4 counts/min had an average decontamination factor of 11, and samples exposed at 920°F with initial activities of almost 2×10^4 counts/min had an average decontamination factor of 67. Other samples exposed at lower temperatures and those more remote from the fission-product source had much lower initial activities and were decontaminated essentially to background. The higher temperature samples were thinly coated with a dark oxide, which was lightened in color or removed by the steam blast.

Characterization of Gas-Borne Fission Products (W. E. Browning, Jr., R. D. Ackley, M. D. Silverman)

The behavior of gas-borne materials depends markedly on their form; consequently, the prediction of their dispersal or transport or the selection and design of systems for their removal from gases requires information as to the distribution of radioactivity between the different forms. Two methods for determining the form of radioactivity in gases were therefore investigated. In one method, diffusion coefficients for fine particles and for radioactive vapors, such as iodine, were determined by measuring the distribution of radioactivity on the walls of a channel previously exposed to gas carrying radioactive materials and flowing under laminar conditions. This method of characterizing gas-borne radioactive materials was applied to the problem of removing millimicron-diameter radioactive particles from air streams. Such particles may be too small in mass for efficient filtration by inertial impaction, but sufficiently large, as compared with molecules of iodine vapor, that diffusion is too slow for efficient deposition. In tests using I^{131}-labeled Al_2O_3 particles with a nominal diameter of 0.004 μ, high-efficiency low-pressure-drop particulate filters exhibited efficiencies ranging from less than 10 up to about 75%. With activated-carbon beds, 0.75 in. deep and 6 × 16 mesh, iodine-vapor removal was essentially complete, but the removal efficiency for 0.003 to 0.006 u particles was observed to be only 75 to 90%, the higher efficiency being associated with the finer particles.

Similar tests were carried out using fog condensation and foam encapsulation to remove millimicron-sized particles from air. In these

tests, removal efficiencies of 85 to 99% were observed. These results are encouraging, but the efficiencies are not high enough to provide the basis for design of a fission-product removal system. Optimization of these processes might provide a partial answer to the problem of small-particle removal.

In the second method, fibrous filters are used for studying the characteristics of radioactive aerosols. The transport of an aerosol through an array of fibers involves the processes of inertial impaction, interception, and diffusion. Since all these processes have important effects on the behavior of radioactive materials in gases, it is useful to be able to characterize radioactive aerosols by measuring their behavior in fibrous beds under carefully controlled conditions. A filter was developed that has a uniform fiber diameter to permit theoretical analysis and a layered structure to facilitate separation of the fiber bed into discrete layers for radioassay after exposure to the aerosol. A radioactive aerosol of 0.004 to 0.03 μ particles containing Zn^{65} was developed for initial tests.

Preliminary results indicate that the techniques used are satisfactory and should provide useful information on aerosol character and on filtration mechanisms. The slope of the distribution curve on a semilog plot equals the coefficient of interaction between the aerosol and the fibers and is composed of terms corresponding to each of the interaction processes. This coefficient is characteristic of the aerosol species. At the lowest linear velocity (~0.4 ft/min), where diffusion would be controlling, collection efficiency is increased by decreased velocity, as expected. At higher flow rates, where the primary mechanism of filtration is interception for particles of this size, the efficiency appears to be independent of velocity, in accord with theory. This investigation is being continued to provide a more specific identification of the mechanisms that produce the distribution patterns observed. Interpretation of distributions in terms of aerosol characteristics will then be possible. It is anticipated that this work will also extend the theory of the performance of fibrous filters to conditions for which little information is now available.

In-Pile Fission-Product-Deposition Experiment MTR-48-6 (M. F. Osborne)

Specimens of type 347 stainless steel, Croloy, AGOT graphite, and silver were exposed in the purge gas stream from experimental assembly MTR-48-6. Each specimen was a thin disk, 0.6 in. in diameter. One specimen of each type was located 1 1/4 in. downstream from the fuel cylinder and another was 2 1/4 in. downstream from the fuel cylinder. During irradiation the temperatures of these specimens were between 600 and 800°F.

After removal from the reactor, each specimen was leached in nitric acid, and the solute was analyzed for the common fission products. The results of these analyses are given in Table 6.9. The silver specimens retained the most fission products, except for Cs^{137}. The very high concentration of Ag^{110} in these specimens was due to neutron activation. The type 347 stainless steel specimens appeared to retain fewer fission products than the other materials.

Release of Fission Products by In-Pile Burning of Irradiated Fueled Graphite

W. E. Browning, Jr.
R. P. Shields
C. E. Miller, Jr.
B. F. Roberts

Three experiments were conducted in the ORR in which pyrolytic carbon-coated uranium carbide particles in a graphite matrix were burned at temperatures up to approximately 1400°C. In these experiments, fission and gamma heat produced a sufficiently high temperature for a large portion of the fuel to burn during the 15-min period in which air was supplied as the sweep gas. The method of running the experiment and the results of the first experiment were described in the previous report.[8] The specifications for the specimen and pertinent experimental conditions are listed below:

Burning conditions

Initial temperature	890°C
Combustion temperature	Up to 1400°C
Air flow rate	400 cm^3/min
Burning duration	15 min

Table 6.9. Fission-Product-Deposition Data for Specimens Exposed in Purge Gas Stream of Experiment MTR-48-6

Specimen[a]	Fission-Product Deposition at Shutdown (atoms)						
	Ce^{144}	Ba^{140}	Cs^{137}	Ag^{110}	Zr^{95}	Y^{91}	Sr^{89}
Silver							
Top[b]	8.55×10^{11}	1.59×10^{14}	$<10^{11}$	1.38×10^{17}	1.5×10^{10}	5.57×10^{12}	1.47×10^{13}
Bottom[b]	1.07×10^{13}	7.9×10^{14}	$<10^{11}$	1.64×10^{17}	6.77×10^{11}	2.57×10^{13}	3.4×10^{13}
Croloy							
Top	1.69×10^{11}	1.62×10^{13}	3.3×10^{12}	1.38×10^{12}	4.22×10^{9}	3.85×10^{12}	1.26×10^{13}
Bottom	1.24×10^{11}	5.67×10^{13}	3.25×10^{12}	9.15×10^{12}	7.57×10^{9}	7.72×10^{12}	1.6×10^{13}
Graphite							
Top	2.02×10^{11}	1.75×10^{13}	3.5×10^{12}	3.05×10^{11}	2.85×10^{9}	3.97×10^{12}	1.31×10^{13}
Bottom	1.79×10^{11}	1.38×10^{13}	3.72×10^{12}	1.07×10^{13}	6.72×10^{9}	7.2×10^{12}	1.47×10^{13}
Bottom[c]	7.27×10^{12}	1.74×10^{12}	9.6×10^{12}	7.15×10^{11}	5.57×10^{11}	5.37×10^{11}	9.55×10^{11}
Type 347 stainless steel							
Top	3.55×10^{11}	3.8×10^{13}	2.06×10^{12}	4.05×10^{11}	3.72×10^{10}	2.32×10^{12}	6.22×10^{12}
Bottom	4.25×10^{10}	4.37×10^{12}	9.22×10^{11}	6.05×10^{11}	2.20×10^{9}	1.39×10^{12}	3.25×10^{12}

[a] Each sample was leached with 25 ml of 8 N HNO_3 at room temperature for a period of 24 hr.

[b] Top specimens were 2 1/4 in. from fuel; bottom specimens were 1 1/4 in. from fuel.

[c] After room-temperature leaching was completed, this sample was boiled for 8 hr using total reflux in 25 ml of 8 N HNO_3.

Fuel specimen	
Particles	Pyrolytic-carbon-coated uranium carbide
Matrix	Graphite
Manufacturer	Minnesota Mining and Manufacturing Co.
Dimensions	0.6-in.-OD bushing, 0.5 in. long with 0.25-in. axial hole
Uranium content	8 to 10 wt % natural uranium

As the graphite matrix burned, some of the fuel particles fell away from the unburned fuel. Metallographic examination of these particles and those in the unburned fuel showed that the damage to particles ranged from none to complete destruction of the coating and oxidation of the uranium carbide. Typical particles that fell away during burning are shown in Fig. 6.22. It was not possible to determine the percentage of particles of each type shown. Some of the particles that remained in the unburned fuel also showed cracks. In experiment 1, a count of the damaged and undamaged particles, obtained by scanning the exposed surfaces, showed that about 45% of the particles had at least one crack in the coating. In experiment 2, the uranium content of the specimens was so low that the results were not analyzed.

The results of experiment 3 confirmed, for the most part, the results of experiment 1. In the first experiment, 58% of the specimen burned, compared with 41% in the third. In the third experiment, most of the uranium carbide in the specimen was concentrated on one side, and this side burned very little; 93% of the uranium was found by analyses to be in the unburned fuel.

Fission-product-release data for experiments 1 and 3 are presented in Table 6.10. A large fraction of some of the fission products was probably retained inside those particles having undamaged pyrolytic carbon coatings, especially those in the unburned fuel. The release of strontium, zirconium, barium, cerium, and uranium from the high-temperature zone of the furnace was very low, but large fractions of iodine, tellurium, and cesium were released. Forty percent of the ruthenium was released from

---

[8]W. E. Browning et al., Release of Fission Products by In-Pile Burning of Irradiated Fueled Graphite, pp. 256–259, "GCRP Semiann. Prog. Rep. Sept. 30, 1962," USAEC Report ORNL-3372, Oak Ridge National Laboratory.

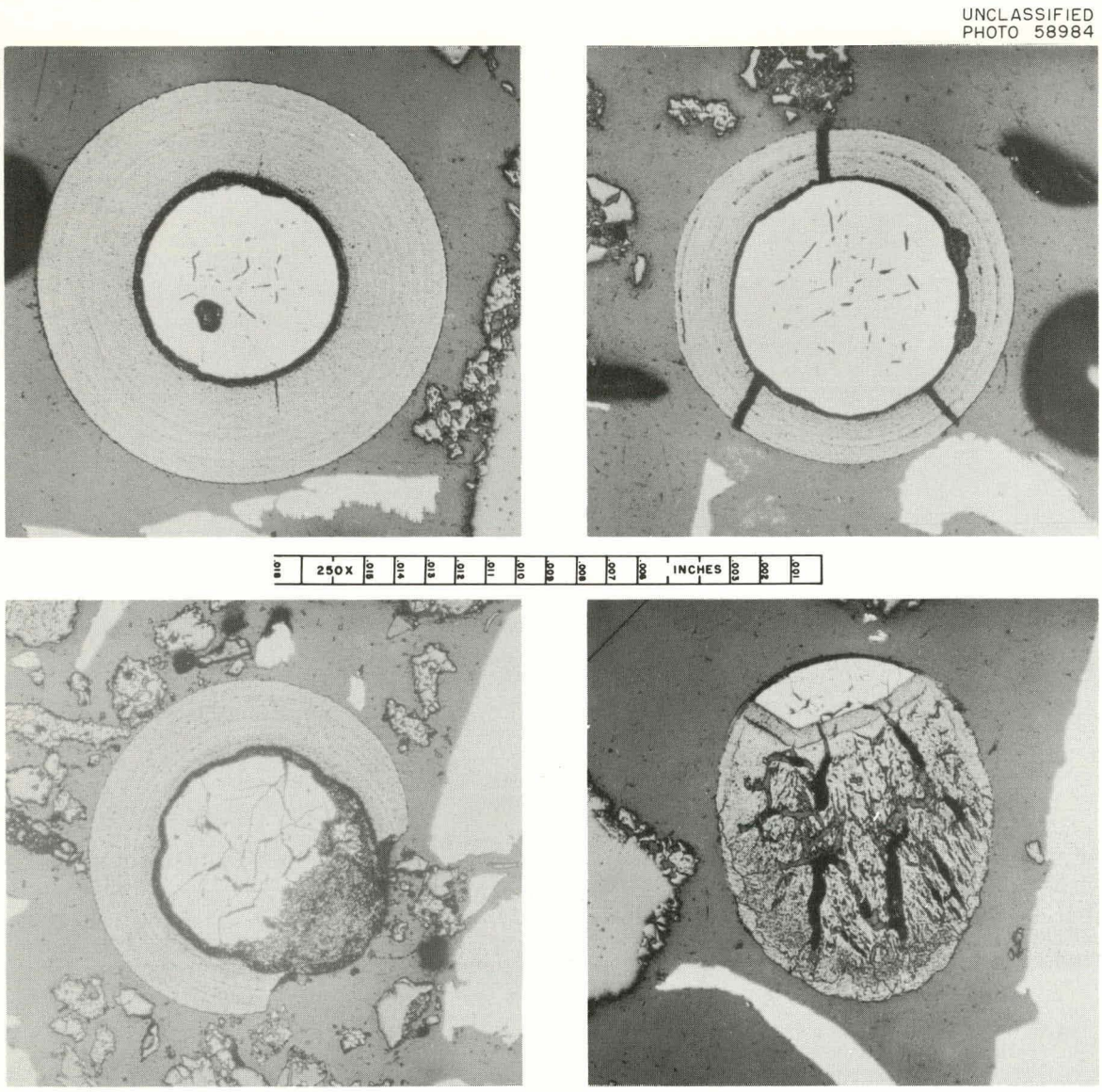

Fig. 6.22. Pyrolytic-Carbon-Coated Uranium Carbide Particles Showing Various Stages of Oxidation.

the furnace in experiment 1 and 5.7% in experiment 3. The loss of ruthenium in the first experiment was probably due to the formation of volatile oxides. Analyses for krypton and xenon were omitted to avoid developing refrigerated adsorbers to operate in air. The following conclusions are based on experiments 1 and 3:

1. Strontium, zirconium, barium, and cerium are retained where they are formed.

Table 6.10. Fission-Product-Release Data from In-Pile Burning Experiments 1 and 3

	Material Found, Expressed as Percentage of Total Material Found in Experimental Assembly								
	Sr^{89}	Zr^{95}	Ru^{106}	I^{131}	Te^{132}	Cs^{137}	Ba^{140}	Ce^{144}	U
Unburned fuel[a]									
Experiment 1	50.6	58.2	27.0	59.7	47.6	38.1	51.7	54.8	61.9
Experiment 3	75.4	83.9	87.0	82.4	76.1	39.1	84.9	85.3	93.9
Outside of fuel residues[b]									
Experiment 1	13.8	3.7	48.2	28.9	42.7	51.3	14.5	9.05	2.12
Experiment 3	13.1	5.04	8.81	16.5	23.2	54.5	6.96	6.98	0.877
Retained in furnace									
Experiment 1	98.8	99.5	59.3	73.2	64.9	63.0	99.5	93.8	99.6
Experiment 3	98.7	98.7	94.3	85.6	85.7	58.4	99.3	97.1	99.8

[a] In experiment 1, 58.6% of the sample was burned; in experiment 3, 41% burned.

[b] Fuel residues included the unburned portion of the specimen, fuel particles, fuel powder, and the floor of the combustion furnace.

2. The unburned fuel retained 88 to 97% of the iodine associated with the uranium of the unburned fuel.

3. Fifteen to 25% of the iodine, 15 to 35% of the tellurium, and 35 to 40% of the cesium was released from the furnace.

4. The release of ruthenium varied between 5 and 40%.

5. An appreciable amount of cesium (10% of total), ruthenium (1%), and iodine (1.5%) penetrated the filter, but tellurium was retained by the filter.

6. The fragments that fell away from the specimen during burning contained the same percentage of carbon as the unburned fuel.

7. These experiments indicate that the uranium carbide-lean side of a heterogeneous specimen burns preferentially.

Compatibility of Pyrolytic-Carbon-Coated Uranium Carbide Particles and Uncoated Fuel Bodies with Water Vapor in Helium

L. G. Overholser J. P. Blakely
J. L. Rutherford

Experimental results were reported previously[9] for the reaction of coated particles from lots 3M-113 and 3M-114 with steam-helium mixtures in the temperature range 700 to 1000°C. The partial pressures of steam employed ranged from 55 to 355 mm Hg at a total pressure of one atmosphere. Although the coatings present in the two lots of particles were both laminar and approximately equal in thickness, the coatings on the 3M-114 particles afforded better protection of the cores against attack by steam than did the coatings on the 3M-113 particles. This difference in protectiveness could not be accounted for by differences in the reaction rates of the respective pyrolytic-carbon coatings with steam. Photomicrographs of the particles following exposure to steam showed that the attack on the 3M-113 particles consisted of localized pitting, whereas more generalized attack occurred on the 3M-114 particles.

---

[9]L. G. Overholser, J. P. Blakely, and N. V. Smith, Compatibility of Pyrolytic-Carbon-Coated Uranium Carbide Particles with Water Vapor in Helium, pp. 259–269, "GCRP Semiann. Prog. Rep. Sept 30, 1962, " USAEC Report ORNL-3372, Oak Ridge National Laboratory.

Samples of pyrolytic-carbon-coated uranium carbide particles from lot 3M-117 were exposed to steam using the equipment described previously.[10] Particles from lot 3M-117 are polygonal in shape with an average diameter of 375 μ, have a laminar coating with a nominal thickness of 100 μ, and contain 44.1% uranium. This material was contacted at 800 to 1100°C with steam-helium mixtures having a partial pressure of steam of either 355 or 635 mm Hg and a total pressure of one atmosphere. Following the exposure to steam, the particles were leached with 8 M HNO_3 at 90°C for 8 hr, the extracted uranium was measured, and the particles were examined microscopically. The rates of reaction of the pyrolytic-carbon with steam were determined from weight changes and represented average rates during the exposures.

The data listed in Table 6.11 show the rates of reaction of the pyrolytic-carbon coatings and also give a measure of the integrity of the coatings as determined by the uranium removed by the HNO_3 leach following the steam treatment at the various temperatures and partial pressures of steam. In agreement with the earlier results,[9] the reaction rates of the pyrolytic-carbon with steam increase with increasing temperature and steam pressure. The rates also are in fair agreement with those given earlier. The results for run 25 show the drastic attack that occurred at 1100°C upon exposure for 1 hr.

The uranium contents of the HNO_3 leach solutions indicate that the coatings on the 3M-117 particles afford less protection to the cores when exposed to high-temperature steam than was found in the case of the 3M-114 particles.[9] They are more protective than the 3M-113 coatings, however. The results obtained at 1000 and 1100°C indicate that the coatings are more protective at the lower temperature, based on comparable removal of pyrolytic carbon (see runs 1, 12, and 25), suggesting that the type of attack is temperature dependent.

Photomicrographs of several of the samples taken after exposure to steam are shown in Figs. 6.23 through 6.27. All particles except those

---

[10] L. G. Overholser, J. P. Blakely, and N. V. Smith, Compatibility of Coated and Uncoated Uranium Carbide Particles with Water Vapor in Helium, pp. 223–224, "GCRP Quar. Prog. Rep. March 31, 1962," USAEC Report ORNL-3302, Oak Ridge National Laboratory.

Table 6.11. Reactivity of 3M-117 Coated Particles with Steam

Sample		Steam Exposure Conditions			Quantity of Pyrolytic Carbon Reacted			Uranium Removed by HNO_3 Leach	
No.	Weight (g)	Time (hr)	Temperature (°C)	Pressure of H_2O (mm Hg)	Gram	Per Cent	Gram per Gram-Hour	Gram	Per Cent
20	2.07	4	800	355	0.069	6.4	0.016	0.004	0.4
16	2.10	1	800	635				0.001	0.1
23	1.98	4	800	635	0.163	16	0.040	0.011	1.3
5	2.06	1	900	355	0.030	2.8	0.028	0.027	3.0
6	2.10	2	900	355	0.075	6.9	0.035	0.057	6.2
22	2.06	4	900	355	0.115	11	0.027	0.032	3.5
17	2.03	4	900	355	0.142	13	0.034	0.053	5.9
21	2.01	4.5	900	355	0.117	11	0.025	0.024	2.7
8	2.13	1	900	635	0.078	7.1	0.071	0.006	0.6
24	1.62	1	900	635	0.052	6.2	0.062	0.032	4.5
7	2.01	2	900	635	0.172	17	0.083	0.037	4.1
3	2.56	1	1000	355	0.084	6.4	0.064	0.050	4.4
2	1.98	2	1000	355	0.186	18	0.092	0.122	14
19	2.05	2	1000	355	0.133	13	0.063	0.031	3.4
12	2.01	4	1000	355	0.417	40	0.10	0.061	6.8
1	2.34	4	1000	355	0.521	43	0.11	0.046	4.5
10	1.92	1	1000	635	0.114	11	0.12	0.036	4.1
25	1.78	1	1100	635	0.421	46	0.46	0.316	40

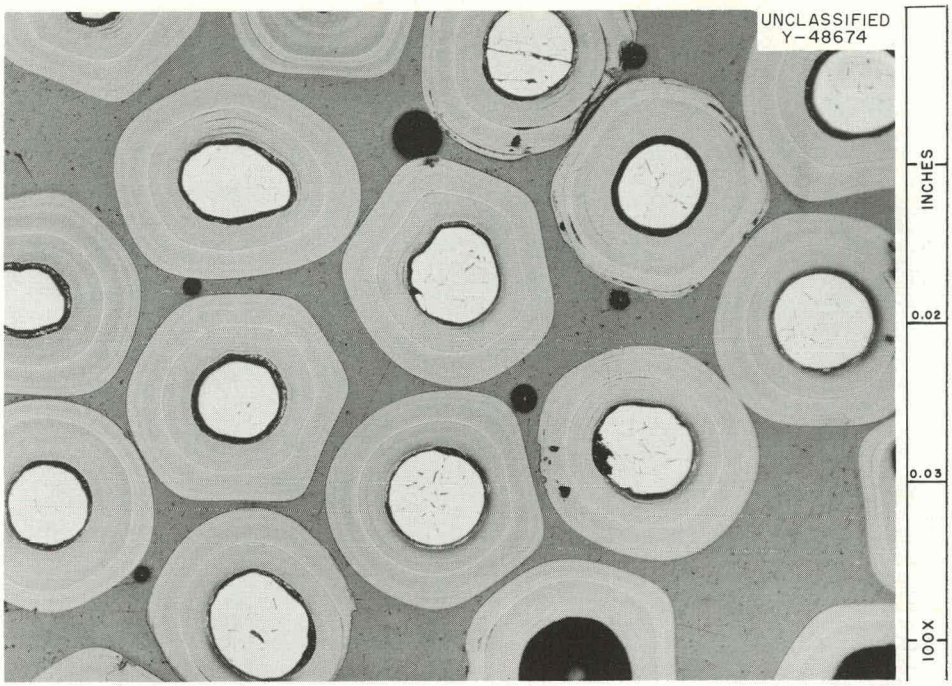

Fig. 6.23. Coated Particles of Run 20 After 4 hr of Exposure at 800°C to Steam at a Partial Pressure of 355 mm Hg. (Original reduced 19%.)

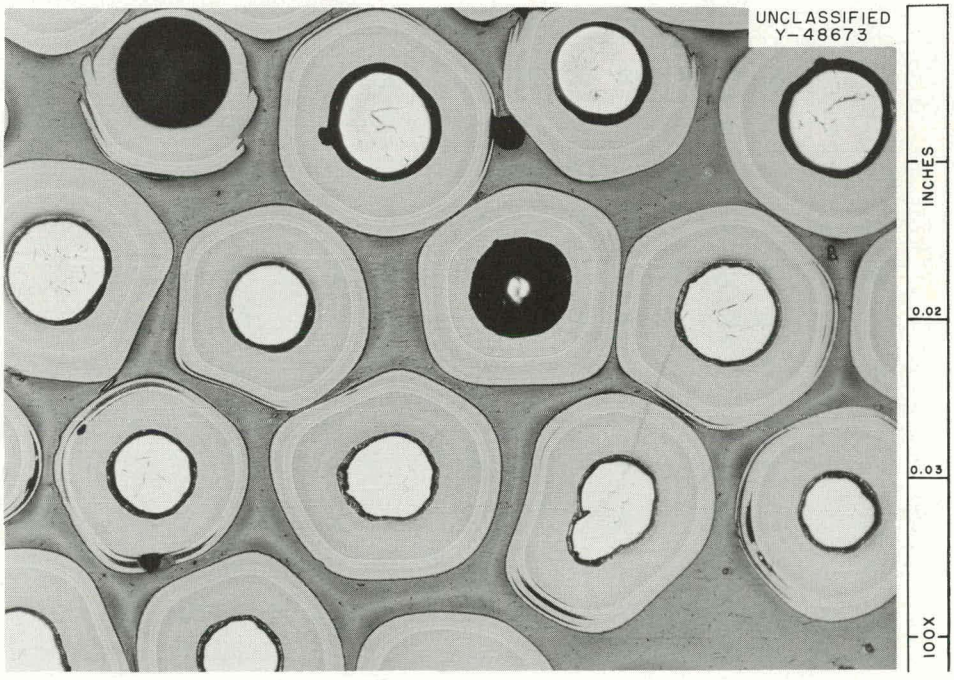

Fig. 6.24. Coated Particles of Run 19 After 2 hr of Exposure at 1000°C to Steam at a Partial Pressure of 355 mm Hg. (Original reduced 19%.)

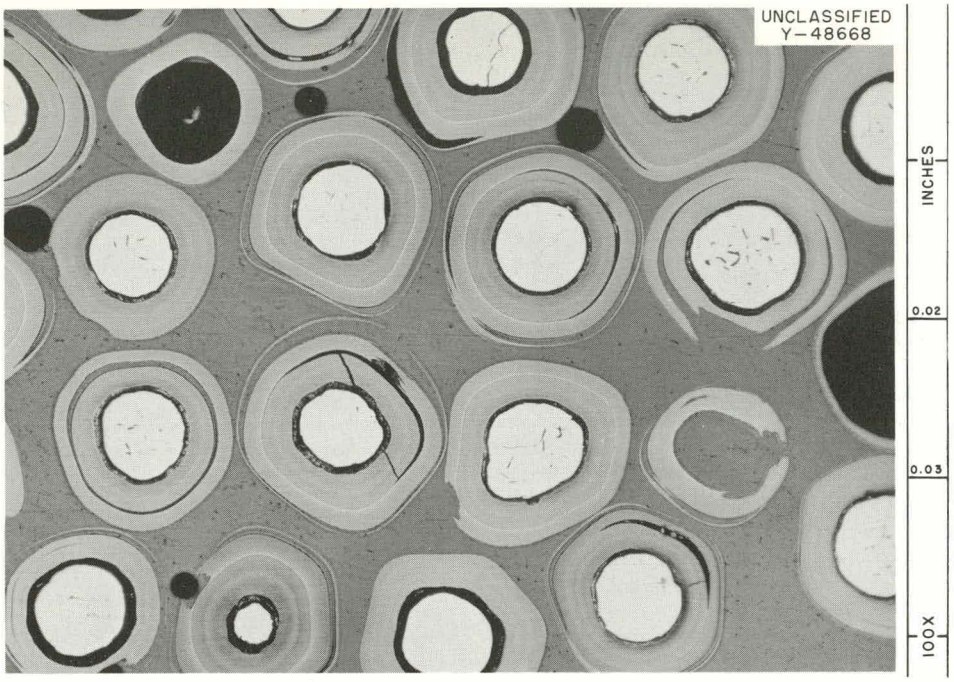

Fig. 6.25. Coated Particles of Run 1 After 4 hr of Exposure at 1000°C to Steam at a Partial Pressure of 355 mm Hg. (Original reduced 19%.)

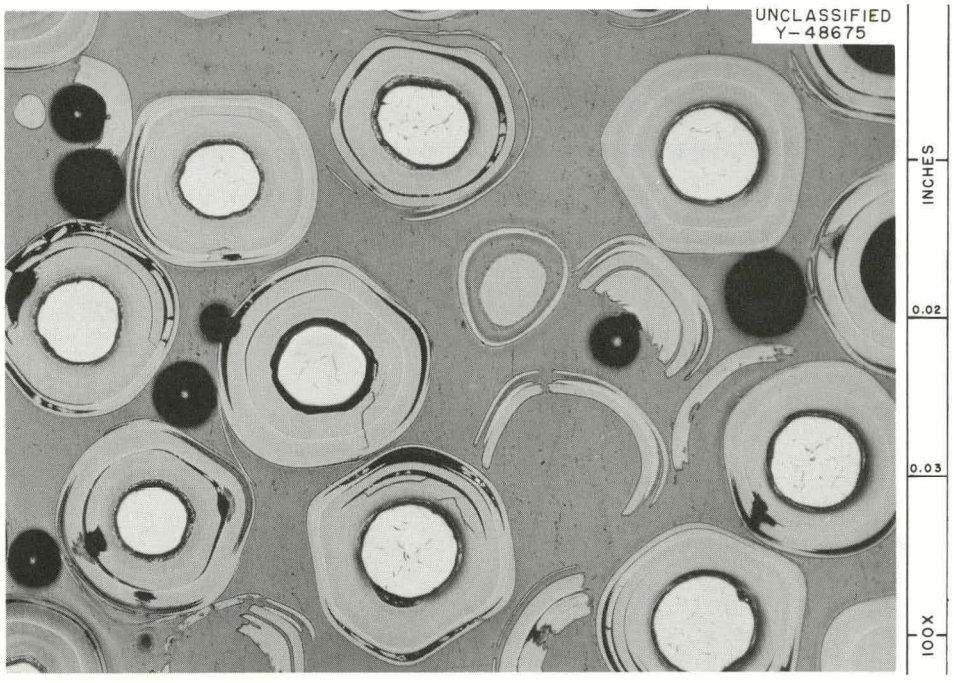

Fig. 6.26. Coated Particles of Run 25 After 1 hr of Exposure at 1100°C to Steam at a Partial Pressure of 635 mm Hg. (Original reduced 19%.)

Fig. 6.27. Coated Particles of Run 25 After 1 hr of Exposure at 1100°C to Steam at a Partial Pressure of 635 mm Hg Prior to HNO_3 Leaching.

shown in Fig. 6.27 were photographed after leaching with HNO_3. Some indications of pitting attack are shown in Fig. 6.23, but, in general, the most conspicuous effect is the separation of the layers of the coatings. The extensive attack that occurred at 1100°C, with peeling, cracking, and pitting very much in evidence, is shown in Fig. 6.26. The residues from the cores may be seen in Fig. 6.27, which is from the same sample as shown in Fig. 6.26 but was photographed prior to leaching with HNO_3.

The results obtained by exposing the various lots of coated particles to steam at elevated temperatures show marked differences in behavior that appear to be associated with different modes of attack by steam under these conditions. The cause of the differences noted among these lots of particles, all of which had laminar coatings, is unknown but must be associated with the conditions used during deposition of the coatings. Relatively small differences in the reaction rates of the coatings with steam

have been observed at comparable conditions of exposure. Much larger differences have been noted in the degree of protectiveness of the coatings after comparable exposure. There is no clear-cut relationship, however, between the amount of pyrolytic-carbon coating removed and the incidence of failure of the coating, as determined by leaching with HNO_3. Extensive failure of the coatings would be expected at 1100°C for short exposures to steam. The results are much more favorable at temperatures of 800°C and below. Experimental evaluation appears necessary before the compatibility of a particular lot of particles with steam at temperatures of 900 to 1000°C can be predicted with any degree of certainty.

Equipment has been assembled and tested for use in the study of the compatibility of various uncoated fuel bodies with steam at temperatures of 800 and 1200°C. Steam from an electrically heated boiler is passed upward through a 2-in. mullite tube containing the sample; the steam is condensed; and the reaction products in the gas stream are sampled and analyzed. A slow bleed of helium (15 cm^3/min) is employed to facilitate sampling of the gas.

Test runs were made at 900 and 1000°C using a 1.5-in. sphere (~50 g) of Speer moderator-2 graphite. Hydrogen generation rates of 4 and 27 cm^3/min were found for the sample at 900 and 1000°C, respectively. Steam flow rates varied from 600 to 1800 cm^3/min at a partial pressure of ~730 mm Hg. The effect of flow rate was small in this range. The study of uncoated fuel bodies in this equipment will be started soon.

Thorium Diffusion in Pyrolytic Carbon

R. B. Evans III J. Truitt

An accelerated investigation of the diffusion characteristics of thorium in carbon and in graphite is under way to provide information needed in the procurement of fuel elements for the German pebble-bed reactor (AVR). These fuel elements are to contain coated thorium-uranium carbide fuel particles in which the thorium-to-uranium ratio will be in the range 9 to 7 and the coatings will consist primarily of pyrolytic carbon with a columnar structure. Similar studies involving uranium carbide have been under way for some time,[11] and some information on pyrolytic-

carbon-coated uranium carbide is presently available;[12] however, companion information on pyrolytic-carbon-coated thorium carbide does not, apparently, exist. Although the diffusion of thorium from a constant-potential carbide source is probably of greater applied interest than the trace layer techniques described here, it was deemed advisable to start the present investigation with the latter. The major factor leading to this decision was a desire to acquire thorium diffusion information as rapidly as possible.

Description of the Carbon

The details of the techniques used in manufacturing the pyrolytic carbon being investigated are not available; however, the structure and properties of this material are comparable with those of carbons that have been prepared by the pyrolytic decomposition of methane at 20 mm Hg (total pressure) and 2000°C. The properties of the gross material are nearly the same as those of the grains that constitute its microstructure.[13] These grains are large and conical in shape and are usually described as columnar grains. The planar surface of the gross material corresponding to the planar surface of deposition is parallel to the crystallographic "a" direction of a large majority of the grains; the "c" direction is perpendicular to the deposition surface. The conical vertices of the grains are adjacent to this surface. The material is dense, with zero open porosity. In coatings, the uranium diffusion would proceed in the "c" direction, starting at the cone vertices.

Procedure for Experimental Studies of Diffusion

The pyrolytic graphite described above was utilized in the form of 0.375-in.-square coupons with a thickness of 0.150 in. The surfaces normal to the diffusion direction were ground flat to within ±2.5 μ. The

---

[11] W. O. Harms, "Coated Particle Fuel Development at Oak Ridge National Laboratory," USAEC Report ORNL-TM-431, Feb. 14, 1963.

[12] R. J. Borg, D. R. McKenzie, and J. R. Wolfe, "The Self-Diffusion of Uranium in Pyrographite," Canadian Report UCRL-6827T, March 15, 1962.

[13] P. L. Walker, Jr., American Scientist, 50(2): 259–358 (1962).

first step in preparing the coupons for experimentation was to heat them at 1770°C for 12 hr under helium to remove adsorbed gases. A very thin layer of thorium was placed on the ground surfaces by mounting the coupons on a rotating target device and bombarding the surfaces with Th^+ ions in an electromagnetic separator (24-in. radius). The results of thorium analyses performed on several coupons at various positions on the target indicated that the thorium was deposited uniformly over the target area. The average surface content of thorium on the pyrolytic carbon coupons after placement was 8.9 μg of thorium per square centimeter. The electromagnetic-separator run was timed to deliver 10 μg of thorium per square centimeter. It was also found that the depth of thorium penetration into the carbon matrix was approximately 5 μ; however, these low values could not be determined accurately by ordinary sectioning techniques.

After thorium placement, the coupons were subjected to diffusion annealing in an evacuated graphite resistance furnace and then activated in the ORNL graphite reactor. The activated coupons were individually cemented to a precision-ground metal cylinder which, in turn, was checked in a precision lapping device for the sectioning step. The most critical operation in regard to lapping was alignment of the plane of the coupon diffusion surface with the plane of lapping (as determined by the characteristics and dimensions of the lapping device). With great care, this operation could be performed so that the two planes were parallel within the original surface tolerances (±2.5 μ). After mounting, the total activity of the coupon was determined, and then sections of the coupon were removed. The activity remaining in the coupon was determined as each section was removed. The count rates were determined by measurement of the 0.31-Mev gamma emission of Pa^{233} (formed by thorium activation) using a scintillation detector in association with a single-channel differential analyzer.

Applicable Diffusion Equations

The diffusion geometry for an infinitely thin layer of thorium on the surface of dense nonporous carbon becomes that of an unreplenished plane source with the diffusion path extending into a semi-infinite matrix

in the direction normal to the plane surface. The solution to the diffusion equation for these boundary conditions is

$$C(x,t') = \frac{Q}{(\pi Dt')^{1/2}} \exp\left(-\frac{x^2}{4Dt'}\right), \tag{1}$$

where t' is the exposure time in seconds for a fixed time interval, x is the depth of penetration normal to the surface in centimeters, C is the concentration as a function of x and t', Q is the total amount of diffusing material placed initially at $x = 0$ in grams per square centimeter, and D is the diffusion coefficient in square centimeters per second.

The measured amount $M(x,t')$ in grams of thorium remaining after removal of Δx parallel to the activated surface can be defined as

$$\frac{M(x',t')}{A} = \int_{x'}^{\infty} C(x,t')\, dx , \tag{2}$$

where x' is a particular depth of sectioning and A is the area normal to diffusion. By substitution of Eq (1) into Eq. (2) and integrating, the fraction of thorium remaining becomes

$$F = \frac{M(x',t')}{AQ} = \frac{2}{(\pi)^{1/2}} \int_{u'}^{\infty} e^{-u^2}\, du = \operatorname{erfc} u , \tag{3}$$

where

$$u' = \frac{x'}{(4Dt')^{1/2}} . \tag{4}$$

Values for the complementary error function (erfc u) have been tabulated in the literature and can be used to calculate experimental values for D based on the distribution data. The relationship is simply

$$D = (x'/u')^2/(4t') ,$$

where the x's and u's correspond to the same F values.

Results

Data are available for four completed experiments involving diffusion annealing for 1, 17, 49, and 100 hr at approximately 1900°C. The first

test of the data correlations was performed by preparing cross plots of the experimentally determined distribution data so that a series of x' versus $(t')^{1/2}$ curves (each at a constant value of F) would be obtained. These curves are presented on Fig. 6.28. It should be noted that the curves do not pass through the origin and do not possess a constant slope. According to Eq. (3), however, these conditions should have been met if (1) an infinitely thin thorium layer were present on the surface at time zero and (2) all the experiments were conducted at the same temperature (the same D), since by Eq. (4) there can be only one value of u for a given F.

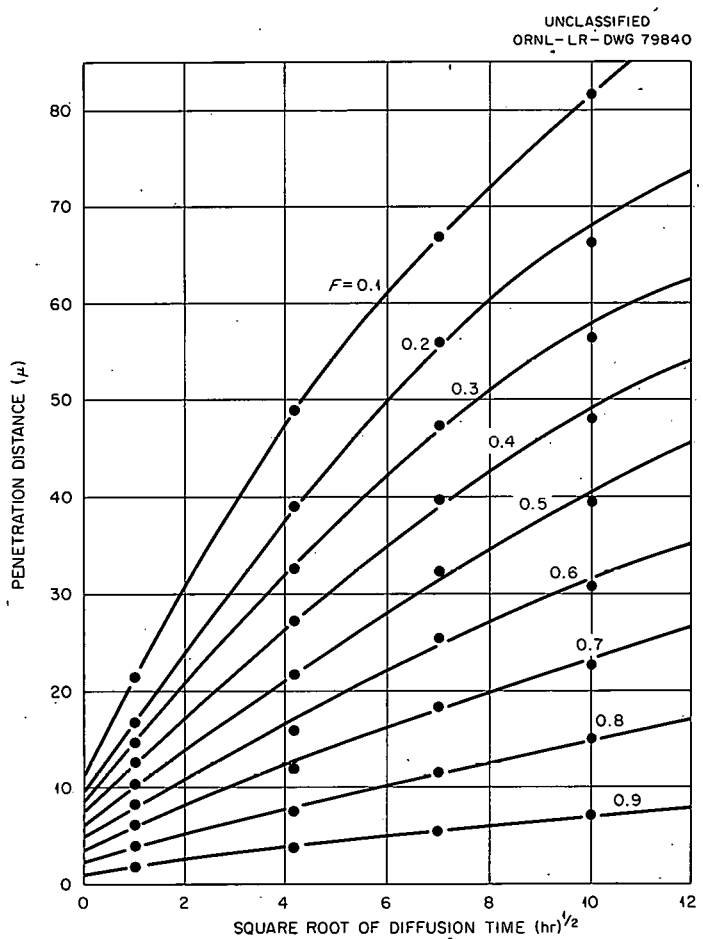

Fig. 6.28. Penetration Versus Time for Various Fractions, F, of Thorium Remaining in Pyrolytic Carbon After Diffusion Annealing at 1900°C.

It was not surprising to find a nonzero intercept for the curves on Fig. 6.28, since small penetrations were observed on unannealed coupons and a small amount of diffusion occurred during the heatup period. These effects were taken into account by assuming that an initial distribution, as described by Eq. (3), existed at time zero and that a "dummy" $(Dt)_0$, common to all the experiments, could be applied in the calculations. The $(Dt)_0$ value utilized was 7.5×10^{-7} cm^2. The computed D values employing the small $(Dt)_0$ correction were 6.6×10^{-11}, 5.6×10^{-11}, and 4.2×10^{-11} cm^2/sec at 17, 49, and 100 hr, respectively. It was clear that D still varied either with t' or x', even with the zero-time correction. Since the structure did not alter during the diffusion annealing period, t' was excluded as a possible cause of the variations in D. This led to the tentative conclusion that the variations in D were the result of variations in structure along x. It should be mentioned that the positive x direction for the diffusion observed in these experiments was in the "c" direction of the structure as measured from the initial to the final deposition planes.

As a final check of the data, a generalized plot of the 17-, 49-, and 100-hr results was prepared using an average D value of 5.47×10^{-11} cm^2/sec. This curve is presented on Fig. 6.29. The agreement between the experimental and theoretical u values is good, considering the complex structure of the pyrolytic carbon. Additional experiments to determine D values at different temperatures are under way.

Uranium Migration in Porous Graphite

C. M. Blood J. Truitt

Studies of the migration of uranium in porous graphite are of important practical significance to the design of the fueled-graphite systems presently being considered for a number of reactors. Fuel consisting of uranium carbide in a graphite matrix is to be employed in the Dragon Reactor Experiment in England,[14] the HTGR-Peachbottom reactor being built

[14] G. E. Lockett and R. A. U. Huddle, Nuclear Power, 5: 112 (1960).

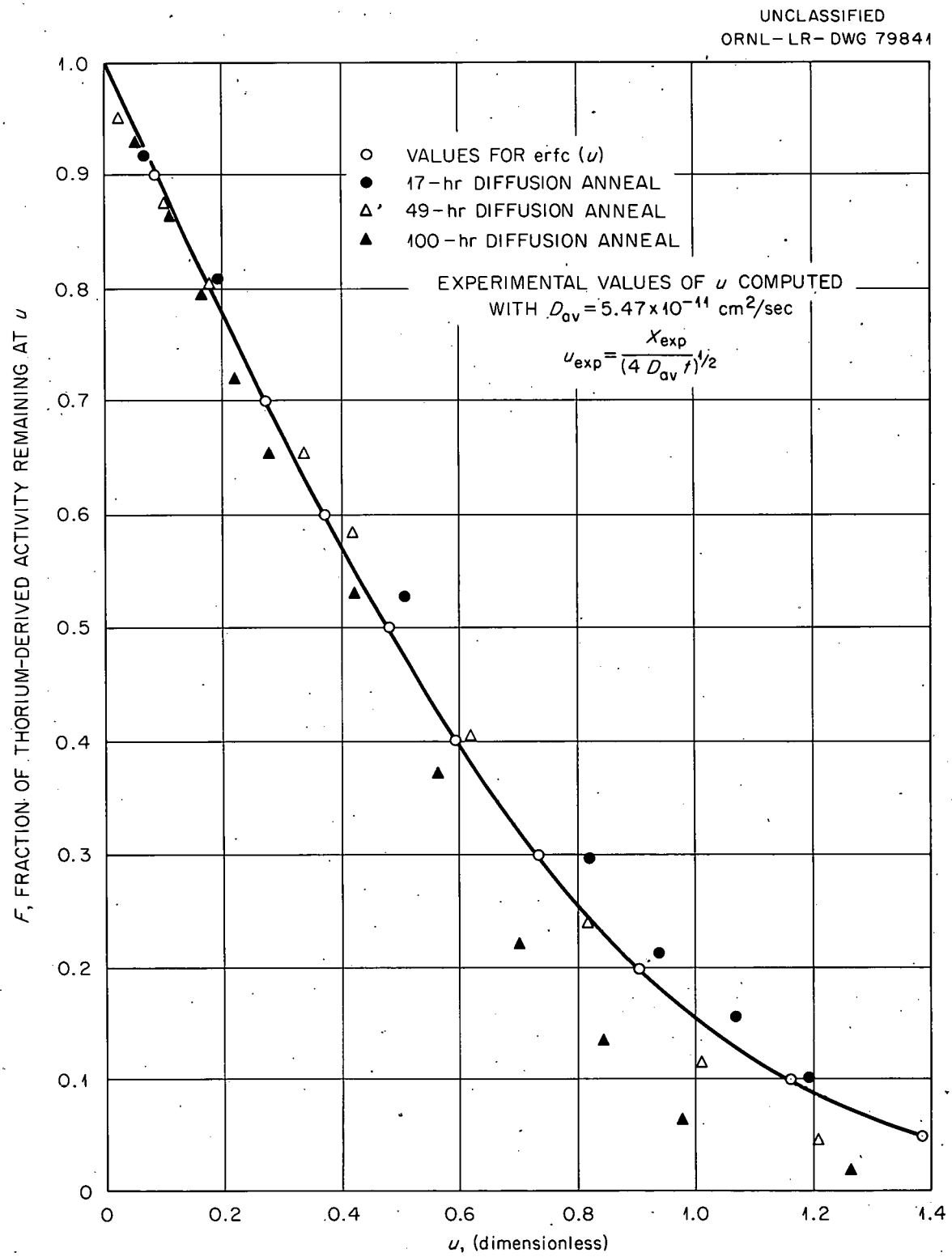

Fig. 6.29. Generalized Diffusion of Thorium into Pyrolytic Carbon at 1900°C.

by General Atomic near Philadelphia,[15] the UHTREX reactor at Los Alamos,[16] and the AVR pebble-bed reactor in Germany.[17] The fuel elements of each reactor consist of fueled-graphite bodies encased in an unfueled graphite sleeve (or shell) that is cooled by helium. Recently, use of the newly developed pyrolytic-carbon coated fuel particles in the fueled-graphite bodies has been under serious consideration. The use of such particles would be justified by the favorable fission-product-retention properties of the coating material (see previous sections of this chapter, especially Fig. 6.12). Although coatings may be designed with a suitable estimated lifetime, uranium migration through the permeable graphite matrix and the encasement sleeve could be a problem if an appreciable number of coatings prematurely ruptured. Therefore studies of the rates of migration of uranium from uranium carbide through porous graphite were initiated along with similar studies on pyrolytic carbon.

The experimental work was begun with the AGOT graphite and uranium carbide system. Suitable couples appeared to have been fabricated, as described previously,[18] by heating uranium-metal foil placed between two graphite coupons. Microscopic examination of the uranium carbide-graphite interface revealed that the U^{o}-UC liquids had penetrated the pores of graphite during the conversion of U^{o} to UC_2 and UC-UC_2. This system was soon abandoned because the concentration profiles were hidden by the porous penetration, which was 2 to 5 mils in depth.

The next experimental effort with porous graphite involved using graphite uniformly impregnated with uncoated UC_2 (25 wt %) as the source layer, furfural-impregnated graphite, and carbon cement. A diffusion couple "sandwich" was made by placing a source layer between two coupons of furfural-impregnated graphite; one coupon had the source layer cemented

---

[15]General Atomic, "Peachbottom Preliminary Hazards Summary Report," NP-9115, Part B, Vol. I and II, August 1961.

[16]Los Alamos Scientific Laboratory, "Ultra-High Temperature Reactor Experiment Hazards Report," USAEC Report LA-2689, April 1962.

[17]D. Machnig et al., Nuclear Power, 6: 63 (1961).

[18]C. M. Blood, Diffusion of Fuel and Nonvolatile Fission Products in Fueled Graphite, pp. 173–178, "GCRP Quar. Prog. Rep. Dec. 31, 1961," USAEC Report ORNL-3254, Oak Ridge National Laboratory.

to it, and the second was simply placed on top of the opposite side of the source layer without cement. The couple was securely held together and subjected to a diffusion anneal in an evacuated graphite resistance furnace. Portions of both coupons of the "sandwich" were sectioned by the wedge technique and also by slicing in planes parallel to the original interface. Sections obtained by the wedge technique, designated "A" samples, were designed to obtain steep concentration profiles near the interface; and sections obtained by slicing parallel to the interface, designated "B" samples, were designed to supply profiles for relatively rapid migration processes.

Penetration data were obtained from each of the two respective coupons of four couples that were prepared as described above and annealed at 1900°C. The uranium concentrations of the A samples taken from respective coupons did not show concentration gradients near the interfaces. The uranium contents of these samples in the isothermal region of a coupon were nearly the same. Therefore the average value of all the uranium analyses obtained from a given coupon were interpreted as representative of the over-all concentration of uranium in an unsectioned coupon. These data are reported in Table 6.12.

Table 6.12. Uranium Migration in a Porous Uranium Carbide-Impregnated Graphite System at an Average Temperature of 1900°C

Couple No.	Diffusion Annealing Period[a] (hr)	Uranium Concentration[b] of Porous Graphite Coupons (g/cm^3)	
		Cemented	Uncemented
		$\times 10^{-4}$	$\times 10^{-4}$
1	0.083	0.02	0.04
2	0.083	0.21	0.08
3	26.5	3.8	3.3
4	208.3	13.6	13.4

[a]Time required to reach 1900°C was approximately 1 hr in each experiment.

[b]Based on a graphite density of 1.782 g/cm^3 and the total uranium content of the A samples.

Analyses of A samples in the non-isothermal sections of a coupon, which were usually discarded, indicated less uranium migration at lower temperatures. The B samples taken from other portions of the coupons listed in Table 6.12 provided the approximate concentration profiles presented in Fig. 6.30.

A comparison of the data reported above for the A samples of two coupons comprising a couple show that the cement layer at the interface of the couple has no apparent effect on the rate and amount of mass transfer of uranium into porous graphite. This indicates that the cement layer does not make the porous graphite less penetrable, even though some of the pores may have become plugged.

The parabolic shape of the concentration profiles obtained from B samples, shown in Fig. 6.30, does not correlate with that predicted for uniform solid-state migration (Fick's law). Such predicted profiles show the largest concentration gradients near the interface, while those in Fig. 6.30 show the least for the porous graphite. It appears that the uranium penetration is much faster than what might be expected for solid-

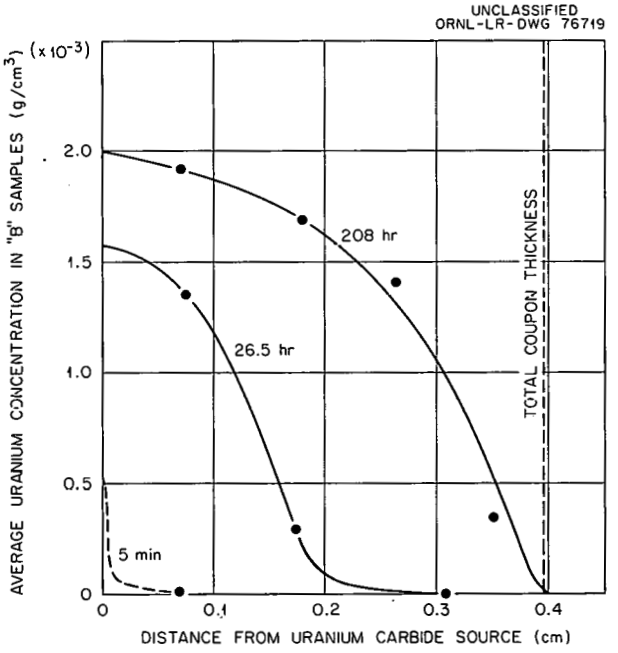

Fig. 6.30. Concentration Profiles Resulting from the Migration of Uranium into Porous Graphite at 1900°C. The points are based on averages of values for both cemented and uncemented coupons.

state migration described by semi-infinite and constant-potential boundary conditions. This premise is further supported by the profile obtained from the 208-hr exposure at 1900°C, which shows a slight accumulation of uranium at the back boundary. These experimental results suggest that there is an additional source of uranium within the couple beyond the interface and that the mechanism of mass transfer of uranium is complex. It is probably caused by pore and surface effects coupled with an adsorption-desorption phenomenon, in addition to solid-state migration. Although the experiments were conducted at a higher temperature than that for reactor operation, the same mechanism of mass transfer would be expected to exist at lower temperatures.

Further examination of the data in Fig. 6.30 raises the question of the value of the concentration, C_o. It is clear that the driving force or apparent saturation of uranium in a particular graphite at x = 0, defined as C_o, is a variable with temperature; but it is not entirely clear that it is a function of time also. The approximated concentration profiles in Fig. 6.30 were extrapolated to x = 0 and, therefore, specific conclusions concerning C_o should not be drawn without first obtaining concentration-penetration data in the region nearest the interface. Experiments designed to provide this information are under consideration.

Decontamination of Type 304 Stainless Steel from I^{131} and Te^{132} Deposited from Heated Helium

A. B. Meservey

Treatment with 0.4 to 0.5 M oxalic acid or oxalate salt solutions containing 0.1 M fluoride and various amounts of hydrogen peroxide was satisfactory for removing I^{131} and Te^{132} deposited at 800°C and below from helium onto type 304 stainless steel pipe. The pipe had been contaminated from heated, irradiated UC_2 and UO_2. Resistance to decontamination was highest in the high-temperature zone where some metal oxidation had occurred because of slight inleakage of air. Decontamination was much easier where the metal was unoxidized and the temperature had been lower.

In the oxidized zone contaminated at 800°C, where the comparatively low level of gamma activity was more than half due to Te^{132} and the

remainder was I^{131}, the decontamination factor was only about 2, mostly from I^{131} removal, after periods of up to several hours in hot alkali or hot noncorrosive oxalate-peroxide solutions. Oxide dissolution and decontamination to almost background level (DF = 5.1) were achieved in 1 hr in 0.4 M $H_2C_2O_4$–0.1 M NaF–0.015 M H_2O_2 at 95°C.

In the deposition zone that was at 330°C, where the gamma activity was higher than in the zone contaminated at 800°C by a factor of 10^4, the deposit was chiefly I^{131}, with some Te^{132}. There was also a pale brown oxide coating. The gamma decontamination factor after boiling for 20 min in 10% NaOH was 36, with the I^{131} being removed in preference to the Te^{132}. Both iodine and tellurium were soluble at 95°C in oxalate-peroxide solution at a pH of 4, the gamma decontamination factor being 39 in 20 min and 180 in 7 hr. In 1 hr at 95°C in the acidic fluoride solution containing 0.015 M H_2O_2, the decontamination factor was 1.7×10^3.

The region of pipe contaminated at 175°C, which had no discoloration and was about one-tenth as contaminated as the region treated at 330°C, was the easiest to decontaminate. Here boiling 10% NaOH removed nearly all the I^{131} in 1 hr (gamma DF = 73), leaving the Te^{132}. Both contaminants were soluble at 95°C in oxalate-peroxide solution at a pH of 4, with a gamma decontamination factor of 68 in 20 min and 318 in 7 hr.

A special study was made of the fluoride and peroxide effects in the section of pipe contaminated at 400°C, which showed a dark oxide and was contaminated with I^{131}, Te^{132}, and Te^{129}. A series of 0.5 M $H_2C_2O_4$–0.1 M

Table 6.13. Effects of Fluoride and Peroxide Additions to 0.5 M $H_2C_2O_4$ on Corrosion and Decontamination Factors of I^{131}- and Te^{132}-Contaminated Type 304 Stainless Steel in a 1-hr Treatment at 95°C

Peroxide Content (molar)	Decontamination Factor		Corrosion (mil/hr)	
	With 0.1 M F^-	Without F^-	With 0.1 M F^-	Without F^-
0	7	11	0.01	0.005
0.015	50	49	0.02	<0.001
0.1	85	28	0.005	<0.001
1	118	22	0.003	<0.001

NaF solutions containing 0 to 1 M H_2O_2 was compared in corrosivity and decontamination effectiveness with the same series of H_2O_2 solutions containing no fluoride (Table 6.13). On this type of deposit, fluoride and peroxide were both of significant benefit, and the fluoride solution containing enough H_2O_2 to decrease corrosion was even more effective than the low-peroxide solution of high corrosivity.

7. CLAD FUEL DEVELOPMENT

A. Goldman O. Sisman
D. B. Trauger

Irradiation Effects on Swaged and Tamp-Packed UO_2-ThO_2

D. F. Toner H. E. Robertson
J. G. Morgan E. L. Long, Jr.

Two type 304 stainless steel capsules (03-5 and 06-5) containing vibration-compacted ThO_2–2.9 wt % UO_2 prepared by the "Sol-Gel D" process were irradiated in the ORR poolside facility. The capsules and the irradiation conditions are described in Table 7.1. The postirradiation examinations consisted of dimensional measurements, leak testing, gamma scans, gas analyses, and burnup analyses. The metallographic examination is still in progress. Dimensional measurements showed that the cladding of capsule 03-5 became distorted during irradiation. The diameter decreased 0.008 in. at midplane and increased 0.005 in. at each end. In

Table 7.1. Description of Capsules 03-5 and 06-5 and Conditions of Irradiation in ORR Poolside Facility

Capsule length: 7 in.
Capsule outside diameter: 0.625 in.
Cladding wall thickness: 0.020 in.
Flux: 6×10^{13} neutrons/cm^2·sec
Expected burnup of heavy metal: 5000 Mwd/MT
Irradiation period: 215.2 full-power days at 30 Mw

	Capsule 03-5	Capsule 06-5
Cladding surface temperature, °F	1300	1000
Fuel central temperature, °F	3011	2726
Uranium burnup, Mwd/MT		
Based on Ce^{144}	181,200	95,930
Based on Cs^{137}	175,670	105,730
Thorium plus uranium burnup, Mwd/MT		
Based on Ce^{144}	5,320	2,810
Based on Cs^{137}	5,150	3,095

addition, the over-all length decreased 0.1 in. A similar length decrease was noted in capsule 06-5, but no significant diameter changes were observed. Scans of gross gamma activity indicated no distinct fuel shifting, but the activity level at the bottom end of capsule 06-5 was about 10% higher than at the top end. Samples were selected from the midplane of each element for radiochemical burnup analyses. As indicated in Table 7.1, capsule 03-5 achieved the desired burnup but capsule 06-5 did not. These analyses are being checked.

The NaK coolant from each experimental assembly was analyzed for Cs^{137} activity, and none was detected. Subsequently, each capsule was examined for cladding leaks or other failures by immersion in silicone oil under vacuum. No bubbles indicating leaks were observed.

Samples of gas were collected from each capsule prior to sectioning. The results of the gas analyses are presented in Table 7.2. The high N_2 + CO content in capsule 06-5 is thought to be the result of decomposition of uranium nitride. Only the Kr^{85} released from capsule 03-5 is reported because the pressure data taken during the sampling of capsule 06-5 were not accurate.

Loose, unsintered fuel was found in each capsule when sectioned. A longitudinal section of capsule 03-5 is shown in Fig. 7.1. The fuel had

Table 7.2. Analyses of Gas From Capsules 03-5 and 06-5

Gas Species	Content (vol %)	
	Capsule 03-5	Capsule 06-5
H_2	1.04	0.58
He	29.33	37.79
CH_4	0.71	0.27
H_2O	0.08	2.33
HC	0.18	0.04
N_2 + CO	0.38	14.78
O_2	0.02	
Kr	8.89	5.55
Xe	59.37	38.66
Kr^{85}[a]	0.3	

[a]Percentage of total generated.

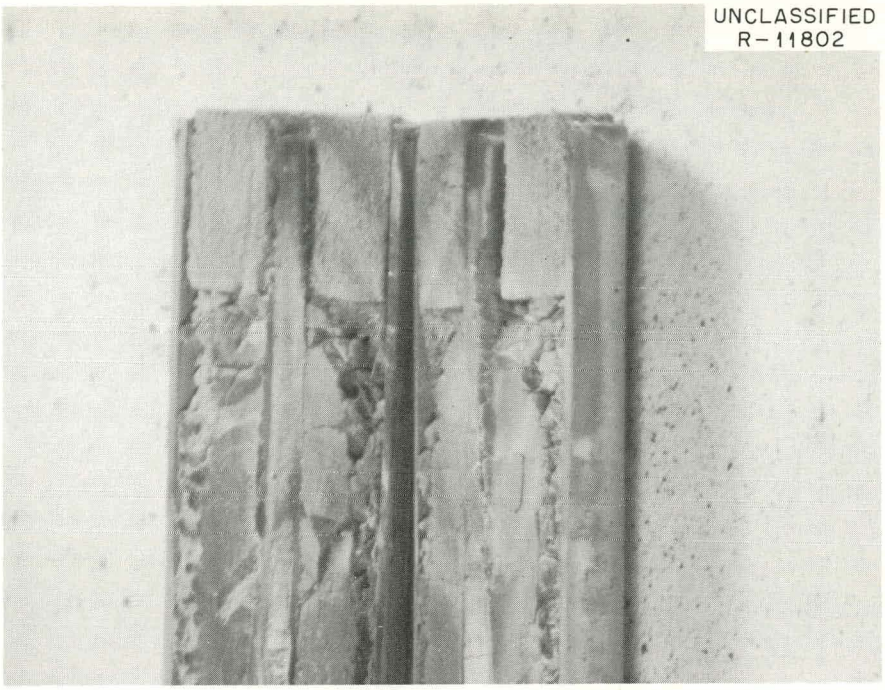

Fig. 7.1. Longitudinal Section of Capsule 03-5. Note sintered fuel in central portion and unsintered loose fuel near the cladding. Mating halves of the fuel element shown.

sintered in the central regions of both capsules, but less fuel densification was evident in capsule 06-5 (Figs. 7.2 and 7.3). Since capsule 06-5 had a measured central temperature of 2726°F compared with 3011°F for capsule 03-5, the fuel densification was expected to be greater in capsule 03-5.

High-Temperature Irradiation of UO_2 in LITR Miniature Capsules

R. R. Sellers F. R. McQuilkin

Operating data for the miniature fueled capsules irradiated in the LITR during this report period are given in Table 7.3. Two capsules, L-CP6 and L-HT2, previously inserted, achieved the desired burnup and were discharged. The irradiation of capsule L-HT3 was initiated and completed. Irradiation of capsule L-CP5X was continued, and irradiation of capsule L-HT4 was initiated.

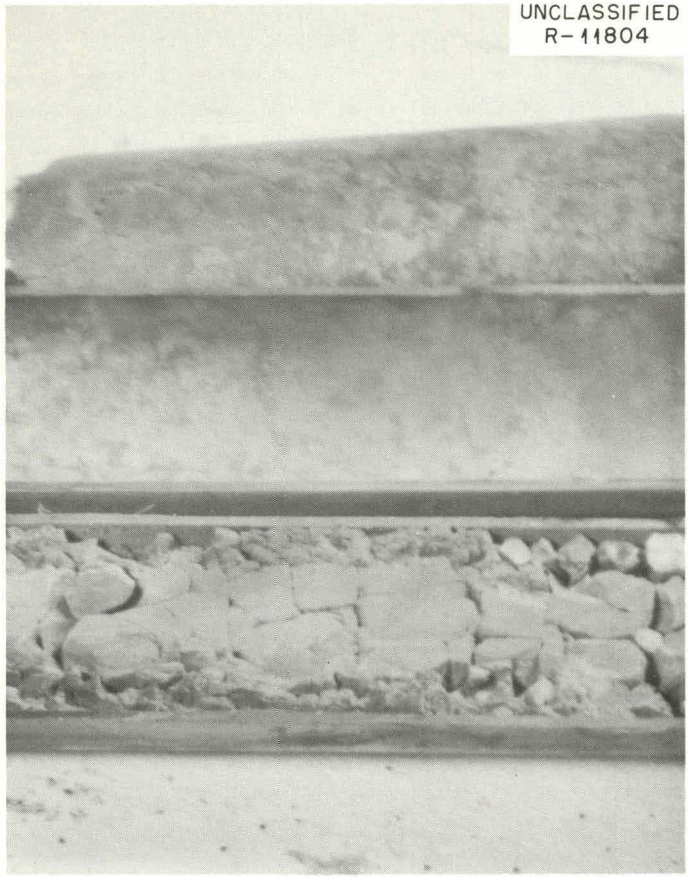

Fig. 7.2. Longitudinal Section Through Capsule 06-5. Note powdered fuel near cladding.

Fig. 7.3. Transverse Section of Capsule 06-5. Note sintered fuel surrounding central thermocouple.

Table 7.3. Irradiation Conditions of Miniature Capsules in LITR

Capsule Designation	Fuel Description		LITR Insertion Date	First Day Fuel Central Temperature (°F)		Removal Date	Burnup (at. % of heavy metal)
	Type	Batch No.		Section a	Section b		
L-CP5X	Pyrolytic-carbon-coated $(U + Th)C_2$	GA-1332-46E	6-19-62	1935	2115	In-pile	4.1
L-CP6	Pyrolytic-carbon-coated UC_2	NCC-AD	3-27-62	1840	2020	9-18-62	7.3
L-HT2	UO_2 cylinders	ORNL-1043	9-25-62	(a)	(a)	10-2-62	
L-HT3	UO_2 cylinders	ORNL-1043	1-7-63	(a)	(b)	1-8-63	
L-HT4	UO_2 cylinders	ORNL-1043	1-8-63	(a)	(b)	In-pile	

[a]Thermocouple calibration values for W-5% Re vs W-26% Re are uncertain above 4200°F; however, by using corrected millivolt values and extrapolating, temperatures in the range 4200 to 4500°F were indicated.

[b]Central temperature was not monitored in section b.

The L-CP capsules contain loose particles of UC_2 (capsule L-CP6) or $(U + Th)C_2$ (capsule L-CP5X) with pyrolytic carbon coatings. The design of these capsules was described previously.[1] Postirradiation examinations of these capsules will be discussed in the subsequent report under the heading "Investigations of Fueled-Graphite Systems."

Capsules L-HT2, -HT3, and -HT4 complete the series of four high-temperature UO_2 irradiations described previously.[2] Capsule L-HT1 was irradiated for five weeks; L-HT2, one week; L-HT3, 19 hr; and L-HT4 is scheduled to be irradiated for three months; all irradiations are conducted at a central temperature higher than 2000°C. In all but capsule L-HT1, the thermocouples for the measurement of the fuel central temperature are tantalum-sheathed, BeO-insulated, tungsten–5% rhenium vs tungsten–26% rhenium. The corrected millivolt output from these thermocouples during the first few hours of irradiation exceeded the maximum given in calibration tables, and therefore the reported initial temperatures were determined by extrapolation. For example, the initial central thermocouple readings on capsule L-HT2 were 37.6 mv (including correction for the emf generated at the thermocouple-to-lead wire splice), and calibration data are available only to 36 mv. An extrapolation of the calibration curve yielded an estimate of 4420°F. Shortly after the reactor reached full power, the temperature indication drifted down sharply. After 5 hr of operation, the a-specimen central thermocouple indicated 3895°F and the b-specimen central thermocouple indicated 3945°F; 19 hr later these temperatures were 3810 and 3865°F, respectively. The negative drift continued with decreasing slope throughout the period of irradiation. Immediately before reactor shutdown for removal of the capsule, the central thermocouples indicated 3510°F for the a-specimen and 3550°F for the b-specimen. In the case of capsule L-HT3, the initial a-specimen temperature was estimated to have been between 4200 and 4500°F.

---

[1]F. R. McQuilkin and W. E. Thomas, Miniature Capsule Fission-Gas-Release Experiments in LITR, p. 161, "GCRP Quar. Prog. Rep. Sept. 30, 1961," USAEC Report ORNL-3210, Oak Ridge National Laboratory.

[2]F. R. McQuilkin and R. R. Sellers, Miniature Capsule Irradiations in LITR, p. 238, "GCRP Semiann. Prog. Rep. Sept. 30, 1962," USAEC Report ORNL-3372, Oak Ridge National Laboratory.

After 3 hr of irradiation, the temperature indication had drifted to 4030°F, where it remained steady for the remainder of the 19-hr test. The central temperature indication for capsule L-HT4 has been much like that for capsule L-HT3, except that the drift has continued downward. On February 26, the indicated central temperature was 3280°F.

Ratchetting of Metal-Clad Fuel Elements During Thermal Cycling

W. R. Martin

It has been reported[3,4] that thermal cycling of metal-clad fuel elements can result in plastic deformation of the thin-walled cladding. The common cause of elongation of the elements during thermal cycling is contact between cladding and fuel. This condition can be achieved in the metal-clad fuel elements by collapse of the cladding about the fuel because of external pressure, radial expansion of the fuel in excess of the diametral expansion of the cladding, or a combination of the two. The results and interpretation of data from an evaluation program that emphasized fuel and cladding interactions and utilized the internal heater device as a test apparatus in out-of-pile tests are the following:

1. Fuel and cladding interactions can result in cladding strains that exceed the fracture strain of the material under irradiation and therefore can be the limiting factor in the metallurgical lifetime of metal-clad fuel elements.

2. Axial plastic strains resulting from cladding and fuel interactions increase as the cladding thickness is reduced.

3. Experiments with 0.015- and 0.020-in.-thick tubing show that increasing the pressure differential across the cladding wall increases the axial deformation rate for a given cladding thickness and material. This can be interpreted as meaning that the relative movement of cladding and

---

[3]W. R. Martin and J. R. Weir, "Dimensional Behavior of the Experimental Gas-Cooled Reactor Fuel Element at Elevated Temperatures," USAEC Report ORNL-3103, Oak Ridge National Laboratory, July 1961.

[4]M. F. Lyons, F. A. Comprelli, V. E. Hazel, and H. E. Townsend, "Plastic Strain in Thin Fuel Element Cladding Due to UO_2 Thermal Expansion," USAEC Report GEAP-3739, General Electric Company, July 1961.

fuel decreases as the coolant pressure is increased because of increased frictional forces between cladding and fuel. This results in a larger total strain in the cladding.

4. Axial loads caused by thermal expansion of the fuel exceeding the thermal expansion of the cladding cannot exceed the frictional force between cladding and fuel.

5. For a given load on the cladding, the plastic strain per cycle can decrease as the elastic moduli, cross-sectional area, elastic limit strain, and creep strength of the cladding are increased.

6. Increasing the thermal expansion of fuel with respect to the cladding increases the magnitude of the total strain that can be introduced in the cladding.

7. The loads causing cladding deformation can be repetitive with each cycle because of the difference in magnitude of the frictional forces during the heating and cooling portions of the thermal cycle.

8. Decreasing the magnitude of the frictional forces between cladding and fuel increases the relative movement and thereby reduces the magnitude of the total strain introduced in the cladding. Experiments utilizing graphite and calcium fluoride as fuel element lubricants were successful in reducing the plastic strain rate of 0.005- and 0.010-in.-thick tubing during thermal cycling. Although graphite is of no practical value because of the carburizing reaction with stainless steel, no apparent reaction was found between calcium fluoride and stainless steel, as shown in Fig. 7.4.

9. Circumferential ratchetting of thin-walled cans was observed for 0.005- and 0.010-in.-thick smooth-walled tubes, 0.710 in. ID. The result of the ratchetting was the formation of an axial wrinkle that increased until the bending strains in tension were equal to the fracture strain of the cladding.

These results define the factors related to the mechanism of axial growth of fuel elements during thermal cycling and are in reasonable agreement with experimental thermal-cycling data obtained from different types of test apparatus.[3-6] The extension of the cladding by the fuel when the frictional forces are sufficient to prevent relative movement results in plastic strain by two mechanisms. If the total strain introduced

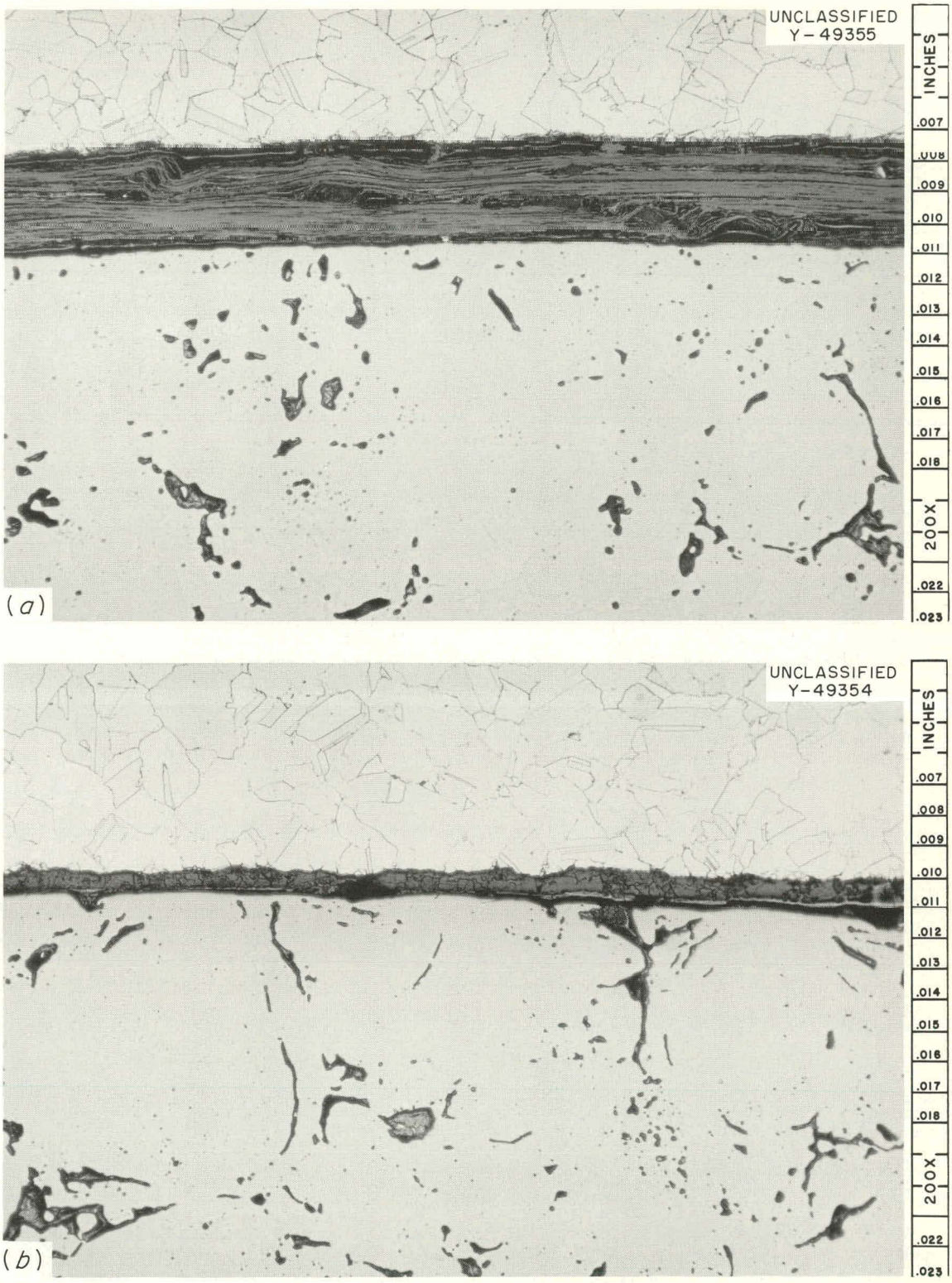

Fig. 7.4. Cross Sections of 0.010-in.-Thick Stainless Steel Cladding and Fuel with CaF_2 in the Gap Between Cladding and Fuel. Note the difference in structure of the CaF (a) in the middle of the element, and (b) at the end of the element. Etchant: aqua regia.

into the cladding is less than the elastic limit strain of the cladding material, the cladding will plastically deform only at elevated temperatures by the mechanism of stress relaxation. When the total strain exceeds the elastic limit strain of the cladding, that magnitude of strain greater than the elastic strain is of course permanent and can be observed regardless of cladding temperature. For the latter case at elevated temperatures, plastic strain is obtained by both mechanisms, that is, short-time tensile strains and stress relaxation.

It is recommended that, whenever possible, rates of temperature change in reactors containing metal-clad fuel elements be reduced to a low value to minimize the difference in expansion of fuel and cladding. A feasible maximum heating rate for the EGCR, for example, would be 150°F/min.

Mechanical properties of the cladding materials could be increased to reduce the magnitude of the plastic strains. The increased strength alone would not prevent plastic strains in fuel element cladding at all reactor conditions and hence the ductility of the cladding in the presence of radiation should be increased.

The problem of circumferential ratchetting could be the limiting factor in the use of thin-walled cladding. This problem should be investigated relative to lubrication techniques and smooth walls versus ribbed walls. The static coefficient of friction between fuel and cladding at elevated temperatures as a function of contact pressure should be evaluated. The problems of end-plenum gaps in fuel elements, thermal expansion of UO_2, and axial deformation of cladding during thermal cycling are related, with the common factor being frictional forces between cladding and fuel. Perhaps the differences[7,8] of opinion regarding the relative

---

[5]R. E. Hodson and R. D. Stacey, "Out-of-Pile Studies of the Ratchetting of Stainless Steel Clad UO_2 Fuel Elements," United Kingdom Atomic Energy Authority Report DEG-296s, January 1961.

[6]R. E. Hodson and R. D. Stacey, "Out-of-Pile Evaluation of Windscale AGR Mk-2 Fuel Elements and Fuel Element Assemblies," United Kingdom Atomic Energy Authority Report TRG-269, March 1962.

[7]C. N. Spalaris, "Uranium Dioxide Cladding Interactions: Axial Expansion of UO_2 Column in Fuel Elements," Trans. Am. Nucl. Soc., 5(1): pp. 228–229 (June 1962).

movement between cladding and fuel can be resolved by carefully determining the static coefficient of friction between cladding and fuel for a given fuel element condition, particularly since the in-pile thermal expansion of UO_2 pellets has been measured.[9]

Experimental Tube-Burst Tests

J. T. Venard

The investigation of the stress-rupture properties of the British 20% Cr–25% Ni stainless steel tubing was continued. This material is stabilized with approximately 0.6% Nb. The out-of-pile control tests were completed, except for a few long-time tests that are now in progress, and the test results are presented in Fig. 7.5. The maximum strains at fracture ranged from 4 to 16% at 650°C, 8 to 21% at 750°C, and 9 to 24% at 850°C. The strain values obtained in flowing CO_2 with 5% CO are comparable with those obtained in argon with 1% O_2. Virtually no end-closure failures were experienced.

Two irradiation experiments on this same material were performed in an ORR poolside facility and the results are compared in Fig. 7.6 with the out-of-pile data. The data indicate a slight loss of strength at 650°C and little or no effect at 750°C; however, the average strains at fracture were lower by 30 to 50% in the in-pile tests than in the out-of-pile tests. It is also important to note that several of the in-pile specimens failed at or near the welds. This may have been a result of poor welds, but in view of the strain data, it is possibly an indication of some irradiation-induced embrittlement at the weld.

At least two more irradiation experiments will be performed to obtain data for times greater than 1000 hr and at 850°C. Metallographic examinations of both control and in-pile samples are in progress and will perhaps provide information on the weld failures.

---

[8]M. J. F. Notley, "The Relative Axial Expansions Under Irradiation of Stacks of UO_2 Pellets in Zircaloy Sheaths," Canadian Report CRFD-1092, August 1962.

[9]W. E. Baily, "Relative Thermal Expansion of UO_2 Fuel Inpile," Report CVNA-152, Carolina Virginia Nuclear Power Associates, Inc., June 1962.

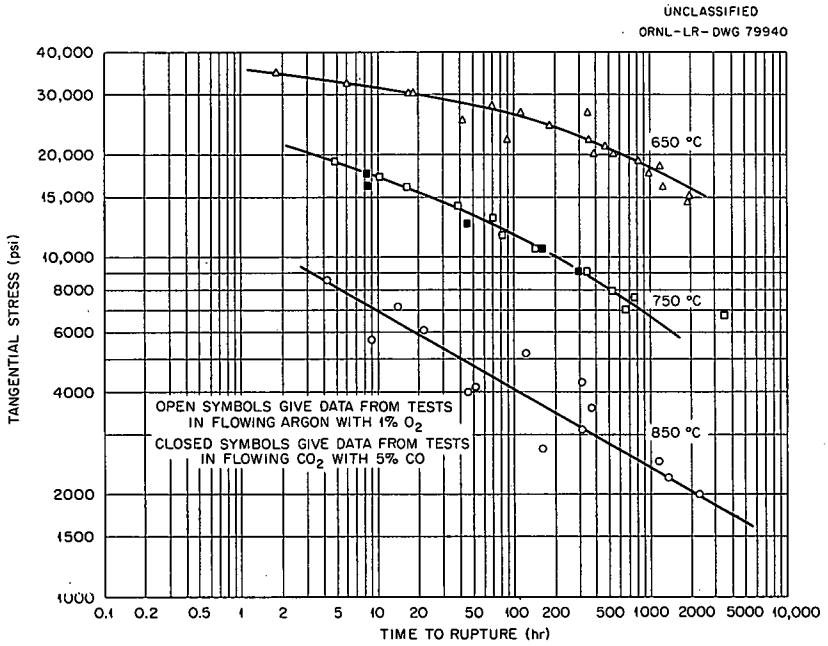

Fig. 7.5. Results of Tube-Burst Test on British 20% Cr, 25% Ni, Niobium-Stabilized, Cast Stainless Steel Tubing, Lot L-16. As-received and welded. Pressurized with argon.

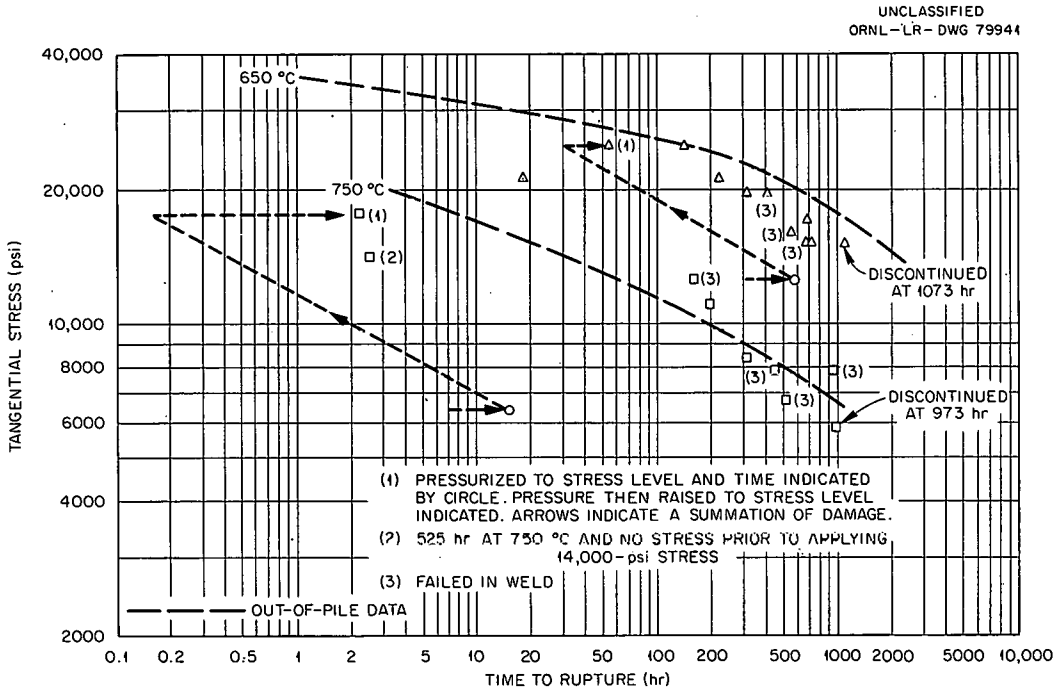

Fig. 7.6. Comparison of Results of In-Pile and Out-of-Pile Tube-Burst Tests of British Stainless Steel Containing 20% Cr and 25% Ni. As-received and welded. Tested in-pile in helium with 1% O_2.

Tensile Properties of Stainless Steel After Irradiation

W. R. Martin

Numerous stainless steel specimens are being irradiated at temperatures in the range 150 to 815°C at fast-neutron (>1 Mev) doses of the order of 5×10^{13} neutrons/cm^2·sec. After irradiation to total doses of 10^{19} to 10^{21} neutrons/cm^2, the specimens will be tensile tested under various conditions. The results will be compared with those for control specimens heat treated to obtain thermal histories equivalent to those of the irradiated specimens.

Brazing of Beryllium

R. G. Gilliland

The wetting behavior of liquid silver, gold, germanium, aluminum, copper, and the alloys Pd–2.1 wt % Be, Zr–5 wt % Be, and Ti–6 wt % Be on the surface of solid beryllium was studied. In general, the wetting of these metals was investigated at 50 and 100°C above their melting points in argon and in vacuum with the use of sessile-drop techniques.

Measurements of the contact angles indicated that the wetting of beryllium by liquid aluminum, germanium, silver, Pd–2.1 wt % Be alloy, and Ti–6 wt % Be alloy was greater in an argon atmosphere rather than in vacuum. The wetting of beryllium by liquid gold, copper, and Zr–5 wt % Be alloy was either unaffected by the test atmosphere or better in vacuum than in an argon atmosphere. The wetting of beryllium by the liquid metals tested was in agreement with basic wettability theory in that wetting was promoted by increasing the temperature.

An extensive metallographic examination of the samples revealed that only aluminum, Zr–5 wt % Be alloy, and Ti–6 wt % Be alloy produced little or no alloying with the beryllium. Alloying of beryllium with the other liquid metals included in the investigation was so extreme that in some cases liquid-phase penetration of greater than 50% of the thickness of the beryllium pad was found.

Surface tension properties of the materials found to produce little or no beryllium reaction were calculated. The data revealed that the

liquid-vapor and solid-liquid surface tensions were greater for the nonwetting aluminum than for the wetting liquid alloys Ti–6 wt % Be and Zr–5 wt % Be. The alloy Ti–6 wt % Be was found to have the lowest calculated liquid-vapor and solid-liquid surface tensions, and Zr–5 wt % Be alloy and aluminum were next in order.

Calculations were also made of the work of adhesion and of the coefficient of spreading for aluminum, Zr–5 wt % Be alloy, and Ti–6 wt % Be alloy. The data qualitatively indicated that these parameters were greatest for the highly wetting Ti–6 wt % Be alloy.

Diffusion of Carbon in Dissimilar-Metal Welds

G. M. Slaughter

The diffusion of carbon in ferritic steel-to-austenitic stainless steel joints at elevated temperatures is being studied at Virginia Polytechnic Institute. A preliminary microstructural analysis of the bond zone was described previously,[10] with major emphasis on the decarburized area of the ferritic material. It now appears that in a joint consisting of a ferritic material and an austenitic material, the carburized zone of the austenitic material may be a better indication of carbon migration. This is particularly true in ferritic steels containing strong carbide-forming elements where no definite decarburized zone has been found. The diffusion couples were made from type 304 stainless steel and ferritic steel containing 2 1/4 wt % Cr, 1 wt % Mo, and 1/2 wt % Ti.

Experiments have indicated that the addition of a carbide-forming element to the ferritic material has little or no effect on the over-all diffusion of carbon from ferrite to austenite. The diffusion coefficient remains constant, as indicated in Table 7.4, and a plot of the square of the width of the carburized zone vs time gives a straight line, Fig. 7.7.

---

[10] G. M. Slaughter, Diffusion of Carbon in Dissimilar-Metal Welds, pp. 46–48, "GCRP Quar. Prog. Rep. Dec. 31, 1961," USAEC Report ORNL-3254, Oak Ridge National Laboratory.

Table 7.4. Extent of Carbon Migration from 2 1/4 wt % Cr–1 wt % Mo–1/2 wt % Ti Ferritic Steel to AISI Type 304 Stainless Steel at 1300°F

Contact Time (hr)	Width of the Carburized Zone (mm)	Diffusion Coefficient (cm^2/sec)
		$\times 10^{-11}$
500	0.015	1.531
1,000	0.150	1.563
15,000	0.185	1.584
2,000	0.210	1.531

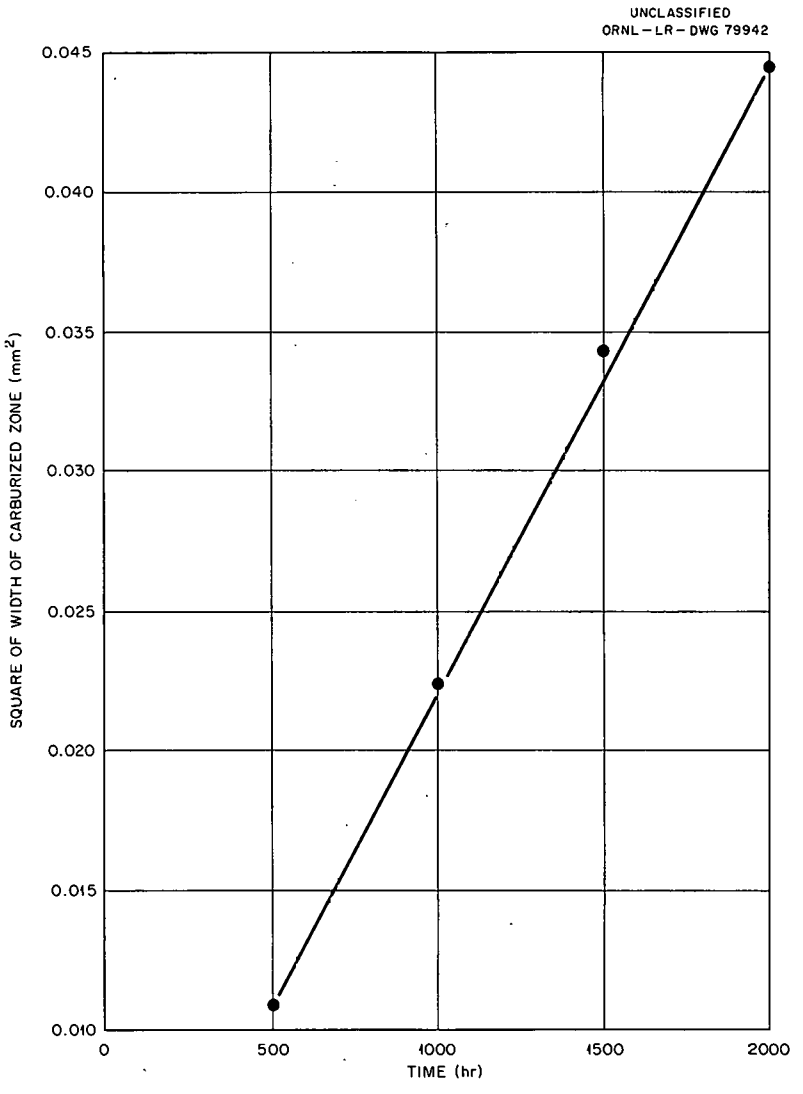

Fig. 7.7. Effect of Time at 1300°F on Growth of Carburized Zone on AISI Type 304 Stainless Steel Side of Composite Diffusion Joint.

Thermal Conductivity of UO_2

T. G. Godfrey D. L. McElroy

The fourth heating cycle on 93.4%-dense UO_2 in the radial heat flow apparatus was terminated by a failure of the specimen core heater at 1400°C.[11] In order to avoid further difficulties the cooling capacity of the containment shell was increased, and the cylindrical muffle length was doubled. The muffle now consists of three bifilar-wound heaters (5, 10, and 5 in., respectively), each independently controlled. Kovar seals were added to allow independent power control, and new, simple, thermocouple seals were installed to facilitate future use of other types of thermocouples.

The diameter of the two end guard heaters was decreased to allow them to be positioned within the lengthened muffle at the junctions of the new extensions, and seven new thermocouples were added, two for the end guard heaters and five for the lengthened muffle and monitoring. The core heater was doubled in length, wound on a very true 99+% Al_2O_3 grooved tube, and extended well outside the specimen stack. The specimen system remains essentially unchanged; however, the new end guard heater placement will permit testing of a smaller diameter, shorter specimen stack, which should aid in future specimen fabrication. All these changes were made to provide for easier and faster assembly, a greater degree of control, extension of the operating regime, and better realization of the boundary conditions assumed to exist in the radial heat flow experiment.

An evaluation of the data generated in runs 1 through 4 has indicated the existence of a heat-transfer mechanism operating above 1200°K that is more powerful than internal radiation transmission. The same mechanism is indicated by the data of Howard and Gulvin[12] for their UO_2 specimen No. 2. The evidence for this mechanism is obtained by a plot of

---

[11] T. G. Godfrey and D. L. McElroy, Thermal Conductivity of UO_2, p. 294, "GCRP Semiann. Prog. Rep. Sept. 30, 1962," USAEC Report ORNL-3372, Oak Ridge National Laboratory.

[12] V. C. Howard and T. F. Gulvin, "Thermal Conductivity Determinations on Uranium Dioxide by Radical Flow Method," UKAEA IG-Report 51 (RD/C), 1961.

the thermal resistance (1/k) vs temperature. This plot is linear for runs 1 through 4 to about ±1% from 500 to 1200°K; however, above 1200°K a real negative deviation, or turndown, of the plot occurs. The linear portion of the curve is the expected behavior of an electrically insulating or semiconducting solid for which the heat transport is predominantly by phonons. The turndown means that some other heat-transport mechanism is becoming operative. A line was placed through the few points obtained above 1200°K during run 4 and the difference in the thermal conductivity, Δk, was calculated between values of k obtained from this curve and values of k obtained from the extrapolation of the straight portion of the data. This Δk evidently represents the effects of the summation of the extra heat-transport mechanism. A plot of the log of Δk vs $1/T$ yielded a straight line with a slope of -6.1×10^3°K, indicating an apparent activation energy of 1.2 ev. The Howard and Gulvin[12] data treated similarly also yielded a straight line with a slope of -4.9×10^3°K, indicating an activation energy of about 1.0 ev. If internal radiation were the exclusive cause of the Δk, simple theory would predict that Δk would be proportional to T^3. If this were the case, a plot of log Δk vs $1/T$ would yield a curve with a slope at any temperature equal to -1.3 T, which is equivalent to an activation energy of approximately 0.35 ev in the temperature range of the turndown of the plot. Therefore, a mechanism more powerful than predicted by simple radiation transmission may be operative, since the observed activation energies are so large. Similar behavior was observed by Taylor[13] for beryllium oxide at much higher temperatures.

The UO_2, k, k_{ex}, and Δk values used in this analysis are listed in Table 7.5. The values were obtained from 1/k curves drawn through the fourth-run data and similar curves drawn through the data of Howard and Gulvin[12] for their specimen No. 2. The k_{ex} values were obtained from the extrapolation of the linear portion of the 1/k plots.

It should be pointed out that the numbers were taken from curves through the actual data points. There were not sufficient data on UO_2 in the turndown region to give anything but a hint of high-temperature heat-

---

[13]R. F. Taylor, "Thermal Conductivity and Expansion of Beryllia at High Temperatures," J. Am. Ceram. Soc., 45: 74 (1962).

Table 7.5. Thermal Conductivity Calculations Based on Data for UO_2

T (°K)	1/T (°K^{-1})	Data from Fourth Run (w/cm·°K)			Data from Howard and Gulvin (w/cm·°K)		
		k	k_{ex}	Δk	k	k_{ex}	Δk
	× 10^{-3}						
1173	0.853	0.0310	0.0310	0.0	0.0312	0.0310	0.0002
1273	0.786	0.0291	0.0289	0.0002	0.0296	0.0291	0.0005
1373	0.728	0.0275	0.0270	0.0005	0.0284	0.0274	0.0010
1473	0.679	0.0263	0.0253	0.0010	0.0277	0.0259	0.0018
1573	0.636	0.0256	0.0239	0.0017	0.0272	0.0245	0.0027

Table 7.6. Thermal Conductivity Values Obtained for 93.4% Dense UO_2 in Run No. 5

Temperature (°C)	Thermal Conductivity (w/cm·°C)	
	Measured	Corrected to Theoretical Density
109	0.06497	0.06956
110	0.06508	0.06965
201	0.05813	0.06222
200	0.05763	0.06172
296.5	0.05147	0.05512
298.5	0.05120	0.05481
400	0.04600	0.04925
400	0.04568	0.04891
501	0.04090	0.04380
501	0.04110	0.04400
601.5	0.03726	0.03990
601.5	0.03750	0.04015
700	0.03441	0.03685
700	0.03443	0.03686
798	0.03195	0.03420
798	0.03190	0.03416
900	0.02977	0.03187
998	0.02775	0.02971
1050	0.02697	0.02888
1099	0.02628	0.02814
1099	0.02624	0.02810

transport mechanisms. Run 5 is presently in progress with the goal of accruing data above 1200°K, as well as sufficient data below 1200°K, to adequately determine the slope of the linear portion of the 1/k curve.

Results obtained to 1100°C, presented in Table 7.6, reflect the previously noted linear relation between thermal resistance and temperature. A slight modification of the operating conditions was made between the tests at 800°C and those at 900°C, and this caused the thermal-resistance values between 900 and 1100°C to be about 1% below the values predicted by the results below 900°C. It is believed that the changed operating procedure caused a new heat flow pattern within the specimen, with the resulting change of 1% in the measured thermal conductivity values between 900 and 1100°C. This effect is being studied, and efforts to extend run 5 to 1500°C are in progress.

8. INVESTIGATIONS OF MODERATOR MATERIALS

A. Goldman B. L. Greenstreet
G. M. Watson H. W. Savage

Mechanical Properties of Graphite

C. R. Kennedy

Tests for evaluating graphite as a structural material were continued.[1] The program consists of a large number of mechanical and physical property tests of various grades and extrusion sizes of graphite to obtain data for statistical comparisons. Tensile and compressive tests have been conducted on a 6 × 6-in. extrusion of TSX graphite, a 4 3/8 × 4 3/8-in. extrusion of AGOT graphite, a 2 1/4 × 2 1/4-in. extrusion of GCB-MSR graphite, and an AGOT graphite block representative of the EGCR moderator blocks. Data from these tests are presented in Tables 8.1 and 8.2. Comparison of the results for the EGCR material with those for the smaller size AGOT extrusion indicates greater scatter in the results for the EGCR material. The spread indicates that the data taken previously[1] from only one section of an 18 × 18-in. EGCR block did not represent the strength of a typical section of a moderator column. In fact, it appears that there is no typical section, inasmuch as the strength varies greatly in the axial direction, as well as across the sections.

The data for the 4 3/8 × 4 3/8-in. AGOT material did not exhibit the scatter shown for the larger blocks. The data scatter was small both for axial and cross-section samples, and the fracture stress and strain average values were much higher than those for the larger EGCR blocks.

The TSX material was very anisotropic. The average axial strength was higher than that of AGOT; however, the average transverse strength was much lower. The internal defects in this block were found to be aligned in a direction normal to the weakest transverse direction. It is interesting to compare the compression test results with the tensile

---

[1] C. R. Kennedy, Mechanical Properties of Graphite, pp. 287–290, "GCRP Semiann. Prog. Rep. Sept. 30, 1962," USAEC Report ORNL-3372, Oak Ridge National Laboratory.

Table 8.1. Tensile Tests of Moderator Graphite

Sample	Direction of Sampling[a]	Number of Specimens	Average Fracture Stress (psi)	Coefficient of Variation of Fracture Stress (%)	Average Fracture Strain (%)	Average Modulus of Elasticity (psi)
						$\times 10^6$
AGOT graphite blocks from EGCR material						
Bar 266	Parallel	35	1610	24.7	0.16	1.29
Bar 246	Parallel	35	1481	19.5	0.18	1.08
Bar 272	Parallel	35	1696	16.4	0.18	1.08
AGOT graphite extrusion (4 3/8 × 4 3/8 in.)	Parallel	24	2179	11.2	0.24	1.54
	Perpendicular No. 1[b]	12	1750		0.32	0.68
	Perpendicular No. 2[b]	12	1427		0.27	0.69
TSX graphite extrusion (6 × 6 in.)	Parallel	25	2940		0.17	2.35
	Perpendicular No. 1	5	1337		0.28	1.03
	Perpendicular No. 2	4	370		0.07	0.70
GCB-MSR graphite extrusion (2 1/4 × 2 1/4 in.)	Parallel	10[c]	4910–6210		0.2–0.26	2.75–3.35
	Parallel	8[d]	1510–4270		0.04–0.20	

[a] With respect to extrusion axis.

[b] Perpendicular No. 1 and Perpendicular No. 2 taken at right angles.

[c] Apparently not affected by axial cracks.

[d] Apparently affected by axial cracks.

Table 8.2. Compression Tests on Moderator Graphite

Sample	Direction of Sampling[a]	Number of Specimens	Average Fracture Stress (psi)	Average Fracture Strain (%)	Average Modulus of Elasticity (psi)
					$\times 10^6$
TSX graphite extrusion (6 × 6 in.)	Perpendicular No. 1	4	4760	3.24	0.34
	Perpendicular No. 2	3	5297	5.33	0.18
AGOT graphite extrusion (4 3/8 × 4 3/8 in.)	Parallel	6	6095	2.24	0.58

[a]With respect to extrusion axis.

test results in that the maximum strength directions are reversed. These results add considerable significance to a maximum principal strain criterion for fracture. The maximum tensile strain direction in compression is rotated 90 deg to that in tension; thus, in compression, parallel cracks have a significant effect in reducing strength and fracture strain.

The MSR-GCB graphite specimens were taken from a bar which had severe axial cracks. Eight of 18 specimens had a pronounced stair-step fracture surface with axial crack lengths greater than 1/4 in. The fracture appeared to be a two-stage process where the axial crack caused one side of the specimen to fracture and transfer the load to the opposite side. The nonaxial loading was sustained in some cases by the remaining side. When a further load was applied, however, complete fracture occurred. The fracture in these cases was always detected by two audible snapping sounds. This two-stage process implies a certain resistance to crack propagation in graphite. The ten specimens that did not appear to be affected by axial cracks, that is, did not exhibit the stair-step fracture surface, yielded high strength values, although the fracture strains were similar to those of other grades of graphite.

In-Pile Creep of Graphite

C. R. Kennedy

The effect of irradiation-induced creep on the ability of graphite moderator blocks to sustain the strains expected in a gas-cooled reactor of the EGCR type is being investigated in in-pile creep experiments. The experiments consist of loading contilever parabolic beams of AGOT graphite by bellows, as shown in Fig. 8.1. The parabolic beam specimen, cut parallel to the extrusion axis, has a 6-in. free length and is 1/2 in. square at the base. The experimental facility can take nine specimens per experiment. Seven linear-film graphite resistors and two variable-permeance transducers are provided to indicate deflection of the graphite beam.

In the first experiment, the two variable-permeance transducers lost all sensitivity within the first 50 hr, and readings could not be accepted

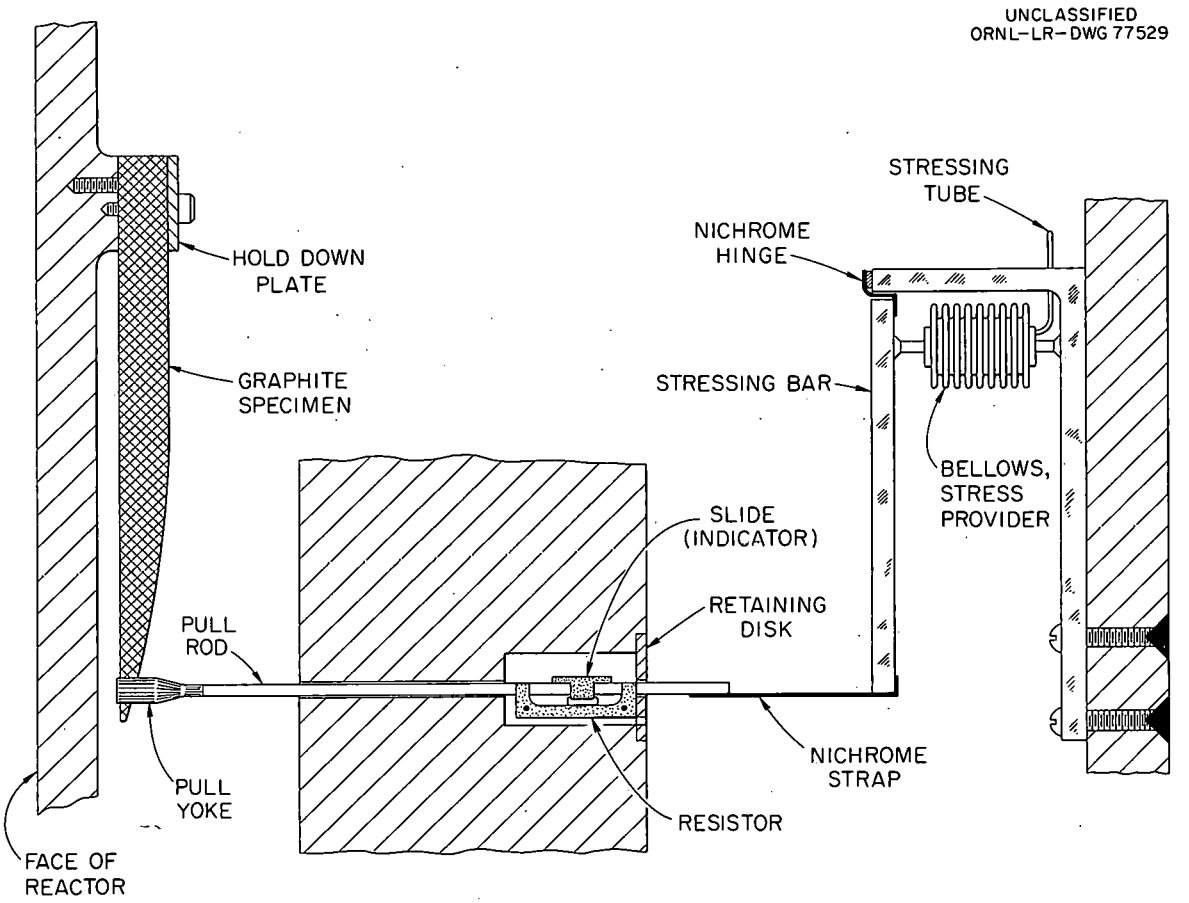

Fig. 8.1. Extensometer Arrangement in ORR Poolside Facility for Studying the In-Pile Creep of Graphite.

as valid. The seven resistance transducers responded satisfactorily, with the loss of only one after 150 hr. The sliding contact on the linear film resistor gives a deflection sensitivity of 10^{-4} in., which yields a sensitivity in strain measurement of 1×10^{-6} in./in. The specimens are heated only by gamma activity, and their resulting temperature is 450 ± 50°F. Each specimen has a temperature gradient of about 75°F, with the higher temperature at the tip of the beam.

The experimental facility occupies a poolside position in the ORR where the flux (>0.2 Mev) is estimated to be 1×10^{17} neutrons/cm^2·hr. This is roughly equivalent to 1 Mwd/At per hour. Flux monitors are now being processed to determine the actual flux spectrum.

The results obtained during an initial ORR-cycle exposure are shown in Fig. 8.2. The characteristic curves are similar to those obtained in

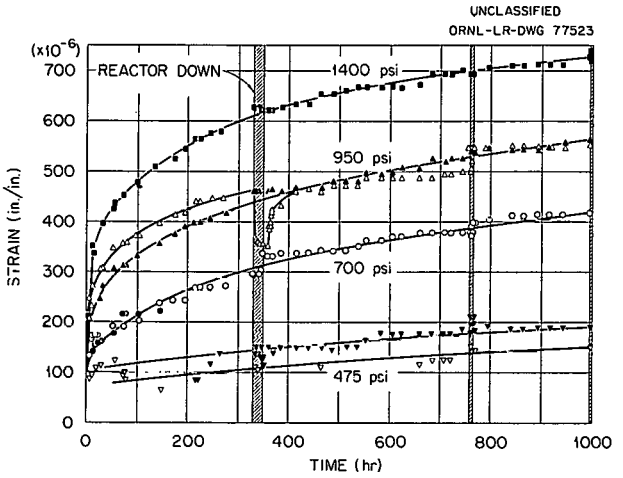

Fig. 8.2. Creep of AGOT Graphite Under Irradiation, ORR Experiment 104.

out-of-pile tests, as shown in Fig. 8.3, except for the greater creep rates. The out-of-pile creep rates demonstrate Newtonian viscosity, as shown in Fig. 8.4. As may be seen from Fig. 8.2, the in-pile creep rates decelerate with time, but it is questionable whether a linear rate was established by the end of the cycle. Tangential creep rates, shown in Fig. 8.5, demonstrate a linear stress function similar to that found out of pile. A linear stress function is also shown in Fig. 8.6, where the zero-intercept, a measure of the primary creep, is plotted versus stress for both in-pile and out-of-pile test data. The linear stress function

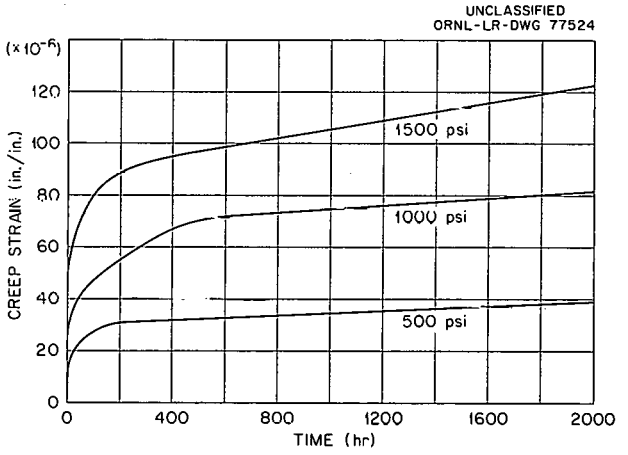

Fig. 8.3. Creep of Unirradiated AGOT Graphite in Bending Under a 1/3 Point Loading.

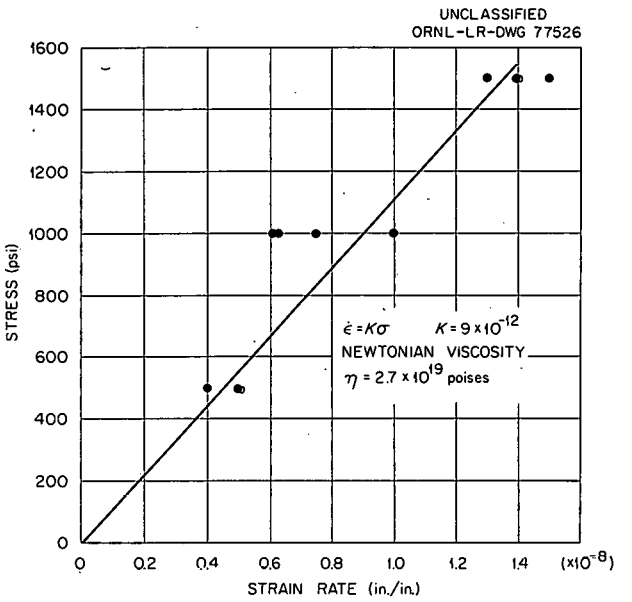

Fig. 8.4. Stress vs Strain for Unirradiated AGOT Graphite.

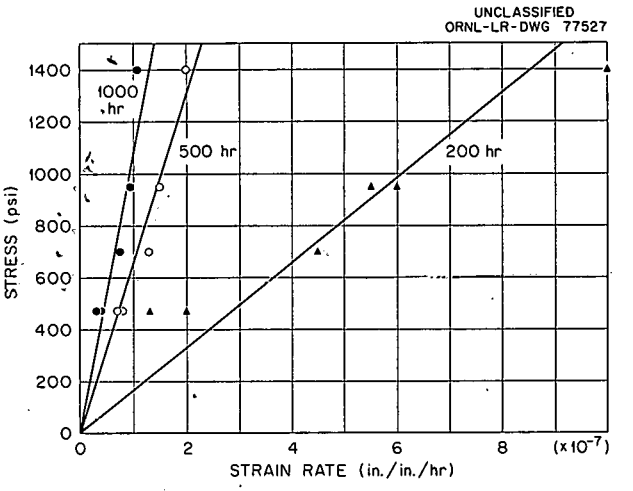

Fig. 8.5. Tangential Creep Rates of AGOT Graphite Under Irradiation, ORR Experiment 104.

indicates that the stress distribution in the beam under bending loads will not vary with time or strain.

The data obtained thus far indicate that the creep of graphite under irradiation and in the absence of irradiation is a linear function of stress. The prime objective of demonstrating the ability of graphite to

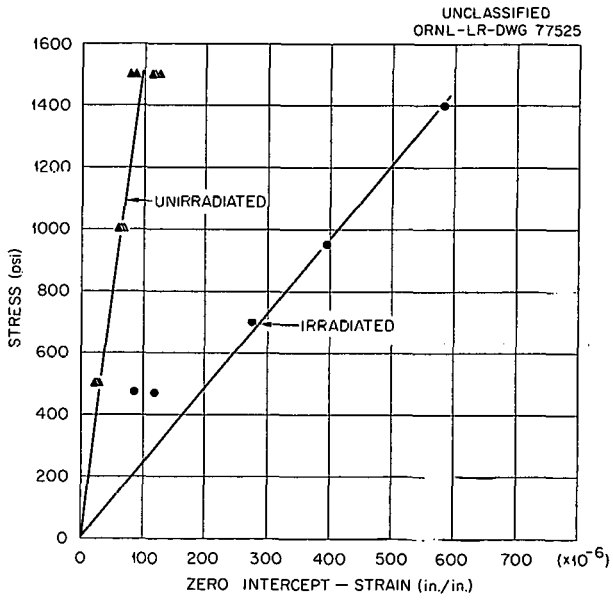

Fig. 8.6. Comparison of Creep of Irradiated and Unirradiated AGOT Graphite.

sustain large strains under irradiation cannot, however, be attained with the original test parameters unless the experiment is permitted to run for ten years. Therefore, as soon as it is established that a linear rate will or will not be attained, the stress levels will be increased until significant strain is absorbed in the specimens.

Graphite-Metal Compatibility Studies

B. Fleischer

The compatibility of type 304 stainless steel and AGOT graphite in intimate contact is being investigated in vacuum in the temperature range 1000 to 1300°F. As reported previously,[2] extensive bonding and carburization of stainless steel disks against graphite was observed at 1200 and 1300°F. More recent tests showed that carburization can occur at temperatures as low as 1000°F; however, there is no bonding, and the degree of

[2]B. Fleischer, Graphite-Metal Compatibility Studies, pp. 53–56, "GCRP Quar. Prog. Rep. March 31, 1962," USAEC Report ORNL-3302, Oak Ridge National Laboratory.

carburization is relatively minor after 1000 hr. Data presented in Table 8.3 show the interdependence of contact pressure and the extent of carburization at 1100°F.

Table 8.3. Effect of Contact Pressure on the Carburization of Type 304 Stainless Steel in Contact with Graphite at 1100°F for 1000 hr in Vacuum

Apparent Contact Pressure (psi)	Carbon Content[a] (%)					
	Test F	Test H-1	Test H-2	Test H-3	Test H-4	Test H-5
300		0.026	0.044	0.037	0.022	0.039
600		0.064	0.085	0.068	0.029	0.042
1200	0.083	0.108	0.103	0.108	0.025	0.120
2400	0.182					
5100	0.327					

[a]As-received material contained 0.025% C; all data are total carbon in specimen; since there were carbon gradients within each specimen, the data are essentially qualitative.

It is assumed that increasing the contact pressure serves to bring more graphite and metal into intimate contact at the interface and thus increases the effective concentration of the reactants, and an effort was made recently to verify this assumption. A test was conducted to determine whether the contact pressure caused permanent deformation of the graphite at the interface and whether the degree of permanent deformation was directly related to the contact pressure. Also, it was thought that the greater the deformation, the greater would be the effective contact area. Thus, the initial load applied across the interface should determine the effective area and the extent of carburization. It should then be possible to employ a high load for a short period followed by a lower load for the duration of the test, and the resultant degree of carburization should be the same as that found when using the high load for the entire test period. The test was performed at 1100°F. An initial contact load of 720 lb was applied across the interface at temperature for 1 hr and subsequently reduced to 180 lb for the remainder of the test period (1000 hr). The test results, reported in Table 8.4, do not confirm the

Table 8.4. Effect of Initial Contact Pressure on Carburization of Type 304 Stainless Steel in Contact with Graphite at 1100°F for 1000 hr in Vacuum

Initial Contact Pressure (psi)	Subsequent Contact Pressure (psi)	Carbon Content[a] (%)
4800	1200	0.073
2400	600	0.059
1200	300	0.040

[a]Average value of total carbon in five specimens.

assumptions when compared with the data of Table 8.3. An analysis is being made to determine whether the test conditions and results are sufficient to rule out the proposed analysis.

Graphite Reactions in Helium Containing CO_2

L. G. Overholser J. P. Blakely

Rates were reported previously[3] for the reaction of CO_2 with Speer Moderator-2 graphite in the temperature range 875 to 1025°C at CO_2 concentrations of 550 and 1100 ppm by volume in helium. An activation energy of approximately 55 kcal/mole and an apparent order of the reaction of less than one with respect to partial pressure of CO_2 were indicated.

Reaction rates at 975°C and additional CO_2 concentrations were subsequently determined in the range 100 to 1800 ppm by volume using the same graphite specimen. Prior to attempting to measure the reaction rates at CO_2 concentrations below 500 ppm, a concerted effort was made to improve the stability of the output of the Burrell K-7 gas chromatograph and reduce the weight losses arising from inleakage and contamination of

[3]L. G. Overholser, J. P. Blakely, and N. V. Smith, Gas-Graphite Reactions, pp. 279–281, "GCRP Semiann. Prog. Rep. Sept. 30, 1962," USAEC Report ORNL-3372, Oak Ridge National Laboratory.

the helium. Replacement of the filament in the detector had no apparent effect on either the sensitivity or stability of the gas chromatograph. A temperature regulator was installed in the takeoff block heating circuit, and a sensitive flow regulator was installed to control the flow of gas more closely through the columns. A stabilized potential was applied to the grid to establish whether the potential supplied by the battery pack was responsible for the unstable output. Some improvement in the operating characteristics of the instrument resulted from these changes, but the instrument is still not completely satisfactory. Rather large changes in the sensitivity frequently occur from day to day or even during a single day and require too frequent calibration of the instrument against the gas standards. It appears that the instability is inherent in the design of the detector and will continue to exist until another type of detector becomes available. The blank arising from contaminants in the helium stream was reduced to a permissible value by reconstructing the gas-handling system.

Following these modifications, reaction rates were measured at 975°C using CO_2 concentrations of 100, 300, 550, 1100, and 1800 ppm in helium at a total pressure of one atmosphere and a flow rate of approximately 125 cm^3/min. The data are not sufficiently precise to establish the apparent order of the reaction with respect to partial pressure of CO_2. The apparent order shown by the results is less than unity, and there is evidence that it changes with concentration of CO_2 in the range studied. Surprisingly large values for the reaction rate were measured at 100 ppm CO_2. The data are being withheld until additional measurements are made at CO_2 concentrations below 550 ppm. Similar measurements will be made in the near future using uncoated fuel bodies in place of moderator-grade graphite.

Transport of Gases Through Graphite

A. P. Malinauskas

Contaminant migration in the gaseous phase in gas-cooled reactors is possible because of the simultaneous existence of gradients in the temperature, pressure, and concentration of the gas across the graphite

septum. The specification of conditions conducive to suppression of this undesirable transport thus requires that the transfer mechanisms associated with these driving forces be reasonably well understood.

For transport caused solely by the presence of a concentration gradient, a model that describes the graphite barrier as a localized agglomeration of uniformly distributed, giant gas molecules (dust) has already been shown to be amenable to experiment.[4,5] Although a theoretical extension of this model to include pressure gradients has been reported[6] and compared with experimental results,[7] as previously remarked,[8] only an empirical relation is possible because of the failure of the model to accommodate other than a diffusive mechanism. No important advances have been made with respect to a removal of this defect, although it appears feasible to consider an additivity relation between the viscous and diffusive effects. The main difficulty arises from the complex manner in which the viscosity is dependent upon composition. A similar complexity caused by a composition dependence has limited a more recent extension of the model to include thermal gradients to the case involving only a pure gas (thermal transpiration).[9] In this instance, the additivity relation, whose application is reasonably straightforward, was assumed and appears to be valid. A significant result of this work has been the development

---

[4]R. B. Evans III, G. M. Watson, and E. A. Mason, "Gaseous Diffusion in Porous Media at Uniform Pressure," J. Chem. Phys., 35: 2076 (1961).

[5]R. B. Evans III, G. M. Watson, and J. Truitt, "Interdiffusion of Gases in a Low Permeability Graphite at Uniform Pressure," J. Appl. Phys., 33: 2682 (1962).

[6]R. B. Evans III, G. M. Watson, and E. A. Mason, "Gaseous Diffusion in Porous Media. II. Effect of Pressure Gradients," J. Chem. Phys., 36: 1894 (1962).

[7]R. B. Evans III, G. M. Watson, and J. Truitt, "Interdiffusion of Gases in a Low-Permeability Graphite. II. Influence of Pressure Gradients," J. Appl. Phys. (to be published, 1963).

[8]R. B. Evans III, A. P. Malinauskas, and J. Truitt, Gaseous Transport in Graphite, pp. 281-287, "GCRP Semiann. Prog. Rep. Sept. 30, 1962," USAEC Report ORNL-3372, Oak Ridge National Laboratory.

[9]E. A. Mason, R. B. Evans III, and G. M. Watson, "Gaseous Diffusion in Porous Media. III. Thermal Transpiration," J. Chem. Phys. (to be published, 1963).

of a relation between the thermal transpiration maximum and the contribution to the heat conductivity of the gas because of translational degrees of freedom. Exploratory experimental investigations intended primarily to determine the optimum conditions under which the phenomenon might be studied have been completed. A refined thermal transpiration apparatus, based upon the knowledge gained from an operation of the prototype, is presently under construction.

Another facet involving gas transport through graphite that has been investigated concerns stratified media.[10] In this regard it has been demonstrated that the presence of strata of differing permeability along the length of the flow path does not invalidate the flow relations obtained for the over-all medium when the medium is considered to be uniform in the same sense that each of the strata are considered uniform. Thus, for example, the permeability, K, of the medium was found to obey the linear relationship

$$K = \frac{B_o}{\eta} \bar{p} + \frac{4}{3} \bar{v} K_o \,, \tag{1}$$

where $\bar{p}$ is the arithmetic mean of the pressures on the entrance and exit sides of the barrier, η is the viscosity of the gas, $\bar{v}$ is the average thermal velocity of the gas molecules, and B_o and K_o are constants characteristic of the septum. Furthermore, the validity of the approximate formulas

$$\frac{1}{B_o} = \sum_i \frac{1}{\alpha_i B_{o,i}} \tag{2}$$

and

$$\frac{1}{K_o} = \sum_i \frac{1}{\alpha_i K_{o,i}} \tag{3}$$

were established under conditions where the over-all pressure difference was small and where

---

[10] A. P. Malinauskas, R. B. Evans III, and J. Truitt, "Gas Transport Through Stratified Porous Media," unpublished internal communication.

$$\alpha_i = (A/L)_i/(A/L) \tag{4}$$

represented the fractional area-to-length ratio of the ith stratum.

Similarly, no deviations as a result of septum inhomogeneity were observed when the equation

$$\frac{J_1 - J\delta_1\, x_1(L)}{J_1 - J\delta_1\, x_1(0)} = \exp\left(\frac{JL}{nD'_{12}}\right), \tag{5}$$

which is strictly applicable only to isotropic media, was employed to describe the uniform pressure binary-gas diffusion results obtained with a stratified barrier. In addition, an argument utilizing only the requirement that matter be conserved yields the relation

$$\frac{1}{nD'_{12}} = \sum_i \frac{1}{\alpha_i (nD'_{12})_i}, \tag{6}$$

if each of the i septa are sufficiently similar for the δ_i to be considered identical.

The symbols introduced in Eq. (5) have the following significance:

$J = J_1 = J_2$ = net flux of molecules through the septum,

nD'_{12} = the pressure-independent product of the molecular density and the effective binary mutual diffusion coefficient,

$x_1(z)$ = mole fraction of component 1 at the point z along the length of the septum,

L = length of the septum in the direction of transport,

$\frac{1}{\delta_1} = 1 + \frac{D'_{12}}{\frac{4}{3}\bar{v}_1 K_o}$, is a measure of the relative contribution to flow due to intermolecular interactions.

Geometry Studies of Irradiation-Induced Changes in Graphite

F. J. Witt

One of the important objectives in designing graphite structures for use in nuclear reactors is to provide elements for which the stresses and

distortion associated with irradiation-induced dimensional changes are minimized without sacrificing the ability to meet other requirements. This objective can be realized only through a careful analysis of all potentially acceptable geometries for a given core. A generalized study applicable to all reactors cannot be made because of differences in fast-neutron damage distributions; however, the results for specific cases provide a guide for evaluating the geometry effects for other applications. Therefore studies based on a plane-strain, anisotropic, elastic model are being made, with the damage distributions taken as being independent of the axial coordinate. The stresses are being calculated using an IBM 7090 computer program, the nonhomogeneous biharmonic code (NBC),[11] which was developed for analyzing the EGCR graphite.

The basic geometries considered for graphite elements in gas-cooled reactors are cylinders with circular, hexagonal, or square cross sections. The bodies may have single or multiple channels through them, and the cross sections may be subdivided in various ways.

Cylindrical bodies subdivided into sector units are often considered for use in moderator structures when the cross-sectional dimensions of the cylinders required are large, as in pebble-bed reactors. The adoption of sectors allows for a reduction in extrusion or molding size over that required for a complete cylinder, and a reduction in maximum stress is also realized. Hence, studies were made on cylinders with a central channel and sectors of these cylinders.

The fast-neutron exposure distribution used was given by

$$\phi = 1.12 \times 10^4 \, e^{-0.26d} ,$$

where d is distance in in. from the inner surface of the cylinder and ϕ is exposure in Mwd/At per year. The physical properties assumed for the graphite are

$$E_z = 1.5 \times 10^6 \text{ psi},$$
$$E_x = 1.11 \times 10^6 \text{ psi},$$
$$\gamma_z = -3.4 \times 10^{-7} \text{ (in./in.)/(Mwd/At)},$$

[11] F. J. Witt, S. E. Moore, and B. C. Sparks, Thermal Analysis of Structures Using the Biharmonic Program, pp. 27–31, "GCRP Quar. Prog. Rep. Sept. 30, 1961," USAEC Report ORNL-3210, Oak Ridge National Laboratory.

$$\gamma_x = -1.3 \times 10^{-7} \text{ (in./in.)/(Mwd/At)},$$
$$\nu_{zx} = 0.35,$$

where E is the modulus of elasticity, γ is the dimensional change coefficient, ν_{zx} is the ratio of unit strains, ϵ_x/ϵ_z, when stressed in the z direction, and subscripts x and z denote directions transverse and parallel to the extrusion axis, respectively. Two cylinders with an inside diameter of 30 in. were considered. In the first case the outside diameter was 54 in., and in the second, it was 90 in.

The procedures used in deriving the axial stresses must be understood to interpret the results. For example, in analyzing thick-walled cylinders under axisymmetrical loadings, all tractions give, for plane-strain assumptions, self-equilibrating forces, except in the axial direction. Hence, the axial strain, ϵ_z, must be chosen to satisfy the axial force conditions imposed on the body. In the general case, the axial strain must be specified so that all axial constraint conditions, including moments and force, are satisfied.[12] At the same time, however, the plane-strain equations used in deriving the in-plane stresses must not be altered. The most general expression for axial strain, ϵ_z, is then

$$\epsilon_z = F_1 x + F_2 y + F_3 , \tag{1}$$

where F_1, F_2, and F_3 are constants to be determined, and x and y are in-plane coordinates. The axial stress, σ_z, is thus given by

$$\sigma_z = E_z(F_1 x + F_2 y + F_3 - \gamma_z \phi) + \nu_{zx}(\sigma_x + \sigma_y) . \tag{2}$$

The axial constraint conditions studied are: (1) full axial constraint, in which case the axial strain is zero; (2) constraint against bowing or warping, in which case the axial force is zero but the parallel plane cross sections remain plane and parallel after loading; and (3) no axial constraint, in which case the force and moments associated with the axial stress are zero. There is not sufficient freedom allowed by Eq. (1) to satisfy exactly and everywhere the equilibrium conditions for the body, but it is possible to enforce the conditions that the resultant

---

[12] B. A. Boley and J. H. Weiner, Theory of Thermal Stresses, pp. 307–311, John Wiley and Sons, Inc., New York, 1960.

forces and moments satisfy specified values. With the aid of St. Venant's principle, this gives a good estimate of the stresses except near the ends of the body.

For condition 2, the following integral must be satisfied:

$$\int_A \sigma_z \, dA = 0 \, , \tag{3}$$

where A is the cross-sectional area. The constants F_1 and F_2 in Eq. (1) are zero. Condition 3 is satisfied by taking

$$\int_A \sigma_z \, dA = \int_A \sigma_z x \, dA = \int_A \sigma_z y \, dA = 0 \, . \tag{4}$$

For a case where the stress distribution in a body possesses symmetry, as in the example cited above, conditions 2 and 3 are identical. This is also true, in general, if the stress distribution possesses symmetry about axes in the plane.

The cylinders and sectors were analyzed for all three constraint conditions and the results are given in Table 8.5. From this table it is seen that the in-plane stresses of the sectors are much lower than those of the complete cylinder and that they decrease with decreasing sector angle. Also, the constraint condition on the body greatly influences the axial stress. Significant reductions in axial stresses are shown for sectors with no axial constraint as compared with the other constraint conditions. For the cases considered, the maximum axial and in-plane stresses are always located at the intersection of the sector angle bisector and the inner surface, whereas the minimum axial stress is along a radial edge. The minimum in-plane stress is either inside the body or on the inner surface.

The maximum stresses may also be reduced by using nested, thin-walled cylinders[13] in place of a single, thick-walled cylinder. Thus, an analysis for a 30-in.-ID cylinder with various radial thicknesses up to 12 in. was made. Sectors were also examined on a maximum axial stress

---

[13]A. P. Fraas et al., "Preliminary Design of a 10-Mw(t) Pebble-Bed Reactor Experiment," Oak Ridge National Laboratory, May 8, 1961, unpublished report.

Table 8.5. Irradiation-Induced Stresses in Complete Cylinders and in Sectors

	Stresses (psi per year)							
	In-Plane		Axial					
			Complete Axial Constraint		Constrained Against Bowing or Warping		No Axial Constraint	
	Maximum	Minimum	Maximum	Minimum	Maximum	Minimum	Maximum	Minimum
	$\times 10^3$	$\times 10^3$	$\times 10^3$	$\times 10^3$	$\times 10^3$	$\times 10^3$	$\times 10^3$	$\times 10^3$
Complete cylinder[a]	2.48	−0.76	6.57	0	5.03	−1.55	5.03	−1.55
180° sector	1.80	−0.98	6.30	0.26	4.79	−1.28	4.23	−2.04
90° sector	0.78	−0.28	5.98	0.26	4.44	−1.28	3.13	−1.80
45° sector	0.51	−0.44	5.80	0.26	4.34	−1.28	2.24	−0.63
Complete cylinder[b]	3.12	−0.37	6.79	0.17	6.33	−0.56	6.33	−0.56
90° sector	1.71	−1.43	6.30	0	5.83	−0.20	4.05	−1.15

[a] With dimensions of 30 in. ID and 54 in. OD.

[b] With dimensions of 30 in. ID and 90 in. OD.

versus thickness basis. Since the in-plane stresses for sectors are small, the contributions from them are negligible; this is especially true for small sector angles. Therefore, the sector analyses were made disregarding the in-plane stresses.

The results of studies on sectors and complete cylinders are shown in Fig. 8.7, where the maximum tensile stress (maximum axial stress) is plotted as a function of sector angle and thickness. The bodies are assumed to have no axial constraint (condition 3). The 2π sector angle actually applies to a complete cylinder. The results for 12-in.-thick units are those from Table 8.5. It is significant that the stresses for thin sectors change little with sector angle between $\pi/2$ and 2π, but the change increases with increasing radial thickness.

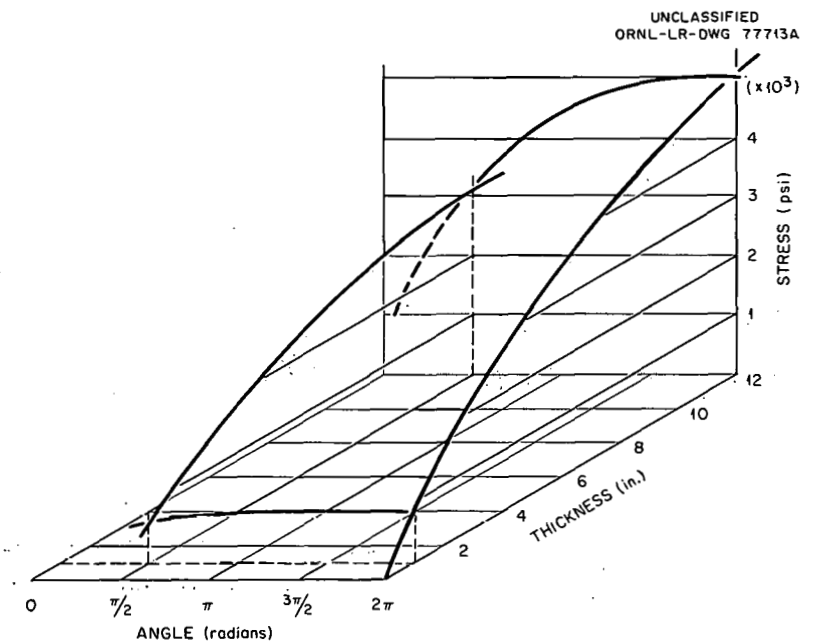

Fig. 8.7. Maximum Tensile Stress as a Function of Sector Angle and Thickness.

Design Criteria for Graphite Components

S. E. Moore J. G. Merkle

The tensile strength of graphite, which ranges from about 1000 to 2000 psi, and the fracture elongations, 0.1 to 0.4%, are low when

compared with the stresses or total strains to be sustained by graphite bodies used in nuclear reactors. Thus calculations indicate that fracture of these bodies will occur during service. The obvious consequence has been to design reactors[14,15] so that the graphite can be removed when the useful lifetime of the component has been exhausted.

A study is therefore being conducted to establish adequate design criteria for graphite components. The behavior of bodies under complex stress states is being examined through experimental and analytical studies on specimens with simple geometries subjected to single loadings.

In the analysis of bodies that are loaded to failure, the ability to make accurate predictions depends, in part, on the accuracy with which the stress-strain relationships are represented. Generally, analyses are made in one of two ways; the material is assumed to behave elastically over the range of loading or an elastoplastic analysis is made.

When the behavior of the material is typified by that of graphite in uniaxial tension, neither assumption for the stress-strain relationship is correct; however, the errors involved depend upon the sensitivity to this factor. Thus calculations were made to study the importance of the stress-strain relationship upon the stress and strain distributions in bodies under external load.

A homogeneous, isotropic material giving a stress-strain diagram both in tension and compression similar to that for graphite was considered. Three approximations to the stress-strain relationship were selected. The first was a linear relationship with the slope equal to the slope of the actual curve at the origin; the second was an elastic-ideally plastic curve with the slope of the elastic portion being the same as for the first relationship and the area under the curve equal to the area under the measured curve. Finally, a linear relationship obtained by drawing a straight line between the origin and the fracture point was used. These relationships and the actual stress-strain diagram for AGOT graphite are

---

[14]Oak Ridge National Laboratory, "Conceptual Design of the Pebble Bed Reactor Experiment," USAEC Report ORNL-TM-201, May 17, 1962, pp. 179–184.

[15]Oak Ridge National Laboratory, "The ORNL GCR-3, A 750-Mw(e) Gas-Cooled Clad-Fuel Reactor Power Plant," USAEC Report ORNL-3353, December 27, 1962, pp. 2.26–2.42.

shown in Fig. 8.8, where the approximations are labeled 1, 2, and 3, respectively.

The fracture stress and elongation for the specimen tested were 2600 psi and 0.21%. The modulus of elasticity for assumed relationships (1) and (2) was 1.76×10^6 psi, and the value for the third was 1.27×10^6

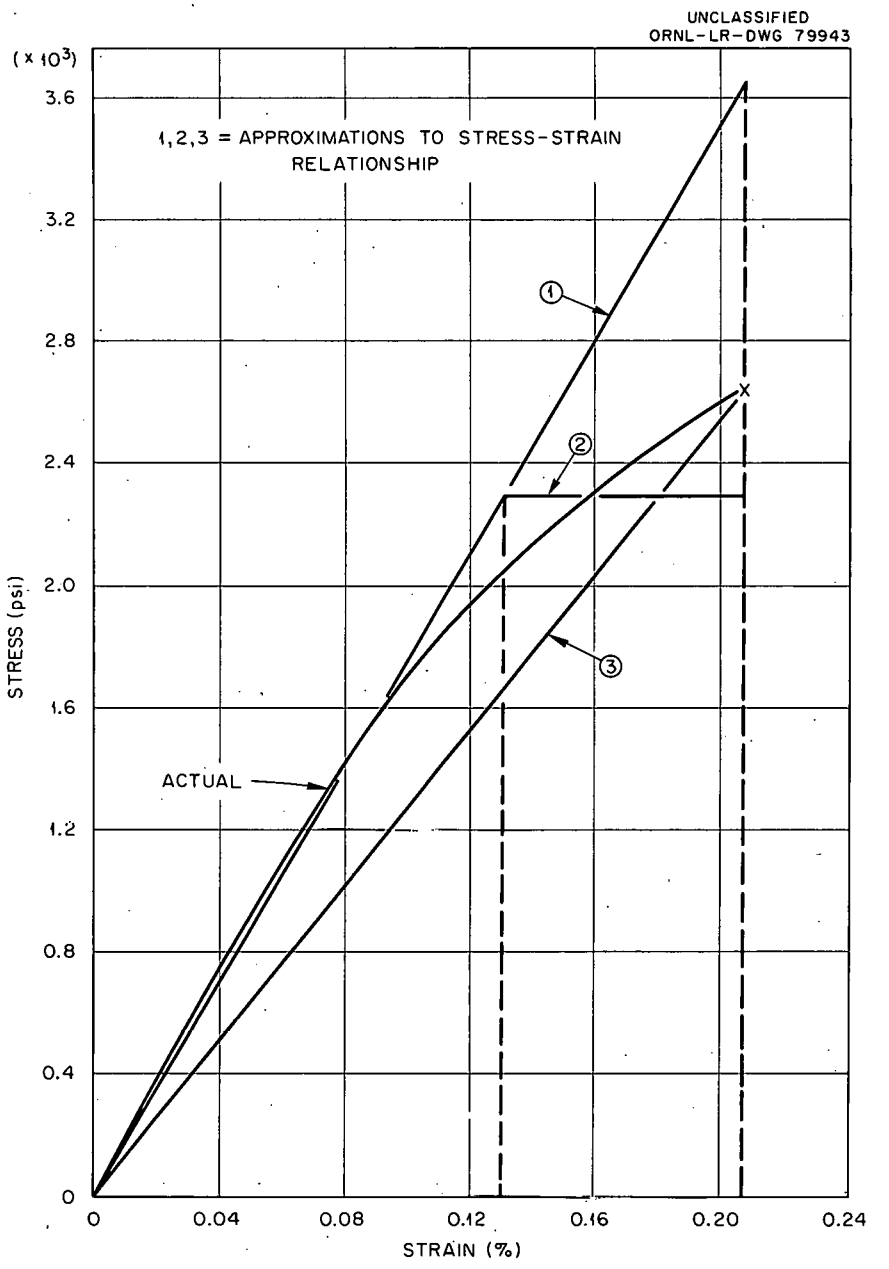

Fig. 8.8. Stress-Strain Diagram for AGOT Graphite Tensile Tested at Room Temperature.

psi. The yield stress, σ_y, for the elastic-ideally plastic case was 2300 psi.

The bodies initially examined were thick-walled cylinders under internal pressure loadings. The pressure was selected to give a maximum tensile strain for the elastoplastic case near the fracture strain of the material. The results for cylinders with an inside radius-to-outside radius ratio, a/b, of 0.5 are shown in Figs. 8.9 and 8.10. In Fig. 8.9

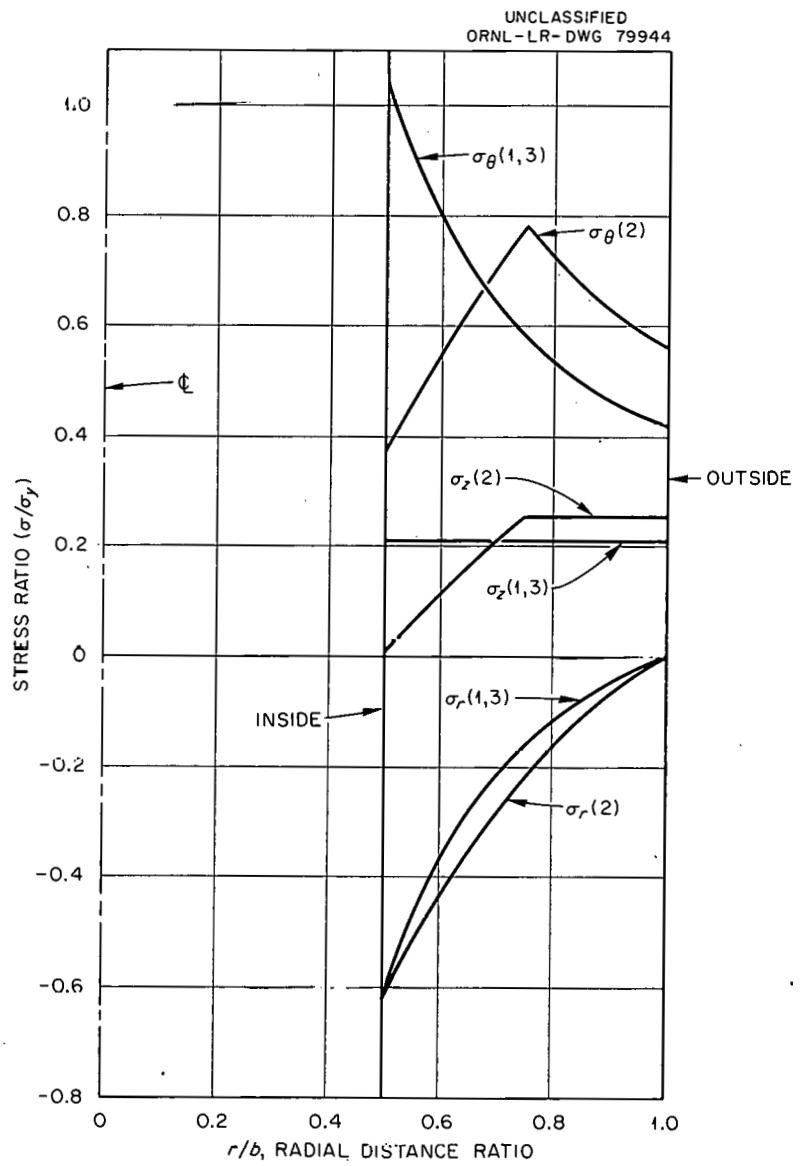

Fig. 8.9. Stress Ratios for Thick-Walled Graphite Cylinder Subjected to an Internal Pressure Loading.

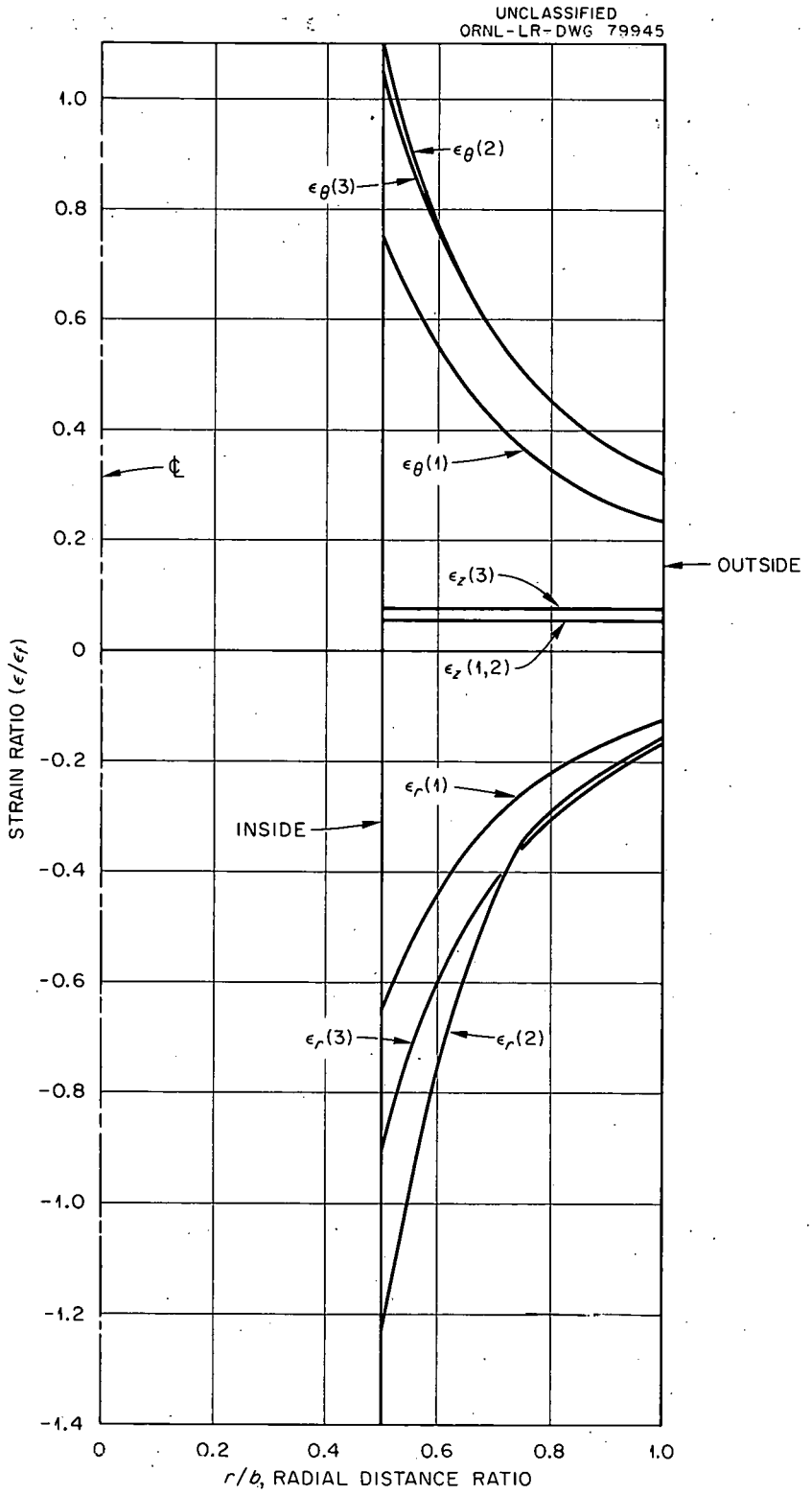

Fig. 8.10. Strain Ratios for Thick-Walled Graphite Cylinder Subjected to an Internal Pressure Loading.

the ratios of the principal stresses to the yield stress of the elastoplastic case are plotted versus the radius ratio, r/b, and in Fig. 8.10 the ratios of principal strains to the fracture strain are shown. The subscripts r, θ, and z refer to the radial, tangential, and axial directions, respectively. The internal pressure is 1435 psi and Poisson's ratio is 0.30 for the elastic regions.

The plastic front for the elastoplastic analysis occurs at r/b = 0.75, as may be seen by the discontinuities in the axial and tangential stress curves. It may also be seen from Fig. 8.9 that the stress distributions for stress-strain relationship (2) are much different from those for (1) and (3). In the case of strains, relationships (2) and (3) do not give significantly different results in the axial and tangential direction; however, the radial strains are strongly affected by the stress-strain relationship. Similar results were obtained for cylinders with other a/b ratios.

Since the quantities that could be measured in a thick-walled cylinder test are the axial and tangential strains, it would be difficult to differentiate between relationships (2) and (3). Therefore, the studies will be extended to include other cases. Thermal loadings will be examined on the same basis, and the anisotropy of the material must be factored into the study.

Compatibility of Graphite and Metals in Hydrogen

A. M. Smith R. E. MacPherson

Further tests were conducted in the study of reactions of hydrogen, graphite, and metals in high-temperature autoclaves.[16] Following the initial test at 1000 psig and 1500°F, which was terminated after approximately 200 hr because of a gradual pressure loss, the inner surface of one of the three autoclave units was preoxidized and a pressure-decay test conducted at the same conditions. Results of this test showed a significant increase in the leakage rate compared with the leakage rate in a similar

[16]A. M. Smith and R. E. MacPherson, Compatibility of Hydrogen and Graphite, pp. 291–292, "GCRP Semiann. Prog. Rep. Sept. 30, 1962," USAEC Report ORNL-3372, Oak Ridge National Laboratory.

test at 1000 psig and ambient conditions, that is, 2×10^{-2} versus 6×10^{-4} cm^3 (STP)/sec. When the hydrogen in the unit (still at 1500°F) was replaced with helium, however, the leakage rate was reduced to 4.8×10^{-4} cm^3 (STP)/sec, which compared favorably with the leakage rate of hydrogen at ambient conditions. Consequently it was felt that most of the pressure loss resulted from the diffusion of hydrogen through the hot wall of the autoclave unit.

Since it appeared logical to expect similar experience with the remaining units, a decision was made to operate two units (tests No. 2 and 3) at 1500°F and offset the losses by numerous repressurizations. Type AGOT graphite plus specimens of type 304L and 310 stainless steel, Inconel, and a control specimen of 19-9DL steel were used in both tests, which were of 1000 hr duration at an average pressure of 850 psig.

Analyses of the hydrogen used in test No. 2 showed a steady increase in CH_4 concentration over the entire test period, with a maximum value of 16.8 vol % at the end of the test. Analyses of hydrogen used in test No. 3 showed a similar trend; however, because of a smaller volume ratio of hydrogen to graphite, the maximum CH_4 value was only 5.3 vol %.

Behavior of Beryllium Oxide Compacts Under Fast-Neutron Irradiation

G. W. Keilholtz J. E. Lee, Jr.
R. E. Moore

Postirradiation examinations of specimens from BeO irradiation experiment 7 were completed, and the results are discussed below. The irradiation in the ETR of experimental unit 9 was completed in January, and hot-cell disassembly is under way. This unit received a fast-neutron (>1 Mev) dose of about 3.5×10^{21} neutrons/cm^2. Experimental unit 8, which is similar to unit 9, will continue to be irradiated in the ETR until June 1963, for an expected exposure of 6×10^{21} to 8×10^{21} neutrons/cm^2. The irradiation of experimental unit 10, an uninstrumented, water-cooled assembly, was started in January. The planned exposure is about 10^{21} neutrons/cm^2. A summary of the irradiation conditions for experimental units 6 through 10 was given in a previous report.[17]

Postirradiation Examinations of Specimens from Experimental Unit 7

Metallographic Examination. (E. J. Manthos, E. L. Long, Jr.) Photomicrographic evidence of grain-boundary separation in irradiated BeO, which can account for much of the observed change in physical properties, was presented previously.[17] The metallographic study of the specimens irradiated in experiment 7 is now complete, and the results confirm earlier conclusions.

The effect of temperature on the degree of grain-boundary separation is illustrated in Figs. 8.11 and 8.12. Very little separation can be seen in Fig. 8.11, which shows cold-pressed material irradiated to an exposure of 2.25×10^{21} neutrons/cm^2 at 1100°C in capsule 8. On the other hand, the cold-pressed BeO in capsule 1, which received a much lower fast-neutron

[17] G. W. Keilholtz, J. E. Lee, Jr., and R. E. Moore, Behavior of BeO Under Irradiation, pp. 269–279, "GCRP Semiann. Prog. Rep. Sept. 30, 1962," USAEC Report ORNL-3372, Oak Ridge National Laboratory.

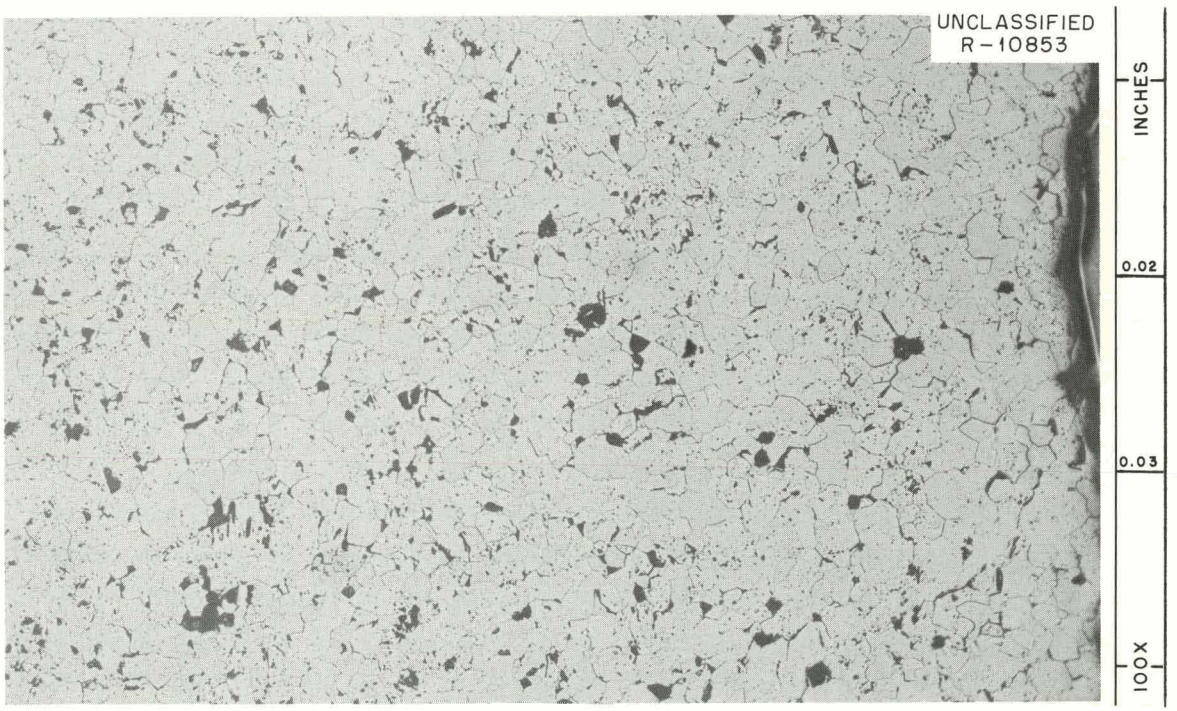

Fig. 8.11. Irradiated Cold-Pressed and Sintered BeO Specimen 7-8-2, Which Was Exposed to a Fast-Neutron (>1 Mev) Dose of 2.25×10^{21} Neutrons/cm^2 at 1100°C in Experiment 41-7. As polished.

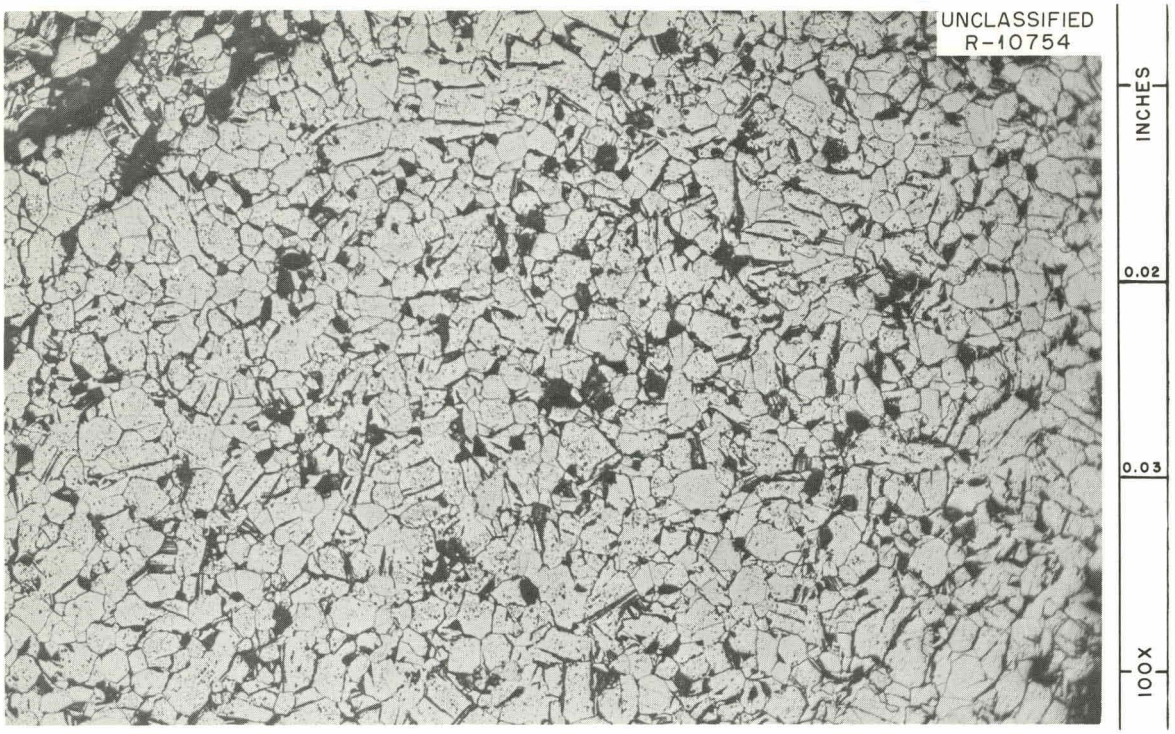

Fig. 8.12. Irradiated Cold-Pressed and Sintered BeO Specimen 7-1-5, Which Was Exposed to a Fast-Neutron (>1 Mev) Dose of 1.20×10^{21} Neutrons/cm^2 at 583°C in Experiment 41-7. As polished.

dose, 1.2×10^{21} neutrons/cm^2, at a much lower temperature, 583°C, exhibited a high degree of grain-boundary separation, as can be seen in Fig. 8.12.

A comparison of the complete series of photomicrographs of both types of as-polished specimens substantiated an earlier conclusion that hot-pressed BeO underwent more extensive grain-boundary separation than cold-pressed BeO under the same conditions of fast-neutron exposure and temperature. Also, there is a correlation of volume increase of the specimens with the degree of grain-boundary separation estimated from visual inspection of the photomicrographs.

Grain sizes of the cold-pressed and sintered specimens ranged from 20 to 40 μ; the average was 27.5 μ. The hot-pressed material was homogeneous because the cylinders were machined from very large pieces; the range of measured grain sizes was 28 to 33 μ, with the average 30 μ. The grain-size measurements show no evidence of grain growth under the conditions of the experiment.

Thermal Conductivity. The loss in thermal conductivity of specimens in capsules 3 and 5 was calculated from in-pile temperature difference measurements and plotted against fast-neutron dose in Fig. 8.13. The thermal conductivity decreased at a greater rate in the higher flux region (capsule 5), but appeared to level off at about 40 to 45% of the original value as the neutron dose approached 4×10^{21} neutrons/cm^2. Experimental unit 7 was not designed to achieve separation of the neutron-dose and neutron-flux variables, but the fact that capsules 3 and 5 were irradiated at very nearly the same temperature permits a separation of the variables for the specimens from these capsules. The slopes of the curves in the lower dose range ($<10^{21}$ neutrons/cm^2) are uncertain, however, because of the widely scattered values of temperature difference.

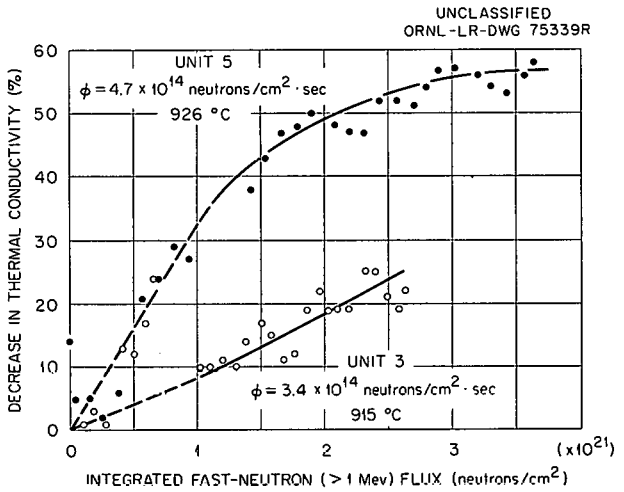

Fig. 8.13. Decrease in Thermal Conductivity of BeO vs Integrated Fast-Neutron Flux in Experimental Unit 41-7.

X-Ray Diffraction Examinations. (H. L. Yakel) X-ray diffraction studies of finely ground specimens from experimental unit 7 were recently completed. The fractional c parameter increase, $\Delta c/c_o$, was quite small (<0.0015), as was expected in view of the high temperatures, but it was approximately proportional to the neutron dose above 900°C, as can be seen in Fig. 8.14. The effect of temperature is illustrated by the relatively high value of $\Delta c/c_o$ at 583°C and low values at 1100°C. There was a large

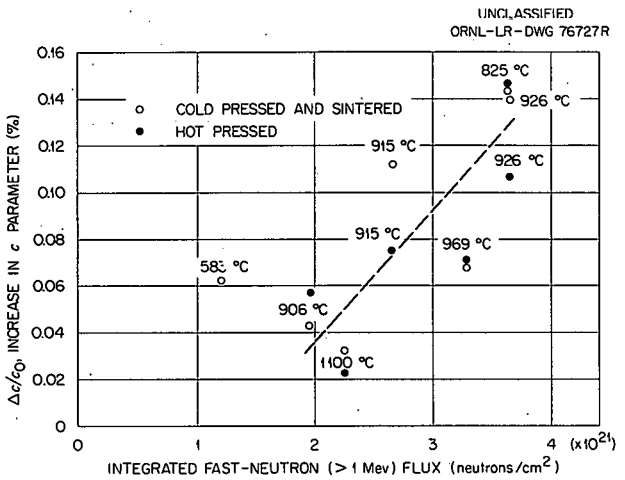

Fig. 8.14. Increase in c Parameter vs Integrated Fast-Neutron Flux in Experimental Unit 41-7.

variation in the anisotropic expansion ratios, $(\Delta c/c_o)/(\Delta a/a_o)$, but the average (~8) was near that for other experiments.

Marked symmetrical broadening of all reflections $hk\cdot\ell$ with ℓ large, which may be indicative of lattice-defect agglomeration between certain of the planes perpendicular to the c-axis, was noted in all patterns, except those for specimens in capsule 7. These two patterns were anomalously sharp, and the lattice parameters were anomalously low. Metallographic examination of the steel cladding of capsule 7 (see subsequent section of this chapter) indicated, however, a period of operation at a higher temperature than the average temperature of 935°C for this capsule. Partial annealing of the lattice damage to the BeO in the capsule could have occurred during this period.

Lattice parameters and anisotropic expansion ratios of corresponding hot-pressed and cold-pressed samples are in fair agreement. The increase in volume calculated from the lattice parameters is only about 4% of the total volume increase of the hot-pressed compacts and only about 8% of that of the cold-pressed material. Nevertheless, as can be seen in Fig. 8.15, there is a correlation of total volume increase for both types of BeO with the c parameter increase.

Gas Content. The tritium generated in the specimens of experimental unit 7 was nearly completely lost, as in previous experiments at high temperatures, and about 50% of the helium escaped during exposure to high

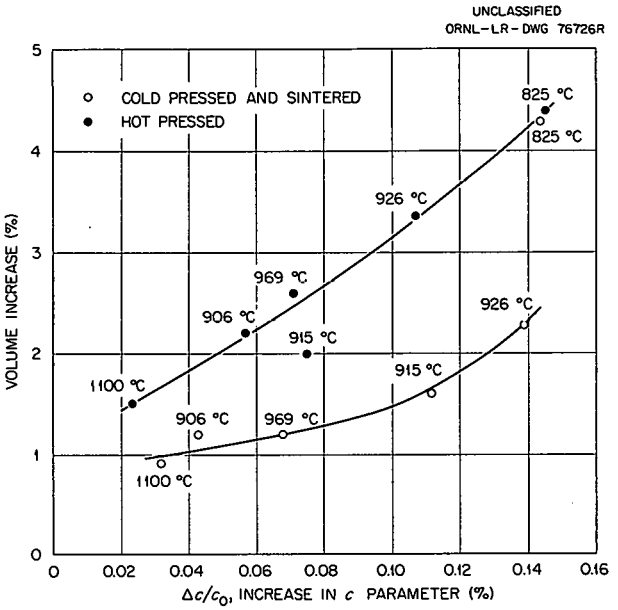

Fig. 8.15. Volume Increase of BeO Specimens vs Increase in c Parameter, Experimental Unit 41-7.

fast-neutron doses ($>3 \times 10^{21}$ neutrons/cm^2). The grain-boundary separation that occurred at the high doses may have permitted some of the helium to diffuse out of the compacts. Results[17] of experiment 6 indicated a helium loss of about 60% after a much lower exposure ($<10^{21}$ neutrons/cm^2). The BeO used in this experiment was, however, of very low density and quite porous; consequently, loss of helium by diffusion was expected.

Discussion of Results of Experiment 7

The increase in volume of BeO compacts exposed to high fast-neutron doses is one of the important criteria of irradiation damage. The fractional volume increase may be represented by the approximate equation

$$\frac{\Delta V_T}{V_o} = \frac{\Delta V_\ell}{V_o} + \frac{\Delta V_d}{V_o} + \frac{\Delta V_g}{V_o} ,$$

in which

ΔV_T = total volume increase,
ΔV_ℓ = volume increase calculated from lattice parameters,
ΔV_d = volume increase caused by lattice-defect agglomeration,

ΔV_g = volume increase caused by grain-boundary separation,

V_o = unirradiated volume.

The lattice parameter expansion, $\Delta V_\ell / V_o$, which can be calculated from measured values of the c and a parameters, is much less at high temperatures than at very low temperatures.[18] Nevertheless, it is still approximately proportional to the neutron dose at temperatures above 900°C. Evidence from the x-ray diffraction patterns[19] shows that the defect-volume increase, $\Delta V_d / V_o$, like $\Delta V_\ell / V_o$, is anisotropic and produces an additional preferred growth in the direction of the c axes of individual crystals. Values of $\Delta V_d / V_o$ can be obtained from measurements of the densities and lattice parameters of single crystals included in experiments now in progress. It should be possible therefore to calculate the values of $\Delta V_g / V_o$ for corresponding sintered compacts.

The two principal mechanisms proposed for grain-boundary separation in pure BeO are (1) anisotropic expansion of the crystals that results in stresses at the grain boundaries which ultimately overcome the intergranular bonding forces and (2) the breaking apart of grain boundaries by the pressure of the helium that diffuses to the grain boundaries after its production by neutron reactions within the crystals. It seems certain that the first mechanism applies at low neutron doses and low temperatures, because under these conditions grain-boundary separation occurs with very low helium production.[20] The question of whether this mechanism is also dominant at high temperatures and high neutron dose is still unanswered, because there was no separation of the neutron-flux and neutron-dose parameters in experiment 7, except in the in-pile thermal conductivity measurements. The correlation of c parameter increase with total volume increase (Fig. 8.15) does not, in itself, substantiate the anisotropic

---

[18] R. P. Shields, J. E. Lee, Jr., and W. E. Browning, Jr., "Effects of Fast-Neutron Irradiation and High Temperatures on Beryllium Oxide," USAEC Report ORNL-3164, Oak Ridge National Laboratory, March 16, 1962.

[19] H. L. Yakel and B. S. Borie, Acta. Cryst. (1963) (in press).

[20] J. Elston, "Radiation Damage in Solids," Proceedings of Symposium on Radiation Damage in Solids and Reactor Materials, Venice, May 7–11, 1962, Vol. II (Vienna, IAEA, 1962).

expansion mechanism, because $\Delta c/c_o$ is also proportional to the neutron dose (Fig. 8.14).

The experimental units now being evaluated and undergoing irradiation are statistically designed[21] to separate the parameters of grain size, density, specimen size, neutron flux, neutron dose, and temperature. More than 300 cold-pressed cylindrical compacts made from the same starting material and sintered at the same temperature, as well as single-crystal specimens, are included. The statistical design should permit a test of the proposed damage mechanisms, and the results should provide quantitative reactor-design information.

Metallographic Examination of Cladding and End Caps from BeO Experimental Unit 41-7 (E. J. Manthos)

It was noted during the disassembly[17] of experimental unit 7 that the type 430 stainless steel cladding surfaces of capsules 7 and 8 appeared to be large grained. The average operating temperatures were 935 and 1100°C, respectively. The end caps of these capsules, originally flat, were bowed, and shiny crystalline metal deposits were present at the ends of the interior surfaces of the cladding. Capsule 4 presented a normal appearance even though it operated at a higher temperature (970°C) than capsule 7. Metallographic examination revealed, however, that the grains of the steel cladding of capsules 7 and 8 were similar and much larger than those of capsule 4. In addition, the microhardness (DPH, 500-g load) of a control specimen and cladding sections of capsules 4, 7, and 8 were 202, 147, 142, and 140, respectively.

Metallographic evidence thus indicates that capsule 7 operated for a period of time at a temperature greater than the average operating temperature of 935°C and possibly at a temperature as high as that of capsule 8, 1100°C. The crystalline type 430 stainless steel deposits may have resulted from vaporization of metal from the sides of the end caps and subsequent condensation on the adjacent cooler capsule walls. Preferential

---

[21] D. A. Gardiner, "The Experimental Design for BeO Irradiation Experiments ORNL-41-8 and ORNL-41-9," USAEC Report ORNL-3310, Oak Ridge National Laboratory, July 2, 1962.

diametral expansion of BeO may have forced the capsule walls away from the end caps, which would result in overheating of the end caps.

9. STUDIES OF ADVANCED SYSTEMS

GCR-3 Power Cycle Studies

W. R. Gall

The steam power cycle proposed in the GCR-3 study[1] included six regenerative feedwater heaters to provide a feedwater temperature of 450°F. In order to provide an adequate temperature difference between the gas and steam in the steam generator, it would be necessary to return the gas to the blowers at 550°F. The blower power required to circulate the gas would vary as follows:

$$Q_b = \frac{Q_T}{\eta} \frac{T_1}{(T_2 - T_1)} \left[\rho_c^{(k-1)/k} - 1\right] ,$$

where

Q_b = work done on the gas by the blowers,
Q_T = total thermal energy, including Q_b and the reactor heat,
η = efficiency of the blowers,
T_1 = blower suction temperature (absolute),
T_2 = reactor outlet temperature (absolute),
ρ_c = compression ratio,
k = adiabatic exponent of the gas.

For the conditions of the GCR-3 design Q_T = 2000 Mw, η = 0.85, k = 1.659, T_1 = 1010°R, T_2 = 1610°R, and $[\rho_c^{(k-1)/k} - 1]$ = 0.0231; so Q_b/Q_T = 0.0452 or 4.5% of the total energy of the system.

In terms of the blower suction temperature, the blower work for the GCR-3 system is

$$\frac{Q_b}{Q_T} = \frac{0.0272 T_1}{1610 - T_1} .$$

---

[1] M. Bender and W. R. Gall, "The ORNL GCR-3, A 750 Mw(e) Gas-Cooled Clad-Fuel Reactor Power Plant, A Joint Design Study," USAEC Report ORNL-3353, Oak Ridge National Laboratory, January 1963.

Thus the suction temperature affects the blower work both by changes in the compressive work per pound and by the total number of pounds pumped. This effect was calculated by adding heaters to and subtracting them from the heat-balance diagram for the GCR-3 cycle, and the results presented in Table 9.1 were obtained. Enthalpies were held constant throughout the cycle, and the total thermal energy available at the steam generator was held at 2000 Mw.

Table 9.1. Effect of Feedwater Temperature on Performance of GCR-3 Power Cycle

Feedwater temperature, °F	93.6	265.1	342.7	386.9	450.1	533.0
Number of heaters	0	2	4	5	6	7
Blower inlet temperature, °F	366	452	494	517	550	598
Reactor inlet temperature, °F	388	476	519	543	578	627
Blower work, % of reactor heat	2.95	3.68	4.11	4.37	4.83	5.49
Heat rate, Btu/kwhr	9716	9148	8955	8932	8937	8990
Net plant efficiency, %	35.5	38.0	39.0	39.2	39.3	39.3

The data presented in Table 9.1 are shown graphically in Fig. 9.1. The most noticeable feature of the curves of Fig. 9.1 is the broad flat shape of the efficiency and heat-rate curves between feedwater temperatures of 350 and 530°F. The change in efficiency in this range is only 0.2% of 39%. This is a considerably flatter efficiency peak than is typical for conventional power plants.

The economics also differ from those of conventional plants. Since efficiency changes little with feedwater temperature, the fuel cost also changes little, and the significant economic factors are the effects of the temperature on the capital cost of equipment. Costs of blower equipment, gas piping, feedwater heaters, and the reactor core increase with increases in the feedwater temperature, whereas the steam generator cost decreases. Before final selection of the feedwater temperature is made, a careful evaluation of these economic effects is required.

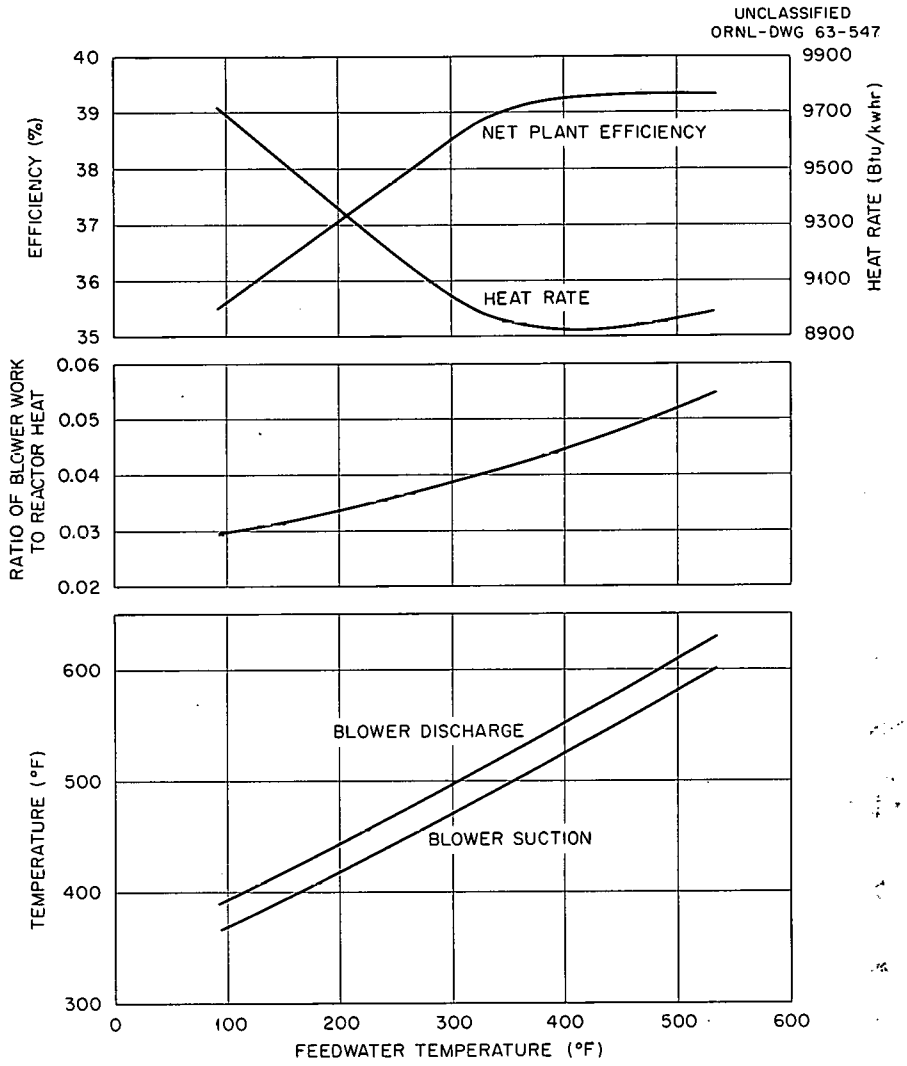

Fig. 9.1. Effect of Feedwater Temperature on Performance of the GCR-3 Power Cycle.

GCR-4 Design Studies

W. R. Gall

The GCR-3 study[1,2] showed that it would be possible to generate power in a gas-cooled reactor power plant for as little as 4.5 mills/kwhr. The study was based on a reactor gas outlet temperature of only 1150°F in order to be below the temperature level attainable with clad fuels.

---

[2]W. R. Gall, GCR-3 Design, pp. 340–403, "GCRP Semiann. Prog. Rep. Sept. 30, 1962," USAEC Report ORNL-3372, Oak Ridge National Laboratory.

The Westinghouse Electric Corporation has now completed a preliminary parametric study of a combined gas-turbine and steam-generator power cycle of the type shown in Fig. 9.2. The basic steam conditions assumed for the study were

Steam pressure, psia	2415
Initial temperature, °F	1000
Reheat temperature, °F	1000
Steam exhaust flow, lb/hr	3,000,000
Exhaust pressure, in. Hg abs.	1.5

Heat balances were developed for three values of feedwater temperature, 96.1, 269.4, and 450.3°F, corresponding to 0, 3, and 6 stages of heating,

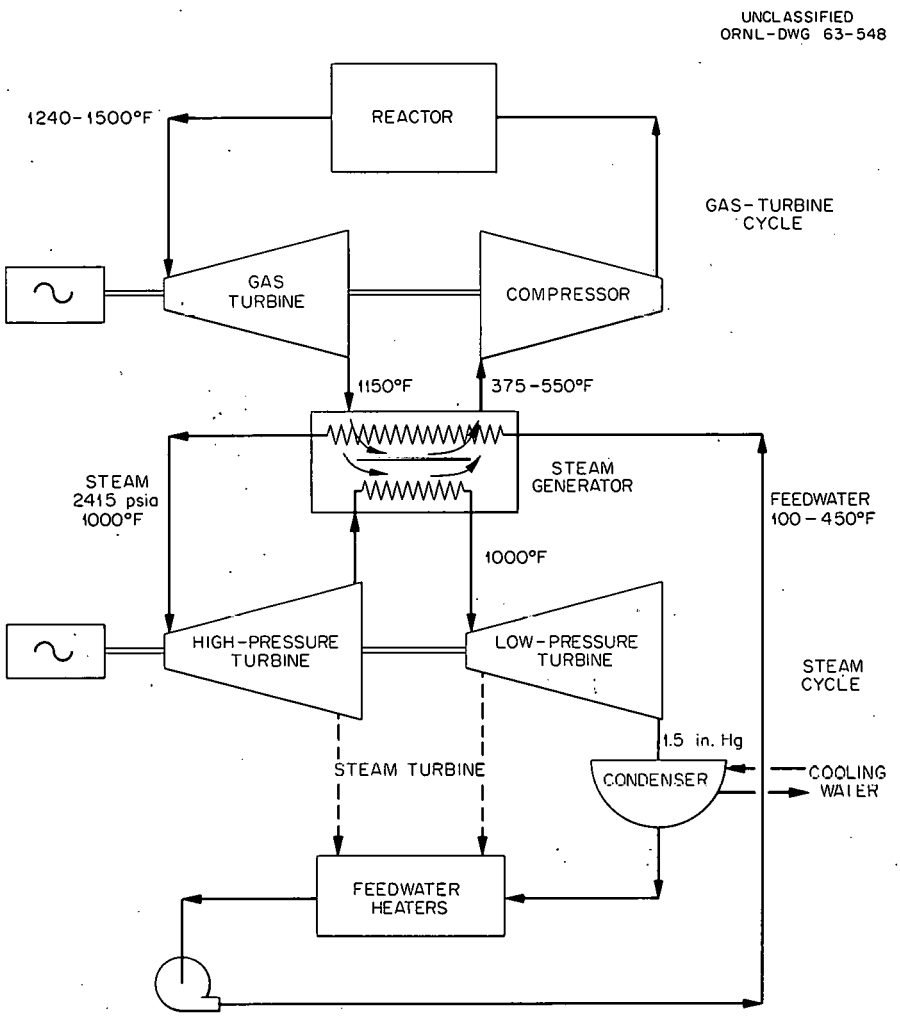

Fig. 9.2. Schematic Diagram of Combined Gas Turbine and Steam-Generator Power Cycle for a Gas-Cooled Reactor.

respectively. The results of the three heat-balance determinations are listed in Table 9.2. In all three cases it was assumed that the boiler feed pumps were driven by steam turbines and the gas circulators were driven by gas turbines. For the three feedwater temperatures the corresponding gas temperatures at the compressor suction were:

Feedwater Temperature (°F)	Gas Suction Temperature (°F)
96.1	375
269.4	470
450.3	550

The turbine exhaust temperature was 1150°F for all cases, and the exhaust gas went to the steam generator, as shown by Fig. 9.2. The compression ratio required to overcome frictional resistance was assumed to be 1.06.

Table 9.2. Heat Balances for Various Feedwater Temperatures

Feedwater temperature, °F	96.1	269.4	450.3
Stages of heating	0	3	6
Exhaust steam flow, lb/hr	3,008,059	3,002,107	3,009,522
Throttle flow, lb/hr	3,116,000	3,700,000	4,500,890
Steam turbine power, kw	578,476	658,925	714,434
Heat rate, Btu/kwhr	8,660	8,064	7,760

Ten gas turbine and compressor arrangements were studied as topping cycles for the three steam cycles. In three of these the gas turbines provided only enough power to drive the compressors. The other seven were selected to show the effect on over-all plant performance of generating various amounts of net power in the gas turbines with gas temperatures up to 1500°F at the turbine inlet. The results are given in Table 9.3 and Figs. 9.3, 9.4, and 9.5.

For the simple case where the gas turbine is used only to drive the gas circulator, a reactor exit temperature of 1240°F is adequate, as shown in Fig. 9.3, if no feedwater heating is used. A gain in efficiency results from further increases in the reactor exit temperature, however, since it permits a higher feedwater temperature and thus higher efficiency in the steam cycle, which establishes the net capability of the system. For a

Table 9.3. Results of Parametric Study of Various Gas-Turbine and Steam Generator Combinations

Compressor Suction Temperature (°F)	Number of Compression Stages	Turbine Inlet Temperature (°F)	Net Gas-Turbine Power (kw/lb·sec)[a]	Total Flow of Helium (lb/sec)	Net Gas-Turbine Power (kw)	Total Power Output of Plant (kw)	Reactor Inlet Temperature (°F)	Reactor Thermal Power (kw)	Efficiency (%)
375	12	1240.3	0	1436.4	0	578,476	465.3	1,467,754	39.41
470	18	1288.2	0	1736.5	0	658,925	607.9	1,557,583	42.30
550	28	1368.6	0	2053.4	0	714,434	768.4	1,624,970	43.97
375	28	1421.7	66.94	1436.4	96,153	674,629	693.4	1,568,697	43.01
470	28	1390.5	27.75	1736.5	48,188	707,113	688.4	1,607,496	43.99
375	23	1368.6	47.30	1436.4	68,660	647,135	555.6	1,539,721	42.03
470	26	1368.6	21.98	1736.5	38,168	697,093	671.1	1,596,964	43.65
375	18	1308.2	25.56	1436.4	36,714	615,190	512.9	1,506,199	40.84
470	37	1475.0	49.62	1736.5	86,165	745,090	755.5	1,647,334	45.23
550	43	1500.0	21.72	2053.4	44,600	759,034	882.7	1,671,267	45.42

[a]Based on helium as the circulated gas.

feedwater temperature of 450°F the reactor exit temperature required is 1368.6°F and the efficiency of the plant is 43.97%, as compared with 39.4% at the lower temperature.

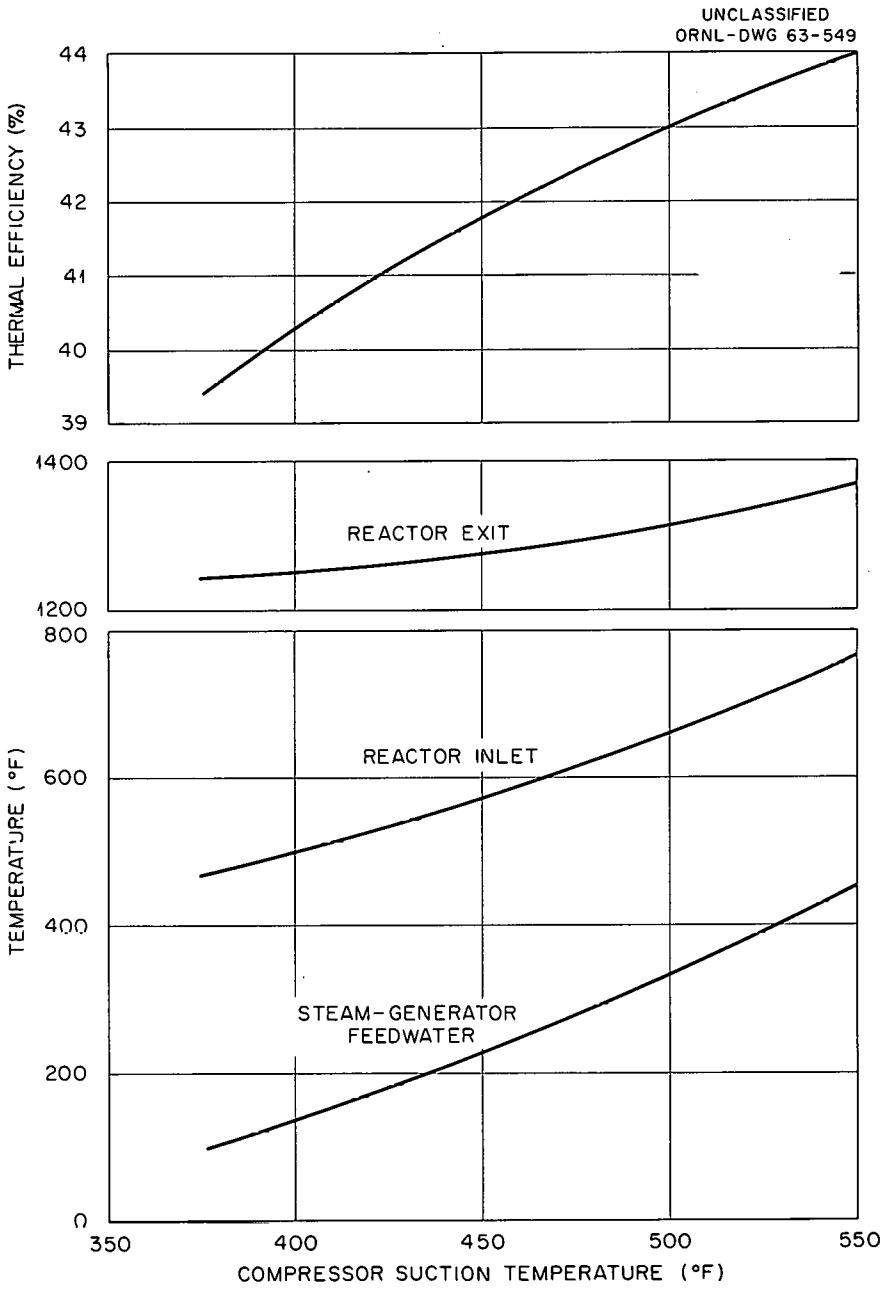

Fig. 9.3. Effect of Compressor Suction Temperature on Thermal Efficiency and Reactor-Exit, Reactor-Inlet, and Steam-Generator Feedwater Temperatures. Gas turbines used only to drive compressors and exhausted to steam generator at 1150°F. Friction loss pressure ratio = 1.06.

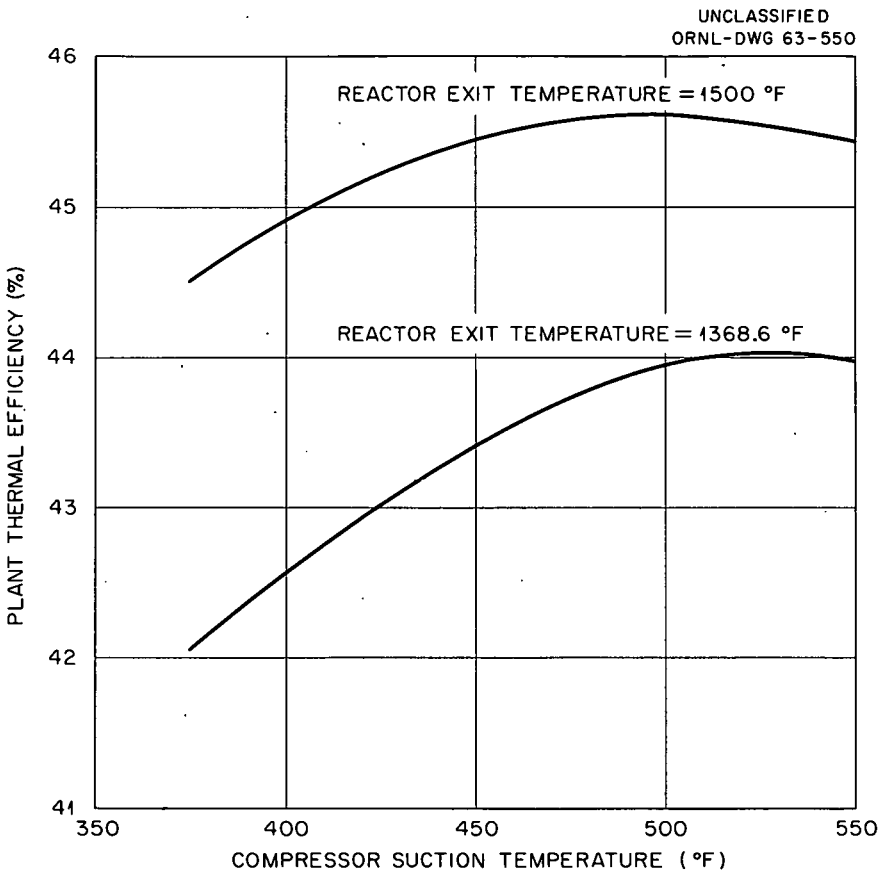

Fig. 9.4. Effect of Compressor Suction Temperature on Thermal Efficiency of the Combined Gas Turbine and Steam-Generator Power Cycle at Reactor Exit Temperatures of 1368.6 and 1500°F. Calculated for the cycle shown in Fig. 9.2.

For a given reactor exit temperature, the maximum efficiency occurs at a lower compressor suction temperature than 550°F, as shown in Fig. 9.4, where efficiency curves for reactor exit temperatures of 1368.6 and 1500°F are presented. The lower curve corresponds to the reactor outlet temperature at which no net gas-turbine power is generated at a suction temperature of 550°F. At lower suction temperatures, however, some excess power is available, so this curve is higher at all other points than the efficiency curve of Fig. 9.3. At the higher reactor exit temperature of 1500°F, a greater fraction of the plant output is generated by the gas turbine, so the effect of a higher feedwater temperature carries less weight and the maximum efficiency occurs at a still lower temperature for better gas-turbine performance.

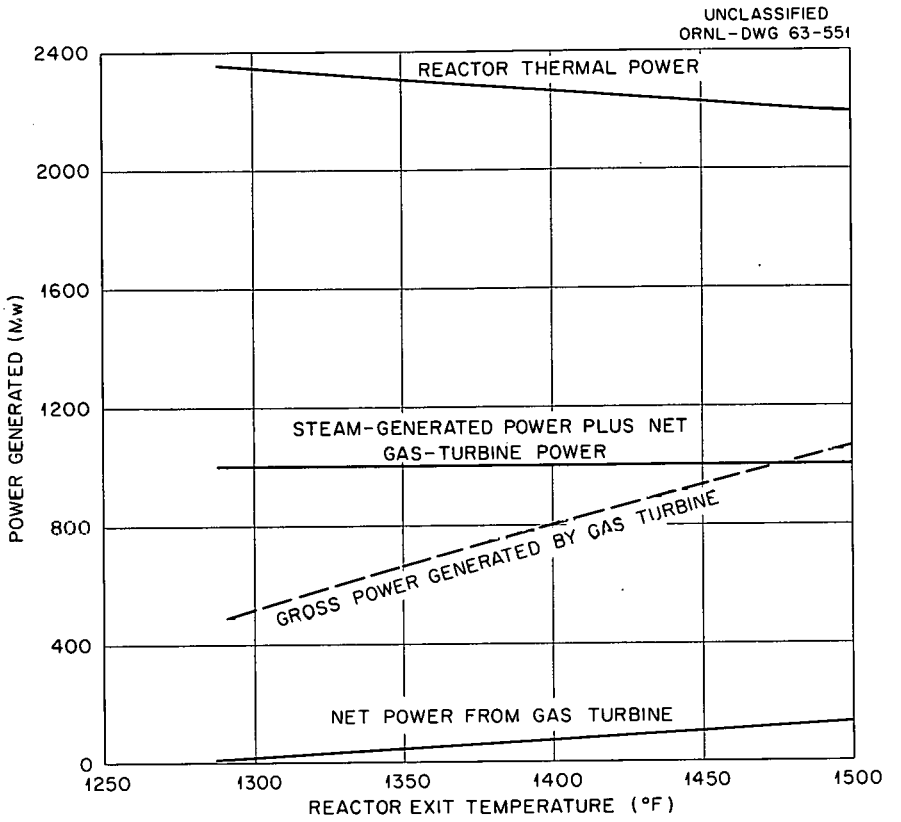

Fig. 9.5. Reactor Thermal Power and Net and Total Electrical Power from Gas Turbine for Combined Gas-Turbine and Steam-Generator Power Plant Generating 1000 Mw of Electricity. Calculated for the cycle shown in Fig. 9.2 with a compressor suction temperature of 470°F and a feedwater temperature of 269.4°F.

Figure 9.5 indicates the effect of increasing the reactor exit temperature on the required reactor thermal power and on the net power from the gas turbine for a power plant with an electrical output of 1000 Mw using a fixed compressor suction temperature of 470°F and the basic conditions of the parametric study of the system shown in Fig. 9.2. The fraction of net power supplied by the gas turbine is small at all temperatures below 1500°F, amounting to only 13.3% at 1500°F. At 1500°F, however, the gross power generated by the gas turbine alone is more than 100% of the net electrical output of the plant (1060 Mw vs 1000 Mw). The difference between the gross and net gas-turbine power is the work done on the gas by the compressor. Studies are under way to determine the economics of the system using a suction temperature of 470°F; a feedwater

temperature of 270°F, a reactor exit temperature of approximately 1500°F, and a plant designed for a total electrical output of 1000 Mw.

Comparison of Coolants for Gas-Cooled Reactors

G. Samuels M. E. Lackey

The relative merits of coolants for gas-cooled reactors were studied on the basis of their molecular weight, specific heat, thermal conductivity, and viscosity. The radiation and thermal stability and the corrosion effects of the gases or their products were not considered. The hydrocarbons, which are known to be thermally unstable at temperatures of interest, were not included, and chlorine compounds were omitted because of their high neutron-absorption cross section.

For comparing the coolants, the GCR-3 system[1] was used as the base design, and the system was divided into four components: the core, the piping, the steam generators, and the blowers. In all cases, the gas temperature, power output, and fuel element surface temperature were held constant. For evaluating core performance, both the channel diameter and the surface roughness of the fuel elements were varied to maintain the same maximum fuel surface temperature. In the steam generators, the spacing between the tubes was varied so that the total heat transferred and total surface area remained constant. This attempt to hold conditions as nearly constant as possible resulted in rather severe penalties for some of the coolants, especially for CO_2 and SO_2 in the steam generator. The thermal, nuclear, and physical properties and the performance characteristics of the coolants investigated are summarized in Tables 9.4 and 9.5.

It may be seen from Table 9.5 that H_2, SiH_4, CF_4, SiF_4, SF_6, and C_2F_6 are all superior to helium, with SiH_4, SF_6, and C_2F_6 being the best. Also, SO_2 is a very poor coolant for the GCR-3 operating condition and would be of interest only in unusual applications in which the blower suction temperature was in the range 300 to 350°F and the system pressure about 1000 to 1100 psi.

A determination was also made of the cost to a reactor system of using a mixture of neon and helium in place of helium. The following

Table 9.4. Thermal, Nuclear, and Physical Properties of Coolants for Gas-Cooled Reactors

Gas	Molecular Weight	Microscopic Absorption Cross Section at Thermal Energy (cm^{-1})	Thermal and Physical Properties at 860°F		
			Specific Heat (Btu/lb·°F)	Thermal Conductivity (Btu/hr·ft·°F)	Viscosity (lb/hr·ft)
He	4	1.95×10^{-4}	1.245	0.162	0.0885
H_2	2	1.87×10^{-2}	3.501	0.215	0.0380
CO_2	44	1.15×10^{-5}	0.269	0.0289	0.0763
SO_2	64	1.45×10^{-2}	0.190	0.0195	0.0727
SiH_4	32	4.27×10^{-2}	0.540	0.0618	0.0598
CF_4	88	1.22×10^{-3}	0.267	0.0291	0.0830
SiF_4	104	6.42×10^{-3}	0.224	0.0240	0.0785
SF_6	146	1.62×10^{-2}	0.239	0.0264	0.081
C_2F_6	138	1.88×10^{-3}	0.252	0.0225	0.080

tabulation gives an approximate value of the required pumping power for neon-helium mixtures compared with 100% helium:

Gas (vol %)		Required Pumping Power Relative to That for 100% Helium
Neon	Helium	
20	80	1.80
10	90	1.40
5	95	1.20
2.5	97.5	1.10
0	100	1.00

In attempting to place a value on the pumping power, the GCR-3 design and cost figures were used, along with the following assumptions:

1. The plant gross output remains the same.

2. All plant equipment remains the same except for the blower drives and shaft.

3. The base cost of the drives and shaft is $2,500,000 and increases as the 0.6 power of the required power input.

4. The increased power to the drives causes a like decrease in the net plant output.

5. The GCR-3 system volume is 1.5×10^6 ft^3.

Table 9.5. Performance Characteristics of Coolants for Gas-Cooled Reactors Relative to the Characteristics of Helium

Gas	Relative Pressure Drop			Relative Weight Flow	Blower Requirements		
	Core	Steam Generator	Total		Head (ft)	Suction Volume Ratio	Pumping Power Ratio
He	1.0	1.0	1.0	1.0	22,500	1.0	1.0
H_2	0.227	0.370	0.267	0.356	11,200	0.682	0.177
CO_2	2.749	10.711	4.531	4.628	10,500	0.528	2.156
SO_2	4.702	26.229	9.600	6.553	19,600	0.809	5.698
SiH_4	0.739	1.080	0.804	2.306	2,230	0.285	0.228
CF_4	1.409	5.509	2.311	4.663	2,450	0.229	0.506
SiF_4	1.784	8.245	3.231	5.558	2,990	0.245	0.740
SF_6	1.094	7.431	2.557	5.209	1,650	0.157	0.381
C_2F_6	1.168	6.275	2.311	4.941	1,560	0.155	0.341

6. The loss rate of coolant is 1 1/3 charges per year.

7. Total plant output is 5.4×10^9 kwhr/year and is valued at 6 mills/kwhr.

8. The capital cost rate is 14.5%.

For the gas mixture with 2.5 vol % neon, as an example, the pumping power would increase from 10 to 11% of plant output, the cost of the blower drives would increase about 6%, and the plant output would decrease by 1%. The yearly cost of these effects would be the following:

$$\text{Cost of larger drives} = 2.5 \times 10^6 \times 0.06 \times 0.145 = \$21,800$$

$$\text{Value of power lost} = 5.4 \times 10^9 \times 0.006 \times 0.01 = \$324,000$$

$$\text{Total cost per year} = \$346,000$$

The saving, S (per 1000 ft^3 of gas), required in the cost of the coolant to offset the above penalty would be

$$[(1500 \times 0.145) + 2000]S = \$346,000 ,$$

and thus the required decrease in coolant cost to justify a 2 1/2% addition of neon to helium would be \$156 per 1000 ft^3. Considering the linear relation between the neon content and pumping power, the saving

required for each 1% increase in neon content would be about $62.50 per 1000 ft^3 of coolant.

Parametric Study of Large Pebble-Bed Reactors

J. W. Michel

A study was made of the heat transfer and fluid flow parameters for the core of a pebble-bed reactor designed for operation in the thermal power range 2500 to 100,000 Mw. The study was limited primarily to applying the reactor heat to make saturated steam at a maximum temperature of 300°F and to optimizing the steam generator design using the recently developed GCSG computer code.[3]

Four general types of core geometries were examined before selecting the radial-flow type for a more detailed analysis. The four types were (1) upflow (levitation limited and restrained), (2) downflow, (3) folded flow, and (4) radial flow. The basic design parameters selected in an attempt to arrive at a feasible minimum-cost plant are listed below:

Thermal power level, Mw	25,000
Coolant gas	Helium
Coolant pressure, psia	1000
Core inlet temperature, °F	350
Core outlet temperature, °F	1050
Minimum core dimension, ft	15
Allowable power density for 1 1/2-in.-diam fueled spheres, w/cm^3	240

It was further assumed that a prestressed concrete pressure vessel of up to 60 ft in inside diameter could be built to contain helium at 1000 psia.

The three typical radial outflow designs studied are described in Table 9.6, which indicates the effects of changing the core geometry and the fuel-sphere size. The relative importance of the cost of the blower drive equipment as affected by the system pressure drop should be noted. To a first order approximation, the optimization of the associated steam

---

[3]A. P. Fraas and M. N. Ozisik, "Steam Generators for High-Temperature Gas-Cooled Reactors," USAEC Report ORNL-3208, Oak Ridge National Laboratory, April 8, 1963.

Table 9.6. Characteristics of Three Radial-Outflow Pebble-Bed Cores

Design	1	2	3
Core inside diameter, ft	20	20	15
Core outside diameter, ft	50	50	45
Height, ft	26	41	48
Fuel-sphere diameter, in.	4	5	5
Ratio of pumping power to heat removal	0.011	0.0036	0.0039
Pressure drop through core, psi	16.8	5.45	5.91
Core power density (maximum allowable), w/cm^3	20.6	13.1	13.1
Flow rate, lb/hr	115×10^6	115×10^6	115×10^6
Blower suction capacity, cm	4.2×10^6	4.2×10^6	4.2×10^6
Number of spheres in pebble bed	1.35×10^6	1.11×10^6	0.95×10^6
Bed volume, ft^3	42,900	69,000	67,500
Weight of spheres in bed, tons	1,400	2,200	2,150
Core inlet velocity for double entry, with 1 1/2-ft-thick reflector, ft/sec	130	130	260
Core inlet pressure drop, psi	0.37	0.37	1.5
Blower head required, ft	12,960	7,870	8,430
Drive power required for 85% blower efficiency, hp	752,000	456,000	489,000
Cost of drive equipment at $15 per unit of power required	$\$11.3 \times 10^6$	$\$6.84 \times 10^6$	$\$7.34 \times 10^6$
Estimated cost of pressure vessel at $40 per cubic foot of internal volume	$\$4.18 \times 10^6$	$\$5.71 \times 10^6$	$\$5.35 \times 10^6$
Total cost of drive equipment and pressure vessel	$\$15.5 \times 10^6$	$\$12.6 \times 10^6$	$\$12.7 \times 10^6$

generator was computed using the GCSG code. The design of one of the six axial-flow steam generators assumed to be required is described below:

Tube diameter, in.	1 1/2
Tube bundle diameter, ft	16.4
Tube bundle length, ft	66.0
Ratio of pumping power to heat removal	0.005
Steam mass flow rate, $lb/ft^2 \cdot sec$	70
Estimated tube-bundle cost, dollars	3×10^6

Fuel-Cycle Cost Study for a Large Pebble-Bed Reactor

A. M. Perry H. F. Bauman J. G. Delene

Fuel-cycle costs and conversion ratios were calculated for large fueled-graphite reactors of the pebble-bed type. Such high-temperature gas-cooled reactors have, among other features desirable in large power reactors, highly efficient power cycles and the capability of high conversion ratios, or even breeding, using a thorium cycle with fully enriched uranium.[4] The core of the reactor was assumed to be in the form of an annular bed that provided for radial flow of the coolant gas from a central gas duct outward through the fuel bed. In the reference design, the pebble-bed inside diameter was 15 ft, the outside diameter was 45 ft, and the height was 45 ft. The annular bed, starting radially from the centerline of the core, consisted of (1) the central gas duct, (2) a 1-ft-thick reflector, (3) an inner blanket, (4) the core region, (5) an outer blanket, and (6) a 2-ft-thick reflector. There was also a 2-ft-thick reflector above and below the core. At a power density of about 14 w/cm^3 of bed, the thermal power generated in a reactor of this size would be 25,000 Mw.

The reference pebble bed consisted of fuel spheres of graphite impregnated with thorium and uranium and blanket spheres of graphite containing thorium. At equilibrium the core spheres would contain, typically, 0.5 wt % uranium (U^{233} plus U^{235}) and 10 wt % thorium and the blanket spheres would have 0.3 wt % uranium and 25 wt % thorium. It was assumed

---

[4]H. F. Bauman and J. G. Delene, "Fuel-Cycle Cost Study for a Very Large Pebble-Bed Reactor," USAEC Report ORNL-TM-572, Oak Ridge National Laboratory (to be published).

that the fuel would be reprocessed on site and that the uranium and thorium would be recycled to the reactor. In the calculations the reflector thickness was held constant while the various other factors affecting fuel-cycle costs were studied individually to provide basic information applicable to a wide range of possible pebble-bed reactor designs.

MODRIC,[5] a one-dimensional, multigroup, diffusion-theory code, was used to make preliminary optimization studies and criticality calculations. For equilibrium cycle calculations the MERC code[6] was used. This code uses the MODRIC code and the ERC equilibrium code as chain links and calculates the composition of the reactor so that criticality and equilibrium conditions are simultaneously satisfied. The calculational model assumes that the uranium processed from both the core and blanket is recycled to the core and that there is continuous feed and uniform exposure of the core and blanket spheres. The cross sections used were the 34-group set tabulated by Nestor,[7] and the treatment of the thorium resonance cross sections was the same as that described by Miller.[8]

The fuel element fabrication and processing costs for a large pebble-bed reactor of this type are not presently known. Most of the economic optimizations were made at $50 per kilogram of heavy elements, but the effects of processing costs in the range from $10 to $100 per kilogram were also examined.

Fuel-Cycle Cost Optimization

The purpose of the fuel-cycle cost optimization was to determine the important variables and the way they affect the fuel-cycle costs. Each of the variables was studied, in turn, over a wide range, while the other

---

[5]J. Replogle, "A One-Dimensional Neutron Diffusion Code for the IBM-7090," USAEC Report K-1520, Oak Ridge Gaseous Diffusion Plant, September 6, 1962.

[6]L. G. Alexander, Oak Ridge National Laboratory, personal communication to H. F. Bauman, Oak Ridge National Laboratory.

[7]C. W. Nestor, Jr., "Multigroup Neutron Cross Sections," USAEC Report ORNL-CF-61-6-87, Oak Ridge National Laboratory, June 23, 1961.

[8]J. W. Miller, "Thorium Resonance Cross Sections for Thermal Breeder Reactor Study," Oak Ridge National Laboratory, January 1961, unpublished internal communication.

variables were held at their estimated optimum values. The parameters studied were blanket thickness, blanket thorium concentration, fuel burnup, blanket burnup, reactor height-to-diameter ratio, power density, moderator-to-fuel ratio, and central duct diameter. The core thorium concentration was selected automatically in the calculation based on achieving criticality at the specified conditions.

Blanket Thickness and Concentration

It was expected that the thickness and thorium concentration of the blanket would have little interaction with the other variables in the optimization. For this reason, the blanket thickness and concentration were fixed first in a preliminary study using the MODRIC code.

Blanket Thickness. Somewhat arbitrarily, but from consideration of the mechanics of sphere flow, it was decided that a blanket thickness of less than 1 ft was not practical in a reactor of this size. The effects of various combinations of blanket thickness and thorium concentration were calculated based on estimated equilibrium concentrations for the nuclides in the reactor and the simplifying assumption that blanket fissions were negligible. It was found for blanket thicknesses of 1.0, 1.5, and 2.0 ft and for thorium concentrations ranging from 6 to 40 wt % that the effect of blanket thickness was small compared with the effect of the total quantity of thorium in the blanket. Since any desired portion of the neutrons available could be absorbed in the blanket by adjusting the thorium concentration without increasing the thickness, the blanket thickness was fixed at 1 ft for the remainder of the study.

Blanket Concentration. The blanket thorium concentration was fixed by balancing the economic gain from higher neutron economy with an increase in thorium concentration against the accompanying increase in inventory charges. Preliminary calculations with the MODRIC code indicated that the optimum blanket thorium concentration was about 25 wt %, and this value was used in the remainder of the study. Later MERC equilibrium cost calculations confirmed this value.

Equilibrium Calculations

The effects of the variables obtained from equilibrium recycle calculations with the MERC code are shown in Figs. 9.6 through 9.11 and

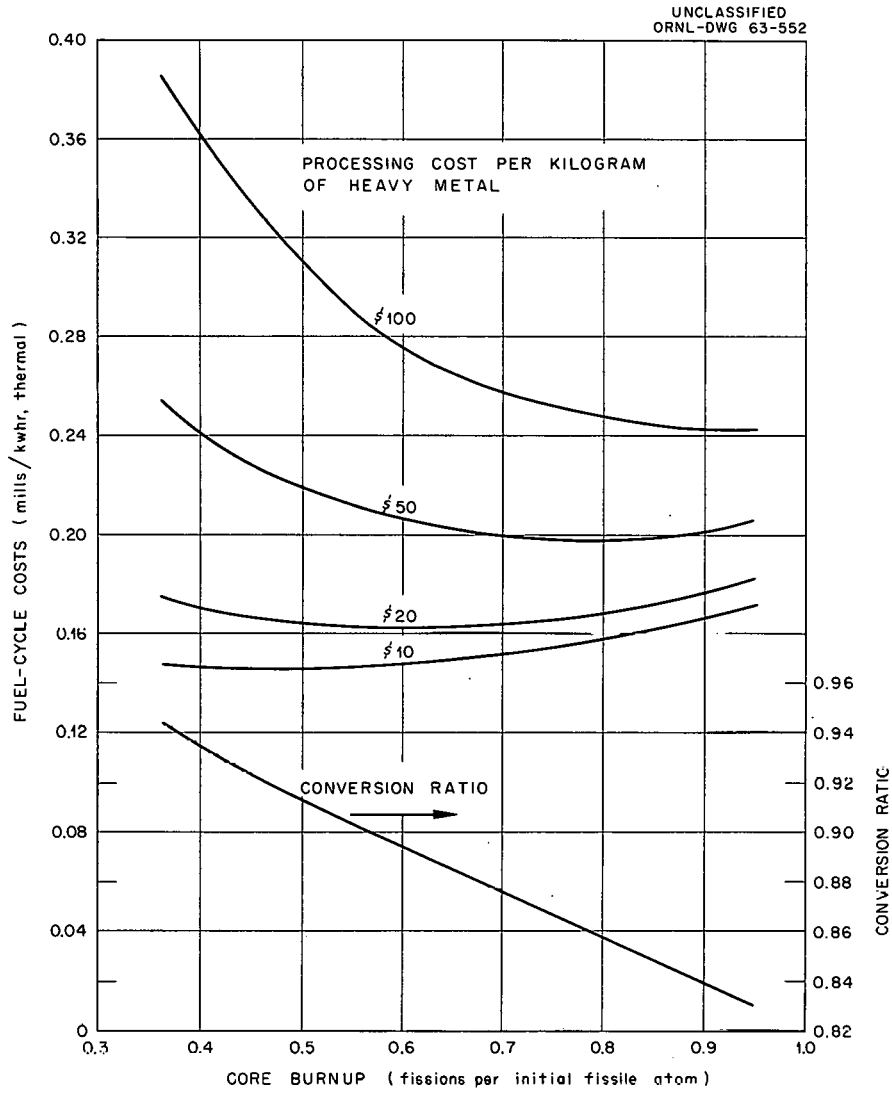

Fig. 9.6. Fuel-Cycle Costs Versus Core Burnup for Unit Processing Cost of $10 to $100 per Kilogram of Heavy Metal and a Blanket Burnup of 5.4 to 5.5%.

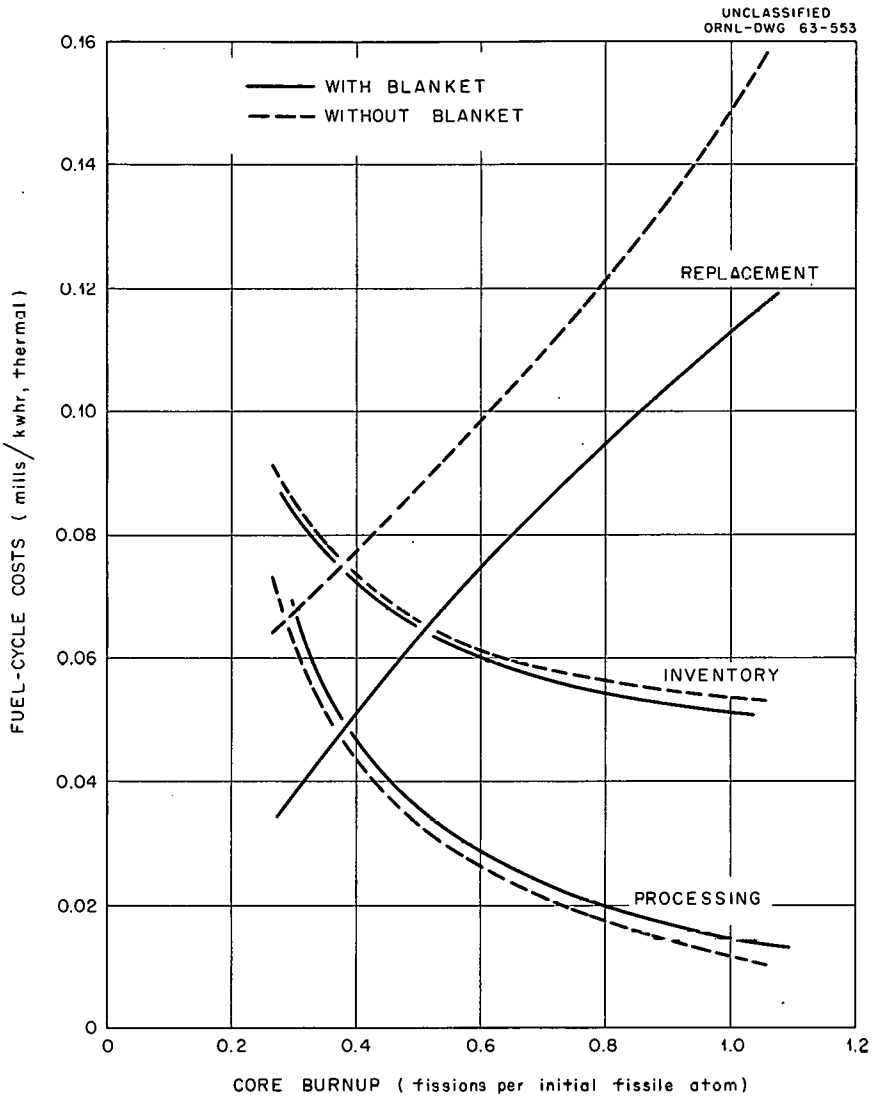

Fig. 9.7. Components of Fuel-Cycle Costs Versus Core Burnup Based on a Unit Processing Cost of $20 per Kilogram of Heavy Metal and a Blanket Burnup of 5.4 to 5.5%.

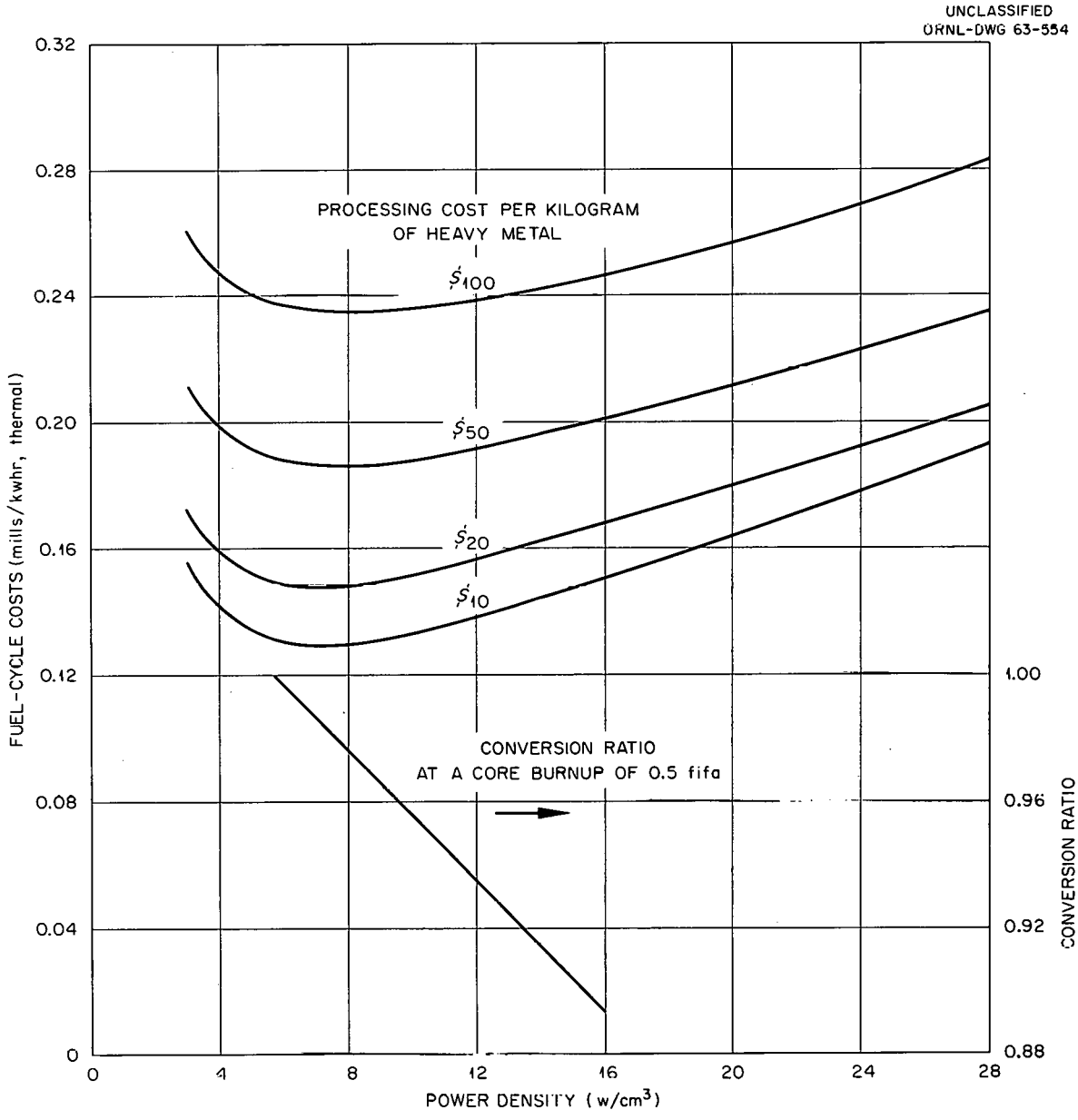

Fig. 9.8. Fuel-Cycle Costs Versus Power Density at Optimum Core Burnup for Unit Processing Costs of $10 to $100 per Kilogram of Heavy Metal.

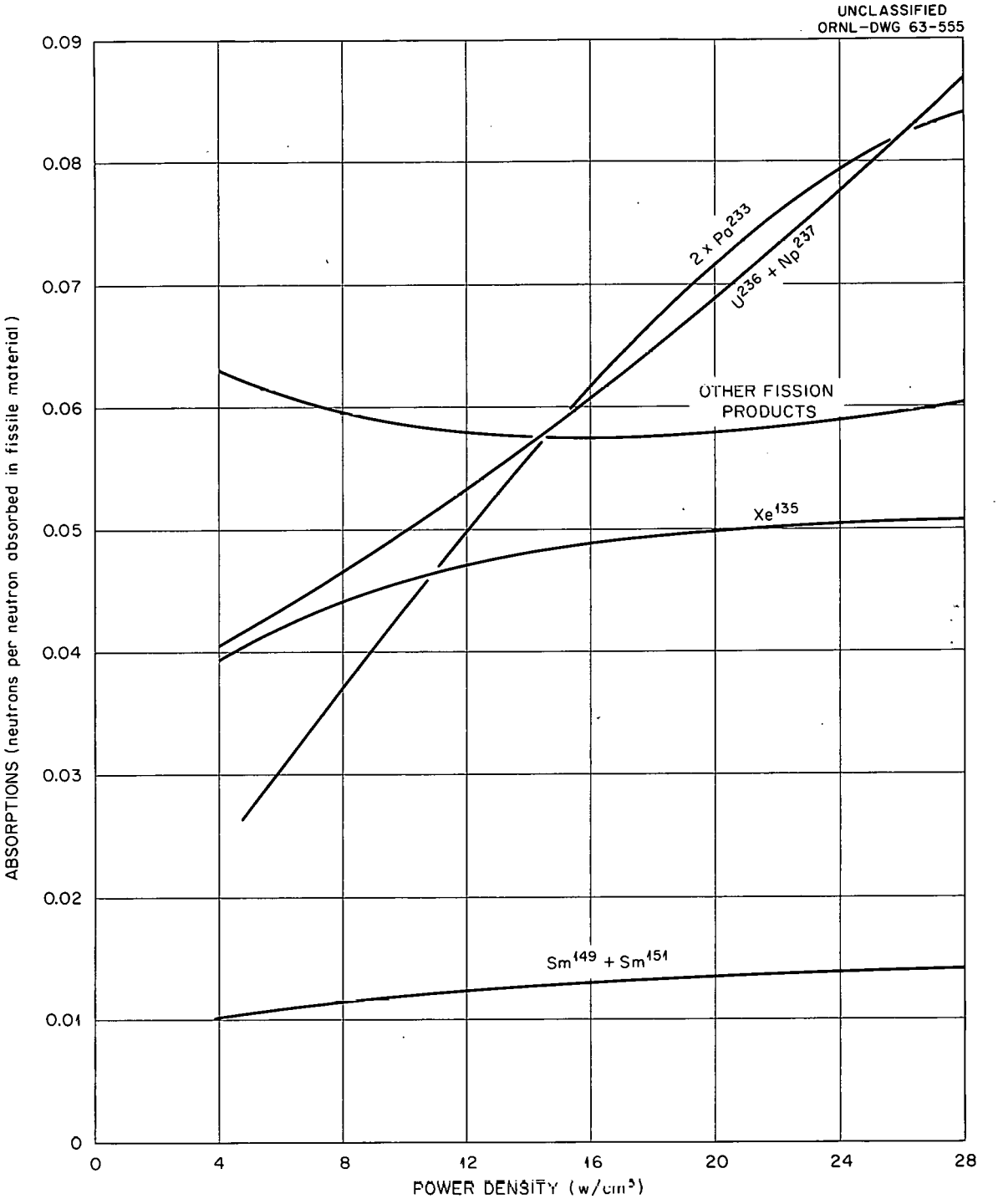

Fig. 9.9. Absorptions Versus Power Density for a Core Burnup of 0.61 to 0.86 fifa and a Blanket Burnup of 5.3 to 5.6%.

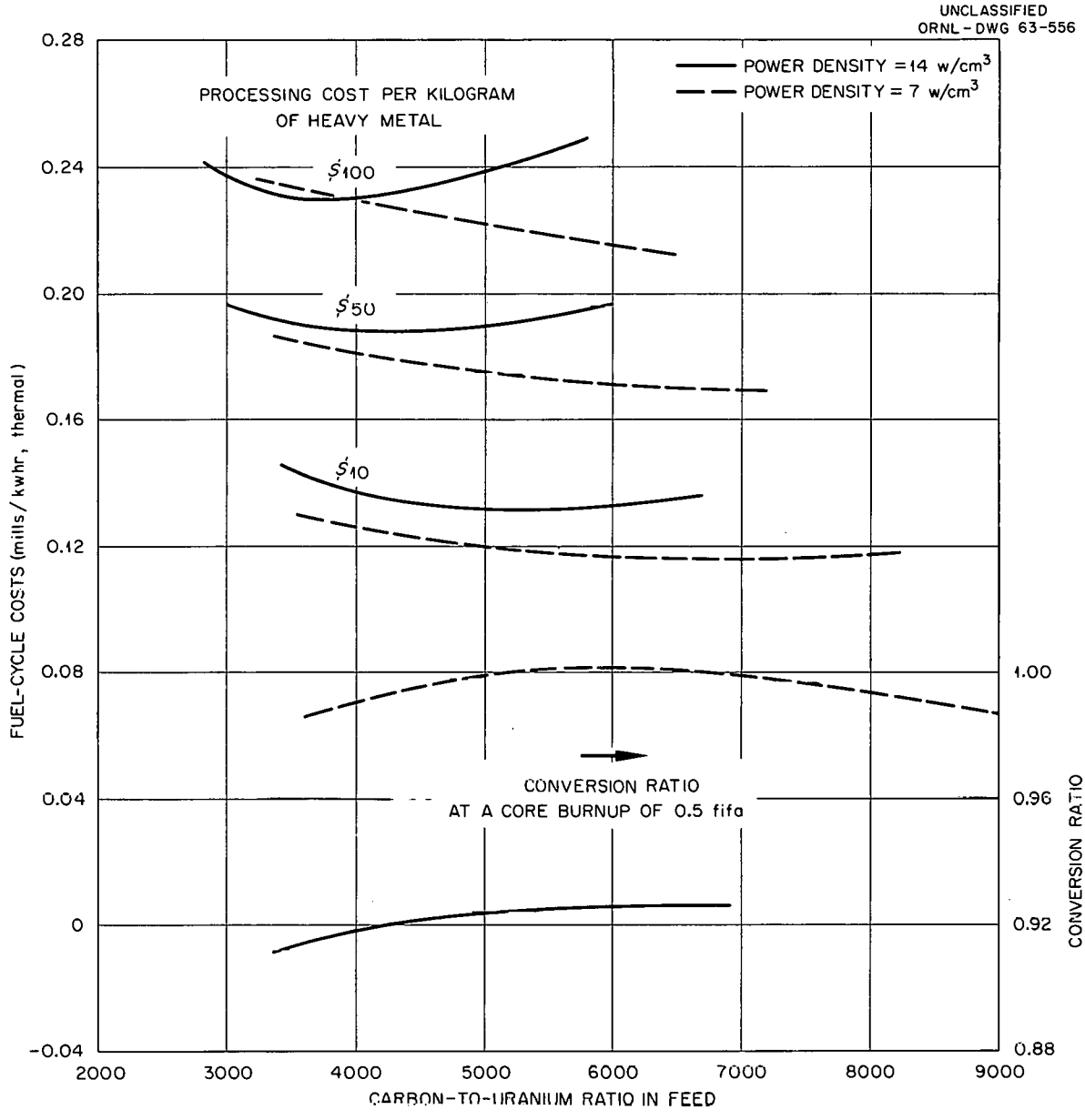

Fig. 9.10. Fuel-Cycle Costs Versus Moderator-to-Fuel Ratio at Optimum Core Burnup for Unit Processing Costs of $10 to $100 per Kilogram of Heavy Metal.

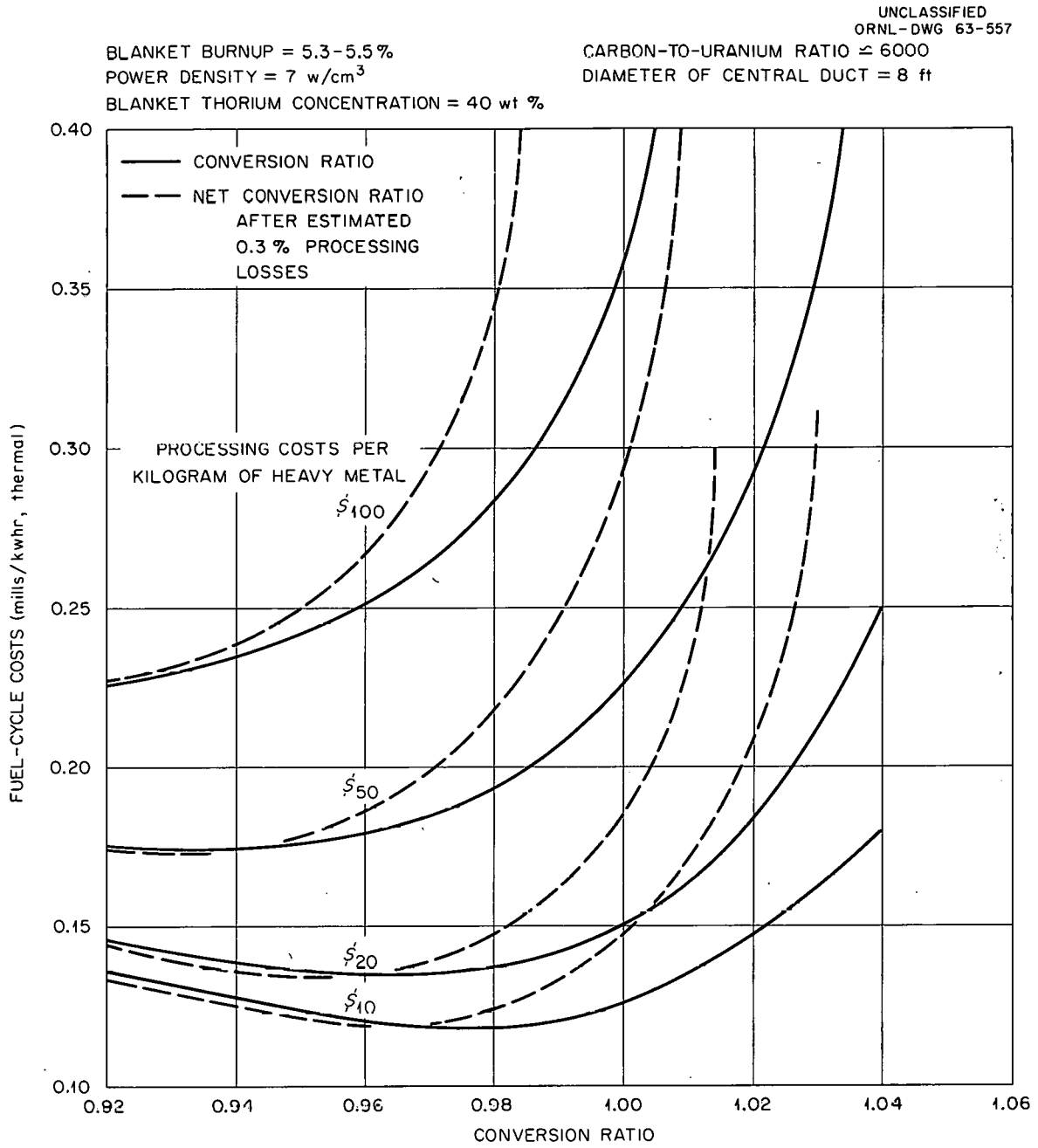

Fig. 9.11. Fuel-Cycle Costs Versus Conversion Ratio at Optimum Breeding Conditions.

described in the following sections. Unless otherwise indicated in the figures, the following reference conditions apply:

Blanket thickness, ft	1.0
Blanket thorium concentration, wt %	25
Height-to-diameter ratio	1.0
Power density, over-all average, w/cm^3	14
Carbon-to-fissile-uranium atomic ratio in feed	~3000
Inside diameter of central duct, ft	13

The economic factors that were fixed for this study are given in the following list:

Cost of fuel (by isotope)	
U^{235}	
Unit cost, $/kg	12,000
Interest, %/yr	4.75
U^{233}	
Unit cost, $/kg	12,000
Interest, %/yr	4.75
Th^{232}	
Unit cost, $/kg	19
Interest, %/yr	14
Reprocessing and fabrication time	
Core	
Cooling and processings, days	130
Fabrication, days	20
Blanket	
Cooling and processing, days	96
Fabrication, days	20
Reserve supply of core and blanket spheres, days	30
Processing losses	
Thorium, %	2.0
Uranium and Pa^{233}, %	0.3
Pa^{233} throwaway losses	
Core, %	3.5
Blanket, %	8.7
Plant factor	0.8

The unit processing costs used in the calculations included all processing and fabrication costs, and the calculations were made for processing costs of $10, $20, $50, and $100 per kilogram of heavy metal processed.

Core and Blanket Burnup. The reactor fuel-cycle costs are shown in Fig. 9.6 to be strongly influenced by core burnup, and the optimum burnup (i.e., the burnup which gives the minimum fuel-cycle cost) changes markedly with the processing costs assumed; the optimum burnup for a processing cost of $50 per kilogram of heavy elements is about 0.78 fifa (fissions per initial fissile atom). The conversion ratio decreases almost linearly with core burnup.

The blanket burnup, in contrast, has very little effect on the fuel-cycle costs. The blanket burnup is expressed as the percentage of thorium atoms that absorb neutrons per initial thorium atom. A broad, flat minimum in the fuel-cycle costs (at a unit processing cost of $50/kg) occurs at about 5.5% burnup of the blanket. The conversion ratio has a very flat maximum at the same point. The core burnup calculations were made at about the optimum blanket burnup (5.5%), and the blanket calculations were made at optimum core burnup (about 0.78 fifa).

The three main components of the fuel-cycle costs are plotted versus core burnup in Fig. 9.7 for cores with and without blanket regions. The pebble-bed configuration was the same for both core models; in the model without a blanket, the blanket spheres were replaced by fuel spheres. The processing costs shown in Fig. 9.7 are for a unit cost of $20 per kg of heavy metal; other assumed unit costs would result in simple multiples of the processing costs shown (e.g., if the unit cost were doubled, the processing costs shown would be doubled). The inventory and processing costs are nearly identical for cores with and without blanket regions; the replacement cost is consistently lower, however, for the core with a blanket because of the higher conversion ratio obtained.

Blanket Thorium Concentration. With the core and blanket burnups held at approximately their optimum values, the effect of the blanket thorium concentration was calculated. A broad optimum was found between 25 and 40 wt % thorium that was unaffected by the assumed unit processing cost. The conversion ratio increased with thorium concentration, although the effect was small at high concentrations.

Height-to-Diameter Ratio. The results presented above are for a pebble-bed with equal height and diameter, that is, 45 ft, because a cylinder with a height-to-diameter ratio of one has a minimum surface-to-volume ratio, and a reactor of this shape would be expected to have close to minimum leakage. There are possible advantages to higher ratios, however, such as: (1) a shorter flow path through the pebble bed, which would give a lower coolant pressure drop and a lower pumping cost; (2) a smaller pressure vessel diameter (but a greater height), which might result in a capital cost saving; and (3) a larger interface between core and blanket so that more neutrons would enter the blanket and give a greater blanket conversion ratio. Therefore the effects of the height-to-diameter ratios from 1.0 to 3.0 (at the same bed volume) were calculated for cores with and without blanket regions. The optimum core burnup was determined for each set of conditions, and the resulting minimum costs were calculated.

For the cores with blanket regions, there was little change in the fuel-cycle costs over the range studied. Likewise, there was little change in the over-all conversion ratio. For the cores without blanket regions, the fuel-cycle costs increased with the height-to-diameter ratio; however, the increase was small below a ratio of 2.0.

Power Density. The fuel-cycle costs at the optimum core burnup are given in Fig. 9.8 for each of several power densities. The minimum in fuel-cycle costs occurs at a power density of about 7 w/cm^3, and the optimum power density is little affected by the unit processing cost assumed.

The size of the core and, hence, the capital cost of items related to core size are inverse functions of power density. Therefore the power density of 14 w/cm^3 assumed for the other portions of this cost study may be nearer to optimum with regard to power costs, even though it is twice the optimum power density based on fuel-cycle costs alone.

The conversion ratio increases steeply as the power density is decreased. This increase results almost entirely from decreased parasitic absorptions in U^{236}, Np^{237}, and Pa^{233}, as shown in Fig. 9.9.

Moderator-to-Fuel Ratio. The fuel-cycle costs at the optimum core burnup for each of several moderator-to-fuel ratios are shown in Fig. 9.10. At a power density of 14 w/cm^3, the initial estimate of the optimum

carbon-to-uranium ratio in the core feed of about 3000 was somewhat low; the optimum for a unit processing cost of $50 per kilogram of heavy metal is actually somewhat above 4000.

A number of cases were calculated at a power density of 7 w/cm^3 to investigate the interaction of power density with moderator-to-fuel ratio at the optimum core burnup. These data are shown as dashed curves in Fig. 9.10. The minimums shift toward higher carbon-to-uranium ratios at the lower power density. There is a broad maximum in the conversion ratio at a carbon-to-uranium ratio of about 6000 for a core burnup of 0.5 fifa and either power density.

Size of the Central Duct. The size of the central duct was found to have little effect on the fuel-cycle costs over the range of interest. As the largest duct diameter (18 ft) studied was approached, the conversion ratio decreased slightly and the fuel-cycle costs slightly increased.

Optimum Fuel-Cycle Cost. The optimum fuel-cycle cost (i.e., the costs at the optimum moderator-to-fuel ratio and core burnup) at a power density of 14 w/cm^3 based on $50 per kilogram of heavy metal as the most probable unit processing cost was found to be 0.187 mill/kwhr (thermal). This is about 12% less than the corresponding cost for a reactor without a blanket. The optimum fuel-cycle cost at the optimum power density of 7 w/cm^3 was found to be 0.169 mill/kwhr (thermal).

Economic Breeding

The foregoing fuel-cycle cost study showed that the optimum reactor from an economic standpoint would have a conversion ratio somewhat greater than 90%. An extension of this study was made to determine what conditions might yield a breeder reactor with a minimum increase in fuel-cycle costs.

The following conditions, which are favorable to a high conversion ratio at little or no cost penalty, were selected:

Blanket burnup, % of thorium	5.5
Power density, w/cm^3	7
Blanket thorium concentration, wt %	40
Carbon-to-fissile uranium atomic ratio in feed	~6000
Inside diameter of central duct, ft	8
Height-to-diameter ratio	1.0

A series of cases was calculated for various core burnups, and, since the conversion ratio is a function of core burnup, it was convenient to plot the resulting fuel-cycle costs against the conversion ratio, as shown in Fig. 9.11.

The solid curves give the nuclear conversion ratio, that is, the ratio without recycle losses. As may be seen, a substantial breeding gain is possible with little cost penalty for unit processing costs of the order of $10 to $20 per kilogram of heavy metal.

The dashed curves give the net conversion ratio based on recycle losses of 0.3% of the fissile material, an arbitrary but reasonable assumption. Breeding is possible under this assumption, but at a substantial fuel-cycle cost penalty.

Processing Cost. If the unit processing cost (which includes fabrication) is reduced by a factor of 10 from $100 to $10, the optimum fuel-cycle costs, as shown in Fig. 9.11, are reduced by a factor of 2, and the corresponding conversion ratio is increased by 8% from 0.90 to 0.98; however, even for a zero unit processing cost (but normal inventory charges for material being processed), the conversion ratio is only 1.00 at the optimum fuel-cycle costs. The major factor is the inventory charge on the external inventory of fuel, which imposes an increasing economic penalty at the higher processing rates required to achieve increased breeding ratios.

Blanket. In every core studied the use of a blanket resulted in lower fuel-cycle costs and higher conversion ratios compared with the corresponding core without a blanket. Attempts to increase the over-all conversion ratio by increasing the conversion in the blanket beyond that obtained with a "minimum" blanket were not, however, successful. Increasing the transport of neutrons from the core to the blanket by changing the shape of the reactor (increasing the height-to-diameter ratio or the diameter of the inner duct) did increase the conversion in the blanket but at the cost of an even greater loss of conversion in the core. The effect on the blanket conversion of changing the core carbon-to-uranium ratio was negligible.

The transport of neutrons to the blanket could be increased by lowering the fuel element density or increasing the core void fraction. These factors were not, however, investigated in the present study.

AVR Fuel Management Study

A. M. Perry R. S. Carlsmith J. G. Delene

Various fuel management procedures are being studied for the first core loading of the German pebble-bed reactor (AVR). The objective of the study is to find a fuel composition that will give a high rate of burnup and, at the same time, be representative of fuel likely to be employed in full-scale power reactors of the pebble-bed type. The fuel must also meet the requirement that there would be no reactivity rise in the event of an accident in which steam entered the core.

The core consists essentially of a right circular cylinder, 300 cm high and 300 cm in diameter, surrounded by a graphite reflector. The core is filled with graphite spheres, 6 cm in diameter, some of which are fueled. Criticality is maintained by varying the compositions of the spheres in the core, and the four control rods are used only for shutdown.

The combined weight fraction of uranium and thorium in the spheres that contain fuel has been tentatively set at 5%. This is the lower limit of the range which economic studies of full-scale pebble-bed reactors indicate to be of interest; also, since this was to have been the loading for the PBRE, the fuel testing program has to date produced more information on this composition than on heavier loadings. The fraction of the spheres to contain fuel in the initial loading has been tentatively set at one-third. A lower fueled fraction would result in higher temperatures in the fueled spheres, while a higher fraction would give a decreased rate of burnup. Some calculations have been made with smaller loadings in the fueled spheres or with smaller fueled fractions in order to determine how much the burnup rate could be increased. The uranium enrichment is to be 90%.

Two basic methods of controlling reactivity during burnup are available. In the first, the initial uranium loading is made greater than necessary for criticality (i.e., the thorium-to-uranium ratio is less than that required for criticality), and the excess reactivity is offset by poisoning some of the nonfueled spheres. The poisoned spheres are then gradually removed and replaced by graphite spheres as uranium burnup proceeds. The available lifetime for the fuel is determined by the thorium-

to-uranium ratio, as indicated in Table 9.7. Spheres poisoned with thorium, boron, and a rare earth mixture have been considered. If thorium were used for the poisoned spheres in a core with fueled spheres with a thorium-to-uranium ratio of 4.3, 67,000 poisoned spheres containing 5 wt % thorium would be required, that is, all the unfueled spheres would be poisoned. The same amount of poisoning would be obtained with only 1000 spheres containing 0.5 wt % boron or 560 spheres containing 0.5 wt % Lindsay Mix (rare earth oxides).

Table 9.7. Effect of Thorium-to-Uranium Ratio on Fuel Lifetime and Burnup

	Case 1	Case 2	Case 3
Initial thorium-to-uranium ratio in fuel spheres	12.6	7.3	4.3
Fuel lifetime, days	0	268	727
Fuel burnup, Mwd/T	0	36,300	98,400

In the second method, a thorium-to-uranium ratio is chosen that makes the reactor just critical when the desired initial fraction of spheres is fueled. Reactivity is then maintained by inserting new fueled spheres (of the same or different composition from the original fueled spheres) in place of nonfueled spheres or in place of fueled spheres. In the cases calculated thus far, the spheres used to maintain criticality all contained the uranium concentration of the original spheres but contained either no thorium, one-half the thorium of the original spheres, or the full thorium concentration of the original spheres. The results of these calculations are presented in Table 9.8.

Calculations were also made for a combination of the two methods of reactivity control in which poisoned sphere removal was followed by the addition of more fueled spheres. The burnups achieved for three different starting conditions are given in Table 9.9.

The calculations were performed with a one-dimensional diffusion-theory model in 27 energy groups, that is, the MODRIC code with the Modburn lifetime feature. In all cases where only one-sixth of the spheres were

Table 9.8. Calculated Fuel Characteristics at the End of 350 and 700 Days of Operation Based on Three Types of Reactivity Control by Fuel Addition

	Conditions At 350 Days	Conditions At 700 Days
Reactivity Control by Addition of Spheres Containing Original Quantity of Uranium and No Thorium		
Number of spheres initially fueled	1/3	1/3
Initial thorium-to-uranium ratio in fueled spheres	12.6	12.6
Fuel burnup, Mwd/T	33,000	54,000
Fraction of barren spheres replaced by fueled spheres	0.415	0.775
Number of spheres initially fueled	1/6	1/6
Initial thorium-to-uranium ratio in fueled spheres	7.6	7.6
Fuel burnup, Mwd/T	45,000	80,000
Fraction of barren spheres replaced by fueled spheres	0.152	0.352
Reactivity Control by Addition of Spheres Containing Original Quantity of Uranium and One-Half the Original Quantity of Thorium		
Number of spheres initially fueled	1/3	1/3
Initial thorium-to-uranium ratio in fueled spheres	12.6	12.6
Fuel burnup, Mwd/T	30,000	46,000
Fraction of barren spheres replaced by fueled spheres	0.552	1.011
Number of spheres initially fueled	1/6	1/6
Initial thorium-to-uranium ratio in fueled spheres	7.6	7.6
Fuel burnup, Mwd/T	45,200	75,700
Fraction of barren spheres replaced by fueled spheres	0.252	0.466
Reactivity Control by Addition of Fueled Spheres of Initial Composition		
Number of spheres initially fueled	1/6	1/6
Initial thorium-to-uranium ratio in fueled spheres	7.6	7.6
Fuel burnup, Mwd/T	44,700	70,700
Fraction of barren spheres replaced by fueled spheres	0.294	0.556

Table 9.9. Calculated Fuel Characteristics for Three Starting Conditions Based on Reactivity Control by Poisoned Sphere Removal Followed by Uranium Addition

	Case 1	Case 2	Case 3
Number of spheres initially fueled	1/3	1/3	1/4
Initial thorium-to-uranium ratio in fueled spheres	9.4	7.8	5.5
Percentage of unfueled spheres initially poisoned[a]	0.30	0.54	0.62
Maximum rate of poisoned sphere removal, spheres per day	4.9	3.5	3.6
Maximum rate of uranium addition, spheres per day	53.4	45.8	35.8
Operating time to boron burnout, days	82	195	249
Fuel burnup at time of boron burnout, Mwd/T	11,100	26,400	44,800
Total fuel lifetime, days	700	700	700
Total fuel burnup, Mwd/T	66,100	75,500	101,500
Fraction of barren spheres replaced with fueled spheres	0.479	0.336	0.206

[a]Poisoned spheres contain 0.5 wt % boron.

fueled initially, the reactor was assumed to operate initially at one-half of full power so that the average power density in the fueled spheres would not exceed the average rating of 1.4 kw per sphere. The fuel burnup values in the tables are for the initial fuel loading only.

A comparison of the results for cores with one-third of the spheres fueled indicates that greater burnup can be obtained if poison removal is used; however, the thorium-to-uranium ratios necessary to obtain a full two years of lifetime using poison removal give a positive steam reactivity coefficient. Further calculations indicated that no reactivity rise would result from the addition of any amount of steam if the thorium-to-uranium ratio was at least 7.8 for a hot core and at least 9.4 for a cold core when one-third of the spheres were fueled. If one-fourth of the spheres were fueled, the minimum thorium-to-uranium ratio would be 5.5 for a hot core.

The fuel compositions that would give a zero steam coefficient with a hot core were investigated further. Since with these thorium-to-uranium ratios the removal of poison would not by itself give two years of lifetime, a combination of removal of poison followed by an addition of fuel would be required. Boron was used as the initial poison. When all the boronated spheres had been removed, spheres containing only uranium would be added to maintain criticality. The results of these calculations are presented in Table 9.9. (The reactor here was assumed to operate at full power even when less than one-third of the spheres were fueled, since the results obtained apply equally well to a case with one-third of the spheres fueled with a composition of 3.75 wt % uranium plus thorium.)

Analyses of Nozzle-to-Shell Attachments

B. L. Greenstreet R. L. Maxwell

One of the basic problems associated with pressure vessel design is the design of nozzle attachments. In the case of spherical shells, the theoretical analysis of single radially attached nozzles is now in the development stage. Theoretical methods for examining nozzles that are nonradially attached (hillside nozzles) do not exist, however, and definitive experimental results are needed before methods now being considered can be evaluated.

In order to obtain the required data, an experimental program is being conducted to examine the stress distributions around both radially and nonradially attached nozzles in test models made of steel and instrumented with strain gages. Attachment angles of 0, 15, 30, and 45 deg are being investigated. Other parameters are nozzle diameter and thickness and the influence of internal nozzle stubs. The models are being subjected to axial, moment, and transverse (or normal) loads on the nozzles and to internal pressures. The results will be used for making design correlations and for comparison with stresses calculated from existing theories for radially attached nozzles.

In the test program, single nozzles will be sequentially attached to a hemispherical shell. The nozzles are divided into series according

to outside diameter, and the nozzles in each series will be tested at all attachment angles before a new series is started. The dimensions of the nozzles are given in Table 9.10, where

L_o = length of external nozzle, in.

L_i = maximum length of internal stub, in.

a = radius to middle of nozzle wall, in.

h = thickness of nozzle wall, in.

t = thickness of hemispherical shell, in.

r = radius to middle of hemispherical shell, in.

β = inverse of characteristic length of nozzle

$$= \left[\frac{3(1-\nu^2)}{a^2h^2}\right]^{1/4},$$

βL = dimensionless length of nozzle,

ν = Poisson's ratio.

The radius and thickness of the hemispherical shell are given in the heading of Table 9.10. As may be seen, the common factors of the test series are the radius-to-thickness ratios.

Table 9.10. Nozzle Dimensions for Test Series I, II, and III with r = 15.254 in. and t = 0.375 in.[a]

Test Series	L_o	L_i (b)	a	h	Outside Diameter of Nozzle (in.)	a/h	t/h	r/a	β	βL
I	4	4	1.188	0.25	2.625	4.75	1.5	12.85	2.35	9.4
	4	4	1.25	0.125	2.625	10.0	3.0	12.20	3.24	12.96
	4	4	1.281	0.0625	2.625	20.5	6.0	11.91	4.55	18.20
II	6	6	2.5	0.25	5.25	10.0	1.5	6.10	1.618	9.71
	6	6	2.563	0.125	5.25	20.5	3.0	5.95	2.315	13.89
III	10	10	3.75	0.375	7.875	10.0	1.0	4.07	1.078	10.78
	10	10	3.844	0.1875	7.875	20.5	2.0	3.97	1.964	19.64

[a] See text for definition of terms.

[b] For a nonradially attached nozzle, this dimension will have to be reduced.

The model with the first radial nozzle described in Table 9.10 was fabricated and instrumented, and tests were completed for an internal pressure load and an axial load on the nozzle. The remaining loads to be applied to the model with this nozzle configuration are a pure bending moment, a side force, and a torque on the nozzle.

Strain gages of 1/8-in. gage length were mounted in identical positions along meridional lines 180 deg apart on the nozzle and shell. In this way, duplicate readings were obtained for each gage position. A 90-deg, two-gage rosette, with the gages aligned in the principal stress directions, was used at each position. Corresponding gages were placed on the outer and inner surfaces. The gages inside the model were positioned radially opposite those on the outside. The gages on the inside make it possible to separate the total stresses into bending and membrane components. Additional instrumentation will be installed for the three remaining tests.

The model and the associated test equipment are shown in Fig. 9.12, and curves of the total principal stresses on the outer surfaces of the shell and nozzle are presented in Figs. 9.13 through 9.16. Figures 9.13

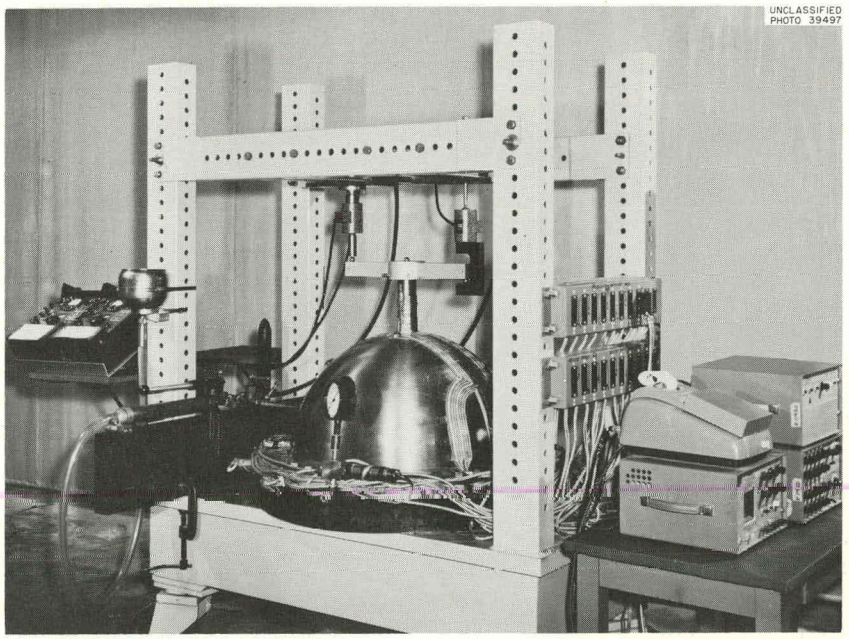

Fig. 9.12. Test Model and Equipment for Obtaining Experimental Data on Stress Distributions Around Nozzle-to-Shell Attachments.

and 9.14 are for an internal pressure loading and Figs. 9.15 and 9.16 are for an axial loading on the nozzle. The points on the curves are data points corresponding to gage locations.

The data of Figs. 9.13 through 9.16 indicated that additional gages were required in the immediate vicinity of the nozzle-to-shell junction

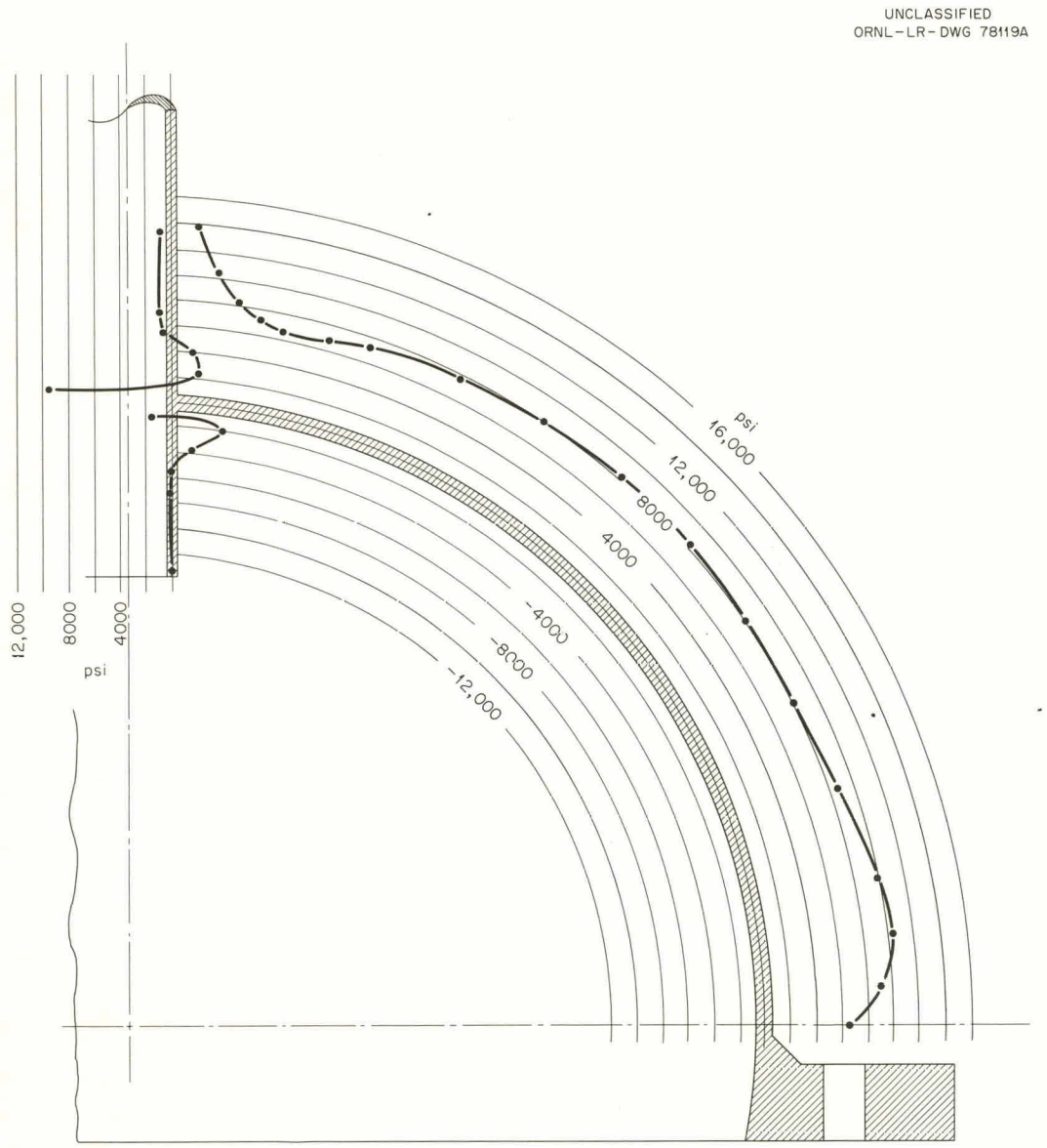

Fig. 9.13. Total Stresses in Meridional and Axial Directions on Outer Surfaces of Shell and Nozzle Under Internal Pressure Loading of 400 psi.

before the peak stresses could be adequately determined from the experimental data alone. Therefore additional strain gages with a gage length of 1/32 in. have been installed on the outer surfaces at the junction.

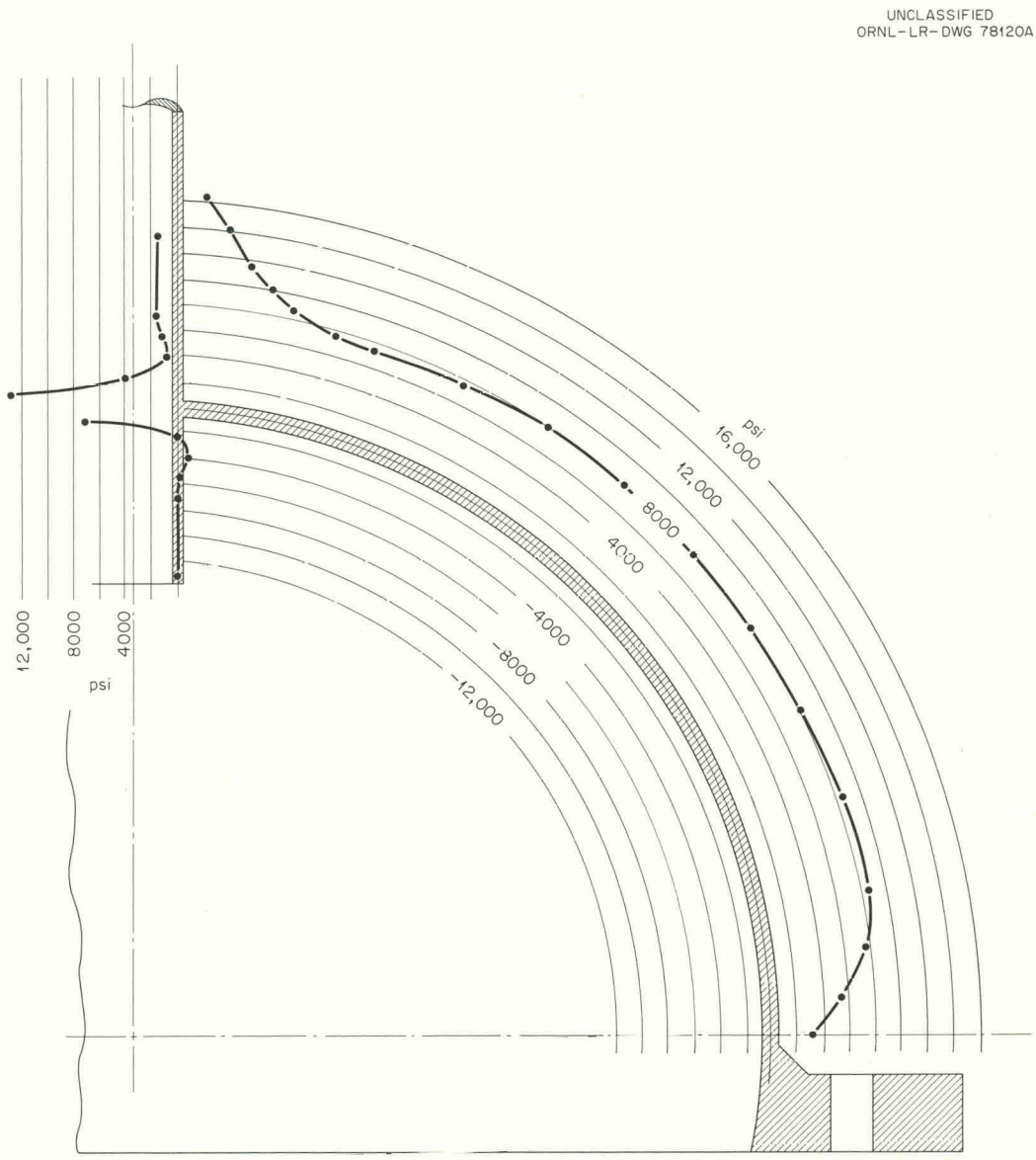

Fig. 9.14. Total Stresses in Parallel or Circumferential Directions on Outer Surfaces of Shell and Nozzle Under an Internal Pressure Loading of 400 psi.

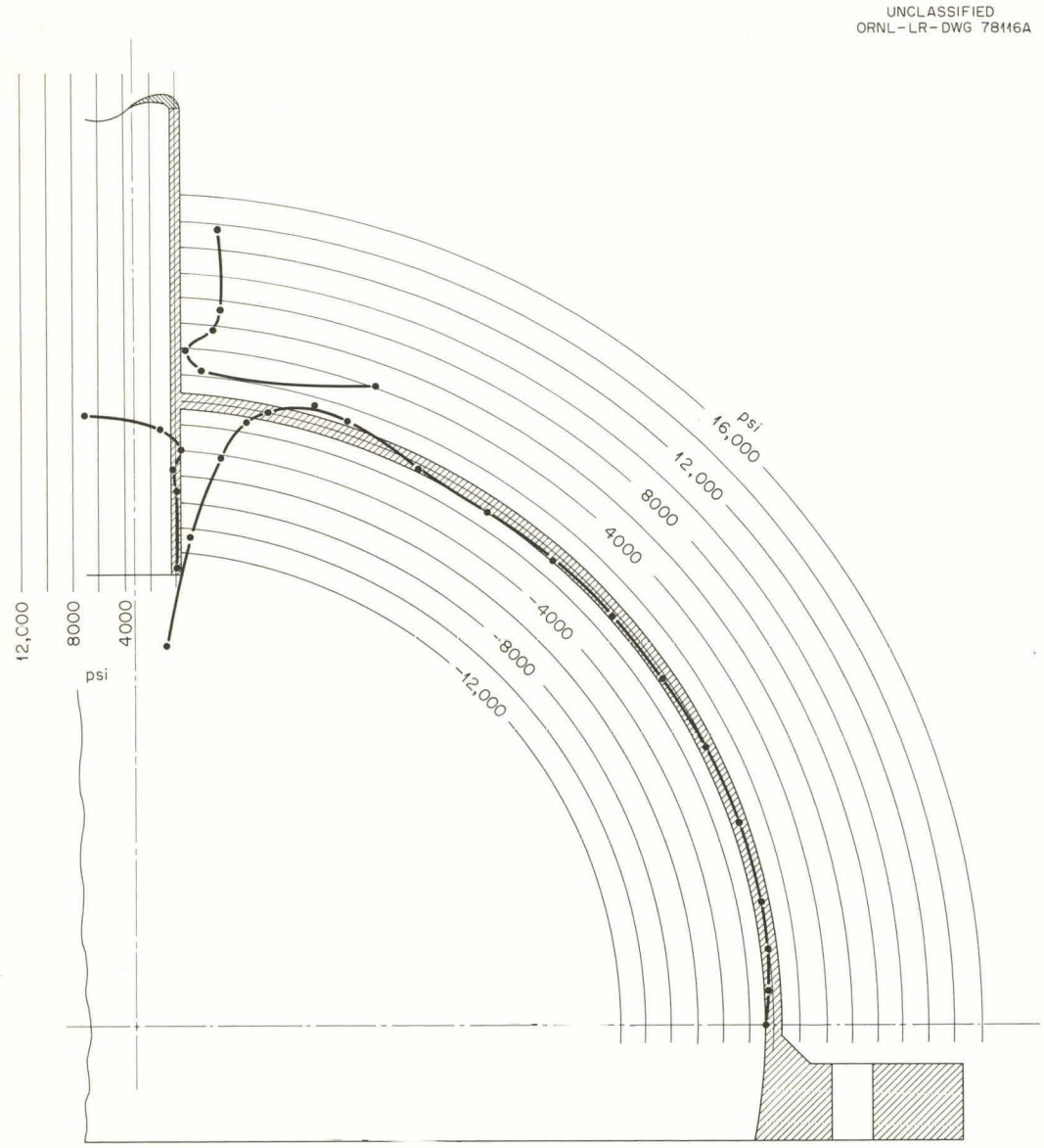

Fig. 9.15. Total Stresses in Meridional and Axial Directions on Outer Surfaces of Shell and Nozzle Under an Axial Load on the Nozzle of 6000 lb.

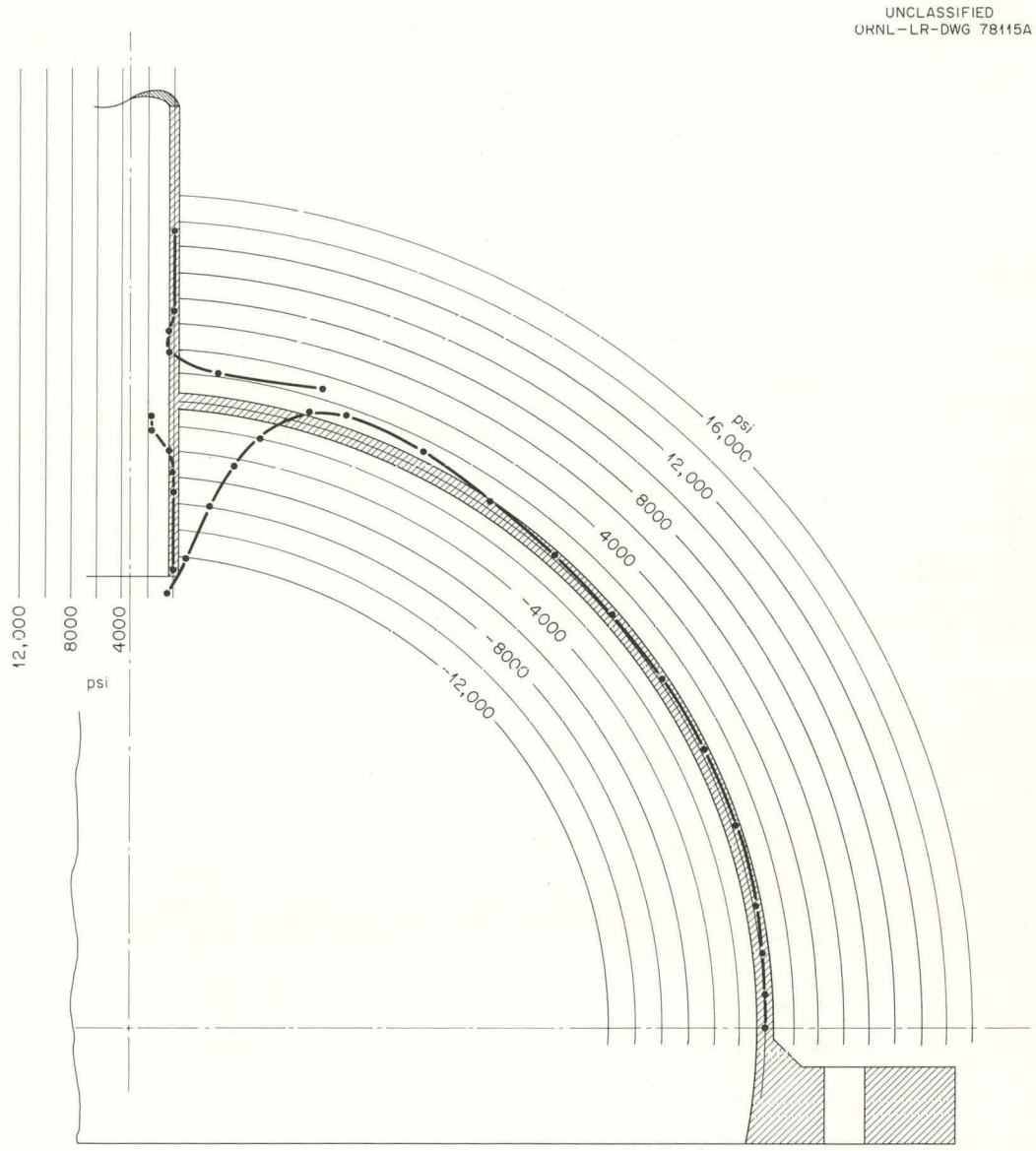

Fig. 9.16. Total Stresses in Parallel or Circumferential Directions on Outer Surfaces of Shell and Nozzle Under an Axial Load on the Nozzle of 6000 lb.

Neutron Captures in Second- and Higher-Generation Fission-Product Poisons

A. M. Perry W. E. Thomas R. S. Carlsmith

It has been recognized for many years (see for example ref. 9) that neutron capture in fission-product poisons may produce other nuclides having appreciable neutron capture cross sections and that, as a consequence, the total poisoning effect of fission fragments and their products may significantly exceed that which would be expected from the primary fission-product poisons. Interest in the problem of allowing correctly for this effect has increased with the interest in reactors having the potential for large fractional burnup of the fuel, such as fueled-graphite gas-cooled reactors. In order to establish the magnitude of the contribution of secondary poisons to the total neutron capture rate under conditions of interest to the gas-cooled reactor program, a study was performed in which the individual contribution of each nuclide in the group ranging from Nd^{145} to Eu^{155}, both to the primary and to the secondary fission-product poisoning, was calculated and recorded.

The chain studied is depicted below:

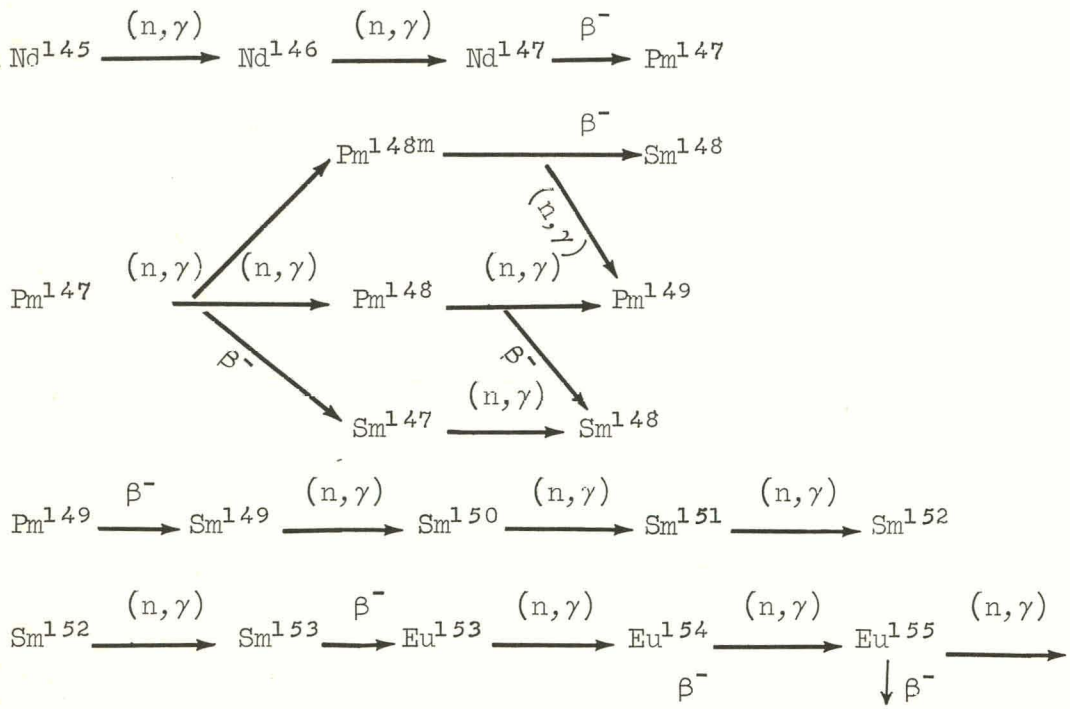

This group of nuclides was selected because it accounts for roughly one-half the total poisoning (exclusive of Xe^{135}) and is expected to contribute a large portion of the secondary poisoning.

In this study, primary poisons were defined as those produced directly from fission or by one or more beta decays from a primary fission fragment. Secondary poisons were defined as those produced by neutron capture in a nuclide which might itself be either a primary or a secondary poison or by beta decay of a secondary poison; that is, secondary poisons were considered to be those derived from primary poisons by one or more neutron captures. It was considered that a given nuclide could be both a primary and a secondary poison. The poisoning effect of the nuclide chain depicted above was defined as the neutron capture rate in these nuclides divided by the neutron capture rate in fissile material averaged over the life of the fuel. This quantity was computed as a function of neutron spectrum, fuel specific power, and fractional fuel burnup (expressed in fissions per initial fissile atom, or fifa). Calculations were made for both U^{235} and U^{233} fuel and on either of two assumptions regarding fuel concentration, namely, that fissile material was replaced at a rate equal to the burnup rate or that it was replaced at a rate equal to 40% of the initial burnup rate. The flux was kept constant.

The calculations were performed with the aid of the computer code NUCY[10] (programmed for the IBM 7090 computer), which provides simultaneous solutions of the equations

$$N_i = S_i - \alpha_i N_i ,$$

where N_i is the concentration of the ith nuclide, S_i is a source term involving direct yield from fission or production from a precursor by beta decay or by neutron capture, and α_i is the destruction probability involving decay, neutron capture, or both. Results of the calculations

---

[9]J. B. Sampson et al., "Poisoning in Thermal Reactors Due to Stable Fission Products," USAEC Report KAPL-1226, Knolls Atomic Power Laboratory, Oct. 4, 1954.

[10]D. R. Vondy, "Development of a General Method of Explicit Solution to the Nuclide Chain Equations for Digital Machine Calculations," USAEC Report ORNL-TM-361, Oak Ridge National Laboratory, Oct. 17, 1962.

are summarized in Table 9.11, where the spectral index is the fraction of fissions produced by epithermal neutrons, the specific power is given in megawatts of heat per kilogram of fissile material, and the fuel replacement rate is given as an initial conversion ratio, although it should be understood that the replacement fuel is the same as burned fuel, that is, U^{235} is replaced with U^{235} and U^{233} is replaced with U^{233}.

It is to be noted again that the poison fractions given are averaged over the fuel life. They are thus not terminal values but are more representative of the average performance at any time in a reactor fueled by continuous fuel charge and discharge (uniform graded-exposure fuel distribution). The details of these calculations, which show the captures in individual nuclides for all cases, will be published in a separate report, but the data given in Table 9.11 are sufficient to demonstrate the significance of the secondary captures and to illustrate their dependence on key reactor parameters.

Fast-Neutron Flux Monitors

A. M. Perry C. A. Preskitt

A number of authors have studied the use of foil activation for the measurement of neutron fluxes in the Mev energy range. A recent article by Passell and Heath[11] summarizes much of the available information. In most applications of this technique, some means is used to define an effective threshold and an associated effective cross section in such a way that the activation may be assumed to integrate the flux above the effective threshold.

In nearly every case the reactions are not, strictly speaking, threshold reactions at all; that is, the (n,p) reactions commonly used for this purpose nearly all have positive Q values so that the reaction takes place even for zero-energy neutrons. The reaction cross section is, nevertheless, a steeply rising function of neutron energy because of the coulomb barrier of the nuclear charge to the escaping protons. Various methods

[11] T. O. Passell and R. L. Heath, "Cross Sections of Threshold Reactions for Fission Neutrons: Nickel as a Fast Flux Monitor," Nucl. Sci. Eng., 10(4): 308–315 (August 1961).

Table 9.11. Poison Fractions for Nuclides from Nd^{145} to Eu^{155}

Fuel	Fraction of Epithermal Fissions	Initial Conversion Ratio	Specific Power (Mw/kg)	Fuel Burnup (fifa)	Poison Fraction		Secondary Poisons as Percentage of Total Poisons
					Total Poisons	Secondary Poisons	
					$\times 10^{-4}$	$\times 10^{-4}$	
U^{235}	0.1	1.0	1.0	0.5	294	71	24.3
	0.1	1.0	1.0	1.0	446	144	32.4
	0.1	1.0	1.0	1.5	569	213	37.4
	0.1	0.4	1.0	0.5	333	91	27.2
	0.1	0.4	1.0	1.0	589	226	38.4
	0.1	0.4	1.0	1.5	850	390	45.9
	0.3	1.0	0.5	0.5	413	122	29.7
	0.3	1.0	0.5	1.0	614	231	37.6
	0.3	1.0	0.5	1.5	771	327	42.0
	0.3	1.0	1.0	0.5	434	138	31.8
	0.3	1.0	1.0	1.0	655	258	39.4
	0.3	1.0	1.0	1.5	825	364	44.2
	0.3	1.0	2.0	0.5	442	147	33.2
	0.3	1.0	2.0	1.0	681	279	40.9
	0.3	1.0	2.0	1.5	863	394	45.6
	0.3	0.4	0.5	0.5	474	155	32.7
	0.3	0.4	0.5	1.0	796	339	42.5
	0.3	0.4	0.5	1.5	1130	571	50.5
	0.3	0.4	1.0	0.5	499	173	34.7
	0.3	0.4	1.0	1.0	859	388	45.1
	0.3	0.4	1.0	1.5	1197	623	52.0
	0.3	0.4	2.0	0.5	509	183	36.0
	0.3	0.4	2.0	1.0	881	414	47.0
	0.3	0.4	2.0	1.5	1247	665	53.3
U^{233}	0.3	1.0	0.5	0.5	206		20.9
	0.3	1.0	0.5	1.0	305		28.4
	0.3	1.0	0.5	1.5	386		33.4
	0.3	1.0	1.0	0.5	218		23.4
	0.3	1.0	1.0	1.0	329		30.7
	0.3	1.0	1.0	1.5	418		35.1
	0.3	1.0	2.0	0.5	226		25.2
	0.3	1.0	2.0	1.0	345		32.6
	0.3	1.0	2.0	1.5	445		37.0
	0.3	0.4	0.5	0.5	231		23.6
	0.3	0.4	0.5	1.0	399		34.2
	0.3	0.4	0.5	1.5	574		41.5
	0.3	0.4	1.0	0.5	245		26.0
	0.3	0.4	1.0	1.0	430		36.1
	0.3	0.4	1.0	1.5	618		43.0
	0.3	0.4	2.0	0.5	255		27.8
	0.3	0.4	2.0	1.0	452		37.7
	0.3	0.4	2.0	1.5	650		44.4

have been used in the past to define an effective threshold energy, but none of these have been based directly on the intended application to flux monitoring.

If the neutron energy spectrum is known for some case, an effective cross section can be defined for any threshold energy, E_o, as

$$\sigma_{eff}(E_o) \equiv \frac{\text{total reaction rate}}{\text{integrated flux above } E_o} .$$

Mathematically this definition may be written as

$$\sigma_{eff}(E_o) = \frac{\int_0^\infty \sigma(E)\,\phi(E)\,dE}{\int_{E_o}^\infty \phi(E)\,dE} ,$$

where $\phi(E)$ is the energy dependence of the neutron flux spectrum and $\sigma(E)$ that of the cross section in question. The numerator of this equation is the total reaction rate and may be determined, for example, from the intensity of some activity resulting from the reaction. For any value of E_o, this cross section will obviously depend on the shape of the neutron energy spectrum, and if flux monitoring is the objective, a reasonable choice of E_o is the value that results in as nearly as possible the same value of $\sigma_{eff}(E_o)$ for a range of differing spectra.

The basis given above for determining the effective threshold and effective cross section was applied to the (n,p) reactions for Ni^{58} and S^{32} and to the fission of Np^{237}. These cross sections were analyzed in spectra computed by the GAM-I code[12] for the cores of typical water-moderated test reactors (ORR, GETR) and the core of a graphite reactor (EGCR). The method is illustrated for the case of Np^{237} fission in Fig. 9.17. The expression given above for $\sigma_{eff}(E_o)$ is evaluated as a function of E_o for the two spectra and the intersection of the two curves defines the value

---

[12] G. D. Joanou and J. S. Dudek, "GAM-I: A Consistent P_1 Multigroup Code for the Calculation of Fast Neutron Spectra and Multigroup Constants," USAEC Report GA-1850, General Atomic, June 28, 1961.

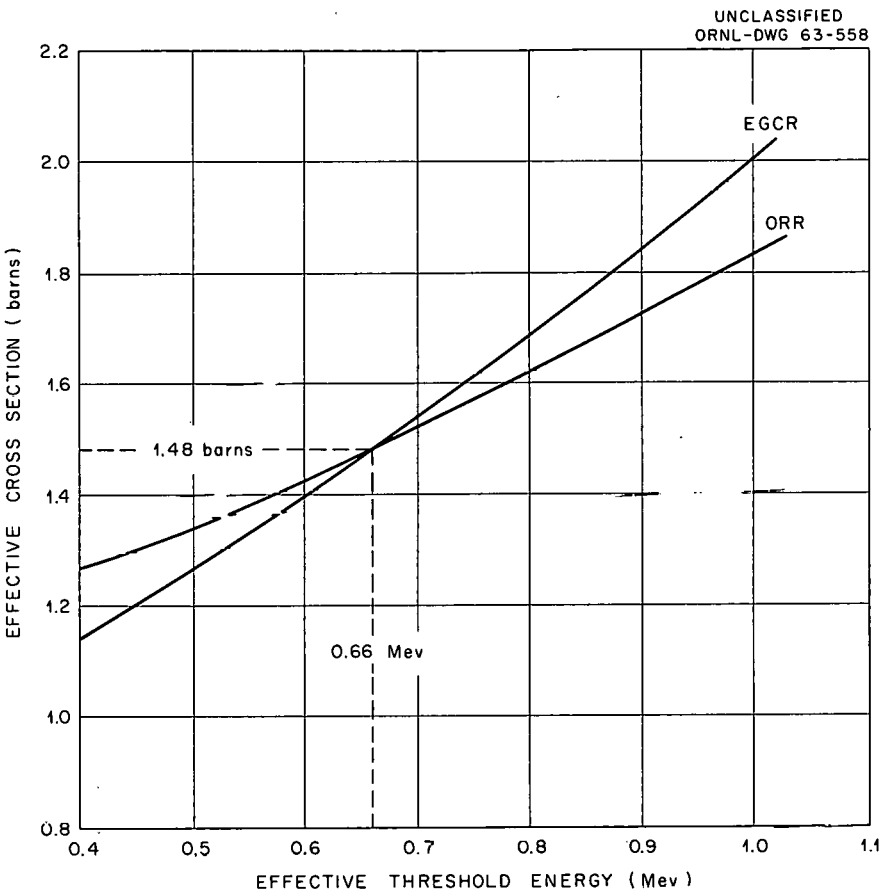

Fig. 9.17. Determination of Effective Threshold and Effective Fission Cross Section for the $Np^{237}(n,f)FP$ Reaction.

of E_o for which the monitoring will be exact for both spectra. The cross section data used for this example were obtained from Hughes and Schwartz.[13]

The relatively low energy (0.66 Mev) of the effective threshold for the fission of Np^{237} has led to its frequent use as a fast-neutron monitor for irradiation experiments. Since the decay of selected fission products is used to determine the number of Np^{237} fissions which have occurred, it is of interest to estimate their yield from the other fission reactions that may take place. Specifically, since Np^{237} has a large capture cross section for low-energy neutrons, the yield from the following chain was calculated for a typical irradiation in the ORR:

---

[13]D. J. Hughes and R. B. Schwartz, Neutron Cross Sections, USAEC Report BNL-325, Brookhaven National Laboratory, July 1, 1958.

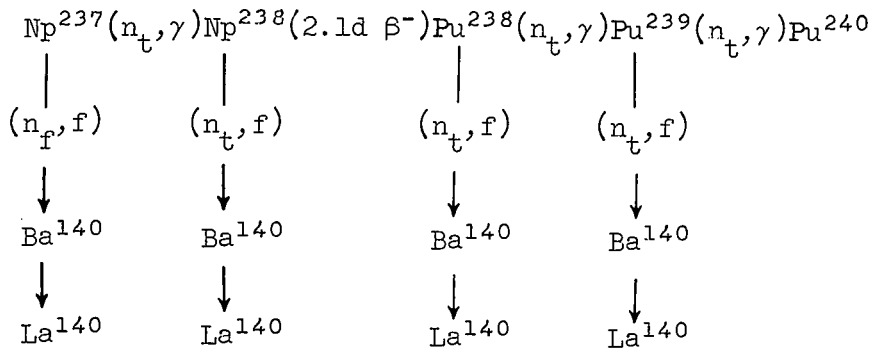

The symbol n_t represents a reaction by predominantly low-energy neutrons, and n_f represents one by predominantly fast neutrons. The calculations were performed with the NUCY program for the IBM-7090 computer.[14]

The Ba^{140} concentrations resulting from the four fission reactions shown above are given in Table 9.12. The conventional, or 2200 m/s, flux was taken to be 1×10^{14} neutrons/cm^2·sec, and the flux integrated above the effective Np^{237} fission threshold was taken to be 1.8×10^{14}. All other constants used in the calculation are given in Table 9.13. In some cases the cross sections were chosen with only a superficial examination

[14]D. R. Vondy, "Development of a General Method of Explicit Solution to the Nuclide Chain Equations for Digital Machine Calculations," USAEC Report ORNL-TM-361, Oak Ridge National Laboratory, Oct. 17, 1962.

Table 9.12. Ba^{140} Concentrations Resulting from Fission Reactions

Source of Ba^{140}	Ratio of Ba^{140} Concentration to Initial Np^{237} Concentration		
	Irradiation Time (days)		
	5	30	100
Np^{237}	7.0×10^{-6}	2.3×10^{-5}	2.6×10^{-5}
Np^{238}	8.3×10^{-6}	4.9×10^{-5}	5.8×10^{-5}
Pu^{238}	5.5×10^{-8}	2.8×10^{-6}	1.4×10^{-5}
Pu^{239}	1.5×10^{-8}	5.2×10^{-6}	9.2×10^{-5}
Ratio of Ba^{140} from Np^{237} to total Ba^{140}	0.46	0.29	0.14

Table 9.13. Cross Sections and Other Constants Used in Calculation of Np^{237} Chain

Isotope	Cross Sections (barns)[a]				λ, Decay Constant (sec^{-1})
	σ_{2a}	σ_{2f}	σ_{1a}	σ_{1f}	
Np^{237}	169	0	1.48	1.48	0
Np^{238}	1600	1600	0	0	3.83×10^{-6}
Pu^{238}	403	16.8	0	0	0
Pu^{239}	1400	1000	0	0	0
Ba^{140} (b)	0	0	0	0	6.24×10^{-7}
La^{140} (c)	0	0	0	0	0

[a]The subscripts have the following meanings: f = fission, a = absorption, 1 = energy interval above an effective Np^{237} fission threshold of 0.66 Mev, 2 = conventional, or 2200 m/s, flux.

[b]Total fission yield taken to be 0.06 for all fissionable isotopes.

[c]This isotope included as a dummy stable element to retain information on number of Ba^{140} decays.

of the appropriate averages, but the results are not grossly affected by these approximations.

After a five-day irradiation at the assumed flux levels, the activity from Np^{237} fission is less than half the total Ba^{140} activity of the sample. After a 100-day irradiation, this activity is only one-seventh of the total Ba^{140} activity.

These results illustrate the difficulty encountered in the use of bare neptunium samples in the presence of a high thermal flux. The calculations are presently being extended to determine (1) the production of fissionable Pu^{239} by the chain $Np^{238}(n,\gamma)Np^{239}(\beta^-)Pu^{239}$, (2) the effect of the use of cadmium covers, and (3) the effects of other assumed values for the flux levels.

10. EXPERIMENTAL INVESTIGATIONS OF HEAT TRANSFER AND FLUID FLOW

H. W. Hoffman G. Samuels

Resistance-Heated-Tube Heat-Transfer Experiment

G. J. Kidd, Jr.

The constants in the correlating equation describing the dependence of the Nusselt modulus on the Reynolds modulus and the axial position,[1] as developed from data obtained with the model-4 heat-transfer apparatus,[2] have been redetermined using all available data. The resulting equation is

$$N_{Nu,x} = 0.041\ (N_{Re,x})^{0.77}\ (x/d_e)^{-0.15}\ ,$$

$$\text{for } \begin{cases} 5 \leq x/d_e \leq 25 \\ 38{,}000 \leq N_{Re,x} \leq 63{,}000 \end{cases} . \quad (1)$$

In this equation, $N_{Nu,x}$ is the local Nusselt modulus and $N_{Re,x}$, the local Reynolds modulus. The axial position, x/d_e, is measured by the number of channel diameters from the nearest upstream obstruction. For the inlet section of the cluster, this is taken as the distance from the downstream edge of the end spider; in the second section, the zero position corresponds to the downstream edge of the mid-cluster spacer ($x/d_e = 23$).

The constants in Eq. (1) were developed as follows:

1. The x/d_e variation was established by correlation with the local Nusselt modulus at the mean N_{Re} for the channel.

2. The N_{Re} variation was determined next by correlation with values of the local Nusselt modulus at each x/d_e position.

---

[1] G. J. Kidd, Jr., Resistance-Heated-Tube Heat Transfer Experiment, pp. 404–414, "GCRP Semiann. Prog. Rep. Sept. 30, 1962," USAEC Report ORNL-3372, Oak Ridge National Laboratory.

[2] W. J. Stelzman, Resistance-Heated-Tube Heat Transfer Experiment, pp. 63–68, "GCRP Quar. Prog. Rep. June 30, 1961," USAEC Report ORNL-3166, Oak Ridge National Laboratory.

3. The multiplying constant was taken as the arithmetic mean of the values obtained from the correlation of step 2.

Equation (1) describes the heat transfer for all seven tubes of the cluster, with one or both clusters heated, at all relative cluster orientations. The error in prediction, based on the measured values, was found to range from +6 to −8%.

Roughened-Surface Pressure Drop

G. J. Kidd, Jr. J. L. Wantland

The effects of surface roughness on the pressure-loss coefficients in clusters of long rods are being studied in a series of experiments for establishing (1) the performance of modified EGCR-type clusters and (2) the characteristics of clusters of advanced design.

For the first type of investigation, the apparatus consists of two seven-rod clusters arranged in series within a 3-in.-ID Plexiglas channel. Each cluster is constructed from approximately 52-in.-long, 0.75-in.-OD rods located at a 2-in. bolt-circle diameter (2:1 ligament-ratio spacing). In order to emphasize the effects of surface roughness in contrast with other influences, the cluster length is 33% more than that of an EGCR element and the mid-cluster spacer has been omitted. The resulting uninterrupted flow-path is $x/d_e = 85$; whereas, for the EGCR fuel element, the free-passage length is only 22 diameters. The downstream cluster is instrumented with five equally spaced piezometer rings to provide for studying flow development. The working fluid is dry air at approximately room temperature. The roughened rod surfaces to be examined are shown in Fig. 10.1. The upper surface shown has Whitworth threads at 32 threads per inch with a root diameter of 0.75 in.; the lower surface is a 0.75-in.-OD rod spirally wrapped with 0.006-in.-diam wire at a pitch spacing of 0.060 in.

Smooth surfaces were studied in this apparatus with air flow in the Reynolds modulus range from 20,000 to 80,000, and the friction factors for the inlet cluster were found to be consistently lower than those for the second cluster. This suggests a rather sensitive dependence on the

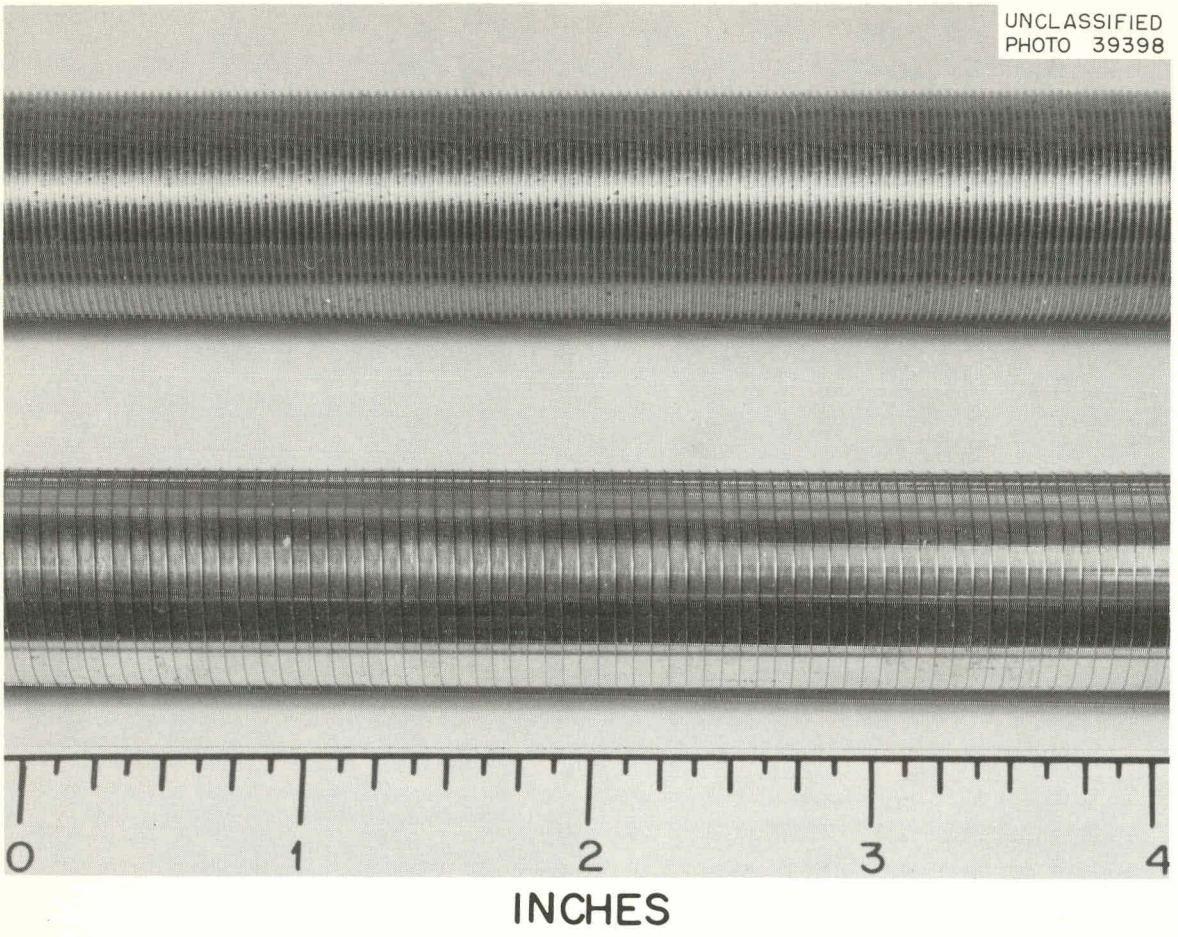

Fig. 10.1. Magnified Sections of Roughened-Surface Rods. Upper, 32 Whitworth threads per inch; lower, spirally wound 0.006-in.-diam wire at 0.060-in. pitch.

inlet geometry. Data for the axial variation of the friction factor in the downstream cluster showed an unexpectedly large scatter; this has been attributed to uncontrolled oscillation in the flow. This situation will be corrected before continuing with further tests.

The second type of study was designed to provide information needed in the development of advanced clad fuel elements. The effect of roughening the surface, lengthening the cluster to eliminate a number of end spiders, and introducing additional spacers at the original positions of the end spiders were investigated. The apparatus assembled for this study consisted of a single seven-rod cluster fabricated from 72 1/4-in.-long, 0.8-in.-OD rods, with a 2:1 ligament-ratio spacing (2.667-in. bolt-circle

diameter, 4-in.-ID channel). Spacers of the EGCR type[3] were attached to the rods at 14 1/2-in. intervals, giving five cluster sections. Static pressure taps were located at the mid-points of the third and fifth sections.

Pressure-loss coefficients were determined over a Reynolds modulus range from 2000 to 200,000 for bare rods and for rods spirally wrapped with 0.006-in.-diam wire on a 0.036-in. pitch (pitch-to-height ratio of 6:1). The pressure-loss coefficients, K_t, per section are shown in Fig. 10.2; K_t is defined by the equation,

$$K_t = K_s + f_B \frac{L}{d_e} , \qquad (2)$$

where K_s is the loss coefficient associated with one cluster spacer, f_B is the Blasius friction factor, L is the section length, and d_e is the cluster equivalent diameter. At low N_{Re}, approaching laminar flow, both surfaces exhibit similar characteristics; at higher N_{Re}, the roughened surface produces greater pressure-loss coefficients. For $N_{Re} > 10^5$, K_t for the wire-wrapped surface is approximately twice that for the smooth-tube cluster.

---

[3]Oak Ridge National Laboratory, "GCRP Quar. Prog. Rep. March 31, 1960," USAEC Report ORNL-2929, Fig. 2.1, p. 17.

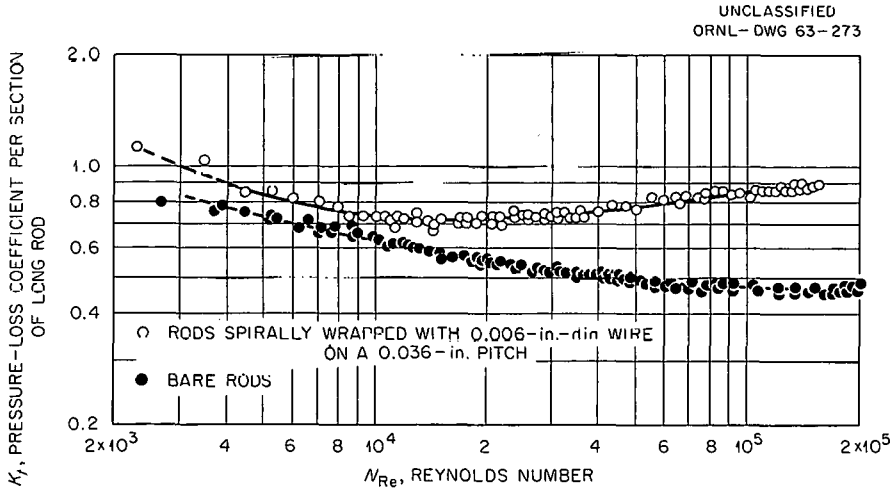

Fig. 10.2. Pressure-Loss Coefficients per Section for Clusters of Long Rods.

Interrupted-Surface Heat-Transfer Experiment

J. L. Wantland

Assembly work on apparatus for the study of heat transfer from rough surfaces[4,5] was continued. The device for inserting, spacing, and removing the interrupter rings was completed, and operational tests indicated satisfactory performance. A Borescope was optically modified to provide a means for visually inspecting the placement of the wire rings, both before and during operation, and thus it will be possible to check for any shifting of the rings at frequent intervals.

Surface temperatures are to be indicated by a digital read-out voltmeter with axial traversing accomplished by a solid-state switching device. Malfunctions in the latter unit have occasioned considerable delay. A 16-mm motion-picture camera that is capable of single-frame exposures will photographically record the emf displayed by the voltmeter along with the thermocouple location number. Synchronous-motor-operated cam switches will advance the switching unit in single steps and, after voltmeter balancing, activate a triggering solenoid that will move the film one frame and actuate the camera shutter.

Mass Transfer in Clusters of Roughened-Surface Rods

J. L. Wantland

Experimental difficulties, the correction of which would require extensive redesign and modification of the existing apparatus, prompted termination of this study of the characteristics of roughened surfaces as determined by a naphthalene mass-transfer technique. Specifically, it was found that with the present system the time involved in insertion and removal of the active rod was of the order of the exposure time. Thus a

---

[4]J. L. Wantland, Interrupted-Surface Heat-Transfer Experiment, pp. 245–246, "GCRP Quar. Prog. Rep. Dec. 31, 1961," USAEC Report ORNL-3254, Oak Ridge National Laboratory.

[5]J. L. Wantland, Interrupted-Surface Heat-Transfer Experiment, pp. 425–426, "GCRP Semiann. Prog. Rep. Sept. 30, 1962," USAEC Report ORNL-3372, Oak Ridge National Laboratory.

significant error was introduced into the data. At a Reynolds modulus of 85,000, and with all other controllable factors equal, apparent mass-transfer j-factors varied from 0.0037 to 0.0048 for experiments with smooth surfaces. Using the wire-wrapped configuration, where the exposure times must be severely restricted in order to avoid collapse of the wire coil because of loss of support through excess mass removal, the data scatter would be even greater.

Annulus Flow Experiments

R. S. Holcomb F. E. Lynch

An experimental facility was placed in operation that was designed to provide data for determining the friction factor and the heat transfer coefficient of air in an annulus with a roughened inner surface and a smooth outer surface. The apparatus consists of an inlet and an exit plenum flanged to a sleeve. These components are made of stainless steel. Six sleeves have been fabricated that range in inside diameter from 1.27 to 2.5 in. Three static pressure taps are located 120° apart, 10, 16, 22, and 28 in. from the inlet end of the sleeve. Two velocity probe stations are located 180° apart, 13, 16, and 19 in. from the inlet end. Three screws for centering the inner rod are located 2 and 31 1/2 in. from the inlet end. The plenums have insulated sealing flanges to allow heated tubes 0.75, 0.875, and 1 in. in diameter to extend through the plenums to make electrical and thermocouple connections.

The air flow is measured with sharp-edged orifice plates of three different orifice diameters in a 3-in.-diam orifice run. The orifice pressure drop is read on a water micromanometer with a range of 0 to 40 in. of water with 0.001-in. scale divisions. The test-section pressure drop is measured between a piezometer ring connecting the three taps at 10 in. and a ring connecting the three taps at 28 in. and is read on a water micromanometer or U-tube mercury manometer, depending on the Reynolds number. The air temperature is measured just below the orifice run and in the inlet and exit plenums with exposed-junction Chromel vs Alumel thermocouples made of 0.010-in.-wire. The thermocouple emf can be read on a potentiometer or on a strip-chart temperature recorder.

Pressure drop tests were completed on solid stainless steel rods 0.75 in. in diameter inside the 1.272-in.-ID sleeve. A smooth inner rod and rods wrapped with 0.0113-in.-diam wire with the following pitches were tested: 0.0385, 0.0769, 0.125, 0.182, and 0.286 in. The wire was wound over a 24-in. length and spot welded at the ends, and it was wound tightly enough that it was undisturbed by the air flow. The inlet end of the rod was placed at the sleeve inlet flange, and the pressure drop was measured over an 18-in. length of roughened surface preceded by 5-in. of smooth surface and 3-in. of roughened surface.

The Fanning friction factor was calculated for the annulus from the measured flow and pressure drop by the equation

$$\frac{2fG^2L}{gd_e} = \frac{G^2}{g} \ln \frac{P_2}{P_1} - \frac{M}{2RT}(P_2^2 - P_1^2) ,$$

where

f = Fanning friction factor,
G = mass velocity,
L = length of test section,
g = gravitational constant,
d_e = annulus equivalent diameter,
P_1 = upstream static pressure,
P_2 = downstream static pressure,
M = molecular weight,
R = absolute temperature.

The annulus equivalent diameter was taken as the inside diameter of the outer sleeve minus the diameter of the smooth rod. This equivalent diameter was used for the wire-wound rods as well as the smooth rod.

The friction factors for the six surfaces tested are plotted versus Reynolds number in Fig. 10.3. The smooth annulus curve shows completion of the transition to the turbulent flow at a Reynolds number of about 5000. The slope of the curve for the smooth annulus increases with Reynolds number from 5000 to 30,000 and then remains fairly constant. The curves for the rough annuli approach the smooth curve at a Reynolds number of 2000,

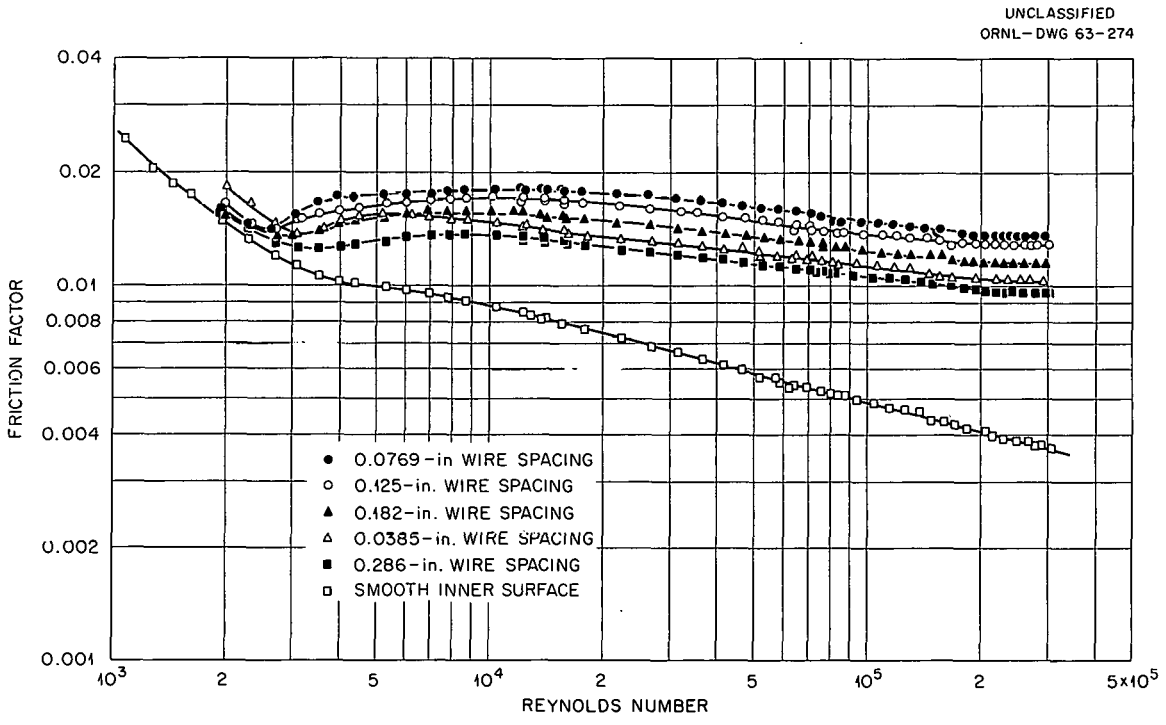

Fig. 10.3. Friction Factor Versus Reynolds Number for Air Flowing in Annulus Formed by 0.75-in.-diam Rods Inside 1.272-in.-ID Sleeves. Inner rod was smooth or wrapped with 0.0113-in.-diam wire at the spacing indicated.

except for the rod wrapped at a 0.0385-in. pitch. The difficulty here probably lies in the choice of the equivalent diameter used to calculate the friction factor. If the equivalent diameter were defined as the sleeve inside diameter minus the diameter of the cylinder passing tangent to the wire on the inner rod, the friction factor would be reduced about 10%. This would be more realistic as the pitch becomes so tight that the gas cannot flow along the rod surface. If applied to the 0.0385-in. pitch curve, the redefined equivalent diameter would lower the friction factor so that it would approach that for the smooth-surface curve in the laminar regime.

The friction factor goes through a maximum as a function of pitch at constant Reynolds number. This is seen to be necessary, since the wire-wound surface approaches a smooth surface as the coils get closer together or become very far apart. The wire wrapped at a 0.076-in. pitch had the maximum value of the five wires tested.

Heat Transfer and Fluid Flow in Packed-Sphere Beds

H. W. Hoffman

Hot-Spot Factors (D. G. Thomas)

Common usage in the reactor literature assigns the name "hot-channel hot-spot factors" to the safety factors in the design that account for unknown or inaccurate values of design parameters. These factors are usually applied to the average values for the hottest channels to obtain the maximum safe operating temperature. In making detailed calculations, some of the factors relate to the over-all temperature rise through the reactor, ΔT, while others are used with the local film temperature rise, Δt. For a prismatic fuel-element geometry, the hot-spot factors related to over-all and film temperatures most probably apply in the same channel. In contrast, for a geometry in which the fuel is contained in randomly distributed spheres, the maximum over-all temperature rise and the maximum film-temperature rise will not necessarily occur at the same radial location. This latter situation results because the maximum value of the film-temperature drop may be associated with local clusters which, in regions away from the wall, are randomly distributed through the bed and are not necessarily coincident with the maximum axial-temperature-rise location. The worst possible case in a packed bed occurs for a cluster at the radial position of the maximum over-all temperature rise.

Once individual hot-spot factors have been evaluated from estimated accuracies of design and fabrication procedures, it is necessary to determine the probability of the occurrence of such events in order to obtain realistic values for the over-all hot-spot factor.[6] The determination of these probabilities can be accomplished in most cases in the same manner as for other reactors; that is, by estimating the uncertainties in the heat-transfer, pressure-drop, and flow-rate expressions used in the design. An added complication, of course, is the effect of the random arrangement of spheres in the packed bed and the fact that this arrangement

---

[6] F. H. Abernathy, "The Statistical Aspects of Nuclear Reactor Fuel Element Temperature," USAEC Report ORNL CF-60-7-31, Oak Ridge National Laboratory, July 13, 1960.

changes with time as fuel is added and withdrawn from the reactor. The factors to be considered in the hot-spot analysis and the temperature rise with which each is associated are listed in Table 10.1. This table

Table 10.1. Hot-Spot Factors Affecting Packed-Bed Nuclear Reactor Design

	To Be Applied to		Typical Hot-Spot Factors[a]	
	Axial ΔT	Film Δt	Value	Probability
Flow distribution				
Clustering		X	1.5[b]	(10^{-5})[c]
Velocity profile				
Mean	X		1.05[d]	
Entrance region		X	1.05[d]	
Exit region		X	1.05[d]	
Interconnected channels	X			
Pressure drop	X		1.1[e]	
Heat transfer				
Average heat-transfer coefficient	X		1.1	
Radiation cooling		X		
Local heat-transfer coefficient		X	1.1	
Bed flow				
Sphere flow-velocity profile	X		1.02	
Broken-sphere factor	X	X	1.5	Small
Physics				
Radial peak-to-average power density	X		1.01	
Axial peak-to-average power density	X		1.01	
Manufacturing tolerances				
Nonuniform fuel loading		X	1.01	
Variation in sphere diameter		X	1.01	
Sphere density		X	1.01	
Operation				
Reactor power level	X		1.01	
Gas inlet temperature	X		±40°F	
Gas outlet temperature	X		±25°F	
Thermocouple error	X		±25°F	

[a] Unless otherwise indicated, all values are taken from ref. 7.

[b] N. Ozisik, R. B. Korsmeyer, and C. L. Rhoden, "Heat Transfer Analysis of Pebble Bed Reactors and Comparison with Prismatic Cores," USAEC Report ORNL-CF-61-6-16, Oak Ridge National Laboratory, June 19, 1961.

[c] D. G. Thomas, Evaluation of Cluster Formation, pp. 155–157, "GCRP Semiann. Prog. Rep. Sept. 30, 1962," USAEC Report ORNL-3372, Oak Ridge National Laboratory.

[d] From following section, R. D. Bundy, "Full-Scale Packed-Bed Reactor Core Experiments."

[e] D. G. Thomas, Pressure Drop Evaluation, pp. 148–150, "GCRP Quar. Prog. Rep. March 31, 1962," USAEC Report ORNL-3302, Oak Ridge National Laboratory.

also gives representative values of the hot-spot factor as derived for various gas-cooled reactors.[7] For packed-bed reactors, the over-all temperature rise may be in the range 700 to 1200°F, while the film-temperature drop may be in the range 150 to 200°F. Thus in terms of the margin required for safe operation of a packed-bed reactor, a much larger hot-spot factor can be tolerated for the film-temperature drop than for the axial-temperature rise. From inspection of Table 10.1, the cumulative factor (obtained by successive multiplication of the individual factors) for the Δt term (1.93) is found to be approximately one-third greater than that for the ΔT term (1.45) when the broken-sphere factor is neglected as being of low probability of occurrence. In fact, the results obtained by application of the factors of Table 10.1 are significantly modified by inclusion of the probability term; for example, tests giving information on the product of the probability and the hot-spot factor suggest that under most circumstances there need be little concern over the clustering factor.[8] Experiments are currently under way, however, to verify this for the specific geometry being studied.[9]

The product of the factors from Table 10.1 and the last three items in the table give a maximum (and quite pessimistic) temperature allowance for uncertainties in design, fabrication, and operation of 500 to 650°F for the mean temperature rise through the reactor. If the probability of the simultaneous occurrence of all the "worst" possible events is 0.5, the safety factor may be reduced to 250 to 325°F.

Full-Scale Packed-Bed Reactor Core Experiments (R. D. Bundy)

The study of the static and dynamic characteristics of a randomly packed bed of 1 1/2-in.-diam graphite spheres within a full-scale model

---

[7] Power Reactor Technology, 4(1): 30–32 (December 1960); 3(4): 30–31 (September 1960).

[8] C. B. Von der Decken et al., "The Determination of Heat Transfer from a Pebble Bed to a Through Flowing Gas Using the Mass-Transfer Analogy," Chem. Ingr.-Tech., 32: 591 (1960).

[9] See following section, F. N. Peebles et al., "Mass-Transfer Studies."

of a packed-bed reactor core was continued.[10,11] A description of the experiments performed is given in Table 10.2. Beds 1, 2, and 3 were studied before inclusion of the full-scale core model in the reactor mockup, and hence experiments were restricted to static conditions. It was observed that for 86% of the spheres the velocity at the exit of the injection tube was in the range 0.7 to 5.2 ft/sec; the maximum injection velocity measured was 11.3 ft/sec. Details of the bed loading conditions are given in Table 10.2. In the following discussion, the results are keyed to the experiment by adding the bed designation number to a prefix indicating the experiment performed; for example, VF-5 indicates the void-fraction measurement for bed 5, as listed in column 3 of Table 10.2.

Void-Fraction and Angle-of-Repose Measurements. The static bed characteristics, void fraction, and mean angle of repose for the beds studied are given in the final columns of Table 10.2. Void fractions were determined by calculation from the measured bed height and the known volume of the spheres and the core; as noted in the table, a water-volume technique was also used for measuring the void fractions of beds 1 through 3. The instruments used in establishing the bed height are shown in Figs. 10.4 and 10.5.

The void fractions for beds 4 and 5 (0.394 and 0.398, respectively) fall within the scatter band previously indicated for the results obtained with beds 1 through 3 (0.401 ± 2%).[11] Bed 5 was formed from bed 4 by withdrawing spheres in groups of about 65 from the core bottom and readmitting them singly at the core top. As indicated by the numbers given above, no significant effect on the void fraction was noted.

There exists the finite possibility that levitation of the bed will occur sometime during its lifetime. Therefore the effects of this were studied in beds 6 and 7. In forming bed 6, the air flow through the core was raised to the levitation value, at which point a severe, cyclic,

---

[10]R. D. Bundy, PBRE-Core Flow Characteristics, pp. 153–155, "GCRP Quar. Prog. Rep. March 31, 1962," USAEC Report ORNL-3302, Oak Ridge National Laboratory.

[11]R. D. Bundy, Full-Scale PBRE-Core Experiments, pp. 158–169, "GCRP Semiann. Prog. Rep. Sept. 30, 1962," USAEC Report ORNL-3372, Oak Ridge National Laboratory.

Table 10.2. Description of Packed-Sphere-Bed Experiments

Bed Designation	Experimental Determinations	Experiment Designation	Bed Loading Conditions				Static Characteristics	
			Technique	Sphere Impact Velocity (ft/sec)		Gas Flow During Loading ($lb/ft^2 \cdot sec$)	Angle of Repose (deg)	Void Fraction[a]
				At Bottom	At Top			
1	Void fraction Angle of repose	VF-1 AR-1	Spheres added singly at center from 6 1/2 in. above core model top	17.3	9.0	(b)	20–26	0.410
2	Void fraction Angle of repose	VF-1 AR-1	Spheres added singly at center from 6 1/2 in. above core model top	15.4	2.8	(b)	20–28	0.396
3	Void fraction	VF-3	Spheres added off-center (4 in. from wall) from 6 1/2 in. above core model top	15.4	3.6	(b)	23	0.397
4	Void fraction Pressure distribution Levitation velocity Angle of repose	VF-4 PD-4 LV-4 AR-4	Spheres added singly at center from 6 1/2 in. above core model top	18.3–19.1	10.9–12.0	0	23	0.394
5	Void fraction Pressure distribution Levitation velocity Velocity profile Angle of repose	VF-5 PD-5 LV-5 VP-5 AR-5	Spheres of bed 4 cycled once by batch removal (65 spheres) from bottom and single addition at top		10.9–12.0	0	18–25	0.398
6	Void fraction Pressure distribution Levitation velocity Velocity profile	VF-6 PD-6 LV-6 VP-6	Bed 5 levitated and allowed to settle slowly			1.56	0	0.418
7	Void fraction	VF-7	Bed 6 levitated and allowed to settle abruptly			1.56	0	0.419
8[c]	Void fraction Pressure distribution Levitation velocity Velocity profile Angle of repose	VF-8 PD-8 LV-8 VP-8 AR-8	Spheres added singly at center from 6 1/2 in. above core model top	(c)	(c)	0.51	19–22	(c)

[a]Obtained by calculation from height and volume measurements; for beds 1 through 3, data obtained by water addition and withdrawal yielded 0.403 for bed 1, 0.399 for bed 2, 0.401 for bed 3.

[b]Static experiments performed in full-scale core model before inclusion in reactor mockup.

[c]Experiment incomplete.

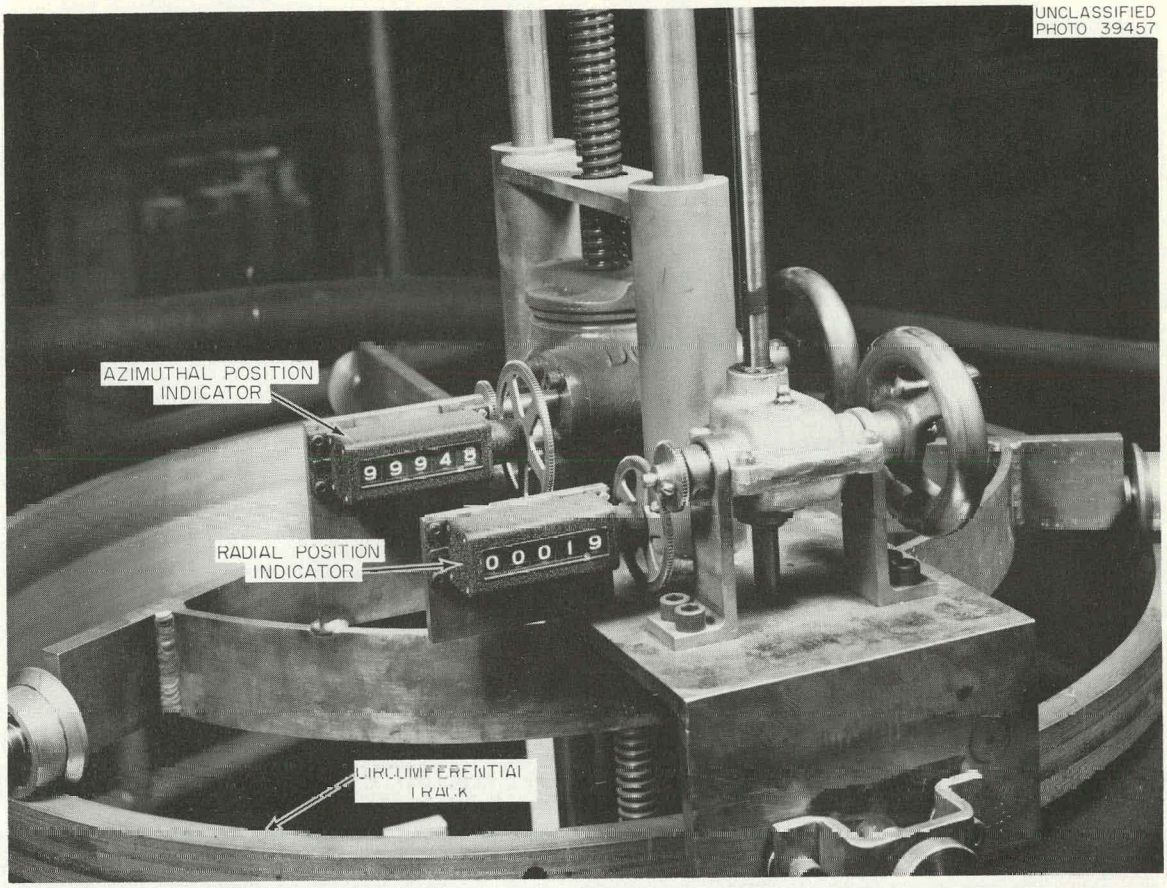

Fig. 10.4. Probe-Positioning Mechanism for Studies of Velocity and Bed Top-Face Profiles.

churning action was observed. The air flow was then slowly decreased to zero so that the bed progressively stabilized, beginning at the bottom. In contrast, for bed 7, the air flow was abruptly shut off after levitation. As indicated by the values listed in Table 10.2, a significant (5%), residual expansion of the bed resulted. There was no discernable influence on the void fraction of the means by which the bed reverted to the settled condition following levitation. The experiments with bed 8 have not yet been completed. In this case, the bed was produced by adding spheres singly to an initially empty core, while maintaining a counter gas flow at a level approximately one-third that required to levitate a full bed.

In addition to the void-fraction determinations, the angle of repose of the spheres in the fill cone at the top of the bed was also measured for those beds in which the spheres were added singly; the results are

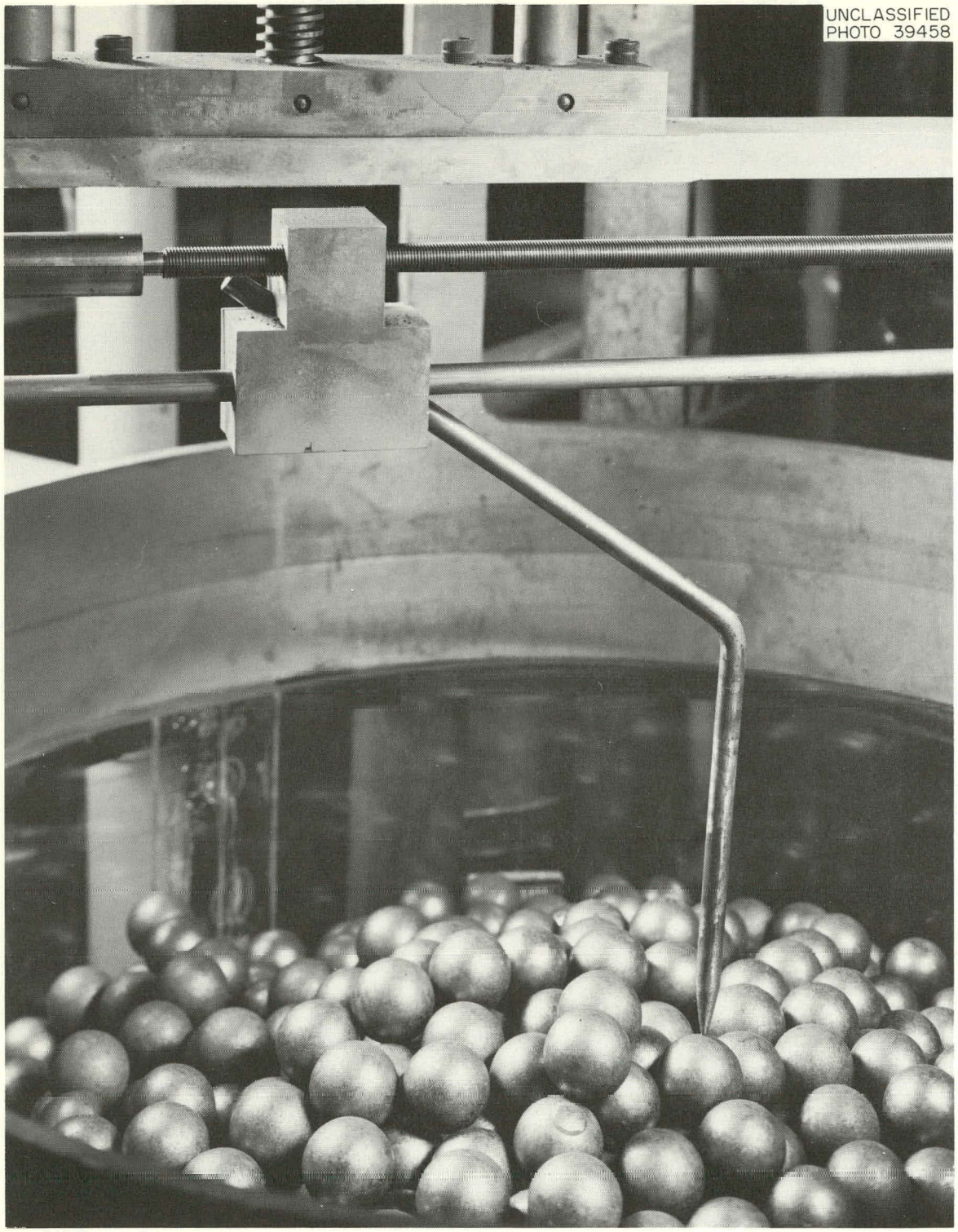

Fig. 10.5. Probe for Determining Profile of Top Face of Packed-Sphere Bed.

listed in Table 10.2. The superficial angle of repose is defined as the angle between the horizontal and a line connecting with the extreme spheres in the fill cone (at the wall and at the top). The range values of the data in Table 10.2 reflect the bounds obtained from measurements along several radii; where a single value is listed, only one measurement was made. Good agreement was observed for the results from the most recent experiments (beds 4, 5, and 8) and those reported earlier[11] (beds 1, 2, and 3). The data spread seemed to be somewhat reduced for the situation in which the spheres were charged to the core against air flow (bed 8), but this will require further verification.

The angle of repose as a function of the impact velocity is shown in Fig. 10.6. Again, reasonable agreement was found between the data obtained after inclusion of the core model in the reactor mockup (shaded area) and that obtained earlier (open circles).

Pressure Distribution. As described previously,[10] the full-scale model was provided with static-pressure taps distributed over the core wall and the bottom surface. In all, there were 33 such pressure-tap locations arranged in sets of 11 (eight along the core wall and three on the bottom) at each of three 120-deg separated positions. Nine additional

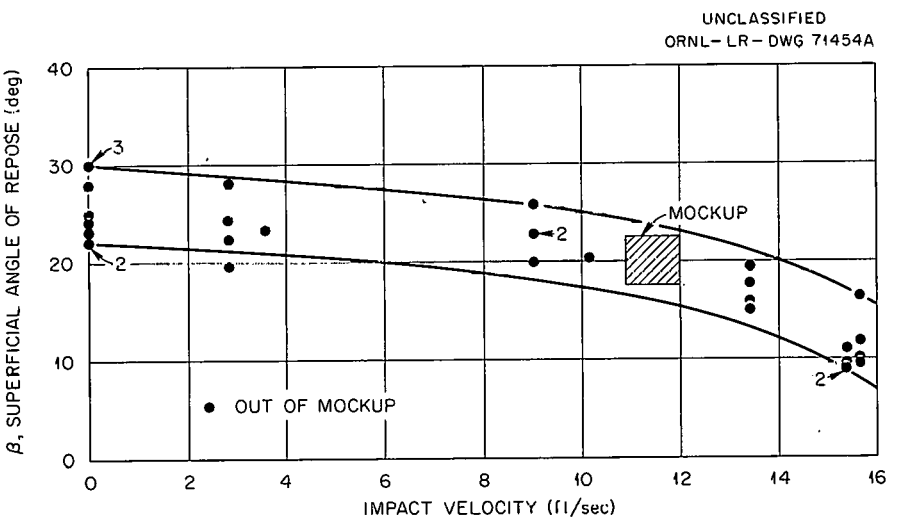

Fig. 10.6. Effect of Impact Velocity on Angle of Repose in Packed-Sphere Bed.

taps gave information on the over-all core pressure drop and the losses in the inlet line.

In the course of these experiments, the air flow through the core was varied over the range from 25 to 93% of the levitation velocity ($N_{Re,p}$ from 2,500 to 10,000). At all flows, pressures observed at the same height but at different angular locations agreed to within the precision of the measurements. It thus appears that no gross crossflow maldistributions exist.

Two friction factors were calculated from the pressure-drop data: (1) an over-all factor based on the total pressure difference across the bed, which is specific to the geometry studied, and (2) a more general factor calculated from the constant portion of the pressure-gradient curve, which characterizes fully developed flow in a packed bed. Since the pressure gradient in the inlet region of the core was, in general, less than that in regions of established flow, the over-all factors were determined to be of lesser magnitude than those developed from the data for the cylindrical part of the core. The results are presented in Fig. 10.7, and, for reference, the mean line through the data of Denton et al.[12] and the curves predicted by the correlation of Ergun[13] (at two values of the void fraction) and of Bakhmeteff and Feodoroff[14] are included in the figure.

Two facts are noted from the data. First, both the over-all and the established-flow friction factors showed a −0.2 dependence on the Reynolds modulus (i.e., $f \sim N_{Re}^{-0.2}$) over the full range of the experiments. Even at the higher flows, there was no indication of any leveling off of the friction-factor curve, such as that indicated by the Ergun correlation. Second, the friction factor does not appear to depend simply on the void fraction. Thus, the decrease in the friction factor from that obtained in experiment PD-4 to that in PD-5 or PD-8 was greater than anticipated

---

[12]W. H. Denton, C. H. Robinson, R. S. Tibbs, "The Heat Transfer and Pressure Loss in Fluid Flow Through Randomly Packed Spheres," British Atomic Energy Authority Report AERE-HPC-35, June 1949.

[13]S. Ergun, "Fluid Flow Through Packed Columns," Chem. Eng. Progr., 48: 89–94 (1952).

[14]B. A. Bakhmeteff and N. V. Feodoroff, "Flow Through Granular Media," J. Appl. Mech., 4: A97–A104 (September 1937).

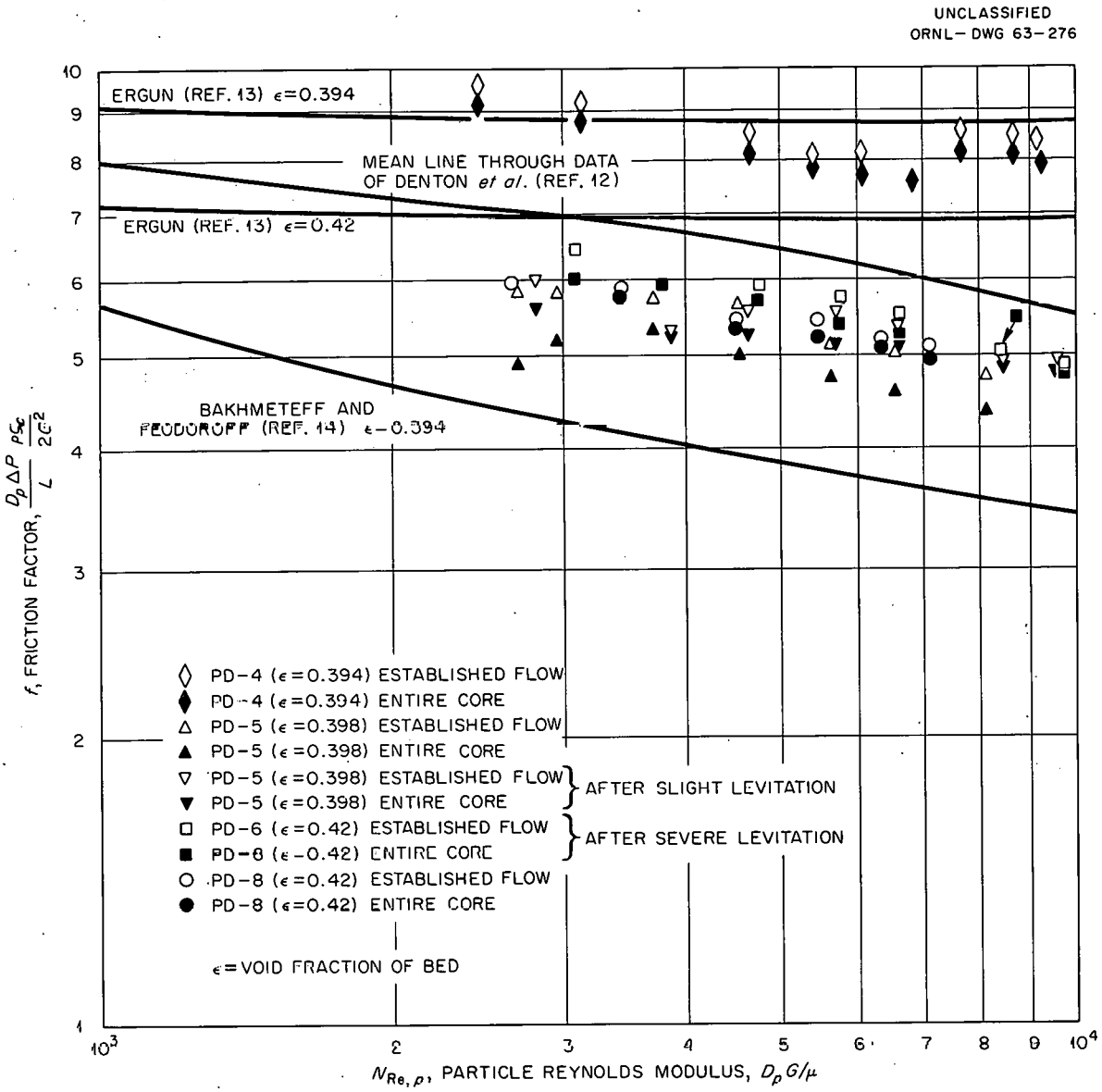

Fig. 10.7. Experimental Friction Factors as Determined in Full-Scale Packed-Bed-Reactor Core Model.

from the increase in void fraction. Further, the PD-5 data indicate a lower flow resistance than was observed for PD-6 in which the void fraction was 5% greater (0.418 vs 0.398). The possibility thus exists that oriented flow passages were present in beds 5 and 8. These could have been created in bed 5 by the batch removal of spheres at the bottom and in bed 8 by the upward air flow during charging. Velocity profile determinations (discussed further in a following section) at the exit face

of bed 5 tend to confirm this hypothesis. The friction factors evaluated in experiment PD-4 agree well with those previously reported by Peebles et al.[15] for flow through a 3/8-scale model randomly packed with smooth, 9/16-in.-diam plastic spheres.

Levitation Velocity. As the flow through a packed bed is increased, a gas velocity will be reached at which the pressure difference (drop) across the bed is equivalent to the weight per unit cross section of the bed. At velocities slightly greater, the void fraction sharply increases and the bed tends toward an arrangement of individual spheres suspended (floating) in a gaseous medium. This phenomenon is termed levitation. The quantitative delineation of the levitation velocity presents some problems, however, in that (1) there is no sharp point of demarcation between a static bed and a levitated bed (i.e., the bed does not lift and expand abruptly) and (2) the gas velocity can only be defined in terms of the superficial velocity at the bed exit. It was experimentally observed that a definite progression of events, beginning with sphere motion on the upper face of the bed, precedes full-bed levitation. The choice of any of these events (see Fig. 10.8) as indicative of incipient levitation rests on what the observer considers a detrimental condition from the viewpoint of the end application. Further, the lift experienced by an individual sphere depends on the geometry of the local region in which it is embedded. Thus, at a given exit superficial velocity, a bed of rhombohedrally arranged spheres may levitate, and a randomly packed bed may remain static.

In the data discussed below and summarized in Table 10.3, levitation is defined in terms of the ratio of the pressure gradient across the bed to the bulk bed density ($dp/\rho dz$) rather than in terms of the gas velocity. This avoids some of the problems considered above. The behavior of the spheres at the top of the bed was observed visually and photographically while the air flow was slowly increased and decreased at a velocity near that required to levitate the bed.

---

[15]F. N. Peebles, B. M. Phillips, J. M. Rhodes, Mass Transfer Studies, pp. 169–174, "GCRP Semiann. Prog. Rep. Sept. 30, 1962," USAEC Report ORNL-3372, Oak Ridge National Laboratory.

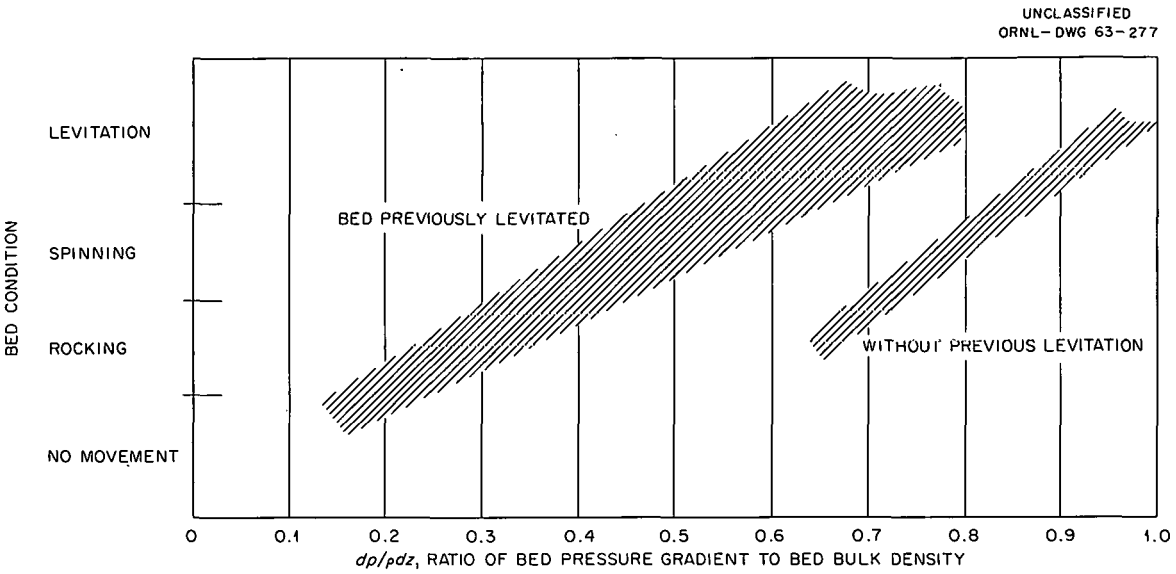

Fig. 10.8. A Qualitative Representation of the Phenomena Preceding Full-Bed Levitation.

Three distinct phenomena characterized the approach to full levitation, and all were noted to occur in local areas without involving the full exit face of the bed. These were the following:

1. a rocking motion of a few spheres when the pressure gradient was equivalent to 60% of the bulk bed density,
2. the initiation of spinning of some spheres when the pressure gradient-to-bed density ratio was 0.80,
3. physical lifting of spheres for values of dp/ρdz in excess of 0.90.

As the flow was decreased from its maximum value, the same phenomena occurred in reverse order. These observations are consistent with those reported by Randall and Millwright.[16]

A graphical presentation of the results listed in Table 10.3 is given in Fig. 10.8. Since quantitative criteria describing the various regimes have not been defined, the figure shows only that in certain ranges of dp/ρdz certain phenomena occur. A distinct discrimination between beds with and without levitation prior to the observations is, however, apparent. This difference was found regardless of whether the full bed had

[16]D. E. Randall and S. S. Millwright, "Experimental Determinations of the Pressure Drop Through a Pebble Bed," Sandia Corporation Report SC-4354(TR), September 1959.

been levitated (as in LV-6) or only the top face (as in LV-4 and LV-5). For either situation, if previous levitation had occurred, subsequent levitation was achieved at pressure gradients equal to only 60% of the

Table 10.3. Summary of Results of Levitation Studies of Packed-Sphere Beds

Experiment	Ratio of Pressure Gradient to Bulk Density	Comments
LV-4-1	0.65	A few spheres began to rock[a]
-2	0.80	One sphere only was spinning; others were rocking[a]
-3	0.95	Physical levitation of some spheres[a]
-4	0.61	Physical levitation of some spheres
-5	0.62	Physical levitation of some spheres
-6	0.61	Physical levitation of some spheres
-7	0.60	Physical levitation of some spheres
LV-5-1	0.98	Physical levitation of some spheres[a]
-2	0.63	Physical levitation of some spheres
-3	0.61	Physical levitation of some spheres
-4	0.62	Physical levitation of some spheres
-5	0.65	Physical levitation of some spheres
-6	0.67	Physical levitation of some spheres
-7	0.58	Physical levitation of some spheres
LV-6-1	0.35	A few spheres began to rock
-2	0.60	A few spheres were spinning; others were rocking
-3	0.65	Physical levitation of some spheres
-4	0.14	All movement by spheres ceased
-5	0.18	One sphere only began to rock
-6	0.35	A few spheres began to rock
-7	0.44	One sphere only was spinning; others were rocking
-8	0.64	Physical levitation of some spheres
-9	0.59	Levitation ceased but spheres continued to spin and rock
-10	0.41	All spheres stopped spinning; some still rocked
-11	0.18	All movement by spheres ceased
-12	0.30	One sphere only began to rock
-13	0.37	A few spheres began to rock
-14	0.60	Physical levitation of some spheres

[a]Measurements were for beds not previously levitated.

bulk density. Other indications of approaching levitation were observed at correspondingly lower values of pressure gradient.

Consideration of the arrangement of spheres in the top layers of the bed provided an explanation for the observed data separation. Agitation of the top of the bed during levitation permitted spheres to assume a minimum potential-energy configuration (rhombohedral). In following experiments, this denser packing created a steeper pressure gradient at the bed exit face and, hence, occasioned levitation at lower values of $dp/\rho dz$. This description is true even for those beds which had been fully levitated (e.g., bed 6). For these beds, even though the over-all void fraction was increased, the top surface showed closer packing. This hypothesis was qualitatively confirmed by manually disturbing the ordered packing at the bed face while the gas flow was just sufficient to maintain levitation; all indications of levitation immediately ceased.

Velocity Profiles. A knowledge of the flow distribution within a packed bed is needed for estimating the heat transfer (local or over-all) from the bed. Measurements of the velocity inside the bed are difficult and not a part of the immediate scope of this study. Information relative to the gross distribution of the superficial velocity can be obtained, however, from data on the velocity at the exit face of the bed.

A hot-wire probe, supported and positioned by the mechanism used in the bed-height measurements, was used to measure the velocity. The traverses were made at a level six sphere diameters (9 in.) above the bed in order to minimize the effects of the wakes from the individual spheres while retaining sensitivity to local variations in the superficial velocity. The probe was calibrated in an empty pipe.

The results obtained from the beds studied (see Table 10.2) are presented, in part, in Figs. 10.9, 10.10, and 10.11. It was observed that, at any given radial distance from the core wall, the local velocity varied significantly with angular position. This is shown in Fig. 10.9, in which the radial variation in the local maximum and minimum velocities (determined by circumferential traverses at each radial position) and in certain averaged velocities (30- and 360-deg sectors) is given dimensionlessly as a velocity ratio based on the bed average. The data depicted are for run VP-5A in which the average bed velocity was 5.7 ft/sec. From Fig. 10.9,

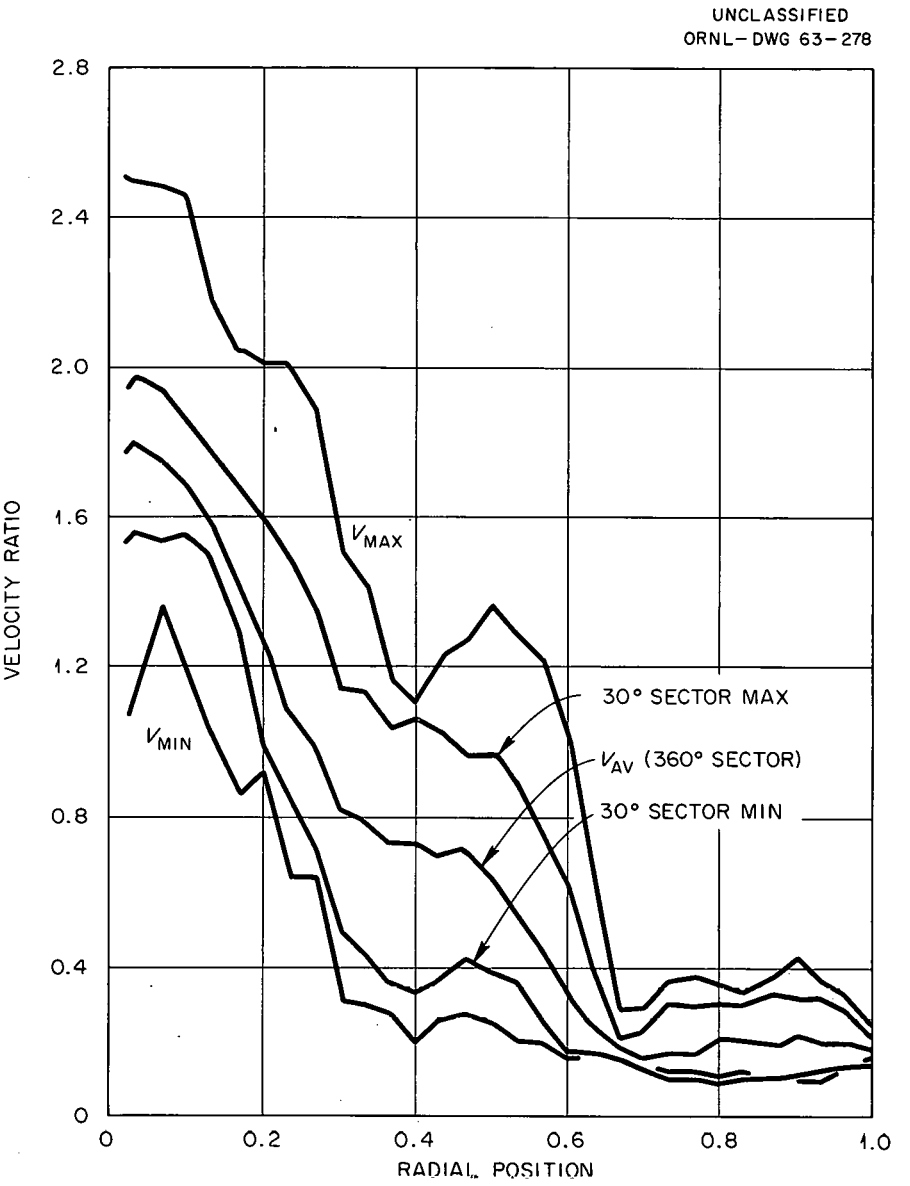

Fig. 10.9. Experimental Velocity Spectrum Obtained with Peaked Bed Top (VP-5A) and an Average Bed Velocity of 5.7 ft/sec.

it is noted that the spread in the ratio of local maximum-to-minimum velocities is of the order of 2 to 6. The angular location of the extreme values varied randomly between traverses, reflecting local variations in void fraction (probably in the uppermost levels of the bed). This aspect will be examined further by removing successive layers from the top face of the bed and observing the changing pattern in the distribution of local

velocities. Velocities averaged over 30-deg sectors show a lesser variation in the maximum-to-minimum ratio. While the local velocities reflect conditions near the exit face of the packed bed, the average of these

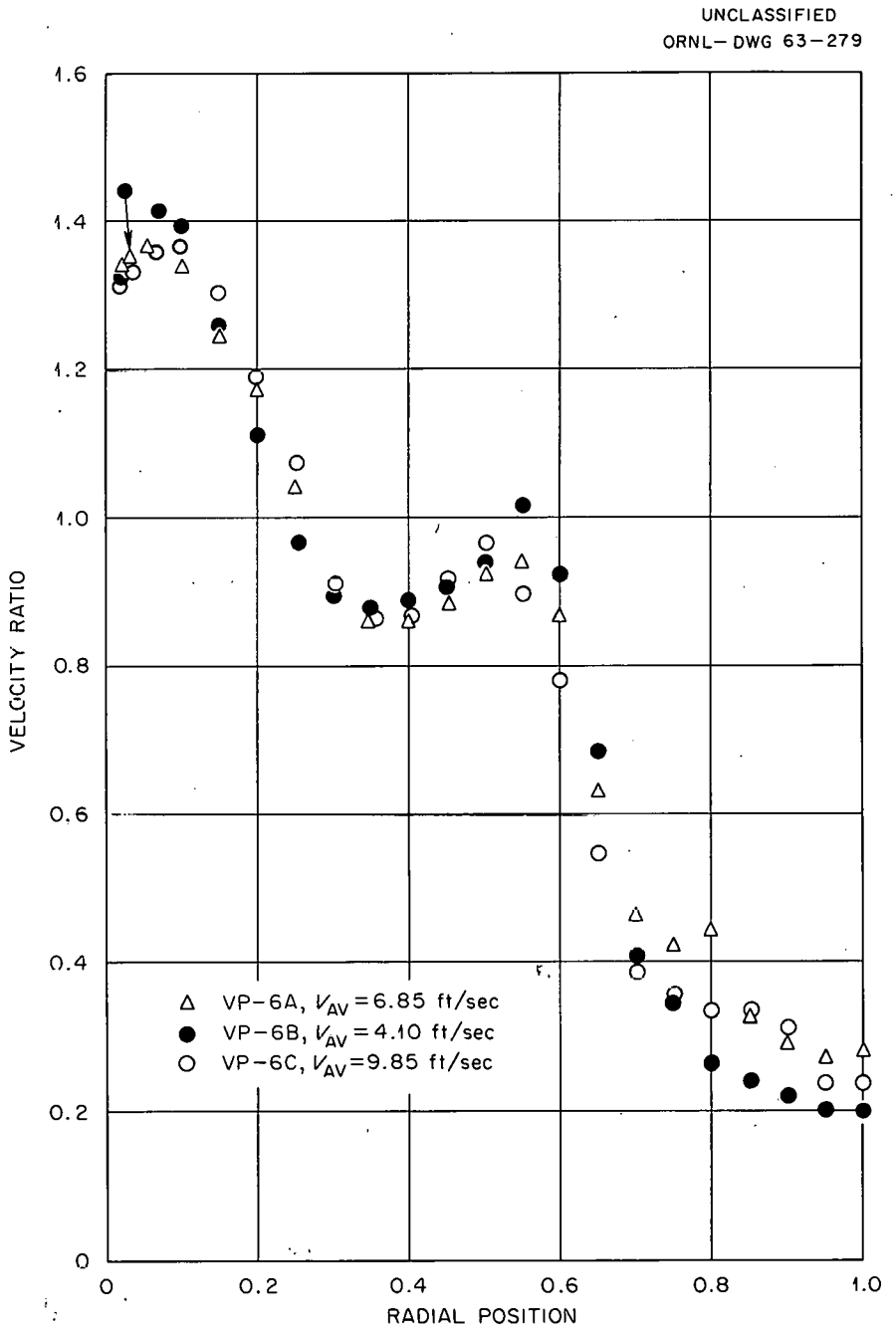

Fig. 10.10. Experimental Mean Superficial Velocity Profiles for a Completely Levitated Bed.

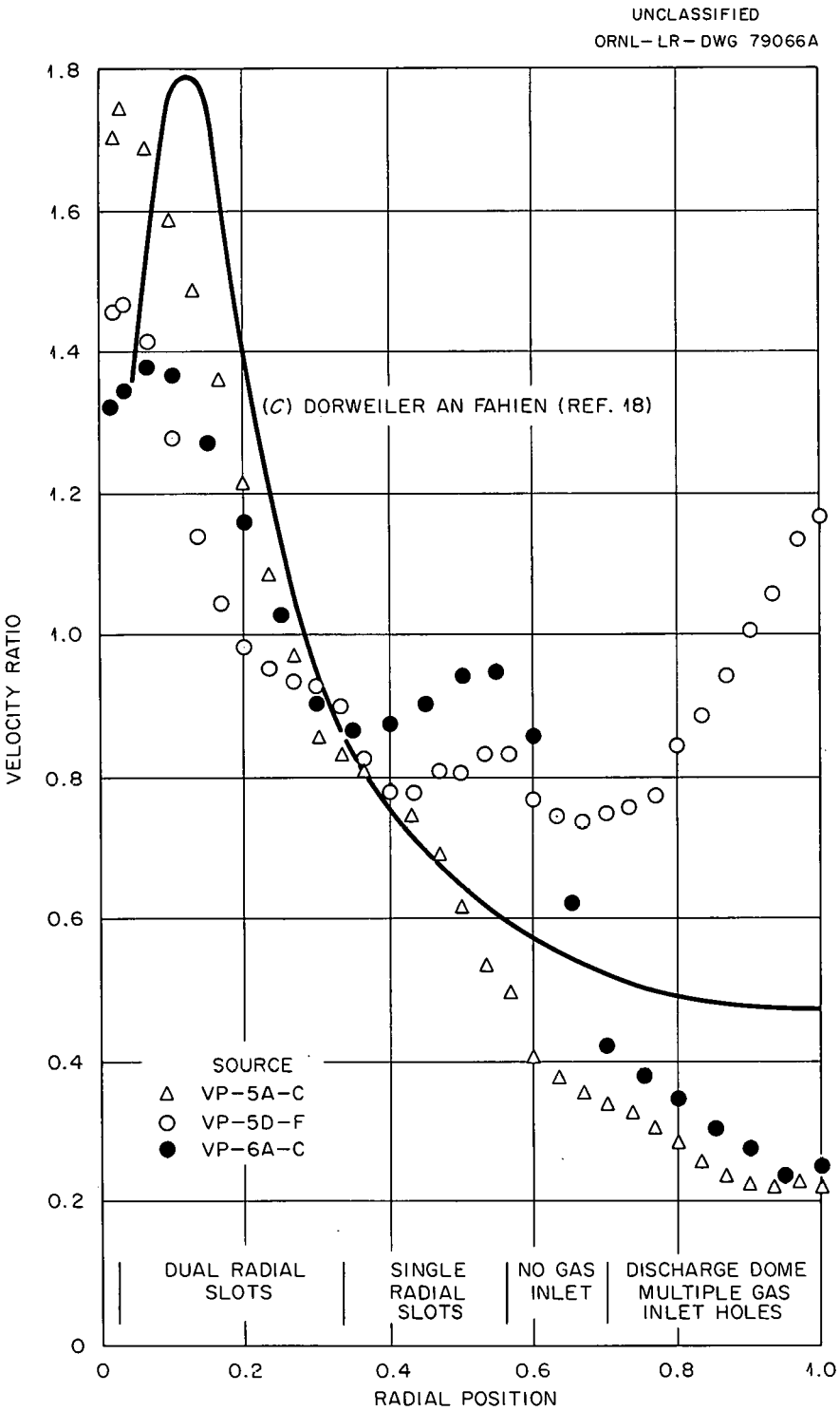

Fig. 10.11. Mean Superficial Velocity Profiles for Beds 5 and 6.

velocities over the full 360-deg sector should reasonably characterize the gross distribution of the superficial velocity within the bed; this will be checked by observing changes in this profile (curve labeled V_{av} in Fig. 10.9) in the aforementioned experiment.

A series of experiments was performed (VP-6A, VP-6B, VP-6C) in which the effect of the bed average velocity on the radial variation of the mean circumferential velocity was examined. The results, presented in Fig. 10.10, indicate that a 2.4-fold change in the average velocity did not significantly affect the shape of the radial velocity profile; the variation between the profiles was less than the estimated ±5 to 7% error associated with the measurement. This result is consistent with the conclusions of other investigators.[17-19]

The velocity data obtained for several differently formed beds (5 and 6) are compared in Fig. 10.11 with results reported by Dorweiler and Fahien.[18] The regions delineated along the abscissa in Fig. 10.11 have reference to the geometric structure of the core bottom, as shown in Fig. 10.12; gas-inlet holes in the central sphere-discharge dome are not shown in this photograph. The effect of the inlet gas distribution on the velocity profile is discernible in the data of Fig. 10.11. Results for the VP-5A through 5C runs are in best agreement with the Dorweiler and Fahien profile; the differences can be explained in terms of the structure of the beds studied. Dorweiler and Fahien examined a flat-topped bed contained by a right-circular cylinder; whereas, for the mockup, the bottom and top faces were both roughly conical. The higher resistance to flow in the mockup bed caused both a shift of the point of maximum velocity toward the wall and a decrease in flow through the central region. To verify this, the upper face of bed 5 was leveled prior to runs VP-5D through VP-5F by levitating the top layers of spheres. The results, while somewhat inclusive, show that the velocity maximum moved away from the

---

[17]M. Collins, "Velocity Distribution of Packed Beds," M.E. Thesis, University of Delaware (June 1958).

[18]V. P. Dorweiler and R. W. Fahien, "Mass Transfer at Low Flow Rates in a Packed Bed Column," A.I.Ch.E. J., 5: 193 (1959).

[19]C. E. Schwartz and J. M. Smith, "Flow Distribution in Packed Beds," Ind. Eng. Chem., 45: 1209 (1953).

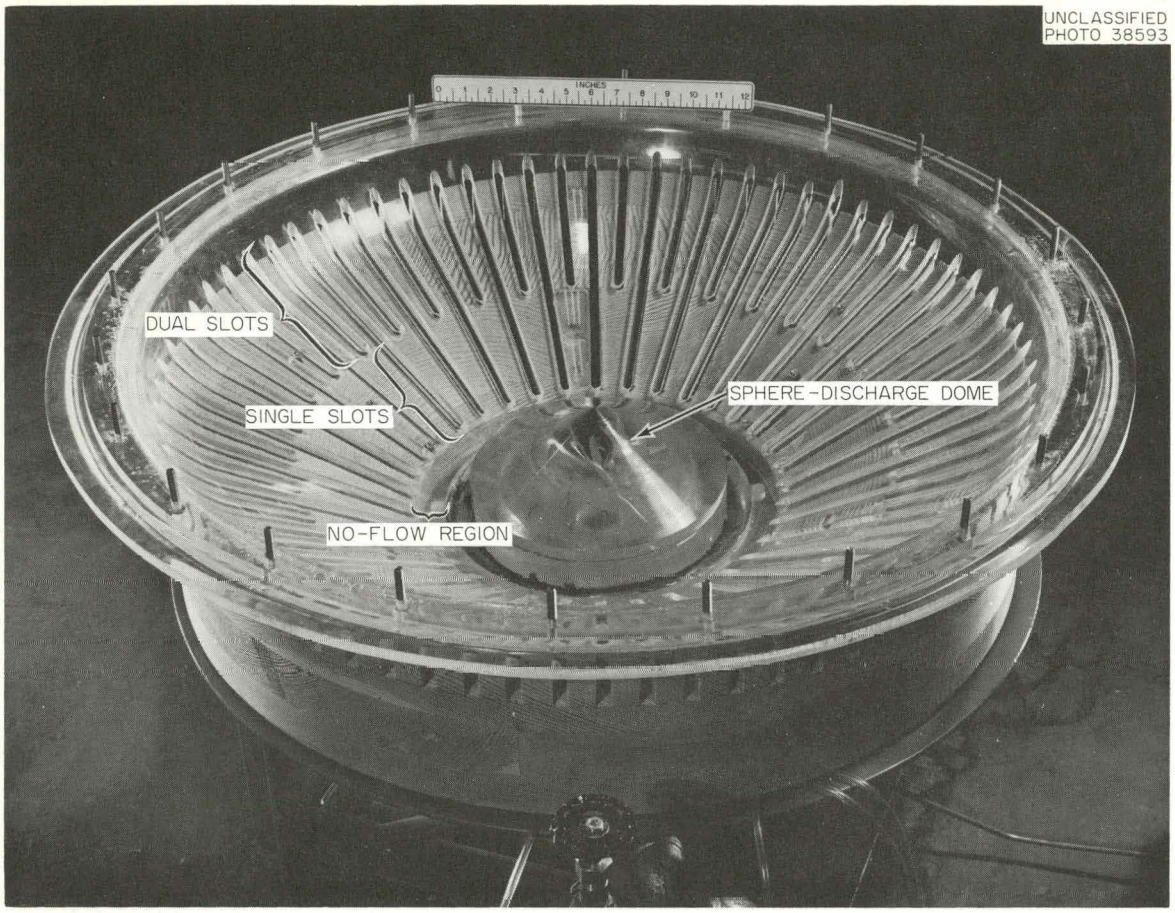

Fig. 10.12. Core Mockup Inlet Geometry. In a later version, gas-inlet holes were added in sphere-discharge dome.

wall and that the central flow was increased. Interpretation of this data is complicated by the fact that levitation resulted in the formation of (1) large clusters (extending through the upper four or five layers) of rhombohedral spacing and (2) vertically oriented channels in the region of the central dome. With the bed flattened, a strong velocity maximum appeared at the core center; and a secondary maximum occurred in the vicinity of the outer edge of the central dome (in VP-5A-C an inflection was noted in this region). Further modification of the bed (VP-6A-C) by complete levitation resulted in lower relative velocities near the wall, an additional displacement of the velocity maximum toward the core center, and the elimination of the high central velocity; the secondary maximum was somewhat amplified. While the packing arrangement within the bed was

difficult to estimate, the results suggest an increased density in those regions in which the velocity was originally greatest (although the overall bed density decreased).

Mass-Transfer Studies[20] (F. N. Peebles, B. M. Phillips, J. M. Rhodes)

Consideration of the local heat-transfer phenomena in packed-sphere cores leads to the conclusion that substantial temperature excesses could exist in and near clusters of closely packed fueled spheres. To furnish data on the severity of this condition, an experiment was initiated to measure the rates of mass transfer for spheres within and around a cluster. Corresponding rates of heat transfer were then calculated by application of the heat transfer-mass transfer analogy.[21]

A 3/8-scale core model with 9/16-in.-diam plastic spheres to simulate the spheres of the full-scale mockup study was described earlier.[22] Mass-transfer tests were delayed because of two ruptures of the plastic core model. Modifications of the test section to provide additional reinforcement of the cemented plastic joints were completed, and hydraulic tests showed that particle Reynolds moduli between 10^3 and 10^4 could be obtained.

Benzoic acid test spheres (9/16-in.-diam) for the cluster experiment were satisfactorily prepared by pressing cp-grade crystals in a spherical die, rather than by machining the test spheres from crude pressings as in the earlier work.[23] Preassembled closely packed clusters with benzoic acid test spheres in the center of the test cluster are shown in Fig. 10.13. Mass-transfer tests will be made with the closely packed clusters manually positioned in the otherwise randomly packed bed of inert plastic spheres.

---

[20]Work performed under subcontract by Department of Chemical and Metallurgical Engineering, University of Tennessee, Knoxville, Tennessee.

[21]C. O. Bennett and J. E. Myers, Momentum, Heat and Mass Transfer, pp. 331–488, McGraw-Hill Company, Inc., New York, 1962.

[22]F. N. Peebles, B. M. Phillips, and J. M. Rhodes, Mass-Transfer Studies, pp. 169–174, "GCRP Semiann. Prog. Rep. Sept. 30, 1962," USAEC Report ORNL-3372, Oak Ridge National Laboratory.

[23]J. M. Rhodes and F. N. Peebles, "Local Rates of Mass Transfer from Spheres in Ordered Arrays," Department of Chemical and Metallurgical Engineering, University of Tennessee, Knoxville, Tennessee, August 1962.

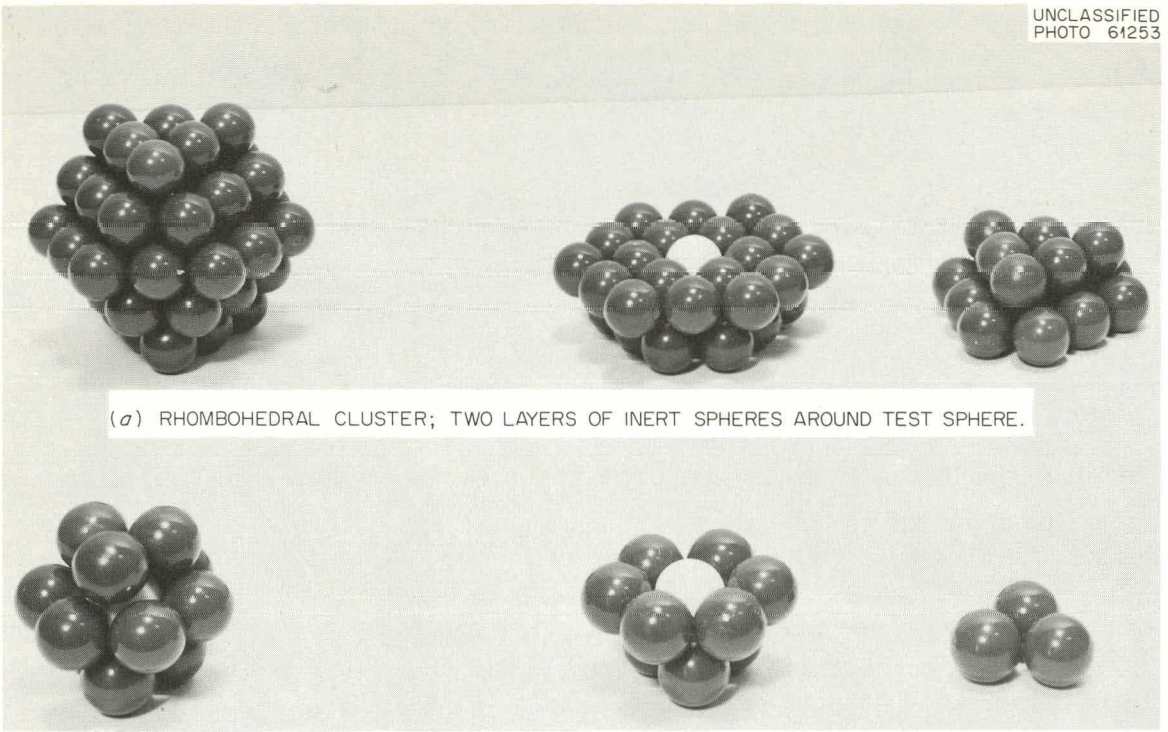

(*a*) RHOMBOHEDRAL CLUSTER; TWO LAYERS OF INERT SPHERES AROUND TEST SPHERE.

(*b*) RHOMBOHEDRAL CLUSTER; ONE LAYER OF INERT SPHERES AROUND TEST SPHERE.

Fig. 10.13. Closely Packed Clusters of Inert Plastic Spheres with Soluble Benzoic Acid Test Sphere in Center of Cluster.

Further experiments on local mass-transfer rates from spheres in ordered arrays were initiated to extend the data of Rhodes and Peebles[23] to higher particle Reynolds moduli (up to 10^5) and lower Schmidt moduli (200 to 1000). This information is needed in the interpretation of data from random-bed experiments and in more precise thermal analyses of packed-bed reactor cores.

Design calculations showed that a 9- by 9-in. test section with five layers of 3-in.-diam spheres could be used in the existing hydraulic facility to attain particle Reynolds moduli up to 104,000. As in the earlier mass-transfer studies, benzoic acid test spheres will be placed in arrays of otherwise inert spheres. Infinite-bed packings will be simulated by use of partial spheres machined to fit the square test section.

The apparatus used by Rhodes and Peebles[23] for measuring local radius changes on mass-transfer test spheres was modified to make use of a linear variable-differential transformer (LVDT, Columbia Model S-125-SZR) to

UNCLASSIFIED
PHOTO 61249

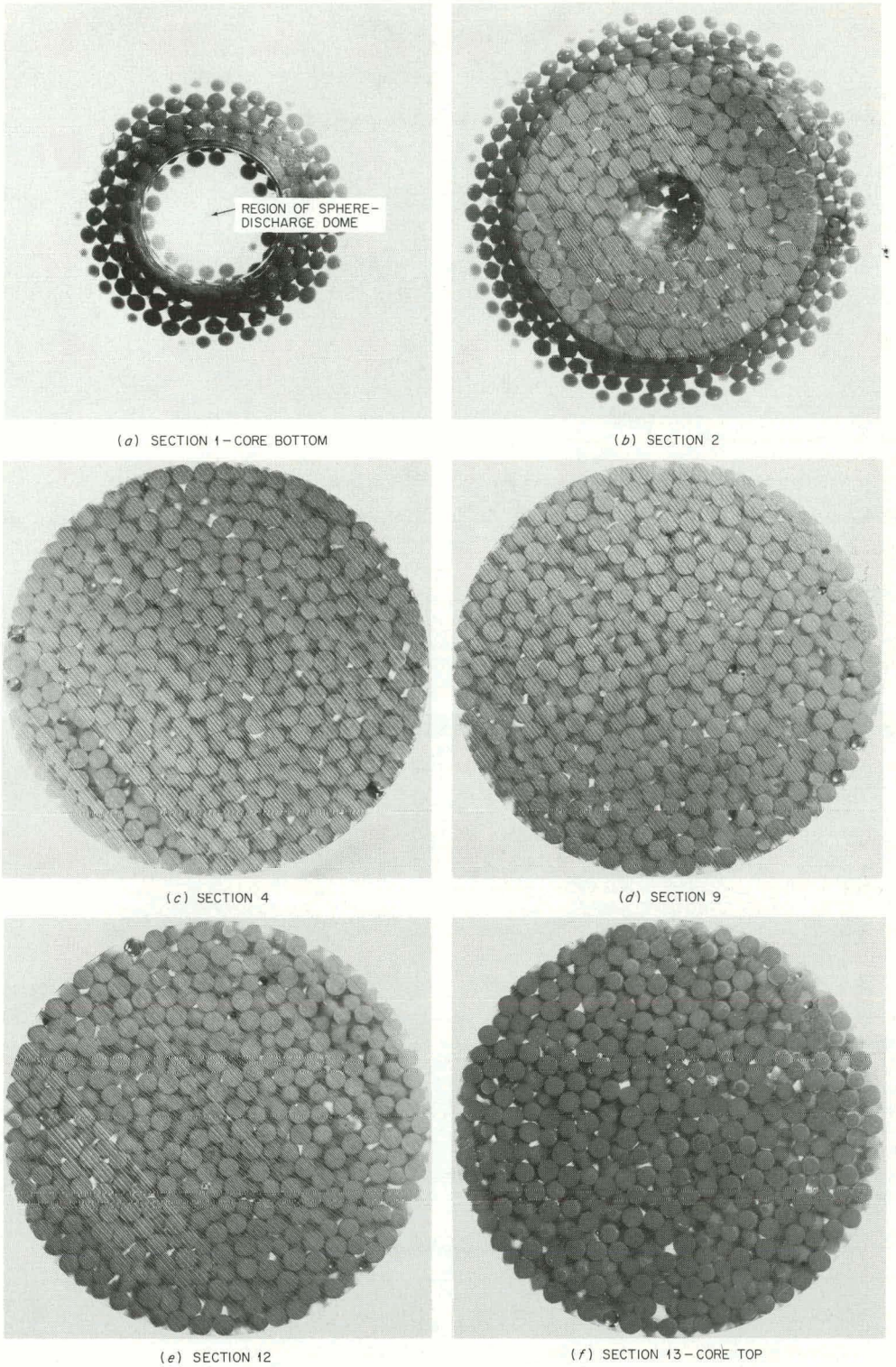

(a) SECTION 1 – CORE BOTTOM

(b) SECTION 2

(c) SECTION 4

(d) SECTION 9

(e) SECTION 12

(f) SECTION 13 – CORE TOP

Fig. 10.14. Disks Cut from Solid Replication of a Random Sphere Bed for Study of Voidage Distribution. Sections are numbered upward from model bottom.

detect dimensional changes. The output voltage from the LVDT is being used to drive a recorder that plots the local radius versus position on the test sphere. Referènce measurements and calibration of this device are in progress.

Void Distribution in Random Sphere Beds (F. N. Peebles, M. C. Thadani)

An experimental study of the spatial distribution of voidage in randomly packed beds of spheres in reduced-scale packed-sphere beds was initiated to furnish data needed to resolve uncertainties in thermal design. Replication of the bed of spheres randomly packed in the test model was obtained by filling the void with a liquid resin, which was then solidified by polymerization. X-ray pictures of disks cut from the solid replications will yield data for determination of the radial, axial, and circumferential variations in voidage.

Typical disks cut from a 1/4-scale model filled with 3/8-in.-diam plastic spheres are shown in Fig. 10.14. The disks are 3/4 in. thick, and the lower faces are pictured. In a qualitative way the disks reveal no excessive axial variation in voidage. Detailed x-ray analysis of these disks from the solid replication of the core model is in progress.

11. FACILITIES AND EQUIPMENT

GCR-ORR Loop No. 2 Construction

J. Zasler

Installation of the GCR-ORR loop No. 2 in-pile section and the first experimental assembly was completed, and loop operation was initiated January 31, 1963. The experiment assembly being irradiated is a low-power unit for determining the neutron flux by the argon-activation technique described by Carroll.[1] It consists of a 1-in.-diam, 1-in.-long cylinder that can be moved axially over the 9 in. to be occupied by fuel specimens in future experiments.

The neutron flux was measured with the in-pile section in four positions: fully inserted, withdrawn 6 in., withdrawn 12 in., and withdrawn 21 in. The results of the measurements are presented in Fig. 11.1.

The outer surface of the cylinder was coated with a thin layer of UO_2 in an attempt to generate recoil fission products. Samples were taken that indicated small amounts of fission products in the loop.

The bypass purification system is operating and appears to be quite effective in removing gaseous impurities. A typical analysis of the loop gas follows:

Constituents	Quantity (ppm)
H_2	6
H_2O	3
N_2 + CO	8
CO_2	1
O_2	<1
Ar	18

The argon in the gas sample was introduced during final assembly and testing of the loop and can be removed by purging.

The loop is presently operating with a maximum gas temperature of 1200°F. The heater control circuitry is performing well in providing constant temperature gas to the test section.

---

[1] R. M. Carroll, "Argon Activation Measures Irradiation Flux Continually," Nucleonics, February 1962.

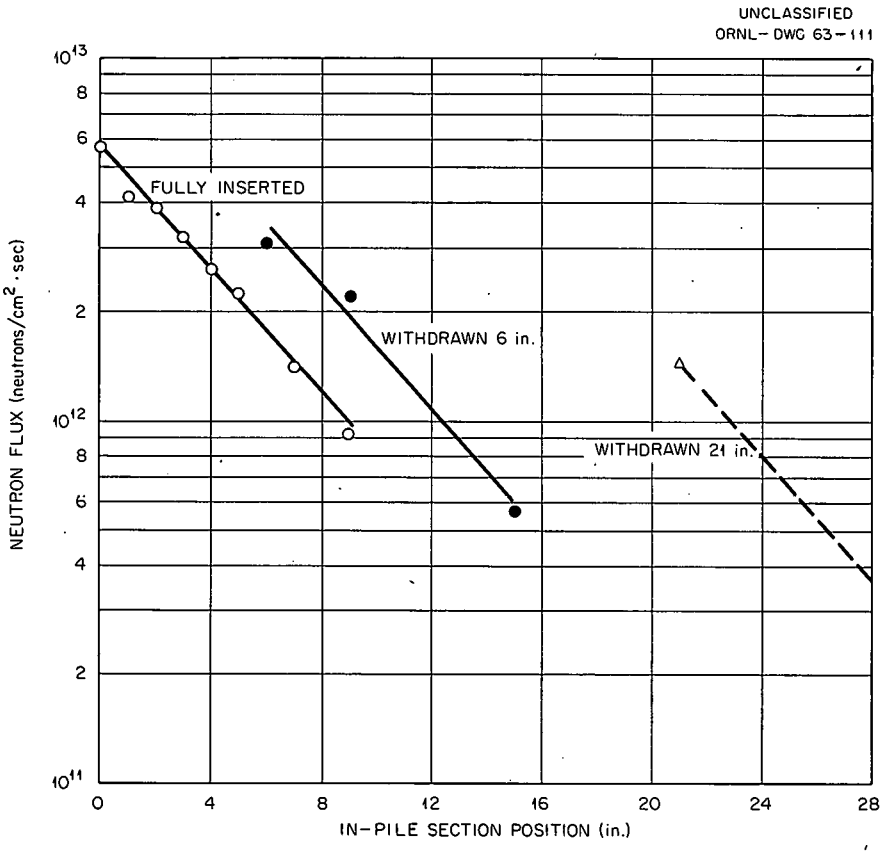

Fig. 11.1. Neutron Flux Measurements in In-Pile Section of GCR-ORR Loop No. 2 During ORR Cycle 45.

Measurements and calculations were made to determine the gamma-energy transferred to the gas that cools the in-pile section. The value appears to be between 2 and 3 kw, which is considerably lower than the 17 kw assumed in the design and hazards calculations. The implications of this for future operation of the loop are being examined.

Compressor Development

W. F. Boudreau

Gas-Bearing Compressors for GCR-ORR Loop No. 2 (D. L. Gray)

A second series of tests was run to obtain additional operating data on gas-bearing compressors. The instrumented Bristol Siddeley gas-bearing compressor was used for these tests. The internal thermocouples were relocated prior to these tests to obtain temperature data in the region

of the front journal bearing. Four attempts were made to operate the compressor at design temperature and pressure (600°F and 295 psia), and in each case indications of rubbing of the journal bearings were found as the temperature approached 500°F.

Upon disassembly of the compressor it was found that no apparent damage had occurred to the journal bearings but that contact had occurred between the cylindrical heat shields and the thermocouple fastened to the front journal bearing diaphragm. It was believed that this had caused the diaphragm to deform and thus cause misalignment of the front journal bearing. The heat shields were notched to eliminate this difficulty.

The compressor was reassembled, and it operated successfully at speeds up to 11,400 rpm at 600°F and 295 psia. Attempts to operate at higher speeds resulted in touching of the journal bearings. When the compressor was disassembled, it was found that the leading edge of the rear end of the top pad on the front journal bearing showed evidence of rubbing. The shaft was scored at this location to the extent that a decision was made to replace it and to install new journal bearings. Further investigation gave rise to the belief that the difficulties could have resulted from unbalance in the rotating assembly caused by shifting of the impeller on the shaft during assembly.

The rotary assembly was removed and balanced, and means for ensuring correct repetitive positioning of the impeller were studied. A set of journal and thrust bearings surfaced with Glacier "DU" are to be installed in this compressor. Glacier "DU" is a proprietary material that consists of a 0.010-in.-thick layer of sintered bronze attached to a steel backing. The bronze is impregnated with Teflon. It has been found in European tests that this material gives good results for starting and stopping in very dry helium, whereas all known metallic materials are subject to galling under these conditions. A process for impregnating the surface of the shaft with MoS_2 has also been developed in Europe, but it has not been effective in all cases in preventing damage with dry helium. Since it will be necessary to make new bearings, studies are being made of the optimum configuration to overcome all the known problems in this type of compressor.

Continental Bearing Research Corporation Experimental Gas-Bearing Compressor (D. L. Gray)

Evaluation tests of the experimental gas-bearing compressor supplied by the Continental Bearing Research Corporation were continued. The compressor was installed in the test loop and operated for approximately 2 hr at a suction pressure of 92 psig and a temperature of 89°F. It was stopped to replace the overload heater in the electrical circuit breaker and then operated for a second period of 2 hr at 160 psig and 99°F at speeds from 9,000 to 15,000 rpm. At the end of this time the compressor stopped and could not be restarted. A considerable amount of debris of various types was found when the impeller was removed. Part of the debris consisted of metal chips, and most of the remainder appeared to be fragments from the ceramic motor insulation. It was also found that one of the pivot pads in the lower journal bearing had been installed backward. All three pads were welded to the shaft.

It was concluded that the failure was caused by the debris. The motor insulation was examined, and it was determined that it would be very difficult to prevent further chipping of the insulation in service, since it seemed probable that most of the problem was caused by differential expansion between the metal retainer strips in the stator slots and the ceramic insulation. No further tests will be made with this unit unless a more adequate type of high-temperature insulation can be found.

Regenerative Grease-Lubricated Compressors (I. K. Namba)

The regenerative compressors in GCR-ORR loop No. 1 continued to operate satisfactorily during irradiation test cycles. Since the previous report period, the operating time of the compressors has increased from 3300 (three test cycles) to 4400 hr (four test cycles) without replacement of the bearings. Inspection of the compressors indicates that an additional 1100 hr of operation should be feasible, for a total operating period of 5500 hr.

The set of regenerative compressors in GCR-ORR loop No. 2 was operated intermittently during the loop shakedown period and has continued to operate satisfactorily during the initial test cycle.

A small regenerative compressor that was designed and fabricated at ORNL was installed in the control-rod-drive testing facility. This compressor was operated intermittently during various phases of loop shakedown testing. Tests were also made with several alternate impeller and volute geometries to obtain data on the fluid dynamics of the regenerative impeller. Analysis of the data is in progress.

A second, small, regenerative compressor was assembled for use in testing the EGCR burst slug detection system in GCR-ORR loop No. 2.

Blower and Compressor Evaluation Studies (W. F. Boudreau, D. L. Gray)

A study was made of the possible use of a hermetically sealed, motor-driven compressor for the EGCR emergency cooling loop. Such units could eliminate problems associated with conventional shaft seals exposed intermittently to high pressures. It would also be possible to reduce the physical size of the compressors and thereby reduce their cost. It was decided that it would be possible to design such compressors that would utilize hydrostatic gas-lubricated bearings but that it would not be feasible to demonstrate the operation of these bearings at an early enough date to permit their consideration for EGCR use.

During the course of the investigation it became apparent that hydrostatic gas bearings offer attractive possibilities for use in large blowers and compressors. It was therefore decided to initiate an investigation of the operation of this type of bearing. An available test unit is being modified for this study.

Development of Shaft Seals (Subcontract No. 2118, University of Tennessee, W. K. Stair)

Four additional reports on the development of shaft seals were completed and published by the University of Tennessee. Five of the total of six reports have now been made available to the Office of Technical Services for distribution.[2-6]

---

[2]Frederick Arnold and W. K. Stair, "The Labyrinth Seal — Theory and Design," ME 5-62-1, University of Tennessee, March 1962, USAEC Report TID-15986.

Equipment for Helium Analyses

A. S. Meyer C. M. Boyd

Development work was completed on the Greenbrier process chromatograph, which was adapted for analysis of radioactive helium samples from GCR-ORR loop No. 2. The separation and flow-directing valves that were described previously[7] were used in the final instrument; however, minor modifications, including a change in column packing, improved flow- and pressure-regulating components, and modifications of the bridge circuits to reduce the effect of temperature variations, were required to obtain consistent analyses.

In order to complete an analysis cycle within a 20-min period and obtain a more effective elimination of the fission-product gases krypton and xenon, the columns originally selected (an 18-in.-long, 1/4-in.-OD, silica-gel column and a 36-in.-long, 1/4-in.-OD, type 5A molecular sieve column) were replaced. The new columns consist of a 11-in.-long, 1/4-in.-OD column of Burrell high-activity silica gel and a 12-ft-long, 3/16-in.-OD column packed with 20-30 mesh type 13X molecular sieves. The new columns yielded a chromatogram similar to that obtained with the previous columns. The peaks were somewhat more sharply resolved and the spacing between nitrogen and methane was increased to provide additional flushing time to remove the radioactive krypton. Also, with this column combination, the retention time of carbon dioxide is increased so that it is

---

[3]Wm. K. Stair, "The Visco Seal — A Survey," ME 5-62-2, University of Tennessee, March 1962, USAEC Report TID-15987.

[4]Wm. H. Carden, "The Mechanical Face Seal," ME 5-62-TN-3, University of Tennessee, March 1962, USAEC Report TID-15988.

[5]Wm. K. Stair, "The Bearing Seal — A Design Evaluation," ME 5-62-TN-2, University of Tennessee, April 1962, USAEC Report TID-16358.

[6]Wm. K. Stair, "A Research Program on Dynamic Shaft Seals," ME 5-62-3, University of Tennessee, published as Paper No. 10 in "Rotating Machinery for Gas-Cooled Reactor Application," Proceedings of Meeting at Oak Ridge National Laboratory April 2-4, 1962, USAEC Report TID-7631.

[7]A. S. Meyer, Jr., C. M. Boyd, and J. E. Attrill, Gas Chromatographic Analysis of Helium, pp. 252–256, "GCRP Quar. Prog. Rep. Dec. 31, 1961," USAEC Report ORNL-3254, Oak Ridge National Laboratory.

eluted from the silica-gel column and measured during the interval in which krypton is being flushed from the sieve column.

The resolution obtained with the 13X sieves was equal or superior to that obtained with the type 5A sieves for all components except carbon monoxide. The peak originally obtained for carbon monoxide was highly asymmetric and yielded poor linearity and lower sensitivity, particularly for ppm concentrations. By contaminating the sieves with water and carbon dioxide to empirically selected levels, the position of the carbon monoxide peak is translated conveniently close to the methane peak, and the asymmetry is substantially eliminated. At the necessary level of sieve contamination, bleeding of water from the column is negligible, but bleeding of CO_2 contributes a concentration of 10 to 20 ppm in the effluent carrier. This CO_2 is quantitatively removed from the column effluent by absorbing CO_2 in a short section of 1/4-in. tubing packed with ascarite and magnesium perchlorate.

The total leak rate of all components that may contain radioactive gases was reduced to less than 10^{-6} cm^3/sec. The Phillip-type valves were demonstrated to be a satisfactory, although difficult, solution to the problem of effecting the complex flow-switching operations necessary to the chromatographic analysis while maintaining the rigorous leak specification necessary for radioactive systems. In the Phillips valves, closure of flow paths between adjacent parts is effected by the application of actuating pressure to a region of a Teflon diaphragm that is clamped between two flat plates. Because of minor imperfections in these surfaces, no satisfactory seal could be obtained in the valves as received from the manufacturer. After lapping the surfaces with 900 grit abrasive and ceria, reducing the thickness of the Teflon diaphragm to 2 mils, and using a thick gasket to distribute the force of the clamping nut, the leak rate was reduced to a value below the limit of detection of a helium leak tester. No detectable leaks in the three valves have developed during a six-month period of intermittent operation. In order to maintain satisfactory flow switching, it is necessary to scrupulously exclude particulate water from the gas stream. Switching difficulties with these valves were eliminated only after blowing out all lines with high-pressure helium to

remove dust and scale and sealing the ends of the columns with glass wool backed up by 5-μ fritted metal disks.

In order to eliminate contamination of the carrier gas by atmospheric gases, a pressure regulator equipped with a metal diaphragm was originally specified for this instrument. Since this regulator provided inadequate pressure control for measurements at ppm concentration levels, it was replaced with a special regulator assembled from Moore Product Company components. In this improved regulator, diffusion of atmospheric gases through the elastomer diaphragm is minimized by a continuous purge of the atmospheric side of the diaphragm with a 10 cm^3/min flow of helium. A Moore back-pressure regulator with adjacent buffer volumes was used to reduce the effects of variations in the carrier gas pressure caused by fluctuations in the pressure of the disposal system. No base-line perturbations attributable to such pressure variations were observed.

The instrument has now been in intermittent service in GCR-ORR loop No. 2 for more than three months. It has been used for preliminary evaluations of the helium cleanup system and is now providing analyses for the first low-power test run of the loop. In measurements at the 100-ppm concentration level, the reproducibility is better than 5 ppm for all components except hydrogen and better than 40 ppm for hydrogen.

Thermocouples for High-Temperature Measurements

G. W. Keilholtz R. L. Bennett

Thermocouple Material Tests in Contaminated Helium

Preliminary screening tests were conducted, as reported previously,[8] on wires exposed to helium containing 500 ppm H_2 and 500 ppm CO. In these tests, which were made at 760 and 982°C, the wires were suspended over graphite. Since there was the possibility of one type of wire influencing the attack on another by cross contamination or modification of the gaseous atmosphere, a second group of experiments was started in which

[8]W. T. Rainey, Jr., R. L. Bennett, and H. L. Hemphill, Thermocouples for High-Temperature Measurements, pp. 436–440, "GCRP Semiann. Prog. Rep. Sept. 30, 1962," USAEC Report ORNL-3372, Oak Ridge National Laboratory.

sets of 25 types of wires are located in small holes drilled in 12-in. AGOT graphite blocks. The wires are in direct contact with the graphite and are isolated from other types of wires. Wires of each type are removed at selected intervals. A set was withdrawn after 36 days, and the wires are being compared with as-received wires for changes in thermoelectric output at 420°C against a platinum standard wire.

The results for the wires that have been checked are listed in Table 11.1, and it may be concluded that at the lower temperature only Chromel-A and type 347 stainless steel gave significant error (greater than 0.5% of the output against platinum). At 982°C, however, large thermoelectric changes occurred in all wires checked thus far, except 50% Mo–50% Re wire. The other 16 wires will be checked, and another set of wires will be checked after an exposure of greater than 100 days.

The individual wires listed in the first column of Table 11.1 were coupled with a platinum wire, and the temperature errors at 420°C were obtained. The temperature errors if the wires were coupled with wires

Table 11.1. Effect of Exposure to Helium Containing H_2 and CO on Accuracy of Thermocouple Wires

Wire	Error in Output at 420°C			
	Exposed at 760°C		Exposed at 982°C	
	EMF Drift (mv)	Temperature Error (°C)	EMF Drift (mv)	Temperature Error (°C)
Regular Chromel-P	+0.05[a]	+1.7[b]	−0.25	−8.3
Special Chromel-P	+0.04	+1.3	−0.25	−8.3
Geminol-P	0	0	+0.56	+33.0
50% Mo–50% Re	+0.01	+0.8	−0.04	−0.5
Chromel-A	+0.22	+14.0	+0.64	+41
Type 347 stainless steel	−0.21	−30.5	−0.34	−49
Molybdenum	−0.01	−0.5	−0.21	−10.9
Rhenium	+0.01	+3.0	+0.80	+229
Platinum-10% rhodium	0	0	−0.95	−120

[a]Based on comparison with as-received wire.

[b]These values represent the temperature error of a thermocouple of the individual wire coupled with a standard platinum wire at 420°C.

other than platinum would be different, with the magnitude and sign of the temperature error being dependent of the relative positions of the two wires in the thermal emf series. The emf errors given in the table are characteristic of the individual wires only and represent the output of an as-received wire coupled against an exposed wire.

Tests of Stainless-Steel-Sheathed Chromel-P vs Alumel Thermocouples

Type 304 stainless steel-sheathed Chromel-P versus Alumel thermocouples insulated with MgO have been tested in various atmospheres for extended times. The results of several of these tests are summarized in Table 11.2.

Table 11.2. Drift Data on Type 347 Stainless Steel-Sheathed Chromel-P Versus Alumel Thermocouples in Various Atmospheres

Atmosphere	Test Temperature (°C)	Test Time (days)	EMF Drift (mv)	Temperature Error (°C)
CO at 7 psig	870	194	+0.27	+7
H_2 at 7 psig	870	155	−4.02	−100
H_2 at 150 psig	870	92	−0.01	0
He at 7 psig in a graphite system	700	161	−0.20	−5

Thermal emf errors along the wires were determined by withdrawing them from a 400°C isothermal tube furnace. The error data for the individual wires exposed to CO and H_2 are presented in Fig. 11.2. Metallographic samples were taken of an as-received thermocouple and at 1/4-in. intervals along the regions where error was noted. The as-received thermocouple is shown in Fig. 11.3, and selected photomicrographs of samples taken at the points indicated on Fig. 11.2 are shown in Figs. 11.4 through 11.7. All the photomicrographs are transverse cross sections and are oriented with the Chromel wire at the bottom. The correspondence between the error curves and the microstructural changes was definite, except in one case. In the CO test, no microstructural change was detected that corresponded to the dip in the Chromel emf error curve at the 11-in.

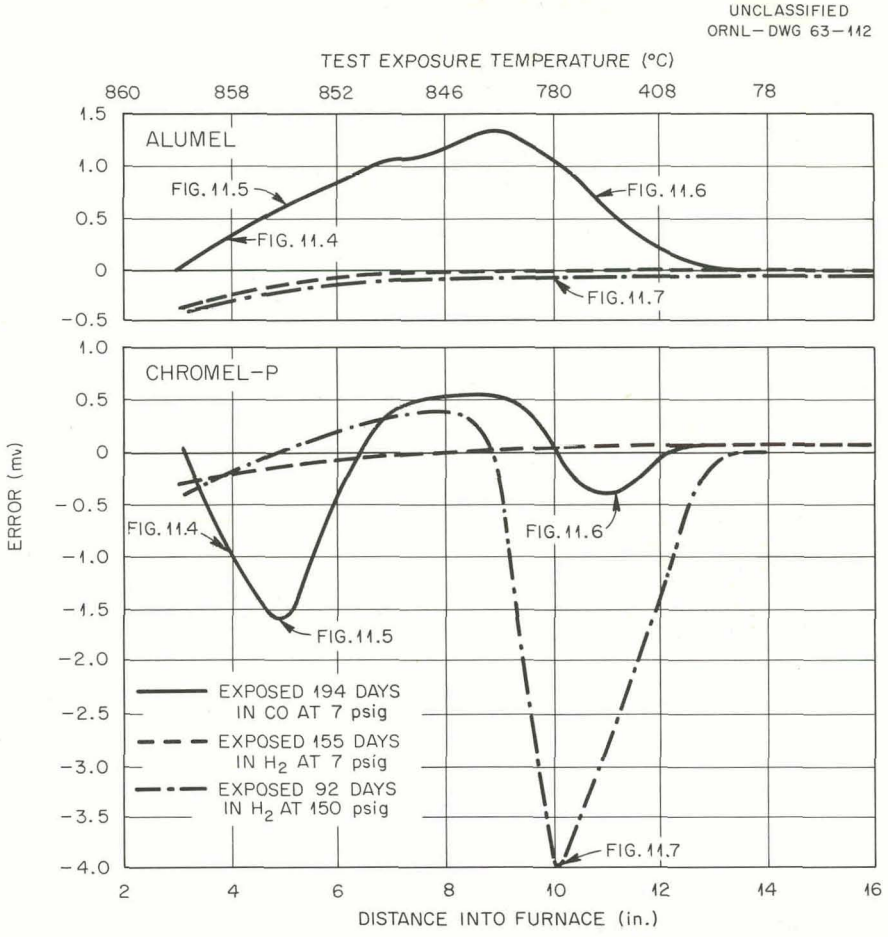

Fig. 11.2. Thermal-Gradient EMF Error Curves for Individual Wires of MgO-Insulated, Type 304 Stainless Steel-Sheathed, Chromel-P Versus Alumel Thermocouples Tested in Various Atmospheres. Figure numbers indicate locations at which metallographic samples were taken.

position (Fig. 11.6). This probably means that the thermoelectric drift was more sensitive in revealing a change than the photomicrographs.

The emf error curve for the thermocouple tested in helium at 7 psig in a graphite system is shown in Fig. 11.8. The helium atmosphere contained H_2 and CO degassed from the graphite. There is good correlation between the two maximum error peaks and microstructural changes indicated in Figs. 11.9 and 11.10. The oxide shown on the sheath contained Fe_3O_4.

Tests of Refractory Metal Thermocouples

The tests of tungsten-rhenium thermocouples were continued. The instability of these thermocouples in low concentrations of oxygen (10 to

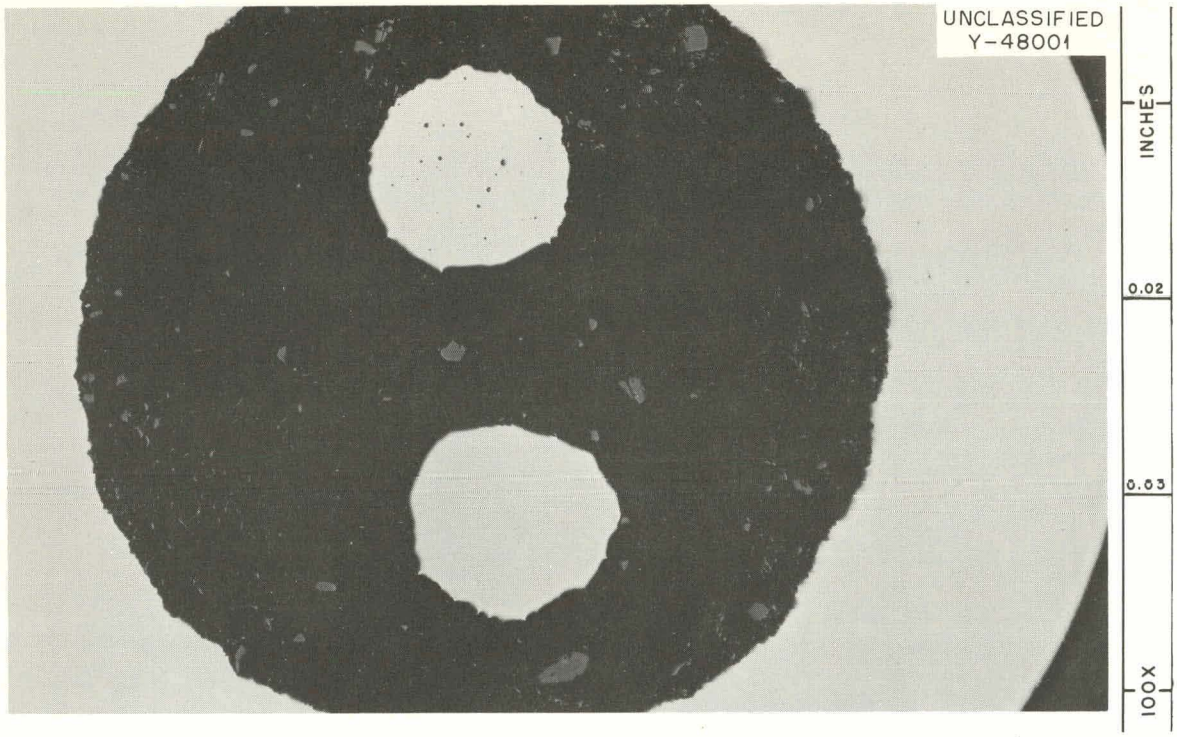

Fig. 11.3. Section of As-Received, MgO-Insulated, Type 304 Stainless Steel-Sheathed, Chromel-P Versus Alumel Thermocouple.

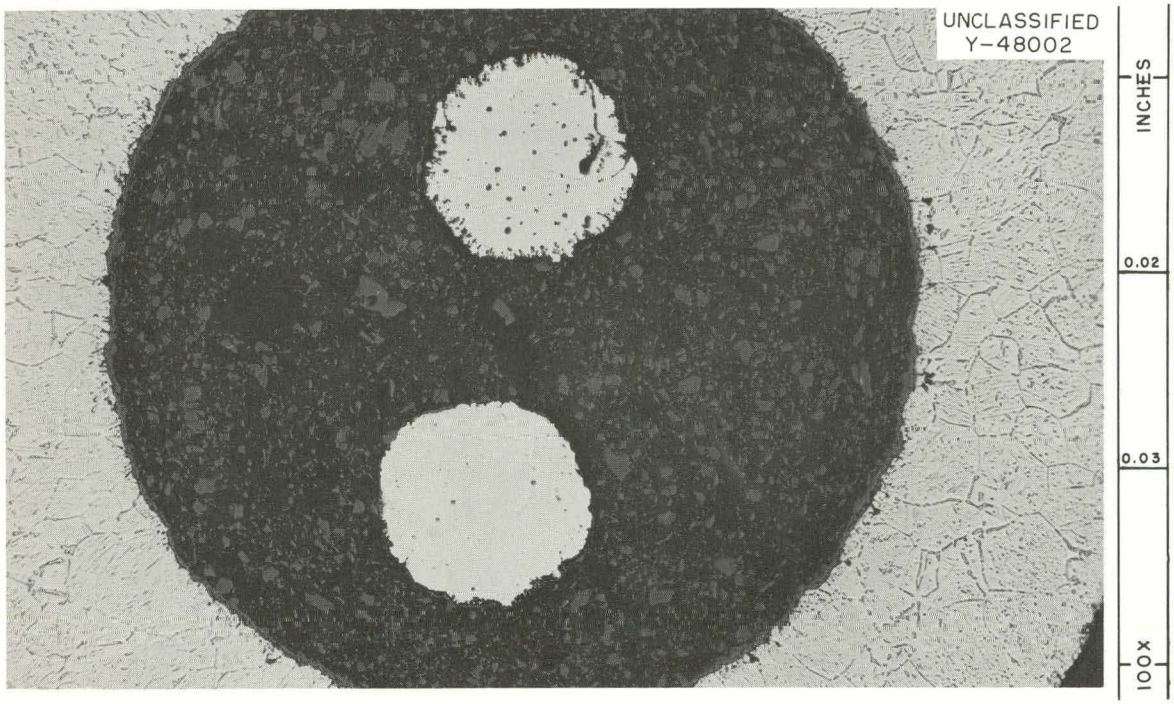

Fig. 11.4. Cross Section of Thermocouple Exposed to CO at 7 psig at a Position 4 in. Inside Furnace. Note beginning of oxidation of Alumel wire at top of section.

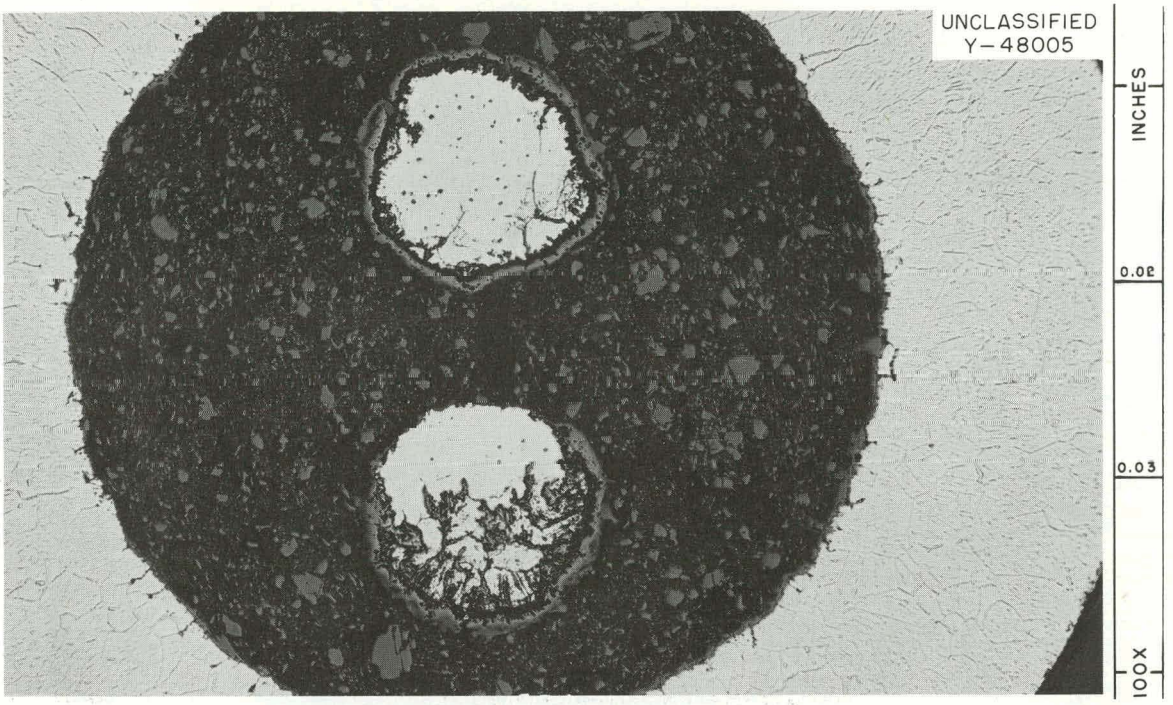

Fig. 11.5. Cross Section of Thermocouple Exposed to CO at 7 psig at a Position 4 3/4 in. Inside Furnace. Note sharp increase in oxidation of Chromel wire (compared with that shown in Fig. 11.4) and more gradual increase in oxidation of Alumel wire.

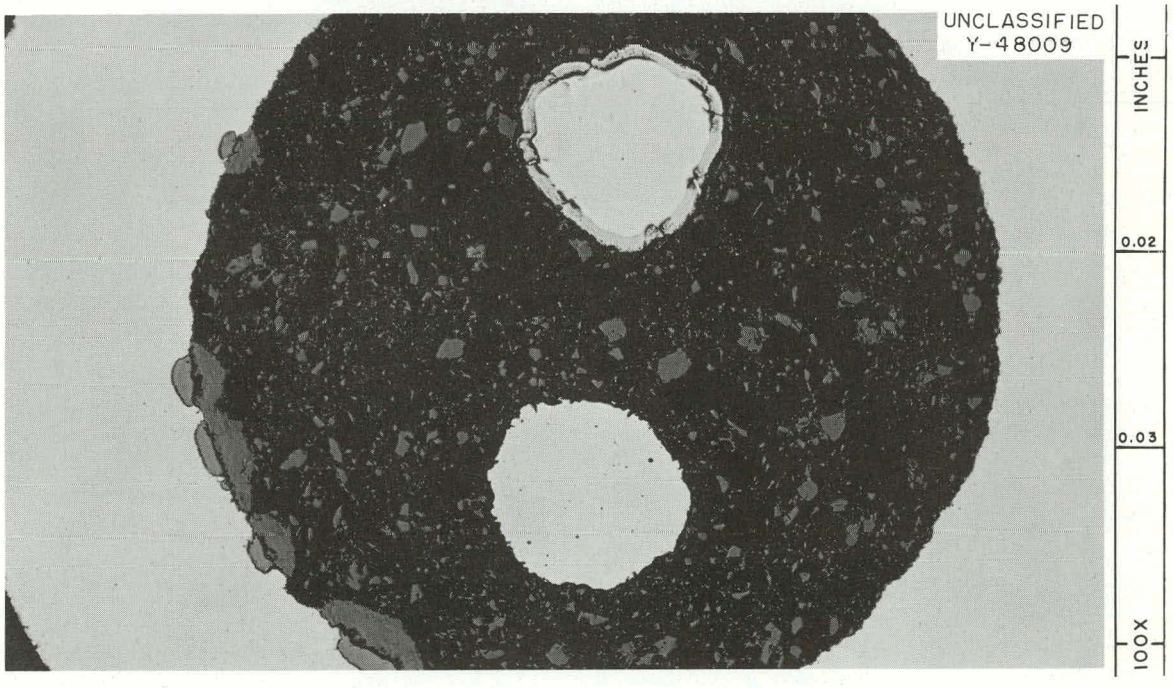

Fig. 11.6. Cross Section of Thermocouple Exposed to CO at 7 psig at a Position 11 in. Inside Furnace. Note decrease in oxidation of Chromel and Alumel wires.

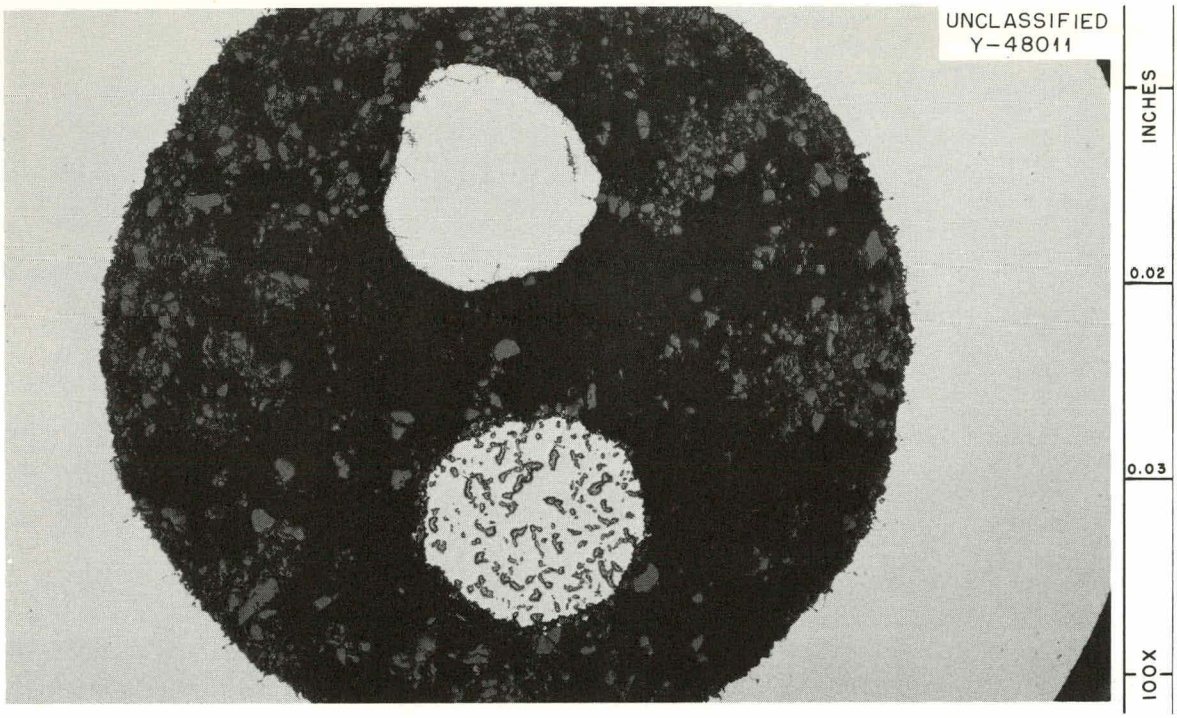

Fig. 11.7. Cross Section of Thermocouple Exposed to H_2 at 7 psig at a Position 10 in. Inside Furnace.

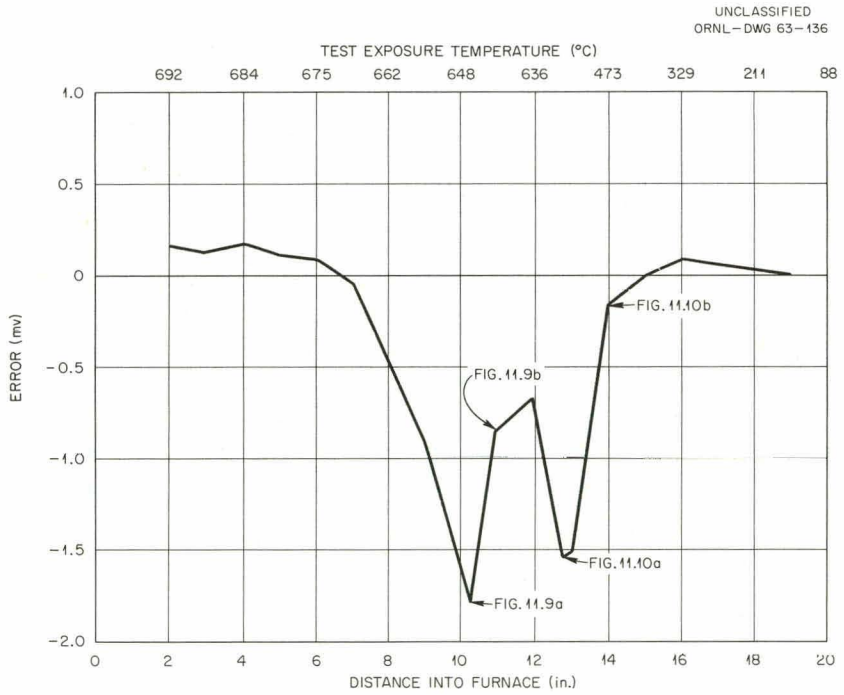

Fig. 11.8. Thermal-Gradient EMF Error Curves for an MgO-Insulated, Type 304 Stainless Steel-Sheathed, Chromel-P Versus Alumel Thermocouple Tested in 7-psig Helium in a Graphite System.

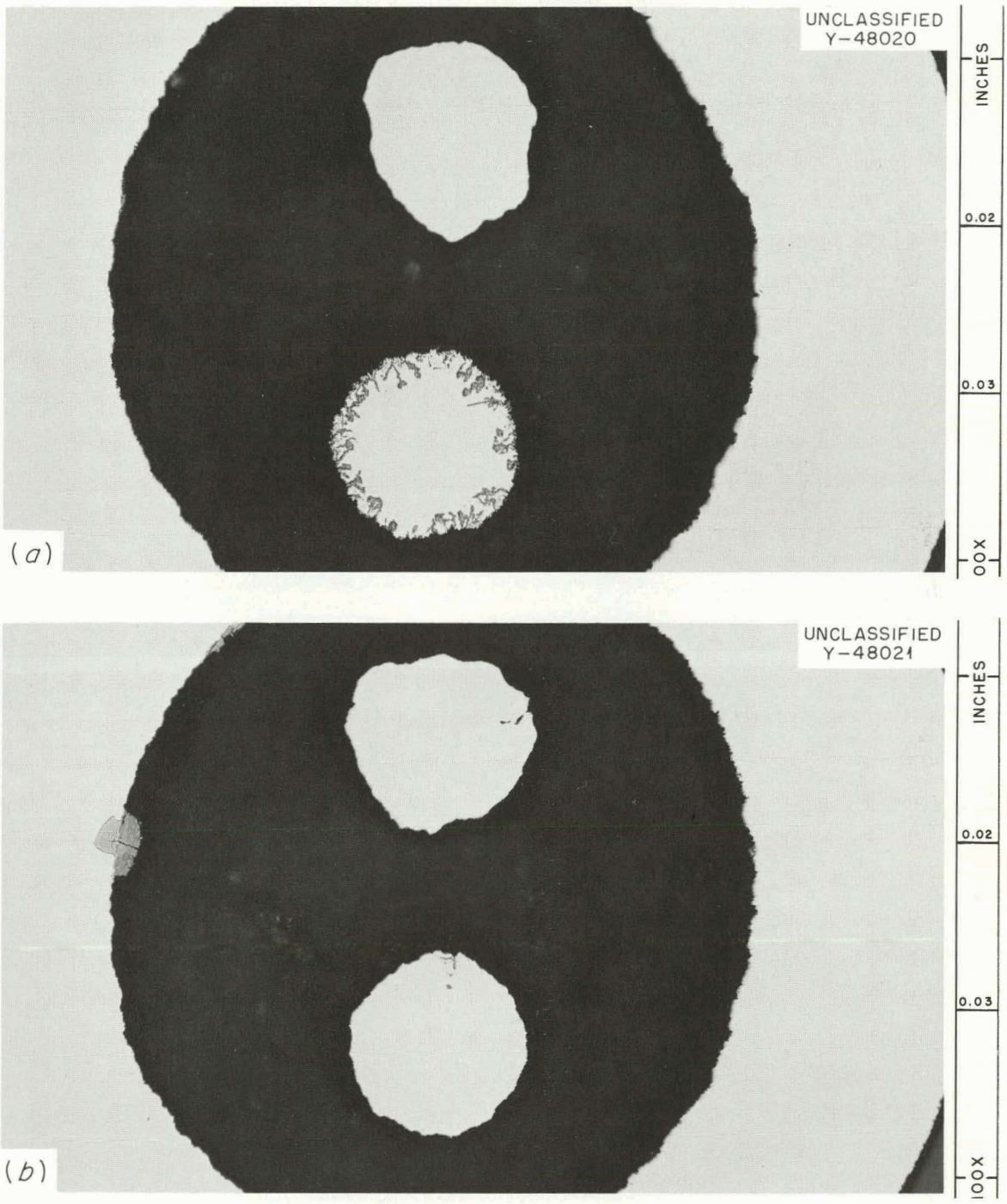

Fig. 11.9. Cross Sections of Thermocouple Exposed to Helium at 7 psig in a Graphite System. (a) Section taken 10 1/4 in. inside furnace. (b) Section taken 11 in. inside furnace.

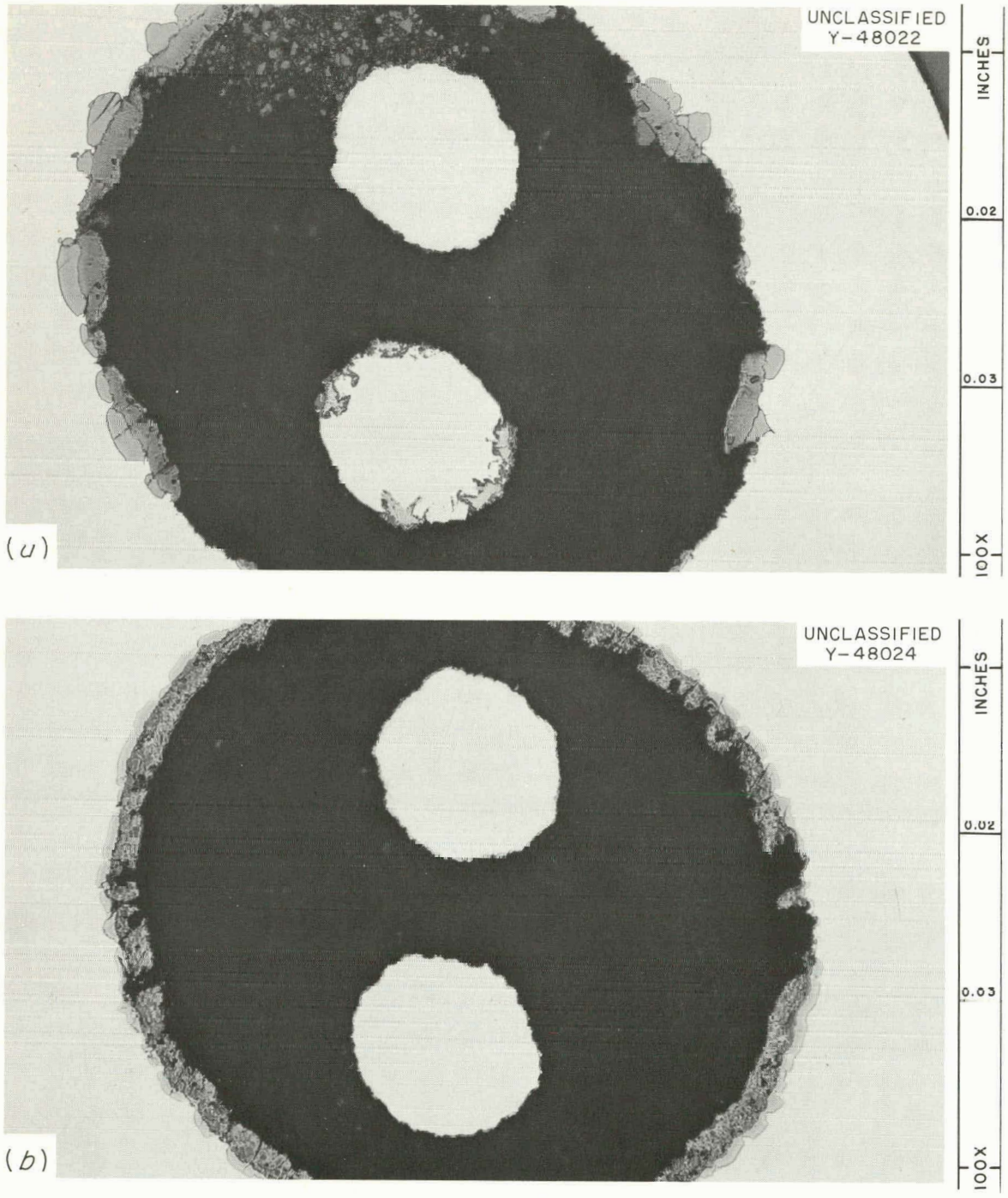

Fig. 11.10. Cross Sections of Thermocouple Exposed to Helium at 7 psig in a Graphite System. (a) Section taken 12 3/4 in. inside furnace. (b) Section taken 14 in. inside furnace.

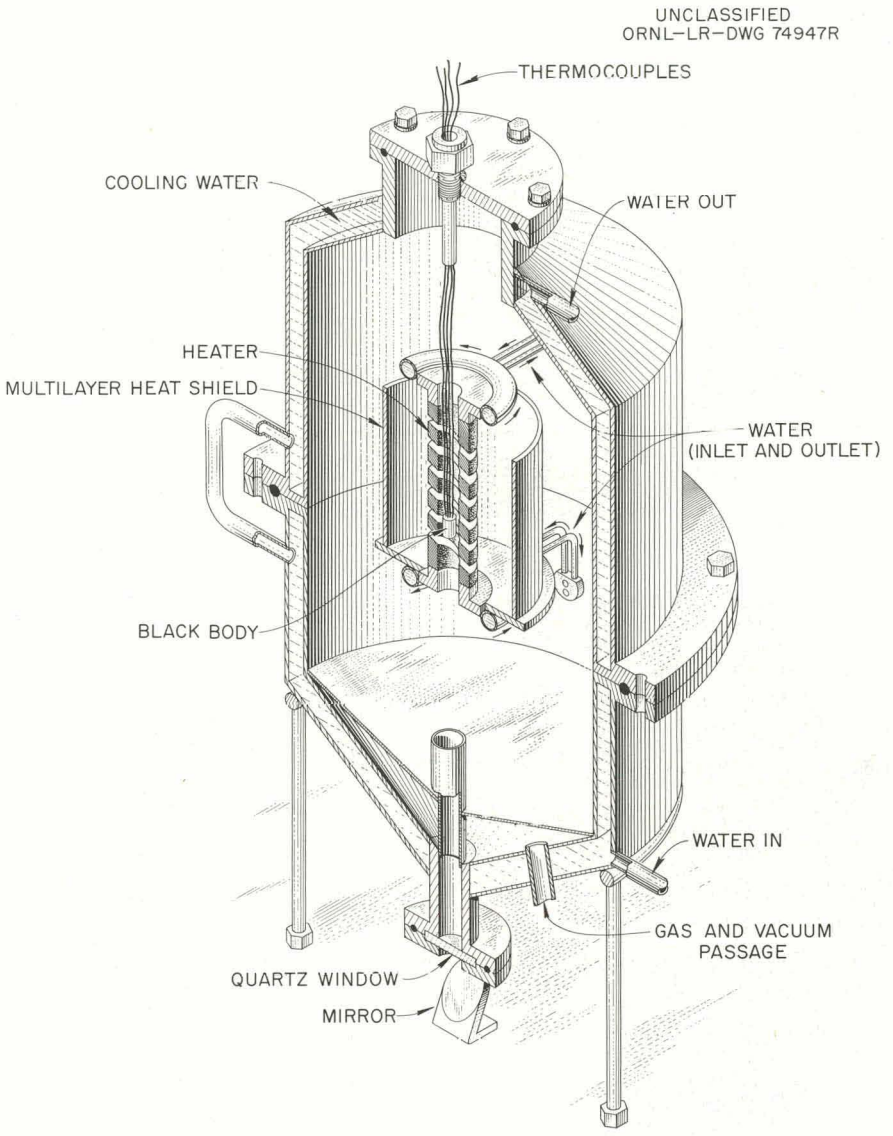

Fig. 11.11. Apparatus for Tests of Thermocouples at High Temperatures.

100 ppm) and CO (100 ppm) in helium was described previously.[8] Pure tungsten wires 0.010 and 0.020 in. in diameter were compared thermoelectrically against pure rhenium during long exposures in helium containing 100 ppm CO at about 1000°C. For 240 hr, only minor emf variations were noted, but rapid emf drift, equivalent to about 150°C in 100 hr, was observed upon raising the temperature to 1200°C.

Thermocouples of all combinations of tungsten, tungsten–5% rhenium, tungsten–26% rhenium, and pure rhenium were found to drift at 1750°C in helium containing 25 ppm CO at approximately the same rate as in helium containing 100 ppm CO. In general the drift rates were rather rapid for the first 100 hr of exposure and then leveled off for the duration of the 260-hr test.

The spiral graphite furnace previously used for the refractory metal tests in helium-CO atmospheres was modified to flatten the thermal gradient in the high-temperature region. The length of the heater section was increased from 2.5 to 5 in., and checks have shown a heating section length of 1.25 in. to be within ±6°C of 1000°C with 2400-w input. The impedance of the graphite heater is well matched to the power supply, so most of the 10-w power should be available. For a 0.5 × 0.25-in. tungsten black body with a 0.063-in.-diam cavity, the optical pyrometer agreed with the thermocouple output within ±5°C at 1200°C. The modified furnace is shown in Fig. 11.11.

Previous reports in this series are:

ORNL-2500	Part 1–4, issued April 1, 1958
ORNL-2505	Issued June 19, 1958
ORNL-2510	Issued September 18, 1958
ORNL-2676	Period Ending December 31, 1958
ORNL-2767	Period Ending June 30, 1959
ORNL-2835	Period Ending September 30, 1959
ORNL-2888	Period Ending December 31, 1959
ORNL-2929	Period Ending March 31, 1960
ORNL-2964	Period Ending June 30, 1960
ORNL-3015	Period Ending September 30, 1960
ORNL-3049	Period Ending December 31, 1960
ORNL-3102	Period Ending March 31, 1961
ORNL-3166	Period Ending June 30, 1961
ORNL-3210	Period Ending September 30, 1961
ORNL-3254	Period Ending December 31, 1961
ORNL-3302	Period Ending March 31, 1962
ORNL-3372	Period Ending September 30, 1962

THIS PAGE

WAS INTENTIONALLY

LEFT BLANK

ORNL-3445

Reactor Technology
TID-4500 (20th ed., Rev.)

Internal Distribution

1. G. M. Adamson
2. S. E. Beall
3. M. Bender
4. R. G. Berggren
5. D. S. Billington
6. E. P. Blizard
7. E. G. Bohlmann
8. C. J. Borkowski
9. G. E. Boyd
10. R. B. Briggs
11. F. L. Carlsen
12. W. B. Cottrell
13. J. A. Cox
14. F. L. Culler
15. J. H. DeVan
16. D. A. Douglas
17. R. B. Evans
18. D. E. Ferguson
19. L. M. Ferris
20. J. L. Fowler
21. A. P. Fraas
22. J. H. Frye, Jr.
23. W. R. Gall
24-25. A. E. Goldman
26. R. J. Gray
27. B. L. Greenstreet
28. W. R. Grimes
29. W. O. Harms
30. M. R. Hill
31. E. C. Hise
32. H. W. Hoffman
33. A. Hollaender
34. A. S. Householder
35. W. H. Jordan
36. C. P. Keim
37. M. T. Kelley
38. E. M. King
39. J. A. Lane
40. C. E. Larson (K-25)
41. R. S. Livingston
42. H. G. MacPherson
43-62. W. D. Manly
63. R. W. McClung
64. F. R. McQuilkin
65. A. B. Meservey
66. H. J. Metz
67. J. G. Morgan
68. K. Z. Morgan
69. F. H. Neill
70. M. L. Nelson
71. L. G. Overholser
72. M. N. Ozisik
73. P. Patriarca
74. A. M. Perry
75. D. Phillips
76. C. A. Preskitt
77. M. E. Ramsey
78. M. W. Rosenthal
79. G. Samuels
80. H. W. Savage
81-82. A. W. Savolainen
83. J. L. Scott
84. O. Sisman
85. E. D. Shipley
86. M. J. Skinner
87. G. M. Slaughter
88. A. H. Snell
89. I. Spiewak
90. J. C. Suddath
91. J. A. Swartout
92. E. H. Taylor
93. D. B. Trauger
94. C. S. Walker
95. J. L. Wantland
96. G. M. Watson
97. M. S. Wechsler
98. A. M. Weinberg
99. J. R. Weir
100. J. C. White
101. Gale Young
102. J. Zasler
103-105. ORNL-Y-12 Technical Library Document Reference Section
106-108. Central Research Library
109-166. Laboratory Records Department
167. Laboratory Records Department, ORNL, R.C.

External Distribution

168-170. S. Matovich, Allis-Chalmers Mfg. Co.
171-173. P. D. Bush, Kaiser Engineers
174. R. A. Charpie, UCC Research Administration, New York, N.Y.
175. W. R. Cooper, Tennessee Valley Authority
176-177. David F. Cope, Reactor Division, AEC, ORO
178-179. R. W. Coyle, Vallecitos Atomic Laboratory
180. E. Creutz, General Atomic
181-183. R. B. Duffield, General Atomic
184. H. L. Falkenberry, Tennessee Valley Authority
185. D. H. Fax, Westinghouse Atomic Power Division
186. M. Janes, National Carbon Research Laboratories, Cleveland, Ohio
187. T. Jarvis, Ford Instrument Co.
188. James R. Johnson, Minnesota Mining and Manufacturing Company, Saint Paul, Minn.
189. Richard Kirkpatrick, AEC, Washington
190. C. W. Kuhlman, United Nuclear Corp.
191-192. H. Lichtenburger, General Nuclear Engineering Corp.
193. J. P. McGee, Bureau of Mines, Appalachian Experiment Station
194. R. W. McNamee, Manager, UCC Research Administration, New York, N.Y.
195. S. G. Nordlinger, AEC, Washington
196. R. E. Pahler, High-Temperature Reactor Branch, Reactor Division, AEC, Washington
197. H. B. Rahner, Savannah River Operations Office
198. Corwin Rickard, General Atomic
199. M. T. Simnad, General Atomic
200. Nathanial Stetson, Savannah River Operations Office
201. Donald Stewart, AEC, Washington
202. Philip L. Walker, Pennsylvania State University
203. R. E. Watt, Los Alamos Scientific Laboratory
204-205. W. L. Webb, East Central Nuclear Group, Inc.
206. C. E. Winters, UCC, Cleveland, Ohio
207. Lloyd R. Zumwalt, General Atomic
208. Division of Research and Development, AEC, ORO
209-821. Given distribution as shown in TID-4500 (20th ed., Rev.) under Reactor Technology category (75 copies - OTS)